# From Concepts Towards Application: Tailored Hydrogel Systems as Versatile Materials in the Biomedical Field

DISSERTATION

Zur Erlangung des Grades eines Doktors

der Naturwissenschaften

vorgelegt von

Fiona Wiesner (geb. Diehl)

Eingereicht bei der Naturwissenschaftlich-Technischen Fakultät

der Universität Siegen

Siegen 2025

Betreuer und erster Gutachter

Prof. Dr. Ulrich Jonas

Universität Siegen

Zweiter Gutachter

Prof. Dr. Ulrike Ritz

Universitätsmedizin der Johannes-Gutenberg Universität Mainz

Tag der mündlichen Prüfung

2. Juli 2025

*„Our greatest weakness lies in giving up.*
*The most certain way to succeed is always to try just one more time.”*

Thomas Alva Edison (1847–1931)

## Summary

The rapidly evolving field of biomedicine demands innovative solutions to complex medical challenges, necessitating interdisciplinary approaches in materials development. Polymeric materials, particularly hydrogels, have emerged as vital components in addressing biomedical challenges due to their unique physicochemical properties and biocompatibility.

This work investigates the development and application of hydrogel systems across three critical biomedical domains: biosensors, wound therapy, and implant technology. While these applications present distinct challenges, they share the fundamental requirement to precisely engineer the polymer architecture and the respective crosslinking mechanism.

The research focuses on polymers based on 2-oxazoline and on acrylamide derivatives, respectively, which were selected for their synthetic versatility and adaptability to diverse application requirements. Various crosslinking strategies were systematically investigated, including simultaneous deprotection and crosslinking, multiphoton as well as one-photon photocrosslinking. For that, each methodology was evaluated within its specific application context. Specifically, the investigation encompasses comprehensive characterization of the resulting hydrogel systems, with particular emphasis on thermoresponsive behavior and surface properties including antifouling, anti-adhesive, and antibacterial characteristics.

This thesis provides fundamental insights into both the underlying principles of tailored polymer network formation and their specific biomedical applications, contributing to the broader understanding of hydrogel-based materials in biomedicine.

# Zusammenfassung

Das Gebiet der Biomedizin entwickelt sich rasch und erfordert innovative Lösungen für komplexe medizinische Fragestellungen. Aus diesem Grund sind interdisziplinäre Ansätze in der Materialentwicklung erforderlich. In diesem Zusammenhang haben sich polymere Materialien, insbesondere Hydrogele, aufgrund ihrer einzigartigen physikochemischen Eigenschaften und Biokompatibilität zu essenziellen Komponenten bei der Bewältigung biomedizinischer Herausforderungen entwickelt.

Diese Arbeit untersucht die Entwicklung und Anwendung von Hydrogelsystemen in drei wichtigen biomedizinischen Bereichen: Biosensoren, Wundtherapie und Implantattechnologie. Während diese Anwendungen unterschiedliche Problemstellungen repräsentieren, teilen sie grundlegende Anforderungen an präzise entwickelte Polymerarchitekturen und deren spezifische Vernetzungsmechanismen.

Die hier dargestellte Forschung konzentriert sich insbesondere auf Polymere, die aus 2-Oxazolin- und Acrylamidderivaten aufgebaut sind, welche aufgrund ihrer synthetischen Vielseitigkeit und Anpassungsfähigkeit an verschiedene Anwendungsanforderungen ausgewählt wurden. Für die Darstellung der Poylmernetzwerke wurden unterschiedliche Vernetzungsstrategien systematisch untersucht. Dazu gehören simultane Entschützung und Vernetzung, die Multiphotonen- sowie die Einphotonen-Photovernetzung. Dabei wurde jede dieser Methodiken im Kontext ihrer spezifischen Anwendung evaluiert. Dies umfasst eine umfangreiche Charakterisierung der resultierenden Hydrogelsysteme, mit besonderem Fokus auf thermoresponsives Verhalten und Oberflächeneigenschaften, einschließlich Anti-Fouling, Anti-Adhäsions- und antibakterieller Effekte.

Diese Dissertation liefert grundlegende Einblicke sowohl in die zugrundeliegenden Prinzipien der maßgeschneiderten Polymernetzwerke als auch in ihre spezifischen biomedizinischen Anwendungen und trägt damit zum breiteren Verständnis hydrogelbasierter Materialien in der Biomedizin bei.

# Table of Contents

Index of Abbreviations ..... 1

1 Scope of this Thesis ..... 6

2 Overall Introduction: From Monomer to Hydrogel ..... 12

3 Plasmonic Nanomaterials with Responsive Polymer Hydrogels for Sensing and Actuation ..... 18

4 Microstructuring of Thermoresponsive Biofunctional Hydrogels by Multiphoton Photocrosslinking ..... 57

5 Plasmon-Enhanced Multiphoton Polymer Crosslinking for Selective Modification of Plasmonic Hotspots ..... 73

6 Thiol-Substituted Poly(2-oxazoline)s with Photolabile Protecting Groups - Tandem Network Formation by Light ..... 84

7 Thermoresponsive and Photocrosslinkable Poly(2-alkyl-2-oxazoline) Toolbox – Customizable Ultralow-Fouling Hydrogel Coatings for Blood Plasma Environments ..... 96

8 Hydrogel-Based Diffusion Barriers for Drug-Loaded Wound Dressings ..... 113

9 Antiadhesive and Antibacterial Coatings for Short-Term Titanium Implants ..... 124

10 Patent: Nonstick Polymer Coatings for Short-Term Implants ..... 140

11 General Conclusion and Outlook ..... 163

Acknowledgements ..... 165

Appendix ..... 166

# Index of Abbreviations

| | |
|---|---|
| 3D | three-dimensional |
| AaAm | *N*-(2-acetic acid) acrylamide |
| AAHAQ | 2-acrylamido-3-hydroxyanthraquinone |
| ADA | adamantane amine |
| AEAm | *N*-(2-aminoethyl) acrylamide |
| AEAm-Boc | Boc-protected *N*-(2-aminoethyl) acrylamide |
| AFM | atomic force microscopy |
| AHAQ | 2-amino-3-hydroxyanthraquinone |
| AIBN | 2,2'-azobis(isobutyronitrile) |
| AIPC | 2,2'-azobis [2-(2-imidazolin-2-yl) propane] dihydrochloride |
| Am | acrylamide |
| ANCO | conjugated regions of AAHAQ and MAAHAQ |
| AP | anchor polymer |
| APAm | *N*-(3-Aminopropyl) acrylamide |
| APAm-Boc | Boc-protected *N*-(3-aminopropyl)acrylamide |
| AuNP | gold nanoparticle |
| AzOxa | 2-(3-azidopropyl)-4,5-dihydro-1,3-oxazole |
| $\beta$ | mass concentration |
| B35A | Brij35 acrylate |
| BCH | conjugated region of BPQAAm |
| BNCO | conjugated region of BPAm |
| Boc | *tert*-butyloxycarbonyl |
| BPAm | *N*-(4-benzophenyl) acrylamide |
| BPdiS | benzophenyl disulfide |
| BPOxa | 2-[3-(4-benzoylphenoxy)propyl]-4,5-dihydro-1,3-oxazole |
| BPQAAm | [(4-benzoylphenyl)methyl]dimethyl[3-(prop-2-enamido)propyl] azanium bromide |
| CA | contact angle |
| CB | 3-[dimethyl(prop-2-yn-1-yl)ammonio]propanoate |
| CCD | charge-coupled device |

| | |
|---|---|
| CEA | 2-carboxyethyl acrylate |
| CFU | colony forming unit |
| ConA | concanavalin A |
| COOH | 4-pentynoic acid |
| CROP | cationic ring opening polymerization |
| CTA | chain transfer agent |
| CuAAC | copper(I)-catalyzed azide-alkyne cycloaddition |
| *Đ* | dispersity |
| DFU | diabetic foot ulcer |
| DLS | dynamic light scattering |
| DMAA | *N*,*N*-dimethylacrylamide |
| DMAc | *N*,*N*-dimethylacetamide |
| DMF | dimethylformamide |
| DMP | 2-{[(dodecylthio)-carbonothioyl]thio}-2-methylpropanoic acid |
| DMSO | dimethyl sulfoxide |
| EA | elemental analysis |
| EBL | electron beam lithography |
| EDX | energy-dispersive X-ray |
| EMP | 2-{[(Ethylthio)-carbonothioyl]thio}-2-methylpropanoic acid |
| ESEM | environmental scanning electron microscopy |
| EtOAc | ethyl acetate |
| EtOH | ethanol |
| EtOxa | 2-ethyl-2-oxazoline |
| EtOxaOTf | oligo(2-ethyl-2-oxazoline)-2-ethyl-2-oxazolinium trifluoromethanesulfonate |
| Fc | ferrocene |
| FRET | fluorescence resonance energy transfer |
| FRP | free radical polymerization |
| fs | femtosecond |
| GEMA | glycosyloxyethyl methacrylate |
| GPC | gel permeation chromatography = SEC |
| HBP | human blood plasma |
| HEAm | *N*-(2-hydroxyethyl) acrylamide |

| | |
|---|---|
| HEMA | 2-hydroxyethyl methacrylate |
| HMPP | 2-hydroxy-2-methylpropiophenone |
| HPAm | *N*-(2-hydroxypropyl) acrylamide |
| iPrOxa | 2-*iso*-propyl-2-oxazoline |
| LCST | lower critical solution temperature |
| LPA | lysophosphatidic acid |
| $l_s$ | segment length |
| LSP | localized surface plasmon |
| LSPR | localized surface plasmon resonance |
| MAA | methacrylic acid |
| MAAHAQ | 2-methacrylamido-3-hydroxyanthrquinone |
| MeOH | methanol |
| MeOTf | methyl trifluoromethanesulfonate |
| $M_n$ | number average molecular weight |
| mol% | molar percentage |
| $M_p$ | molar mass peak maximum |
| MPB | multivalent protein binding |
| MPC | multiphoton crosslinking |
| NbMEtOxa | 2-{2-[(2-nitrobenzyl) thio]ethyl}-4,5-dihydrooxazole |
| $n_h$ | refractive index (hydrogel) |
| NHS | *N*-hydroxysuccinimide |
| NIPAm | *N*-isopropylacrylamide |
| NIR | near-infrared |
| NMR | nuclear magnetic resonance |
| NP | nanoparticle |
| nPrOxa | *n*-propyl-2-oxazoline |
| OD | optical density |
| OEG | oligo(ethylene glycol) / 2-{2-[2-(prop-2-yn-1-yloxy)ethoxy]ethoxy}ethan-1-ol |
| OEG-SB | 3-{dimethyl{2-[2-(prop-2-yn-1-yloxy)ethoxy]ethyl}ammonio}propane-1-sulfonate |
| OWS | optical waveguide spectroscopy |
| pAA | poly(allylamine) |

| | |
|---|---|
| pAAc | poly(acrylic acid) |
| pAAm | poly(acrylamide) |
| pANI | poly(aniline) |
| PBS | phosphate-buffered saline |
| pDEAEMA | poly(2-(diethylamino)ethyl methacrylate) |
| PEF | plasmon-enhanced fluorescence |
| PEG | poly(ethylene glycol) |
| PE-MPC | plasmon-enhanced multiphoton crosslinking |
| PET | poly(ethylene terephtalate) |
| PETA | pentaerythritol tetraacrylate |
| pNIPAAm | poly(*N*-isopropyl acrylamide) |
| pNIPMAM | poly(*N*-isopropylmethacrylamide) |
| POxa | poly(2-oxazoline) |
| PPG | photoremovable protecting grroup |
| PSP | propagating surface plasmon |
| $Q_V$ | volume swelling ratio |
| $R(\theta)$ | reflectivity value |
| r.t. | room temperature |
| RAFT | reversible addition-fragmentation chain transfer |
| RAFTP | reversible addition-fragmentation chain transfer polymerization |
| RGD | Arg-Gly-Asp |
| RI | refractive index |
| SAM | self-assembled monolayer |
| SB | 3-[dimethyl(prop-2-yn-1-yl)ammonio]propane-1-sulfonate |
| SEC | size-exclusion chromatography = GPC |
| SEF | surface-enhanced fluorescence |
| SEM | scanning electron microscopy |
| SERS | surface-enhanced Raman scattering |
| SPR | surface plasmon resonance |
| $T_c$ | cloud point temperature |
| TEM | transmission electron microscopy |
| TFA | trifluoroacetic acid |

| | |
|---|---|
| TFAA | trifluoroacetic anhydride |
| TFA-NHS | *N*-trifluoroacetoxy succinimide |
| THF | tetrahydrofuran |
| TLC | thin layer chromatography |
| UCST | upper critical solution temperature |
| UV/VIS | ultraviolet/visible |
| UV-LIL | UV laser interference lithography |
| V/V | volume-to-volume ratio |
| VPA | vinylphosphonic acid |
| VPTT | volume phase transition temperature |
| wt% | percentage by weight |
| $\Phi_p$ | polymer volume fraction |
| $\beta$-CD | $\beta$-cyclodextrin |
| $\nu_c$ | crosslink density |

# 1 Scope of this Thesis

Biomedicine represents a modern, rapidly advancing interdisciplinary field that investigates topics of medical relevance. As global life expectancy continues to rise, healthcare systems face increasingly complex challenges that require innovative solutions. The development of smart materials for medical applications demands close collaboration across multiple research disciplines, with polymeric materials — particularly hydrogels — emerging as crucial components in addressing these challenges.[1,2]

Hydrogels, classified as soft matter materials, consist of hydrophilic crosslinked polymer networks capable of absorbing substantial quantities of water, which leads to significant volume expansion through swelling.[3] Their biocompatibility and soft, tissue-like characteristics, make them particularly advantageous for applications in contact with the human body.[4,5] The effective encapsulation of therapeutic molecules and selective permeability of hydrogel network structures offers additional functions as soft membranes or controlled drug release systems.[6–8] Through their highly hydrophilic character, hydrogels are prone to inhibit the fouling of surfaces.[9-13] By that, hydrogels are found in a plethora of biomedical applications, for example in tissue engineering scaffolds,[4,5,14–17] contact lens materials,[18,19] wound dressings,[20–22] and antifouling coatings.[23–25] Additionally, their integration into plasmonic biosensor platforms further demonstrates their utility in diagnostics.[26–29]

While there has been a lot of research in biomedicine focusing on polymeric hydrogels, their exploration has by far not reached its limit. As such, the presented research aims to address a range of biomedical applications of hydrogels by investigating polymers that are based on 2-oxazoline and acrylamide derivatives, chosen for their synthetic accessibility and versatility.[30,31]

For a deeper understanding of the underlying network-forming mechanisms, a range of photo-induced crosslinking strategies is explored, including (i) tandem-deprotection-crosslinking, (ii) multiphoton crosslinking, and (iii) one-photon crosslinking. These photocrosslinking approaches are particularly valuable for achieving high-resolution network structures on demand.[32–35] Each strategy is thoroughly investigated and evaluated within the context of its intended application with a focus on plasmonic sensor matrices.

Advanced hydrogel systems are further developed and examined by investigating (i) thermoresponsive behavior, (ii) antifouling properties, (iii) permeability, (iv) biocompatibility, (v) antiadhesive characteristics, and (vi) antibacterial effects. All these intricate qualities play an important role in unlocking the full potential of hydrogels designed for resolving health care related questions.

Finally, these benefits of polymeric hydrogels are exploited in three primary applications:

1. Thermoresponsive and antifouling hydrogels are investigated for their function as (plasmonic) biosensor materials, especially after microstructuring them *via* multiphoton crosslinking processes.

2. For their application as diffusion barriers in drug-loaded wound dressings, the key characteristics of permeability and biocompatibility are targeted.

3. Antiadhesive and antibacterial hydrogels are employed as thin coatings for titanium implants that require removal after completed bone healing.

## References


1. Chen, G.; Tang, W.; Wang, X.; Zhao, X.; Chen, C.; Zhu, Z. Applications of Hydrogels with Special Physical Properties in Biomedicine. Polymers (Basel) **2019**, 11, 1420, doi:10.3390/polym11091420.

2. Ho, T.-C.; Chang, C.-C.; Chan, H.-P.; Chung, T.-W.; Shu, C.-W.; Chuang, K.-P.; Duh, T.-H.; Yang, M.-H.; Tyan, Y.-C. Hydrogels: Properties and Applications in Biomedicine. Molecules **2022**, 27, 2902, doi:10.3390/molecules27092902.

3. Bashir, S.; Hina, M.; Iqbal, J.; Rajpar, A.H.; Mujtaba, M.A.; Alghamdi, N.A.; Wageh, S.; Ramesh, K.; Ramesh, S. Fundamental Concepts of Hydrogels: Synthesis, Properties, and Their Applications. Polymers (Basel) **2020**, 12, 2702, doi:10.3390/polym12112702.

4. El-Sherbiny, I.M.; Yacoub, M.H. Hydrogel Scaffolds for Tissue Engineering: Progress and Challenges. Glob Cardiol Sci Pract **2013**, 2013, 38, doi:10.5339/gcsp.2013.38.

5. Lee, K.Y.; Mooney, D.J. Hydrogels for Tissue Engineering. Chem Rev **2001**, 101, 1869, doi:10.1021/cr000108x.

6. Huang, G.; Gao, J.; Hu, Z.; St. John, J. V; Ponder, B.C.; Moro, D. Controlled Drug Release from Hydrogel Nanoparticle Networks. Journal of Controlled Release **2004**, 94, 303, doi:10.1016/j.jconrel.2003.10.007.

7. He, H.; Cao, X.; Lee, L.J. Design of a Novel Hydrogel-Based Intelligent System for Controlled Drug Release. Journal of Controlled Release **2004**, 95, 391, doi:10.1016/j.jconrel.2003.12.004.

8. Ashley, G.W.; Henise, J.; Reid, R.; Santi, D. V. Hydrogel Drug Delivery System with Predictable and Tunable Drug Release and Degradation Rates. Proceedings of the National Academy of Sciences **2013**, 110, 2318, doi:10.1073/pnas.1215498110.

9. Zou, W.; Chen, Y.; Zhang, X.; Li, J.; Sun, L.; Gui, Z.; Du, B.; Chen, S. Cytocompatible Chitosan Based Multi-Network Hydrogels with Antimicrobial, Cell Anti-Adhesive and Mechanical Properties. Carbohydr Polym **2018**, 202, 246, doi:10.1016/j.carbpol.2018.08.124.

10. Lee, S.Y.; Lee, Y.; Le Thi, P.; Oh, D.H.; Park, K.D. Sulfobetaine Methacrylate Hydrogel-Coated Anti-Fouling Surfaces for Implantable Biomedical Devices. Biomater Res **2018**, 22, doi:10.1186/s40824-017-0113-7.

11. Liu, S.; Guo, W. Anti-Biofouling and Healable Materials: Preparation, Mechanisms, and Biomedical Applications. Adv Funct Mater **2018**, 28, doi:10.1002/adfm.201800596.

12. Murosaki, T.; Ahmed, N.; Ping Gong, J. Antifouling Properties of Hydrogels. Sci Technol Adv Mater **2011**, 12, 064706, doi:10.1088/1468-6996/12/6/064706.

13. Wiesner (née Diehl), F.; Petri, C.; Hageneder, S.; Kunzler, C.; Klees, S.; Frank, P.; Pertiller, M.; Dostalek, J.; Knoll, W.; Jonas, U. Thermoresponsive and Photocrosslinkable Poly(2-alkyl-2-oxazoline) Toolbox – Customizable Ultralow-Fouling Hydrogel Coatings for Blood Plasma Environments. Macromol Rapid Commun **2024**, 45, doi:10.1002/marc.202300549.

14. Drury, J.L.; Mooney, D.J. Hydrogels for Tissue Engineering: Scaffold Design Variables and Applications. Biomaterials **2003**, 24, 4337, doi: 10.1016/s0142-9612(03)00340-5.

15. Qin, X.H.; Ovsianikov, A.; Stampfl, J.; Liska, R. Additive Manufacturing of Photosensitive Hydrogels for Tissue Engineering Applications. BioNanoMaterials **2014**, 15, 49, doi:10.1515/bnm-2014-0008.

16. You, S.; Li, J.; Zhu, W.; Yu, C.; Mei, D.; Chen, S. Nanoscale 3D Printing of Hydrogels for Cellular Tissue Engineering. J Mater Chem B **2018**, 6, 2187, doi:10.1039/c8tb00301g.

17. Spicer, C.D. Hydrogel Scaffolds for Tissue Engineering: The Importance of Polymer Choice. **2020**, 11, 184, doi:10.1039/c9py01021a.

18. Kita, M.; Ogura, Y.; Honda, Y.; Hyon, S.-H.; Cha, W.-I.; Ikada, Y. Evaluation of Polyvinyl Alcohol Hydrogel as a Soft Contact Lens Material. Graefe's Archive for Clinical and Experimental Ophthalmology **1990**, 228, 533, doi:10.1007/BF00918486.

19. Childs, A.; Li, H.; Lewittes, D.M.; Dong, B.; Liu, W.; Shu, X.; Sun, C.; Zhang, H.F. Fabricating Customized Hydrogel Contact Lens. Sci Rep **2016**, 6, 34905, doi:10.1038/srep34905.

20. Koehler, J.; Brandl, F.P.; Goepferich, A.M. Hydrogel Wound Dressings for Bioactive Treatment of Acute and Chronic Wounds. Eur Polym J **2018**, 100, 1, doi:10.1016/j.eurpolymj.2017.12.046.

21. Li, M.; Liang, Y.; He, J.; Zhang, H.; Guo, B. Two-Pronged Strategy of Biomechanically Active and Biochemically Multifunctional Hydrogel Wound Dressing To Accelerate Wound Closure and Wound Healing. Chemistry of Materials **2020**, 32, 9937, doi:10.1021/acs.chemmater.0c02823.

22. Liang, Y.; He, J.; Guo, B. Functional Hydrogels as Wound Dressing to Enhance Wound Healing. ACS Nano **2021**, 15, 12687, doi:10.1021/acsnano.1c04206.

23. Banerjee, I.; Pangule, R.C.; Kane, R.S. Antifouling Coatings: Recent Developments in the Design of Surfaces That Prevent Fouling by Proteins, Bacteria, and Marine Organisms. Advanced Materials **2011**, 23, 690, doi:10.1002/adma.201001215.

24. He, Z.; Yang, X.; Wang, N.; Mu, L.; Pan, J.; Lan, X.; Li, H.; Deng, F. Anti-Biofouling Polymers with Special Surface Wettability for Biomedical Applications. Front Bioeng Biotechnol **2021**, 9, doi:10.3389/fbioe.2021.807357.

25. Erathodiyil, N.; Chan, H.-M.; Wu, H.; Ying, J.Y. Zwitterionic Polymers and Hydrogels for Antibiofouling Applications in Implantable Devices. Materials Today **2020**, 38, 84, doi:10.1016/j.mattod.2020.03.024.

26. Li, J.; Yu, X.; Herberg, A.; Kuckling, D. Biomolecule Sensor Based on Azlactone-Modified Hydrogel Films. Macromol Rapid Commun **2019**, 40, e1800674, doi:10.1002/marc.201800674.

27. Liu, B.; Liu, X.; Shi, S.; Huang, R.; Su, R.; Qi, W.; He, Z. Design and Mechanisms of Antifouling Materials for Surface Plasmon Resonance Sensors. Acta Biomater **2016**, 40, 100, doi: 10.1016/j.actbio.2016.02.035.

28. Jiang, Y.; Colazo, M.G.; Serpe, M.J. Poly(N-Isopropylacrylamide) Microgel-Based Sensor for Progesterone in Aqueous Samples. Colloid Polym Sci **2016**, 294, 1733–1741, doi:10.1007/s00396-016-3926-3.

29. Fong, C.-C.; Wong, M.-S.; Fong, W.-F.; Yang, M. Effect of Hydrogel Matrix on Binding Kinetics of Protein–Protein Interactions on Sensor Surface. Anal Chim Acta **2002**, 456, 201–208, doi:10.1016/S0003-2670(02)00033-8.

30. Sennakesavan, G.; Mostakhdemin, M.; Dkhar, L.K.; Seyfoddin, A.; Fatihhi, S.J. Acrylic Acid/Acrylamide Based Hydrogels and Its Properties - A Review. Polym Degrad Stab **2020**, 180, 109308, doi:10.1016/j.polymdegradstab.2020.109308.

31. de la Rosa, V.R. Poly(2-Oxazoline)s as Materials for Biomedical Applications. J Mater Sci Mater Med **2014**, 25, 1211–1225, doi:10.1007/s10856-013-5034-y.

32. Hennink, W.E.; van Nostrum, C.F. Novel Crosslinking Methods to Design Hydrogels. Adv Drug Deliv Rev **2012**, 64, 223–236, doi:10.1016/j.addr.2012.09.009.

33. Prucker, O.; Brandstetter, T.; Rühe, J. Surface-Attached Hydrogel Coatings via C,H-Insertion Crosslinking for Biomedical and Bioanalytical Applications (Review). Biointerphases **2018**, 13, 010801, doi:10.1116/1.4999786.

34. Torgersen, J.; Qin, X.H.; Li, Z.; Ovsianikov, A.; Liska, R.; Stampfl, J. Hydrogels for Two-Photon Polymerization: A Toolbox for Mimicking the Extracellular Matrix. Adv Funct Mater **2013**, 23, 4542–4554, doi:10.1002/adfm.201203880.

35. Accardo, A.; Blatché, M.C.; Courson, R.; Loubinoux, I.; Vieu, C.; Malaquin, L. Two-Photon Lithography and Microscopy of 3D Hydrogel Scaffolds for Neuronal Cell Growth. Biomed Phys Eng Express **2018**, 4, doi:10.1088/2057-1976/aaab93.

# 2 Overall Introduction: From Monomer to Hydrogel

The fundamental prerequisite for hydrogel formation is a polymer network based on interconnected hydrophilic polymer chains. Such polymer chains can be derived from both synthetic and natural sources. Synthetic monomers include acrylates,[1] acrylamides, [2] and 2-alkyl-2-oxazolines,[3–5] while natural sources encompass materials like dextrans,[6] alginates,[7,8] polypeptides,[9] or hyaluronic acid.[10,11] Synthetic polymers offer the advantage to adjust their properties by synthesis and the possibility to incorporate specific functional groups into the polymer chains. The preparation of these polymers can be achieved through various polymerization methods, whereas for each specific application the most suitable polymerization method is to be identified individually.

Free radical polymerization (FRP) is a simple and versatile polymerization technique that is relatively insensitive to impurities (with the exception of oxygen).[12] However, the resulting polymers exhibit broad mass dispersities (*Đ*), as multiple reactions take place simultaneously, including initiator decay, chain growth, branching through backbiting, and termination *via* combination or disproportion. These individual reaction steps acting simultaneously during the growth of each polymer chain result in a wide spread for the numbers of repeat unit per chain.

In contrast to FRP, Reversible Addition-Fragmentation Chain Transfer Polymerization (RAFTP) is a controlled radical polymerization method that yields narrower molar mass distributions with dispersities *Đ* as low as 1.1.[13] The polymerization is performed by addition of a so-called chain transfer agent (CTA) to the reaction mixture that intermittently and reversibly acquires the radical character and thus the growing chain switches between a dormant and an active state. Consequently, the presence of a CTA ensures a living-like characteristic of the radical polymerization reaction. However, this method has drawbacks including higher sensitivity to inhibition compared to FRP and the presence of remaining CTA groups at the polymer chain ends. Such residual CTA groups may lead to unwanted cytotoxicity in biological applications.[14] Both FRP and RAFTP are suitable for a broad range of monomers containing a polymerizable double bond.[12,13]

Cationic Ring-Opening Polymerization (CROP) requires specific monomers such as 2-alkyl-2-oxazolines that are susceptible to the attack of an active cationic chain end. Poly(2-alkyl-2-

oxazoline)s are particularly interesting polymers for biomedical applications due to their high biocompatibility resulting from their peptide-like chemical structure.[5,15,16] The CROP method is very sensitive to water and must be performed under anhydrous conditions. When this requirement is met, this quasi-living polymerization method allows for narrow molar mass distributions near $Đ$ ~ 1.1, similar to RAFTP.[17,18]

The network formation required for the crosslinked polymer architecture in hydrogels can be attained through two primary mechanisms: Physical networks arise from non-covalent interactions such as chain entanglements and ionic interactions.[12] In contrast, chemical networks are formed through covalent bonds. The covalent crosslinking can be established through two main approaches: *in-situ* crosslinking and *post-polymerization* crosslinking.[19,20]

*In-situ* crosslinking occurs during the polymerization process by incorporation of multifunctional monomers, e.g., bis-acrylamide, resulting in direct network formation. The final shape of the hydrogel is determined during this polymerization stage, though in some cases, small hydrogel particles can be produced for subsequent shape manipulation.

*Post-polymerization* crosslinking employs crosslinkers containing at least one functional group that can be activated by external stimuli, such as temperature or light.[21,22] This approach is particularly advantageous for creating thin hydrogel layers suitable for coating applications.[19,23,24] Commonly used crosslinkers exhibit groups that operate through specific pairing mechanisms (such as Diels-Alder reactions or click chemistry) or unspecific reactions like C-H insertion.[22,25] *Post-polymerization* crosslinking can be further divided into two approaches employing external and internal crosslinkers. External crosslinker molecules require at least two interconnecting units. These must be compatible with the polymer matrix and are usually added to the tailored pre-formed polymer by mixing.[26] In contrast, internal crosslinkers in the form of comonomers contain both chain-extending and crosslinking units. They are copolymerized with the main monomers and bound to the polymer backbone by the chain-extending moiety. For both internal and external post-polymerization crosslinkers, the material can then be processed into the desired form through dissolution, spreading, and drying. The final network structure is formed by activating the crosslinking reaction upon exposure to the appropriate stimulus.

Additional parameters to consider include several architectural aspects (e.g., sandwich structure, composite materials, surface attachment). Further details on such tailored hydrogel preparation can be found in the review article *Plasmonic nanomaterials with responsive polymer hydrogels for sensing and actuation*[27] (see page 18), specifically in the chapters "1. Introduction" and "2. Responsive hydrogels".

## References


1. Serrano-Aroca, Á.; Deb, S. Acrylic-Based Hydrogels as Advanced Biomaterials. In Acrylate Polymers for Advanced Applications; IntechOpen, **2020**, doi: 10.5772/intechopen.92097.

2. Sennakesavan, G.; Mostakhdemin, M.; Dkhar, L.K.; Seyfoddin, A.; Fatihhi, S.J. Acrylic Acid/Acrylamide Based Hydrogels and Its Properties - A Review. Polym Degrad Stab **2020**, 180, 109308, doi:10.1016/j.polymdegradstab.2020.109308.

3. Hoogenboom, R. Poly(2-Oxazoline)s: A Polymer Class with Numerous Potential Applications. Angewandte Chemie - International Edition **2009**, 48, 7978, doi:10.1002/anie.200901607.

4. Dargaville, T.R.; Forster, R.; Farrugia, B.L.; Kempe, K.; Voorhaar, L.; Schubert, U.S.; Hoogenboom, R. Poly(2-Oxazoline) Hydrogel Monoliths via Thiol-Ene Coupling. Macromol Rapid Commun **2012**, 33, 1695, doi:10.1002/marc.201200249.

5. de la Rosa, V.R. Poly(2-Oxazoline)s as Materials for Biomedical Applications. J Mater Sci Mater Med **2014**, 25, 1211, doi:10.1007/s10856-013-5034-y.

6. Kim, S.H.; Won, C.Y.; Chu, C.C. Synthesis and Characterization of Dextran-Based Hydrogel Prepared by Photocrosslinking. Carbohydr Polym **1999**, 40, 183, doi:10.1016/S0144-8617(99)00053-3.

7. Paredes Juárez, G.A.; Spasojevic, M.; Faas, M.M.; de Vos, P. Immunological and Technical Considerations in Application of Alginate-Based Microencapsulation Systems. Front Bioeng Biotechnol **2014**, 2, 1, doi:10.3389/fbioe.2014.00026.

8. Wen, H.; Xiao, W.; Biswas, S.; Cong, Z.Q.; Liu, X.M.; Lam, K.S.; Liao, Y.H.; Deng, W. Alginate Hydrogel Modified with a Ligand Interacting with $\alpha 3\beta 1$ Integrin Receptor Promotes the Differentiation of 3D Neural Spheroids toward Oligodendrocytes in Vitro. ACS Appl Mater Interfaces **2019**, 6, 5821, doi:10.1021/acsami.8b19438.

9. Hou, X.; Dai, X.; Yang, J.; Zhang, B.; Zhao, D.; Li, C.; Yin, Z.; Zhao, Y.; Liu, B. Injectable Polypeptide-Engineered Hydrogel Depot for Amplifying the Anti-Tumor Immune Effect Induced by Chemo-Photothermal Therapy. J Mater Chem B **2020**, 8, 8623, doi:10.1039/d0tb01370f.

10. Leach, J.B.; Schmidt, C.E. Characterization of Protein Release from Photocrosslinkable Hyaluronic Acid-Polyethylene Glycol Hydrogel Tissue Engineering Scaffolds. Biomaterials **2005**, 26, 125, doi:10.1016/j.biomaterials.2004.02.018.

11. Liu, X.; Huang, R.; Su, R.; Qi, W.; Wang, L.; He, Z. Grafting Hyaluronic Acid onto Gold Surface to Achieve Low Protein Fouling in Surface Plasmon Resonance Biosensors. ACS Appl Mater Interfaces **2014**, 6, 13034, doi:10.1021/am502921z.

12. Young, R.J.; Lovell, P.A. Introduction to Polymers; 3rd ed.; CRC Press, **2011**; ISBN 978-0-8493-3929-5.

13. Perrier, S. 50th Anniversary Perspective : RAFT Polymerization—A User Guide. Macromolecules **2017**, 50, 7433, doi:10.1021/acs.macromol.7b00767.

14. Pissuwan, D.; Boyer, C.; Gunasekaran, K.; Davis, T.P.; Bulmus, V. In Vitro Cytotoxicity of RAFT Polymers. Biomacromolecules **2010**, 11, 412, doi:10.1021/bm901129x.

15. Hoogenboom, R. Poly(2-oxazoline)s: A Polymer Class with Numerous Potential Applications. Angewandte Chemie International Edition **2009**, 48, 7978, doi:10.1002/anie.200901607.

16. Hoogenboom, R.; Schlaad, H. Bioinspired Poly(2-Oxazoline)s. Polymers (Basel) **2011**, 3, 467, doi: 10.3390/polym3010467.

17. Chen, T.; Zhao, C.; Lai, T.; Zhao, J. Cationic Ring-Opening Polymerization of 2-Oxazolines in γ-Butyrolactones Using Various Initiators. Polym Chem **2025**, 16, 903, doi:10.1039/D4PY01422G.

18. Piotti, M.E.; Padmanabhan, R. Living Cationic Polymerization. In Reference Module in Materials Science and Materials Engineering; Elsevier, **2016**, doi: 10.1016/B978-0-12-803581-8.03749-8.

19. Mateescu, A.; Wang, Y.; Dostalek, J.; Jonas, U. Thin Hydrogel Films for Optical Biosensor Applications. Membranes (Basel) **2012**, 2, 40, doi: 10.3390/membranes2010040.

20. Hennink, W.E.; van Nostrum, C.F. Novel Crosslinking Methods to Design Hydrogels. Adv Drug Deliv Rev **2012**, 64, 223, doi:10.1016/j.addr.2012.09.009.

21. Haslinger, C.; Zahoranová, A.; Baudis, S. Synthesis of Coumarin-Containing Poly(2-Oxazoline)s and Light-Induced Crosslinking for Hydrogel Formation. Monatsh Chem **2023**, 154, 459, doi:10.1007/s00706-022-03013-8.

22. Prucker, O.; Brandstetter, T.; Rühe, J. Surface-Attached Hydrogel Coatings via C,H-Insertion Crosslinking for Biomedical and Bioanalytical Applications (Review). Biointerphases **2018**, 13, 010801, doi:10.1116/1.4999786.

23. Toomey, R.; Freidank, D.; Rühe, J. Swelling Behavior of Thin, Surface-Attached Polymer Networks. Macromolecules **2004**, 37, 882, doi:10.1021/ma034737v.

24. Beines, P.W.; Klosterkamp, I.; Menges, B.; Jonas, U.; Knoll, W. Responsive Thin Hydrogel Layers from Photo-Cross-Linkable Poly(N-Isopropylacrylamide) Terpolymers. Langmuir **2007**, 23, 2231, doi:10.1021/la063264t.

25. Kotrade, P.F.; Rühe, J. Malonic Acid Diazoesters for C−H Insertion Crosslinking (CHic) Reactions: A Versatile Method for the Generation of Tailor-Made Surfaces. Angewandte Chemie **2017**, 129, 14597, doi:10.1002/ange.201704486.

26. Mateescu, A.; Wang, Y.; Dostalek, J.; Jonas, U. Thin Hydrogel Films for Optical Biosensor Applications. Membranes (Basel) **2012**, 2, 40, doi:10.3390/membranes2010040.

27. Diehl, F.; Hageneder, S.; Fossati, S.; Auer, S.K.; Dostalek, J.; Jonas, U. Plasmonic Nanomaterials with Responsive Polymer Hydrogels for Sensing and Actuation. Chem Soc Rev **2022**, 51,3926, doi: 10.1039/D1CS01083B.

# 3 Plasmonic Nanomaterials with Responsive Polymer Hydrogels for Sensing and Actuation

**Published as:**

**Fiona Diehl**, Simone Hageneder, Stefan Fossati, Simone K. Auer, Jakub Dostalek and Ulrich Jonas, *Chem. Soc. Rev.*, **2022**, 51, 3926, doi: 10.1039/d1cs01083b.

**Author Contributions:**

***Fiona Wiesner (née Diehl):*** Conception, Coordination, Writing (Abstract, 1. Introduction, 2. Responsive hydrogels, 6. Summary, Conclusion and Outlook), Reviewing, Editing

*Simone Hageneder:* Coordination, Writing (4. Plasmonic (bio)sensors), Reviewing, Editing

*Stefan Fossati:* Writing (5. Thermoresponsive hydrogel actuators), Reviewing, Editing

*Simone K. Auer*: Writing (3. Responsive plasmonic nanomaterials), Reviewing, Editing

*Jakub Dostalek:* Conception, Coordination, Writing (Abstract, 1. Introduction, 3. Responsive plasmonic nanomaterials, 6. Summary, Conclusion and Outlook), Reviewing, Editing, Funding, Corresponding author

*Ulrich Jonas:* Conception, Coordination, Writing, Writing (Abstract, 1. Introduction, 2. Responsive hydrogels, 6. Summary, Conclusion and Outlook), Reviewing, Editing, Funding, Corresponding author

Chem Soc Rev

REVIEW ARTICLE

View Article Online
View Journal | View Issue

Open Access Article. Published on 26 April 2022. Downloaded on 9/25/2023 10:08:45 AM.
This article is licensed under a Creative Commons Attribution 3.0 Unported Licence.

Check for updates

Cite this: *Chem. Soc. Rev.*, 2022, **51**, 3926

# Plasmonic nanomaterials with responsive polymer hydrogels for sensing and actuation

Fiona Diehl,[a] Simone Hageneder,[b] Stefan Fossati,[b] Simone K. Auer,[bc] Jakub Dostalek *[bd] and Ulrich Jonas *[a]

Plasmonic nanomaterials have become an integral part of numerous technologies, where they provide important functionalities spanning from extraction and harvesting of light in thin film optical devices to probing of molecular species and their interactions on biochip surfaces. More recently, we witness increasing research efforts devoted to a new class of plasmonic nanomaterials that allow for on-demand tuning of their properties by combining metallic nanostructures and responsive hydrogels. This review addresses this recently emerged vibrant field, which holds potential to expand the spectrum of possible applications and deliver functions that cannot be achieved by separate research in each of the respective fields. It aims at providing an overview of key principles, design rules, and current implementations of both responsive hydrogels and metallic nanostructures. We discuss important aspects that capitalize on the combination of responsive polymer networks with plasmonic nanostructures to perform rapid mechanical actuation and actively controlled nanoscale confinement of light associated with resonant amplification of its intensity. The latest advances towards the implementation of such responsive plasmonic nanomaterials are presented, particularly covering the field of plasmonic biosensing that utilizes refractometric measurements as well as plasmon-enhanced optical spectroscopy readout, optically driven miniature soft actuators, and light-fueled micromachines operating in an environment resembling biological systems.

Received 17th November 2021

DOI: 10.1039/d1cs01083b

rsc.li/chem-soc-rev

[a] *Macromolecular Chemistry, Department of Chemistry and Biology, University of Siegen, Adolf Reichwein-Straße 2, 57074 Siegen, Germany. E-mail: jonas@chemie.uni-siegen.de*

[b] *Biosensor Technologies, AIT-Austrian Institute of Technology GmbH, Konrad-Lorenz-Straße 24, 3430 Tulln an der Donau, Austria. E-mail: jakub.dostalek@ait.ac.at*

[c] *CEST Competence Center for Electrochemical Surface Technologies, 3430 Tulln an der Donau, Austria*

[d] *FZU-Institute of Physics, Czech Academy of Sciences, Na Slovance 2, Prague 182 21, Czech Republic*

## 1. Introduction

Metallic nanoparticles and nanostructured thin metallic films exhibit unique optical properties associated with collective oscillations of electron density coupled with the respective electromagnetic field. These oscillations are referred to as surface plasmons, and their resonant optical excitation allows for tight confinement of light energy, strong increase of its

**Fiona Diehl**

*Fiona Diehl started studying chemistry at University of Siegen, Germany in 2014, while earning her BSc in 2017 and her MSc in 2019. Since 2016, she is a member of the Macromolecular Chemistry group chaired by Professor Ulrich Jonas. Currently, she is working there as a research assistant and accomplishing her PhD studies with focus on the synthesis of tailored responsive and non-responsive polymer systems for hydrogels with applications in antifouling coatings, sensors, actuators, and wound dressings.*

**Simone Hageneder**

*Simone Hageneder received her Master's degree in Biotechnology (2015) and her PhD (2021) from the University of Natural Resources and Life Sciences, Vienna, Austria. She was working at the Austrian Institute of Technology as Junior Scientist until 2022. Her doctoral research was focused on interfaces and plasmonic nanostructures for detection of biomarkers. She is currently a postdoctoral researcher at BiomedX in Heidelberg, Germany.*



This journal is © The Royal Society of Chemistry 2022

Open Access Article. Published on 26 April 2022. Downloaded on 9/25/2023 10:08:45 AM.
This article is licensed under a Creative Commons Attribution 3.0 Unported Licence.

intensity, and enhancement of local density of optical states.[1] The progress in understanding of the design rules and gradual advancing of fabrication precision of plasmonic nanostructures paved the way towards a plethora of applications of surface plasmon resonance that range from efficient amplification of weak optical spectroscopy signal,[2,3] analytical biosensor technologies for detection of minute amounts of chemical and biological species,[4–6] light manipulation in highly miniaturized devices and optical integrated circuits,[7,8] to systems serving for trapping of light in photovoltaic technologies.[9] Metallic nanostructures can be prepared by chemical synthesis in liquid media and subsequently assembled into more complex architectures,[10] or they can be directly fabricated by various lithography-based techniques on solid substrates.[11,12] However, these metallic structures are typically static, meaning their optical characteristics are determined by the chosen geometry and typically cannot be reconfigured after the preparation step.

To further extend the spectrum of functionalities plasmonic materials can provide, on-demand tunable plasmonic architectures attracted a great deal of attention in the research community.[13] For instance, inorganic materials with rapidly actuated refractive index have been proposed for fast plasmonic modulators.[14] Moreover, we witnessed additional approaches based on decorating the metallic nanostructures with photoswitchable organic molecules such as azobenzene derivatives.[15,16] A different approach that is particularly attractive in the bioanalytical field is based on merging metallic nanostructures with responsive hydrogels[17] in order to harness their stimulus-sensitive characteristics and benefit from their biocompatible properties. Such responsive hydrogels are composed of water-swollen networks with interconnected responsive polymer chains, and their physical properties can be toggled between different states by applying an external stimulus.[18] They can be prepared by numerous versatile synthetic routes[19] and constitute an important class of soft matter

**Stefan Fossati**

*Stefan Fossati studied physics at the University of Technology Vienna and joined the Austrian Institute of Technology in 2015 where he since pursued his research activities as PhD and PostDoc in the group of Jakub Dostalek. Since 2019 he is lecturer at the IMC University of Applied Science Krems, Austria. His research interest focuses on nanophotonics, in particular plasmonics, for biosensor applications.*

**Simone K. Auer**

*Simone Auer completed her bachelor's degree in physics at the University of Vienna 2019 and is currently finalizing her master's degree in biomedical engineering at the Technical University of Vienna. Since 2018 she has been working as a student assistant in the Biosensor Technology Group of the Austrian Institute of Technology AIT in Vienna, Austria.*

**Jakub Dostalek**

*Jakub Dostalek received his PhD in 2006 from the Charles University in Prague and worked as a research assistant at the Institute of Photonics and Electronics, Czech Academy of Sciences (CAS) until 2006. After his postdoctoral training at Max Planck Institute for Polymer Research in Mainz, he moved in 2009 to the Austrian Institute of Technology in Vienna, where he holds Senior Scientist position from 2015. Since 2020, he serves as a lecturer at the University of Natural Resources and Applied Life Sciences in Vienna. In 2021, he assumed Senior Researcher position at the Institute of Physics, CAS, in Prague.*

**Ulrich Jonas**

*Ulrich Jonas studied chemistry at the University in Mainz, Germany, at the University of California, Santa Barbara, USA, and at the ETH Zurich, Switzerland. After receiving his PhD in 1996 from the University in Mainz he worked as postdoctoral Feodor Lynen fellow at the Lawrence Berkeley National Laboratory in Berkeley, California, USA. In 1999 he joined the Max-Planck-Institute for Polymer Research in Mainz as project leader before his appointment as director of research at the Foundation for Research and Technology-Hellas in Crete, Greece in 2009. Since 2012 he is professor at the University in Siegen, Germany teaching Macromolecular Chemistry.*

Open Access Article. Published on 26 April 2022. Downloaded on 9/25/2023 10:08:45 AM.
This article is licensed under a Creative Commons Attribution 3.0 Unported Licence.

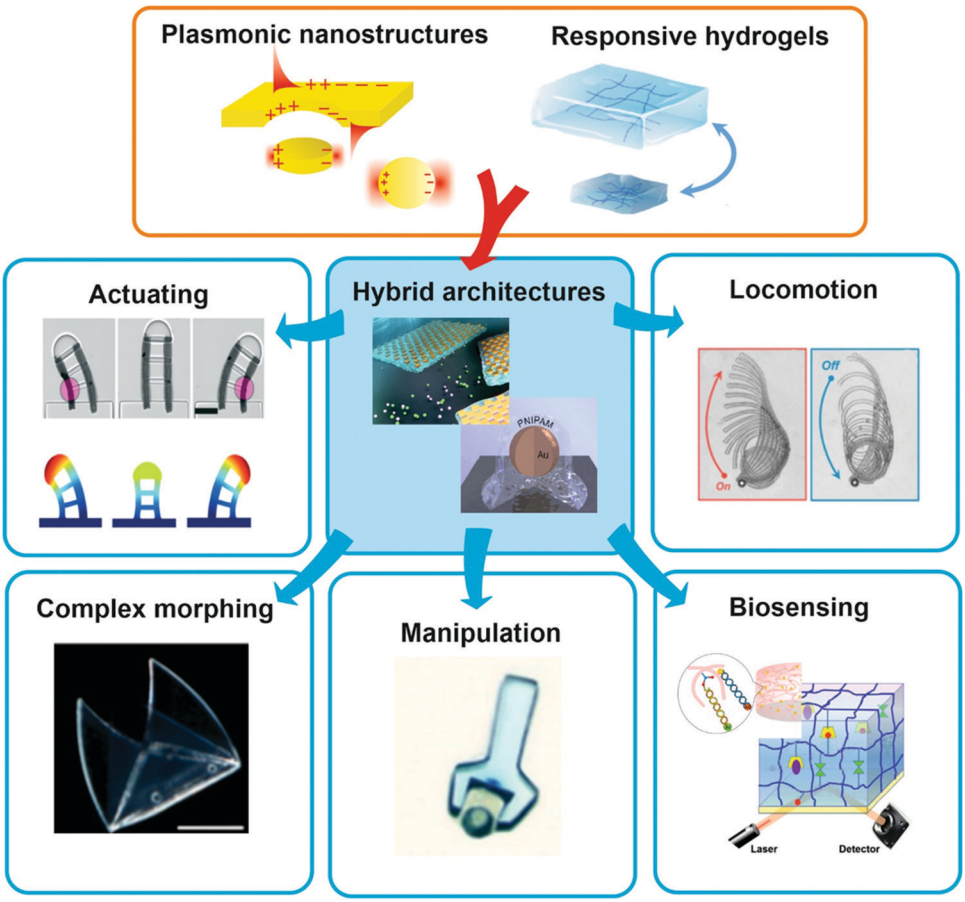


Fig. 1 Schematic representation of the combination of plasmonic nanostructures with hydrogels to yield advanced hybrid architectures that can further be employed in the fields of sensors and actuators. All shown examples will be discussed in the corresponding chapters further below, respectively. Adapted under CC-BY from ref. 21–24 and with permissions from ref. 25–27 and 28 ©2020 American Chemical Society, and ref. 29 © IOP Publishing. All rights reserved.

with switchable features that already routinely serve in the prominent fields of biomedical devices, drug delivery systems, and tissue engineering.[20]

This review highlights current activities in the plasmonic research community devoted to novel functionalities and applications enabled by the marriage of responsive hydrogels with plasmonic metallic nanostructures (Fig. 1). Following a tutorial approach, these two key elements are individually introduced. Starting in Chapter 2, responsive hydrogels, their characteristics, means of preparation, and implementation within miniature devices are discussed. Chapter 3 then focuses on the key rules in designing plasmonic nanostructures, routes for their preparation, and possible strategies for integration into crosslinked polymer networks. Subsequently, novel biosensing modalities that benefit from actively tunable plasmonic materials are presented in Chapter 4, including those with colorimetric and refractometric readout as well as plasmonically amplified fluorescence and surface-enhanced Raman spectroscopy. In particular, we focus on systems in which the open, permeable network structure of the responsive hydrogel is modified with functional biomolecules that specifically interact with the target analyte present in a liquid sample that is contacted with the structure. The capture of target analytes can then serve as an internal stimulus itself. In addition, external triggering of the collapse of the responsive hydrogel matrix with the captured analyte is exploited for compacting the analyte at the so-called plasmonic hotspot. There it can be efficiently probed by the intense surface plasmon field and thus the plasmon-enhanced optical spectroscopy readout can reach the highest sensitivity. Taking the design strategies to the next level in Chapter 5, the concept of exploiting responsive hydrogel plasmonics for actively shape-changing materials is scrutinized and discussed in the context of actuation and locomotion. Here, recent efforts in developing miniature optically-driven machines that can perform mechanical work using plasmonic heating-based actuation are presented. It should be noted that the combination of plasmonic nanomaterials with responsive hydrogels finds also its way to other important applications such as the prominent field of drug delivery[30–32] that has been covered by recent reviews,[33–35] but which is beyond the scope of this present review.

Open Access Article. Published on 26 April 2022. Downloaded on 9/25/2023 10:08:45 AM.
This article is licensed under a Creative Commons Attribution 3.0 Unported Licence.

## 2. Responsive hydrogels

### 2.1 Definitions: hydrogels

Polymeric gels[36] play an essential role in the development of innovative soft matter applications due to their unique characteristics, like viscoelasticity and swelling behavior. These polymeric systems are distinguished from inorganic gels, like silica gels consisting of inorganic $SiO_2$ particles, which are not in the scope of this review. By definition, a polymeric gel is a highly solvent-swollen polymer network of macromolecular chain segments held together by interconnections, *i.e.* crosslinks, which can either be of chemical or physical nature. The chain segments are characterized by the number of repeat units between two crosslinks, which defines their segment length $l_s$. The crosslinks prevent the macromolecular system from dissolving as individual chains and allow for a substantial uptake of liquid by chain solvation, resulting in swelling of the gel. Based on this attribute, the volume swelling ratio $Q_V$ is defined by the quotient of the total volume of the swollen system, including the polymer network and the associated solvent, divided by the volume of only the polymer network, and corresponds directly to the inverse of the polymer volume fraction $\Phi_p$ (symbols are used in analogy to ref. 36). The swelling ratio depends directly on the number of crosslinks per volume element in the polymer network, referred to as crosslink density $\nu_c$. For a given polymer, the swelling ratio $Q_V$, crosslink density $\nu_c$, and segment length $l_s$ are interrelated as follows: the higher the crosslink density $\nu_c$, the shorter the segment length $l_s$, the lower the swelling ratio $Q_V$, and *vice versa*. If the gel is swollen specifically with water, it is called a hydrogel.[37] Consequently, the primary requisite for a hydrogel is the strong affinity of the underlying macromolecular structure to water. The required hydrophilicity of the repeat units in the polymer chain is provided by functional moieties with high polarity, such as hydroxyl, amino, carboxyl, ionic, or even zwitterionic groups.[38] The polymers may be derived from hydrophilic monomers based on synthetic sources (like acrylates,[39] acrylamides,[40] 2-oxazolines,[41] and sulfo- or carboxy-betaines[42]), or originating from natural sources (such as dextrans,[43] alginates,[44] polypeptides,[45] proteins,[46] hyaluronic acid,[47] and chitosan[48]). The water-swollen, soft materials with high chemical versatility, which hydrogels represent, can mimic living tissue,[49] be easily integrated into biological systems,[50] and serve as a binding matrix material in bioanalytical application technologies as well as artificial muscles in soft robotics.[24,51–53]

### 2.2 Definitions: thermo-, iono-, and pH-responsive hydrogels

A particularly interesting category of hydrogels draws on the intricate properties of stimuli-responsive polymers that undergo physical transformations induced by an external stimulus, like due to a change in illumination (photoresponsive),[54] ionic strength (ionoresponsive),[55] proton concentration (pH-responsive),[56] or temperature (thermoresponsive).[57] Such transformations may occur in the form of shape and volume changes, sol–gel transitions, assembling and disassembling, or switching between hydrophobic and hydrophilic interactions.[58] In order to yield a multiresponsive hydrogel, several polymer classes, which are sensitive to different triggers, may be integrated into the same network structure.[59,60] In this review, we mainly focus on responsive hydrogels, in which a volume change is triggered by a shift in temperature, light, pH, or salt concentration. The mechanism responsible for volume changes of thermoresponsive hydrogels is found in the temperature-dependent interaction of polymeric substructures with the surrounding solvent. For freely dissolved polymer chains, this transition is manifested as a cloud point temperature ($T_c$), at which the optical transmittance of the solution is either decreased by precipitation or increased due to dissolution of the polymer (Fig. 2, left). The transition temperature for a given polymer structure specifically depends on the type of solvent (water in the case of hydrogels), the concentration of the solution, and the heating or cooling rate.[61] There are two general types of transitions with either an abrupt dissolution at the upper critical solution temperature (UCST)[61] or precipitation at the lower critical solution temperature (LCST)[62] upon temperature increase. Below the $T_c$, an LCST-type polymer exists in a solvated state as equilibrated coil. Upon exceeding the $T_c$ the polymer chains can undergo a coil-to-globule transition, releasing water from the solvation shell, and typically precipitate (if not colloidally stabilized).[63] For UCST-type polymers, the opposite behavior is observed, being insoluble at low temperatures and dissolving when reaching the $T_c$. A commonly used technique to determine the $T_c$ of a polymer solution is turbidimetry. For this method, transmittance of the solution with given concentration is measured while heating or cooling the sample at constant rate. With this method, the influence of several parameters on the transition behavior of responsive polymers was investigated.[64,65] In an earlier publication, the synthesis of different LCST-type copolymers by postmodification of poly(2-vinyl-4,4-dimethylazlactone)s with appropriate substituents (here: tetrahydrofurfuryl, *n*-pentyl, or di(ethylene glycol) methyl ether side chains) was described to shift the transition temperature.[64] The dependency of the $T_c$ on the polymer structure with varying side group type and ratio was demonstrated *via* turbidimetry (Fig. 2A). While the increase in hydrophobicity of the copolymer by the *n*-pentyl side chain leads to a decrease of $T_c$, the di(ethylene glycol) methyl ether side chains are more hydrophilic and consequently increase the $T_c$. In a second publication, turbidity measurements of an UCST-type sulfobetaine copolymer at different sodium chloride concentrations (Fig. 2B) are reported.[65]

Besides the structural influence of the copolymer composition on the transition temperature, the effect of ion concentration on $T_c$ is of high importance. As the solubility of the sulfobetaine copolymer is enhanced by the addition of sodium chloride, the $T_c$ shifts to lower temperatures for higher salt content. With this ionoresponsiveness, it is possible to shift the phase transition to a desired temperature range by adjusting the ion concentration. The same principle is exploited with pH-responsive polymers, which exhibit a particular solubility behavior affected by the proton concentration. For these systems, acidic or basic groups (carboxylic acids, amines, *etc.*) in the polymer structure provide a pH response.[56] In order to use light as a stimulus, various polymer systems have been realized with

Open Access Article. Published on 26 April 2022. Downloaded on 9/25/2023 10:08:45 AM.
This article is licensed under a Creative Commons Attribution 3.0 Unported Licence.

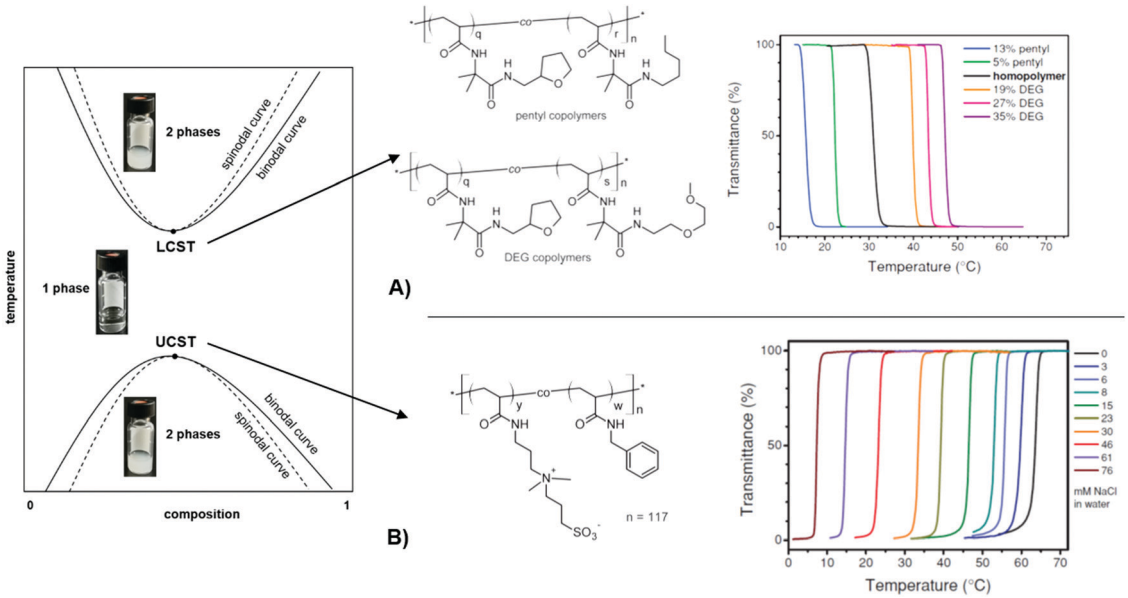


Fig. 2 Schematic phase diagram for UCST/LCST-type polymer solutions at different concentrations and temperatures. The photographs visualize the phase transitions of a thermoresponsive polymer in water. (A) Transmittance curves of LCST-type copolymers illustrating the influence of side-chain architecture and compositions on the cloud point. Adapted with permission from ref. 64, ©2013, American Chemical Society. (B) Transmittance curves of a UCST-type, sulfobetaine-based copolymer in water at varying salt concentrations, showing enhanced solubility with an increased salt concentration. Adapted with permission from ref. 65 ©2014, American Chemical Society.

photochromic motifs (*e.g.* benzospiran, azobenzene, or triphenylmethane leuconitrile groups).[66–68] These chromophore moieties undergo a structural change of their molecular framework upon excitation with light (like a *cis–trans* isomerization in the azobenzene group or decomposition into an ion pair in the case of triphenylmethane leuconitrile groups). By this, the state of the photosensitive polymer can be reversibly switched, yielding photoresponsive polymer structures. In particular, light features the benefit of being stringently controllable in wavelength, intensity, duration, and spatial resolution. These discussed concepts of tailored thermoresponsiveness, ionioresponsiveness, lightresponsiveness, and pH responsiveness can be transferred from single polymer chains to polymer networks. Since the polymer chains in a network are interconnected, they cannot be completely dissolved. Consequently, for a hydrogel composed of crosslinked thermoresponsive polymers, the temperature-induced transition between a swollen and a collapsed state of the chain segments at $T_c$ leads to a macroscopic volume change by incorporation or expulsion of solvent from the hydrogel matrix, which has been exploited in a broad range of applications. For example, the adaptable responsiveness and the switchable permeability of the water-swollen hydrogel matrix is appealing for biomedical applications like drug delivery.[69] In this context, both the temperature and pH sensitivity of responsive hydrogels are exploited for the release of loaded drug cargo at a particular temperature (*e.g.* at human body temperature),[70] and pH values of the target milieu (*e.g.* blood, stomach, or intestine).[71] In case of a polymer network scaffold built from photoresponsive polymer chains, the light-induced molecular transitions can be exploited to switch between different states, like closed and open valves,[72,73] or fouling and antifouling surfaces for so-called "self-cleaning" purposes.[74] In general, stimulus-triggered response affects the material properties at different length scales and thus allows to exploit these transitions in a variety of functionalities in microscopic as well as macroscopic devices. This is demonstrated in Fig. 3 by characteristic examples of actuators and sensor systems that take advantage of (multi-)responsive hydrogels.

At the nanoscopic scale, the combination of thermoresponsiveness and ionoresponsiveness was demonstrated for dual responsive hydrogel spheres with diameters around 100 nm, which is shown in Fig. 3A.[75] These systems were utilized as $K^+$ sensors by visualizing changes in the fluorescence resonance energy transfer (FRET) intensity that are caused by particle swelling and contracting upon variation of the ion concentration and temperature. Such swelling-dependent sensing can as well be achieved by exploiting the plasmonic response of small hydrogel beads with incorporated gold nanostructures. These plasmonic systems respond chain segment elongation inside the polymeric network leading to the modulation in near-field optical coupling that can be perceived as a color change, as discussed in the corresponding chapters below in more detail.[77] In the microscopic domain, there was demonstrated the application of volume-changing hydrogels in microfluidic valves that can be opened and closed by a light stimulus (Fig. 3B).[76] A macroscopic example was provided with composite gel sheets exhibiting a size in the cm range, which show dual-responsiveness towards pH and ion concentration by reversible folding and stretching in opposite directions (Fig. 3C).[60] Based on the complex stimuli-induced shape change, self-folding tubes were prepared that change diameter

Open Access Article. Published on 26 April 2022. Downloaded on 9/25/2023 10:08:45 AM.
This article is licensed under a Creative Commons Attribution 3.0 Unported Licence.

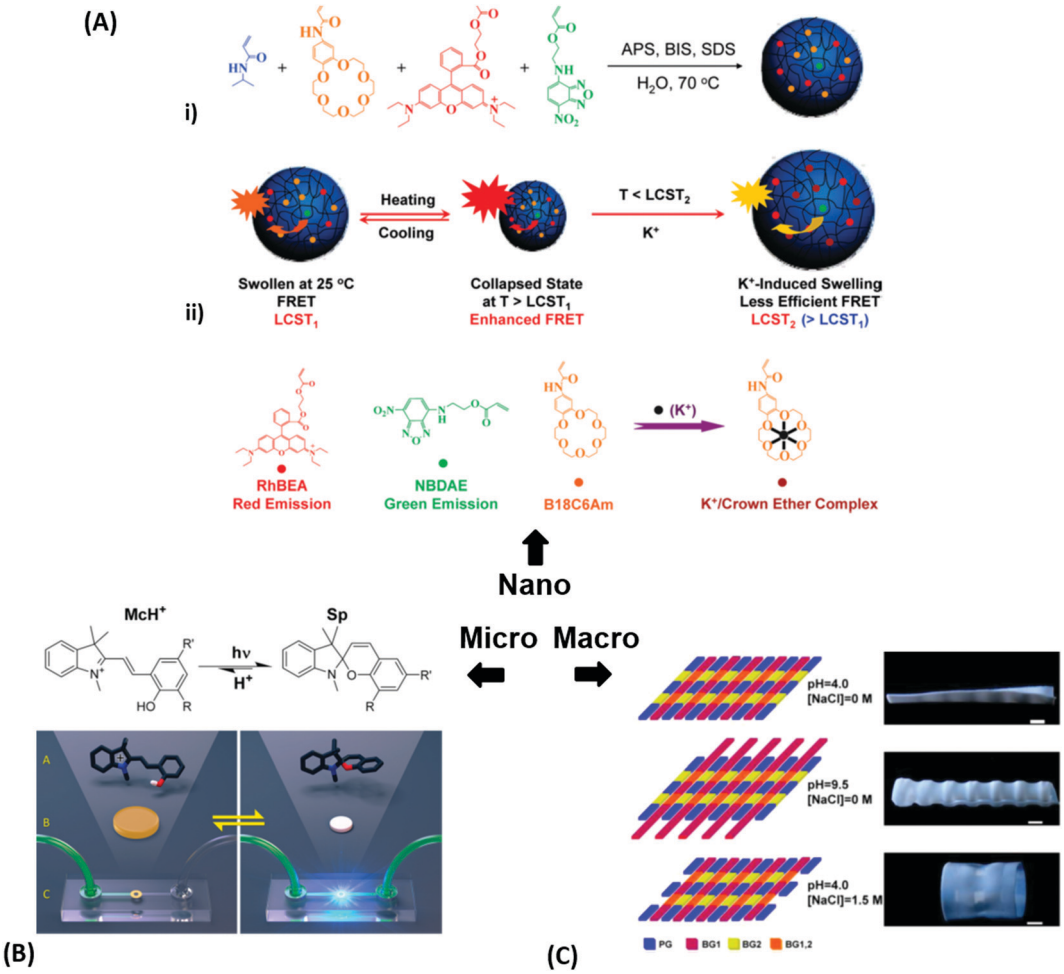


Fig. 3 (A) – (i) Synthesis scheme for the preparation of thermoresponsive and $K^+$ responsive hydrogel particles in the 100 nm size range. (ii) Illustration of fluorescence resonance energy transfer (FRET) within the hydrogel particles induced by changes in temperature, $K^+$ ion concentration, and a combination of both. Adapted with permission from ref. 75 ©2010, American Chemical Society. (B) – Effect of structural isomerization of a photoresponsive molecular probe inside a polymer network on the swelling state of the hydrogel by irradiation with light, which serves as light-switchable valve in a microfluidic device. Adapted with permission from ref. 76 ©2013, American Chemical Society. (C) Multiple shape transformations of pH- and ionoresponsive composite gel sheets. At pH = 4 and [NaCl] = 0, the gel sheet acquires a planar shape. At pH = 9.5 and [NaCl] = 0, the hydrogel forms a long cylinder. At pH = 4 and [NaCl] = 1.5 M, the gel adopts a drum shape. The thickness of the rectangular hydrogel sheet is 0.44 mm and the scale bars are 0.5 cm. Adapted with permission from ref. 60 ©2013, American Chemical Society.

and length in response to the solute composition in the liquid medium. These three examples provide only a brief glimpse into the limitless possibilities and the immense potential that multiresponsive hydrogel systems may offer to soft matter research. In order to tap into this rich arsenal of polymer-based hydrogel materials, first, their synthetic fundamentals need to be embraced.

### 2.3 Hydrogel preparation: polymerization and crosslinking

Water-attracting interconnected polymer chains are the prerequisite for hydrogels and the following paragraph expatiates their most common synthesis considerations and crosslinking strategies. The hydrophilic polymer chains are formed by common polymerization methods,[78] like free radical polymerization, ring-opening polymerization, or polycondensation, in which the crosslinks can be introduced either during or after chain formation, as specified further below. Crosslinks can be of chemical nature, like permanent covalent bonds, or they are based on reversible physical interactions, such as entanglements, host-guest interactions, hydrogen bonding, ion-pairing, or van der waals forces.[79] Entanglements affect the polymer behavior once the chain exceeds a critical length that is about twice the segment length $l_s$ between two entanglements.[78] Host-guest systems involve the complexation of a molecular entity (guest) within a molecular cavity (host), as given for the azobenzene guest inserted into a cyclodextrin host, depicted in Fig. 4A.[80] Hydrogen bonding typically exists between polar groups with high electron density (*e.g.* carbonyl oxygen), so-called acceptors, and groups with a labile bond to a hydrogen (*e.g.* amide proton), referred to as donor (Fig. 4B).[81] Such hydrogen bonding motives acting as crosslinks can either be intentionally integrated into the polymer backbone during

Open Access Article. Published on 26 April 2022. Downloaded on 9/25/2023 10:08:45 AM.
This article is licensed under a Creative Commons Attribution 3.0 Unported Licence.

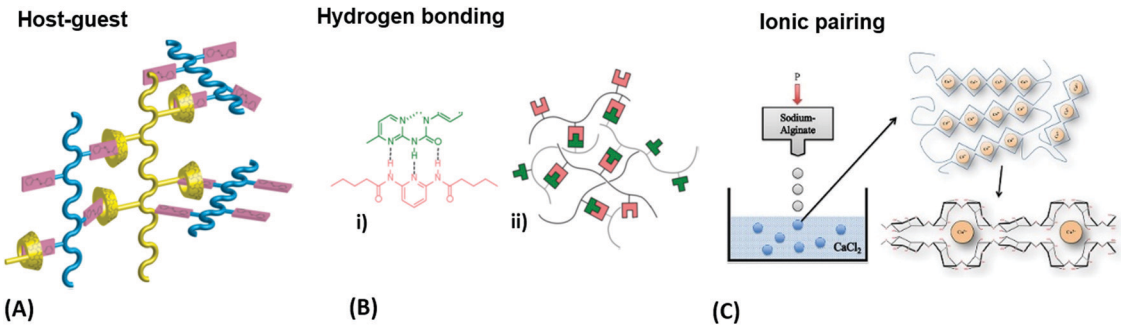


Fig. 4 (A) Schematic illustration of a host-guest network with physical crosslinks from a mixture of azobenzene copolymers and α-cyclodextrin copolymers. Adapted with permission from ref. 80. (B) Exploitation of hydrogen bonding motifs for multivalent crosslinking of macromonomers: (i) the underlying chemical complex and (ii) schematic representation of the hydrogen-bonded network. Adapted with permission from ref. 81. (Further permissions related to the material excerpted should be directed to the ACS.) (C) Gelation process of alginate by crosslinking of the polysaccharide chains with calcium ions after injecting sodium alginate into a calcium chloride solution. Adapted under CC-BY 3.0 from ref. 83.

synthesis *via* the introduction of appropriate functional groups or be intrinsically present in certain polymer classes, like in gelatin.[82] Depending on the solvent and the type of ionic interaction, ion-pairing may lead to a physical network, as illustrated by the example of calcium-induced crosslinking of sodium alginate (Fig. 4C),[83] where the exchange of the monovalent sodium ions with the divalent calcium ions transforms the soluble polymer into a hydrogel by ion bridging.

The strategies mentioned above, yielding reversible, physical crosslinks are suitable for applications, in which transient networks and temporary gel formation are desired. Such reversible network junctions provide a responsive structure component for reconfiguration of the gel scaffold *via* the action of an external stimulus. By opening or closing the network junctions, the crosslink density $\nu_c$ is varied, which has a direct influence on the mechanical properties and the swelling behavior. This responsiveness can be exploited for mechanical work in actuator applications or as transducer elements in gel-based biosensors.[84] However, often enhanced stability and durability of the hydrogel scaffold are required, demanding permanent covalent network junctions. Depending on the target hydrogel structure and application, chemical crosslinks can be introduced during (*in situ*) or after polymerization (post-synthetic).[38] For *in situ* crosslinking, multifunctional crosslinkers (monomers that can engage in more than two covalent bonds) are employed as comonomers in the polymerization reaction, which yields branches and crosslinks directly. In contrast, the post-synthetic approach requires an additional reaction step after polymerization to activate the crosslinker to interconnect the polymer chains. Such crosslinker functionality can be integrated into the polymer backbone during polymerization by a comonomer with a dormant reactive site (here referred to as internal crosslinker), which can be independently activated to form covalent bonds with neighboring chains. Alternatively, a polymer with appropriate functional groups can be reacted by addition of a small molecular agent (here referred to as external crosslinker) to generate the network in the post-synthetic step. Consequently, internal crosslinkers exhibit one chain-extending unit (*e.g.* double bond for polymerization) and at least one crosslinking unit (introducing a branching point for chain interconnection), while external crosslinkers should carry at least two interconnecting units. The crosslinkers for post-synthetic network formation may be activated by irradiation with light, by temperature increase, or by other stimuli. An external crosslinker is further required to be well miscible with the polymer matrix in order to prevent phase separation of the system. Internal crosslinking can be performed in two different ways following distinct generic mechanisms, either by specific pairing of complementary functional groups or by unspecific covalent linkage with the surrounding molecular framework. In the first case, the internal crosslinkers undergo specific reactions, like [2+2]-cycloaddition (Diels-Alder reaction),[85] Michael addition ("click-chemistry"),[86] or 1,3-cycloaddition.[38] The advantage of this specific post-synthetic crosslinking method lies in the predictability of the target structure for the network junctions. However, if the concentration and the mobility of the specific crosslinker units are too low, the probability for an encounter to form the covalent network link by reaction is strongly reduced.[87] In the second case, unspecific crosslinker units (*e.g.*, aromatic ketones,[88] azides,[87] or diazo groups[85]) may react by an unspecific C–H insertion reaction after activation by heat or light. As an advantage, such unspecific crosslinkers can act at very low concentrations as they do not require a specific reaction partner but rather undergo covalent linkage with either polymer backbones or side chains. Even more so, they can induce concurrent anchoring to a suitable substrate carrying the required C–H groups.[41,85,89] This simultaneous crosslinking and surface-attachment strategy is of great interest for the fabrication of sensors, actuators, and antifouling surface coatings.[18] Furthermore, the above outlined strategy to activate the post-synthetic crosslinker by irradiation with light can be conveniently exploited to spatially address network formation to yield advanced constructs with predetermined 2D patterns and 3D geometries, as described further below.

### 2.4 Hydrogel characteristics: tailoring of properties

In order to provide the most suitable features of a hydrogel for the specifically targeted application, its characteristic properties can be tailored by the following four aspects.

Open Access Article. Published on 26 April 2022. Downloaded on 9/25/2023 10:08:45 AM.
This article is licensed under a Creative Commons Attribution 3.0 Unported Licence.

**1. Molecular basis.** The specific chemical structure and dedicated functional groups of the underlying monomeric building blocks, as well as their combination in copolymers, provide the foundation for the desired hydrogel characteristics. For example, the monomer *N*-isopropylacrylamide (NIPAAm) was used to introduce the thermoresponsiveness in LCST-type hydrogels.[90–92] Equally, highly hydrophilic betaine monomers were employed in polymers to implement a UCST response and potentially resistance against unspecific sorption of biomolecules from complex biological fluids.[42] Such antifouling properties were exploited in applications, where biomolecular adhesion is not desired, like on ship hull surfaces,[93] medical devices and implants,[94] or biosensor chip interfaces.[42]

**2. Network design.** The crosslink density $\nu_c$ influences the degree of swelling and associated mechanical and diffusive properties. A higher number of crosslinks reduces the swelling capacity and consequently increases the stiffness of the gel. Inversely, a lower crosslink density $\nu_c$ entails a higher swelling ratio $Q_V$ and the associated larger, solvent-filled voids between the polymer segments allow an enhanced diffusion of small solute molecules through the network structure.

**3. Network modification.** The material properties of the network can be further tuned by post-synthetic functionalization or by blending with other constituents to form a hybrid or composite material. Such functionalization strategies may employ integrated carboxyl groups for subsequent conjugation with biomolecules such as immunoglobulin G antibodies,[91] or with other specific biological receptors[95,96] *via* amine coupling. Furthermore, the inclusion of nanoparticles allows targeting special properties of the hydrogel composite system,[97] like plasmonic heating *via* embedded gold nanoparticles,[92] mechanical reinforcement,[98] or magnetic manipulation.[99]

**4. Architectural aspect.** The hydrogel material can be furthermore sculptured to adopt complex shapes and structures at length scales from the nanoscopic level up to macroscopic dimensions. The methods to precisely control the geometry and dimensionality of the hydrogel structures can be chosen from a large pool of patterning techniques, which are covered further below. The generic structure classes can be distinguished as bulk hydrogel, micro or nanogel particles,[100] surface-attached hydrogel layers,[87] and polymer brushes.[101] While the unconfined gel material in the bulk or particle form can freely swell in three dimensions, confined networks can only swell with reduced dimensionality. These include 2D swelling in the valve structures shown in Fig. 5,[99] or 1D swelling in surface-attached hydrogels and polymer brushes deployed at planar substrates, where swelling occurs primarily in the direction perpendicular to the surface.[38] The concept of 1D swelling hydrogels is of high relevance for antifouling coatings,[69] sensing,[20,102,103] and actuation applications.[104,105] Strictly speaking, polymer brushes do not represent a true category of hydrogel networks since the main feature of a hydrogel – the presence of crosslinks interconnecting the polymer chains – is missing. However, they exhibit similar properties like surface-attached polymer networks, and the brush layers can be produced with crosslinks, which are termed brush-gels.[106,107]

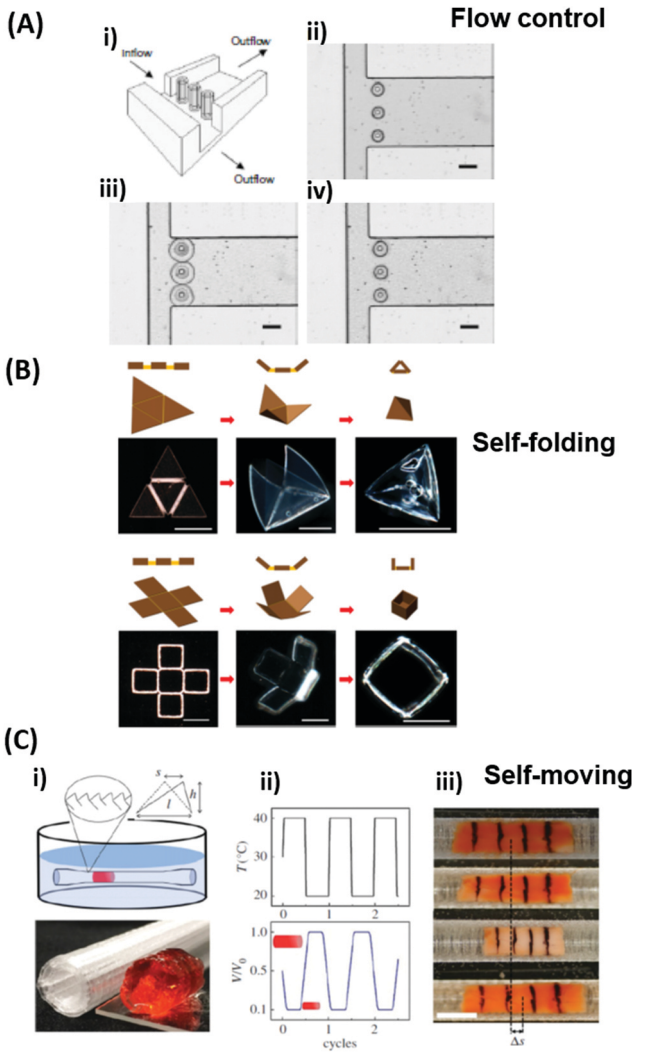


Fig. 5 (A) Temperature-switchable valve structures based on rigid posts in a microchannel coated with thermoresponsive hydrogels. (i) Model of the flow regulation system. (ii) Optical micrograph of the actual device in the open state after polymerization of the hydrogel. (iii) In the closed valve state the swollen hydrogel jackets block the side channel. (iv) Reverted to the open valve state the contracted hydrogels allow fluid to flow down the side branch. Scale bars, 300 μm. Adapted by permission from Springer Nature from ref. 99 ©2000. (B) Schematic and optical microscopy images showing thermally responsive self-folding hydrogel structures of different shapes, such as a pyramidal and a cubic capsule. The optical images were taken while increasing the temperature from 25 °C to 60 °C. All scale bars are 300 μm. Adapted with permission from ref. 108 © IOP Publishing. All rights reserved. (C) Temperature-driven pNIPAAm-based hydrogel crawler. (i) Schematic of the experimental set-up. (ii) Schematic plots showing the periodic change of temperature of the fluid and the resultant swelling/collapsing of the hydrogel. (iii) Sequential snapshots of the hydrogel in one collapsing/swelling cycle in the channel. Scale bar: 1 cm. Adapted with permission from ref. 105.

Since many strategies are available to tailor hydrogel properties towards a target application, their combination leads to an even larger variety of achievable features, as demonstrated with the following three examples. In the earlier developments, there was pursued pH-responsive valve based on functional

Open Access Article. Published on 26 April 2022. Downloaded on 9/25/2023 10:08:45 AM.
This article is licensed under a Creative Commons Attribution 3.0 Unported Licence.

hydrogel architecture of hydrogel layers attached to supporting posts that were prepared inside a microfluidic device (Fig. 5A).[99] For this purpose, a mixture of acrylic acid (for pH response) and 2-hydroxyethyl methacrylate (HEMA, hydrophilic comonomer for water uptake) was polymerized using the *in situ* crosslinker ethylene glycol dimethacrylate in the presence of a photoinitiator and with the help of a photomask. The modified microfluidic device allowed flow control of liquid through the side channel by the pH-responsive valve, which could collapse or swell within seconds upon pH change. A similar flow regulation system based on light-induced plasmonic heating of optically independently addressable gold colloids and nanoshells to trigger a thermoresponsive hydrogel collapse was exemplarily introduced.[109] A later report was published on self-folding 3D hydrogel scaffolds with micrometer dimensions, which were pH- and thermoresponsive. There were lithographically inscribed zones with different crosslink density $\nu_c$ and gradients into the hydrogel network to exploit the resulting difference in mechanical properties and swelling behavior as rigid walls and flexible hinges (targeted network design, Fig. 5B).[108] The utilized photoreactive hydrogel precursor was composed of an *n*-butanol solution of thermoresponsive LSCT-type p(NIPAAm), NIPAAm monomer, pH-responsive acrylic acid, the *in situ* crosslinker *N*,*N*′-methylenebisacrylamide, and a photoinitiator. Structural elements of the 3D scaffold were generated from the hydrogel precursor by irradiation through a photomask. The highly swellable hinges were built by thin, gradiently crosslinked regions, while the rigid, low swelling panels were made from thick sections with high crosslink densities. When immersing these geometric hydrogel structures in water and increasing the temperature over the $T_c$ of pNIPAAm, the temperature-induced self-folding of the 3D scaffold took place (see Fig. 5B). In a more recent example, self-crawling hydrogel particles are reported that move inside a surface-modified channel upon periodical temperature changes, falling below or exceeding $T_c$.[105] Their actuation system was based on thermoresponsive LCST-type hydrogels formed by pNIPAAm chains, confined in a narrow, cylindrical channel with rough, anisotropic surface structure (Fig. 5C, left). The NIPAAm-based hydrogel corpus collapsed, when immersing this system into an aqueous medium with a temperature below $T_c$, and expanded, after immersion into a water bath tempered above $T_c$. A periodical decrease/increase in temperature resulted in an expansion/shrinkage of the hydrogel inside the channel and a longitudinal movement due to the friction between the hydrogel and the anisotropic surface of the tube (Fig. 5C, right). The main underlying concepts for hydrogel crawlers are discussed in more detail in the later chapter dedicated to hydrogel actuators. Even more complex functionality can be achieved with these responsive hydrogel systems by integration into sophisticated architectures described in the following section.

### 2.5 Structured hydrogels: realization of complex architectures

An intrinsic structuring can be found in composite hydrogel materials obtained by modification of polymeric gels with filler components, like fibers or nanoparticles. Depending on the properties of the individual components, this approach can result in responsive composites with complex architectures. Such hydrogel composites can be prepared by three strategies, being (1) addition of the respective filler component to the preformed hydrogel matrix, (2) mixing of the filler with a polymer solution prior to the polymer crosslinking, or (3) polymerization of the hydrogel-forming monomer in the presence of filler particles and fibers.[97] For example, such composite materials can provide increased mechanical stability compared to the parent hydrogel (Fig. 6A). In this approach, recent work exploited silica nanoparticles that were integrated into the thermoresponsive pNIPAAm network in order to reinforce the soft hydrogel matrix.[98] In general, the sophisticated combination of the specific filler properties with the responsiveness of the polymer network can be employed as stimulus transducer, for example a hydrogel collapse induced by plasmonic heating *via* optical irradiation of embedded gold nanoparticles. As stimulus transducers are essential components of sensor systems, these responsive hydrogel composites may be directly applied as sensing matrices. One of the most common architectures in sensor and actuator platforms consists of a thin hydrogel layer covalently attached to a surface, which shows 1D swelling perpendicular to the surface. The surface acts as solid support and can simultaneously be involved in the transduction and sensing process, which is exploited with the plasmonic response of gold surfaces. Depending on the actual hydrogel layer thickness, different preparation methods have to be employed. For ultra-thin polymer brush layers with the thickness defined by a single polymer chain, two general synthesis techniques are employed, referred to as ''grafting-to'' and ''grafting-from'' method.[42] The grafting-from method allows the formation of attached polymer chains by polymerizing the monomers away from the surface starting at a surface-attached initiator species, while grafting-to refers to the deposition of the preformed polymer chains. These polymer brush layers can also be laterally patterned, as outlined in Fig. 6B. For preparation of thicker hydrogel films, doctor blading, printing, spin coating, dip coating, or spray coating of the polymeric precursor can be employed, followed by crosslinking activated with an external stimulus (*e.g.* heat or light).[110] Often, a covalent surface attachment of the hydrogel network is simultaneously achieved in this crosslinking step. Furthermore, hydrogel layers may be prepared by an assembly of pre-formed hydrogel beads (micro- and nanogels) on the substrate surface. A standard deposition method is the Langmuir–Blodgett technique, in which the particles are transferred to a solid substrate by its slow withdrawing through an air-liquid interface, at which the particles self-assemble.

For precursor polymers with photosensitive crosslinker units, photolithography can be utilized to directly generate intricate patterns of small hydrogel structures by light-induced crosslinking. The required spatially controlled irradiation can be achieved by either illumination through a photomask or by a focused optical beam. By the first method, only areas irradiated by UV light are photocrosslinked, whereas the

Open Access Article. Published on 26 April 2022. Downloaded on 9/25/2023 10:08:45 AM.
This article is licensed under a Creative Commons Attribution 3.0 Unported Licence.

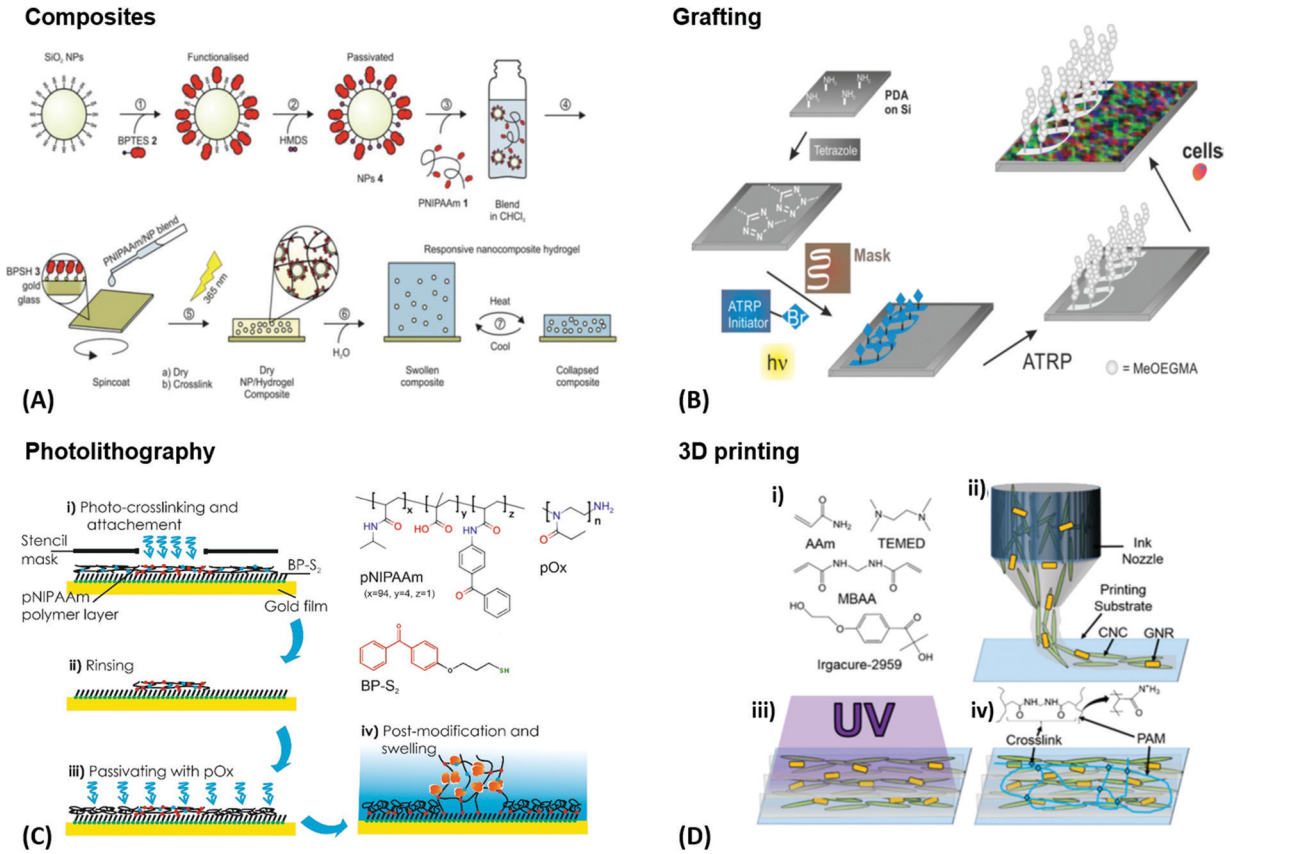


Fig. 6 (A) Preparation of photoreactive functionalized $SiO_2$ nanoparticles and their application in responsive nanocomposite hydrogels for mechanical stabilization. Adapted with permission from ref. 98. (B) Surface patterning of silicon wafers and their resistance to cell adhesion. A film was functionalized with a photoactive tetrazole. A maleimide-based initiator for atom transfer radical polymerization was photopatterned *via* irradiation through a photomask. Polymer brushes were then grown on the patterned areas, showing full resistance towards cell adhesion while the rest of the surface was coated by a confluent layer of cells. Adapted with permission from ref. 111. (C) Application example for the photolithography process. A photocrosslinkable polymer is spin coated and irradiated with UV light through a stencil mask. Non-irradiated (and therefore non-crosslinked) areas are washed off. An additional passivation step may be implemented as well. (D) – (i) Underlying chemical structures that are mixed with gold nanorods and cellulose nanocrystals to make the gel precursor. (ii) Cellulose nanocrystals and gold nanorods are orientationally aligned along the flow of the gel precursor by a 3D printing process. (iii) Curing of the printed sol with UV light. (iv) Resulting composite gel with crosslinked poly(acrylamide) chains. Adapted with permission from ref. 112. (Further permissions related to the material excerpted should be directed to the ACS.)

polymer chains on the surface area protected by the lithography mask stay unreacted and can be washed away after the process, as presented in Fig. 6C. The latter one, two-photon polymerization of hydrogel precursors, represents a more advanced technique to fabricate 3D hydrogel structures by direct laser writing with high resolution below the 100 nm limit and structure dimensions up to macroscopic length scales, also referred to as nanoscale 3D printing.[113–116] In order to achieve rapid fabrication of macroscopic hydrogel scaffolds and objects, various 3D printing technologies are available for fully automated printing of a precursor polymer with subsequent crosslinking. An example of this technique was demonstrated to yield well-defined poly(acrylamide) composites with co-aligned cellulose nanocrystals and plasmonic gold nanorods, as shown in Fig. 6D.[112] In 4D printing, the above-mentioned structuring tool provided by 3D printing is combined with the unique properties of responsive hydrogel materials to transform the shape of the object by application of an appropriate stimulus after printing. In the following chapters, the combination of responsive hydrogel materials and plasmonic structures is highlighted with recent examples of sensor and actuator applications.

## 3. Responsive plasmonic nanomaterials

Metallic nanoparticles and nanostructured metallic thin films increasingly serve as building blocks for the assembly of materials with precisely tailored optical properties. These structures enable to tightly confine energy of light at their surface by the resonant excitation of surface plasmons that originate from coupled collective oscillations of electron density and associated electromagnetic field. The combination of metallic nanostructures with responsive hydrogels paved the way to numerous important features and functionalities,

Open Access Article. Published on 26 April 2022. Downloaded on 9/25/2023 10:08:45 AM.
This article is licensed under a Creative Commons Attribution 3.0 Unported Licence.

including facile means to modify metallic surfaces with functional biomolecules (for biosensor applications), 'on-demand' tuning their optical properties (serving in enhanced optical spectroscopy and adaptive optical materials), as well as performing light-fueled mechanical work and actuating (in micro- and nano-machines).

### 3.1 Optical properties of plasmonic nanostructures

The optical properties of metallic nanostructures and architectures they constitute can be efficiently controlled by their architecture design. The particular parameters that allow tuning such characteristics include the shape and material from which the individual metallic nanoparticles are made, their spatial arrangement, and optical properties of the surrounding dielectric. In general, the use of responsive hydrogels as materials hosting the metallic nanostructures enables 'on demand' controlling the latter two parameters, which open doors for developing new class materials that exhibit actively tunable characteristics. As illustrated in Fig. 7, the swelling and collapsing of the responsive hydrogel matrix can be utilized to reversibly modulate refractive index $n_h$ (due to the variations in polymer volume fraction $\Phi_p$) and the distance between metallic nanoparticles $d$ (through volumetric change of the polymer networks). These parameters thus serve as facile handles to actuate the resonant coupling of light to localized surface plasmons (LSPs) supported by metallic nanoparticles and propagating surface plasmons (PSPs) that travel along the continuous metallic films.

The first approach presented in Fig. 7A shows actuating of LSPs supported by an individual metallic nanoparticle by changing the refractive index $n_h$ of the surrounding responsive hydrogel shell. In general, collapsing of the hydrogel shell adjacent to the metallic core leads to a local increase in the refractive index $n_h$ that red-shifts the resonant excitation of LSPs to longer wavelengths. For instance, a collapse of about 100 nm thick pNIPAAm-based hydrogel shell was exploited for detuning the LSPs on chemically synthesized spherical gold nanoparticles with a diameter of 15–50 nm in dynamic light scattering studies.[92] A higher sensitivity of the LSPs to refractive index changes can be achieved for other shapes of metallic nanoparticles as was, for instance, shown for chemically synthesized rod-shaped gold nanoparticles with pNIPAAm shell.[117] Alternatively, lithography allows for the preparation of controlled shape of metallic nanoparticles at a solid surface and, for example, arrays of cylindrical gold nanoparticles were fabricated and wrapped by pNIPAAm-based hydrogel caps for their rapid actuating by applied external stimulus.[118]

Metallic nanoparticles separated by a responsive hydrogel from a flat metal surface constitute the second widely used design of tunable plasmonic geometry, see Fig. 7B. It allows for efficient actuation of LSPs that form a plasmonic mode which tightly confines the energy of light in the gap. This gap is defined by the distance $d$ between the surfaces of the metal film and the nanoparticle occupied by the responsive hydrogel material. In this architecture, a responsive pNIPAAm-based hydrogel spacer was demonstrated to enable thermal reversible

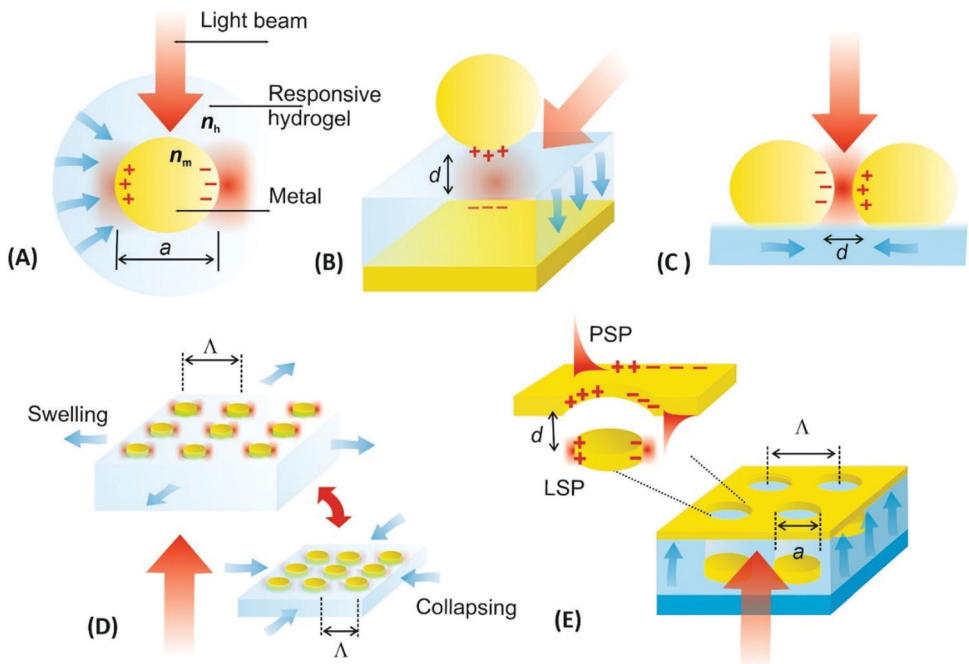


Fig. 7 Overview of actuated geometries supporting localized surface plasmon (LSP) and propagating surface plasmon (PSP) modes by the use of responsive hydrogels: (A) individual metallic nanoparticle responding to changes in refractive index $n_h$ of the hydrogel capping shell, (B) metallic nanoparticle placed at tunable distance $d$ from a flat metallic surface, (C) plasmonic nanoparticle dimer with actuated separation distance $d$, (D) lattice of metallic nanoparticles with modulated period $\Lambda$ and (E) example more complex structure where responsive hydrogel induced variations in both refractive index $n_h$ and near-field coupling responding to $d$.

Open Access Article. Published on 26 April 2022. Downloaded on 9/25/2023 10:08:45 AM.
This article is licensed under a Creative Commons Attribution 3.0 Unported Licence.

modulating the distance $d$ between 18 and 63 nm for gold spherical with a diameter of 78 nm.[119] In order to actuate narrower gaps, pNIPAAm or pDEAEMA brushes[120,121] can be tethered to a flat metal surface to serve as a tunable spacer instead of polymer networks forming a thin hydrogel. Moreover, chemically synthesized gold nanoparticles were capped with pNIPAAm polymer and attached to a flat gold surface with the actuated distance $d$ between 8 and 20 nm.[122]

Metallic nanoparticle dimers that are sketched in Fig. 7C, or more generally, aggregates of multiple plasmonic nanoparticles, represent another system for tuning LSPs by near-field coupling. For these architectures, the observed LSP resonance is red-shifted to a longer wavelength when reducing the distance $d$ between the metallic nanoparticles to comparable or smaller separation than their size $a$. This shift originates from the interaction of LSPs supported by the individual nanoparticles, leading to the occurrence of a LSP mode that also confines the energy in the gap. Such LSP coupling has been implemented with metallic nanoparticles attached to the surface of responsive microgels, that are pushed closer to each other upon the collapse of the responsive microgel core.[123] For gold nanorods attached to pNIPAAm microgel with a diameter of $\sim$500 nm, a reversible LSPR wavelength shift of $\Delta\lambda >$ 100 nm was observed.[124] Another possible utilization of this concept was explored by loading chemically synthesized silver nanospheres inside a pNIPAAm microgel body that was made reversibly collapsing and swelling upon temperature modulation.[125] Morover, an aggregation of gold chemically synthesized nanoparticles capped with pNIPAAm polymer shell allowed for reversible assembly and disassembly of clusters exhibiting distinct plasmonic properties.[126]

By lithography approaches, more precise control of the prepared geometry can be achieved. As Fig. 7D illustrates, two-dimensional periodic arrays of metallic nanoparticles can be prepared for dynamic tuning of LSPs by modulating the period $\Lambda$. This type of structure was realized with a poly(acrylic acid) (pAAc) hydrogel membrane that carried rectangular gold nanoparticles fabricated by electron beam lithography (EBL).[127] It exhibited a particle-particle gap of 15 nm that was much narrower than the period $\Lambda$ of about 100 nm. By swelling and collapsing of the pAAc membrane due to the ionic strength variations, the period $\Lambda$ was modulated between 100 nm and 200 nm. These changes lead to the variations in near-field coupling between the LSPs on neighboring nanoparticles, and decreasing the period $\Lambda$ was accompanied by a strong red-shift in the LSP wavelength of $\Delta\lambda = 70$ nm. A similar type of structure was obtained by UV-laser interference lithography (UV-LIL) on the top of a free-standing hydrogel membrane based on pNIPAAm, featuring a longer period $\Lambda$ and wider gap between the metallic nanoparticles of several hundreds of nanometers. Swelling and collapsing of the hydrogel allowed changing the arrays period $\Lambda$ between 360 and 600 nm. In this range, the neighboring LSPs interact *via* diffraction, and thus, opposite evolution of the occurs and LSP wavelength blue-shifts (with maximum change of about $\Delta\lambda \sim 150$ nm) when decreasing the period $\Lambda$ (see Fig. 8A).[128]

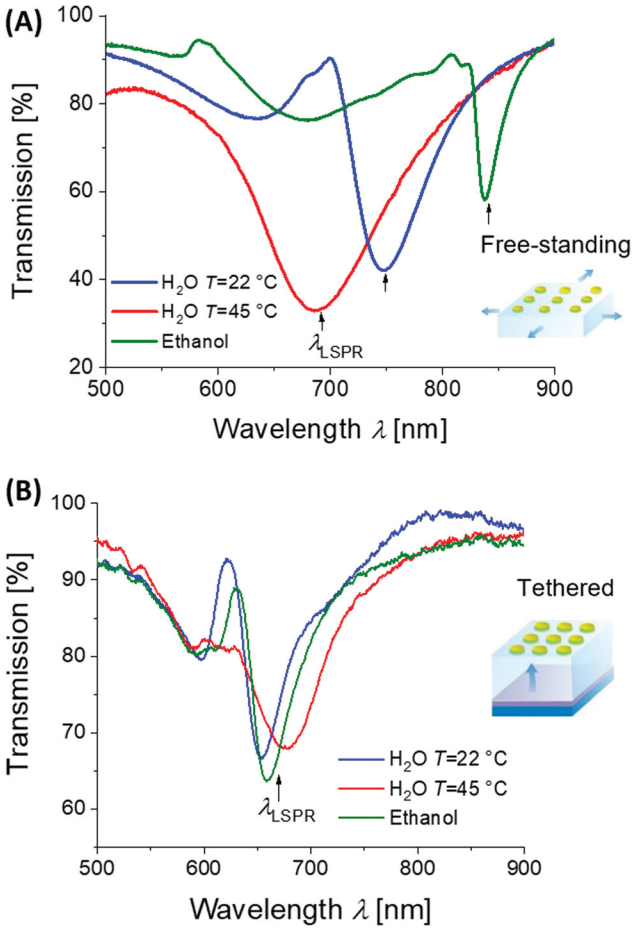


Fig. 8 Example of plasmonic properties of lithographically prepared arrays of cylindrical gold nanoparticles on top of a thin pNIPAAm-based hydrogel cushion. (A) Optical response to variations in the period of the structure $\Lambda$ with free-standing membrane, (B) optical response to refractive index changes for the surface-attached structure. Adapted under CC-BY from ref. 128.

It should be noted that more complex geometries allow for modulation of a richer spectrum of surface plasmon modes by hydrogel actuation, as indicated in Fig. 7E. This schematic shows a metallic film perforated by an array of nanoholes that are contacted with an array of metallic nanoparticles. These nanoparticles are separated from the holes by a distance $d$ controlled by swelling and collapsing of the responsive hydrogel cushion. The spectral response of series of resonances associated with the excitation of LSPs (confined at the nanoparticles and the nanoholes) and PSPs (traveling along the bottom and top metal film interface) were investigated.[129] The observed variations in spectral features encoded to the reflected and transmitted waves were ascribed to the competing effects of near-field coupling (driven by variations in $d$) and changes in the refractive index of the responsive hydrogel $n_h$ (induced by variations in the hydrogel swelling ratio $Q_v$).

Moreover, hydrogels exhibit a refractive index $n_h$ that is close to that of water and thus they allow for embedding the metallic nanoparticles in a refractive index-symmetrical geometry when exposed to acqueous environment. Arranging them in sparse

Open Access Article. Published on 26 April 2022. Downloaded on 9/25/2023 10:08:45 AM.
This article is licensed under a Creative Commons Attribution 3.0 Unported Licence.

arrays then enables efficiently decreasing the damping of LSP resonances. This phenomenon occurs due to phase-matching of light that is resonantly scattered at the periodic arrays of metallic nanoparticle leading to establishing a new type of lattice (also called collective) LSP modes.[130] As illustrated in Fig. 8A and B, the collective LSPs excitation can occur on periodic arrays of cylindrically shaped gold nanoparticles attached to a swollen hydrogel membrane in contact with water. It is manifested as an angular dispersive dip in the transmission spectrum that is spectrally narrower than that for conventional LSPs excited on gold nanoparticles attached to a substrate with a higher refractive index. The excitation of these two types of LSP modes can be reversibly switched by collapse and swelling of the hydrogel, accompanied by a modulation of the refractive index $n_h$ (thus perturbing and re-establishing the symmetry). Such behavior was observed for the metallic structures prepared on top of a responsive pNIPAAm-based hydrogel cushion,[128] as well as for self-assembled architectures with synthetically prepared gold/pNIPAAm hydrogel core/shell nanoparticles.[131]

### 3.2 Preparation of architectures composed of plasmonic nanostructures and responsive hydrogels

As expounded further below, several distinct types of approaches can be identified for the preparation of materials that combine metallic nanostructures and responsive hydrogels. Typically, metallic nanoparticles are fabricated separately and then either embedded into hydrogel materials, attached to their surface, or caped with a responsive polymer network shell for subsequent assembly into the desired composite architectures.

In the first fabrication approach to yield extended arrays of hydrogel-embedded metallic nanoparticles, the metallic nanostructures can be prepared on a solid substrate by using lithography followed by their transfer to the responsive hydrogel material. A wide range of lithography methods has been established for the preparation of such metallic nanostructures, including EBL,[132] UV-LIL,[133] and colloidal lithography.[11] As illustrated in the example presented in Fig. 9, periodic arrays of cylindrical gold nanoparticles were prepared on a glass substrate by a UV-LIL method. Afterwards, these nanoparticles were attached to a NIPAAm-based polymer network in order to obtain thin responsive plasmonic membranes.[128] This polymer network was prepared either by irradiation of a photocrosslinkable pNIPAAm-based copolymer carrying benzophenone groups or by direct polymerization of monomers in contact with the surface carrying metallic nanostructures. The first route yielded a hydrogel film with a thickness of 2.2 μm, while the second route allowed a significant increase of the attainable thickness to about 40 μm (both in swollen state). Such hydrogel membranes with embedded metallic nanoparticles were then stripped from the substrate to be used as surface-attached or a free-standing structure (see Fig. 9).

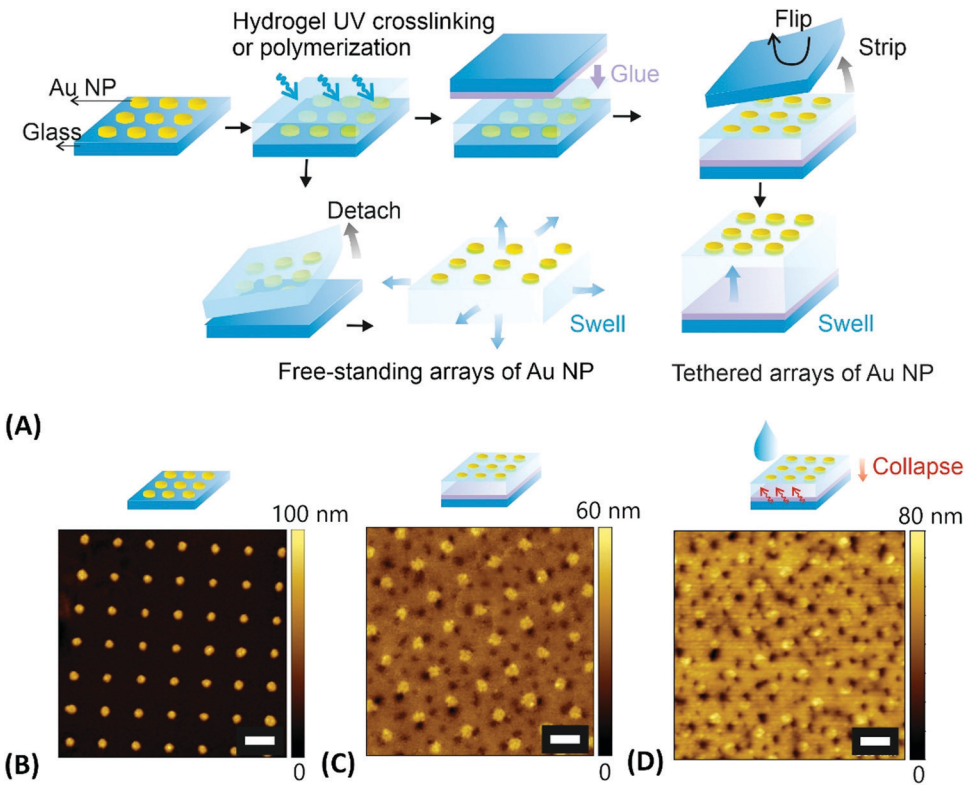


Fig. 9 (A) Overview of the preparation steps for embedding gold nanoparticles arrays into tethered and free-standing pNIPAAm-based hydrogel films. AFM observation of (B) the gold nanoparticle arrays prepared by UV-LIL, (C) stripped structure that was attached to the crosslinked pNIPAAm polymer in the dry state in air, (D) same structure under water at a temperature above the LCST. Scale bars correspond to 500 nm. Adapted under CC-BY from ref. 128.

Open Access Article. Published on 26 April 2022. Downloaded on 9/25/2023 10:08:45 AM.
This article is licensed under a Creative Commons Attribution 3.0 Unported Licence.

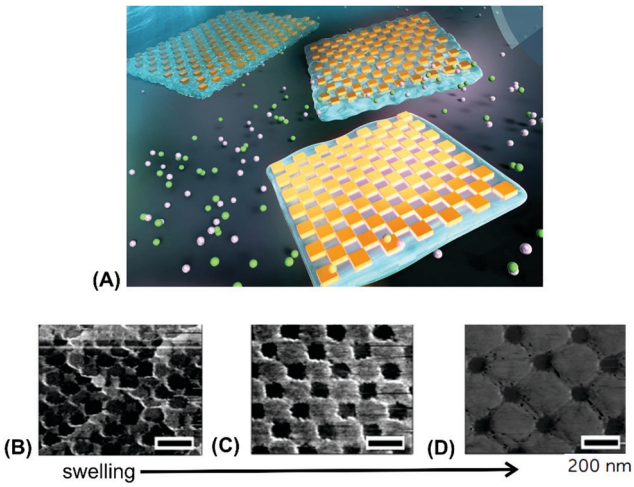


Fig. 10 (A) Illustration of a free-standing pAAc membrane with embedded arrays of rectangular gold nanoparticles prepared by EBL. (B)–(D) AFM images of the structures upon gradual swelling. Scale bars correspond to 200 nm. Adapted under CC-BY 3.0 from ref. 127.

A similar strategy was utilized for embedding periodic arrays of rectangular gold nanoparticles into a free-standing pAAc hydrogel membrane (Fig. 10A).[127] The closely packed rectangular gold nanoparticles were prepared on a Si substrate by EBL and then transferred onto a thin pAAc hydrogel membrane that was allowed to swell in an aqueous medium. This membrane was prepared by polymerization in a narrow mold and exhibited a thickness of 1 millimeter in the swollen state. Fig. 10B–D shows the AFM images of the surface structures, where the distance between the corners of neighboring rectangular gold nanoparticles was actively controlled by gradual swelling of the supporting pAAc membrane.

In the second approach, the employed metallic nanoparticles are prepared by chemical synthesis. Research in this field lead to the development of a plethora of protocols enabling precise control of the particle morphology ranging from spherical, rod, core–shell to hyperbranched shapes.[134] These metallic nanostructures can be either capped by a responsive hydrogel,[135] embedded in small hydrogel particles (microgels or nanogels)[136] or formed inside the already prepared responsive polymer network structure.[137] These systems can be subsequently assembled as individual building blocks into the desired periodic[138] or more complex[139] geometries. A common technique takes advantage of the self-assembly process of such nanoparticles occurring at the liquid–liquid or liquid–air interface.[110] Thereby, periodic two-dimensional hexagonal arrays are typically prepared. The schematics in Fig. 11 illustrate such an assembly process with subsequent transfer to a solid substrate and further processing of the monolayer (embedding in polymer layer and photocrosslinking) to yield the final optical device.[131]

In the third possible approach, the chemically synthesized metallic nanostructures are either attached to the object surface or dispersed within the polymer matrix upon the formation of the hydrogel. When molding the hydrogel by polymerization in cavities, the size of the resulting responsive devices is typically $>10$ μm and the metallic nanoparticles are trapped inside the crosslinked polymer network.[140] Alternatively, preformed responsive microgels can be employed as building blocks that are decorated with metallic nanoparticles. From these raspberry-like structures, the bulk hydrogel material is formed by casting inside the mold, see the example in Fig. 12.[77]

Responsive hydrogel structures with sub-micrometer features were obtained from photocrosslinkable polymers on the top of plasmonic substrates by more precise lithography methods. For example, arrays of 100 nm-wide responsive hydrogel nanopillars were prepared by UV-NIL with nanostructured soft polymer stamp casted to a layer of photocrosslinkable polymer.[141] Furthermore, by crosslinking a thin pNIPAAm-based polymer film with a UV interference pattern, responsive

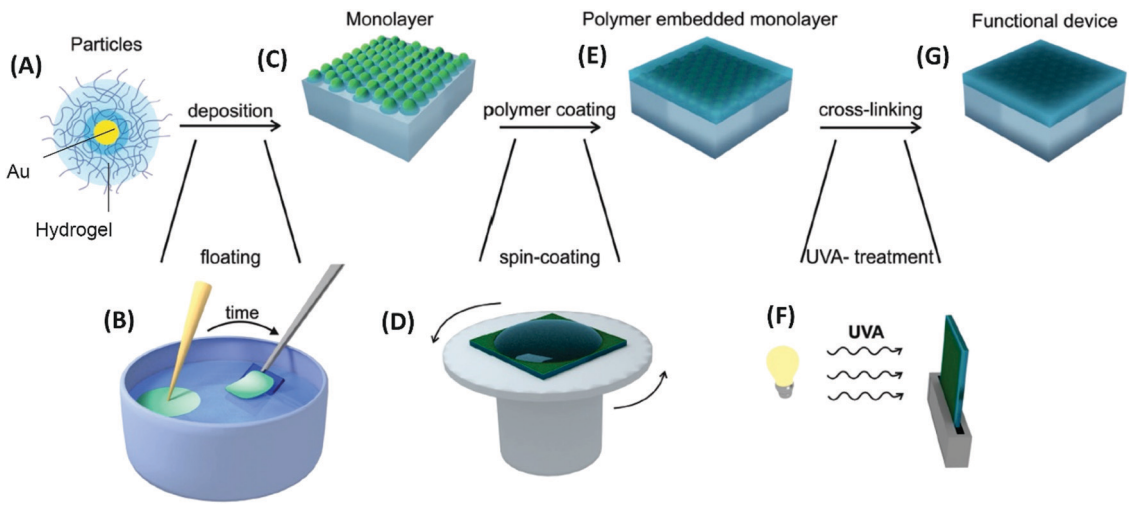


Fig. 11 Flow diagram for (A) pNIPAAm-capped gold nanoparticles that are (B) self-assembled at the liquid–air interface and (C) transferred to a solid substrate followed by (D)–(F) embedding into a polymer layer. Adapted with permission from ref. 131.

Open Access Article. Published on 26 April 2022. Downloaded on 9/25/2023 10:08:45 AM.
This article is licensed under a Creative Commons Attribution 3.0 Unported Licence.

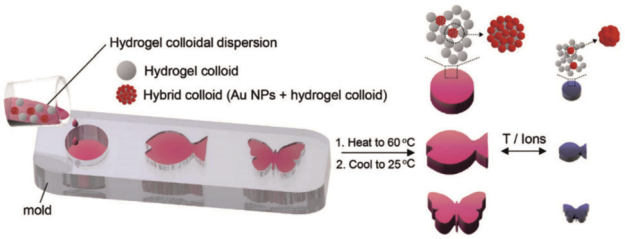


Fig. 12 Preparation of plasmonic hydrogel objects with tunable optical absorption by casting responsive microgels with and without gold nanoparticle decoration in an appropriate mold. A color change due to plasmonic coupling of the gold nanoparticles is observed upon swelling and collapsing of the responsive polymer colloids upon an external temperature or ionic stimulus. Adapted under CC-BY from ref. 77.

hydrogel relief gratings with a period <300 nm could be attached to a flat gold film.[142] Similarly, this approach was adopted by using four-beam UV-LIL for the preparation of non-connected arrays of responsive pNIPAAm-based hydrogel domains with a diameter <200 nm that were wrapped around lithographically-made gold nanocylinders.[118]

Let us note that there is often the necessity to chemically link responsive polymer networks to the surface of the metallic or oxide nanostructures in order to yield a stable system. For the networks that are prepared *via* photocrosslinking of polymer chains in contact with these nanostructures, linker molecules bearing thiol headgroups can be employed that form self-assembled monolayers on most commonly used gold surfaces (see Fig. 6C) or silane headgroups reacting with oxide materials. For such photoactive groups, benzophenone[143] or anthraquinone molecules[144] can be used to simultaneously attach and crosslink the polymer chains to plasmonic or other type of optical structures upon irradiation with UV light[143,145] or by exploiting a two-photon absorption process.[144]

### 3.3 Plasmonic heating

As numerous thermoresponsive polymers have been discovered, among possible stimuli available for actuating responsive hydrogels temperature is arguably the most commonly used. A temperature change stimulus $\Delta T$ can be applied with electronic devices such as Peltier elements or resistive microheaters. However, these devices typically allow for temperature control of macroscopic bulk volumes and thus are inevitably slow and not suitable for rapid actuating of miniaturized responsive hydrogel structures. An attractive solution to this problem offers a technique that is referred to as plasmonic heating.[146] It allows for rapid and spatially confined heating of small volumes that comprise metallic nanostructures by using optical excitation of LSPs and their dissipation to heat by Ohmic losses. The rate of heating and dissipation of the heat to the surrounding medium depends on the particular design of the plasmonic structures. As illustrated in Fig. 13A, irradiation of an individual metallic nanoparticle leads to harvesting of the light energy followed by its conversion to heat with an absorption cross-section of $\sigma_{abs}$. Then, the nanoparticle functions as a

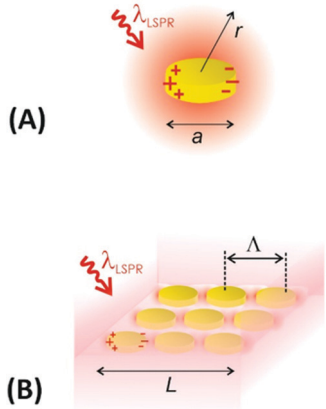


Fig. 13 Schematics of plasmonic heating by energy dissipation of optically excited LSPs for (A) an individual nanoparticle and (B) collective heating of closely packed plasmonic nanoparticle arrays.

local heat source, and the temperature locally increases at its surface by:

$$\Delta T = \frac{I\sigma_{abs}}{4\pi a\kappa} = I\frac{2\pi n_h a^2}{\lambda\kappa}\mathrm{Im}\left\{\frac{n_m^2 - n_h^2}{n_m^2 + 2n_h^2}\right\}, \quad (1)$$

where $I$ is the irradiation intensity of the heating light beam that impinges with a wavelength $\lambda$ on a metallic nanoparticle with size $a \ll \lambda$. The generated heat is dissipated to the surrounding dielectric medium with thermal conductivity $\kappa$ and density $\rho$. The right-hand-side of the eqn (1) holds for the $\sigma_{abs}$ of a spherical metallic nanoparticle with a diameter $a$, metal refractive index $n_m$, and the refractive index $n_h$ of the surrounding dielectric material. The temperature change $\Delta T$ decreases with the distance $r$ from the nanoparticle as $1/r$ (for $r \gg a$) and responds to changes in the irradiation intensity $I$ with a time constant:

$$\Delta t = \frac{a^2}{\kappa/\rho c_p}, \quad (2)$$

where $c_p$ is the heat capacity. The factor $\kappa/\rho c_p$ is of $\sim 10^{-3}$ cm$^{-2}$ s$^{-1}$ for a structure surrounded by water that is kept at ambient room temperature.

Importantly, the time response $\Delta t$ and temperature change $\Delta T$ can differ substantially when ensembles of nanoparticles are used, as a collective heating effect may occur. Assuming 2D metallic nanoparticle arrays that are arranged with a period $\Lambda$ and which are irradiated by a light beam with a footprint diameter of $L$, the contribution by collective heating become important. These two regimes can be distinguished *via* the following dimensionless parameter:

$$\xi = \frac{\Lambda^2}{3La}. \quad (3)$$

For large $\xi > 1$, each nanoparticle serves as an independent source that quickly heats only its close vicinity. However, the collective heating effect becomes dominant for small $\xi < 1$ and is accompanied by a stronger increase of temperature $\Delta T$ over the whole irradiated area with a footprint diameter $L$.

Open Access Article. Published on 26 April 2022. Downloaded on 9/25/2023 10:08:45 AM.
This article is licensed under a Creative Commons Attribution 3.0 Unported Licence.

Consequently, the time constant $\Delta t$ is then substantially prolonged to:

$$\Delta t = \frac{L^2}{\kappa/\rho c_p}. \quad (4)$$

### 3.4 Plasmonic characterization of responsive hydrogel films and microgels

The metallic nanostructures embedded or contacted to responsive hydrogels allow for the optical measurement of the polymer network characteristics, including volumetric changes, the swelling ratio $Q_V$ and the polymer volume fraction $\Phi_p$. These can be measured in equilibrium for static structures, but also their optical interrogation can provide a means for rapid probing of the time-dependent swelling and collapsing process of the polymer networks.

The detuning of the LSPR wavelength on arrays of metallic nanoparticles due to a refractive index change $\Delta n_h$ was exploited for rapid monitoring of swelling and collapsing of thermoresponsive polymers occurring within the tightly confined surface plasmon field. This approach offers the possibility to rapidly heat *via* LSP excitation and simultaneously probe the swelling state utilizing the same metallic nanostructures. In a recent work, arrays of elliptical-shaped nanoparticles were prepared by EBL and employed to characterize the responsive properties of pNIPAAm polymer chains that were grafted to these structures.[147] The collective heating effect was dominant, and irradiating a footprint diameter of $L = 3$ μm with a near-infrared heating beam allowed to generate temperature changes with a time constant of $\Delta t \sim 16$ μs. The pNIPAAm chains forming a brush with a thickness of 30 nm responded to a quick temperature variation across the LCST with a transition time of 160 μs. A similar approach was reported for the observation of pNIPAAm network layers with a thickness of 800 nm (in the swollen state) that covered arrays of elliptical gold nanoparticles prepared by UV-LIL, see Fig. 14A and B.[148] As seen in Fig. 14C, when monitoring the LSPR wavelength variations over time for the collapse (manifested as a gradual increase in LSPR wavelength) and swelling (seen as a gradual decrease of LSPR wavelength), transition times of several milliseconds were determined. The response of such pNIPAAm networks is substantially slower compared to the pNIPAAm brushes, which can be ascribed to the effect of the crosslink junctions in the polymer network, hindering diffusion of water molecules through the networks and giving rise to additional collective effects related to the imposed stress. Moreover, additional, substantially slower rearrangement of the polymer chains occurs simultaneously at longer time scales.[18]

Contrary to such slow transitions, a dramatically faster sub millisecond response was observed for gold nanoparticle aggregates with attached pNIPAAm chains.[149] Such a fast transition was monitored for clusters of near field-coupled aggregated gold nanoparticles that expanded by the rapid (spring-loaded) conversion of pNIPAAm chains from a hydrophobic globular state to a hydrophilic stretched conformation. LSPR on metallic

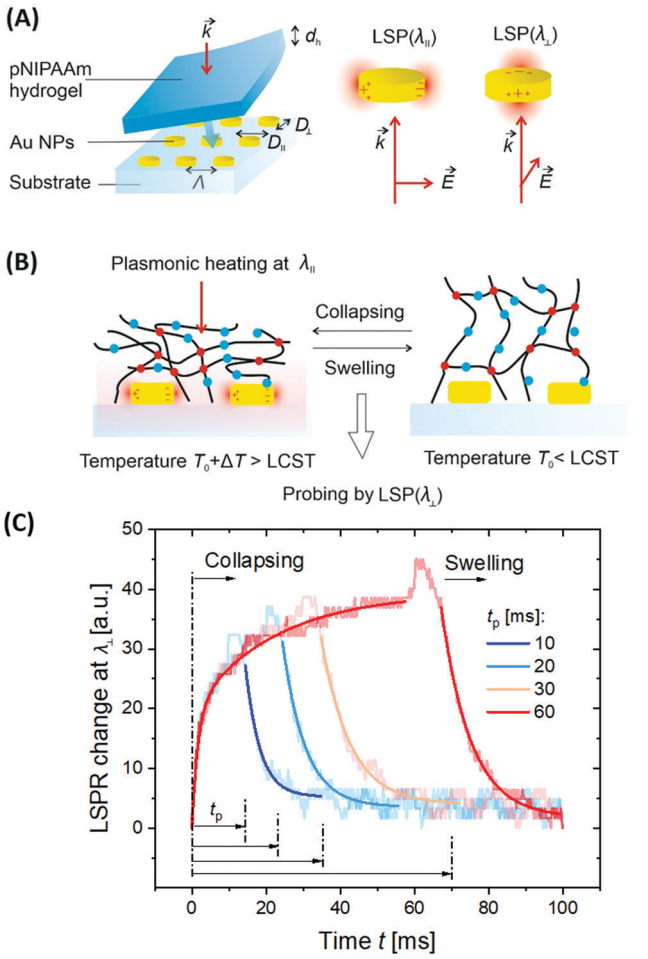


Fig. 14 (A) Schematic illustration of the optical structure designed to monitor (B) rapid swelling and collapsing of NIPAAm-based polymer networks with (C) example of the obtained kinetics. Adapted with permission from ref. 148.

colloidal nanoparticles is associated with an enhanced scattering crosssection, which can be utilized to track their motion in suspension by dynamic light scattering (DLS). Furthermore, the influence of plasmonic heating on the diffusion behaviour of gold nanoparticles capped with a pNIPAAm hydrogel shell was studied by DLS.[92] The observed effect was attributed to a change in local solvent viscosity as well as to a variation of the hydrodynamic radius by swelling and collapsing of the pNIPAAm shell.

LSPR supported by nanoscopic gold rods was also applied for the investigation of polymers responsive to other, different stimuli. Polyaniline (pANI) can be incorporated into hydrogels,[92] which makes it responsive to pH changes and electro-oxidation/reduction. The electronic response was first investigated on arrays of cylindrical and rod-shaped gold nanoparticles prepared by EBL on an ITO substrate and coated with a 100 nm pANI film. A reversible wavelength shift of the LSPR by 70 nm was measured with a (non-optimized) switching time <10 s.[150] To increase the magnitude of the LSPR wavelength shift, a particular architecture of chemically synthesized

Open Access Article. Published on 26 April 2022. Downloaded on 9/25/2023 10:08:45 AM.
This article is licensed under a Creative Commons Attribution 3.0 Unported Licence.

gold rod-shaped nanoparticles was proposed that were capped over their whole surface with a pANI shell of about 8 nm thickness. The structure enabled repeated shifting of the LSPR by 149 nm with the applied voltage.[151] A similar approach to monitor the switching between a proton-doped and non-doped states upon changing the pH was reported for pANI-coated gold nanoparticles with a transition time of several tens of seconds.[152]

Besides LSPR, also propagating surface plasmons – PSPs – can be utilized for the observation of responsive hydrogels optical systems with Kretschmann configuration that typically support SPR biosensors. For thin hydrogel films on flat gold surfaces, additional guided modes can travel along the polymer film as it exhibits a higher refractive index $n_h$ than that of the adjacent aqueous medium. On this basis, SPR and optical waveguide spectroscopy (OWS) were combined to monitor the responsive characteristics of pNIPAAm-based hydrogels.[153] The example in Fig. 15 shows angular reflectivity spectra for a pNIPAAm-based hydrogel film that gradually collapses upon increasing temperature $T$ from below to above the phase transition of the polymer network. The density gradient of the hydrogel layer, represented by the polymer volume fraction $\Phi_p$, was reconstructed from the analysis of the resonances in the spectrum associated with the coupling of the incident light to PSPs and hydrogel optical waveguide modes (manifested as a series of narrow dips in the angular reflectivity in Fig. 15A). Moreover, OWS studies were employed to characterize pNIPAAm-nanoparticle composite films on solid supports,[98] or free-standing membranes,[154] that were tailored for blocking or opening the structure for the diffusion of target molecules to the plasmonic sensor surface. It is worth noting that swelling of surface-attached responsive hydrogel films is predominantly restricted to the direction perpendicular to the surface (1D swelling) due to lateral confinement by covalent bonding to the substrate. This effect establishes a strain along the interface that is partially released by buckling of the hydrogel surface, as observed from the increased scattering of light resonantly coupled to guided PSPs and hydrogel optical waveguide modes. Besides flat films, swelling and collapsing of periodic arrays of pNIPAAm features attached to a flat gold film were probed by PSP-enhanced diffraction,[141] and by PSP Bragg scattering.[142] These studies were performed in order to elucidate the different contributions by 1D swelling/collapsing in the direction perpendicular to the surface and by lateral swelling of the topographic features in the lateral direction, resulting in a quasi-3D swelling behavior.

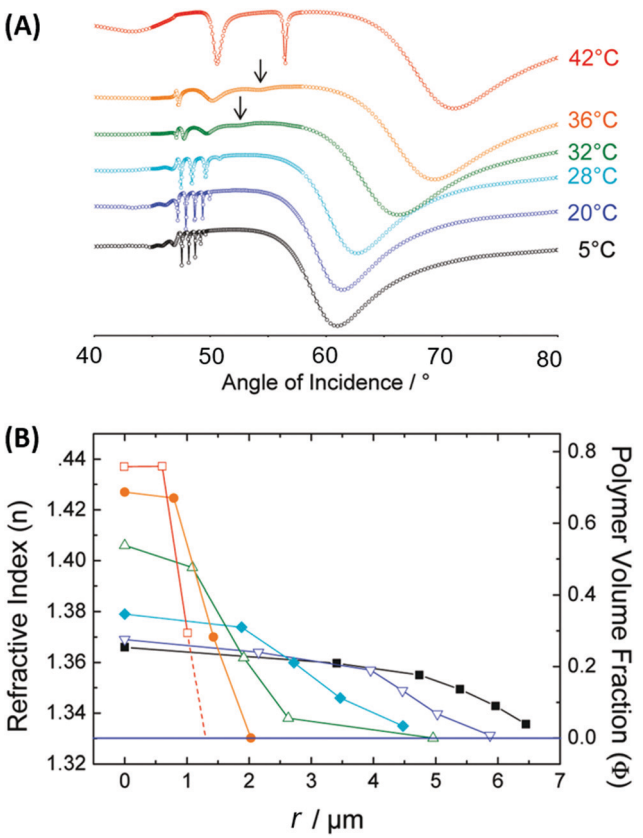


Fig. 15 (A) Measured angular reflectivity spectra in combined SPR and OWS observation of the temperature-induced collapse of a pNIPAAm-based hydrogel film. (B) Reconstructed profile of the refractive index $n_h$ and polymer volume fraction $\Phi_p$ as a function of a distance $r$ from the interface, to which the hydrogel film is attached. Adapted with permission from ref. 55 ©2010, American Chemical Society.

## 4. Plasmonic (bio)sensors

### 4.1 Surface plasmon resonance-based readout

Plasmonic nanostructures, combined with responsive hydrogels, were employed in optical sensors and biosensors. The optical sensor response is generated by a physical stimulus or by specific interaction with the target species present in the analyzed liquid sample *via* induced changes in the responsive hydrogel characteristics. This type of optical readout can be implemented *via* functional moieties incorporated into the hydrogel polymer network in order to translate the specific interaction with a target analyte to variations in the crosslink density $\nu_c$, to a change in the hydrophilicity of the network, or other effects that affect the swelling ratio $Q_v$. In general, such stimulus-induced modulation of the swelling ratio $Q_v$ can be converted to an optical signal *via* SPR probing of the associated refractive index changes $\delta n_h$ or through LSPR near-field coupling on the metallic nanostructures responding to hydrogel volumetric variations. These mechanisms were exploited in physical sensors (temperature, pH) as well as in chemical sensors and biosensors for the detection of molecular analytes related to medical diagnosis (glucose, cancer biomarkers).

pNIPAAm microgels conjugated with gold nanoparticles were implemented as plasmonic sensor elements in a smart wearable device that allows naked-eye readout of temperature variations in contact with skin (Fig. 16A).[155] These stretchable sensor elements allowed to track temperature variations in the range between 25 to 40 °C within one second by the wavelength shift of the LSPR extinction peak due to the induced swelling ratio variation $\delta Q_v$ and a respective modulation of the distance-

Open Access Article. Published on 26 April 2022. Downloaded on 9/25/2023 10:08:45 AM.
This article is licensed under a Creative Commons Attribution 3.0 Unported Licence.

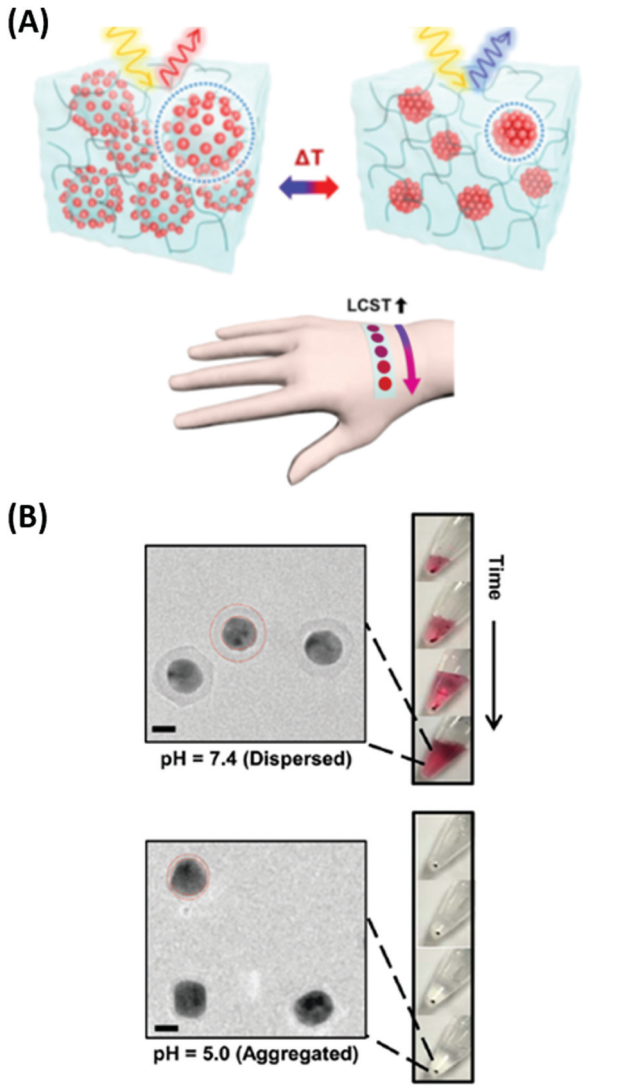


Fig. 16 (A) Colorimetric sensor utilized by plasmonic microgels contacted with human skin and responding to variations in temperature. Adapted with permission from ref. 155. (B) TEM images of the deposited Au-CEA2 NPs in a dispersed and aggregated state that were used for the monitoring of intracellular pH. Scale bars: 10 nm. Adapted with permission of RSC from ref. 39.

dependent LSP near-field coupling (see Fig. 16A). Another approach has been adopted to follow a pH change in the range from 1 to 12 by measuring the refractive index variations associated with swelling and collapsing of an acrylamide-based hydrogel.[156] There, a fiber optic probe was used to observe the resonant excitation of PSPs in the transmission wavelength spectrum of a layered architecture comprising silver, indium tin oxide, aluminum, and a pH-responsive hydrogel. Monitoring of pH changes in very small volumes was shown recently.[39] Here, gold nanoparticles capped with a thin layer of poly(methacrylic acid) (MAA) or poly(2-carboxyethyl acrylate) (CEA) were introduced to HeLa cells. Intracellular pH changes triggered the shell swelling (see Fig. 16B) and led to an aggregation of the nanoparticles accompanied by a red-shift and a broadening of the LSPR bands, observable as color changes in dark-field optical microscopy.

Sensors based on a hydrogel binding matrix with incorporated boronic acid moieties were reported for the selective detection of glucose molecules.[157] The responsiveness derives from the reversible, pH-dependent formation of a boronate ester between the boronic acid and the *cis*-diol-motif present in glucose (see Fig. 17A),[58,158] resulting in a transition of the hydrogel matrix from a lesser to a more hydrophilic state and consequently leading to a volumetric increase. This volume increase can be optically measured by the plasmonic response of gold nanoparticle arrays made by lithography and covered by a glucose-responsive HEMA-based hydrogel layer with incorporated boronic acid moieties. Upon binding of glucose molecules, the hydrogel swelled, and the LSPR wavelength was reversibly blue-shifted (see Fig. 17B). Additionally, the hydrogel matrix kept larger molecules away from the plasmonically probed surface, prohibiting unspecific binding of other constituents, like proteins, in medical samples and enabling the non-invasive continuous monitoring of this target analyte in tear fluid. The same interaction mechanism was employed in a glucose sensor, where a pNIPAAm-based microgel with 3-aminophenyl boronic acid moieties was deposited on a perforated metallic film at an optical fiber tip.[159] Here, the binding of glucose was accompanied by a swelling of the gel and an increase in its $Q_v$, which blue-shifts the wavelength at which PSP modes were resonantly excited at the fiber optic probe, as monitored in the reflected wavelength spectrum (see Fig. 17C).

Sensors relying on the variation of the crosslinking density $\nu_c$ mediated by target analyte-binding in responsive hydrogels were also utilized in another approach for the detection of glucose. In this modality, a displacement assay relying on the specific interaction of glucose with concanavalin A (ConA) moieties was exploited.[160] For SPR readout, a poly(NIPAAm-*co*-glycosyloxyethyl methacrylate) microgel film was fabricated on a gold layer, which contracted upon addition of multivalent ConA due to an increase of the crosslinking density $\nu_c$. Competitive binding of glucose from the analyzed sample by the incorporated ConA units inside the hydrogel led to a disruption of the ConA crosslinks, subsequent microgel reswelling, and an increase in $Q_v$ accompanied by a decrease in the refractive index $n_h$ (Fig. 18A).

A system with the reversed modulation of crosslinking density $\nu_c$ was pursued with bioresponsive p(NIPAAm-*co*-AAc) nanogels carrying multivalent protein binding (MPB) moieties for detection of PD-1 proteins (Fig. 18B).[161] Small multivalent cations (*e.g.*, $Ca^{2+}$, $Fe^{2+}$, and $Fe^{3+}$) can be distinguished by SPR over monovalent cations (*e.g.*, $Na^+$ and $K^+$) as they form a protein complex with the analyte. Multivalent binding of polyclonal antibodies was also explored by using a pNIPAAm microgel to detect progesterone by the optical etalon principle.[162] Like in the previous work, an increase in the hydrogel cross-linking density $\nu_c$ due to the specific interaction with the analyte was monitored *via* the induced changes in the hydrogel refractive index $n_h$.

Open Access Article. Published on 26 April 2022. Downloaded on 9/25/2023 10:08:45 AM.
This article is licensed under a Creative Commons Attribution 3.0 Unported Licence.

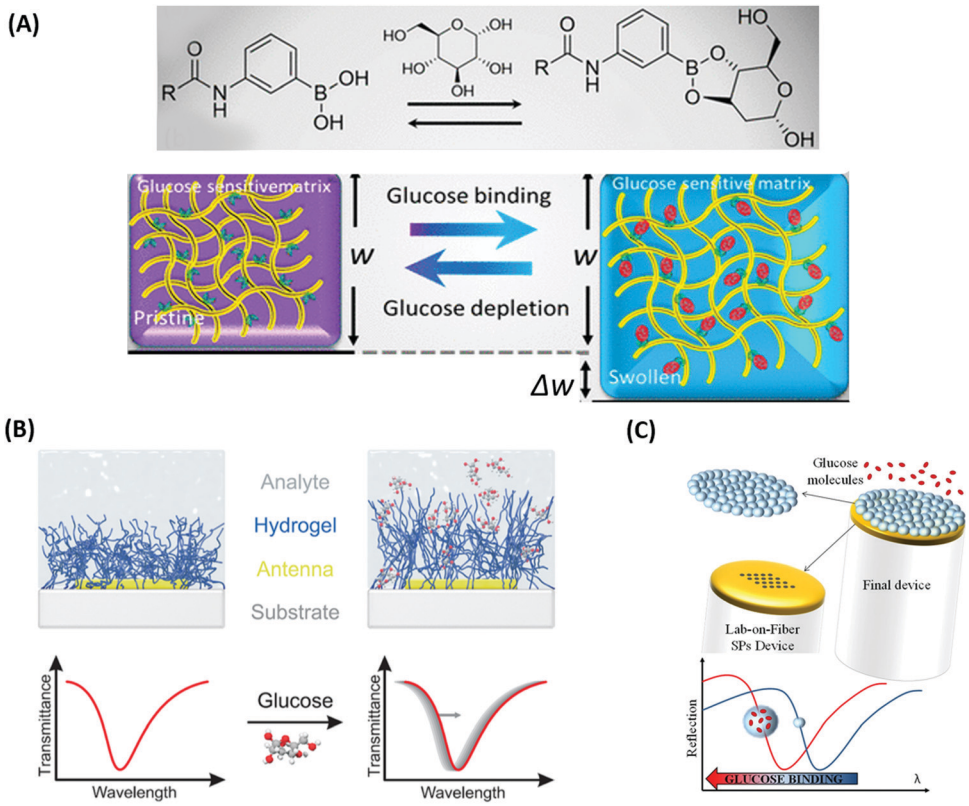


Fig. 17 (A) Illustration of the glucose binding-induced swelling of the phenylboronic acid-functionalized hydrogel matrix that generates a change in the refractive index. Adapted under CC-BY, 4.0 from ref. 158. (B) Layout and sensing principle relying on plasmonic nanoparticles supporting LSPs that probe responsive hydrogel swelling due to a refractive index change induced by glucose binding. Adapted with permission from ref. 157, © 2015, American Chemical Society. (C) Detection scheme for probing with PSPs a glucose-responsive microgel matrix attached to a perforated gold film on an optical fiber tip. Adapted under CC-BY from ref. 159.

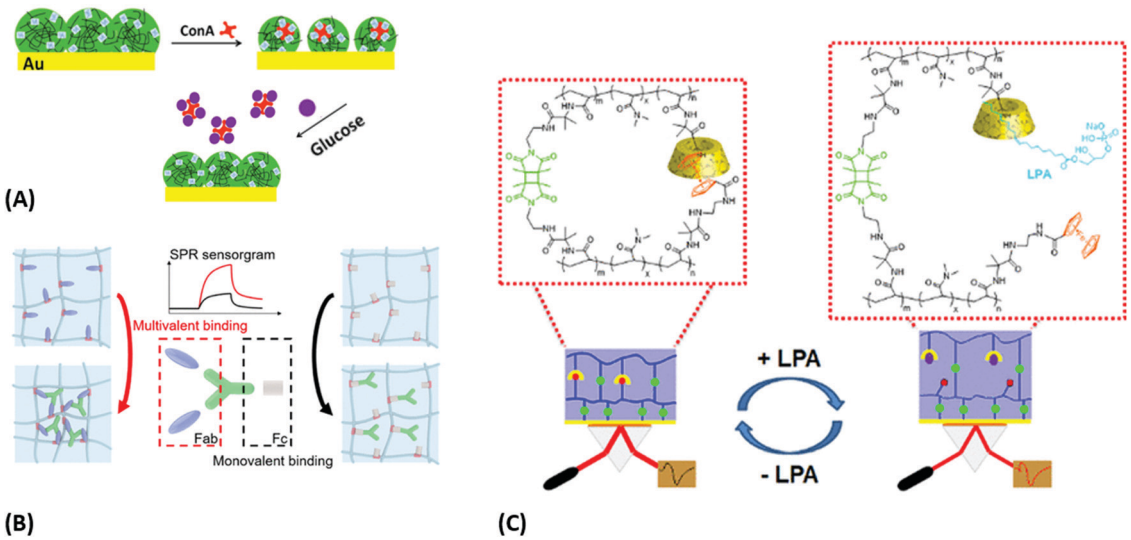


Fig. 18 Plasmonic sensor concepts based on a modulation of crosslinking density: (A) platform with p(NIPAAm-*co*-glycosyloxyethyl methacrylate) microgels for glucose binding. Adapted with permission from ref. 160, © 2019, American Chemical Society. (B) Principle of multivalent protein binding and corresponding sensorgram, discriminating multivalent (left) and monovalent binding (right). Adapted with permission from ref. 161, ©2020, American Chemical Society. (C) Schematic of the sensor and its response mechanism based on disrupting β-CD and Fc complexes with target molecule LPA. Adapted with permission from ref. 163, ©2020, American Chemical Society.

Open Access Article. Published on 26 April 2022. Downloaded on 9/25/2023 10:08:45 AM.
This article is licensed under a Creative Commons Attribution 3.0 Unported Licence.

Another report communicated bioresponsive supramolecular hydrogels that were probed by SPR and OWS techniques (Fig. 18C).[25,163] A reversible sensor platform exhibiting two different crosslinks was demonstrated: a covalent photocrosslinker and a host-guest recognition pair from β-cyclodextrin (β-CD) and ferrocene (Fc). Increased swelling in the presence of the small targets adamantane amine (ADA) and the cancer marker lysophosphatidic acid (LPA) occurred due to breaking of the non-covalent bond between β-CD and Fc, which led to a decrease in the refractive index $n_h$. Monitoring these changes allowed to determine the analyte concentration with a limit of detection of $2.43 \times 10^{-5}$ M for ADA and 2 μM for LPA under plasma-like conditions. The achieved results document the potential of this approach to establish a new direction for small analyte sensing with direct detection format.

An alternative sensing principle was proposed with an ionoresponsive hydrogel for the detection of estradiol 17β in milk samples by a Fabry–Perot etalon-based sensor system.[164] In this setup, a responsive microgel layer was sandwiched between two metallic layers, with the outer layer being porous and modified with a DNA aptamer. The affinity interaction of the aptamer with the target analyte estradiol 17β led to blocking of the pores and a hindered diffusion of $Na^+$ or $Ca^{2+}$ ions into the cavity with the responsive microgel. When estradiol 17β was bound to the aptamer, ion diffusion and subsequent collapse of the microgel layer was hindered, which could be observed as a change in the Fabry–Perot fringes. In this detection scheme, the external stimulus of the responsive hydrogel is spatially separated from the specific analyte recognition (see Fig. 19).

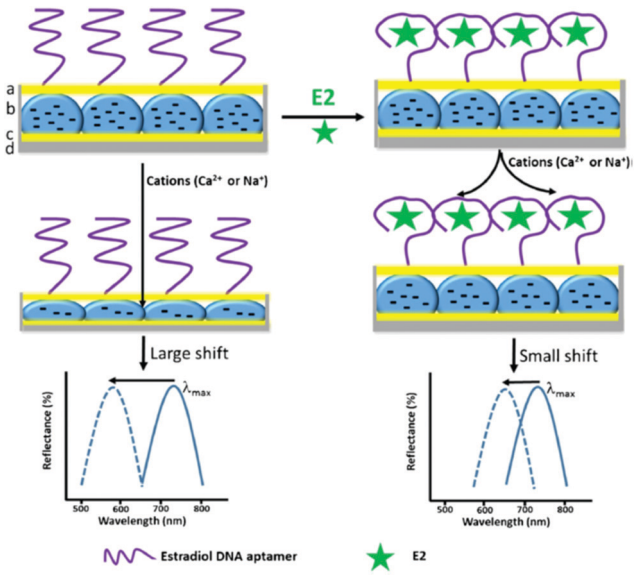


Fig. 19 Schematics of an optical etalon showing the sensing mechanism, with the DNA aptamer binding estradiol 17β (E2) and forming a specific secondary structure that blocks $Na^+$ or $Ca^{2+}$ from entering the etalon microgel layer. The extent of blocking is directly proportional to the concentration of E2 in the sample, as documented by the typical reflectance spectrum obtained from this optical setup. Adapted by permission from Springer Nature, ref. 164, ©2018.

### 4.2 Plasmonically-enhanced optical spectroscopy readout

Besides probing the changes in refractive index $n_h$ and $Q_v$ that occur inside responsive hydrogels designed to specifically interact with the target analyte, these materials can also serve in optical spectroscopy-based detection of species trapped in their network. The responsive hydrogel material is typically utilized to enhance the collection efficiency of target analyte from the liquid sample capitalizing on the large surface area of permeable 3D mesh structure of the polymer network. After trapping the analyte, the responsive hydrogel binding matrix can be collapsed with an external stimulus, and by this allows compacting the captured analyte in the vicinity to metallic nanostructures. These zones represent the most sensitive region of the sensor and thus the initially weak optical spectroscopy signal is then amplified by the hydrogel collapse. At this stage, the optical readout is performed by the confined surface plasmon field that exhibits increased intensity and is associated with enhanced local density of optical states. In addition, the possible reconfiguration of plasmonic nanostructures using responsive hydrogels offers attractive means to actively form plasmonic hotspots (volume where the optical field is tightly confined) for probing the locally captured target analyte with advanced readout sensitivity and reproducibility.

In surface plasmon-enhanced spectroscopy (PEF, also referred to as surface-enhanced fluorescence SEF), the plasmonic nanostructures are tuned to confine the electromagnetic field intensity at wavelengths that are coincident with the absorption and emission bands of chosen emitters. These emitters are typically organic fluorophores, serving as labels when conjugated with the biomolecules to constitute an assay for the target analyte. The possibility to post-modify the permeable structure of responsive hydrogels with functional biomolecules as ligands was pursued to increase the binding capacity of the sensor surface and thus improve the probability of the specific analyte capture.[91] It should be noted that depending on the density of ligand molecules in the hydrogel matrix, the target analyte can diffuse inside the gel only a certain distance from its outer interface in contact with the analyzed liquid sample, which is typically several hundreds of nanometres.[165] However, such thick binding matrices cannot be efficiently probed with the confined field of surface plasmons that probe depth below several tens of nanometres for LSPs or about a hundred nanometres for PSPs. Therefore, there was investigated a sensing concept, where the efficient analyte capture in the swollen gel state is followed by triggering the gel collapse in order to drag the analyte to a smaller volume probed with the confined surface plasmon field.

The realization of this sensing concept was reported for the immunoassay-based detection of IgG molecules labelled with Alexa Fluor 647 fluorophore using a pNIPAAm-based hydrogel binding matrix attached to a gold surface.[166] The matrix exhibited a thickness of about 750 nm in the swollen state, and after the analyte capture it as collapsed to about 180 nm by increasing the ionic strength with 5 M NaCl solution. This collapse led to an increase in the plasmon-enhanced fluorescence intensity by a factor of about 3.1 when the interface was

Open Access Article. Published on 26 April 2022. Downloaded on 9/25/2023 10:08:45 AM.
This article is licensed under a Creative Commons Attribution 3.0 Unported Licence.

probed by PSP modes at the wavelength matching the fluorophore label absorption band. In order to utilize a more convenient temperature stimulus, an immunoassay detection scheme was developed that employs arrays of cylindrical gold nanoparticles wrapped with a pNIPAAm-based network of about 200 nm thickness in the swollen state, which compacts around the gold nanoparticles when exceeding the transition temperature of the polymer, Fig. 20A.[118] The hydrogel network was postmodified with an IgG antibody ligand, and the affinity binding of target IgG antibody that was conjugated with a fluorophore was monitored by the LSP-enhanced fluorescence signal. As can be seen in Fig. 20B, the affinity binding manifests itself as a gradually elevated fluorescence intensity. After the affinity binding experiment, temperature $T$ was increased above the phase transition temperature $T_c$ of the unmodified pNIPAAm. However, a respective fluorescence signal intensity increase of only 20% was observed (marked as red arrow in Fig. 20B), which can be attributed to the fact that the thermoresponsive properties of the pNIPAAm-based network are severely impaired after the postmodification with large molar mass ligands such as IgG. By studying this effect in more detail, it was observed that the temperature-induced collapse of similar pNIPAAm layers led to a decrease in the swelling ratio $Q_v$ by a factor of 4.7, but after its postmodification with IgG this ratio dropped to only 1.6.[167] This work suggests that a possible route to circumvent this problem is using ligands with lower molar mass imposing smaller changes to the thermoresponsive characteristics of the pNIPAAm binding matrix. Fig. 20C shows for the polymer matrix modified with a smaller peptide ligand that the temperature-induced collapse led to a similar change in the swelling ratio $Q_v$ by a factor of 4.3 as in the case of the pristine gel layer.

At short distances $d < 15$ nm from the metal surface of plasmonic nanostructures, a strong effect of fluorescence quenching competes with the PEF. Therefore, small metallic nanoparticles that exhibit a tighter confined LSP field than PSPs on continuous metallic films are typically less efficient in PEF due to the strongly pronounced effect of quenching occurring at their close proximity. The effect of quenching of fluorescence was reported for colloidal silver nanoparticles with about 50 nm thick polymer shells based on a pNIPAAm hydrogel.[168] In this study, the absorption wavelength of the selected emitters was tuned to match the LSP wavelength of the particles. It was shown that upon collapse of the pNIPAAm shell towards the surface of silver core nanoparticles, the fluorescence intensity of the hydrogel-associated emitters decreased in comparison to the swollen state. Nevertheless, this type of material is attractive for the amplification of weak Raman scattering signals and can serve as an efficient SERS substrate since it is not prone to quenching. Fig. 21A shows no measurable Raman signal when bringing Raman-active analyte molecules in contact with silver nanoparticles capped by a densely collapsed pNIPAAm shell at an elevated temperature. However, when decreasing the temperature below the phase transition, the hydrogel structure swells and becomes permeable for the Raman active molecule, which can diffuse to the silver surface,

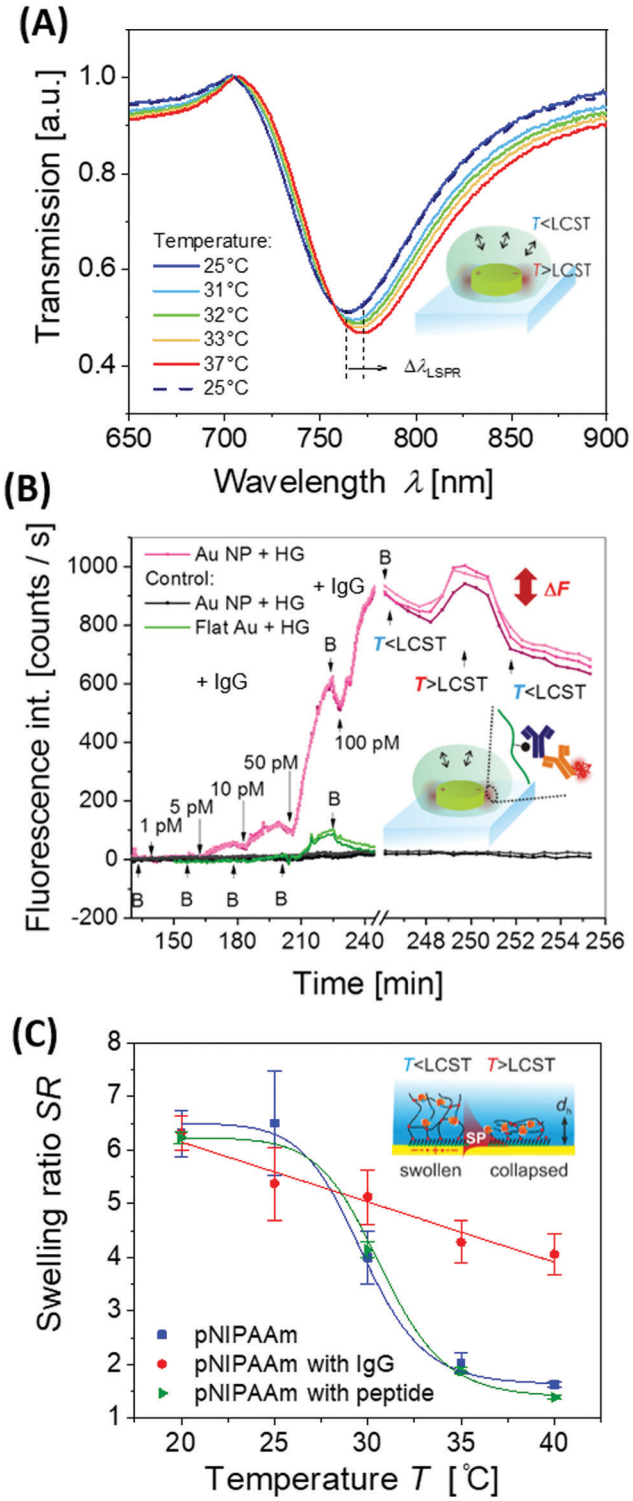


Fig. 20 (A) Example LSPR spectra and (B) PEF readout upon affinity binding to an IgG-functionalized pNIPAAm binding matrix wrapped around gold nanoparticles in an arrays after active compacting of the captured analyte at the plasmonic hotspot by a temperature stimulus. Adapted under CC-BY 4.0 from ref. 118. (C) Changes in responsive properties of a pNIPAAm-based hydrogel layer due to its post-modification with a high molar mass protein ligand (IgG antibody) and a low molar mass peptide ligand. Adapted under BY-NC-ND 4.0 from ref. 167.

Open Access Article. Published on 26 April 2022. Downloaded on 9/25/2023 10:08:45 AM.
This article is licensed under a Creative Commons Attribution 3.0 Unported Licence.

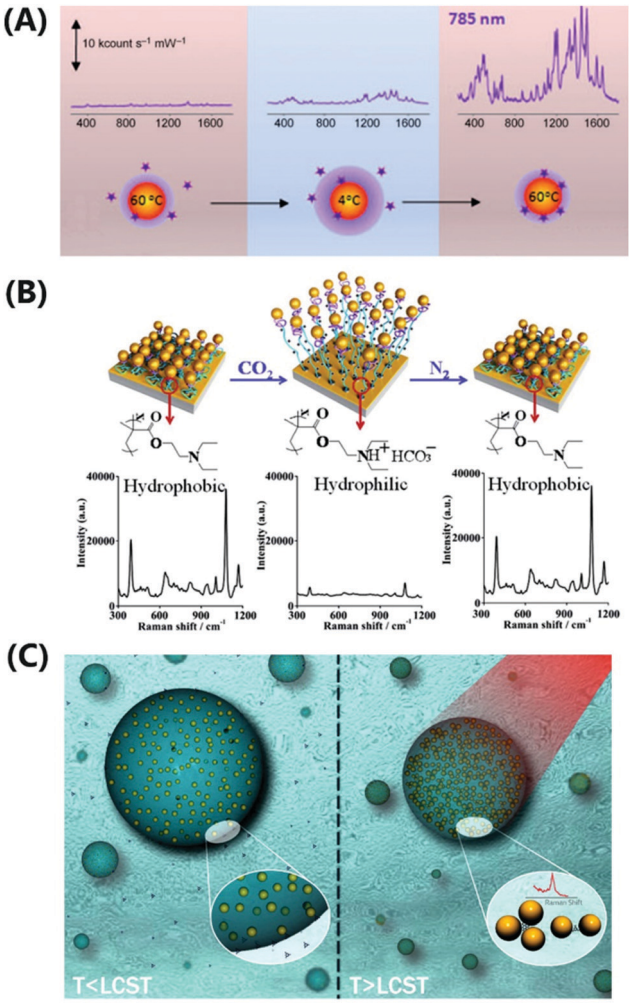


Fig. 21 Overview of geometries utilized for the SERS detection that combine the responsive polymer and metallic nanostructure building blocks: (A) individual metallic nanoparticle capped with a pNIPAAm hydrogel shell for collecting and compacting of target molecules on its surface within the plasmonic hotspot. Adapted with permission from ref. 168. (B) Plasmonic nanoparticles attached to a flat metallic surface *via* a responsive polymer brush architecture that allows to control over their distance and formation of a tightly confined plasmonic hotspot. Adapted with permission from ref. 168 and 121. (C) Thermoresponsive microgel beads loaded with metallic nanoparticles for collection and trapping of a target analyte in the plasmonic hotspot formed upon the collapse of the network. Adapted with permission Royal Society of Chemistry from ref. 169.

as observable by the appearance of Raman peaks. This signal is strongly enhanced by subsequent heating above the hydrogel phase transition, which drives the Raman-active molecules locked inside the polymer network towards the plasmonic hotspot at the silver surface. Interestingly, these data show that the pNIPAAm network itself does not show pronounced Raman peaks.

With the design of more complex architectures and engineering of the plasmonic hotspot, the Raman scattering efficiency by the plasmonic nanoparticles can be further increased. In order to achieve stronger confinement of the electromagnetic field (and respective enhancement of the field intensity), near-field coupling of metallic nanostructures has been investigated. The implementation of this concept was described in a recent publication with a layer of pNIPAAm microgels sandwiched between a flat gold layer and a permeable film of gold nanoislands.[170] At temperatures below the hydrogel phase transition, the polymer network provides a permeable structure that allows the diffusion of target analyte molecules. Upon a temperature increase these molecules are trapped inside the hydrogel matrix by the microgel collapse, which also reduces the gap between the gold nanoislands and the flat gold film. In consequence, a plasmonic hotspot is formed that leads to an increased SERS signal. This concept was demonstrated for the detection of trinitrotoluene, L-tyrosine, and DNA at detection limits of $10^{-11}$ M. Similar phenomena were exploited by nanostructured gratings coated with a pNIPAAm layer for sensing of azobenzene dyes at a concentration as low as $10^{-14}$ M.[171]

Temperature-controlled near-field coupling between synthetically prepared gold nanoparticles and a flat gold film was reported with a pNIPAAM brush as a linker.[120] The gold nanoparticles were decorated with a Raman-active methylene blue dye *via* click coupling. The SERS signal intensity of the system increased upon raising temperature above the polymer phase transition $T_c$ through compaction of the pNIPAAm-based linker as the gap between the gold nanoparticles and the flat gold surface was reduced. A similar geometry was utilized to construct a $CO_2$ sensor based on SERS readout.[121] In this case, a diblock copolymer brush of poly(*N*,*N*-diethylaminoethyl methacrylate) (pDEAEMA) and pAAm was attached to the gold surface, followed by coupling of chemically synthesized gold nanoparticles. These nanoparticles were conjugated with 4-mecaptophenol to serve as Raman-active reporter, see Fig. 21B. When this sensor architecture was exposed to $CO_2$ in aqueous medium, the pDEAEMA block was protonated and formed ion pairs with the carbonic acid, which led to an increased swelling. Consequently, the gold nanoparticles moved further away from the gold surface (from 15 to 26 nm) and a decrease in SERS signal was detected.

Another class of sensor architectures that allows modulation of the near-field coupling between metallic nanoparticles has been realized with microgels that were loaded with metallic nanostructures in their core, see Fig. 21C. Specifically, a pNIPAAm microgel with embedded 30 nm silver nanoparticles was employed as the SERS transducer.[172,173] Temperature changes then modulate the swelling state of the thermoresponsive microgels and by this means the distance between the nanoparticles is controlled. Accordingly, there is increased the SERS signal originated from analyte molecules that infiltrated the microgel polymer network. An analogous increase of the SERS signal was observed with a scaffold of gold nanoparticles coated with pNIPAAm by trapping and locally concentrating analyte molecules in the plasmonic hotspots through a temperature increase.[169] Limits of detection was determined for adenine ($10^{-6}$ M), melamine ($10^{-5}$ M), and 2-naphthalenethiol ($10^{-6}$ M) in an aqueous solution. By employing gold nanorods with a copolymer coating of NIPAAm and *N*-vinyl-2-pyrrolidone, SERS enhancement upon a temperature-induced collapse was demonstrated with the herbicide diquat as analyte.[174]

Open Access Article. Published on 26 April 2022. Downloaded on 9/25/2023 10:08:45 AM.
This article is licensed under a Creative Commons Attribution 3.0 Unported Licence.

In most of these examples, the SERS enhancement factor and the hotspot formation were tuned by a temperature variation and the associated collapse of the thermoresponsive microgels. An alternative approach was proposed by a combination of SERS and colorimetric readout for pH sensing operating in the range of 1 to 12.[175] In this platform, the pH trigger acted on pANI-coated gold nanorods that were encapsulated in microgels of poly(ethylene glycol)diacrylate.

In order to increase the target analyte collection efficiency in the SERS-based detection, there was utilized its selective pre-concentration at the surface silver nanoparticles by their coupling to molecular-imprinted polymer cavities and thermoresponsive pNIPAAm.[176] Binding and release of the target analyte rhodamine 6G was controlled by adjusting the pNIPAAm swelling state *via* the temperature. At 30 °C the target analyte was selectively captured inside the imprinted cavities with the highest affinity and the strongest Raman signal was observed, whereas at higher temperatures, this effect diminished. The sensor was able to detect the target analyte at concentrations as low as $10^{-12}$ M.

## 5. Thermoresponsive hydrogel actuators

Mechanical actuators have become ubiquitous tools in modern society, assisting where the precision or strength of the human hand is not sufficient or the environment does not allow human presence.[177] They are commonly composed of rigid mechanical components that allow to perform a series of reproducible operations and thus provide specific functions in applications ranging from automatic door openers to robotic assembly of cars and precise surgery within the human body.[178] Despite all those achievements, such hard robots possess inherent shortcomings,[179] particularly in environments with continuously changing surroundings, where direct contact of the robotic structures with humans, animals and soft objects is envisioned. Such limitations are being addressed in the emerging field of soft robotics by employing, for example, functional soft materials that undergo shape changes upon an external stimulus. Hydrogels responsive to pH, ionic strength, electric field gradients, temperature and light have been investigated for this purpose. Light stands out among those stimuli since it can be remotely applied with high spatial-temporal resolution and fast switching times. Metallic nanoparticles that sustain LSPR and which are embedded within a thermoresponsive hydrogel composite allow the efficient absorption of light to induce rapid local plasmonic heating and an associated volume change of the thermoresponsive polymer network. The present chapter discusses how this volume change can be translated into a controlled motion in order to deliver mechanical work, followed by examples of selected applications of photothermally driven actuators.

### 5.1 Shape morphing

Responsive hydrogel objects can react to an applied stimulus by a homogeneous volumetric expansion and contraction or by more complex anisotropic transition with specific deformation of its shape. As discussed further below, the simple homogenous volume change of the object without altering its specific geometric shape can serve in applications such as opening and closing valves[99] or for optical indicators.[46] However, more complex transformations associated with controlled time-dependent shape morphing of responsive hydrogels are needed to accomplish more sophisticated functionalities such as artificial motility and other intricate mechanical motions.[180]

For sufficiently large objects composed of homogenous responsive hydrogel material, applying a spatially nonuniform stimulus can generate local deformations that lead to their shape morphing.[181] Practically, a gradient of electrical[182] or magnetic[183] field intensity or spatially patterned illumination[76] and local heating[153] have been employed for this purpose. It should be noted that light is particularly well-suited as a spatially non-uniform stimulus due to the high resolution and fast switching characteristics of available optical systems. In general, the application of spatially nonuniform stimuli provides a convenient tool for operation of responsive hydrogel devices by simple manipulation methods. However, it can impose increasing complexity to the system needed to establish the locally confined trigger of the stimulus and often requires tracking of the specific location and positioning during deformation of the device for precise control.

In another possible approach, a spatially uniform stimulus is employed to drive devices prepared from an inhomogeneous responsive hydrogel material. An architecture of this type studied in detail is the bilayer system composed of a rectangular thermoresponsive pNIPAAm sheet attached to a thin gold layer depicted in Fig. 22A. Depending on the ratio between length $L$, width $w$, and thickness $h$, swelling and collapsing of the sheet reversibly bends the structure with rigid metal layer along one of the main axes to adopt a spiral or cylindrical tube shape or, when bending along both main axes simultaneously, it can form a helical structure. Self-folding bilayer structures composed of stacks of pNIPAAm and pMMA hydrogel layers were designed to facilitate multiple folding steps.[184] The resulting folding process is driven by the propagation of the diffusion front through the layers, which depends on the specific hydrogel material utilized. Tubular structures can be formed at the edges during the first folding step and act as reinforcements, while softer regions (for example, vertices) serve as hinges in succeeding deformation steps (see Fig. 22B). Photolithography allows controlled structuring of light-sensitive, photocrosslinkable polymers by spatially patterning the crosslinking density $\nu_c$. By combining stiff and highly crosslinked regions with less crosslinked softer sections that act as hinges, self-folding structures have been devised as illustrated in Fig. 22C and D. Self-folding hinge regions can be realized using a gradient in crosslinking density $\nu_c$ across the sheet thickness that causes a bending motion upon a temperature increase above the LCST of the employed thermoresponsive hydrogel material.[108] A different approach for the self-folding of patterned pNIPAAm hydrogel devices was pursued using a nanocomposite material with spatially patterned plasmonic absorbers by locally

Open Access Article. Published on 26 April 2022. Downloaded on 9/25/2023 10:08:45 AM.
This article is licensed under a Creative Commons Attribution 3.0 Unported Licence.

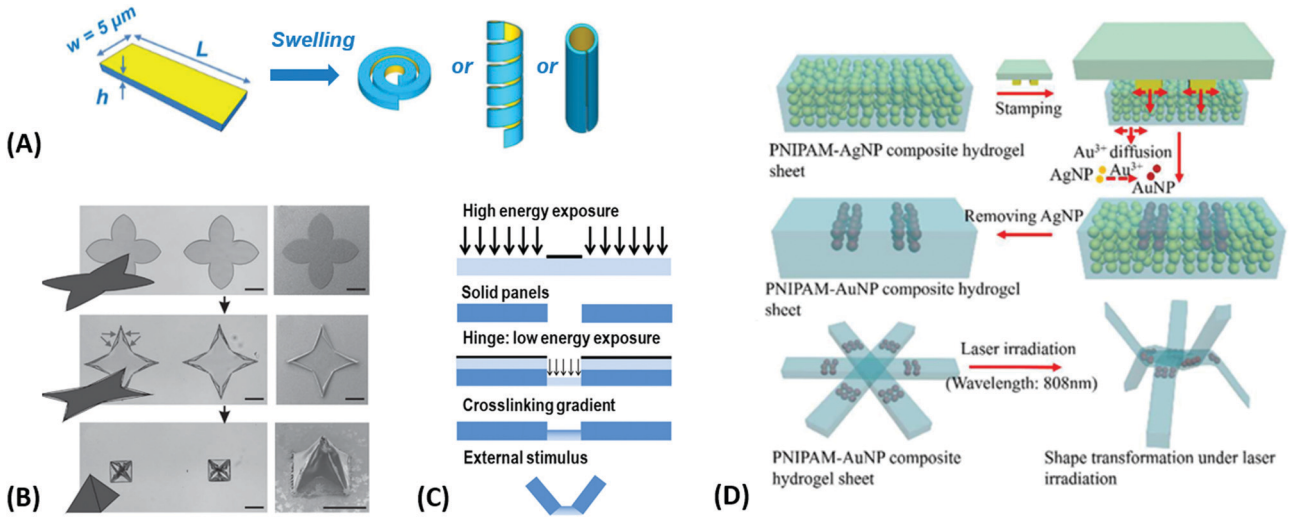


Fig. 22 Shape morphing of devices composed of inhomogeneous responsive hydrogel material: A thermoresponsive hydrogel sheet is combined with (A) non-expandable gold layer (adapted under ACS AuthorChoice license from ref. 186 © 2017 American Chemical Society) and (B) a non-responsive hydrogel layer. (adapted with permission from ref. 184) (C) a system with locally varied hydrogel crosslinking density $\nu_c$, (adapted with permission from ref. 29 ©2014 IOP Publishing, Ltd), and (D) device with locally deposited absorbers enabling local heating of its thermoresponsive body. Adapted with permission from ref. 187 © 2013 Royal Society of Chemistry.

embedding gold nanoparticles.[185] To generate the pattern, a hydrogel stamp was soaked in $HAuCl_4$ and contacted with a hydrogel with embedded silver nanoparticles. Gold ions diffuse into the composite and undergo a replacement reaction by locally converting silver nanoparticles to gold nanoparticles. Upon etching of the remaining silver nanoparticles using an aqueous solution of $NH_3$ and $H_2O_2$, a patterned pNIPAAm-gold nanoparticle composite is obtained, see Fig. 22D.

Additional means to trigger shape morphing of responsive hydrogel devices are based on using anisotropic hydrogel composite materials that can be actuated by a spatially uniform stimulus. Anisotropic composites can be formed by embedding oriented 2D nanostructures inside the hydrogel matrix. Before gelation of the hydrogel body, these inclusions can be oriented by an electric field (graphene flakes)[188] or magnetic field (titanate nanosheets)[33] followed by their fixation in the gel. The embedded 2D nanostructures restrict expansion of the composite hydrogel material leading to anisotropic swelling with one preferred direction, as shown in Fig. 23A. Remarkably, the interaction between the nanostructure inclusions can significantly dominate the hydrogel swelling properties. For example, the nanocomposite of titanate nanosheets embedded in pNIPAAm hydrogel was shown to expand in one direction when increasing the temperature above its LCST – in stark contrast to regular pNIPAAm hydrogel materials that only shrink.[33] The temperature-induced dehydration and

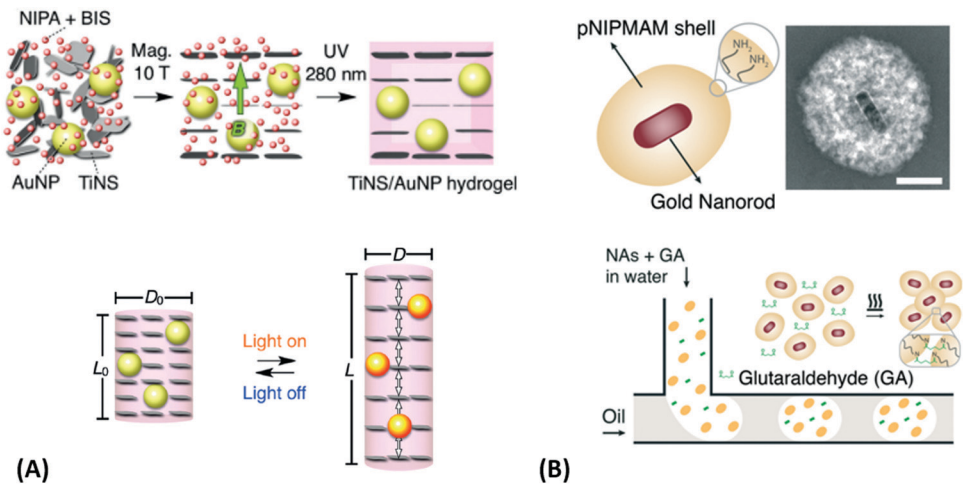


Fig. 23 Shape morphing of composite materials relying on (A) thermoresponsive hydrogel system with anisotropic properties due to the embedding of oriented 2D nanostructures to a hydrogel polymer network. Adapted under CC-BY from ref. 33. (B) Nanoactuators formed by gold nanoparticles capped with responsive pNIPAAm-based shell are assembled to larger microactuators using microfluidics. Adapted under CC-BY-NC 3.0 from ref. 22.

Open Access Article. Published on 26 April 2022. Downloaded on 9/25/2023 10:08:45 AM.
This article is licensed under a Creative Commons Attribution 3.0 Unported Licence.

rehydration of the hydrogel modulate the electrostatic permittivity, and thus, the repulsion between the inclusions leads to isovolumetric expansion. Since this mechanism is not associated with the diffusion of water molecules in and out of the polymer network, it can respond faster and is less limited by the overall size of the device.

An alternative route to accelerate the response time of thermoresponsive hydrogels, such as those based on pNIPAAm, employs a hierarchical architecture that minimizes the distance over which water needs to diffuse within the polymer network. This strategy was pursued for example in a bottom up approach where gold nanorods with a LSPR in the NIR part of spectrum were coated with a thermoresponsive poly(*N*-isopropylmethacrylamide) (pNIPMAM) shell that decreases in thickness when heated above the LCST at $T_c$.[189] The free amino groups in these building blocks were covalently crosslinked by glutaraldehyde inside a microfluidic device (see Fig. 23B). The obtained internally structured materials were employed as microactuators with dimensions between 5 μm and 50 μm, and were demonstrated to respond by two orders of magnitude faster than conventional homogenous bulk hydrogel devices of the same size.

### 5.2 Hydrogel valves

Responsive hydrogels found application in microfluidics for rapid and reversibly actuated valves needed in designs where conventional mechanical or hydraulic solutions are too bulky. Valves based on responsive gels can be designed such that fluid can flow freely through a microfluidic channel passed the collapsed gel, and upon application of the external stimulus, the expanding gel fills the channel and blocks the liquid flow. This concept was implemented by a thermoresponsive pNIPAAm-based hydrogel that was modified with spiropyran moieties to quickly respond to irradiation with light.[76] The hydrogel valve schematically shown in Fig. 24A was deployed in a circular chamber with a 2.6 mm diameter that was connected to an inlet and outlet microfluidic channels with a width of 1 mm. This device was placed on top of a blue light-emitting diode, and by modulating the irradiation power, the swelling degree of the gel valves was tuned to regulate the flow rate through the valve. With a flow sensor and controller, a highly reproducible and stable flow control[72,190] with a valve response time in the order of 10 s for increasing and 30–40 s for reducing the flow was demonstrated.

In general, optical actuation of such thermoresponsive hydrogels is beneficial for rapid and spatially addressable switching. Furthermore, it can be implemented into composite materials with dispersed metallic nanoparticles, capitalizing on plasmonic heating. They exhibit a higher absorption cross-section and, contrary to organic dye molecules, they do not photobleach. Selective actuation of microfluidic valves composed of such composite thermoresponsive material was demonstrated by wavelength division multiplexing.[109] Two spatially separated valves were prepared from a thermoresponsive copolymer hydrogel based on NIPAAm and acrylamide, which comprised different plasmonic nanoparticles exhibiting spectrally distinct LSPR at a wavelength of 530 nm and 830 nm, respectively (Fig. 24B). Irradiating the microfluidic T-junction at these respective wavelengths allows to selectively open and close the integrated valves individually and thus direct the flow of liquid samples to the desired arms of the microfluidic channels. The response time of this system was below 5 seconds when illuminated with an intensity of 1.6 W $cm^{-2}$ for 532 nm and 2.7 W $cm^{-2}$ for 832 nm.

### 5.3 Hydrogel grippers

The ability to grasp and move objects is a crucial task of robotic applications at all length scales. Conventional robotics uses stiff mechanical grippers, suction cups, or magnetic grippers to pick up objects. The actuators are typically designed to manipulate specific types of objects and struggle with handling objects of arbitrary shape. Soft robotics addresses these

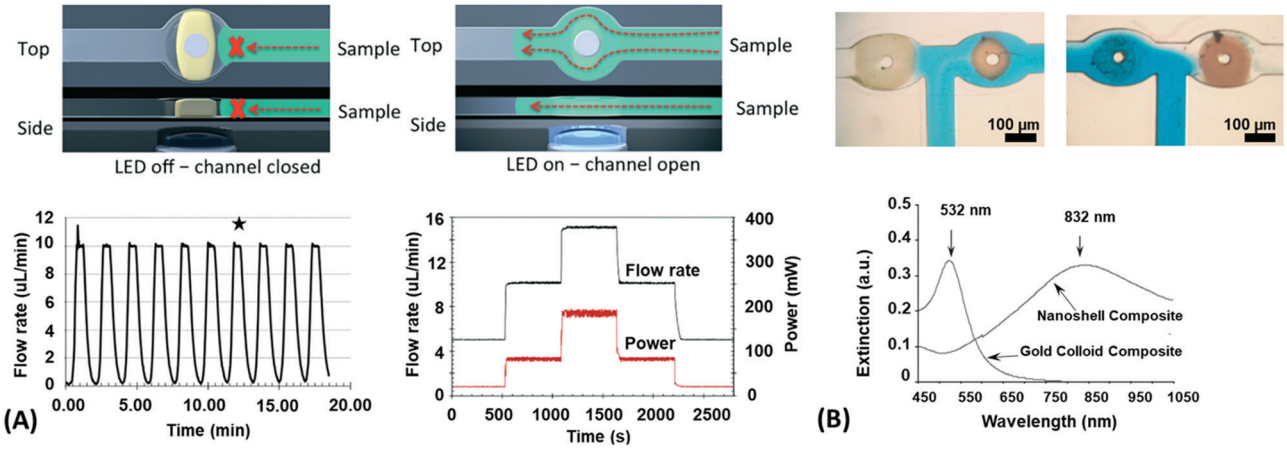


Fig. 24 (A) Precise flow control through a microfluidic channel actuated by a photoresponsive hydrogel valve by modulating the irradiation power. Adapted with permission from ref. 190 ©2001 Royal Society of Chemistry. (B) Microfluidic T-junction with two photothermal responsive valves with embedded plasmonic nanoparticles with distinct LSPR wavelengths that can be independently actuated by using wavelength division multiplexing. Adapted with permission from ref. 109, ©2005 Wiley-VCH.

Open Access Article. Published on 26 April 2022. Downloaded on 9/25/2023 10:08:45 AM.
This article is licensed under a Creative Commons Attribution 3.0 Unported Licence.

challenges by employing actuators that are sufficiently flexible to adapt with respect to the object shape and they ensure a firm grip by switching between an elastic and a stiff state. On a macroscopic scale, hydraulic actuators offer fast response times with high force levels while maintaining compatibility with standard hydraulic or pneumatic controls. While the response time of stimulus-responsive hydrogels is severely limited in macroscopic devices (size exceeding millimeter scales), they can still provide unique opportunities when using hydraulic actuation. It was recently demonstrated that such actuators made of polyacrylamide (pAAm) can provide an advantage in camouflaged optical or sonar observations,[191] capitalizing on the fact that the refractive index and the sonic impedance of such gels closely match the properties of the surrounding medium. Such a hydraulic actuation mechanism requires physical connecting of the device to a driving unit and consequently the implementation of stimuli-responsive hydrogels that can be controlled remotely have been found more attractive.

For example, an universal microgripper based on a dual-network microgel composed of the shape-memory polymer sodium alginate and the thermoresponsive hydrogel pNIPAAm as been presented.[192] The microgel is brought in contact with the object conforming to its shape. The shape is then locked by the shape-memory component of the gel by addition of $Ca^{2+}$ ions that crosslink guluronic acid blocks in the sodium alginate by ionic bonds. To further tighten the grip, the temperature is then increased above the LCST of the thermoresponsive pNIPAAm component of the microgel, compressing the mixed polymer network. The process is fully reversible by a decrease of temperature and removal of the $Ca^{2+}$ ions by either addition of ethylenediaminetetraacetic acid (EDTA) that coordinates with the $Ca^{2+}$ or the introductions of ion such as $Na^{+}$ and $K^{+}$ that replace the $Ca^{2+}$. Microgel spheres of about 500 μm diameter have shown holding forces up to 400 μN on a spherical object, sufficient to carry metallic objects of this size. The shape was fixed within seconds upon introduction of $Ca^{2+}$ and the original shape of the gripper was restored within 2 minutes after introduction of EDTA, fully releasing the gripped object. Attached to a lithographically prepared magnetically movable body as shown in Fig. 25A, and integration of

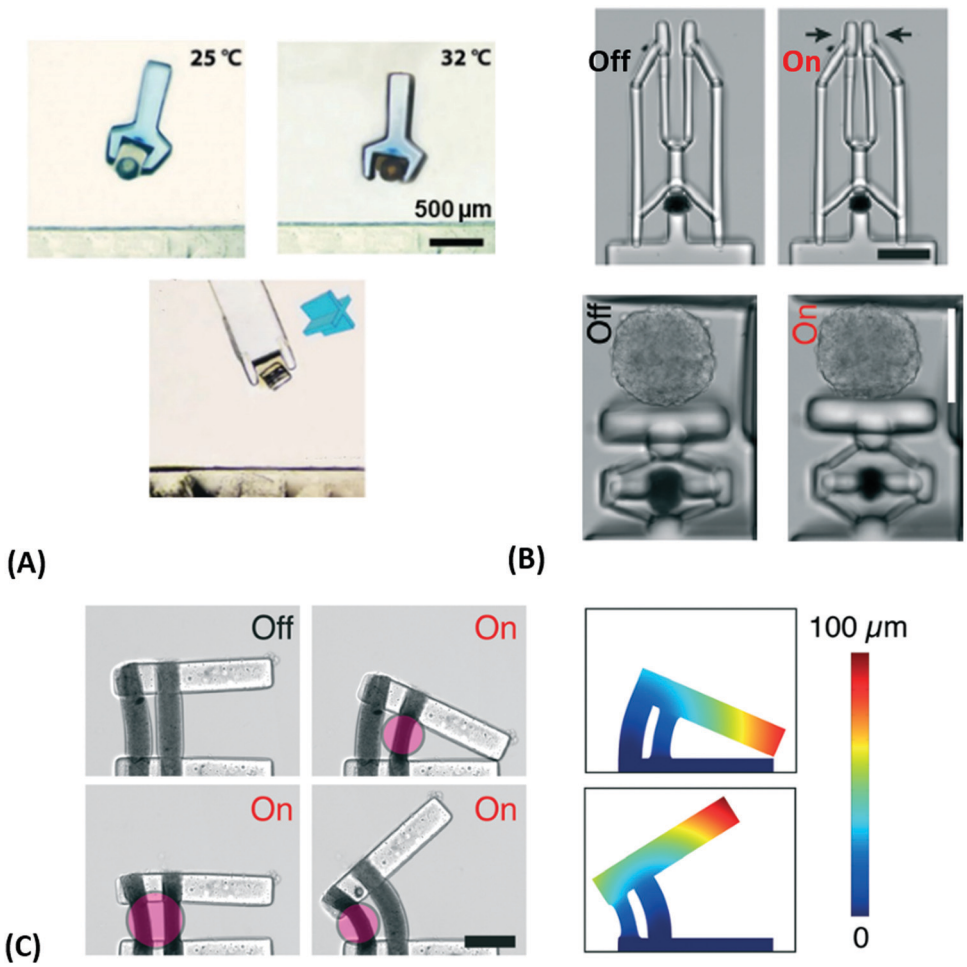


Fig. 25 (A) A universal microgripper based on a hierarchal body is composed of crosslinked pNIPAAm microgel that allows pickup of complex shaped objects and is integrated into a magnetically steerable microbot. Adapted with permission from ref. 26. ©2018 Wiley-VCH. (B) Microactuators that drive a parallel jaw mechanism (top) and a pressure plate (bottom). Adapted under CC-BY-NC 3.0 from ref. 22. (C) A mechanical device composed of two extruded microactuator pillars, which is capable of a range of motion motifs (scale bar of 100 μm). Adapted under CC-BY-NC 3.0 from ref. 22.

Open Access Article. Published on 26 April 2022. Downloaded on 9/25/2023 10:08:45 AM.
This article is licensed under a Creative Commons Attribution 3.0 Unported Licence.

plasmonic absorbers into the hydrogel for remote heating, the fully remotely controlled gripper was used to repeatedly grab and move objects without signs of degradation.

A modular approach to the design of smaller and more complex mechanical devices with sub-millimeter dimensions and photothermal actuation was explored by using maskless projection photolithography.[189] The active part of the systems was made of a composite hierarchical material with crosslinked nanoactuators (see Fig. 23A) that can be rapidly contracted by irradiation with light at a wavelength resonant with the embedded plasmonic nanoparticles. This material is mechanically coupled with other elements prepared from a non-responsive material based on poly(ethylene glycol)diacrylate. The examples in Fig. 25B show a parallel jaw gripper and a microscale piston, compressing a spheroid of epithelial cells. These systems were demonstrated to be remarkably durable, with the piston performance unchanged after 1000 cycles. Using an additive manufacturing approach, the crosslinked nanoactuators were encapsulated in an ionically-crosslinked porous alginate gel and extruded to form pillar-shaped 'muscles'. Combining two such artificial muscles with a nonresponsive bar, shown in Fig. 25C, allowed to perform a range of motions. Plasmonic heating of a single actuator pillar leads to tilting, while simultaneous illumination of both actuator pillars induces movement of the lever parallel to the base. Remarkable are the observed response times of actuator pillars with 50 μm diameter that exhibit 80% contraction within 25 ms and subsequent expansion to 70% of original size within 0.5 s.

### 5.4 Hydrogel swimmers

Propelled microbots attract particular attention due to their potential applications in the biomedical field.[193,194] At micrometer length scales, such devices have to operate in aqueous environments in the regime of low Reynolds number, where the viscous resistance dominates and repeated shape morphing allows for propulsion only if non-reciprocal forward and backward transformation occurs. In this context, thermoresponsive hydrogels with embedded plasmonic absorbers were investigated as actuators. With such materials, a microswimmer based on a helical bilayer system (see Fig. 22) was devised based on torsional transformation upon swelling and deswelling.[140] By rapid heating of the device at a time scale that is faster than the water diffusion-driven swelling and shrinking of the pNIPAAm hydrogel body, non-equilibrium transitions accompanied by a nonreciprocal transformation are induced, resulting in rotation along the two main device axes and performing a net forward motion in a confined channel, see Fig. 26A. A similar autonomous motion was observed for a semi-helical device that can perform rotations (see Fig. 26B).

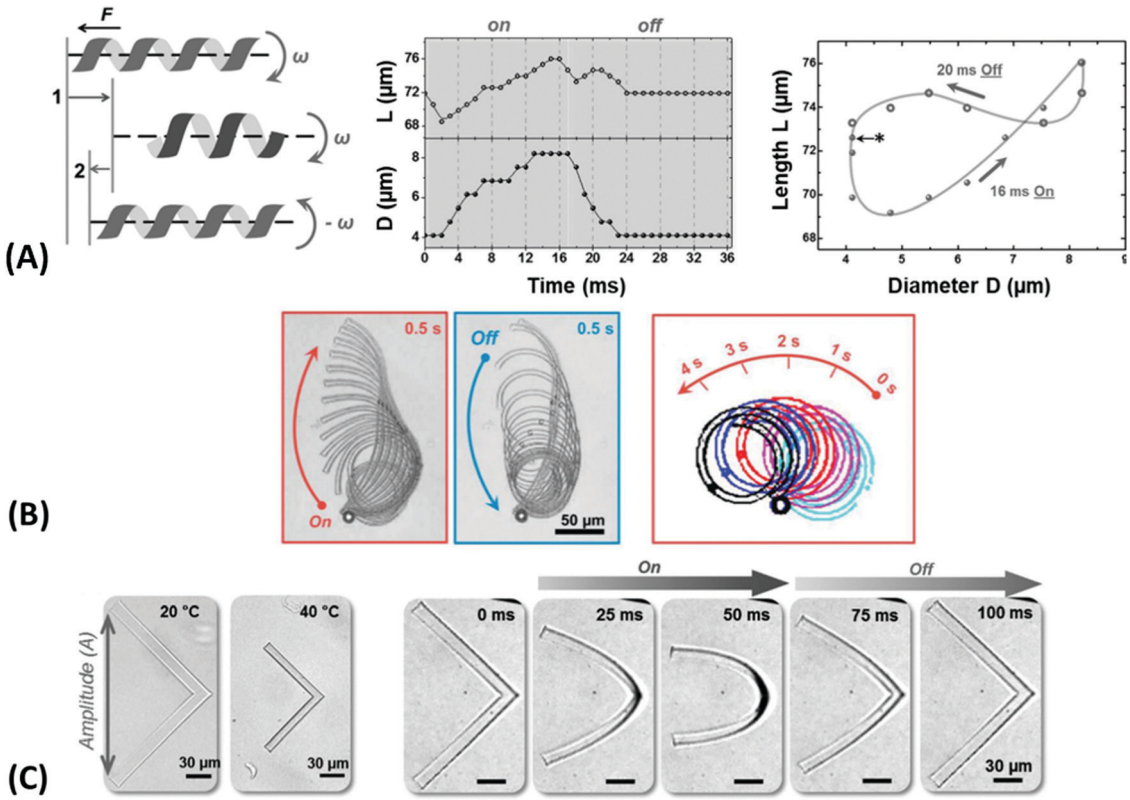


Fig. 26 (A) Forward movement of different hydrogel ribbons in response to photothermal heating. Adapted with under CC-BY 4.0 from ref. 140. (B) Expansion and shrinking of a helical hydrogel ribbon resulting in rotation and net forward movement. Adapted under CC-BY from ref. 24 (C) L-shaped hydrogel structure showing (left) isotropic change in dimensions for slow temperature modulation and (right) forward movement resulting from fast photothermal heating. Adapted with under CC-BY 4.0 from ref. 140.

Open Access Article. Published on 26 April 2022. Downloaded on 9/25/2023 10:08:45 AM.
This article is licensed under a Creative Commons Attribution 3.0 Unported Licence.

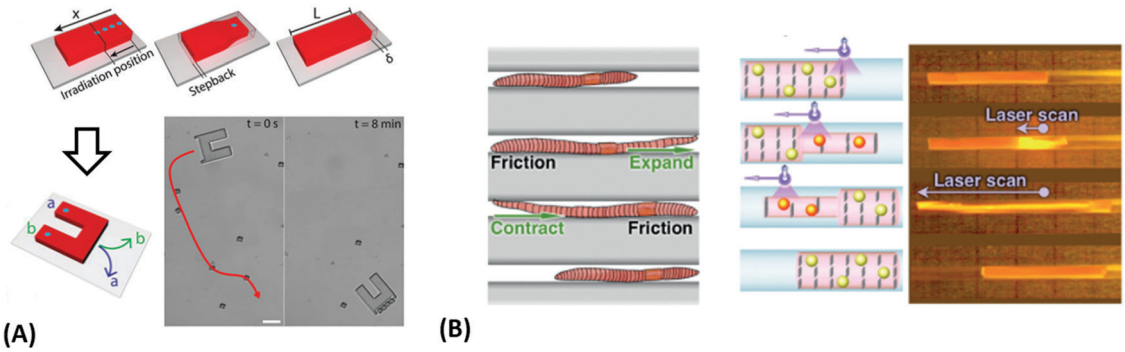


Fig. 27 (A) Light-driven crawler actuated by peristaltic deformation of a pNIPAAm hydrogel with embedded gold nanoparticles upon non-uniform irradiation, which induces modulation of friction between the polymer network and the solid substrate. Scalebar = 100 μm. Adapted with permission from ref. 195, ©2019 Mary Ann Liebert Inc. (B) Microbot mimicking worm-like motion based on an anisotropic hydrogel composite that locally responds to nonuniform irradiation. Reproduced with permission from ref. 33, ©2018 Wiley-VCH.

In another design approach for devices capable of translational motion, shape morphing by rapid heating of an L-shaped ribbon made of thermoresponsive hydrogel with an arm length of 100 μm, a width of 10 μm, and a thickness of 5 μm (see Fig. 26B) is exploited.[140] During slow temperature modulations that allow equilibrium swelling and shrinking, the hydrogel device does not alter its geometrical shape, but only its overall dimensions. However, when rapid plasmonic heating and cooling is implemented by a series of laser pulses with a wavelength of 808 nm and an intensity of 1.7 W mm$^{-2}$, a time-dependent-deformation is induced by the non-equilibrium kinetics of water diffusion into and out of the polymer networks, associated with stress in the hydrogel material. This is demonstrated in Fig. 26C, where the L-shaped device legs are bent faster during the contracting phase of the heating cycle with the optical beam on than the relaxing phase upon cooling when the irradiating beam is switched off. These anisotropic deformations result in nonreciprocal motion and respective progressive movement.

### 5.5 Hydrogel crawlers

Another format of motile hydrogel microsystems is realized with worm-like robots, which are designed to move by mimicking peristaltic motion by applying a time-dependent, spatially nonuniform stimulus. This mode of actuation can be achieved *via* structured illumination of a homogenous responsive hydrogel system to reduce friction upon local contraction and allowing part of the body to move while the remaining body stays at rest. Propagating the deformation along the body in cycles provides progressive forward movement.

For this purpose, the adhesion of pNIPAAm-based hydrogel devices on a glass surface was studied.[195] In sliding experiments on a tilted surface under heating cycles, the friction of the contracted state was found to be significantly reduced compared to the swollen state. A worm-like microbot was then devised consisting of pNIPAAm hydrogel composites with embedded gold nanoparticle absorbers for photothermal actuation. Locally confined irradiation of only a part of the device with a focused laser beam induces local plasmonic heating and shrinking of the irradiated part, as shown in Fig. 27A. By scanning the laser beam over the body (100 μm × 50 μm × 30 μm), the region of reduced friction upon shrinking propagates along the main axis of the device yields net forward motion. Repeated unidirectional scanning of the laser beam transforms the device into a light-driven linear motor. Two such motors were combined to form a remotely controlled, steerable microbot used to collect cargo on a surface.

A relatively fast-moving microbot with dimensions in the millimeter range was demonstrated with an earthworm-like crawler[33] built from a nanocomposite of cofacially aligned titanate nanosheets and plasmonic gold nanoparticles embedded in a pNIPAAm hydrogel. The charged nanosheets constrain swelling of the gel in two dimensions and add strain by electrostatic repulsion. By increasing the temperature, electrostatic permittivity variations of the hydrogel close to its LCST at $T_c$ are induced that modulate the electrostatic repulsion between the nanosheets and subsequently lead to a uniaxial expansion of the structure normal to the nanosheet planes (see Fig. 23B). Contrary to regular pNIPAAm-based devices, this deformation occurs without expelling water from the device, so due to volume conservation, the uniaxial expansion is accompanied by the contraction along the two orthogonal directions. Scanning a laser beam along the device body translates into a peristaltic motion (Fig. 27B) through sequential, local expansion along the scan direction with contraction in the perpendicular directions. As a result, the illuminated segment moves forward against the friction of the non-irradiated segments of the device. The large expansion of up to 70% perpendicular to the nanosheets allows a 15 mm long hydrogel cylinder with 1.2 mm diameter to move by 7 mm, almost half the body length, within a single scan at a speed of 3.4 mm s$^{-1}$.

## 6. Summary, conclusions and outlook

In this review, we take a deeper look into the properties of responsive hydrogels and plasmonic systems by firstly discussing the requirements, architectural adjustments, and their

Open Access Article. Published on 26 April 2022. Downloaded on 9/25/2023 10:08:45 AM.
This article is licensed under a Creative Commons Attribution 3.0 Unported Licence.

broad range of applications. We then focus on the combination of the intriguing characteristics from both material classes to yield plasmonic nanomaterials with responsive polymer hydrogels and the exploitation of their exceptional synergetic properties in applications, such as sensing and actuation.

In the light of the intriguing examples presented in this review, we witness a substantial increase in complexity and functionality of advanced soft materials, which are continously developed and exploited in a wide range of technical, biological and medical applications. Among these, responsive hydrogels stand out as they can transduce minute physical and chemical changes in their environment, such as pH, ionic strength, temperature, illumination, or presence of specific target molecules, to an abrupt transition in their structure. Particularly in connection with metallic nanomaterials, responsive hydrogels provide highly adaptable optical properties forming an important class of 'smart' materials. They can be tailored for applications in modern types of analytical devices paving even the way to the analysis in close contact with the human body. Moreover, responsive hydrogels were employed in light-driven actuators that, up to now, mainly served in microfluidic devices. The majority of recent experiments have been aimed at demonstrating their key functionalities, including remote control of liquid flow, externally-driven locomotion, and manipulation of miniature objects present in aqueous samples. These advances were enabled by a range of fabrication technologies, including lithography, nanoimprinting, colloidal assembly, or rapidly developing additive manufacturing. Research has already established light-propelled microfluidic valves, mechanical grippers, crawlers, and swimmers and is now on the verge of developing functional soft microrobotic devices. The key motivation in these efforts is guided by future applications in the medical field, where microscopic devices prepared from biocompatible materials with length scales of small blood vessels may navigate through organs and perform delicate tasks autonomously or remotely. They may also serve as micro-factories, building structures of micrometer dimensions with unpreceded precision and complexity. Therefore, one can expect that efforts of merging the potential of light-driven remote actuation and sensing within the functionalities of an individual miniature soft device will gaining substantial momentum in the future (see Fig. 28). Such activities will provide new tools for research as well as for applications in important fields of medical diagnostics, drug delivery, or theragnostic.

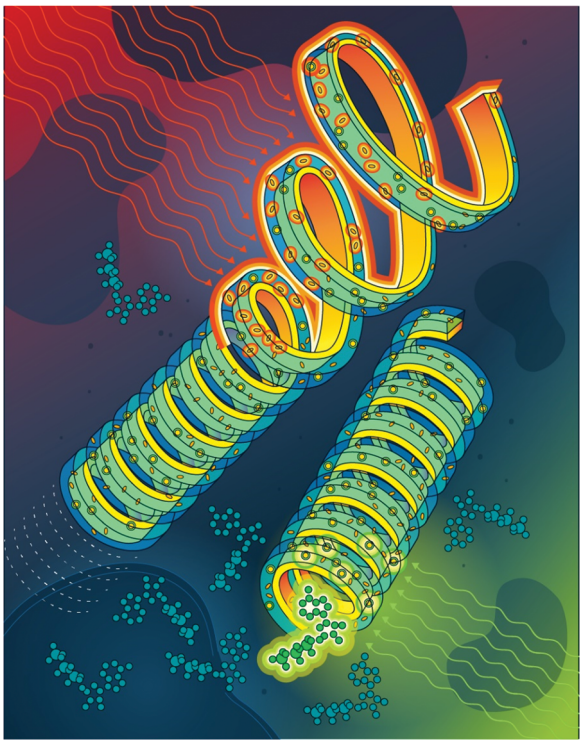

Fig. 28 Schematics of a hypothetical microdevice that performs locomotion and is equipped with a biosensing functionality to detect the spatial and temporal concentration change of monitored target species.

## Abbreviations

| | |
|---|---|
| ADA | Adamantane amine |
| CEA | 2-Carboxyethyl acrylate |
| ConA | Concanavalin A |
| EBL | Electron beam lithography |
| Fc | Ferrocene |
| FRET | Fluorescence resonance energy transfer |
| GEMA | Glycosyloxyethyl methacrylate |
| HEMA | 2-Hydroxyethyl methacrylate |
| LCST | Lower critical solution temperature |
| LPA | Lysophosphatidic acid |
| $l_s$ | Segment length |
| LSP | Localized surface plasmon |
| LSPR | Localized surface plasmon resonance |
| MAA | Methacrylic acid |
| MPB | Multivalent protein binding |
| $n_h$ | Refractive index (hydrogel) |
| NIPAAm | *N*-Isopropyl acrylamide |
| NP | Nanoparticle |
| OWS | Optical waveguide spectroscopy |
| pAA | Poly(allylamine) |
| pAAc | Poly(acrylic acid) |
| pAAm | Poly(acrylamide) |
| pANI | Poly(aniline) |
| pDEAEMA | Poly(2-(diethylamino)ethyl methacrylate) |
| PEF | Plasmon-enhanced fluorescence |
| pNIPAAm | Poly(*N*-isopropyl acrylamide) |
| pNIPMAM | Poly(*N*-isopropylmethacrylamide) |
| PSP | Propagating surface plasmon |
| $Q_V$ | Volume swelling ratio |
| SEF | Surface-enhanced fluorescence |
| SERS | Surface-enhanced Raman scattering |
| SPR | Surface plasmon resonance |
| $T_c$ | Cloud point temperature |
| TEM | Transmission electron microscopy |
| UCST | Upper critical solution temperature |
| UV-LIL | UV laser interference lithography |


This journal is © The Royal Society of Chemistry 2022

Open Access Article. Published on 26 April 2022. Downloaded on 9/25/2023 10:08:45 AM.
This article is licensed under a Creative Commons Attribution 3.0 Unported Licence.

| | |
|---|---|
| β-CD | β-Cyclodextrin |
| $\Phi_p$ | Polymer volume fraction |
| $\nu_c$ | Crosslink density |

## Conflicts of interest

There are no conflicts to declare.

## Acknowledgements

J. D., S. H., S. F. acknowledge support from FFG through the project PLABAN (861578) and from FWF project DIPLAB (I 5119-B), and by Lower Austria project IKTHEUAP number WST3-F-5030820/010-2019. J. D. and S. F. was partially supported by FFG project Easifil (877420) and S. A. is grateful for the support from FWF *via* the project Nanobiosensor (I 2647). In addition, J. D. acknowledges support from the ESIF and MEYS (Project 'FZU researchers, technical and administrative staff mobility' – CZ.02.2.69/ 0.0/ 0.0/18_053/0016627) and Czech Science Fund through the project APLOMA (22-30456J). UJ acknowledges continuous support through the AIT Partner Group cooperation agreement and for financial support through the BMBF funded Project Medistorplast (13GW0349C) for FD.

## References

1 S. A. Maier and H. A. Atwater, Plasmonics: Localization and Guiding of Electromagnetic Energy in Metal/Dielectric Structures, *J. Appl. Phys.*, 2005, 011101, DOI: **10.1063/1.1951057**.

2 T. G. Mayerhöfer and J. Popp, Periodic Array-Based Substrates for Surface-Enhanced Infrared Spectroscopy, *Nanophotonics*, 2018, **7**(1), 39–79, DOI: **10.1515/nanoph-2017-0005**.

3 M. F. Cardinal, E. Vander Ende, R. A. Hackler, M. O. McAnally, P. C. Stair, G. C. Schatz and R. P. Van Duyne, Expanding Applications of SERS through Versatile Nanomaterials Engineering, *Chem. Soc. Rev.*, 2017, **46**(13), 3886–3903, DOI: **10.1039/c7cs00207f**.

4 J. Homola, Surface Plasmon Resonance Sensors for Detection of Chemical and Biological Species, *Chem. Rev.*, 2008, **108**(2), 462–493, DOI: **10.1021/cr068107d**.

5 M. Bauch, K. Toma, M. Toma, Q. Zhang and J. Dostalek, Plasmon-Enhanced Fluorescence Biosensors: A Review, *Plasmonics*, 2014, **9**(4), 781–799, DOI: **10.1007/s11468-013-9660-5**.

6 D. Garoli, H. Yamazaki, N. MacCaferri and M. Wanunu, Plasmonic Nanopores for Single-Molecule Detection and Manipulation: Toward Sequencing Applications, *Nano Lett.*, 2019, 7553–7562, DOI: **10.1021/acs.nanolett.9b02759**.

7 B. Schwarz, P. Reininger, D. Ristanić, H. Detz, A. M. Andrews, W. Schrenk and G. Strasser, Monolithically Integrated Mid-Infrared Lab-on-a-Chip Using Plasmonics and Quantum Cascade Structures, *Nat. Commun.*, 2014, **5**(1), 1–7, DOI: **10.1038/ncomms5085**.

8 A. Karabchevsky, A. Katiyi, A. S. Ang and A. Hazan, On-Chip Nanophotonics and Future Challenges, *Nanophotonics*, 2020, **9**(12), 3733–3753, DOI: **10.1515/nanoph-2020-0204**.

9 V. E. Ferry, M. A. Verschuuren, H. B. T. Li, E. Verhagen, R. J. Walters, R. E. I. Schropp, H. A. Atwater and A. Polman, Light Trapping in Ultrathin Plasmonic Solar Cells, *Opt. Express*, 2010, **18**(S2), A237, DOI: **10.1364/oe.18.00a237**.

10 J. M. Romo-Herrera, R. A. Alvarez-Puebla and L. M. Liz-Marzán, Controlled Assembly of Plasmonic Colloidal Nanoparticle Clusters, *Nanoscale*, 2011, **3**(4), 1304–1315, DOI: **10.1039/c0nr00804d**.

11 B. Ai, Y. Yu, H. Möhwald, G. Zhang and B. Yang, Plasmonic Films Based on Colloidal Lithography, *Adv. Colloid Interface Sci.*, 2014, **206**, 5–16, DOI: **10.1016/j.cis.2013.11.010**.

12 S. Schrittwieser, M. J. Haslinger, T. Mitteramskogler, M. Mühlberger, A. Shoshi, H. Brückl, M. Bauch, T. Dimopoulos, B. Schmid and J. Schotter, Multifunctional Nanostructures and Nanopocket Particles Fabricated by Nanoimprint Lithography, *Nanomaterials*, 2019, **9**(12), 1790, DOI: **10.3390/nano9121790**.

13 N. Jiang, X. Zhuo and J. Wang, Active Plasmonics: Principles, Structures, and Applications, *Chem. Rev.*, 2018, **118**(6), 3054–3099, DOI: **10.1021/acs.chemrev.7b00252**.

14 K. F. MacDonald, Z. L. Sámson, M. I. Stockman and N. I. Zheludev, Ultrafast Active Plasmonics, *Nat. Photonics*, 2009, **3**(1), 55–58, DOI: **10.1038/nphoton.2008.249**.

15 D. S. Sidhaye, S. Kashyap, M. Sastry, S. Hotha and B. L. V. Prasad, Gold Nanoparticle Networks with Photoresponsive Interparticle Spacings, *Langmuir*, 2005, **21**(17), 7979–7984, DOI: **10.1021/la051125q**.

16 G. K. Joshi, K. N. Blodgett, B. B. Muhoberac, M. A. Johnson, K. A. Smith and R. Sardar, Ultrasensitive Photoreversible Molecular Sensors of Azobenzene-Functionalized Plasmonic Nanoantennas, *Nano Lett.*, 2014, **14**(2), 532–540, DOI: **10.1021/NL403576C**.

17 M. Wei, Y. Gao, X. Li and M. J. Serpe, Stimuli-Responsive Polymers and Their Applications, *Polym. Chem.*, 2017, **8**(1), 127–143, DOI: **10.1039/c6py01585a**.

18 M. Toma, U. Jonas, A. Mateescu, W. Knoll and J. Dostalek, Active Control of SPR by Thermoresponsive Hydrogels for Biosensor Applications, *J. Phys. Chem. C*, 2013, **117**(22), 11705–11712, DOI: **10.1021/jp400255u**.

19 I. Pastoriza-Santos, C. Kinnear, J. Pérez-Juste, P. Mulvaney and L. M. Liz-Marzán, Plasmonic Polymer Nanocomposites, *Nat. Rev. Mater.*, 2018, **3**(10), 375–391, DOI: **10.1038/s41578-018-0050-7**.

20 M. A. C. Stuart, W. T. S. Huck, J. Genzer, M. Müller, C. Ober, M. Stamm, G. B. Sukhorukov, I. Szleifer, V. V. Tsukruk, M. Urban, F. Winnik, S. Zauscher, I. Luzinov and S. Minko, Emerging Applications of Stimuli-Responsive Polymer Materials, *Nat. Mater.*, 2010, **9**(2), 101–113, DOI: **10.1038/nmat2614**.

21 Q. Shi, H. Liu, D. Tang, Y. Li, X. J. Li and F. Xu, Bioactuators Based on Stimulus-Responsive Hydrogels and Their Emerging Biomedical Applications, *NPG Asia Mater.*, 2019, **11**(1), 1–21, DOI: **10.1038/s41427-019-0165-3**.

Open Access Article. Published on 26 April 2022. Downloaded on 9/25/2023 10:08:45 AM.
This article is licensed under a Creative Commons Attribution 3.0 Unported Licence.

22 B. Özkale, R. Parreira, A. Bekdemir, L. Pancaldi, E. Özelçi, C. Amadio, M. Kaynak, F. Stellacci, D. J. Mooney and M. S. Sakar, Modular Soft Robotic Microdevices for Dexterous Biomanipulation, *Lab Chip*, 2019, **19**(5), 778–788, DOI: 10.1039/c8lc01200h.

23 S. Hamajima, H. Mitomo, T. Tani, Y. Matsuo, K. Niikura, M. Naya, K. Ijiro, T. Tani, M. Naya, K. Niikura, Y. Matsuo, K. Niikura, M. Naya and K. Ijiro, Nanoscale Uniformity in the Active Tuning of a Plasmonic Array by Polymer Gel Volume Change, *Nanoscale Adv.*, 2019, **1**(5), 1731–1739, DOI: 10.1039/c8na00404h.

24 H. Zhang, L. Koens, E. Lauga, A. Mourran and M. Möller, A Light-Driven Microgel Rotor, *Small*, 2019, **15**(46), 1903379, DOI: 10.1002/smll.201903379.

25 J. Li, C. Ji, X. Yu, M. Yin and D. Kuckling, Dually Cross-Linked Supramolecular Hydrogel as Surface Plasmon Resonance Sensor for Small Molecule Detection, *Macromol. Rapid Commun.*, 2019, **40**(14), 1–5, DOI: 10.1002/marc.201900189.

26 H. Jia, E. Mailand, J. Zhou, Z. Huang, G. Dietler, J. M. Kolinski, X. Wang and M. S. Sakar, Universal Soft Robotic Microgripper, *Small*, 2019, **15**(4), 1803870, DOI: 10.1002/SMLL.201803870.

27 A. Kowalczyk, B. Wagner, M. Karbarz and A. M. Nowicka, A Dual DNA Biosensor Based on Two Redox Couples with a Hydrogel Sensing Platform Functionalized with Carboxyl Groups and Gold Nanoparticles, *Sens. Actuators, B*, 2015, **208**, 220–227, DOI: 10.1016/j.snb.2014.11.029.

28 M. Magnozzi, Y. Brasse, T. A. F. König, F. Bisio, E. Bittrich, A. Fery and M. Canepa, Plasmonics of Au/Polymer Core/Shell Nanocomposites for Thermoresponsive Hybrid Metasurfaces, *ACS Appl. Nano Mater.*, 2020, **3**(2), 1674–1682, DOI: 10.1021/acsanm.9b02403.

29 C. Yoon, R. Xiao, J. Park, J. Cha, T. D. Nguyen and D. H. Gracias, Functional Stimuli Responsive Hydrogel Devices by Self-Folding, *Smart Mater. Struct.*, 2014, **23**(9), 094008, DOI: 10.1088/0964-1726/23/9/094008.

30 F. Howaili, E. Özliseli, B. Küçüktürkmen, S. M. Razavi, M. Sadeghizadeh and J. M. Rosenholm, Stimuli-Responsive, Plasmonic Nanogel for Dual Delivery of Curcumin and Photothermal Therapy for Cancer Treatment, *Front. Chem.*, 2021, **8**, 1235, DOI: 10.3389/fchem.2020.602941.

31 J. H. Kim and T. R. Lee, Discrete Thermally Responsive Hydrogel-Coated Gold Nanoparticles for Use as Drug-Delivery Vehicles, *Drug Dev. Res.*, 2006, **67**(1), 61–69, DOI: 10.1002/DDR.20068.

32 S. Jiang, K. Wang, Y. Dai, X. Zhang and F. Xia, Near-Infrared Light-Triggered Dual Drug Release Using Gold Nanorod-Embedded Thermosensitive Nanogel-Crosslinked Hydrogels, *Macromol. Mater. Eng.*, 2019, **304**(7), 1900087, DOI: 10.1002/mame.201900087.

33 Z. Sun, Y. Yamauchi, F. Araoka, Y. S. Kim, J. Bergueiro, Y. Ishida, Y. Ebina, T. Sasaki, T. Hikima and T. Aida, An Anisotropic Hydrogel Actuator Enabling Earthworm-Like Directed Peristaltic Crawling, *Angew. Chem.*, 2018, **130**(48), 15998–16002, DOI: 10.1002/ange.201810052.

34 C. Wang, X. Liu, V. Wulf, M. Vázquez-González, M. Fadeev and I. Willner, DNA-Based Hydrogels Loaded with Au Nanoparticles or Au Nanorods: Thermoresponsive Plasmonic Matrices for Shape-Memory, Self-Healing, Controlled Release, and Mechanical Applications, *ACS Nano*, 2019, **13**(3), 3424–3433, DOI: 10.1021/acsnano.8b09470.

35 F. Rizzo and N. S. Kehr, Recent Advances in Injectable Hydrogels for Controlled and Local Drug Delivery, *Adv. Healthcare Mater.*, 2021, **10**(1), 2001341, DOI: 10.1002/ADHM.202001341.

36 J. Homola, *Surface Plasmon Resonance Based Sensors*, ed. J. Homola and O. S. Wolfbeis, Springer Series on Chemical Sensors and Biosensors, Springer: Berlin, Heidelberg, 2006, vol. 4, DOI: 10.1007/b100321.

37 A. S. Hoffman, Hydrogels for Biomedical Applications, *Adv. Drug Delivery Rev.*, 2012, **64**, 18–23, DOI: 10.1016/j.addr.2012.09.010.

38 A. Mateescu, Y. Wang, J. Dostalek and U. Jonas, Thin Hydrogel Films for Optical Biosensor Applications, *Membr.*, 2012, **2**(1), 49–69, DOI: 10.3390/membranes2010040.

39 S. Wu, M. Zhu, Q. Lian, D. Lu, B. Spencer, D. J. Adlam, J. A. Hoyland, K. Volk, M. Karg and B. R. Saunders, Plasmonic and Colloidal Stability Behaviours of Au–Acrylic Core–Shell Nanoparticles with Thin PH-Responsive Shells, *Nanoscale*, 2018, **10**(39), 18565–18575, DOI: 10.1039/c8nr07440b.

40 C. K. Pandiyarajan, O. Prucker and J. Rühe, Humidity Driven Swelling of the Surface-Attached Poly(*N*-Alkylacrylamide) Hydrogels, *Macromolecules*, 2016, **49**(21), 8254–8264, DOI: 10.1021/acs.macromol.6b01379.

41 R. Navarro, M. Pérez Perrino, O. Prucker and J. Rühe, Preparation of Surface-Attached Polymer Layers by Thermal or Photochemical Activation of α-Diazoester Moieties, *Langmuir*, 2013, **29**(34), 10932–10939, DOI: 10.1021/la402323k.

42 B. Liu, X. Liu, S. Shi, R. Huang, R. Su, W. Qi and Z. He, Design and Mechanisms of Antifouling Materials for Surface Plasmon Resonance Sensors, *Acta Biomater.*, 2016, **40**, 100–118, DOI: 10.1016/j.actbio.2016.02.035PM-26921775.

43 T. Mutschler, B. Kieser, R. Frank and G. Gauglitz, Characterization of Thin Polymer and Biopolymer Layers by Ellipsometry and Evanescent Field Technology, *Anal. Bioanal. Chem.*, 2002, **374**(4), 658–664, DOI: 10.1007/s00216-002-1488-3.

44 H. Wen, W. Xiao, S. Biswas, Z. Q. Cong, X. M. Liu, K. S. Lam, Y. H. Liao and W. Deng, Alginate Hydrogel Modified with a Ligand Interacting with A3β1 Integrin Receptor Promotes the Differentiation of 3D Neural Spheroids toward Oligodendrocytes in Vitro, *ACS Appl. Mater. Interfaces*, 2019, **11**(6), 5821–5833, DOI: 10.1021/acsami.8b19438.

45 X. Hou, X. Dai, J. Yang, B. Zhang, D. Zhao, C. Li, Z. Yin, Y. Zhao and B. Liu, Injectable Polypeptide-Engineered Hydrogel Depot for Amplifying the Anti-Tumor Immune Effect Induced by Chemo-Photothermal Therapy, *J. Mater. Chem. B*, 2020, **8**(37), 8623–8633, DOI: 10.1039/D0TB01370F.


This journal is © The Royal Society of Chemistry 2022

Open Access Article. Published on 26 April 2022. Downloaded on 9/25/2023 10:08:45 AM.
This article is licensed under a Creative Commons Attribution 3.0 Unported Licence.

46 L. Zhao, X. Zhang, Q. Luo, C. Hou, J. Xu and J. Liu, Engineering Nonmechanical Protein-Based Hydrogels with Highly Mechanical Properties: Comparison with Natural Muscles, *Biomacromolecules*, 2020, **21**(10), 4212–4219, DOI: 10.1021/acs.biomac.0c01002.

47 A. Kirillova, R. Maxson, G. Stoychev, C. T. Gomillion and L. Ionov, 4D Biofabrication Using Shape-Morphing Hydrogels, *Adv. Mater.*, 2017, **29**(46), 1–8, DOI: 10.1002/adma.201703443.

48 K. Nešović, A. Janković, T. Radetić, A. Perić-Grujić, M. Vukašinović-Sekulić, V. Kojić, K. Y. Rhee and V. Mišković-Stanković, Poly(Vinyl Alcohol)/Chitosan Hydrogels with Electrochemically Synthesized Silver Nanoparticles for Wound Dressing Applications, *J. Electrochem. Sci. Eng.*, 2020, **10**(2), 185–198, DOI: 10.5599/jese.732.

49 C. D. Spicer, Hydrogel Scaffolds for Tissue Engineering: The Importance of Polymer Choice, *Polym. Chem.*, 2020, **11**, 184–219, DOI: 10.1039/c9py01021a.

50 N. A. Peppas, J. Z. Hilt, A. Khademhosseini and R. Langer, Hydrogels in Biology and Medicine: From Molecular Principles to Bionanotechnology, *Adv. Mater.*, 2006, **18**(11), 1345–1360, DOI: 10.1002/adma.200501612.

51 F. Ilievski, A. D. Mazzeo, R. F. Shepherd, X. Chen and G. M. Whitesides, Soft Robotics for Chemists, *Angew. Chemie.*, 2011, **123**(8), 1930–1935, DOI: 10.1002/ange.201006464.

52 Z. X. Khoo, J. E. M. Teoh, Y. Liu, C. K. Chua, S. Yang, J. An, K. F. Leong and W. Y. Yeong, 3D Printing of Smart Materials: A Review on Recent Progresses in 4D Printing, *Virtual Phys. Prototyp.*, 2015, **10**(3), 103–122, DOI: 10.1080/17452759.2015.1097054M4-Citavi.

53 S. Li, H. Zhao and R. F. Shepherd, Flexible and Stretchable Sensors for Fluidic Elastomer Actuated Soft Robots, *MRS Bull.*, 2017, **42**(2), 138–142, DOI: 10.1557/mrs.2017.4.

54 H. Schenderlein, A. Voss, R. W. Stark and M. Biesalski, Preparation and Characterization of Light-Switchable Polymer Networks Attached to Solid Substrates, *Langmuir*, 2013, **29**(14), 4525–4534, DOI: 10.1021/la305073p.

55 M. J. N. Junk, I. Anac, B. Menges and U. Jonas, Analysis of Optical Gradient Profiles during Temperature- and Salt-Dependent Swelling of Thin Responsive Hydrogel Films, *Langmuir*, 2010, **26**(14), 12253–12259, DOI: 10.1021/la101185qPM-20504000.

56 M. E. Harmon, D. Kuckling and C. W. Frank, Photo-Cross-Linkable PNIPAAm Copolymers. 2. Effects of Constraint on Temperature and PH-Responsive Hydrogel Layers, *Macromolecules*, 2003, **36**(1), 162–172, DOI: 10.1021/ma021025g.

57 I. Anac, A. Aulasevich, M. J. N. Junk, P. Jakubowicz, R. F. Roskamp, B. Menges, U. Jonas and W. Knoll, Optical Characterization of Co-Nonsolvency Effects in Thin Responsive PNIPAAm-Based Gel Layers Exposed to Ethanol/Water Mixtures, *Macromol. Chem. Phys.*, 2010, **211**(9), 1018–1025, DOI: 10.1002/macp.200900533M4-Citavi.

58 A. J. R. Amaral and G. Pasparakis, Stimuli Responsive Self-Healing Polymers: Gels, Elastomers and Membranes, *Polym. Chem.*, 2017, **8**(42), 6464–6484, DOI: 10.1039/c7py01386h.

59 S. Reinicke, J. Schmelz, A. Lapp, M. Karg, T. Hellweg and H. Schmalz, Smart Hydrogels Based on Double Responsive Triblock Terpolymers, *Soft Matter*, 2009, **5**(13), 2648–2657, DOI: 10.1039/b900539k.

60 H. Thérien-Aubin, Z. L. Wu, Z. Nie and E. Kumacheva, Multiple Shape Transformations of Composite Hydrogel Sheets, *J. Am. Chem. Soc.*, 2013, **135**(12), 4834–4839, DOI: 10.1021/ja400518c.

61 J. Seuring and S. Agarwal, Polymers with Upper Critical Solution Temperature in Aqueous Solution: Unexpected Properties from Known Building Blocks, *ACS Macro Lett.*, 2013, **2**(7), 597–600, DOI: 10.1021/mz400227y.

62 N. Higashi, R. Sonoda and T. Koga, Thermo-Responsive Amino Acid-Based Vinyl Polymers Showing Widely Tunable LCST/UCST Behavior in Water, *RSC Adv.*, 2015, **5**(83), 67652–67657, DOI: 10.1039/c5ra13009c.

63 P. J. Roth, Composing Well-Defined Stimulus-Responsive Materials through Postpolymerization Modification Reactions, *Macromol. Chem. Phys.*, 2014, **215**(9), 825–838, DOI: 10.1002/macp.201400073.

64 Y. Zhu, J. Y. Quek, A. B. Lowe and P. J. Roth, Thermo-responsive (Co)Polymers through Postpolymerization Modification of Poly(2-Vinyl-4,4-Dimethylazlactone), *Macromolecules*, 2013, **46**, 6475, DOI: 10.1021/ma401096r.

65 P. A. Woodfield, Y. Zhu, Y. Pei and P. J. Roth, Hydrophobically Modified Sulfobetaine Copolymers with Tunable Aqueous UCST through Postpolymerization Modification of Poly(Pentafluorophenyl Acrylate), *Macromolecules*, 2014, **47**, 750, DOI: 10.1021/ma402391a.

66 A. Natansohn and P. Rochon, Photoinduced Motions in Azo-Containing Polymers, *Chem. Rev.*, 2002, **102**, 4139–4175, DOI: 10.1021/cr970155y.

67 W. Knoll, *Handbook of Biofunctional Surfaces*, ed. W. Knoll, Jenny Stanford Publishing, 2012. , DOI: 10.1201/B14900.

68 F. P. Nicoletta, D. Cupelli, P. Formoso, G. de Filpo, V. Colella and A. Gugliuzza, Light Responsive Polymer Membranes: A Review, *Membr.*, 2012, **2**(1), 134–197, DOI: 10.3390/MEMBRANES2010134.

69 M. Karg, A. Pich, T. Hellweg, T. Hoare, L. A. Lyon, J. J. Crassous, D. Suzuki, R. A. Gumerov, S. Schneider, I. I. Potemkin and W. Richtering, Nanogels and Microgels: From Model Colloids to Applications, Recent Developments, and Future Trends, *Langmuir*, 2019, **35**(19), 6231–6255, DOI: 10.1021/acs.langmuir.8b04304PM-30998365.

70 A. J. Schmid, J. Dubbert, A. A. Rudov, J. S. Pedersen, P. Lindner, M. Karg, I. I. Potemkin and W. Richtering, Multi-Shell Hollow Nanogels with Responsive Shell Permeability, *Sci. Rep.*, 2016, **6**, 22736, DOI: 10.1038/srep22736PM-26984478.

71 P. Date, A. Tanwar, P. Ladage, K. M. Kodam and D. Ottoor, Biodegradable and Biocompatible Agarose–Poly(Vinyl Alcohol) Hydrogel for the in Vitro Investigation of Ibuprofen Release, *Chem. Pap.*, 2020, **74**(6), 1965–1978, DOI: 10.1007/s11696-019-01046-8.

72 S. Coleman, J. ter Schiphorst, A. Azouz, S. Ben Bakker, A. P. H. J. Schenning and D. Diamond, Tuning Microfluidic

Open Access Article. Published on 26 April 2022. Downloaded on 9/25/2023 10:08:45 AM.
This article is licensed under a Creative Commons Attribution 3.0 Unported Licence.

Flow by Pulsed Light Oscillating Spiropyran-Based Polymer Hydrogel Valves, *Sens. Actuators, B*, 2017, **245**, 81–86, DOI: 10.1016/j.snb.2017.01.112.

73 J. Ter Schiphorst, J. Saez, D. Diamond, F. Benito-Lopez and A. P. H. J. Schenning, Light-Responsive Polymers for Microfluidic Applications, *Lab Chip*, 2018, **18**(5), 699–709, DOI: 10.1039/C7LC01297G.

74 S. N. Ramanan, N. Shahkaramipour, T. Tran, L. Zhu, S. R. Venna, C. K. Lim, A. Singh, P. N. Prasad and H. Lin, Self-Cleaning Membranes for Water Purification by Co-Deposition of Photo-Mobile 4,4′-Azodianiline and Bio-Adhesive Polydopamine, *J. Membr. Sci.*, 2018, **554**, 164–174, DOI: 10.1016/J.MEMSCI.2018.02.068.

75 J. Yin, C. Li, D. Wang and S. Liu, FRET-Derived Ratiometric Fluorescent K+ Sensors Fabricated from Thermoresponsive Poly(*N*-Isopropylacrylamide) Microgels Labeled with Crown Ether Moieties, *J. Phys. Chem. B*, 2010, **114**(38), 12213–12220, DOI: 10.1021/jp1052369.

76 J. Ter Schiphorst, S. Coleman, J. E. Stumpel, A. Ben Azouz, D. Diamond and A. P. H. J. Schenning, Molecular Design of Light-Responsive Hydrogels, for in Situ Generation of Fast and Reversible Valves for Microfluidic Applications, *Chem. Mater.*, 2015, **27**(17), 5925–5931, DOI: 10.1021/acs.chemmater.5b01860.

77 J. E. Song and E. C. Cho, Dual-Responsive and Multi-Functional Plasmonic Hydrogel Valves and Biomimetic Architectures Formed with Hydrogel and Gold Nanocolloids, *Sci. Rep.*, 2016, **6**(1), 1–10, DOI: 10.1038/srep34622.

78 R. J. Young and P. A. Lovell, *Introduction to Polymers*, CRC Press, 3rd edn, 2011.

79 S. Mondal, S. Das and A. K. Nandi, A Review on Recent Advances in Polymer and Peptide Hydrogels, *Soft Matter*, 2020, **16**(6), 1404–1454, DOI: 10.1039/c9sm02127bPMID31984400.

80 Y. Takashima, T. Nakayama, M. Miyauchi, Y. Kawaguchi, H. Yamaguchi and A. Harada, Complex Formation and Gelation between Copolymers Containing Pendant Azobenzene Groups and Cyclodextrin Polymers, *Chem. Lett.*, 2004, **33**(7), 890–891, DOI: 10.1246/cl.2004.890.

81 A. Gooch, N. S. Murphy, N. H. Thomson and A. J. Wilson, Side-Chain Supramolecular Polymers Employing Conformer Independent Triple Hydrogen Bonding Arrays, *Macromolecules*, 2013, **46**(24), 9634–9641, DOI: 10.1021/ma402069b.

82 V. Stroganov, S. Zakharchenko, E. Sperling, A. K. Meyer, O. G. Schmidt and L. Ionov, Biodegradable Self-Folding Polymer Films with Controlled Thermo-Triggered Folding, *Adv. Funct. Mater.*, 2014, **24**(27), 4357–4363, DOI: 10.1002/adfm.201400176.

83 G. A. Paredes Juárez, M. Spasojevic, M. M. Faas and P. de Vos, Immunological and Technical Considerations in Application of Alginate-Based Microencapsulation Systems, *Front. Bioeng. Biotechnol.*, 2014, **2**(AUG), 1–15, DOI: 10.3389/fbioe.2014.00026.

84 A. Harada, Y. Takashima and M. Nakahata, Supramolecular Polymeric Materials via Cyclodextrin-Guest Interactions, *Acc. Chem. Res.*, 2014, **47**(7), 2128–2140, DOI: 10.1021/ar500109h.

85 G. J. Osterwinter, R. Navarro-Crespo, O. Prucker, M. Henze and J. Rühe, Surface-Attached Polymer Networks through Carbene Intermediates Generated from α-Diazo Esters, *J. Polym. Sci., Part A: Polym. Chem.*, 2017, **55**(19), 3276–3285, DOI: 10.1002/pola.28702.

86 Z. C. Wang, X. D. Xu, C. S. Chen, L. Yun, J. C. Song, X. Z. Zhang and R. X. Zhuo, In Situ Formation of Thermosensitive Pnipaam-Based Hydrogels by Michael-Type Addition Reaction, *ACS Appl. Mater. Interfaces*, 2010, **2**(4), 1009–1018, DOI: 10.1021/am900712e.

87 K. Schuh, O. Prucker and J. Rühe, Surface Attached Polymer Networks through Thermally Induced Cross-Linking of Sulfonyl Azide Group Containing Polymers, *Macromolecules*, 2008, **41**(23), 9284–9289, DOI: 10.1021/ma801387e.

88 O. Prucker, T. Brandstetter and J. Rühe, Surface-Attached Hydrogel Coatings via C,H-Insertion Crosslinking for Biomedical and Bioanalytical Applications (Review), *Biointerphases*, 2018, **13**(1), 010801, DOI: 10.1116/1.4999786.

89 A. Kibrom, R. F. Roskamp, U. Jonas, B. Menges, W. Knoll, H. Paulsen and R. L. C. Naumann, Hydrogel-Supported Protein-Tethered Bilayer Lipid Membranes: A New Approach toward Polymer-Supported Lipid Membranes, *Soft Matter*, 2011, **7**(1), 237–246, DOI: 10.1039/c0sm00618a.

90 Y. Osada, J. P. Gong and Y. Tanaka, Polymer Gels, *J. Macromol. Sci., Polym. Rev.*, 2004, **44**(1), 87–112, DOI: 10.1081/MC-120027935.

91 A. Aulasevich, R. F. Roskamp, U. Jonas, B. Menges, J. Dostálek and W. Knoll, Optical Waveguide Spectroscopy for the Investigation of Protein-Functionalized Hydrogel Films, *Macromol. Rapid Commun.*, 2009, **30**(9–10), 872–877, DOI: 10.1002/marc.200800747.

92 N. Carl, J. Sindram, M. Gallei, S. U. Egelhaaf and M. Karg, From Normal Diffusion to Superdiffusion: Photothermal Heating of Plasmonic Core–Shell Microgels, *Phys. Rev. E*, 2019, **100**(5), 052605–052617, DOI: 10.1103/PhysRevE.100.052605.

93 T. Ekblad, G. Bergström, T. Ederth, S. L. Conlan, R. Mutton, A. S. Clare, S. Wang, Y. Liu, Q. Zhao, F. D'Souza, G. T. Donnelly, P. R. Willemsen, M. E. Pettitt, M. E. Callow, J. A. Callow and B. Liedberg, Poly(Ethylene Glycol)-Containing Hydrogel Surfaces for Antifouling Applications in Marine and Freshwater Environments, *Biomacromolecules*, 2008, **9**(10), 2775–2783, DOI: 10.1021/bm800547m.

94 T. R. Thatiparti, A. Kano, A. Maruyama and A. Takahara, Novel Silver-Loaded Semi-Interpenetrating Polymer Network Gel Films with Antibacterial Activity, *J. Polym. Sci., Part A: Polym. Chem.*, 2009, **47**(19), 4950–4962, DOI: 10.1002/pola.23546.

95 O. Andersson, A. Larsson, T. Ekblad and B. Liedberg, Gradient Hydrogel Matrix for Microarray and Biosensor Applications: An Imaging SPR Study, *Biomacromolecules*, 2009, **10**(1), 142–148, DOI: 10.1021/bm801029bPMID19067607.

Open Access Article. Published on 26 April 2022. Downloaded on 9/25/2023 10:08:45 AM.
This article is licensed under a Creative Commons Attribution 3.0 Unported Licence.

96 A. Kausaite-Minkstimiene, A. Ramanaviciene, J. Kirlyte and A. Ramanavicius, Comparative Study of Random and Oriented Antibody Immobilization Techniques on the Binding Capacity of Immunosensor, *Anal. Chem.*, 2010, **82**(15), 6401–6408, DOI: 10.1021/ac100468kPM-20669994.

97 C. Dannert, B. T. Stokke and R. S. Dias, Nanoparticle-Hydrogel Composites: From Molecular Interactions to Macroscopic Behavior, *Polym.*, 2019, **11**(2), 275, DOI: 10.3390/polym11020275.

98 C. R. van den Brom, I. Anac, R. F. Roskamp, M. Retsch, U. Jonas, B. Menges and J. A. Preece, The Swelling Behaviour of Thermoresponsive Hydrogel/Silica Nanoparticle Composites, *J. Mater. Chem.*, 2010, **20**(23), 4827–4839, DOI: 10.1039/b927314j.

99 D. J. Beebe, J. S. Moore, J. M. Bauer, Q. Yu, R. H. Liu, C. Devadoss and B. H. Jo, Functional Hydrogel Structures for Autonomous Flow Control inside Microfluidic Channels, *Nature*, 2000, **404**(6778), 588–590, DOI: 10.1038/35007047.

100 S. Gupta, D. Kuckling, K. Kretschmer, V. Choudhary and H.-J. Adler, Synthesis and Characterization of Stimuli-Sensitive Micro- and Nanohydrogels Based on Photocrosslinkable Poly(Dimethylaminoethyl Methacrylate), *J. Polym. Sci., Part A: Polym. Chem.*, 2007, **45**(4), 669–679, DOI: 10.1002/pola.21846.

101 M. Sharifi, J. E. N. Dolatabadi, F. Fathi, M. Zakariazadeh, A. Barzegar, M. Rashidi, H. Tajalli and M. R. Rashidi, Surface Plasmon Resonance and Molecular Docking Studies of Bovine Serum Albumin Interaction with Neomycin: Kinetic and Thermodynamic Analysis, *BioImpacts*, 2017, **7**(2), 91–97, DOI: 10.15171/bi.2017.12.

102 C. C. Fong, M. S. Wong, W. F. Fong and M. Yang, Effect of Hydrogel Matrix on Binding Kinetics of Protein-Protein Interactions on Sensor Surface, *Anal. Chim. Acta*, 2002, **456**(2), 201–208, DOI: 10.1016/S0003-2670(02)00033-8.

103 S. M. George, S. Tandon and B. Kandasubramanian, Advancements in Hydrogel-Functionalized Immunosensing Platforms, *ACS Omega*, 2020, **5**(5), 2060–2068, DOI: 10.1021/acsomega.9b03816.

104 I. K. Han, T. Chung, J. Han and Y. S. Kim, Nanocomposite Hydrogel Actuators Hybridized with Various Dimensional Nanomaterials for Stimuli Responsiveness Enhancement, *Nano Convergence*, 2019, **6**(1), 18, DOI: 10.1186/s40580-019-0188-zPM-31179510.

105 F. Vernerey and T. Shen, The Mechanics of Hydrogel Crawlers in Confined Environment, *J. R. Soc. Interface*, 2017, **14**(132), 20170242, DOI: 10.1098/rsif.2017.0242.

106 L. Zhai, Stimuli-Responsive Polymer Films, *Chem. Soc. Rev.*, 2013, **42**(17), 7148–7160, DOI: 10.1039/c3cs60023h.

107 R. Barbey, L. Lavanant, D. Paripovic, N. Schüwer, C. Sugnaux, S. Tugulu and H. A. Klok, Polymer Brushes via Surface-Initiated Controlled Radical Polymerization: Synthesis, Characterization, Properties, and Applications, *Chem. Rev.*, 2009, **109**(11), 5437–5527, DOI: 10.1021/cr900045a.

108 C. Yoon, R. Xiao, J. Park, J. Cha, T. D. Nguyen and D. H. Gracias, Functional Stimuli Responsive Hydrogel Devices by Self-Folding, *Smart Mater. Struct.*, 2014, **23**(9), 094008, DOI: 10.1088/0964-1726/23/9/094008.

109 S. R. Sershen, G. A. Mensing, M. Ng, N. J. Halas, D. J. Beebe and J. L. West, Independent Optical Control of Microfluidic Valves Formed from Optomechanically Responsive Nanocomposite Hydrogels, *Adv. Mater.*, 2005, **17**(11), 1366–1368, DOI: 10.1002/adma.200401239.

110 N. Vogel, M. Retsch, C.-A. Fustin, A. del Campo and U. Jonas, Advances in Colloidal Assembly: The Design of Structure and Hierarchy in Two and Three Dimensions, *Chem. Rev.*, 2015, **115**(13), 6265–6311, DOI: 10.1021/cr400081d.

111 C. Rodriguez-Emmenegger, C. M. Preuss, B. Yameen, O. Pop-Georgievski, M. Bachmann, J. O. Mueller, M. Bruns, A. S. Goldmann, M. Bastmeyer and C. Barner-Kowollik, Controlled Cell Adhesion on Poly(Dopamine) Interfaces Photopatterned with Non-Fouling Brushes, *Adv. Mater.*, 2013, **25**(42), 6123–6127, DOI: 10.1002/adma.201302492.

112 A. J. Hess, A. J. Funk, Q. Liu, J. A. De La Cruz, G. H. Sheetah, B. Fleury and I. I. Smalyukh, Plasmonic Metamaterial Gels with Spatially Patterned Orientational Order via 3D Printing, *ACS Omega*, 2019, **4**(24), 20558–20563, DOI: 10.1021/acsomega.9b02418.

113 J. Torgersen, X. H. Qin, Z. Li, A. Ovsianikov, R. Liska and J. Stampfl, Hydrogels for Two-Photon Polymerization: A Toolbox for Mimicking the Extracellular Matrix, *Adv. Funct. Mater.*, 2013, **23**(36), 4542–4554, DOI: 10.1002/adfm.201203880.

114 A. I. Ciuciu and P. J. Cywiński, Two-Photon Polymerization of Hydrogels-Versatile Solutions to Fabricate Well-Defined 3D Structures, *RSC Adv.*, 2014, **4**(85), 45504–45516, DOI: 10.1039/c4ra06892k.

115 S. You, J. Li, W. Zhu, C. Yu, D. Mei and S. Chen, Nanoscale 3D Printing of Hydrogels for Cellular Tissue Engineering, *J. Mater. Chem. B*, 2018, **6**(15), 2187–2197, DOI: 10.1039/c8tb00301g.

116 J. F. Xing, M. L. Zheng and X. M. Duan, Two-Photon Polymerization Microfabrication of Hydrogels: An Advanced 3D Printing Technology for Tissue Engineering and Drug Delivery, *Chem. Soc. Rev.*, 2015, **44**(15), 5031–5039, DOI: 10.1039/c5cs00278h.

117 X. Dong, X. Zou, X. Liu, P. Lu, J. Yang, D. Lin, L. Zhang and L. Zha, Temperature-Tunable Plasmonic Property and SERS Activity of the Monodisperse Thermo-Responsive Composite Microgels with Core–Shell Structure Based on Gold Nanorod as Core, *Colloids Surf., A*, 2014, **452**(1), 46–50, DOI: 10.1016/j.colsurfa.2014.03.090.

118 N. G. Quilis, S. Hageneder, S. Fossati, S. K. Auer, P. Venugopalan, A. Bozdogan, C. Petri, A. Moreno-Cencerrado, J. L. Toca-Herrera, U. Jonas and J. Dostalek, UV-Laser Interference Lithography for Local Functionalization of Plasmonic Nanostructures with Responsive Hydrogel, *J. Phys. Chem. C*, 2020, **124**(5), 3297–3305, DOI: 10.1021/acs.jpcc.9b11059.

119 M. Magnozzi, Y. Brasse, T. A. F. König, F. Bisio, E. Bittrich, A. Fery and M. Canepa, Plasmonics of Au/Polymer Core/

Open Access Article. Published on 26 April 2022. Downloaded on 9/25/2023 10:08:45 AM.
This article is licensed under a Creative Commons Attribution 3.0 Unported Licence.

Shell Nanocomposites for Thermoresponsive Hybrid Metasurfaces, *ACS Appl. Nano Mater.*, 2020, **3**(2), 1674–1682, DOI: 10.1021/acsanm.9b02403.

120 H. Gehan, L. Fillaud, M. M. Chehimi, J. Aubard, A. Hohenau, N. Felidj and C. Mangeney, Thermo-Induced Electromagnetic Coupling in Gold/Polymer Hybrid Plasmonic Structures Probed by Surface-Enhanced Raman Scattering, *ACS Nano*, 2010, **4**(11), 6491–6500, DOI: 10.1021/nn101451q.

121 H. Chen, Y. Wang, X. Li, B. Liang, S. Dong, T. You and P. Yin, A CO2-Tunable Plasmonic Nanosensor Based on the Interfacial Assembly of Gold Nanoparticles on Diblock Copolymers Grafted from Gold Surfaces, *RSC Adv.*, 2018, **8**(39), 22177–22181, DOI: 10.1039/c8ra02934b.

122 S. Cormier, T. Ding, V. Turek and J. J. Baumberg, Actuating Single Nano-Oscillators with Light, *Adv. Opt. Mater.*, 2018, **6**(6), 1701281, DOI: 10.1002/ADOM.201701281.

123 M. Karg, I. Pastoriza-Santos, J. Pérez-Juste, T. Hellweg and L. M. Liz-Marzán, Nanorod-Coated PNIPAM Microgels: Thermoresponsive Optical Properties, *Small*, 2007, **3**(7), 1222–1229, DOI: 10.1002/smll.200700078.

124 C. Fernandez-Lopez, L. Polavarapu, D. M. Solis, J. M. Taboada, F. Obelleiro, R. Contreras-Caceres, I. Pastoriza-Santos and J. Perez-Juste, Gold Nanorod-PNIPAM Hybrids with Reversible Plasmon Coupling: Synthesis, Modeling, and SERS Properties, *ACS Appl. Mater. Interfaces*, 2015, **7**(23), 12530–12538, DOI: 10.1021/am5087209.

125 X. Liu, X. Wang, L. Zha, D. Lin, J. Yang, J. Zhou and L. Zhang, Temperature- and PH-Tunable Plasmonic Properties and SERS Efficiency of the Silver Nanoparticles within the Dual Stimuli-Responsive Microgels, *J. Mater. Chem. C*, 2014, **2**(35), 7326–7335, DOI: 10.1039/c4tc00966e.

126 V. A. Turek, S. Cormier, B. Sierra-Martin, U. F. Keyser, T. Ding and J. J. Baumberg, The Crucial Role of Charge in Thermoresponsive-Polymer-Assisted Reversible Dis/Assembly of Gold Nanoparticles, *Adv. Opt. Mater.*, 2018, **6**(8), 1701270, DOI: 10.1002/ADOM.201701270.

127 S. Hamajima, H. Mitomo, T. Tani, Y. Matsuo, K. Niikura, M. Naya and K. Ijiro, Nanoscale Uniformity in the Active Tuning of a Plasmonic Array by Polymer Gel Volume Change, *Nanoscale Adv.*, 2019, **1**(5), 1731–1739, DOI: 10.1039/c8na00404h.

128 N. Gisbert Quilis, M. van Dongen, P. Venugopalan, D. D. Kotlarek, C. Petri, A. Moreno Cencerrado, S. Stanescu, J. L. Toca Herrera, U. Jonas, M. Möller, A. Mourran, J. Dostalek, N. G. Quilis, M. van Dongen, P. Venugopalan, D. D. Kotlarek, C. Petri, A. M. Cencerrado, S. Stanescu, J. L. T. Herrera, U. Jonas, M. Moeller, A. Mourran and J. Dostalek, Actively Tunable Collective Localized Surface Plasmons by Responsive Hydrogel Membrane, *Adv. Opt. Mater.*, 2019, **7**(15), 1–11, DOI: 10.1002/adom.201900342.

129 D. Kotlarek, S. Fossati, P. Venugopalan, N. Gisbert Quilis, J. Slabý, J. Homola, M. Lequeux, F. Amiard, M. Lamy De La Chapelle, U. Jonas and J. Dostálek, Actuated Plasmonic Nanohole Arrays for Sensing and Optical Spectroscopy Applications, *Nanoscale*, 2020, **12**(17), 9756–9768, DOI: 10.1039/d0nr00761g.

130 B. Auguié and W. L. Barnes, Collective Resonances in Gold Nanoparticle Arrays, *Phys. Rev. Lett.*, 2008, **101**(14), 143902, DOI: 10.1103/PhysRevLett.101.143902.

131 K. Volk, J. P. S. S. Fitzgerald, P. Ruckdeschel, M. Retsch, T. A. F. F. König and M. Karg, Reversible Tuning of Visible Wavelength Surface Lattice Resonances in Self-Assembled Hybrid Monolayers, *Adv. Opt. Mater.*, 2017, **5**(9), 1600971, DOI: 10.1002/adom.201600971.

132 Q. Wang, L. Liu, Y. Wang, P. Liu, H. Jiang, Z. Xu, Z. Ma, S. Oren, E. K. C. Chow, M. Lu and L. Dong, Tunable Optical Nanoantennas Incorporating Bowtie Nanoantenna Arrays with Stimuli-Responsive Polymer, *Sci. Rep.*, 2016, **5**(1), 18567, DOI: 10.1038/srep18567.

133 N. Gisbert Quilis, M. Lequeux, P. Venugopalan, I. Khan, W. Knoll, S. Boujday, M. Lamy De La Chapelle and J. Dostalek, Tunable Laser Interference Lithography Preparation of Plasmonic Nanoparticle Arrays Tailored for SERS, *Nanoscale*, 2018, **10**(21), 10268–10276, DOI: 10.1039/c7nr08905h.

134 M. Grzelczak, J. Pérez-Juste, P. Mulvaney and L. M. Liz-Marzán, Shape Control in Gold Nanoparticle Synthesis, *Chem. Soc. Rev.*, 2008, **37**(9), 1783–1791, DOI: 10.1039/b711490g.

135 Z. Sun, C. Song, C. Wang, Y. Hu and J. Wu, Hydrogel-Based Controlled Drug Delivery for Cancer Treatment: A Review, *Mol. Pharm.*, 2020, **17**(2), 373–391, DOI: 10.1021/acs.molpharmaceut.9b01020.

136 A. C. Manikas, A. Aliberti, F. Causa, E. Battista and P. A. Netti, Thermoresponsive PNIPAAm Hydrogel Scaffolds with Encapsulated AuNPs Show High Analyte-Trapping Ability and Tailored Plasmonic Properties for High Sensing Efficiency, *J. Mater. Chem. B*, 2014, **3**(1), 53–58, DOI: 10.1039/C4TB01551G.

137 P. G. Yin, Y. Chen, L. Jiang, T. T. You, X. Y. Lu, L. Guo and S. Yang, Controlled Dispersion of Silver Nanoparticles into the Bulk of Thermosensitive Polymer Microspheres: Tunable Plasmonic Coupling by Temperature Detected by Surface Enhanced Raman Scattering, *Macromol. Rapid Commun.*, 2011, **32**(13), 1000–1006, DOI: 10.1002/marc.201100143.

138 M. B. Müller, C. Kuttner, T. A. F. König, V. V. Tsukruk, S. Förster, M. Karg and A. Fery, Plasmonic Library Based on Substrate-Supported Gradiential Plasmonic Arrays, *ACS Nano*, 2014, **8**(9), 9410–9421, DOI: 10.1021/nn503493c.

139 M. Á. Fernández-Rodríguez, R. Elnathan, R. Ditcovski, F. Grillo, G. M. Conley, F. Timpu, A. Rauh, K. Geisel, T. Ellenbogen, R. Grange, F. Scheffold, M. Karg, W. Richtering, N. H. Voelcker and L. Isa, Tunable 2D Binary Colloidal Alloys for Soft Nanotemplating, *Nanoscale*, 2018, **10**(47), 22189–22195, DOI: 10.1039/C8NR07059H.

140 A. Mourran, H. Zhang, R. Vinokur and M. Möller, Soft Microrobots Employing Nonequilibrium Actuation via Plasmonic Heating, *Adv. Mater.*, 2017, **29**(2), 1604825, DOI: 10.1002/adma.201604825.

Open Access Article. Published on 26 April 2022. Downloaded on 9/25/2023 10:08:45 AM.
This article is licensed under a Creative Commons Attribution 3.0 Unported Licence.

141 F. Pirani, N. Sharma, A. Moreno-Cencerrado, S. Fossati, C. Petri, E. Descrovi, J. L. Toca-Herrera, U. Jonas and J. Dostalek, Optical Waveguide-Enhanced Diffraction for Observation of Responsive Hydrogel Nanostructures, *Macromol. Chem. Phys.*, 2017, **218**(6), 1–10, DOI: 10.1002/macp.201600400.

142 N. Sharma, C. Petri, U. Jonas and J. Dostalek, Reversibly Tunable Plasmonic Bandgap by Responsive Hydrogel Grating, *Opt. Express*, 2016, **24**(3), 2457, DOI: 10.1364/OE.24.002457.

143 P. W. Beines, I. Klosterkamp, B. Menges, U. Jonas and W. Knoll, Responsive Thin Hydrogel Layers from Photo-Cross-Linkable Poly(*N*-Isopropylacrylamide) Terpolymers, *Langmuir*, 2007, **23**(4), 2231–2238, DOI: 10.1021/la063264t.

144 D. Schwärzle, X. Hou, O. Prucker and J. Rühe, Polymer Microstructures through Two-Photon Crosslinking, *Adv. Mater.*, 2017, **29**(39), 1703469, DOI: 10.1002/ADMA.201703469.

145 N. G. Quilis, S. Hageneder, S. Fossati, S. K. Auer, P. Venugopalan, A. Bozdogan, C. Petri, A. Moreno-Cencerrado, J. L. Toca-Herrera, U. Jonas and J. Dostalek, UV-Laser Interference Lithography for Local Functionalization of Plasmonic Nanostructures with Responsive Hydrogel, *J. Phys. Chem. C*, 2020, **124**(5), 3297–3305, DOI: 10.1021/acs.jpcc.9b11059.

146 G. Baffou, P. Berto, E. Bermúdez Ureña, R. Quidant, S. Monneret, J. Polleux and H. Rigneault, Photoinduced Heating of Nanoparticle Arrays, *ACS Nano*, 2013, **7**(8), 6478–6488, DOI: 10.1021/nn401924n.

147 P. Winkler, M. Belitsch, A. Tischler, V. Häfele, H. Ditlbacher, J. R. Krenn, A. Hohenau, M. Nguyen, N. Félidj and C. Mangeney, Nanoplasmonic Heating and Sensing to Reveal the Dynamics of Thermoresponsive Polymer Brushes, *Appl. Phys. Lett.*, 2015, **107**(14), 141906, DOI: 10.1063/1.4932968.

148 S. K. Auer, S. Fossati, U. Jonas and J. Dostálek, Observation of Rapid Collapsing and Swelling of Crosslinked PNIPAAm-Based Hydrogel Film by Plasmonic Heating and Resonance Detuning, *J. Phys. Chem. B*, 2022, DOI: 10.1021/acs.jpcb.2c01160.

149 T. Ding, V. K. Valev, A. R. Salmon, C. J. Forman, S. K. Smoukov, O. A. Scherman, D. Frenkel and J. J. Baumberg, Light-Induced Actuating Nanotransducers, *Proc. Natl. Acad. Sci. U. S. A.*, 2016, **113**(20), 5503–5507, DOI: 10.1073/pnas.1524209113.

150 Y. R. Leroux, J. C. Lacroix, K. I. Chane-Ching, C. Fave, N. Félidj, G. Lévi, J. Aubard, J. R. Krenn and A. Hohenau, Conducting Polymer Electrochemical Switching as an Easy Means for Designing Active Plasmonic Devices, *J. Am. Chem. Soc.*, 2005, **127**(46), 16022–16023, DOI: 10.1021/ja054915v.

151 J. W. Jeon, J. Zhou, J. A. Geldmeier, J. F. Ponder, M. A. Mahmoud, M. El-Sayed, J. R. Reynolds and V. V. Tsukruk, Dual-Responsive Reversible Plasmonic Behavior of Core–Shell Nanostructures with PH-Sensitive and Electroactive Polymer Shells, *Chem. Mater.*, 2016, **28**(20), 7551–7563, DOI: 10.1021/acs.chemmater.6b04026.

152 N. Jiang, L. Shao and J. Wang, (Gold Nanorod Core)/(Polyaniline Shell) Plasmonic Switches with Large Plasmon Shifts and Modulation Depths, *Adv. Mater.*, 2014, **26**(20), 3282–3289, DOI: 10.1002/adma.201305905.

153 D. Kuckling, M. E. Harmon and C. W. Frank, Photo-Cross-Linkable PNIPAAm Copolymers. 1. Synthesis and Characterization of Constrained Temperature-Responsive Hydrogel Layers, *Macromolecules*, 2002, **35**(16), 6377–6383, DOI: 10.1021/ma0203041.

154 K. Sergelen, C. Petri, U. Jonas and J. Dostalek, Free-Standing Hydrogel-Particle Composite Membrane with Dynamically Controlled Permeability, *Biointerphases*, 2017, **12**(5), 051002, DOI: 10.1116/1.4996952.

155 A. Choe, J. Yeom, R. Shanker, M. P. Kim, S. Kang and H. Ko, Stretchable and Wearable Colorimetric Patches Based on Thermoresponsive Plasmonic Microgels Embedded in a Hydrogel Film, *NPG Asia Mater.*, 2018, **10**(9), 912–922, DOI: 10.1038/s41427-018-0086-6.

156 S. K. Mishra and B. D. Gupta, Surface Plasmon Resonance Based Fiber Optic PH Sensor Utilizing Ag/ITO/Al/Hydrogel Layers, *Analyst*, 2013, **138**(9), 2640–2646, DOI: 10.1039/c3an00097d.

157 M. Mesch, C. Zhang, P. V. Braun and H. Giessen, Functionalized Hydrogel on Plasmonic Nanoantennas for Noninvasive Glucose Sensing, *ACS Photonics*, 2015, **2**(4), 475–480, DOI: 10.1021/acsphotonics.5b00004.

158 M. Elsherif, M. U. Hassan, A. K. Yetisen and H. Butt, Glucose Sensing with Phenylboronic Acid Functionalized Hydrogel-Based Optical Diffusers, *ACS Nano*, 2018, **12**(3), 2283–2291, DOI: 10.1021/acsnano.7b07082.

159 A. Aliberti, A. Ricciardi, M. Giaquinto, A. Micco, E. Bobeico, V. La Ferrara, M. Ruvo, A. Cutolo and A. Cusano, Microgel Assisted Lab-on-Fiber Optrode, *Sci. Rep.*, 2017, **7**(1), 1–11, DOI: 10.1038/s41598-017-14852-5.

160 M. Wei, X. Li and M. J. Serpe, Stimuli-Responsive Microgel-Based Surface Plasmon Resonance Transducer for Glucose Detection Using a Competitive Assay with Concanavalin A, *ACS Appl. Polym. Mater.*, 2019, **1**(3), 519–525, DOI: 10.1021/acsapm.8b00207.

161 H. M. Yang, J. Y. Teoh, G. H. Yim, Y. Park, Y. G. Kim, J. Kim and D. Yoo, Label-Free Analysis of Multivalent Protein Binding Using Bioresponsive Nanogels and Surface Plasmon Resonance (SPR), *ACS Appl. Mater. Interfaces*, 2020, **12**(5), 5413–5419, DOI: 10.1021/acsami.9b17328.

162 Y. Jiang, M. G. Colazo and M. J. Serpe, Poly(N-Isopropylacrylamide) Microgel-Based Sensor for Progesterone in Aqueous Samples, *Colloid Polym. Sci.*, 2016, **294**(11), 1733–1741, DOI: 10.1007/s00396-016-3926-3.

163 J. Li, C. Ji, B. Lü, M. Rodin, J. Paradies, M. Yin and D. Kuckling, Dually Crosslinked Supramolecular Hydrogel for Cancer Biomarker Sensing, *ACS Appl. Mater. Interfaces*, 2020, **12**(33), 36873–36881, DOI: 10.1021/acsami.0c08722.

164 Y. Jiang, M. G. Colazo and M. J. Serpe, Poly(*N*-Isopropylacrylamide) Microgel-Based Etalons for the Label-Free Quantitation of Estradiol-17B in Aqueous Solutions and

Open Access Article. Published on 26 April 2022. Downloaded on 9/25/2023 10:08:45 AM.
This article is licensed under a Creative Commons Attribution 3.0 Unported Licence.

Milk Samples, *Anal. Bioanal. Chem.*, 2018, **410**(18), 4397–4407, DOI: 10.1007/s00216-018-1095-6.

165 C. J. Huang, J. Dostalek and W. Knoll, Long Range Surface Plasmon and Hydrogel Optical Waveguide Field-Enhanced Fluorescence Biosensor with 3D Hydrogel Binding Matrix: On the Role of Diffusion Mass Transfer, *Biosens. Bioelectron.*, 2010, **26**(4), 1425–1431, DOI: 10.1016/j.bios.2010.07.072.

166 C. J. Huang, U. Jonas, J. Dostalek and W. Knoll, Biosensor platform based on surface plasmon-enhanced fluorescence spectroscopy and responsive hydrogel binding matrix, *SPIE Proceedings Optical Sensors*, 2009, **7356**, 510–516, DOI: 10.1117/12.820988.

167 S. Hageneder, V. Jungbluth, R. Soldo, C. Petri, M. Pertiller, M. Kreivi, A. Weinhäusel, U. Jonas and J. Dostalek, Responsive Hydrogel Binding Matrix for Dual Signal Amplification in Fluorescence Affinity Biosensors and Peptide Microarrays, *ACS Appl. Mater. Interfaces*, 2021, **13**(23), 27645–27655, DOI: 10.1021/acsami.1c05950.

168 R. A. Álvarez-Puebla, R. Contreras-Cáceres, I. Pastoriza-Santos, J. Pérez-Juste and L. M. Liz-Marzán, Au@pNIPAM Colloids as Molecular Traps for Surface-Enhanced, Spectroscopic, Ultra-Sensitive Analysis, *Angew. Chem., Int. Ed.*, 2009, **48**(1), 138–143, DOI: 10.1002/anie.200804059.

169 A. C. Manikas, A. Aliberti, F. Causa, E. Battista and P. A. Netti, Thermoresponsive PNIPAAm Hydrogel Scaffolds with Encapsulated AuNPs Show High Analyte-Trapping Ability and Tailored Plasmonic Properties for High Sensing Efficiency, *J. Mater. Chem. B*, 2015, **3**(1), 53–58, DOI: 10.1039/c4tb01551g.

170 R. Elashnikov, D. Mares, T. Podzimek, V. Švorčík and O. Lyutakov, Sandwiched Gold/PNIPAm/Gold Microstructures for Smart Plasmonics Application: Towards the High Detection Limit and Raman Quantitative Measurements, *Analyst*, 2017, **142**(16), 2974–2981, DOI: 10.1039/c7an00419b.

171 O. Guselnikova, P. Postnikov, Y. Kalachyova, Z. Kolska, M. Libansky, J. Zima, V. Svorcik and O. Lyutakov, Large-Scale, Ultrasensitive, Highly Reproducible and Reusable Smart SERS Platform Based on PNIPAm-Grafted Gold Grating, *ChemNanoMat*, 2017, **3**(2), 135–144, DOI: 10.1002/cnma.201600284.

172 Y. Wu, F. Zhou, L. Yang and J. Liu, A Shrinking Strategy for Creating Dynamic SERS Hot Spots on the Surface of Thermosensitive Polymer Nanospheres, *Chem. Commun.*, 2013, **49**(44), 5025–5027, DOI: 10.1039/c3cc40875b.

173 T. Curtis, A. K. Taylor, S. E. Alden, C. Swanson, J. Lo, L. Knight, A. Silva, B. D. Gates, S. R. Emory and D. A. Rider, Synthesis and Characterization of Tunable, PH-Responsive Nanoparticle-Microgel Composites for Surface-Enhanced Raman Scattering Detection, *ACS Omega*, 2018, **3**(9), 10572–10588, DOI: 10.1021/acsomega.8b01561.

174 C. Jiang, X. Ma, M. Xue and H. Z. Lian, Application of Thermoresponsive Hydrogel/Gold Nanorods Composites in the Detection of Diquat, *Talanta*, 2017, **174**(May), 192–197, DOI: 10.1016/j.talanta.2017.06.010.

175 Y. Liu, S. Yue, Y. N. Y. Wang, Y. N. Y. Wang and Z. R. Xu, A Multicolor-SERS Dual-Mode PH Sensor Based on Smart Nano-in-Micro Particles, *Sens. Actuators, B*, 2020, **310**, 127889, DOI: 10.1016/j.snb.2020.127889.

176 H. Li, X. Wang, Z. Wang, J. Jiang, M. Wei, J. Zheng, Y. Yan and C. Li, Thermo-Responsive Molecularly Imprinted Sensor Based on the Surface-Enhanced Raman Scattering for Selective Detection of R6G in the Water, *Dalton Trans.*, 2017, **46**(34), 11282–11290, DOI: 10.1039/c7dt02495a.

177 K. Nagatani, S. Kiribayashi, Y. Okada, K. Otake, K. Yoshida, S. Tadokoro, T. Nishimura, T. Yoshida, E. Koyanagi, M. Fukushima and S. Kawatsuma, Emergency Response to the Nuclear Accident at the Fukushima Daiichi Nuclear Power Plants Using Mobile Rescue Robots, *J. F. Robot.*, 2013, **30**(1), 44–63, DOI: 10.1002/rob.21439.

178 B. Davies, A Review of Robotics in Surgery, *Proc. Inst. Mech. Eng.*, 2000, **214**(1), 129–140, DOI: 10.1243/0954411001535309.

179 J. Hughes, U. Culha, F. Giardina, F. Guenther, A. Rosendo and F. Iida, Soft Manipulators and Grippers: A Review, *Front. Robot. AI*, 2016, 3, DOI: 10.3389/frobt.2016.00069.

180 S. V. Nikolov, P. D. Yeh and A. Alexeev, Self-Propelled Microswimmer Actuated by Stimuli-Sensitive Bilayered Hydrogel, *ACS Macro Lett.*, 2015, **4**(1), 84–88, DOI: 10.1021/mz5007014.

181 A. W. Hauser, A. A. Evans, J. H. Na and R. C. Hayward, Photothermally Reprogrammable Buckling of Nanocomposite Gel Sheets, *Angew. Chem., Int. Ed.*, 2015, **54**(18), 5434–5437, DOI: 10.1002/anie.201412160.

182 M. L. O'Grady, P. L. Kuo and K. K. Parker, Optimization of Electroactive Hydrogel Actuators, *ACS Appl. Mater. Interfaces*, 2010, **2**(2), 343–346, DOI: 10.1021/am900755w.

183 K. C. Hribar, Y. S. Choi, M. Ondeck, A. J. Engler and S. Chen, Digital Plasmonic Patterning for Localized Tuning of Hydrogel Stiffness, *Adv. Funct. Mater.*, 2014, **24**(31), 4922–4926, DOI: 10.1002/adfm.201400274.

184 G. Stoychev, S. Turcaud, J. W. C. Dunlop and L. Ionov, Hierarchical Multi-Step Folding of Polymer Bilayers, *Adv. Funct. Mater.*, 2013, **23**(18), 2295–2300, DOI: 10.1002/adfm.201203245.

185 H. Guo, Y. Liu, Y. Yang, G. Wu, K. Demella, S. R. Raghavan and Z. Nie, A Shape-Shifting Composite Hydrogel Sheet with Spatially Patterned Plasmonic Nanoparticles, *J. Mater. Chem. B*, 2019, **7**(10), 1679–1683, DOI: 10.1039/c8tb01959b.

186 H. Zhang, A. Mourran and M. Möller, Dynamic Switching of Helical Microgel Ribbons, *Nano Lett.*, 2017, **17**(3), 2010–2014, DOI: 10.1021/acs.nanolett.7b00015.

187 H. Guo, Y. Liu, Y. Yang, G. Wu, K. Demella, S. R. Raghavan and Z. Nie, A Shape-Shifting Composite Hydrogel Sheet with Spatially Patterned Plasmonic Nanoparticles, *J. Mater. Chem. B*, 2019, **7**(10), 1679–1683, DOI: 10.1039/c8tb01959b.

188 Y. Yang, Y. Tan, X. Wang, W. An, S. Xu, W. Liao and Y. Wang, Photothermal Nanocomposite Hydrogel Actuator with Electric-Field-Induced Gradient and Oriented Structure, *ACS Appl. Mater. Interfaces*, 2018, **10**(9), 7688–7692, DOI: 10.1021/acsami.7b17907.


This journal is © The Royal Society of Chemistry 2022

Open Access Article. Published on 26 April 2022. Downloaded on 9/25/2023 10:08:45 AM.
This article is licensed under a Creative Commons Attribution 3.0 Unported Licence.

189 B. Özkale, R. Parreira, A. Bekdemir, L. Pancaldi, E. Özelçi, C. Amadio, M. Kaynak, F. Stellacci, D. J. Mooney and M. S. Sakar, Modular Soft Robotic Microdevices for Dexterous Biomanipulation, *Lab Chip*, 2019, **19**(5), 778–788, DOI: 10.1039/c8lc01200h.

190 C. Delaney, P. McCluskey, S. Coleman, J. Whyte, N. Kent and D. Diamond, Precision Control of Flow Rate in Microfluidic Channels Using Photoresponsive Soft Polymer Actuators, *Lab Chip*, 2017, **17**(11), 2013–2021, DOI: 10.1039/c7lc00368d.

191 H. Yuk, S. Lin, C. Ma, M. Takaffoli, N. X. Fang and X. Zhao, Hydraulic Hydrogel Actuators and Robots Optically and Sonically Camouflaged in Water, *Nat. Commun.*, 2017, **8**, 1–12, DOI: 10.1038/ncomms14230.

192 H. Jia, E. Mailand, J. Zhou, Z. Huang, G. Dietler, J. M. Kolinski, X. Wang and M. S. Sakar, Universal Soft Robotic Microgripper, *Small*, 2019, **15**(4), 1803870, DOI: 10.1002/SMLL.201803870.

193 J. Wang and W. Gao, Nano/Microscale Motors: Biomedical Opportunities and Challenges, *ACS Nano*, 2012, **6**(7), 5745–5751, DOI: 10.1021/nn3028997.

194 D. Patra, S. Sengupta, W. Duan, H. Zhang, R. Pavlick and A. Sen, Intelligent, Self-Powered, Drug Delivery Systems, *Nanoscale*, 2013, **5**(4), 1273–1283, DOI: 10.1039/c2nr32600k.

195 I. Rehor, C. Maslen, P. G. Moerman, B. G. P. van Ravensteijn, R. van Alst, J. Groenewold, H. B. Eral and W. K. Kegel, Photoresponsive Hydrogel Microcrawlers Exploit Friction Hysteresis to Crawl by Reciprocal Actuation, *Soft Rob.*, 2020, 1–9, DOI: 10.1089/soro.2019.0169.

# 4 Microstructuring of Thermoresponsive Biofunctional Hydrogels by Multiphoton Photocrosslinking

**Published as:**

Yevhenii M. Morozov, **Fiona Wiesner (née Diehl)**, Jonas J. Grün, Matthias Pertiller, Stefan Fossati, Katharina Schmidt, Nestor Gisbert Quilis, Claudia Gusenbauer, Barbara Zbiral, Jose Luis Toca-Herrera, Sven Klees, Clinton Richard Victor Thiagarajan, Ulrich Jonas, and Jakub Dostalek, *Adv. Funct. Mater.* **2024***,* 2315578, doi: 10.1002/adfm.202315578.

**Author Contributions:**

*Yevhenii M. Morozov:* Conception, Coordination, Writing, Reviewing, Editing, Corresponding author

***Fiona Wiesner (née Diehl):*** Polymer syntheses and analyses, Writing, Reviewing, Editing

*Jonas J. Grün:* Polymer synthesis and analyses

*Matthias Pertiller:* SPRi measurements

*Stefan Fossati:* SPRi measurements

*Katharina Schmidt:* Post-functionalization of the samples

*Nestor Gisbert Quilis:* Assistance with sample preparation

*Claudia Gusenbauer:* Assistance with AFM measurements

*Barbara Zbiral:* AFM measurements

*Jose Luis Toca-Herrera:* AFM measurements

*Sven Klees:* Polymer synthesis and analyses

*Clinton Richard Victor Thiagarajan:* Monomer synthesis and analyses

*Ulrich Jonas:* Conception, Coordination, Writing, Reviewing, Editing, Funding, Corresponding author

*Jakub Dostalek:* Conception, Coordination, Writing, Reviewing, Editing, Funding, Corresponding author

**Supporting Information** can be found in the Appendix, page A1.

Check for updates



ADVANCED FUNCTIONAL MATERIALS
www.afm-journal.de

# Microstructuring of Thermoresponsive Biofunctional Hydrogels by Multiphoton Photocrosslinking

*Yevhenii M. Morozov,* Fiona Wiesner (née Diehl), Jonas J. Grün, Matthias Pertiller, Stefan Fossati, Katharina Schmidt, Nestor Gisbert Quilis, Claudia Gusenbauer, Barbara Zbiral, Jose Luis Toca-Herrera, Sven Klees, Clinton Richard Victor Thiagarajan, Ulrich Jonas,* and Jakub Dostalek**

**A pioneering method is reported for creating thermoresponsive biofunctional hydrogel microstructures using maskless multiphoton lithography. Departing from conventional multiphoton-triggered polymerization-based techniques, this approach relies on simultaneous photocrosslinking and attachment of already pre-synthesized polymer chains onto solid substrates. The method allows improving control over polymer network characteristics and enables facile integration of additional functionalities through postmodification with biomolecules at specific sites. Exploring two distinct benzophenone- and anthraquinone-based photocrosslinkers incorporated into specially designed poly(*N*-isopropyl acrylamide)-based co- and terpolymers, the photocrosslinking efficacy is scrutinized with the use of a custom femtosecond near-infrared laser lithographer. Comprehensive characterization via surface plasmon resonance imaging, atomic force microscopy, and optical fluorescence microscopy reveals swelling behavior and demonstrates postmodification feasibility. Notably, within a specific range of multiphoton photocrosslinking parameters, the surface-attached microstructures exhibit a quasiperiodic topography akin to wrinkle-pattern formation. Leveraging the capabilities of established multiphoton lithographer systems that offer fast pattern writing with high resolution, this approach holds great promise for the versatile fabrication of multifunctional 3D micro- and nanostructures. Such tailored responsive biofunctional materials with spatial control over composition, swelling behavior, and postmodification are particularly attractive in the areas of bioanalytical and biomedical technologies.**

## 1. Introduction

Polymers responsive to a variety of stimuli such as temperature,[1] pH,[2] mechanical force,[3] chemical species,[4] and electric/magnetic field[5,6] have already become essential building blocks serving in the design of advanced functional materials.[7–10] Among these, poly(*N*-isopropyl acrylamide) (pNIPAAm) is one of the most studied responsive polymers. This polymer can be toggled between a coil and globule state in an aqueous solution by changing the temperature below or above the cloud point temperature that occurs close to the human body temperature,[1,11–13] which is a result of its lower critical solution temperature (LCST) characteristics. This material is commonly used for the preparation of networks that act as thermoresponsive hydrogels in the form of free-standing or surface-attached elements. Such pNIPAAm-based structures are typically prepared by UV-triggered photopolymerization in conjunction with casting in miniature molds.[14] In another route, similar photochemistry is exploited in stereolithography by scanning a UV beam,[15] or in shadow mask lithography[16] for the

Y. M. Morozov
Center for Health & Bioresources
AIT-Austrian Institute of Technology
Giefinggasse 4, Vienna 1210, Austria
E-mail: Yevhenii.Morozov@ait.ac.at

F. Wiesner (née Diehl), J. J. Grün, S. Klees, C. R. V. Thiagarajan, U. Jonas
Macromolecular Chemistry
Department of Chemistry and Biology
University of Siegen
Adolf Reichwein-Straße 2, 57076 Siegen, Germany
E-mail: jonas@chemie.uni-siegen.de

M. Pertiller, K. Schmidt, J. Dostalek
LiST-Life Sciences Technology
Danube Private University
Viktor-Kaplan-Straße 2, Wiener Neustadt 2700, Austria
E-mail: dostalek@fzu.cz

The ORCID identification number(s) for the author(s) of this article can be found under https://doi.org/10.1002/adfm.202315578

© 2024 The Authors. Advanced Functional Materials published by Wiley-VCH GmbH. This is an open access article under the terms of the Creative Commons Attribution License, which permits use, distribution and reproduction in any medium, provided the original work is properly cited.

**DOI: 10.1002/adfm.202315578**

fabrication of pNIPAAm-based objects at the micrometer scale. More recently, polymerization triggered by multiphoton absorption has been demonstrated to provide a preparation technique for pNIPAAm-based microstructures with finer structural details.[17] In combination with metallic nanoparticles, the irradiated volume (where photoinitiation and polymerization occur) can be decreased to the nanoscale regime via the excitation of localized surface plasmon resonances in the near-infrared (NIR) part of the spectrum.[18]

Besides multiphoton initiation and polymerization of typically liquid monomers, an alternative approach can be employed for the fabrication of pNIPAAm structures by photocrosslinking of pre-synthesized polymer chains, which are solid in their dry state. This approach enables the preparation of structures from the compact dry polymer layer, without the risk of leaking the residual monomers when swollen, and benefits from facile means to incorporate multiple functionalities during the polymer pre-synthesis step. Additionally, the solid, uncrosslinked polymer layer can act as supporting material during the writing of complex 3D structures, which is a complicated task for the photopolymerization of liquid monomers that cannot support overhanging geometries (if not combined with, e.g., solid particle fillers [19]). In previous works, pNIPAAm-based biofunctional thin hydrogel films with polymer chains simultaneously crosslinked and attached to a gold surface upon irradiation with UV light were prepared with the use of self-assembled monolayer linkers carrying photoactive moieties.[20] The structuring of these layers was achieved by shadow mask lithography,[21] nanoimprint lithography,[22] or UV-laser interference lithography.[23,24] In these reports, pNIPAAm-based terpolymer with photocrosslinkable benzophenone groups and additional moieties for conjugating biomolecules[25] are used in bioanalytical applications as a tunable binding matrix for target analyte molecules.[26] Recently, this approach was further extended through the synthesis of polymers with even higher complexity and several incorporated functionalities in, e.g., thermoresponsive and thermochromic photocrosslinkable polymer systems.[27] Besides UV-triggered photocrosslinking, a multiphoton absorption process was also employed for the preparation of surface-attached 3D hydrogel structures from non-responsive (*N*,*N*-dimethyl acrylamide-based) and n-butylacrylate polymers.[28–30] In the context of biofunctional structures, the usage of an NIR beam for crosslinking of the hydrogel geometry provides the additional advantage of avoiding the risk of damaging delicate groups with UV light.

In the present work, we synthesized a new set of pNIPAAm-based co- and terpolymers bearing photoactive benzophenone and anthraquinone units for simultaneous multiphoton crosslinking and covalent attachment to a solid surface. To the best of our knowledge, this has not yet been demonstrated for this important thermoresponsive polymer and we investigate the efficiency of such fabrication route depending on the structural properties of prepared polymer scaffolds. An adaptable home-built lithographer with a femtosecond NIR laser was employed for structure writing after optimizing the photocrosslinking conditions. A series of optical and atomic force microscopy studies was implemented to reveal the structural and swelling properties of the prepared responsive hydrogel microstructures, as well as to evaluate the possibility of their post-modification with biomolecules.

## 2. Results and Discussion

As **Figure 1a** illustrates, the investigated polymers were deposited on a solid substrate in the form of a thin dry film for subsequent multiphoton writing of microstructures. Such writing was performed by scanning a focused femtosecond NIR laser beam at a wavelength of 785 nm to locally crosslink and anchor the polymer chains at the irradiated zones to the substrate. For this purpose, a series of pNIPAAm-based polymers was synthesized with a set of different photoactive groups, see Figure 1b. Benzophenone crosslinkers were incorporated into the pNIPAAm-based polymer chains by copolymerization of NIPAAm with *N*-(4-benzoylphenyl)acrylamide (BPAm) or [(4-benzoylphenyl)methyl]dimethyl[3-(prop-2-enamido)propyl]azanium bromide (BPQAAm). Anthraquinone side groups were integrated by copolymerization of NIPAAm with 2-acrylamido-3-hydroxyanthraquinone (AAHAQ) as well as 2-methacrylamido-3-hydroxyanthraquinone (MAAHAQ) monomers, respectively. Furthermore, a terpolymer of NIPAAm, BPQAAm, and methacrylic acid (MAA) was synthesized, bearing acid side groups for potential post-modification of the polymer networks enabling additional functionalities. The UV–vis absorption spectra of the corresponding crosslinker monomers in their most appropriate solvents and concentrations are presented in Figure 1c, illustrating their spectral differences.

### 2.1. Polymer Synthesis

For the synthesis of photocrosslinkable polymers, two fundamental strategies are applicable. In the first strategy, polymer molecules with reactive groups along the backbone can be conjugated in a post-polymerization modification with appropriate photocrosslinker units that carry the complementary reactivity. This conjugation approach has the advantage of modularity such that the same polymer system can be conjugated with different types of photocrosslinkers without affecting the degree of polymerization. Yet, an incomplete coupling reaction always results in a somewhat undefined polymer architecture and remaining reactive groups. In the second strategy, the main monomers

S. Fossati, J. Dostalek
FZU-Institute of Physics
Czech Academy of Sciences
Na Slovance 2, Prague 182 21, Czech Republic
N. G. Quilis
Biosensor Technologies
AIT-Austrian Institute of Technology
Konrad-Lorenz-Strasse 24, Tulln an der Donau 3430, Austria
C. Gusenbauer
Institute of Wood Technology and Renewable Materials
University of Natural Resources and Life Sciences
Konrad-Lorenz-Strasse 24, Tulln an der Donau 3430, Austria
B. Zbiral, J. L. Toca-Herrera
Institute of Biophysics
University of Natural Resources and Life Sciences
Muthgasse 11/II, Vienna 1190, Austria


© 2024 The Authors. Advanced Functional Materials published by Wiley-VCH GmbH


16163028, 0, Downloaded from https://onlinelibrary.wiley.com/doi/10.1002/adfm.202315578 by Cochrane Germany, Wiley Online Library on [26/02/2024]. See the Terms and Conditions (https://onlinelibrary.wiley.com/terms-and-conditions) on Wiley Online Library for rules of use; OA articles are governed by the applicable Creative Commons License

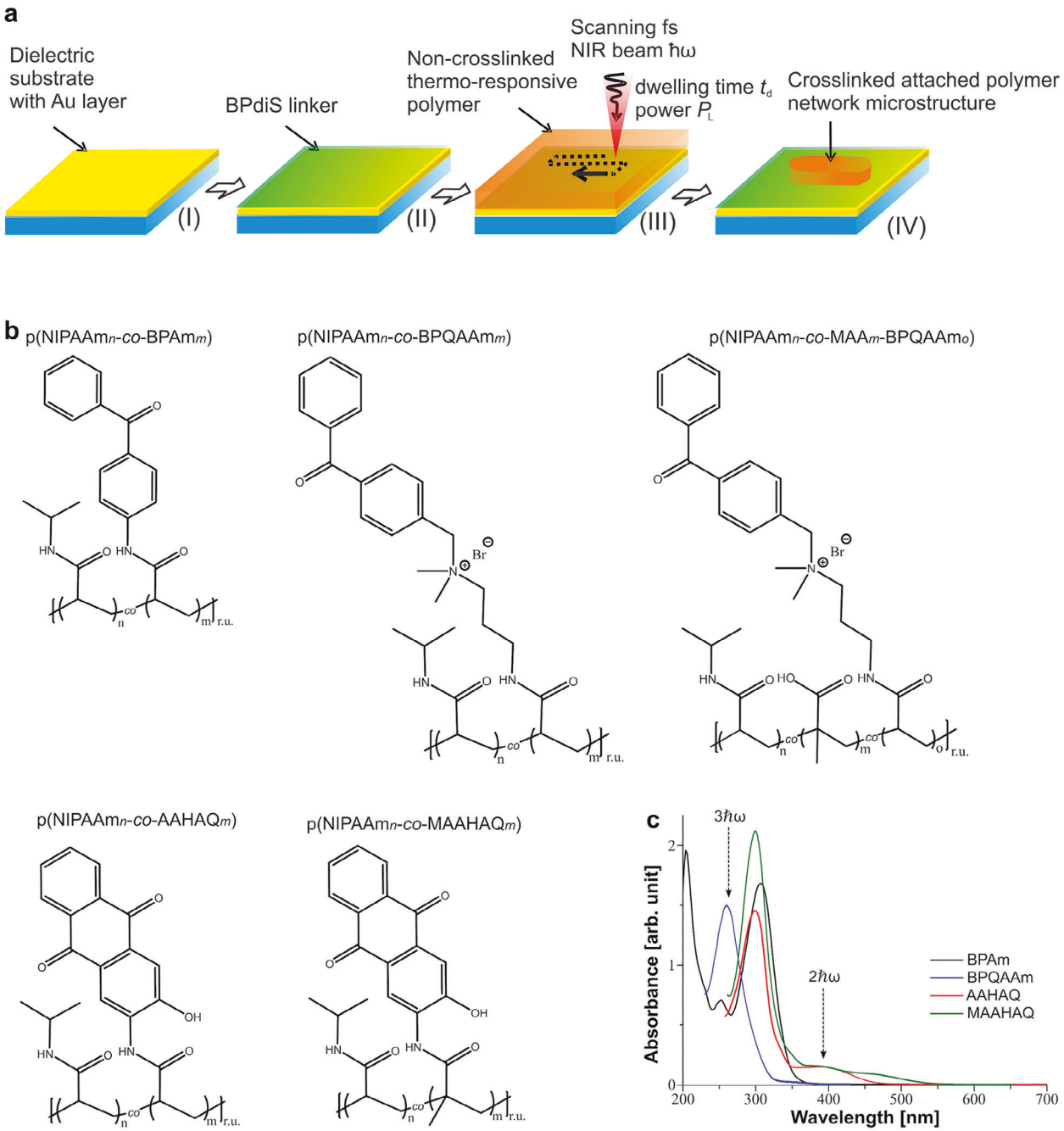


**Figure 1.** a) Schematic of the preparation of polymer network microstructures; b) chemical structures of the polymers and c) respective UV–vis spectra of the photoactive monomers (abbreviated as BPAm, BPQAAm, AAHAQ, and MAAHAQ according to the explanation in the main text) at the concentration of 0.048 g $l^{-1}$ (in EtOH), 0.048 g $l^{-1}$ (in water), 0.040 g $l^{-1}$ (in DMSO), and 0.027 g $l^{-1}$ (in DMSO), respectively after baseline correction for each solvent. The optimal absorption bands for two ($2\hbar\omega$) and three ($3\hbar\omega$) photon excitations are indicated in the spectra by arrows.

that determine the overall behavior of the polymer are copolymerized with comonomers that contain the photocrosslinkable units. This copolymerization approach requires a separate polymerization reaction for each type of photocrosslinker with an inherent slight variation of the resulting polymer structure (degree of polymerization, molar mass dispersity, and comonomer composition) between different samples. Nevertheless, very good control over the reaction conditions can be achieved to allow highly reproducible polymer architectures and the introduction of defined amounts of photocrosslinker units. Also, the combination of different types of comonomers in the same polymer backbone is achievable in this second approach. Thus, for the present paper, we have focused on this copolymerization strategy.

The literature-known BPAm crosslinker was synthesized by a variation of the published procedures.[20,31,32] Briefly,


© 2024 The Authors. Advanced Functional Materials published by Wiley-VCH GmbH


16163028, 0, Downloaded from https://onlinelibrary.wiley.com/doi/10.1002/adfm.202315578 by Cochrane Germany, Wiley Online Library on [26/02/2024]. See the Terms and Conditions (https://onlinelibrary.wiley.com/terms-and-conditions) on Wiley Online Library for rules of use; OA articles are governed by the applicable Creative Commons License

4-aminobenzophenone was exposed to an excess of acryloyl chloride, forming the BPAm monomer with a yield of 88%. The synthesis of BPQAAm was performed in a two-step reaction. In the first step, bromination by a Wohl-Ziegler-type reaction was performed according to the literature.[33] In short, 4-methylbenzophenone was brominated by *N*-bromosuccinimide via radical initiation with azobisisobutyronitrile (AIBN), yielding 84% of 4-bromomethyl benzophenone. In the second step, substitution of 4-bromomethyl benzophenone with *N*-[3-(dimethylamino)propyl]acrylamide in methyl *tert*-butyl ether led to precipitation of the final product BPQAAm as quaternary ammonium bromide in a yield of 90% ($^{1}$H and $^{13}$C NMR spectra of the BPQAAm are shown in Figures S1 and S2, see SI). The anthraquinone-based crosslinker AAHAQ was prepared according to the literature by modification of 2-amino-3-hydroxyanthraquinone with an excess of acryloyl chloride in yields of up to 81%.[28] In an analogous reaction, the synthesis of the corresponding methacrylate MAAHAQ was attempted by treatment of 2-amino-3-hydroxyanthraquinone with a large excess of methacryloyl chloride. Yet, the $^{1}$H NMR analysis of the isolated product (see Figure S3, Supporting Information) indicated incomplete conversion of the anthraquinone. Instead, a ratio of the product and the educt of MAAHAQ to 2-amino-3-hydroxyanthraquinone of 1:0.6 was found even after prolonged reaction times. Nevertheless, this product/educt combination was utilized in a polymerization reaction by adjusting the amount of the starting material mixture based on the above-mentioned ratio with the necessary monomer equivalents. This approach is legitimate, as the starting material without the methacrylic group is not incorporated into the chain during the polymerization reaction.

Copolymers containing the main monomer NIPAAm and one of the four different crosslinker monomers (BPAm, BPQAAm, AAHAQ, and MAAHAQ) were synthesized via free radical polymerization (see Scheme S1, Supporting Information). Specific details about the copolymerization procedures and the copolymer composition can be found in the Figures S4–S16 (Supporting Information).

Overall, the copolymerization of NIPAAm with BPAm or BPQAAm at crosslinker feeds of 1% and 5% resulted in reasonable yields of 60%–80%. As expected from a free radical mechanism, high apparent molar masses (75–150 kDa) and broad molar distributions ($Đ$ = 2.39-2.97) were attained, as determined by size-exclusion chromatography (SEC, see Figure S4, Supporting Information). In contrast, the yields of 22%–51% for the AAHAQ-containing copolymers were significantly lower, the apparent molar masses only amounted to 23–30 kDa, and the molar mass curves from SEC showed a surprisingly narrow and symmetric shape reminiscent of a Poisson distribution (see Figure S5, Supporting Information). It is very striking that nearly all copolymers with AAHAQ prepared by free radical polymerization exhibit narrow dispersities of $Đ$ = 1.3–1.5. Values close to $Đ$ = 1 are typically found for living or controlled radical chain growth mechanisms, such as radical addition-fragmentation chain transfer (RAFT) polymerization.[34,35] Under the assumption that only termination by combination prevails, the theoretical lower limit of the molar mass distribution for free radical polymerization is $Đ$ = 1.5.[36] Thus, the here observed low dispersities for the AAHAQ-containing copolymers suggest a chain transfer reaction mediated by the anthraquinone monomer. A narrow dispersity of $Đ$ = 1.8, which is unusual for free radical polymerizations, was reported in the literature for copolymers composed of AAHAQ and methyl methacrylate,[37] supporting the assumption of the anthraquinone group being involved in the chain growth mechanism. For the MAAHAQ-containing copolymers, the yields of 30%–68% are somewhat higher compared to copolymers with AAHAQ, while they still possess similar apparent molar masses in the range of 27.8–36.9 kDa and narrow dispersities of $Đ$ = 1.3–1.6 (see Figure S6, Supporting Information). As for the copolymerization with AAHAQ, the experimental results indicate an involvement of the MAHAAQ in the chain growth mechanism. However, the postulated transfer mechanism including the anthraquinone crosslinker monomers appears to be complex and was not systematically investigated at this point. This question will be a topic for future studies.

For potential post-modification, 5 mol% methacrylic acid (MAA) was included in the NIPAAm-based terpolymer containing 1 mol% BPQAAm (see Scheme S2, Supporting Information). The carboxylic acid functions of the MAA groups allow the subsequent introduction of molecular fragments (such as biological ligands like antibodies) into the polymer networks after photocrosslinking. The yield of 73% for the terpolymer was comparable to that of the copolymer solely from NIPAAm and BPQAAm, with a similar apparent molar mass of 97 kDa and a dispersity of $Đ$ = 1.89 (see Figure S7, Supporting Information). Furthermore, terpolymers could be prepared from NIPAAm with feeds of 5 mol% MAA and 1 mol% of the two anthraquinone crosslinker monomers, respectively (see Supporting Information).

UV–vis absorption spectra of the used photoactive monomers are shown in Figure 1c and reveal that the spectral position of their absorption peaks varies depending on the crosslinker and the way it is conjugated with the polymer backbone. The BPQAAm monomer exhibits an absorption spectrum with a single peak centered at a wavelength of ≈260 nm, which is close to the energy corresponding to the three-photon absorption process (wavelength of 261 nm) with an NIR light beam at a wavelength of 785 nm. All other crosslinkers show a red-shifted absorption peak located at wavelengths 300–325 nm, which is in the spectral range between a three-photon absorption process (wavelength of 261 nm) and a two-photon absorption process (wavelength of 392 nm). However, AAHAQ and MAAHAQ monomers show an additional shoulder of the absorption peak overlapping with the wavelength of 392 nm making them potentially suitable for a two-photon absorption process. Similar UV–vis absorption bands were observed for the synthesized copolymers (see Figures S12–S15, Supporting Information).

### 2.2. Multiphoton Photochemical Crosslinking of the Polymer Networks

In order to anchor the polymer chains to a gold layer deposited on a BK7 glass substrate, the gold surface was first reacted with 3,3′-disulfanediylbis(N-(4-benzoylbenzyl)propanamide, in short benzophenone disulfide (BPdiS) linker.[38] BPdiS allowed the formation of a self-assembled monolayer (SAM) before the deposition of investigated polymers that were spun on the surface to yield a layer with a thickness of ≈100 nm (as determined by


© 2024 The Authors. Advanced Functional Materials published by Wiley-VCH GmbH

16163028, 0, Downloaded from https://onlinelibrary.wiley.com/doi/10.1002/adfm.202315578 by Cochrane Germany, Wiley Online Library on [26/02/2024]. See the Terms and Conditions (https://onlinelibrary.wiley.com/terms-and-conditions) on Wiley Online Library for rules of use; OA articles are governed by the applicable Creative Commons License

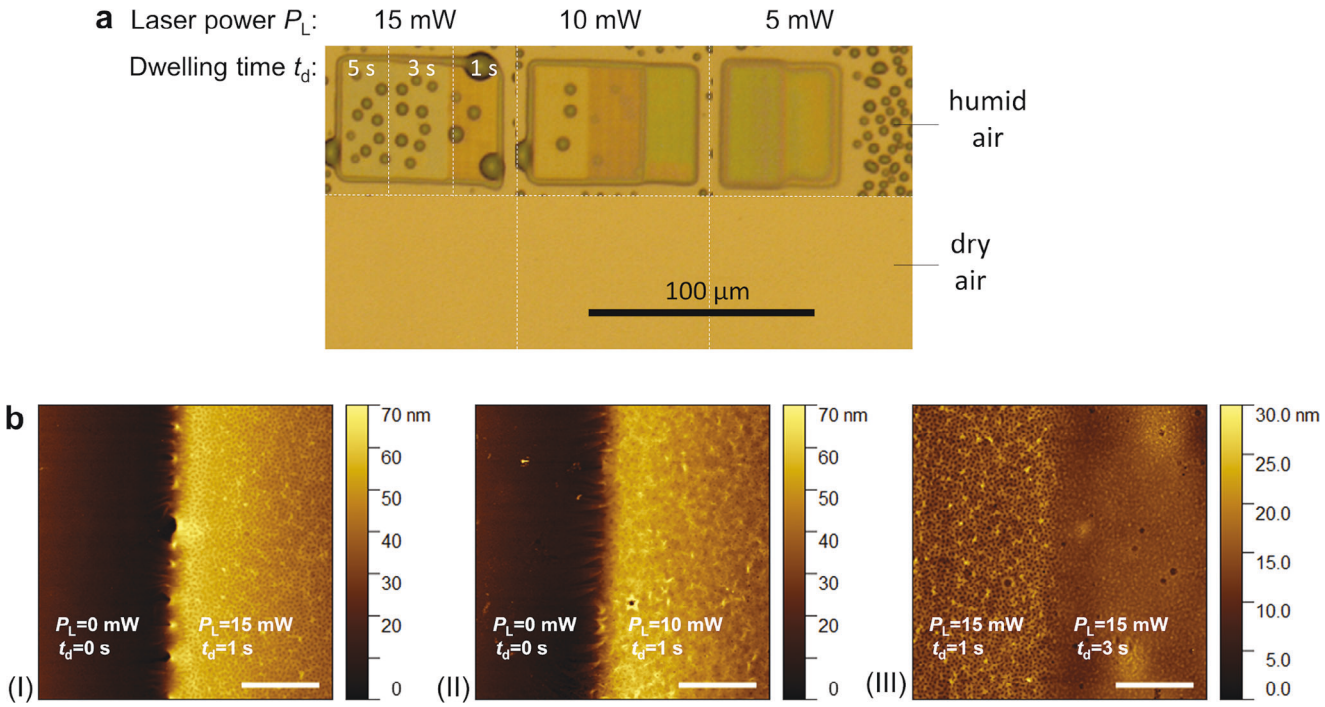


**Figure 2.** a) Bright-field optical microscopy images structures prepared from poly(NIPAAm$_{95}$-*co*-BPQAAm$_5$) with indicated combinations of $P_L$ and $t_d$ when exposed to dry air (bottom row) and humid air in order to form a hydrogel (upper row). b) AFM images of the same poly(NIPAAm$_{95}$-*co*-BPQAAm$_5$) structures on the border of the bare gold substrate and the polymer layer prepared with i) $P_L$ of 15 mW and $t_d$ of 1 s; ii) $P_L$ of 10 mW and $t_d$ of 1 s; and iii) between two polymer network regions made with $P_L$ of 15 mW, $t_d$ of 1 s and $P_L$ of 15 mW, $t_d$ of 3 s; the scale bar is 5 µm.

surface plasmon resonance after drying, see Figure S17, Supporting Information). These substrates were then mounted to a home-built multiphoton lithographer (for more detail see Figure S18, Supporting Information and the Experimental section) that was equipped with a laser emitting ≈100 fs pulses at a repetition rate of 80 MHz. This laser beam was focused through the air on the polymer layer by a 40× objective and the irradiated spot diameter was estimated to be <5 µm (for the given NIR laser beam divergence). The effective power $P_L$ of the beam focused on the polymer sample was controlled between 5 and 15 mW and the overall dose received by the sample at the focal spot was defined by the dwelling time $t_d$ set between 1 and 5 s. The focused beam was raster scanned over the sample by using a motorized stage with a movement step of 1 µm.

To test the ability of the polymer samples to form a hydrogel layer via crosslinking by a multiphoton absorption process, a series of rectangular pads with the size of 75×50 µm$^2$ were recorded in the polymer layers for nine combinations of dwelling time $t_d$ and irradiation power $P_L$ for each polymer type. After the recording, uncrosslinked polymer chains in non-irradiated areas were dissolved by rinsing the substrate with ethanol, eventually leaving only the irradiated pads with successfully crosslinked and attached polymer chains.

First, the presence of the pads in contact with dry and humid air was optically examined by bright-field optical microscopy. The prepared pads were not visible in the dry state, however, water molecules diffused into the polymer network upon exposure to humid air causing their swelling, and then the increased optical contrast allowed for clear observation of their structure. These structures were examined for all synthesized polymers (see Figure S19, Supporting Information) and an example is provided in **Figure 2a** for the poly(NIPAAm$_{95}$-*co*-BPQAAm$_5$). For irradiation laser power set to $P_L$ = 5 mW, the threshold dwelling time $t_d$ that resulted in a stable poly(NIPAAm$_{95}$-*co*-BPQAAm$_5$) network was found to lie above 1 s. For lower irradiation doses no crosslinking took place and the polymer in the irradiated regions did dissolve. When increasing the irradiation power to $P_L$ = 10 and 15 mW, the threshold dwelling time decreased below 1 s. When decreasing the amount of photocrosslinker content in the polymer chains from 5% to 1%, the threshold dwelling time also increased, as can be seen in Figure S20 (Supporting Information) for the poly(NIPAAm$_{99}$-*co*-BPQAAm$_1$). Afterward, the topography of dry samples was examined with atomic force microscopy (AFM), as presented in Figure 2b (AFM images with the corresponding height cross-sections can be found in Figure S21, Supporting Information). The image of the structure edge shows a height of ≈50–60 nm, which is lower than the thickness of the polymer layer before the recording and indicates that a fraction of unbound polymer chains was extracted from the network structures upon rinsing.

Moreover, one can notice a smearing of the structure at the edges, which can be attributed to the effect of swelling. In addition, the stronger crosslinked pads (irradiated with $P_L$ = 15 mW and $t_d$ = 1 s) show a characteristic pore structure resembling wrinkle-patterned hydrogels.[39–41] Besides being of fundamental interest, wrinkle-pattern engineering of the hydrogels offers promising design principles for future smart systems.[42,43]

Interestingly, the polymer poly(NIPAAm$_{95}$-*co*-BPQAAm$_5$) with benzophenone crosslinker BPQAAm (containing a


© 2024 The Authors. Advanced Functional Materials published by Wiley-VCH GmbH

16163028, 0, Downloaded from https://onlinelibrary.wiley.com/doi/10.1002/adfm.202315578 by Cochrane Germany, Wiley Online Library on [26/02/2024]. See the Terms and Conditions (https://onlinelibrary.wiley.com/terms-and-conditions) on Wiley Online Library for rules of use; OA articles are governed by the applicable Creative Commons License

quaternary ammonium fragment) was the only NIPAAm-based polymer that allowed a reliable preparation of thin hydrogel microstructures via the multiphoton absorption crosslinking process. For the other polymer poly(NIPAAm$_{95}$-*co*-BPAm$_5$) with the benzophenone acrylamide crosslinker BPAm (conjugated to the polymer backbone without the ammonium group), we observed that the same illumination conditions did not yield a hydrophilic network and the obtained structures showed a more hydrophobic character that may be ascribed to pyrolysis of the polymer (see Figure S19, Supporting Information). This hypothesis is supported by AFM measurements of the irradiated poly(NIPAAm$_{95}$-*co*-BPAm$_5$) film, which is characterized by inhomogeneous and rather irregular structures (Figure S22, Supporting Information). The difference between the poly(NIPAAm$_{95}$-*co*-BPAm$_5$) and poly(NIPAAm$_{95}$-*co*-BPQAAm$_5$) microstructures is even more obvious when comparing AFM peak force amplitude maps (Figure S23, Supporting Information), where the poly(NIPAAm$_{95}$-*co*-BPAm$_5$) microstructures are reminiscent of a material edge after the laser ablation.[44] The experimentally accessible irradiation conditions for the photocrosslinking of NIPAAm-based polymers with anthraquinone groups – poly(NIPAAm$_{95}$-*co*-AAHAQ$_5$) and poly(NIPAAm$_{95}$-*co*-MAAHAQ$_5$) – apparently did not lead to network formation, as the layers were washed away for all tested dwelling times $t_d$ and irradiation power values $P_L$ (see Figure S19, Supporting Information). On the other hand, a single-photon crosslinking process with 5 mol% AAHAQ crosslinker content in the pNIPAAm polymer at 254 nm irradiation wavelength, starting with a dose of 8.6 J cm$^{-2}$, induced crosslinking and formation of a stable hydrogel after swelling with water (see Figures S25, S26 and Tables S4, S5, Supporting Information). When irradiating at a longer wavelength of 365 nm, an irradiation dose above 10 J cm$^{-2}$ was required to achieve crosslinking. Also, when employing pNIPAAm polymers with only 1 mol% AAHAQ crosslinker content, no network formation was observed under the above irradiation conditions. Similar as reported in the literature,[28,29] the multiphoton-absorption crosslinking led to the formation of polymer networks when using the same AAHAQ crosslinker but exchanging the main monomer with *N,N*-dimethyl acrylamide (DMAA) to yield the polymer poly(DMAA$_{95}$-*co*-AAHAQ$_5$) (see Scheme S3, Figure S20, bottom row, and Figure S27, Supporting Information).

These findings are to be explained by the structural differences of the polymer scaffolds upon variation of the main monomer and the photocrosslinker chromophore, substantially affecting the excitation mechanism of multiphoton-absorption and the crosslinking reaction cascade. Considering first the main monomers, DMAA is a tertiary amide that bears two methyl groups directly bound to the nitrogen atom, while NIPAAm is a secondary amide possessing one hydrogen atom directly attached to the nitrogen (engaging in hydrogen bonding interactions) and one labile hydrogen at the tertiary carbon of the *iso*-propyl group. The latter hydrogen atom at the tertiary carbon is susceptible to radical abstraction by homolytic cleavage, resulting in a carbon radical that is stabilized by hyperconjugation with the tertiary framework. While the NIPAAm-based polymer is indeed able to undergo crosslinking in the *single* photon absorption process for both the AAHAQ-based as well as for benzophenone-based crosslinker comonomers,[20,32,45,46] the *multi*photon crosslinking

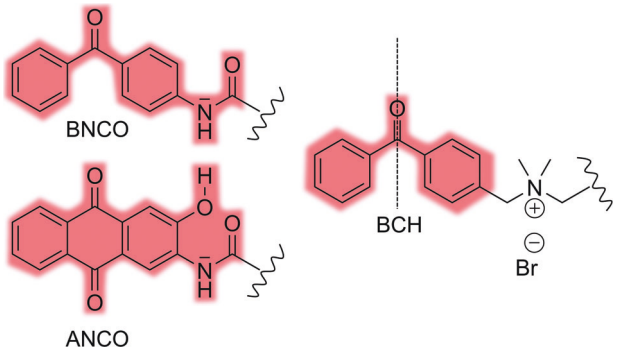


**Figure 3.** Schematics of the three distinct shapes BNCO, BCH, and ANCO for the respective crosslinker chromophores of BPAm, BPQAAm, as well as AAHAQ and MAAHAQ, with the electronically coupled conjugated regions highlighted in red. The black dotted line in BCH indicates the orbital mirror symmetry plane.

was only successful with the BPQAAm unit. Thus, considering only the effects of the main monomer is not sufficient to explain the observed phenomena. In an attempt to elucidate the *multi*photon mechanism, the characteristics of the crosslinker chromophores also need to be scrutinized. In **Figure 3**, the different extensions of the electronic systems are visualized in the four crosslinker monomers employed in the present study. In these schematics, the three distinct shapes of the conjugated regions are abbreviated as BNCO for BPAm, BCH for BPQAAm, and ANCO for both AAHAQ and MAAHAQ. The variation in multiphoton excitation upon irradiation is attributed to the different shapes of these electronic structures, specifically a difference in symmetry, with BCH having a mirror symmetry plane cutting through the carbonyl bond (Figure 3, black dotted line) to support odd-number multiphoton absorption processes (like $3\hbar\omega$). Such mirror plane is missing from BNCO and ANCO, thus they would allow even-number multiphoton absorption processes (like $2\hbar\omega$).

The chromophores BNCO and ANCO exhibit extended conjugated systems involving the amide groups, whereas the conjugation path of BCH only spans over the carbonyl group and the two aromatic rings. The presence of the amide group apparently hampers the multiphoton-induced crosslinking reaction. For BCH a different reaction scenario upon multiphoton excitation can be envisioned, which is displayed in **Figure 4**. The assumed reaction cascade starts with a classical photoexcitation of the carbonyl group in I, where the biradical II is formed at the benzophenone ketone group, as stated in various references of the literature.[46–49] The radical site on the oxygen atom of this carbonyl biradical can abstract a hydrogen atom from a polymer chain in its proximity, resulting in a hydroxyl group on the carbonyl carbon radical and leaving a carbon-based radical site on the participating neighboring polymer chain (III). Following the common mechanism from literature for single-photon crosslinking mentioned above, the carbon radical center of the carbonyl group combines with the carbon-based radical of the adjacent polymer chain, forming a crosslink (see Figure 4, "direct crosslinking (1)" pathway, X).

An alternative reaction pathway for the multiphoton excitation of BCH follows a mesomeric dislocation of the single electron from the carbon-based radical in III via IV to the 4-position in the


© 2024 The Authors. Advanced Functional Materials published by Wiley-VCH GmbH

16163028, 0, Downloaded from https://onlinelibrary.wiley.com/doi/10.1002/adfm.202315578 by Cochrane Germany, Wiley Online Library on [26/02/2024]. See the Terms and Conditions (https://onlinelibrary.wiley.com/terms-and-conditions) on Wiley Online Library for rules of use; OA articles are governed by the applicable Creative Commons License

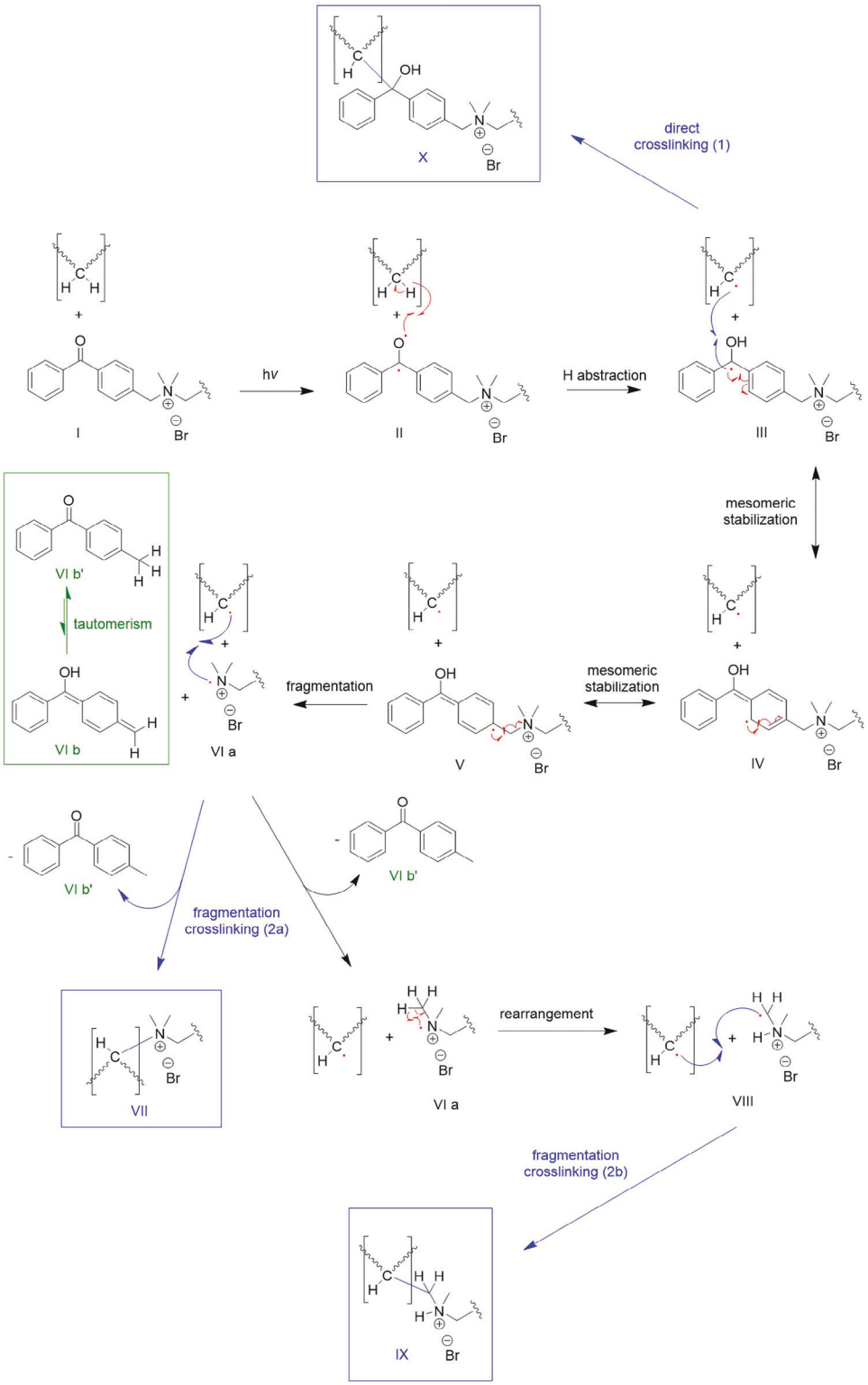


**Figure 4.** The hypothetical mechanism for the multiphoton absorption crosslinking process [fragmentation crosslinking (2a) and fragmentation crosslinking (2b)] of BPQAAm compared with the direct crosslinking mechanism [direct crosslinking (1)]. Square brackets are only schematic indications for a generic polymer chain structure and are not intended to represent the exact repeat unit.

 © 2024 The Authors. Advanced Functional Materials published by Wiley-VCH GmbH



16163028, 0, Downloaded from https://onlinelibrary.wiley.com/doi/10.1002/adfm.202315578 by Cochrane Germany, Wiley Online Library on [26/02/2024]. See the Terms and Conditions (https://onlinelibrary.wiley.com/terms-and-conditions) on Wiley Online Library for rules of use; OA articles are governed by the applicable Creative Commons License

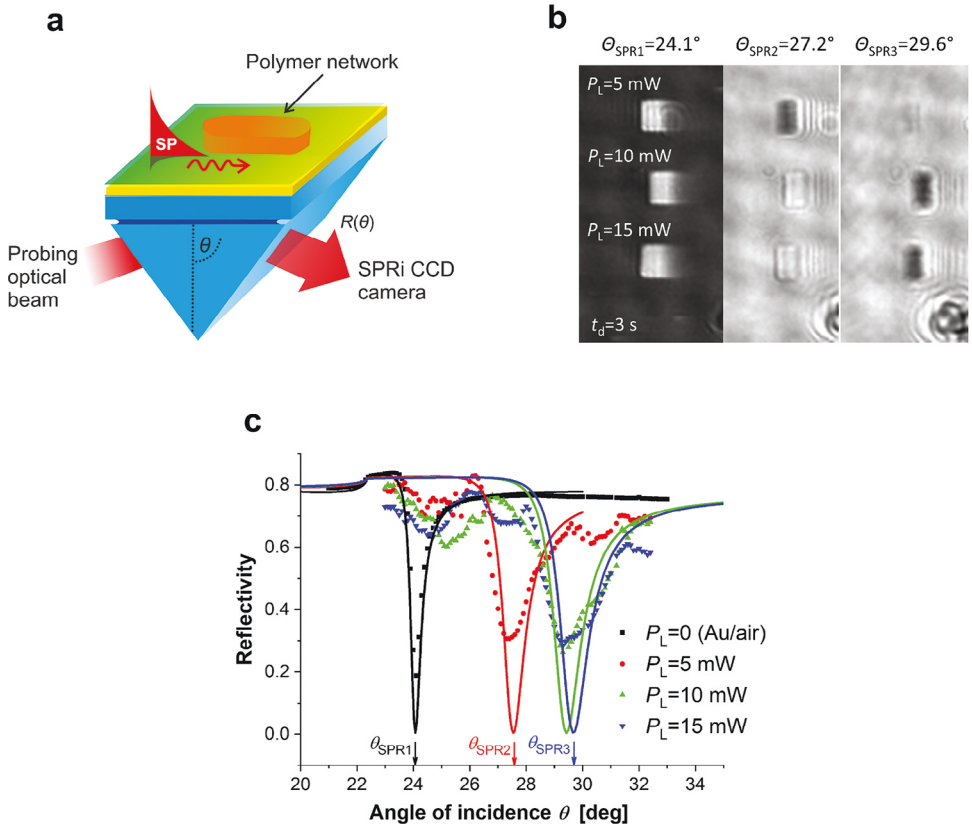


**Figure 5.** a) Schematics of the SPRi setup employed for probing the pNIPAAm-based microstructures in the air; b) SPRi images and c) corresponding angular reflectivity spectra in the air for the case of poly(NIPAAm$_{95}$-*co*-BPQAAm$_5$) structures made with a constant dwelling time of $t_d = 3$ s and varying the laser power $P_L$ between 5, 10, or 15 mW. Solid curves in Figure 5c represent fits calculated with the Fresnel-based reflectivity model.

benzophenone unit (V), where the methylene bridge is attached to a quaternary ammonium group. At this point, a homolytic cleavage of the sigma bond between the methylene carbon and the nitrogen atom from the quaternary ammonium group may take place, resulting in the quinoid form VI b of benzophenone and the fragment VI a with a radical cation on the nitrogen atom. This hypothesis is supported by literature reports on the formation of such nitrogen-based radical cations.[50] This N-radical cation could undergo a crosslinking reaction with an adjacent polymer chain (see Figure 4, "fragmentation crosslinking (2a)" pathway, VII), and forming 4-methylbenzophenone VI b' as the byproduct of the reaction after tautomeric rearrangement of the quinoid benzophenone form VI b.[51]

Yet, an additional reaction pathway may involve a hydrogen shift from the methyl group of the ammonium moiety to the nitrogen radical cation VI a. The formed methylene radical VIII can undergo crosslinking by combination with the polymer backbone radical (see Figure 4, "fragmentation crosslinking (2b)" pathway, IX), also leading to 4-methylbenzophenone (VI b') as a side product.

At this point, we do not have the means of detailed chemical characterization of the crosslinking products of the thin hydrogel films to verify these reaction pathways, but on the basis of existing literature, the drawn assumptions are highly plausible. Nevertheless, the experimental results clearly indicate successful multiphoton crosslinking for the BPQAAm-containing polymers, and further investigation is needed to reveal the underlying photocrosslinking mechanism.

In order to characterize the swelling properties of the prepared hydrogel microstructures, the surface plasmon resonance imaging (SPRi) technique was exploited (**Figure 5a**). A glass substrate was coated with a 50 nm gold film, equipped with a SAM of BPdiS, thin films of the pNIPAAm-based polymers were deposited. After drying, the layers were locally crosslinked and surface-attached by irradiation with a focused laser. The thickness of the prepared pNIPAAm-based polymers layers was adjusted to ≈50 nm (in the dry state as showed by the previous AFM study, see Figure 2) in order to match it with the probing depth of surface plasmon waves (typically reaching 100 nm for used optical parameters). The surface of this substrate was probed by an expanded monochromatic beam that was resonantly coupled to surface plasmon waves traveling along the outer gold interface (for more details about the home-built SPRi setup refer to Figure S28, Supporting Information and the Experimental section). For the resonant excitation of surface plasmon waves, the attenuated total internal reflection method with Kretschmann geometry was used by optically matching the glass substrate to a prism. The spatial distribution of the reflected light intensity was measured by a CCD camera to interrogate changes in surface plasmon resonance (SPR) occurring due to the variations in thermoresponsive hydrogel layers. It manifests itself as a decrease in the reflected intensity that can be tuned by changing the angle


© 2024 The Authors. Advanced Functional Materials published by Wiley-VCH GmbH


16163028, 0, Downloaded from https://onlinelibrary.wiley.com/doi/10.1002/adfm.202315578 by Cochrane Germany, Wiley Online Library on [26/02/2024]. See the Terms and Conditions (https://onlinelibrary.wiley.com/terms-and-conditions) on Wiley Online Library for rules of use; OA articles are governed by the applicable Creative Commons License

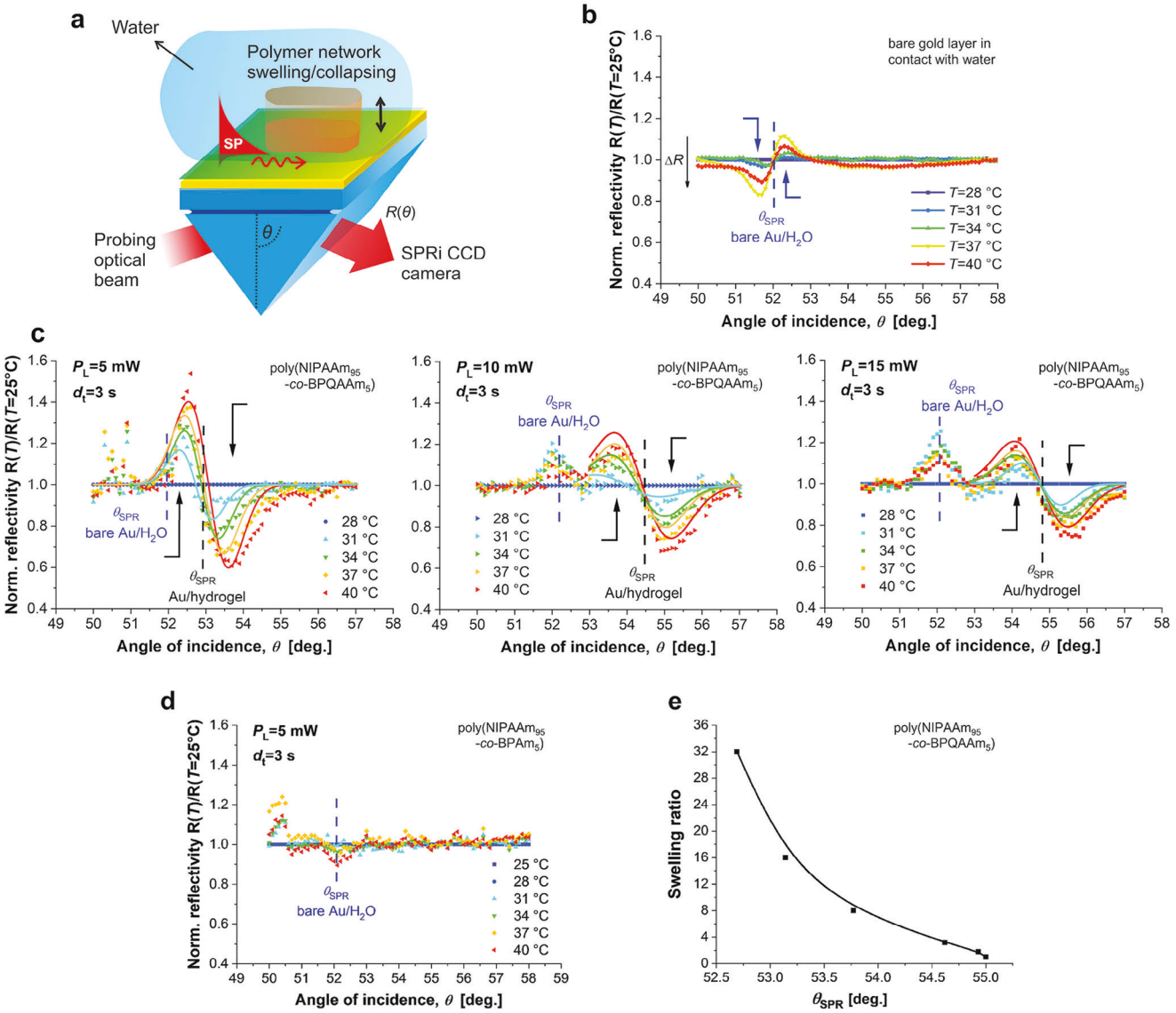


**Figure 6.** a) Schematics of the SPRi employed for probing the pNIPAAm-based microstructures in water. Normalized angular reflectivity spectra in milliQ water with respect to the water temperature for b) the bare gold layer, c) poly(NIPAAm$_{95}$-*co*-BPQAAm$_5$) crosslinked structures at $P_L$ of 5, 10, or 15 mW and $t_d$ = 3 s and d) poly(NIPAAm$_{95}$-*co*-BPAm$_5$) crosslinked structure at $P_L$ of 5 mW and $t_d$ = 3 s; e) dependence between the hydrogel swelling ratio and the SPR angle for the case of the poly(NIPAAm$_{95}$-*co*-BPQAAm$_5$) hydrogel.

of incidence (see Figure 5b). The minimum reflectivity occurs at the resonance angle $\theta_{SPR}$ where surface plasmon waves are excited with the highest efficiency through the resonant optical coupling. From a series of SPRi images acquired at varied angles of incidence, angular reflectivity curves were established for the examined distinct areas carrying the crosslinked pNIPAAm-based microstructures. In this experiment, the dwelling time was set to $t_d$ = 3 s and the laser power $P_L$ varied from 15, 10, to 5 mW to write the polymer network structures, defining three spatially separated pads. The obtained data presented in Figure 5c were acquired for dry polymer pads and were fitted for each crosslinking condition with a model based on the Fresnel multilayer reflectivity formalism to determine the layer thickness. Given a refractive index (RI) for pNIPAAm of 1.49 at $\lambda$ = 785 nm,[52] the fitted thickness for the dry polymer pads prepared with $P_L$ = 5, 10, and 15 mW amounted to 30.5, 41.2, and 42.5 nm, respectively. These thickness values are in good agreement with the data obtained by AFM measurements (compare Figure S21, Supporting Information).

It should be noted that the acquired angular reflectivity spectra show artifacts that are ascribed to interference effects between the surface plasmon waves excited at the bare gold surface and traveling through the pNIPAAm-based structures with those resonantly excited in the polymer-coated areas and due to reflecting of these waves at interfaces. Therefore, for the investigation of the temperature-dependent swelling when in contact with water (**Figure 6a**), the reflectivity curves were measured for increasing temperature $T$ from 28 to 40 °C and normalized with the dependence measured at $T$ = 25 °C. Figure 6b presents such processed reflectivity curves for the bare gold surface in contact with water


© 2024 The Authors. Advanced Functional Materials published by Wiley-VCH GmbH


16163028, 0, Downloaded from https://onlinelibrary.wiley.com/doi/10.1002/adfm.202315578 by Cochrane Germany, Wiley Online Library on [26/02/2024]. See the Terms and Conditions (https://onlinelibrary.wiley.com/terms-and-conditions) on Wiley Online Library for rules of use; OA articles are governed by the applicable Creative Commons License

that serves as a reference. One can see that increasing temperature leads to the occurrence of a feature with an inflection point centered at the angle of incidence corresponding to $\theta_{SPR} = 52°$. This feature exhibits a lower signal at angles $< \theta_{SPR}$ and a higher signal at angles $> \theta_{SPR}$ (which is indicated by blue bent arrows), and it apparently corresponds to the effect of decreasing the SPR angle $\theta_{SPR}$ due to increasing temperature. This agrees with the optical properties of water refractive index which drops when increasing temperature $T$.[53]

When analyzing the normalized curves measured on the areas coated with hydrogel prepared from poly(NIPAAm$_{95}$-*co*-BPQAAm$_5$), a similar feature with the inflection point can be seen at $\theta_{SPR}$ that is shifted to higher angles (see Figure 6c). The reason for this shift is the higher refractive index of the hydrogel with respect to that of water. Importantly, the temperature-induced changes in the vicinity of the inflection point are opposite to that for bare gold, i.e., when increasing the temperature, the signal increases at angles $< \theta_{SPR}$ and decreases at $> \theta_{SPR}$ (which is indicated by black bent arrows). This is a clear signature that the refractive index of pNIPAAm-based networks increases with temperature $T$ upon its collapse. As can be seen in Figure 6c, this effect occurs at temperatures > 31 °C where pNIPAAm has its LCST. For comparison, we included data in Figure 6d measured for poly(NIPAAm$_{95}$-*co*-BPAm$_5$), which does not show a significant response to the temperature changes. This evidence supports the hypothesis that the polymer network was not formed from the polymer with BPAm crosslinker and that no hydrogel structures were formed, e.g., due to pyrolysis of the polymer.

After proving that the pNIPAAm-based hydrogel microstructures prepared by crosslinking with the multiphoton absorption process retain thermoresponsive characteristics, their swelling ratio was deduced from the SPRi analysis. By using a Fresnel-based theory, we established a dependence of the swelling ratio on the SPR angle $\theta_{SPR}$ for the prepared films assuming that the surface mass density is preserved upon the swelling and collapsing and that in the fully collapsed state, the thickness and refractive index of the hydrogel is the same as that determined for the dry films. By comparing the measured $\theta_{SPR} = 53°$ of the weakly crosslinked hydrogel ($t_d = 3$ s, $P_L = 5$ mW) with that determined for the dry film, it can be estimated that the swelling ratio exceeds a factor of 10 (Figure 6e). This quantity refers to the ratio of thickness in the swollen and dry state and the obtained value is higher than that of similar pNIPAAm-based hydrogel films previously prepared by one-photon absorption with the use of UV photocrosslinking.[20,21]

### 2.3. Responsivity and Post-Modification of the Polymer Network with Biomolecules

Besides the binary copolymer of NIPAAm and BPQAAm, a terpolymer with additional MAA units was investigated in order to enable the post-modification of prepared polymer networks. For that purpose, the polymer poly(NIPAAm$_{94}$-*co*-MAA$_5$-BPQAAm$_1$) was synthesized and used for surface-attached microstructures prepared by multiphoton photocrosslinking. Similar terpolymers were also synthesized with the two anthraquinone crosslinkers AAHAQ and MAAHAQ, but no crosslinking with multiphoton irradiation could be achieved in these cases, as observed before with the corresponding copolymers. The swelling and thermoresponsive properties of poly(NIPAAm$_{94}$-*co*-MAA$_5$-BPQAAm$_1$) were examined by AFM operated in contact mode in a liquid medium (milliQ water) kept at a fixed temperature. These measurements were carried out to determine the temperature-dependent mechanical stability of the network as presented in **Figure 7**. The data show that for the hydrogels prepared with $t_d = 3$ s and 5 s and irradiation power $P_L$ of 10 mW, Young's modulus increased from 19 to 26 kPa and from 26 to 30 kPa (respectively) when increasing the temperature from 25 to 40 °C. This documents a collapse of the prepared hydrogel microstructures at temperatures above the pNIPAAm's LCST, yielding a denser and stiffer polymer network.

As this terpolymer bears carboxyl MAA groups, it can be modified with biomolecules through established amine coupling chemistry.[20,54,55] This possibility was demonstrated on a gold-coated substrate with two hydrogel pads fabricated with the $t_d = 3$ s and $P_L = 15$ mW. After recording the structure and developing it by rinsing with ethanol to remove the non-crosslinked polymer chains, the MAA groups were activated by active ester chemistry. Then, IgG protein molecules labeled with Alexa Fluor 647 dye were covalently coupled to the network via their amine groups. The presence of the polymer pads is documented in the bright-field microscopy image, **Figure 8a**. The position of these pads aligns well with the bright areas observed with a confocal fluorescence microscope after the coupling of IgG molecules, Figure 8b. These measurements were performed when the structures were swollen in water, which allowed to increase distance between the metal surface and fluorophores tagged to IgG molecules and thus to reduce quenching. The inset shows an image of one of the pads taken with increased magnification and it interestingly exhibits apparent darker areas resembling the pores observed by AFM for similar hydrogel films (see Figure S21, Supporting Information). It is worth noting that the fluorescence signal originates from anchored IgG molecules tagged with Alexa Fluor 647 . Our previous studies, where a similar pNIPAAm polymer network was used as an affinity binding matrix, showed negligible autofluorescence of the bare structure for the same excitation and emission wavelengths.[21,24]

## 3. Conclusion

This work demonstrates multiphoton absorption–based crosslinking of polymer chains for the facile preparation of thermoresponsive biofunctional NIPAAm-based hydrogel microstructures. A set of NIPAAm-based copolymers and terpolymers was synthesized with controlled amounts of anthraquinone or benzophenone photocrosslinkers conjugated by different structural spacers to the polymer backbone. The study revealed that the ability to crosslink the polymers not only depends on the parameters of the NIR pulsed laser beam scanned over the sample, but also on the choice of the photocrosslinking unit, the spacer between the photocrosslinker and polymer chains, and the nature of the polymer backbone. The results show that for AAHAQ and MAAHAQ crosslinkers attached to the pNIPAAm polymer backbone, the experimentally accessible irradiation dose did not allow reaching the crosslinking


© 2024 The Authors. Advanced Functional Materials published by Wiley-VCH GmbH

16163028, 0, Downloaded from https://onlinelibrary.wiley.com/doi/10.1002/adfm.202315578 by Cochrane Germany, Wiley Online Library on [26/02/2024]. See the Terms and Conditions (https://onlinelibrary.wiley.com/terms-and-conditions) on Wiley Online Library for rules of use; OA articles are governed by the applicable Creative Commons License

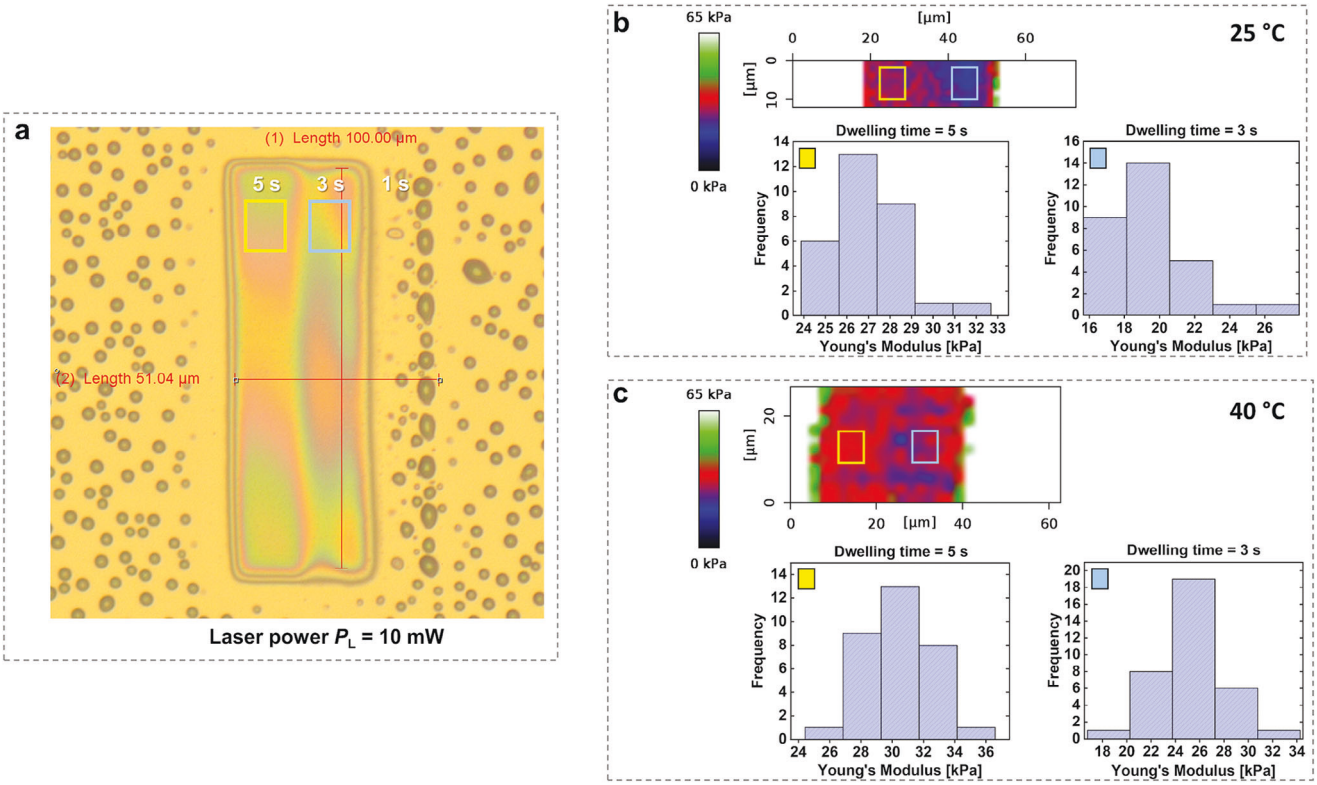


**Figure 7.** Temperature-controlled AFM measurements of Young's moduli for a poly(NIPAAm$_{94}$-*co*-MAA$_5$-BPQAAm$_1$) hydrogel pad made with a laser power $P_L$ of 10 mW and dwelling times $t_d$ of 1, 3, and 5 s on a BK7 substrate. a) Bright-field microscopy image of the formed hydrogels and water condensation patterns after exposure to humid air. Histograms of measured Young's moduli at b) 25 °C and c) 40 °C. Blue and yellow rectangles mark the regions where the modulus distributions were measured.

threshold (however, when changing the polymer backbone to DMAA, successful network preparation was possible). The combination of the BPAm crosslinker with the pNIPAAm polymer backbone assumably showed the effect of pyrolysis and only the BPQAAm crosslinker allowed to yield robust, spatial controllable protocol for the preparation of the pNIPAAm-based polymer networks. The hypothetical pathways for crosslinking mechanism in the case of BPQAAm-based polymer were proposed and discussed; however, a furthermore comprehensive study is needed to confirm the hypothesis. For the identification of the best-performing poly(NIPAAm-*co*-BPQAAm) polymer, the dependence of the threshold on the photocrosslinker amount was determined for different irradiation intensities and dwelling times of the NIR laser beam. Interestingly, the formation of

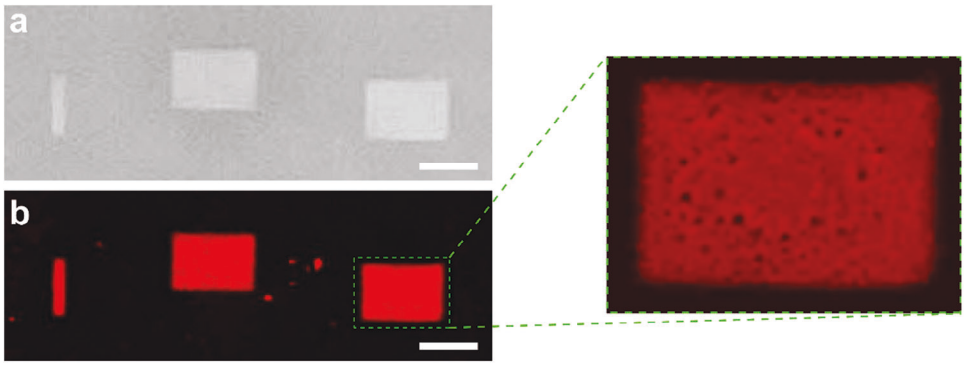


**Figure 8.** a) 10× magnification bright-field microscopy image (in greyscale) of two crosslinked poly(NIPAAm$_{94}$-*co*-MAA$_5$-*co*-BPQAAm$_1$) polymer pads in the dry state before the post-modification and b) 10× magnification confocal fluorescence microscopy image of the corresponding area in the aqueous state after the post-modification. The narrow crosslinked polymer strip was fabricated and used to ease the navigation/orientation over the sample surface. The size of each pad is 75×50 µm$^2$. The scale bar is 50 µm. Inset in Figure 8b presents an image of one of the hydrogel pads recorded with a 40× magnification.


© 2024 The Authors. Advanced Functional Materials published by Wiley-VCH GmbH


16163028, 0, Downloaded from https://onlinelibrary.wiley.com/doi/10.1002/adfm.202315578 by Cochrane Germany, Wiley Online Library on [26/02/2024]. See the Terms and Conditions (https://onlinelibrary.wiley.com/terms-and-conditions) on Wiley Online Library for rules of use; OA articles are governed by the applicable Creative Commons License

wrinkle-patterned topography of collapsed polymer networks was only observed for a specific range of irradiation doses. This characteristic can be beneficial in the context of current interest in wrinkle-pattern engineering of hydrogels.[39–43] In addition, it was shown that a terpolymer poly(NIPAAm-*co*-MAA-*co*-BPQAAm) derived from the best-performing copolymer allows the preparation of thermoresponsive hydrogel structures postmodified with biomolecules. The copolymerization method employed for the synthesis of the photocrosslinkable polymers is a very general approach that can be applied to other types of responsive polymer systems that are prepared by free radical polymerization. As such, the hydrogel networks from multiphoton crosslinking of these polymers can be tailored to respond to other types of stimuli like changes in pH and salt concentrations, to give a few examples.

We believe that the reported approach of multiphoton structuring of thermoresponsive biofunctional hydrogels presented in this publication opens a door for numerous future applications in areas such as externally actuated microstructures serving in micromachines or actively tunable bio-interfaces advancing the performance of bioanalytical technologies. With the use of established multiphoton lithography tools, the reported approach can be adapted for the fabrication of multifunctional 3D nanostructures with higher precision than currently available. The proposed method may offer several advantages with respect to regular approaches using UV-light crosslinking or multiphoton polymerization techniques. For instance, it may allow for the incorporation of cargos (such as a variety of drugs and even viable cells) upon the structure photocrosslinking with a lower risk of their damage. In the same manner, fragile photothermal agents can be coupled with the hydrogel network allowing its spatiotemporal remote control and precise therapy in the biomedical field.[56] Besides, the ability to label with fluorophores and incorporation of biomolecules may allow for the observation and actuating of various microdevices such as responsive hydrogel valves, which can be useful in the lab-on-chip devices[57,58] or be exploited in a new generation of responsive hydrogel-based affinity binding matrices serving in bioanalytical applications. [10]

## 4. Experimental Section

*Chemicals and Working Methods*: Benzophenone disulfide (BPdiS) was synthesized as reported elsewhere.[38] For all reactions, the glassware was dried, and the reactions were carried out under an argon atmosphere. Reaction temperatures were either measured in the center of the aluminum block or inside the used oil bath. All solvents were removed with a rotary evaporator under reduced pressure at 40 °C. Products were either dried with lyophilization or with an oil pump at room temperature if not stated otherwise. Water was demineralized by a Millipore filtration system ($\sigma$ = 18.2 MΩ cm$^{-1}$) (MilliporeQ, USA). Tetrahydrofuran (99%, VWR, Germany) was dried with potassium and distilled before usage. Dimethylformamide (99.8%, Roth, Germany) was dried with potassium carbonate and distilled under vacuum. Magnesium sulfate (99%. Riedel-de Haën, Germany) was dried at 110 °C before usage. AIBN (98%, Fluka Analytic, Germany) was recrystallized twice from methanol. Triethyl amine (99%, Chemsolute, Germany) was distilled before usage. Methacryloyl chloride (97%, containing up to 15% dimer, Alfa Aesar, Germany) was distilled under vacuum before usage. 1,4-Dioxane (99.5%, Roth, Germany) was dried with sodium and distilled before usage. Acetone (99%), hydrochloric acid (37%), dichloromethane (98%), isopropanol (98%), and methanol (98.5%) were all from VWR Chemicals (Germany). *N*-[3-(dimethylamino)propyl]acrylamide was purchased (98%) from TCI (Japan) and used as received. Methyl-*tert.*-butyl ether (99.5%) was bought from Roth (Germany). Silica 60 (0.063 – 0.2 mm, Macherey-Nagel, Germany) was used for column chromatography. Diethyl ether (99.5%), ethyl acetate (99.8%), methanol (99.8%), *n*-hexane, and chloroform (99.8%) were purchased from Fisher Scientific (UK). All deuterated solvents $CDCl_3$ (99.8%), MeOD (99.8%), and DMSO-*d6* (99.8%) were from Deutero GmbH (Germany). Acetic acid (99.5%) and ethanol (99%) were bought from Chemsolute (Germany). Potassium carbonate (98%) was purchased from Bernd Kraft (Germany). 4-Aminobenzophenone (98%), 4-methylbenzophenone (98%), *N*-bromo succinimide (99%), and acryloyl chloride (96%) were bought from Alfa Aesar (Germany). 2-Amino-3-hydroxy anthraquinone (95%) was bought from ABCR GmbH (Germany).

*Monomer Synthesis*: BPAm was synthesized based on analogous procedures in the literature.[20,31,32] BPQAAm was synthesized in a two-step synthesis.

Step 1: Bromination of 4-methylbenzophenone was performed according to the literature.[33] Briefly, 4-methylbenzophenone (1.00 g, 5.09 mmol) and AIBN (1 mg, 6.00 µmol) were dissolved in dichloromethane (6 ml) and *N*-bromo succinimide (1.06 g, 5.95 mmol) was added to obtain a dispersion. The reaction was purged with argon for 10 min and refluxed for 21 h at 60 °C afterward. The orange reaction solution was filtered, and the residue was washed with dichloromethane. The solvent was evaporated, and the solid was washed with *n*-hexane. The process was controlled by thin layer chromatography (silica gel, *n*-hexane/ethyl acetate 10:1, *Rf* = 0.59). After evaporating the solvent, the product was washed with water and dried overnight in a vacuum at 60 °C to obtain 1.17 g (4.25 mmol, 84%) of the product. $^1$H NMR (500 MHz, $CDCl_3$, d/ppm): 4.55 (s, 2 H, $CH_2$-Br), 7.51-7.84 (m, 9 H, -CH = ).$^{13}$C NMR (125 MHz, $CDCl_3$, d/ppm): 32.3, 126.6, 128.3, 128.9, 130.0, 130.3, 130.5, 132.6, 137.4, 137.5, 142.1, 196.0.

Step 2: 4-(Bromomethyl)benzophenone (400 mg, 1.45 mmol) was dissolved in methyl-*tert.*-butyl ether (19 ml) and *N*-[3-(dimethylamino)propyl]acrylamide (272 mg, 1.75 mmol) dissolved in methyl-*tert.*-butyl ether (2 ml) was added dropwise to the solution. The mixture was stirred for 70 h at room temperature. The solvent was decanted and washed with methyl-*tert.*-butyl ether (6×25 ml) and the solvent was removed by decanting. The white solid was dried in a vacuum overnight, and a yield of 563 mg (1.30 mmol, 90%) was obtained. $^1$H NMR (500 MHz, $CDCl_3$, d/ppm): 2.29 (m, 2 H, -$CH_2$-$CH_2$-$CH_2$-), 3.26 (s, 6 H, N-$(CH_3)_2$), 3.49 (q, J = 5.56 Hz, 2 H, N-$CH_2$-$CH_2$), 3.97 (t, J = 8.11 Hz, 2 H, NH-$CH_2$), 5.00 (s, 2 H, N$(CH_3)_2$-$CH_2$-$C_{ar}$), 5.60 (dd, J = 10.01, 1.43 Hz, 1 H, -$CH_2$ = CH-), 6.29 (dd, J = 17.17, 1.43 Hz, 1 H, -$CH_2$ = CH-), 6.47 (dd, J = 16.93, 10.25 Hz, 1 H, -$CH_2$-CH-), 7.51 (m, 2 H, $CH_2$-$C_{ar}$-CH), 7.61 – 7.66 (m, 1 H, -CH = $CH_2$-), 7.79 (m, 4 H, CH-$C_{ar}$-C = O), 7.86 (s, 2 H, -CH = CH-), 8.19 (t, J = 5.25 Hz, 1 H, NH). $^{13}$C NMR (125 MHz, $CDCl_3$, d/ppm): 23.1, 36.4, 50.0, 63.4, 67.3, 110.0, 126.5, 2×128.7, 130.2, 130.6, 131.2, 2×133.3, 136.8, 139.8, 166.8, 195.8.

AAHAQ was synthesized in reference to the literature.[28,59] In short, AHAQ (250 mg, 1.05 mmol) was dispersed in dry 1,4-dioxane (14 ml). Acryloyl chloride (114 mg, 103 µl, 1.25 mmol) dissolved in dry 1,4-dioxane (2) was added dropwise to the dispersion at 0 °C. After complete addition, the reaction was carried out at 110 °C. The reaction mixture turned from black/red to yellow/green and the progress was controlled by thin-layer chromatography (TLC) (silica gel, EtOAc/toluene 60:40, Rf = 0.63). The solid material was filtered off and washed with 1,4-dioxane (5 ml), before removing the excess of acryloyl chloride under vacuum overnight at 70 °C to obtain a yellow powder as the product with yields up to 85%. $^1$H NMR (500 MHz, DMSO-d6, d/ppm): 5.81 (dd, J = 11.92, 1.75 Hz, 1 H, -CH = $CH_2$), 6.34 (m, 1.91 Hz, 1 H, -CH = $CH_2$), 6.85 (m, 1 H, -CH = $CH_2$), 7.64 (m, 1 H, -CH = C-OH), 7.84 – 7.93 (m, 2 H, 2x $CH_{ar}$-C) 8.11 – 8.22 (m, 2 H, 2x ar. -CH = ), 9.01 – 9.08 (m, 1 H, $CH_{ar}$-C-NH), 9.80 (br. s, 1 H, -OH) 11.70 (br. s, 1 H, -NH-). $^{13}$C NMR (125 MHz, DMSO-d6, d/ppm): 111.7, 119.1, 125.8, 126.5, 126.6, 127.9, 129.9, 131.6, 132.2, 133.1, 133.3, 134.0, 134.3, 152.5, 164.0, 181.5, 181.8.


© 2024 The Authors. Advanced Functional Materials published by Wiley-VCH GmbH

16163028, 0, Downloaded from https://onlinelibrary.wiley.com/doi/10.1002/adfm.202315578 by Cochrane Germany, Wiley Online Library on [26/02/2024]. See the Terms and Conditions (https://onlinelibrary.wiley.com/terms-and-conditions) on Wiley Online Library for rules of use; OA articles are governed by the applicable Creative Commons License

For the synthesis of MAAHAQ, AAHAQ (250 mg, 1.05 mmol) was dispersed in dry 1,4-dioxane (14 ml). Methacryloyl chloride (219.5 mg, 204 µl, 2.10 mmol) dissolved in 1,4-dioxane (2 ml) was added dropwise to the dispersion. The conversion was controlled by TLC (silica gel, toluene/EtOAc 80:20, Rf = 0.37). The reaction suspension turned from black to yellow and a solid precipitated. The solid yellow material was washed with 1,4-dioxane (5 ml), before removing the excess of acryloyl chloride in a vacuum overnight at 60 °C to obtain a red-colored product. $^1$H NMR (500 MHz, DMSO-d6, d/ppm): 2.01 – 2.04 (m, 3 H, C-$CH_3$), 5.61 (d, J = 0.95 Hz, 1 H, C-$CH_2$), 7.64 (s, 1 H, -CH = C-OH), 7.86 – 7.91 (m, 2 H, 2x $CH_{ar}$-C), 8.16 (m, J = 10.97 Hz, 2 H, 2x ar. -CH = ), 9.02 (br. s, 1 H, CH-$C_{ar}$-NH), 10.64 (br. s, 1 H, CO-NH), 11.76 (br. s, 1 H, -OH). $^{13}$C NMR (125 MHz, DMSO-d6, d/ppm): 18.3, 109.8, 111.7, 119.0, 125.8, 125.8, 126.5, 126.6, 130.1, 131.8, 133.2, 134.0, 134.3, 139.6, 152.7, 166.2, 181.4, 181.8.

*Copolymer Synthesis*: The masses of the various monomers used for the syntheses of the different polymer samples and the polymer characterization data are provided in Table S1 (Supporting Information). NIPAm (99 or 95 mol%), the crosslinker monomer (BPAm, AAHAQ, MAAHAQ, or BPQAAm, 1 or 5 mol%), and AIBN (0.5 ml%) were dissolved in dry 1,4-dioxane (for BPAm), distilled dimethylformamide (for AAHAQ and MAAHAQ), or methanol (for BPQAAm). The mixture was degassed by three freeze-pump-thaw cycles. The polymerization was started by placing the reaction flask in a preheated aluminum block at 65 °C. After 20 h 20 min, the reaction was quenched by cooling with liquid nitrogen and flushing with air. The polymer was precipitated three times in ice-cold diethyl ether (200 ml). The product was lyophilized from 1,4-dioxane. $^1$H NMR (500 MHz, DMSO-d6, d/ppm) – Poly(NIPAm-*co*-BPAm) (see Figure S8, Supporting Information): 0.85 – 1.15 (CH-$(CH_3)_2$), 1.16 – 1.75 (Backbone, $CH_2$), 1.75 – 2.20 (backbone, CH), 3.70 – 3.98 (CH-$(CH_3)_2$), 6.88 – 7.48 (C-NH), 7.49 – 7.87 ($CH_{ar}$), 9.70 – 10.30 (C-NH). Poly(NIPAm-*co*-BPQAAm) (see SI, Figure S9): 0.85 – 1.15 (CH-$(CH_3)_2$), 1.15 – 1.75 (backbone, $CH_2$), 1.75 – 2.20 (backbone, CH), 2.99 – 3.13 (N-$(CH_3)_2$), 3.70 – 3.95 (CH-$(CH_3)_2$), 6.84 – 7.53 (C-NH) 7.54 – 7.90 ($CH_{ar}$). Poly(NIPAm-*co*-AAHAQ) (see SI, Figure S10): 0.95 – 1.15 (CH-$(CH_3)_2$), 1.16 – 1.75 (backbone, $CH_2$), 1.75 – 2.17 (backbone, CH), 3.70 – 3.97 (CH-$(CH_3)_2$), 6.58 – 7.76 (C-NH), 7.79 – 9.20 ($CH_{ar}$), 11.44 – 11.88 (C-OH). Poly(NIPAm-*co*-MAAHAQ) (see SI, Figure S11): 0.65 – 0.82 (backbone, $CH_3$), 0.83 – 1.15 (CH-$(CH_3)_2$), 1.16 – 1.75 (backbone, $CH_2$), 1.75 – 2.20 (backbone, CH), 3.70 – 3.97 (CH-$(CH_3)_2$), 6.58 – 7.76 (C-NH), 7.79 – 9.10 ($CH_{ar}$), 11.44 – 11.74 (C-OH).

*Terpolymer Synthesis*: Detailed reaction conditions, yields, and the used amounts are shown in Table S2 (Supporting Information). NIPAm (94 or 90 mol%), MAA (5 mol%), the crosslinker monomer (BPAm, AAHAQ, or BPQAAm, 1 or 5 mol%) and AIBN (0.5 mol%) were dissolved in 3.5 ml of distilled dimethylformamide (for AAHAQ), dry 1,4-dioxane (for BPAm), or methanol (for BPQAAm). The mixture was degassed by three freeze-pump-thaw cycles. The polymerization was initiated by placing the reaction flask in a preheated aluminum block at 65 °C. After 20 h 20 min, the reaction was quenched by cooling with liquid nitrogen and flushing with air. The polymer was precipitated three times in ice-cold diethyl ether (200 ml). The product was freeze-dried from 1,4-dioxane.

$^1$H NMR (500 MHz, DMSO-d6, d/ppm): – Poly(NIPAm$_m$-co-MAA$_n$-co-AAHAQ$_o$): 0.74 – 1.15 (CH-$(CH_3)_2$, backbone-$CH_3$), 1.16 – 1.75 (backbone, $CH_2$), 1.75 – 2.20 (backbone, CH), 3.70 – 3.95 (CH-$(CH_3)_2$), 6.65 – 7.75 (C-NH) 7.76 – 9.15 ($CH_{ar}$), 11.37 – 12.20 (C-OH, COOH). Poly(NIPAm$_m$-co-MAA$_n$-co-BPAm$_o$): 0.75 – 1.15 (CH-$(CH_3)_2$, backbone-$CH_3$), 1.16 – 1.75 (backbone, $CH_2$), 1.75 – 2.30 (backbone, CH), 3.70 – 3.95 (CH-$(CH_3)_2$), 6.85 – 7.50 (C-NH), 7.51 – 7.85 ($CH_{ar}$), 11.75 – 12.05 (-COOH). Poly(NIPAm$_m$-co-MAA$_n$-co-BPQAAm$_o$): 0.70 – 1.22 (CH-$(CH_3)_2$, backbone-$CH_3$), 1.2 – 1.75 (backbone, $CH_2$), 1.75 – 2.20 (backbone, CH), 2.99 – 3.10 (N-$(CH_3)_2$), 3.70 – 3.95 (CH-$(CH_3)_2$), 6.85 – 7.54 (C-NH), 7.54 – 8.01 ($CH_{ar}$), 11.75 – 12.05 (-COOH).

*Synthesis of Poly(DMAA$_{95}$-co-AAHAQ$_5$)*: The polymerization of AAHAQ and DMAA was carried out at 75 °C by free radical polymerization in dimethylformamide (DMF) under an inert gas atmosphere. AAHAQ (59.5 mg, 0.203 mmol) and DMAA (384.6 mg, 3.880 mmol) were dissolved in DMF (7 ml). The reaction mixture was degassed by three freeze- and thaw-cycles and initiated by AIBN (3.3 mg, 0.020 mmol). The polymerization was stopped after 24 h by precipitating the reaction mixture in ice-cold diethyl ether. The polymer was purified by dissolving in MeOH and precipitating in ice-cold diethyl ether (2x). The precipitate was separated by centrifugation, dissolved in dioxane (30 ml), and freeze-dried. Yield: 53%, 237.0 mg ($M_w$ = 18.3 kDa, $Đ$ = 2.0). $^1$H NMR spectrum of poly(DMAA$_{95}$-*co*-AAHAQ$_5$) is shown in Figure S24 (see Supporting Information).

*Preparation of Sensor Chips*: BK7 glass substrates were cut into 25 mm × 25 mm pieces and cleaned with a 1% solution of Hellmanex III in an ultrasound bath. These substrates were either coated with a thin SU-8 or by gold layers. SU-8 coating was prepared from a 100 µL drop of a 2% SU-8 (SU-8 from Micro resist technology GmbH, Germany) dissolved in propylene glycol methyl ether acetate (PGMEA) that was spun at 5000 rpm for 60 s followed by drying in a vacuum oven at 50 °C for 2 h. Gold coatings were prepared by vacuum thermal evaporation (UNIVEX 450, Helmut Heller GmbH, Germany), and 2 nm of chromium and 50 nm of gold were subsequently deposited in a vacuum better than $10^{-6}$ mbar. The gold-coated substrates were immersed overnight in a 1 mM solution made of the BPdiS linker 3,3′-disulfanediylbis(N-(4-benzoylbenzyl)propanamide dissolved in dimethyl sulfoxide (DMSO, from Sigma–Aldrich, Austria) in order to form a self-assembled monolayer (SAM). The synthesized pNIPAAm and DMAA polymers were dissolved in EtOH at a concentration of 2% (w/w), 150 µL of this solution was spread over the surface of a gold-coated substrate carrying photoactive linker SAM, and it was spun at 2000 rpm for 60 s. After drying overnight in a vacuum oven at 50 °C, the obtained polymer-coated substrates were stored under an Ar atmosphere before the experiments for less than 2 days.

*Multiphoton Absorption Lithography Setup*: Multiphoton absorption lithography setup was built as schematically shown in Figure S18 (Supporting Information).[60] A compact Er fiber laser (FemtoFiber smart 780, TOptica Photonics) emitting at $\lambda$ = 785 ± 5 nm with a pulse width of ≈100 fs, a repetition rate of 80 MHz, and a maximum output power of 120 mW was used. The beam was focused on the specimen by a 40× reflective objective (LMM-40X-P01, Thorlabs) and scanned by using a 3D scanning stage (MAX381/M, Thorlabs). The instrument was operated by software developed in LabVIEW 2018 Virtual Instrument (VI) including the in-house developed focus-correction algorithm. The developed VI allowed the authors to move the substrates on the stage in a predefined pattern. It is important to highlight that the effective time-averaged irradiation power, $P_L$, delivered to the sample surface was significantly lower than the nominal value of the laser (decreased by a factor of 8). This reduction can be attributed to the use of splitters (enabling a combination with a wide-field optical microscope for navigating and focusing the beam at the sample) and due to not using a beam expander for matching the entrance pupil of the microscope objective lens to avoid spreading the pulses due to dispersion.[61,62] Optical images of prepared crosslinked polymer pads in contact with dry and humid air were taken with the help of a bright-field microscope (Olympus BX41, Japan).

*Surface Plasmon Resonance Imaging Setup*: The schematic of the surface plasmon resonance imaging (SPRi) setup is presented in Figure S28 (Supporting Information). In the setup, light from a superluminescent laser diode with $\lambda_{ex}$ = 785 nm (iBeam Smart 785S, from TOptica, Photonics AG, Gräfelfing, Germany) was collimated and polarized before being coupled to a high refractive index glass prism (LASFN9, $n_p$ = 1.845). A glass substrate with a 50 nm thin gold layer is optically matched to the prism using a high refractive index oil (Cargille Laboratories, cat. No. 1812; $n_o$ = 1.700) and was mounted on a rotation stage. A flow-cell made of transparent silica cover glass (Sico technology) with drilled inlet and outlet ports and an attached polydimethylsiloxane gasket was clamped onto the sensor chip. The respective flow chamber exhibited a volume of 25 µL. The temperature of the sensor surface was controlled using a Peltier element mounted to the flow-cell through which milliQ water flowed under a constant flow rate (50 µL min$^{-1}$) using Tygon LMT-55 tubings (Ismatec, Germany) with an inner diameter of 0.25 mm. The intensity of the reflected laser beam was measured by a CCD camera (piA1000-48ag, Basler AG, Germany). The angle of incidence was varied stepwise between 45 and 60° and images were taken at each angular position. The average intensity of the reflected light at the polymer pads (with a size of 50 × 75 µm$^2$) was determined by using the ImageJ program. The average intensity of


© 2024 The Authors. Advanced Functional Materials published by Wiley-VCH GmbH

16163028, 0, Downloaded from https://onlinelibrary.wiley.com/doi/10.1002/adfm.202315578 by Cochrane Germany, Wiley Online Library on [26/02/2024]. See the Terms and Conditions (https://onlinelibrary.wiley.com/terms-and-conditions) on Wiley Online Library for rules of use; OA articles are governed by the applicable Creative Commons License

similar-sized areas above and below the polymer pads was determined as a reference. The intensity of the reference was then subtracted from the intensity of each polymer pad for the given angle of incidence. For the temperature-controlled experiments, the subtracted data were normalized to the data acquired at a temperature of 25 °C.

*NMR Spectroscopy*: For all NMR spectra, the spectrometer Joel Type ECZ 500 was used. The measurements were performed at room temperature and a Lamor frequency of 500 MHz for the $^{1}$H NMR and at 125 MHz for the $^{13}$C NMR measurements. Chemical shifts of the signals $\delta$ were specified in ppm. The peaks of the non-deuterated solvents were used as an internal standard. The recorded spectra were analyzed with the software ACD/NMR Processor Academic Edition.

*Gel Permeation Chromatography*: For the determination of the molar mass distribution of all polymers, the SECcurity GPC system Agilent Technologies 1260 infinity instrument was used. A so-called Gram Linear M column, equipped with a 10 µm particle size precolumn was utilized at $T \approx 60$ °C. As eluent, *N*,*N*-dimethylacetamide (DMAc) was used mixed with 1 g L$^{-1}$ LiBr, and 20 µL of the polymer samples were injected. For detection, a UV–vis detector adjusted to 260 nm, as well as an RI detector was used.

*UV–vis Spectroscopy*: For UV–vis measurements the Epoch 2 microplate reader from BioTek was used.

*Atomic Force Microscopy*: For topography measurements on pads with dry polymer networks (Figure 2b; Figures S21–S23, Supporting Information), atomic force microscopy (AFM) images were acquired with a Bruker Dimension Icon (Bruker, USA) instrument in tapping mode. For all measurements, triangular sharp silicon nitride SCANASYST-AIR cantilevers (Bruker) with a nominative spring constant of 0.4 N m$^{-1}$, a resonance frequency of 70 kHz (in the air), and a tip radius of 2 nm were used. Before each experiment, the true spring constant in the air was determined via thermal tune calibration after determining the deflection sensitivity. For the hydrogel stiffness measurements in water (Figure 7), AFM force maps were acquired with a JPK III Nanowizard AFM (Bruker, Germany), mounted on an inverted optical microscope, and equipped with a temperature-controlled liquid sample chamber. For all measurements, triangular sharp silicon nitride MLCT "F" cantilevers (Bruker) with a nominative spring constant of 0.6 N m$^{-1}$, a resonance frequency of 125 kHz (in the air), and a tip radius of 20 nm were used. Before each experiment, the true spring constant in the air and in liquid was determined via contact-mode calibration. Force maps were acquired with a sampling rate of 25 kHz and 25 µm$^{-1}$ s. Young's modulus was determined by fitting the approach segment of the force curves with an elastic model (Hertz model with Sneddon extension for geometry).

*Fluorescence Microscopy*: As for the fluorescence observation of the polymer pads, the functional carboxyl groups of the polymer pads were contacted with an aqueous solution of 1-ethyl-3-(3-dimethylami-nopropyl) carbodiimide and *N*-hydroxysuccinimide (200 mM/50 mM) in a petri dish for 20 min. Shortly after rinsing the slide with water, the surface was reacted with AlexaFluor647 anti-human IL-6 antibody (clone MQ2-13A5; cat. number 501 124 from BioLegend, USA) with a mass concentration of 50 µg mL$^{-1}$ in 10 mM sodium acetate buffer (cat. number S8750 from Sigma–Aldrich, Germany) with pH = 5.5 and placed with a cover slide in a humid chamber in the dark for an incubation period of 60 min. Then, the excess IgG molecules were washed off with water and imaged in an aqueous state with a cover slide by a confocal fluorescence microscope (Olympus FV1000).

## Supporting Information

Supporting Information is available from the Wiley Online Library or from the author.

## Acknowledgements

Y.M.M. was supported by the Austrian Science Fund (FWF) through the Lise Meitner Programme (M 2925). J.D. and S.F. acknowledge support from the European Commission EIC Pathfinder project Versilib (#101046217) and from Czech Science Foundation through the project No. 23-05908K. K.S. and J.D. acknowledge support from Gesellschaft für Forschungsförderung Niederösterreich m.b.H. project LS20-014 ASPIS. Further, the authors thank for the financial support through the BMBF funded Project Medistorplast (13GW0349C) for FD. Financial support for CRVT by the BLE-ptble project PermAFog (854798) is acknowledged. MarvinSketch was used for drawing and displaying chemical structures and reactions (https://www.chemaxon.com).

Open access publishing facilitated by Fyzikalni ustav Akademie ved Ceske republiky, as part of the Wiley - CzechELib agreement.

## Conflict of Interest

The authors declare no conflict of interest.

## Data Availability Statement

The datasets related to the data presented in the paper can be found under the following link: https://doi.org/10.17605/OSF.IO/YCNJK (Open Science Framework). In the case of interest in some other data, the data can be obtained from the corresponding authors upon request.

## Keywords

biofunctional coatings, maskless multiphoton lithography, photocrosslinking, pNIPAAm, thermoresponsive hydrogels

Received: December 6, 2023
Revised: January 18, 2024
Published online:

[1] M. Heskins, J. E. Guillet, *J. Macromol. Sci. Part A – Chem.* **1968**, *2*, 1441.
[2] S. Dai, P. Ravi, K. C. Tam, *Soft Matter* **2008**, *4*, 435.
[3] D. A. Davis, A. Hamilton, J. Yang, L. D. Cremar, D. Van Gough, S. L. Potisek, M. T. Ong, P. V. Braun, T. J. Martínez, S. R. White, J. S. Moore, N. R. Sottos, *Nature* **2009**, *459*, 68.
[4] Y. L. Colson, M. W. Grinstaff, Y. L. Colson, M. W. Grinstaff, *Adv. Mater.* **2012**, *24*, 3878.
[5] T. Tanaka, I. Nishio, S. T. Sun, S. Ueno-Nishio, *Science (80-.)*. **1982**, *218*, 467.
[6] J. Thévenot, H. Oliveira, O. Sandre, S. Lecommandoux, *Chem. Soc. Rev.* **2013**, *42*, 7099.
[7] M. Karimi, P. Sahandi Zangabad, S. Baghaee-Ravari, M. Ghazadeh, H. Mirshekari, M. R. Hamblin, *JACS* **2017**, *139*, 4584.
[8] D. Zhang, B. Ren, Y. Zhang, L. Xu, Q. Huang, Y. He, X. Li, J. Wu, J. Yang, Q. Chen, Y. Chang, J. Zheng, *J. Mater. Chem. B* **2020**, *8*, 3171.
[9] A. Bratek-Skicki, *Appl. Surf. Sci. Adv.* **2021**, *4*, 100068.
[10] F. Diehl, S. Hageneder, S. Fossati, S. K. Auer, J. Dostalek, U. Jonas, *Chem. Soc. Rev.* **2022**, *51*, 3926.
[11] S. Gallagher, L. Florea, K. Fraser, D. Diamond, *Int. J. Mol. Sci.* **2014**, *15*, 5337.
[12] P. Winkler, M. Belitsch, A. Tischler, V. Häfele, H. Ditlbacher, J. R. Krenn, A. Hohenau, M. Nguyen, N. Félidj, C. Mangeney, *Appl. Phys. Lett.* **2015**, *107*, 141906.
[13] S. K. Auer, S. Fossati, Y. Morozov, D. Cattozzo Mor, U. Jonas, J. Dostalek, *J. Phys. Chem. B* **2022**, *126*, 3170.
[14] A. Mourran, H. Zhang, R. Vinokur, M. Möller, *Adv. Mater.* **2017**, *29*, 1604825.
[15] I. Rehor, C. Maslen, P. G. Moerman, B. G. P. van Ravensteijn, R. van Alst, J. Groenewold, H. Burak Eral, W. K. Kegel, *Soft Robot* **2021**, *8*, 10.


© 2024 The Authors. Advanced Functional Materials published by Wiley-VCH GmbH

16163028, 0, Downloaded from https://onlinelibrary.wiley.com/doi/10.1002/adfm.202315578 by Cochrane Germany, Wiley Online Library on [26/02/2024]. See the Terms and Conditions (https://onlinelibrary.wiley.com/terms-and-conditions) on Wiley Online Library for rules of use; OA articles are governed by the applicable Creative Commons License

[16] J. ter Schiphorst, S. Coleman, J. E. Stumpel, A. Ben Azouz, D. Diamond, A. P. H. J. Schenning, *Chem. Mater.* **2015**, *27*, 5925.
[17] C. Zheng, F. Jin, Y. Zhao, M. Zheng, J. Liu, X. Dong, Z. Xiong, Y. Xia, X. Duan, *Sens. Actuators, B* **2020**, *304*, 127345.
[18] T. Ding, J. Mertens, A. Lombardi, O. A. Scherman, J. J. Baumberg, *ACS Photon* **2017**, *4*, 1453.
[19] Y. Zhao, J. Zhu, W. He, Y. Liu, X. Sang, R. Liu, *Nat. Commun.* **2023**, *14*, 2381.
[20] P. W. Beines, I. Klosterkamp, B. Menges, U. Jonas, W. Knoll, *Langmuir* **2007**, *23*, 2231.
[21] S. Hageneder, V. Jungbluth, R. Soldo, C. Petri, M. Pertiller, M. Kreivi, A. Weinhäusel, U. Jonas, J. Dostalek, *ACS Appl. Mater. Interfaces* **2021**, *13*, 27645.
[22] F. Pirani, N. Sharma, A. Moreno-Cencerrado, S. Fossati, C. Petri, E. Descrovi, J. L. Toca-Herrera, U. Jonas, J. Dostalek, *Macromol. Chem. Phys.* **2017**, *218*, 1600400.
[23] N. Sharma, C. Petri, U. Jonas, J. Dostalek, *Opt. Exp.* **2016**, *24*, 2457.
[24] N. Gisbert Quilis, S. Hageneder, S. Fossati, S. K. Auer, P. Venugopalan, A. Bozdogan, C. Petri, A. Moreno-Cencerrado, J. L. Toca-Herrera, U. Jonas, J. Dostalek, *J. Phys. Chem. C* **2020**, *124*, 3297.
[25] A. Aulasevich, R. F. Roskamp, U. Jonas, B. Menges, J. Dostalek, W. Knoll, *Macromol. Rapid Commun.* **2009**, *30*, 872.
[26] Y. Wang, C.-J. Huang, U. Jonas, T. Wei, J. Dostalek, W. Knoll, *Biosens. Bioelectron.* **2010**, *25*, 1663.
[27] T. G. Jaik, B. Ciubini, F. Frascella, U. Jonas, *Polym. Chem.* **2022**, *13*, 1186.
[28] D. Schwärzle, X. Hou, O. Prucker, J. Rühe, *Adv. Mater.* **2017**, *29*, 1703469.
[29] N. Geid, J. U. Leutner, J. U. Leutner, O. Prucker, J. Rühe, *Actuators* **2023**, *12*, 124.
[30] D. Song, A. Husari, F. Kotz-Helmer, P. Tomakidi, B. E. Rapp, J. Rühe, *Small* **2023**, 2306682, (Early View).
[31] T. Fadida, J.-P. Lellouche, *J. Polym. Res.* **2012**, *19*, 23.
[32] S. Kommeren, J. Dongmo, C. W. M. Bastiaansen, *Soft Matter* **2017**, *13*, 2239.
[33] E. Tayama, H. Kimura, *Angew. Chem., Int. Ed.* **2007**, *46*, 8869.
[34] A. B. Lowe, C. L. McCormick, *Prog. Polym. Sci.* **2007**, *32*, 283.
[35] G. Moad, E. Rizzardo, S. H. Thang, *Aust. J. Chem.* **2005**, *58*, 379.
[36] R. J. Young, P. A. Lovell, *Introduction to Polymers*, CRC Press, Boca Raton **2011**.
[37] N. S. Allen, G. Pullen, M. Edge, I. Weddell, R. Swart, F. Catalina, *J. Photochem. Photobiol. Chem.* **1997**, *109*, 71.
[38] K. Sergelen, C. Petri, U. Jonas, J. Dostalek, *Biointerphases* **2017**, *12*, 051002.
[39] C. M. González-Henríquez, M. A. Sarabia-Vallejos, C. A. Terraza, A. del Campo-García, E. Lopez-Martinez, A. L. Cortajarena, I. Casado-Losada, E. Martínez-Campos, J. Rodríguez-Hernández, *Mater. Sci. Eng. C* **2019**, *97*, 803.
[40] E. Um, Y.-K. Cho, J. Jeong, *ACS Appl. Mater. Interfaces* **2021**, *13*, 15837.
[41] J. Zhang, S. Shen, R. Lin, J. Huang, C. Pu, P. Chen, Q. Duan, X. You, C.g Xu, B. Yan, X. Gao, Z. Shen, L. Cai, X. Qiu, H. Hou, *Adv. Mater.* **2023**, *35*, 2209497.
[42] Y.-A. Lucy Lee, Z. Mousavikhamene, A. Kottaram Amrithanath, S. M. Neidhart, S. Krishnaswamy, G. C. Schatz, T. W. Odom, *Small* **2022**, *18*, 2103865.
[43] C. M. González-Henríquez, G. E. Medel-Molina, F. E. Rodríguez-Umanzor, C. Terraza Inostroza, M. A. Sarabia-Vallejos, J. Rodríguez-Hernández, *Polymer* **2021**, *231*, 124109.
[44] A. V. Ragutkin, M. R. Dasaev, O. V. Kalakutskaya, O. S. Zilova, E. S. Trushin, *Therm. Eng.* **2022**, *69*, 429.
[45] D. Matsukuma, K. Yamamoto, T. Aoyagi, *Langmuir* **2006**, *22*, 5911.
[46] S. K. Christensen, M. C. Chiappelli, R. C. Hayward, *Macromolecules* **2012**, *45*, 5237.
[47] G. Dorman, G. D. Prestwich, *Biochemistry* **1994**, *33*, 5661.
[48] A. A. Lin, V. R. Sastri, G. Tesoro, A. Reiser, R. Eachus, *Macromolecules* **1988**, *21*, 1165.
[49] G. Porter, F. Wilkinson, *Trans. Faraday Soc.* **1961**, *57*, 1686.
[50] G. J. Smets, S. N. El Hamouly, T. J. Oh, *Pure Appl. Chem.* **1984**, *56*, 439.
[51] L. Anhäuser, N. Klöcker, F. Muttach, F. Mäsing, P. Špaček, A. Studer, A. Rentmeister, *Angew. Chem., Int. Ed.* **2020**, *59*, 3161.
[52] Y. Brasse, M. B. Müller, M. Karg, C. Kuttner, T. A. F. König, A. Fery, *ACS Appl. Mater. Interfaces* **2018**, *10*, 3133.
[53] A. N. Bashkatov, E. A. Genina, *Proc. SPIE* **2003**, 5068.
[54] N. Zammatteo, L. Jeanmart, S. Hamels, S. Courtois, P. Louette, L. Hevesi, J. Remacle, *Anal. Biochem.* **2000**, *280*, 143.
[55] H.-N. Chang, S. Sarkar, J. R. Baker, T. B. Norris, *Opt. Mater. Express* **2016**, *6*, 3242.
[56] Y. Qian, S. Lu, J. Meng, W. Chen, J. Li, *Macromol. Biosci.* **2023**, *23*, 2300214.
[57] A. Beck, F. Obst, D. Gruner, A. Voigt, P. Jan Mehner, S. Gruenzner, R. Koerbitz, M. Hadi Shahadha, A. Kutscher, G. Paschew, U. Marschner, A. Richter, *Adv. Mater. Technol.* **2023**, *8*, 2200417.
[58] J. Liu, L. Jiang, A. Liu, S. He, W. Shao, *Sens. Actuators, B* **2022**, *357*, 131434.
[59] N. S. Allen, J. P. Hurley, D. Bannister, G. W. Follows, *Eur. Polym. J.* **1992**, *28*, 1309.
[60] Y. M. Morozov, N. G. Quilis, F. Diehl, S. Klees, J. Grün, U. Jonas, J. Dostalek, *SPIE Proc* **2022**, *12145*, 1214502.
[61] Z. Bor, *Opt. Lett.* **1989**, *14*, 119.
[62] M. Kempe, U. Stamm, B. Wilhelmi, W. Rudolph, *JOSA B* **1992**, *9*, 1158.


© 2024 The Authors. Advanced Functional Materials published by Wiley-VCH GmbH


16163028, 0, Downloaded from https://onlinelibrary.wiley.com/doi/10.1002/adfm.202315578 by Cochrane Germany, Wiley Online Library on [26/02/2024]. See the Terms and Conditions (https://onlinelibrary.wiley.com/terms-and-conditions) on Wiley Online Library for rules of use; OA articles are governed by the applicable Creative Commons License

# 5 Plasmon-Enhanced Multiphoton Polymer Crosslinking for Selective Modification of Plasmonic Hotspots

**Published as:**

Yevhenii M. Morozov, Nestor Gisbert Quilis, Stefan Fossati, Laura De Laporte, Claudia Gusenbauer, Andreas Weber, Jose Luis Toca-Herrera, **Fiona Wiesner**, Ulrich Jonas, and Jakub Dostalek, *J. Phys. Chem. C* **2024**, 128, 18641, doi: 10.1021/acs.jpcc.4c05936.

**Author Contributions:**

*Yevhenii M. Morozov:* Crosslinking experiments, Conception, Coordination, Writing, Reviewing, Editing, Corresponding author

*Nestor Gisbert Quilis:* Assistance with sample preparation, AFM measurements

*Stefan Fossati:* Assistance with the measurements

*Laura De Laporte:* Assistance with the Photonic Professional (GT) system

*Claudia Gusenbauer:* Assistance with AFM measurements

*Andreas Weber:* AFM measurements

*Jose Luis Toca-Herrera:* AFM measurements

***Fiona Wiesner (née Diehl):*** Polymer syntheses and analyses, Reviewing, Editing

*Ulrich Jonas:* Conception, Coordination, Writing, Reviewing, Editing, Funding, Corresponding author

*Jakub Dostalek:* Conception, Coordination, Writing, Reviewing, Editing, Funding, Corresponding author

**Supporting Information** can be found in the Appendix, page A8.

THE JOURNAL OF PHYSICAL CHEMISTRY C
A JOURNAL OF THE AMERICAN CHEMICAL SOCIETY

Open Access
This article is licensed under CC-BY 4.0

pubs.acs.org/JPCC
Article

# Plasmon-Enhanced Multiphoton Polymer Crosslinking for Selective Modification of Plasmonic Hotspots

Yevhenii M. Morozov,* Nestor Gisbert Quilis, Stefan Fossati, Laura De Laporte, Claudia Gusenbauer, Andreas Weber, Jose Luis Toca-Herrera, Fiona Wiesner, Ulrich Jonas, and Jakub Dostalek*

Cite This: *J. Phys. Chem. C* 2024, 128, 18641−18650

Read Online

ACCESS | Metrics & More | Article Recommendations | Supporting Information

**ABSTRACT:** A novel approach to selectively modify narrow subareas of metallic nanostructures adjacent to plasmonic hotspots, where strong electromagnetic field amplification occurs upon localized surface plasmon (LSP) excitation, is reported. In contrast to surface plasmon-triggered polymerization, it relies on plasmonically enhanced multiphoton crosslinking (MPC) of polymer chains carrying photoactive moieties. When they are contacted with metallic nanostructures and irradiated with a femtosecond near-infrared beam resonantly coupled with LSPs, the enhanced field intensity locally exceeds the threshold and initiates MPC only at plasmonic hotspots. This concept is demonstrated by using gold nanoparticle arrays coated with two specifically designed polymers. Local MPC of a poly(*N*,*N*-dimethylacrylamide)-based copolymer with an anthraquinone crosslinker is shown via atomic force microscopy. Additionally, MPC is tested with a thermoresponsive poly(*N*-isopropylacrylamide)-based terpolymer. The reversible thermally induced collapse and swelling of the MPC-formed hydrogel at specific nanoparticle locations are confirmed by polarization-resolved localized surface plasmon resonance (LSPR) spectroscopy. These hybrid metallic/hydrogel materials can be further postmodified, offering attractive characteristics for future spectroscopic/bioanalytical applications.

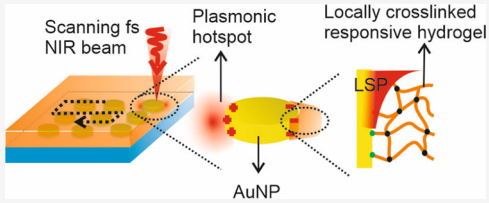


## ■ INTRODUCTION

Optical nanoantennas that allow for nanoscale confinement of the electromagnetic field play a pivotal role in numerous important research fields and application domains relying on optical spectroscopy and photochemical reactions in tightly confined volumes.[1−5] For example, such nanoantennas have enabled the study of fundamental optical phenomena at the single emitter level (such as organic fluorophore molecules, quantum dots, or nitrogen-vacancy centers in diamonds),[6−9] in single biomolecule interaction analysis by using labeling with such fluorescent species,[10] or on hot electron-facilitated catalysis.[11,12] Metallic nanostructures and nanoparticles (NPs) represent key building blocks for the construction of optical nanoantennas. The resonant excitation of localized plasmons (LSPs) on such metallic NPs allows for deep subwavelength confinement of light energy due to collective oscillations of electron density and the associated electromagnetic field.[13,14] The optical excitation of LSPs is accompanied by a strong enhancement of the incident light intensity, which is not homogeneously distributed around metallic NPs but occurs at specific spatially distinct regions (e.g., edges/tips or gaps between closely arranged metallic objects) that are commonly referred to as "plasmonic hotspots".[15] Therefore, various strategies to spatially control the attachment of functional chemical moieties at these regions have been pursued for precise control and to maximize the efficiency of their interaction with LSPs.[15−18] These include the use of photoresist mask windows made by electron beam lithography to overlay with plasmonic hotspots,[19] development of orthogonal surface chemistries,[16,20] and employment of a static electric field gradient for attracting the species at sharp parts of metallic nanostructures.[21] The use of chemical reactions that are locally triggered by LSPs has been explored based on the LSP-generated hot electrons,[22] two-photon polymerization,[23] and by using multiphoton absorption-activated linkers for docking of proteins[24−26] and local photocrosslinking of protein hydrogel.[27] In addition, LSP-induced polymerization has been shown to allow for local attachment of nanoscale photoresist features overlapping with plasmonic hotspots[28−32] and later it was intensively used for the preparation of hybrid polymer/metal materials and probing of local chemical reactions.[33−37]

Multiphoton absorption photochemistry has become particularly important in mask-less lithography[38,39] developed for the preparation of complex structures with a spatial resolution down to a hundred nanometers.[40] Up to now, multiphoton lithography techniques have been utilized for the fabrication of objects with a well-controlled three-dimensional geometry serving in diverse areas including micro-optics,[41−43] micro-

Received: September 2, 2024
Revised: October 7, 2024
Accepted: October 11, 2024
Published: October 22, 2024

Downloaded via 92.72.54.217 on December 8, 2024 at 10:17:44 (UTC).
See https://pubs.acs.org/sharingguidelines for options on how to legitimately share published articles.

ACS Publications
© 2024 The Authors. Published by American Chemical Society

robotics,[44,45] tissue engineering,[46−50] and drug delivery[51] to mention a few examples. The vast majority of materials that are structured with the help of multiphoton absorption lithography rely on a polymerization process.[52] Typically, a femtosecond (fs) pulsed laser beam with a near-infrared (NIR) wavelength is focused and scanned through a liquid monomer to initiate polymerization in a small focal volume, where the threshold for initiation is exceeded.[53] Only along the path of the NIR beam are the included photoinitiator molecules excited by the sequential absorption of photons to initiate a free-radical polymerization reaction locally solidifying the liquid photoresist. Besides multiphoton lithography relying on a polymerization mechanism, a recently reported alternative is based on multiphoton crosslinking (MPC) of soluble polymers employed as solid thin films.[54] Their polymer backbones contain photoactive moieties that were excited by a scanned focused NIR beam to induce MPC, resulting in thermoresponsive biofunctional hydrogels when a postmodification step is utilized.[55] The MPC process was investigated in dependence on the type of crosslinker and its means of conjugation to the polymer backbone.[55] This crosslinking-based approach, in contrast to the more frequently used polymerization, allows for the creation of structures from a compact dry polymer layer, eliminating the risk of residual monomer and/or photoinitiator leakage during swelling and offering the advantage of higher chemical precision when incorporating multiple functionalities during the polymer presynthesis stage.

In the present work, we report on a new generic approach to chemically modify narrow zones of metallic nanostructures, where plasmonic hotspots occur. The strategy employs polymer chains with incorporated photoactive crosslinkers that can be triggered by the multiphoton absorption process for their simultaneous attachment and crosslinking at the plasmonic hotspot where the MPC threshold is locally reached. To the best of our knowledge, in contrast to the plasmonically driven polymerization, this type of plasmonically mediated photochemistry—plasmon-enhanced multiphoton crosslinking (PE-MPC)—has not yet been reported, despite its potential for preparing well-controlled hybrid metal/hydrogel nanomaterials. This method leverages the already established multiphoton lithography tools and offers the capability for selective local postmodification of the resulting structures. The reliability of the approach is demonstrated by using two types of polymers that form locally attached hydrogel nanostructures at plasmonic hotspots after swelling in aqueous media. The successful preparation of such materials is documented for optimized writing conditions by atomic force microscopy (AFM) measurements of the local topography and Young's modulus and by characterizing the nanoscopic domains of the thermoresponsive hydrogel matrix with polarization-resolved localized surface plasmon resonance (LSPR) measurements.

## ■ MATERIALS AND METHODS

**Materials.** Poly(DMAA-*co*-AAHAQ) was synthesized as previously reported.[54] Poly(NIPAAm-*co*-MAA-*co*-BPQAAm) was synthesized as previously reported.[55] Benzophenone disulfide (BPDiS) was synthesized as reported elsewhere.[56] S1805 resist and AZ303 developer were purchased from Micro resist Technology GmbH (Germany). Dimethyl sulfoxide (DMSO) was purchased from Sigma-Aldrich, Austria.

**Preparation of Hydrogel-Coated Gold Particle Arrays.** Periodic arrays of gold nanoparticles (AuNPs) with a diameter $D$ = 185 ± 10 nm and period $\Lambda$ = 400 nm (in the case of structures with poly[DMAA-*co*-AAHAQ]) and with a diameter $D$ = 165 ± 10 nm and period $\Lambda$ = 400 nm (in the case of structures with poly[NIPAAm-*co*-MAA-*co*-BPQAAm] terpolymer) were employed as plasmonic substrates. Briefly, a BK7 glass slide was coated with a 2 nm thick chromium layer and 50 nm thick gold layer by thermal evaporation (UNIVEX 450, Helmut Heller GmbH, Germany). Then, an S1805 positive photoresist (1:2 ratio diluted with propylene glycol monomethyl ether acetate) was spun on the gold surface, yielding a layer with a thickness of 120 nm. A periodic interference pattern was recorded into the photoresist layer by employing a He−Cd laser ($\lambda$ = 325 nm) with Lloyd's mirror setup as previously reported by our group.[57] The well-defined resist particles with subwavelength dimensions were etched by using the AZ-303 developer (1:15 ratio with deionized water). Finally, the inscribed pattern was transferred to the gold film by using dry etching with an argon milling system (IonSys 500, Roth&Rau, Germany). The remaining photoresist was removed by applying an oxygen plasma treatment. The prepared plasmonic substrate was immersed overnight in a 1 mM solution made of BPdiS dissolved in DMSO in order to form a self-assembled monolayer on the pristine gold surface. The photocrosslinkable polymer thin film was subsequently spun (from ethanolic solution with 3 and 2% w/w of poly(DMAA-*co*-AAHAQ) and poly(NIPAAm-*co*-MAA-*co*-BPQAAm), respectively) on top of the AuNP arrays at a rate of 2000 rpm for 60 s and dried overnight in a vacuum oven at $T$ = 50 °C.

**Plasmon-Enhanced Multiphoton Crosslinking of Poly(DMAA-*co*-AAHAQ).** Poly(DMAA-*co*-AAHAQ) was deposited on the top of AuNP arrays carried by a glass substrate, as described above. The substrate was mounted into the Photonic Professional (GT) system from Nanoscribe GmbH for the recording step (with a wavelength of the emitted light centered at 780 nm),[58] with the surface carrying the plasmonic architectures facing a clean coverslip. The interface was selected by focusing on the surface with the gold nanoparticle arrays, and the correct $z$ plane was set by recording square features with the highest writing speed and laser power $P_L$ and visually observing the recording of the micrometer-size features with the equipped microscope camera. Once the proper interface was found, a recording script was loaded and squares (100 × 100 $\mu m^2$) with different parameters were inscribed. The scan speed was varied between 10,000 and 2500 $\mu m\ s^{-1}$ and the laser power $P_L$ = 2−5 mW. After the recording step, the unbound polymer was removed by rinsing with ethanol.

**Plasmon-Enhanced Multiphoton Crosslinking of Poly(NIPAAm-*co*-MAA-*co*-BPQAAm).** Poly(NIPAAm-*co*-MAA-*co*-BPQAAm) was deposited on the top of AuNP arrays carried by a glass substrate, as described above. The substrate was mounted into a home-built general-purpose multiphoton absorption lithography setup for the recording step (details of the setup can be found in refs 55,59). The wavelength of the emitted light of the home-built setup is centered at 785 nm. After the selection of the correct $z$ plane, a rectangular area of 75 × 50 $\mu m^2$ was recorded. The laser power $P_L$ was varied between 10 and 15 mW, and the dwelling time $t_d$ was varied between 1 and 5 s.

**Morphological Characterization.** For topography measurements of the AuNP arrays with attached polymer networks, AFM height topography was acquired with the help of a Bruker's Dimension Icon (Bruker) instrument operated in


https://doi.org/10.1021/acs.jpcc.4c05936
J. Phys. Chem. C 2024, 128, 18641−18650

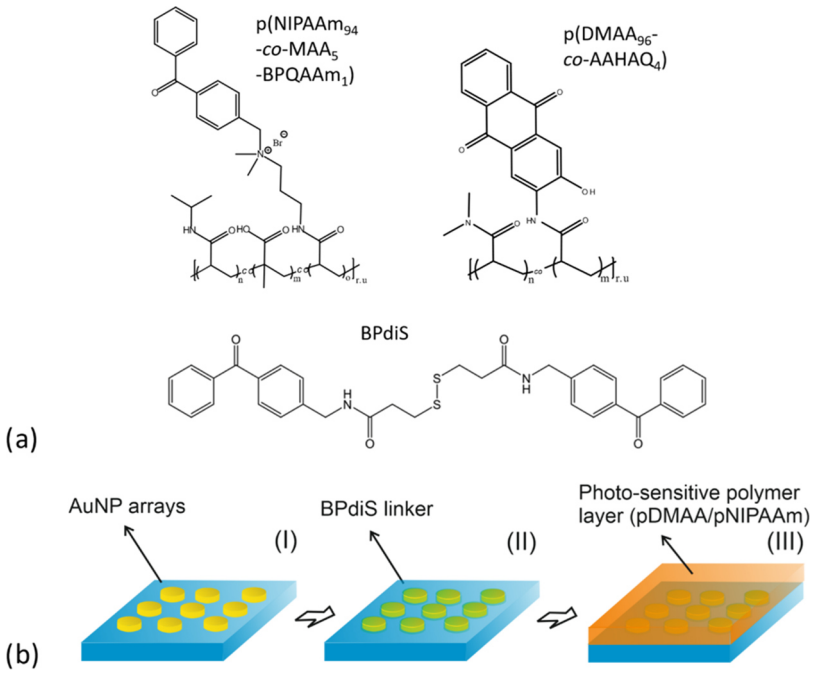


**Figure 1.** (a) Chemical structure of photocrosslinkable poly(DMAA$_{96}$-*co*-AAHAQ$_4$) and poly(NIPAAm$_{94}$-*co*-MAA$_5$-*co*-BPQAAm$_1$) polymers and BPdiS linker and (b) schematics of the preparation procedure for the Au nanoparticle arrays coated with photocrosslinkable polymers.

tapping mode. For all measurements, triangular silicon nitride SCANASYST-AIR cantilevers (Bruker) with a nominative spring constant $k$ of 0.4 N/m, a resonance frequency of 70 kHz (in air), and a tip radius of 2 nm were used. Before each experiment, the true spring constant in air was determined via thermal tuning calibration after determining the deflection sensitivity. The AFM measurements in water were carried out with a Nanowizard (JPK III, Germany) instrument equipped with the inverse microscope and a liquid chamber. Imaging of the samples in water was performed in contact mode and quantitative imaging (QI) mode (0.3 N/m cantilevers with a 10 nm tip radius). The mapping to determine the mechanical properties was conducted in force volume mode both in water and in air (force curve at each pixel with 10 $\mu$m/s, maximum force of 5 nN, up to 200 × 200 resolution for a 2 × 2 $\mu$m image). Young's modulus was determined by fitting the approach section with the elastic model (Hertz model with Sneddon extension for geometry). Cantilever properties: $k$ = 9 N/m (±2), resonance frequency 150 kHz, beam shaped, 175 $\mu$m, Al coating on the backside, OPUS shape (tetrahedral), radius below 7 nm, 35° back angle.

**Electromagnetic Simulations.** The Ansys Lumerical FDTD numerical simulation package was used for all electromagnetic modeling. Geometrical parameters for arrays of AuNPs were used according to those mentioned in the main text and the Supporting Information. Below the AuNPs, a chromium layer with a thickness of 2 nm was assumed. A dielectric medium with a refractive index of 1.5 (non-dispersive) representing the BK7 glass was used as a substrate. As a superstrate, a medium with a refractive index of 1.45 (nondispersive) representing the polymer in a dry state was used. A plane wave made normally incident at the structure was used as an excitation source. Periodic (along the $x$- and $y$-axes) and perfectly matched layer absorbing (at the $z$-axis, 1.2 $\mu$m above and below the structure) boundary conditions were applied. Au and Cr optical properties were taken from the literature.[60,61]

## RESULTS AND DISCUSSION

**Design of Polymers and Plasmonic Nanostructures.** The proposed concept was pursued with two types of photocrosslinkable polymers shown in Figure 1a, which form a polymer network via MPC and subsequently a hydrogel after swelling with water. Details on the mechanism of the photoinitiated crosslinking mechanism was the subject of previous studies,[54,55] and the copolymer poly(*N*,*N*-dimethylacrylamide-*co*-acylamido-3-hydroxyanthraquinone), abbreviated as poly(DMAA$_{96}$-*co*-AAHAQ$_4$), was chosen for the preparation of rigid hydrogel structures. It is ascribed to an apparently higher crosslink density due to a high ratio of anthraquinone-based photocrosslinking units (4% AAHAQ polymerization feed) in the polymer backbone. In addition, the terpolymer poly(NIPAAm$_{94}$-*co*-MAA$_5$-*co*-BPQAAm$_1$) was prepared by copolymerization of *N*-isopropylacrylamide (NIPAAm) with [(4-benzoylphenyl)methyl]dimethyl[3-(prop-2-enamido)-propyl]azanium bromide (BPQAAm) and methacrylic acid (MAA). This polymer carried low amounts of photocrosslinking units (1% BPQAAm in the polymerization feed) and allowed for the preparation of softer thermoresponsive hydrogel features. It was possible to modulate the degree of swelling for this pNIPAAm-based hydrogel with lower critical solution temperature (LCST) behavior by changing the temperature from below the volume phase transition temperature (VPTT), where the polymer network contacting water is in a swollen state, to above the VPTT, where it collapses. In further experiments, the polymers were crosslinked by using a focused beam of pulsed femtosecond (fs) lasers emitting at a wavelength of $\lambda_L$ = 780−785 nm that was scanned over the substrate with a home-built setup[55,59] and alternatively by a commercially available Photonic Professional (GT) system (Nanoscribe GmbH, Germany).[58]


https://doi.org/10.1021/acs.jpcc.4c05936
J. Phys. Chem. C 2024, 128, 18641−18650

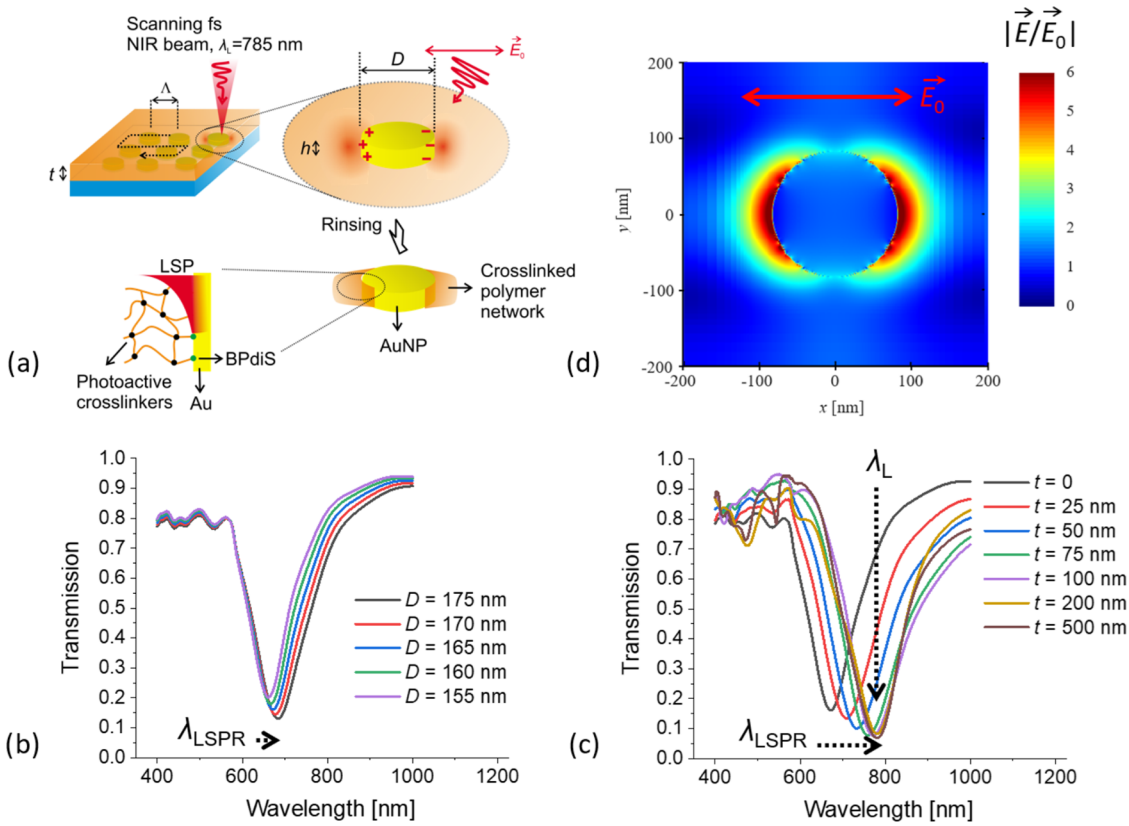


**Figure 2.** (a) Schematics of the crosslinking of polymer layer via PE-MPC. (b) Simulations of transmission spectra for AuNP arrays with varied Au disk diameters $D$ = 155−175 nm and when the polymer overlayer is absent (thickness $t$ = 0). (c) Simulated transmission spectra for $D$ = 165 nm when the polymer overlayer thickness $t$ is increased up to 500 nm. (d) Simulated near-field distribution of the electric field intensity amplitude upon resonant excitation of LSPs on AuNP with $D$ = 165 nm at $\lambda_L$ = 785 nm and $t$ = 100 nm. In all simulations, the period of the AuNP arrays was Λ = 400 nm.

The overall preparation route of the substrates used in PE-MPC experiments is summarized in Figure 1b. Briefly, arrays of cylindrically shaped AuNPs were prepared by using UV laser interference lithography in combination with Ar ion milling (step I).[57] Afterward, the gold surface of AuNPs was reacted with 3,3′-disulfanediylbis(*N*-(4-benzoylbenzyl)propanamide) (BPdiS) to serve as a photoactive linker (step II). Finally, a photocrosslinkable polymer layer (pDMAA- or pNIPAAm-based) with a thickness $t$ of about 100 nm was deposited over the AuNP arrays (step III) prior to MPC with a focused femtosecond NIR laser beam.

The MPC process of the polymer chains at plasmonic hotspots was induced by scanning a focused NIR femtosecond laser beam of a wavelength $\lambda_L$ over the polymer-embedded AuNP arrays, as schematically presented in Figure 2a. The AuNPs are made resonant at a wavelength of $\lambda_{LSPR}$ that is coincident with that of the NIR fs laser beam $\lambda_L$. For the optimum scanning speed and intensity of the NIR fs laser beam $P_L$, the resonant excitation of LSPs increases the electromagnetic field intensity above the threshold of the (nonlinear) multiphoton absorption process that activates crosslinker moieties (BPQAAm or AAHAQ) and allow for the formation of the surface-attached polymer network. The laser beam intensity $P_L$ is chosen such that the NIR electromagnetic field intensity further away from the metallic nanostructure surface stays below the threshold. Therefore, any polymer chains outside the plasmonic hotspots are not crosslinked and upon rinsing with a solvent are washed away. This procedure and parameter optimization are described in our previous work,[55] and it is also important to note that it is crucial to not exceed the threshold, above which the structure is damaged by increased temperature (see Figure S1, where certain laser power and writing speed values resulted in the structural burning of the poly[$DMAA_{96}$-*co*-$AAHAQ_4$] polymer).

The geometry, which enables matching of the LSPR wavelength $\lambda_{LSPR}$ with that of NIR fs laser $\lambda_L$, was identified by using finite-difference time-domain (Ansys Lumerical FDTD) simulations. The optimum Au disk diameter $D$ and thickness of the polymer overlayer $t$ were determined for cylindrically shaped AuNPs with a height of $h$ = 50 nm when arranged in arrays with a period of Λ = 400 nm. As can be seen in Figure 2b, the resonant excitation of LSPs manifests itself as a narrow absorption band in the transmission spectrum with its minimum corresponding to $\lambda_{LSPR}$. The resonant wavelength $\lambda_{LSPR}$ shifts from 650 to 690 nm when increasing the AuNP diameter $D$ from 155 to 175 nm in a structure without the polymer layer (thickness $t$ = 0). Figure 2c shows that the presence of the polymer overlayer red-shifts the resonant wavelength $\lambda_{LSPR}$ and for the AuNP diameter $D$ = 165 and $t$ > 100 nm, it yields $\lambda_{LSPR}$ = 780−790 nm close to the laser wavelength $\lambda_L$. An additional set of FDTD simulations was run to simulate the near-field distribution of electric field intensity upon the resonant excitation of LSPs at $\lambda_L = \lambda_{LSPR}$ = 785 nm for this geometry. The cross section presented in Figure 2d shows that the peak enhancement of the electric field amplitude $|E|$ reaches ∼6 with respect to the incident field $|E_0|$. It exhibits a two-lobe distribution profile that is characteristic of a dipole LSP mode aligned in the direction


https://doi.org/10.1021/acs.jpcc.4c05936
J. Phys. Chem. C 2024, 128, 18641−18650

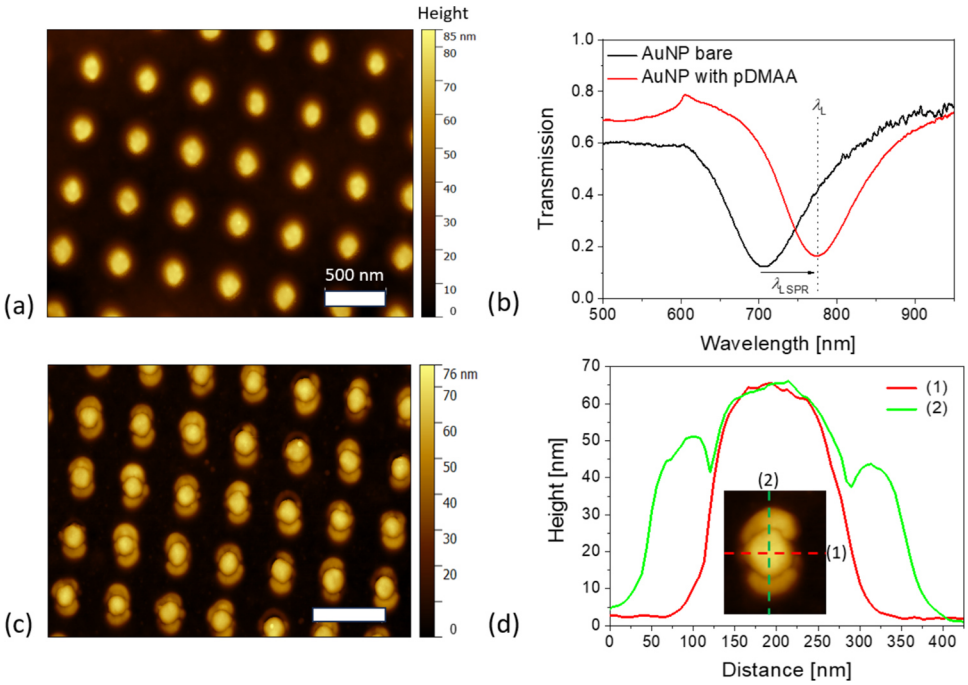


**Figure 3.** (a) AFM topography of the bare AuNP arrays and (b) measured LSPR transmission spectra before (black line) and after the coating (red line) with an uncrosslinked poly(DMAA$_{96}$-*co*-AAHAQ$_4$) layer of thickness $t$ = 154 nm. (c) AFM height topography image of the same AuNP arrays after PE-MPC of poly(DMAA$_{96}$-*co*-AAHAQ$_4$) and rinsing. (d) Respective cross sections for individual AuNPs. All AFM measurements were performed in the air.

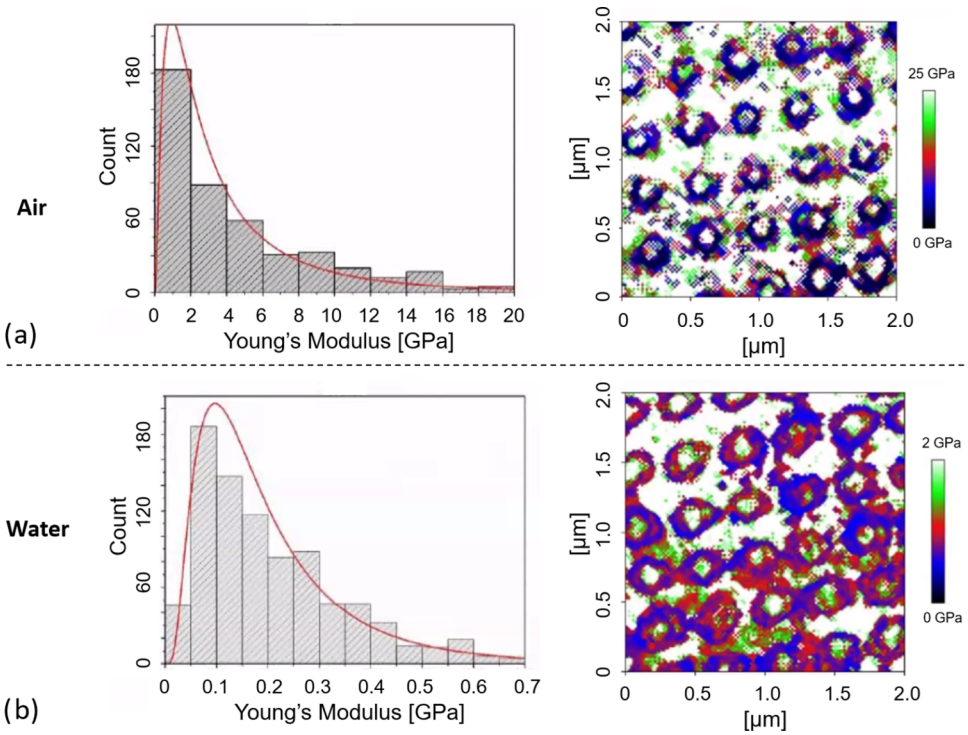


**Figure 4.** Comparison of Young's moduli for the AuNP−polymer network hybrid system in (a) air and (b) water, with histograms on the left-hand side displaying Young's moduli of 30 nanoparticles at random orientations and its corresponding logarithmic fitting.

of the incident field polarization. (A complete set of numerical results for the AuNP array with varying parameters can be found in Figure S2.)

**Topography and Young's Modulus Measurements.** AFM was first used for the observation of morphology and elasticity of the poly(DMAA$_{96}$-*co*-AAHAQ$_4$) polymer networks attached to AuNP plasmonic hotspots. In this experiment, AuNP arrays with a diameter $D$ of 185 ± 10 nm, a height of $h$ = 50 nm, and a period of $\Lambda$ = 400 nm were used with the respective height topography shown in Figure 3a. After depositing the poly(DMAA$_{96}$-*co*-AAHAQ$_4$) copolymer layer with a thickness of $t$ = 154 nm (determined with the surface


https://doi.org/10.1021/acs.jpcc.4c05936
J. Phys. Chem. C 2024, 128, 18641−18650

plasmon resonance measurement; see Figure S3), the LSPR wavelength of the AuNP array was shifted from $\lambda_{LSPR}$ = 700 to 780 nm as confirmed by optical transmission spectroscopy (see Figure 3b). This $\lambda_{LSPR}$ value is close to $\lambda_L$ of the NIR beam of the used multiphoton lithographer, and it agrees with the previous simulations. AuNP arrays coated with poly(DMAA$_{96}$-*co*-AAHAQ$_4$) overlayer were scanned "line-by-line" with a focused NIR fs laser beam using a power of $P_L$ = 4 mW and a writing speed of 2.5 × $10^3$ lines per second (by Nanoscribe Photonic Professional GT system). This condition was below the threshold for MPC without plasmonic amplification (Figure S1). After the MPC recording and ethanol rinsing step, the patterned structures were characterized by AFM, and Figure 3c shows the obtained height topography with detailed cross sections presented in Figure 3d. The successful local attachment of the polymer network changed the shape of the individual AuNPs, which became elongated along one axis, forming two apparent lobes stretching to opposite directions into a distance of 50 nm from the AuNP wall (defined as the distance where the height drops to half of its maximum; see Figure 3d). Such a shape can be attributed to the area of the plasmonic hotspot as simulated by FDTD and presented in Figure 2d. For the same AuNP, these simulations predict that the enhanced field intensity reaches a distance of about 50 nm (from the Au wall where the electric field amplitude drops to half of its magnitude; see Figure S2a) that is close to the experimental results. The orientation of the lobes is expected to be aligned with the polarization of the incident NIR fs beam, and irregularities in the shape can be attributed to variations in the plasmonic properties of individual AuNP associated with their polycrystalline nature[62] and local deviations in shape.[57]

In order to rule out that the polymer features appearing after the irradiation with the fs pulsed laser beam are associated with the effect of burning and to confirm that PE-MPC leads to a polymer network that forms a hydrogel after swelling with water, elastic properties were evaluated by mapping of Young's modulus in air and in water (see Figure 4a,b, respectively).

Both micrographs reveal that around the hard metallic nanoparticles (with Young's modulus >20 GPa), a belt-shaped region with lower stiffness occurs. The evaluation of these data using the elastic contact model according to Hertz with the Sneddon extension for the tip geometry was carried out. It is clearly visible that Young's modulus of the dry polymer network around the AuNPs is around 10 times higher than that for the swollen network immersed in water forming a hydrogel (0−25 GPa for air and 0−2 GPa for water). The values for both Young's moduli in air and water were derived from the histograms of the hydrogel's Young's moduli at random positions (around 30 AuNPs). The maximum of the fitting, representing the most probable value, was then identified as 1.5 ± 0.2 GPa in air and 0.10 ± 0.01 GPa in water. In addition, the degree of swelling of the polymer network was determined by comparing the size of the hydrogel nanostructure (distance between upper and lower) in either air or water ($N$ = 50) from AFM images in contact or QI mode (data not shown). The size of the hybrid features in air was 320.3 ± 2.6 nm, while in water, it was slightly larger at 349.2 ± 2.2 nm, which can be attributed to swelling.

It is worth noticing that selective crosslinking occurs only on substrates with $\lambda_{LSPR}$ of the AuNPs matching the wavelength of the NIR fs laser beam $\lambda_L$. This was demonstrated by employing enlarged AuNPs ($D$ ≈ 210 nm; Figure S4a) with the correspondingly red-shifted LSPR[57] that become detuned from $\lambda_L$. This leads to a lower field amplitude enhancement factor $|E/E_0|$ at $\lambda_L$ (as predicted by simulations in Figure S2c) and, therefore, to a weaker plasmonic enhancement effect for triggering the MPC. In this case, a continuous layer of hydrogel is formed around the particles for conditions above the threshold (as seen in Figure S4b), while below it, no polymer is attached over the entire surface.

The second, pNIPAAm-based, polymer network was attached to AuNPs by an NIR fs beam that was polarized along one of the axes of the AuNP arrays. The home-built lithographer setup was used, and this optical system was designed for "point-by-point" writing of desired structures. For this system, a laser power $P_L$ of 15 mW and a dwelling time $t_d$ of 3 s were previously reported to provide the energy dose above the threshold for direct (nonplasmonically enhanced) MPC for the same poly(NIPAAm$_{94}$-*co*-MAA$_5$-*co*-BPQAAm$_1$) terpolymer.[55] For PE-MPC, the AuNP array with $D$ = 165 ± 10 nm, a height of 50 nm, and a period Λ of 400 nm was exploited, with the LSPR tuned to the used $\lambda_L$ (see Figure S5). Subsequently, the configuration of the scanning NIR femtosecond beam was changed to a decreased power of $P_L$ = 10 mW and a shortened dwelling time of $t_d$ = 1 s, which is below the threshold for the direct MPC recording but above the threshold for PE-MPC. Figure S6b presents the AFM height topography image of an area with AuNPs bearing the attached pNIPAAm-based network that was dried at room temperature after the rinsing step. Apparently, it does not reveal clear localization of the polymer network around the AuNPs, which we ascribed to its high swelling ratio (>10) as documented by our previous work on direct MPC.[55] This effect was previously observed in the case of other pNIPAAm-based hydrogel nanostructures attached to a solid substrate and attributed to the strong surface tension of the water−air interface, which deforms the elastic polymer network and leads to a planarization of the soft crosslinked area as it reaches the hydrogel layer during water evaporation.[63] However, when the same structure is allowed to swell in water at room temperature and subsequently heated to a higher temperature above the pNIPAAm VPTT before drying, the original crosslinked pattern can be retained (this is schematically shown in Figure S7a). To confirm this, we dried the sample at an elevated temperature of $T$ = 80 °C and the results are shown in Figure S7b−d. Specifically, as can be seen from Figure S7c, the hydrogel structure dried at a temperature above its VPTT partially retained the shape, which resembles the plasmonic hotspots (similar to Figure 3c in the case of poly(DMAA$_{96}$-*co*-AAHAQ$_4$) copolymer). However, more pronounced smearing of the prepared hydrogel shape occurs for the poly(NIPAAm$_{94}$-*co*-MAA$_5$-*co*-BPQAAm$_1$) hydrogel when compared to poly(DMAA$_{96}$-*co*-AAHAQ$_4$), which is attributed to the difference in their swelling ratio (swelling of >10 was estimated for the pNIIPAm-based hydrogel, while only 2.3 was determined for pDMAA-based gel from data in Figure S3).

**Polarization-Resolved LSPR Measurements.** AFM observation did not clearly reveal the presence of locally attached polymer networks at the AuNP hotspot for the second polymer poly(NIPAAm$_{94}$-*co*-MAA$_5$-*co*-BPQAAm$_1$) with a lower amount of 1% incorporated photocrosslinker, which we attributed to the softer characteristics of the formed hydrogel associated with a lower crosslink density and high swelling ratio. Therefore, we took advantage of the thermoresponsive properties of this pNIPAAm-based hydrogel


https://doi.org/10.1021/acs.jpcc.4c05936
J. Phys. Chem. C 2024, 128, 18641−18650

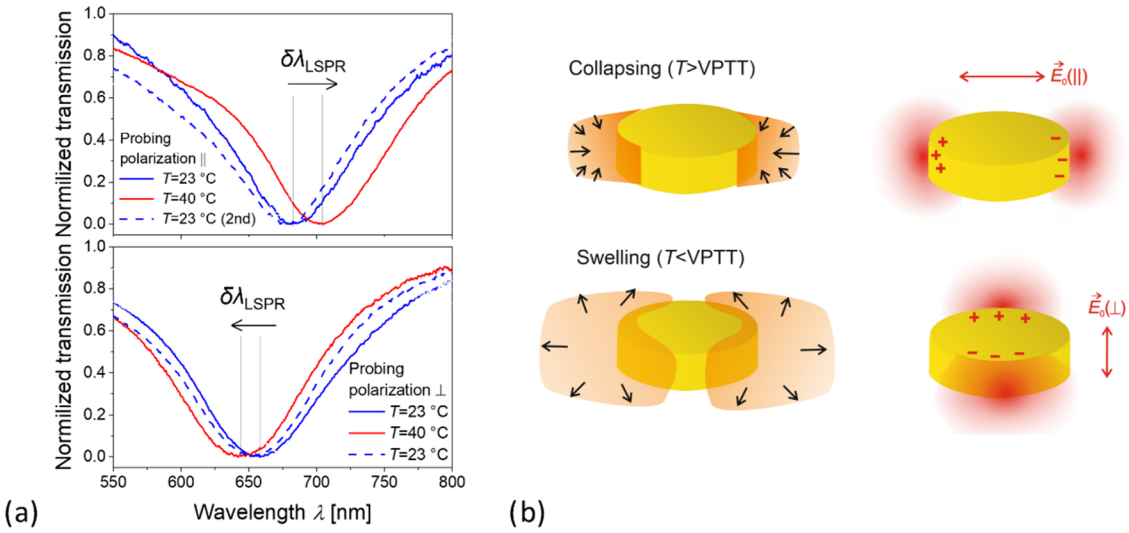


**Figure 5.** Polarization-resolved white-light transmission measurements of the plasmonically enhanced MPC-written poly(NIPAAm$_{94}$-*co*-MAA$_5$-*co*-BPQAAm$_1$) sample: (a) normalized transmission spectra and (b) schematics of the hydrogel swelling and collapsing at the plasmonic hotspots.

and monitored the redistribution of surface mass density around the AuNPs when modulating the temperature above and below the VPTT of pNIPAAm. The LSPR wavelength $\lambda_{LSPR}$ shifts with changes in the refractive index of the medium surrounding the AuNPs with a magnitude that is proportional to the surface mass density of the polymer materials. As the writing NIR femtosecond beam was made polarized for the PE-MPC, the prepared hydrogel nanostructures are expected to be attached only to the AuNP walls that are perpendicular to the incident electric intensity vector of the writing beam (see the near-field distribution in Figure 2d). In the collapsed state, when the temperature of the structure is above the pNIPAAm VPTT, the polymer network should be compacted at these AuNP sides, while below the VPTT in the swollen state, a delocalization and wrapping over the whole AuNPs is expected owing to its high swelling ratio.

In order to test the presence of the locally attached thermoresponsive pNIPAAm-based hydrogel to AuNPs, transmission LSPR spectra were measured with control over the polarization of the impinging optical beam at varying temperature $T$. As shown in Figure 5, the polarization of the probing optical beam was noted as "||-pol." when it is made parallel to, and "⊥-pol." when perpendicular to the polarization of the writing NIR fs laser beam. The substrate carrying AuNPs with the attached pNIPAAm-based nanostructures was mounted on a transparent temperature-controlled flow cell with water in contact with the surface.

First, measurements were done at room temperature ($T$ = 23 °C), then the temperature was increased to $T$ = 40 °C above the pNIPAAm VPTT, and finally, it was decreased again to room temperature ($T$ = 23 °C, second). The corresponding measured transmission spectra in Figure 5a show that as the temperature increases above the pNIPAAm VPTT of 32 °C, the LSPR wavelength $\lambda_{LSPR}$ for ||-pol. (top) red-shifts, while that for ⊥-pol. (bottom) blue-shifts. These shifts are of opposite sign and indicate that the collapse of pNIPAAm leads to asymmetrical redistribution of polymer networks around the AuNPs as an increase in the refractive index on the AuNP walls probed by LSPs with dipole moment parallel to the polarization (||) of the NIR fs laser beam occurs, while on the surface probed by the perpendicular orientation of the polarization (⊥), the refractive index decreases. This unusual behavior can be explained by assuming that the highly swollen pNIPAAm-based hydrogel nanostructure wraps around the whole AuNP in its swollen state. When increasing the temperature $T$ above the LCST, the hydrogel compacts at the AuNP walls where it was attached by the plasmonically enhanced intensity of the NIR fs laser beam (Figure 5b). This effect is accompanied by an increased surface mass density and a higher refractive index of the hydrogel on walls perpendicular to the polarization (||) of the writing beam. On the surface of walls parallel to the fs NIR beam polarization (⊥) where the polymer network is not attached, it therefore retracts toward the plasmonic hotspots and is replaced by water with a lower refractive index of $n_{H_2O}$ = 1.33. Importantly, these transitions are reversible, and as the structure is cooled back to $T$ = 23 °C, which is below the VPTT, the LSPR wavelengths shift to their original position. The magnitude of the LSPR shift for the || probing polarization is $\Delta\lambda_{LSPR}$ = 22 nm (which is close to that measured for a pNIPAAm film that covers the whole area of similar AuNP arrays[64]), and it corresponds to the refractive index change of $\Delta n_h$ = 0.11 with a respective swelling ratio of about 7.5. The measured LSPR shift for the orthogonal polarization ⊥ is of $\Delta\lambda_{LSPR}$ = −14 nm and corresponds to the refractive index change of $\Delta n_h$ = −0.07. This change would translate to a refractive index of the swollen hydrogel of $n_h$ = 1.40, which corresponds to a lower swelling ratio and indicates that local gradients of the swelling process occurring in a quasi-three-dimensional manner play a significant role. Let us also note that the water surrounding the structure also changes its refractive index with temperature with a thermo-optical coefficient of $dn_{H_2O}/dT = -1.2 \times 10^{-4}$ RIU/K, but this effect can be neglected as it is associated with a much smaller decrease in the resonant wavelength of −0.4 nm for the temperature change of 17 K.

## ■ CONCLUSIONS

Selective attachment of polymer networks forming a hydrogel at the plasmonic hotspot regions of metallic nanostructures is achieved. The obtained hybrid polymer−metallic nanostructure was prepared with nanoscale spatial precision by plasmon-enhanced multiphoton crosslinking of the presynthesized


https://doi.org/10.1021/acs.jpcc.4c05936
J. Phys. Chem. C 2024, 128, 18641−18650

polymer chains conjugated with photoactive crosslinkers. With the use of optical configurations already established for a two-photon lithography relying on optically triggered polymerization, the reported alternative approach based on polymer crosslinking[55] provides a facile means for local attachment of the functional hydrogel materials at the areas, where the electromagnetic field is strongly confined. This functionality is highly relevant in the fields of optical bioanalytical technologies and optical spectroscopy that take advantage of the plasmonically enhanced output optical signal. The prepared polymer network can be converted into a hydrogel serving as a three-dimensional large binding capacity matrix when postmodified with biorecognition elements.[65,66] In plasmonic bioanalytical tools, such a binding matrix is designed to efficiently capture target analyte molecules from an analyzed liquid sample contacted with the sensor surface. In combination with the thermoresponsive properties, the optical readout sensitivity can be improved by using a hydrogel matrix that in the swollen state binds the target analyte inside its open network structure followed by its compacting at the plasmonic hotspot via a thermally induced network collapse performed prior to the optical readout. This approach provides dual amplification means, and it was already investigated with a thin pNIPAAm-based hydrogel binding matrix layer collapsing in the direction perpendicular to the surface in conjunction with the optical probing by surface plasmons propagating along the thin metallic film.[67] When using the tighter confined and stronger amplified LSP field generated on metallic nanoparticles, the performance of such a sensor can simultaneously capitalize on stronger optical enhancement and on compacting the captured analyte species at narrower and sparser distributed plasmonic hotspots via a collapse in both perpendicular and parallel directions. The proposed approach may pave the way to such a new class of hybrid plasmonic structures tailored for the optical biosensor and spectroscopy applications with improved accuracy.[66]

## ■ ASSOCIATED CONTENT

### Data Availability Statement

The data that support this study are openly available at 10.17605/OSF.IO/V52GB.

### Supporting Information

The Supporting Information is available free of charge at https://pubs.acs.org/doi/10.1021/acs.jpcc.4c05936.

Additional experimental details and results of electromagnetic numerical simulations, AFM topography of control structures, and used thin film characteristics (PDF)

## ■ AUTHOR INFORMATION


### Corresponding Authors

**Yevhenii M. Morozov** − *Center for Health & Bioresources, AIT-Austrian Institute of Technology, 1210 Vienna, Austria;* orcid.org/0000-0001-9689-8641; Email: yevhenii.morozov@ait.ac.at

**Jakub Dostalek** − *FZU-Institute of Physics, Czech Academy of Sciences, 182 21 Prague, Czech Republic; LiST-Life Sciences Technology, Danube Private University, 2700 Wiener Neustadt, Austria;* orcid.org/0000-0002-0431-2170; Email: dostalek@fzu.cz

### Authors

**Nestor Gisbert Quilis** − *Biosensor Technologies, AIT-Austrian Institute of Technology, 3430 Tulln an der Donau, Austria*

**Stefan Fossati** − *FZU-Institute of Physics, Czech Academy of Sciences, 182 21 Prague, Czech Republic*

**Laura De Laporte** − *DWI-Leibniz Institute for Interactive Materials, D-52074 Aachen, Germany; Institute for Technical and Macromolecular Chemistry, RWTH Aachen University, D-52074 Aachen, Germany; Institute of Applied Medical Engineering, Department of Advanced Materials for Biomedicine, RWTH Aachen University, D-52074 Aachen, Germany;* orcid.org/0000-0002-9438-0977

**Claudia Gusenbauer** − *Institute of Wood Technology and Renewable Materials, University of Natural Resources and Life Sciences, 3430 Tulln an der Donau, Austria;* orcid.org/0000-0003-3520-3732

**Andreas Weber** − *Institute of Biophysics, University of Natural Resources and Life Sciences, 1190 Vienna, Austria*

**Jose Luis Toca-Herrera** − *Institute of Biophysics, University of Natural Resources and Life Sciences, 1190 Vienna, Austria*

**Fiona Wiesner** − *Macromolecular Chemistry, Department of Chemistry and Biology, University of Siegen, 57074 Siegen, Germany*

**Ulrich Jonas** − *Macromolecular Chemistry, Department of Chemistry and Biology, University of Siegen, 57074 Siegen, Germany;* orcid.org/0000-0002-2161-4541

Complete contact information is available at: https://pubs.acs.org/10.1021/acs.jpcc.4c05936


### Author Contributions

The manuscript was written through the contributions of all authors. All authors have approved the final version of the manuscript.

### Notes

The authors declare no competing financial interest.

## ■ ACKNOWLEDGMENTS

Y.M. acknowledges support from the Austrian Science Fund (FWF) through the Lise Meitner Programme (M 2925). J.D. and S.F. are grateful for the support from Operational Programme Johannes Amos Comenius financed by European Structural and Investment Funds and the Czech Ministry of Education, Youth and Sports (Project No. SENDISO - CZ.02.01.01/00/22_008/0004596), the Czech Science Fund through the project APLOMA (22-30456J), and from the European Commission via the project VerSiLib (101046217). Y.M. expresses gratitude to Giorgio Mutinati (Austrian Institute of Technology) for his assistance with the IonSys 500 instrument. Open access publishing facilitated by Fyzikalni ustav Akademie ved Ceske republiky, as part of the ACS - CzechELib agreement.

## ■ ABBREVIATIONS

AAHAQ, acylamido-3-hydroxyanthraquinone; AFM, atomic force microscopy; AuNP, gold nanoparticle; BPdiS, 3,3′-disulfanediylbis(*N*-(4-benzoylbenzyl)propanamide); BPQAAm, quaternary ammonium cation *N*-(4-benzoylphenyl)acrylamide; DMAA, dimethylacrylamide; DMSO, dimethyl sulfoxide; FDTD, finite-difference time-domain; LCST, local critical solution temperature; LSP, localized surface plasmon; LSPR, localized surface plasmon resonance; MAA, methacrylic acid; MPC, multiphoton cross-

linking; NIPAAm, *N*-isopropylacrylamide; NIR, near-infrared; NP, nanoparticle; PE-MPC, plasmon-enhanced multiphoton crosslinking; QI, AFM quantitative imaging mode; VPTT, volume phase transition temperature

## ■ REFERENCES


(1) Gramotnev, D. K.; Bozhevolnyi, S. I. Plasmonics beyond the diffraction limit. *Nat. Photonics* **2010**, *4*, 83−91.

(2) Homola, J.; Yee, S. S.; Gauglitz, G. Surface plasmon resonance sensors: Review. *Sens. Actuators, B* **1999**, *54* (1−2), 3−15.

(3) Christopher, P.; Xin, H.; Linic, S. Visible-light-enhanced catalytic oxidation reactions on plasmonic silver nanostructures. *Nat. Chem.* **2011**, *3*, 467−472.

(4) Wang, X. A.; Kong, X. Review of recent progress of plasmonic materials and nano-structures for surface-enhanced Raman scattering. *Materials* **2015**, *8* (6), 3024−3052.

(5) Rosman, C.; Prasad, J.; Neiser, A.; Henkel, A.; Edgar, J.; Sönnichsen, C. Multiplexed plasmon sensor for rapid label-free analyte detection. *Nano Lett.* **2013**, *13* (7), 3243−3247.

(6) Brasselet, S. Polarization-resolved microscopy in the life sciences. *Opt. Photonics News* **2019**, *30* (4), 34−41.

(7) Zuo, T.; Goldwyn, H. J.; Isaacoff, B. P.; Masiello, D. J.; Biteen, J. S. Rotation of single-molecule emission polarization by plasmonic nanorods. *J. Phys. Chem. Lett.* **2019**, *10* (17), 5047−5054.

(8) Zijlstra, P.; Paulo, P. M. R.; Orrit, M. Optical detection of single non-absorbing molecules using the surface plasmon resonance. *Nat. Nanotechnol.* **2012**, *7*, 379−382.

(9) Liang, L.; Zheng, P.; Jia, S.; Ray, K.; Chen, Y.; Barman, I. Plasmonic nanodiamonds. *Nano Lett.* **2023**, *23* (12), 5746−5754.

(10) Taylor, A. B.; Zijlstra, P. Single-molecule plasmon sensing: Current status and future prospects. *ACS Sens.* **2017**, *2* (8), 1103−1122.

(11) Zhang, X.; Li, X.; Reish, M. E.; Zhang, D.; Su, N. Q.; Gutiérrez, Y.; Moreno, F.; Yang, W.; Everitt, H. O.; Liu, J. Plasmon-enhanced catalysis: Distinguishing thermal and nonthermal effects. *Nano Lett.* **2018**, *18* (3), 1714−1723.

(12) Ezendam, S.; Gargiulo, J.; Sousa-Castillo, A.; Lee, J. B.; Nam, Y. S.; Maier, S. A.; Cortés, E. Spatial distributions of single-molecule reactivity in plasmonic catalysis. *ACS Nano* **2024**, *18* (1), 451−460.

(13) Xia, Y.; Halas, N. J. Shape-controlled synthesis and surface plasmonic properties of metallic nanostructures. *MRS Bull.* **2005**, *30* (5), 338−348.

(14) Moskovits, M. Spot the hotspot. *Nature* **2011**, *469* (7330), 307−309.

(15) Feuz, L.; Jonsson, M. P.; Höök, F. Material-selective surface chemistry for nanoplasmonic sensors: Optimizing sensitivity and controlling binding to local hot spots. *Nano Lett.* **2012**, *12*, 873−879.

(16) Feuz, L.; Jönsson, P.; Jonsson, M. P.; Höök, F. Improving the limit of detection of nanoscale sensors by directed binding to high-sensitivity areas. *ACS Nano* **2010**, *4* (4), 2167−2177.

(17) Beeram, S. R.; Zamborini, F. P. Selective attachment of antibodies to the edges of gold nanostructures for enhanced localized surface plasmon resonance biosensing. *J. Am. Chem. Soc.* **2009**, *131* (33), 11689−11691.

(18) Zhang, N.; Liu, Y. J.; Yang, J.; Su, X.; Deng, J.; Chum, C. C.; Hong, M.; Teng, J. High sensitivity molecule detection by plasmonic nanoantennas with selective binding at electromagnetic hotspots. *Nanoscale* **2014**, *6* (3), 1416−1422.

(19) Piliarik, M.; Kvasnička, P.; Galler, N.; Krenn, J. R.; Homola, J. Local refractive index sensitivity of plasmonic nanoparticles. *Opt. Express* **2011**, *19* (10), 9213−9220.

(20) Oliverio, M.; Perotto, S.; Messina, G. C.; Lovato, L.; de Angelis, F. Chemical functionalization of plasmonic surface biosensors: A tutorial review on issues, strategies, and costs. *ACS Appl. Mater. Interfaces.* **2017**, *9* (35), 29394−29411.

(21) Barik, A.; Otto, L. M.; Yoo, D.; Jose, J.; Johnson, T. W.; Oh, S.-H. Dielectrophoresis-enhanced plasmonic sensing with gold nanohole arrays. *Nano Lett.* **2014**, *14* (4), 2006−2012.

(22) Gargiulo, J.; Berté, R.; Li, Y.; Maier, S. A.; Cortés, E. From optical to chemical hot spots in plasmonics. *Acc. Chem. Res.* **2019**, *52* (9), 2525−2535.

(23) Gruber, C.; Hirzer, A.; Schmidt, V.; Trügler, A.; Hohenester, U.; Ditlbacher, H.; Hohenau, A.; Krenn, J. R. Imaging nanowire plasmon modes with two-photon polymerization. *Appl. Phys. Lett.* **2015**, *106* (8), No. 081101.

(24) Galloway, C. M.; Kreuzer, M. P.; Aćimović, S. S.; Volpe, G.; Correia, M.; Petersen, S. B.; Neves-Petersen, M. T.; Quidant, R. Plasmon-assisted delivery of single nano-objects in an optical hot spot. *Nano Lett.* **2013**, *13* (9), 4299−4304.

(25) Magill, B. A.; Guo, X.; Peck, C. L.; Reyes, R. L.; See, E. M.; Santos, W. L.; Robinson, H. D. Multi-photon patterning of photoactive *o*-nitrobenzyl ligands bound to gold surfaces. *Photochem. Photobiol. Sci.* **2019**, *18* (1), 30−44.

(26) Pin, C.; Ishida, S.; Takahashi, G.; Sudo, K.; Fukaminato, T.; Sasaki, K. Trapping and deposition of dye−molecule nanoparticles in the nanogap of a plasmonic antenna. *ACS Omega* **2018**, *3* (5), 4878−4883.

(27) Rajeeva, B. B.; Hernandez, D. S.; Wang, M.; Perillo, E.; Lin, V.; Scarabelli, L.; Pingali, V.; Liz-Marzán, L. M.; Dunn, V.; Shear, V.; Zheng, Y. Regioselective localization and tracking of biomolecules on single gold nanoparticles. *Adv. Sci.* **2015**, *2* (11), No. 1500232.

(28) Sundaramurthy, A.; James Schuck, P.; Conley, N. R.; Fromm, D. P.; Kino, G. S.; Moerner, W. E. Toward nanometer-scale optical photolithography: Utilizing the near-field of bowtie optical nano-antennas. *Nano Lett.* **2006**, *6* (3), 355−360.

(29) Ueno, K.; Juodkazis, S.; Shibuya, T.; Yokota, Y.; Mizeikis, V.; Sasaki, K.; Misawa, H. Nanoparticle plasmon-assisted two-photon polymerization induced by incoherent excitation source. *J. Am. Chem. Soc.* **2008**, *130* (22), 6928−6929.

(30) Ueno, K.; Juodkazis, S.; Shibuya, T.; Mizeikis, V.; Yokota, Y.; Misawa, H. Nanoparticle-enhanced photopolymerization. *J. Phys. Chem. C* **2009**, *113* (27), 11720−11724.

(31) Nah, S.; Li, L.; Liu, R.; Hao, J.; Lee, S. B.; Fourkas, J. T. Metal-enhanced multiphoton absorption polymerization with gold nanowires. *J. Phys. Chem. C* **2010**, *114* (17), 7774−7779.

(32) Yokoyama, T.; Masuhara, A.; Onodera, T.; Kasai, H.; Oikawa, H. Plasmon-enhanced photopolymerization of SU-8 on rough gold surfaces. *J. Phys. Chem. C* **2010**, *114* (46), 19596−19599.

(33) Kameche, F.; Heni, W.; Telitel, S.; Ge, D.; Vidal, L.; Dumur, F.; Gigmes, D.; Lalevée, J.; Marguet, S.; Douillard, L.; Fiorini-Debuisschert, C.; Bachelot, R.; Soppera, O. Plasmon-triggered living photopolymerization for elaboration of hybrid polymer/metal nanoparticles. *Mater. Today* **2020**, *40*, 38−47.

(34) Kameche, F.; Heni, W.; Telitel, S.; Ge, D.; Vidal, L.; Marguet, S.; Douillard, L.; Fiorini-Debuisschert, C.; Bachelot, R.; Soppera, O. Probing pasmon-induced chemical mechanisms by free-radical nanophotopolymerization. *J. Phys. Chem. C* **2021**, *125* (16), 8719−8731.

(35) Khitous, A.; Molinaro, C.; Gree, S.; Haupt, K.; Soppera, O. Plasmon-induced photopolymerization of molecularly imprinted polymers for nanosensor applications. *Adv. Mater. Interfaces* **2023**, *10* (7), No. 2201651.

(36) Lee, J.; Joshi, P. B.; Wilson, A. J.; Kim, Y. Plasmon-driven near-field photopolymerization in a gold nanoparticle colloid. *J. Phys. Chem. C* **2023**, *127* (17), 8096−8103.

(37) Khitous, A.; Molinaro, C.; Abdallah, S.; Chen, M.; Marguet, S.; Laurent, G.; Vidal, L.; Malval, J.-P.; Fiorini-Debuisschert, C.; Adam, P.-M.; Douillard, L.; Bachelot, R.; Soppera, O. Spatial distribution of the photopolymerization induced by localized surface plasmons: Impact of the morphology of the Au nanoparticles. *J. Phys. Chem. C* **2024**, *128* (31), 13097−13107.

(38) Maruo, S.; Nakamura, O.; Kawata, S. Three-dimensional microfabrication with two-photon-absorbed photopolymerization. *Opt. Lett.* **1997**, *22* (2), 132−134.

(39) Sun, H.-B.; Kawata, S. Two-photon laser precision micro-fabrication and its applications to micro-nano devices and systems. *J. Lightwave Technol.* **2003**, *21* (3), 624−633.




https://doi.org/10.1021/acs.jpcc.4c05936
J. Phys. Chem. C 2024, 128, 18641−18650

(40) Farsari, M.; Chichkov, B. Materials processing: Two-photon fabrication. *Nat. Photonics* **2009**, *3*, 450−452.
(41) Gissibl, T.; Thiele, S.; Herkommer, A.; Giessen, H. Two-photon direct laser writing of ultracompact multi-lens objectives. *Nat. Photonics* **2016**, *10* (8), 554−560.
(42) Florian, C.; Piazza, S.; Diaspro, A.; Serra, P.; Duocastella, M. Direct laser printing of tailored polymeric microlenses. *ACS Appl. Mater. Interfaces* **2016**, *8* (27), 17028−17032.
(43) Gissibl, T.; Thiele, S.; Herkommer, A.; Giessen, H. Sub-micrometre accurate free-form optics by three-dimensional printing on single-mode fibres. *Nat. Commun.* **2016**, *7*, No. 11763.
(44) Avci, E.; Grammatikopoulou, M.; Yang, G. Z. Laser-printing and 3D optical-control of untethered microrobots. *Adv. Opt. Mater.* **2017**, *5* (19), No. 1700031.
(45) Zeng, H.; Martella, D.; Wasylczyk, P.; Cerretti, G.; Lavocat, J. C. G.; Ho, C. H.; Parmeggiani, C.; Wiersma, D. S. High-resolution 3D direct laser writing for liquid-crystalline elastomer microstructures. *Adv. Mater.* **2014**, *26* (15), 2319−2322.
(46) Selimis, A.; Mironov, V.; Farsari, M. Direct laser writing: Principles and materials for scaffold 3D printing. *Microelectron. Eng.* **2015**, *132*, 83−89.
(47) Accardo, A.; Blatché, M. C.; Courson, R.; Loubinoux, I.; Thibault, C.; Malaquin, L.; Vieu, C. Multiphoton direct laser writing and 3D imaging of polymeric freestanding architectures for cell colonization. *Small* **2017**, *13* (27), No. 1700621.
(48) Hippler, M.; Lemma, E. D.; Bertels, S.; Blasco, E.; Barner-Kowollik, C.; Wegener, M.; Bastmeyer, M. 3D scaffolds to study basic cell biology. *Adv. Mater.* **2019**, *31* (26), No. 1808110.
(49) Song, J.; Michas, C.; Chen, C. S.; White, A. E.; Grinstaff, M. W. From simple to architecturally complex hydrogel scaffolds for cell and tissue engineering applications: Opportunities presented by two-photon polymerization. *Adv. Healthcare Mater.* **2019**, *9* (1), No. 1901217.
(50) Jing, X.; Fu, H.; Yu, B.; Sun, M.; Wang, L. Two-photon polymerization for 3D biomedical scaffolds: Overview and updates. *Front. Bioeng. Biotechnol.* **2022**, *10*, No. 994355.
(51) Mckee, S.; Lutey, A.; Sciancalepore, C.; Poli, F.; Selleri, S.; Cucinotta, A. Microfabrication of polymer microneedle arrays using two-photon polymerization. *J. Photochem. Photobiol., B* **2022**, *229*, No. 112424.
(52) Zhou, X.; Hou, Y.; Lin, J. A review on the processing accuracy of two-photon polymerization. *AIP Adv.* **2015**, *5* (3), No. 030701.
(53) Niesler, F.; Hermatschweiler, M. Two-photon polymerization—A versatile microfabrication tool: From maskless lithography to 3D printing. *Laser Tech. J.* **2015**, *12* (3), 44−47.
(54) Schwärzle, D.; Hou, X.; Prucker, O.; Rühe, J. Polymer microstructures through two-photon crosslinking. *Adv. Mater.* **2017**, *29* (39), No. 1703469.
(55) Morozov, Y. M.; Wiesner née Diehl, F.; Grün, J. J.; Pertiller, M.; Fossati, S.; Schmidt, K.; Quilis, N. G.; Gusenbauer, C.; Zbiral, B.; Toca-Herrera, J. L.; Klees, S.; Thiagarajan, C. R. V.; Jonas, U.; Dostalek, J. Microstructuring of thermoresponsive biofunctional hydrogels by multiphoton photocrosslinking. *Adv. Funct. Mater.* **2024**, *34* (26), No. 2315578.
(56) Sergelen, K.; Petri, C.; Jonas, U.; Dostalek, J. Free-standing hydrogel-particle composite membrane with dynamically controlled permeability. *Biointerphases* **2017**, *12* (5), No. 051002.
(57) Gisbert Quilis, N.; Lequeux, M.; Venugopalan, P.; Khan, I.; Knoll, W.; Boujday, S.; de la Chapelle, M. L.; Dostalek, J. Tunable laser interference lithography preparation of plasmonic nanoparticle arrays tailored for SERS. *Nanoscale* **2018**, *10* (21), 10268−10276.
(58) Bunea, A.-I.; del Castillo Iniesta, N.; Droumpali, A.; Wetzel, A. E.; Engay, E.; Taboryski, R. Micro 3D printing by two-photon polymerization: Configurations and parameters for the Nanoscribe system. *Micro* **2021**, *1* (2), 164−180.
(59) Morozov, Y. M.; Quilis, N. G.; Diehl, F.; Klees, S.; Grün, J.; Jonas, U.; Dostalek, J. One- and two-photon crosslinked polymer hydrogel microstructures for optical spectroscopy and biosensing applications. *Proc. SPIE* **2022**, *12145*, No. 1214502.
(60) Johnson, P. B.; Christy, R. W. Optical constants of the noble metals. *Phys. Rev. B* **1972**, *6* (12), 4370.
(61) Johnson, P. B.; Christy, R. W. Optical constants of transition metals: Ti, V, Cr, Mn, Fe, Co, Ni, and Pd. *Phys. Rev. B* **1974**, *9* (12), 5056.
(62) Kejík, L.; Horák, M.; Šikola, T.; Křápek, V. Structural and optical properties of monocrystalline and polycrystalline gold plasmonic nanorods. *Opt. Express* **2020**, *28* (23), 34960−34972.
(63) Sharma, N.; Petri, C.; Jonas, U.; Dostalek, J. Reversibly tunable plasmonic bandgap by responsive hydrogel grating. *Opt. Express* **2016**, *24* (3), 2457−2465.
(64) Auer, S. K.; Fossati, S.; Morozov, Y.; Mor, D. C.; Jonas, U.; Dostalek, J. Rapid actuation of thermo-responsive polymer networks: Investigation of the transition kinetics. *J. Phys. Chem. B* **2022**, *126* (16), 3170−3179.
(65) Mateescu, A.; Wang, Y.; Dostalek, J.; Jonas, U. Thin hydrogel films for optical biosensor applications. *Membranes* **2012**, *2* (1), 40−69.
(66) Diehl, F.; Hageneder, S.; Fossati, S.; Auer, S. K.; Dostalek, J.; Jonas, U. Plasmonic nanomaterials with responsive polymer hydrogels for sensing and actuation. *Chem. Soc. Rev.* **2022**, *51* (10), 3926−3963.
(67) Hageneder, S.; Jungbluth, V.; Soldo, R.; Petri, C.; Pertiller, M.; Kreivi, M.; Weinhäusel, A.; Jonas, U.; Dostalek, J. Responsive hydrogel binding matrix for dual signal amplification in fluorescence affinity biosensors and peptide microarrays. *ACS Appl. Mater. Interfaces* **2021**, *13* (23), 27645−27655.


https://doi.org/10.1021/acs.jpcc.4c05936
J. Phys. Chem. C 2024, 128, 18641−18650

# 6 Thiol-Substituted Poly(2-oxazoline)s with Photolabile Protecting Groups - Tandem Network Formation by Light

**Published as:**

Niklas Jung, **Fiona Diehl** and Ulrich Jonas, *Polymers* **2020**, 12, 1767, doi: 10.3390/polym12081767.

**Author Contributions:**

*Niklas Jung:* Monomer syntheses and analyses, polymer syntheses and analyses, Conception, Coordination, Writing, Reviewing, Editing

***Fiona Wiesner (née Diehl):*** Monomer syntheses and analyses, polymer syntheses and analyses, Writing, Reviewing, Editing

*Ulrich Jonas:* Conception, Coordination, Writing, Reviewing, Editing, Funding, Corresponding author

**Supporting Information** can be found in the Appendix, page A10.

polymers

MDPI

Communication

# Thiol-Substituted Poly(2-oxazoline)s with Photolabile Protecting Groups—Tandem Network Formation by Light

**Niklas Jung, Fiona Diehl and Ulrich Jonas ***

Macromolecular Chemistry, Department Chemistry-Biology, University of Siegen, Adolf-Reichwein-Strasse 2, 57076 Siegen, Germany; Niklas.Jung@uni-siegen.de (N.J.); Fiona.Diehl@uni-siegen.de (F.D.)
* Correspondence: jonas@chemie.uni-siegen.de

Received: 21 July 2020; Accepted: 4 August 2020; Published: 7 August 2020

**Abstract:** Herein, we present a novel polymer architecture based on poly(2-oxazoline)s bearing protected thiol functionalities, which can be selectively liberated by irradiation with UV light. Whereas free thiol groups can suffer from oxidation or other spontaneous reactions that degrade polymer performance, this strategy with masked thiol groups offers the possibility of photodeprotection on demand with spatio-temporal control while maintaining polymer integrity. Here, we exploit this potential for a tandem network formation upon irradiation with UV light by thiol deprotection and concurrent crosslinking via thiol-ene coupling. The synthesis of the novel oxazoline monomer 2-{2-[(2-nitrobenzyl)thio]ethyl}-4,5-dihydrooxazole (NbMEtOxa) carrying 2-nitrobenzyl-shielded thiol groups and its cationic ring-opening copolymerization at varying ratios with 2-ethyl-2-oxazoline (EtOxa) is described. The tandem network formation was exemplarily demonstrated with the photoinitator 2-hydroxy-2-methylpropiophenone (HMPP) and pentaerythritol tetraacrylate (PETA), a commercially available, tetrafunctional vinyl crosslinker. The key findings of the conducted experiments indicate that a ratio of ~10% NbMEtOxa repeat units in the polymer backbone is sufficient for network formation and in-situ gelation in *N*,*N*-dimethylformamide.

**Keywords:** in situ-forming gels; polymer network; chemical bonding; thiol-ene click; poly(2-oxazoline)s; photoremoveable protecting group (PPG)

## 1. Introduction

Poly(2-oxazoline)s are a class of pseudo-polyamides with a polyethyleneimine backbone and pendant amide substituents [1]. Interesting features of this polymer class encompass antifouling [2], biocompatibility [3–5], or therapeutic [1,6] properties. Consequently, in recent years, a large body of research was addressed to this domain [7–9]. For many applications of these poly(2-oxazoline)s, e.g., antifouling surface coatings, crosslinked networks are required [10]. In the literature, various crosslinking mechanisms are described to yield such network architectures, specifically as water-swollen hydrogels. Pioneering work was reported by Seagusa and coworkers at the end of the last century [11–14]. Several years later, different research groups regained interest in poly(2-oxazoline)s as potential precursors for hydrogels [15,16]. A particular elegant strategy to crosslink poly(2-oxazoline)s harnesses the power of the thiol-ene click reaction, as demonstrated by many groups [10,17–24]. There, vinyl-functionalized poly(2-oxazoline)s as network backbone and multi-functional thiol derivatives as small crosslinker units were utilized [22].

To our knowledge, so far no gel has been reported that has been formed from a thiol-functionalized poly(2-oxazoline) and a crosslinker with unsaturated carbon bonds. One advantage of this novel concept concerns the increased stability (e.g., against oxidation) and accessibility of numerous vinyl-

or alkyne-functionalized crosslinker derivatives opposed to their corresponding thiol analogues. Furthermore, the complementary thiol-substituted poly(2-oxazoline)s represent by themselves an interesting class of functional polymers:

a. Targeted functionalization of poly(2-oxazoline)s may be conveniently performed utilizing thiol groups;
b. The biological activity of free thiol groups (e.g., after conversion to asymmetric disulfides) as biologically cleavable linker, which has been proposed in advanced transfection methodologies [25];
c. The thiol group can serve as anchor group for immobilization of poly(2-oxazoline)s on metal surfaces like Au and Ag [26,27];
d. In self-healing materials, the thiol moieties can undergo so-called thiol-disulfide exchange reactions, which is an interesting motive for repair processes [28,29].

Despite these advantages of free thiol groups, such SH–modified poly(2-oxazoline) derivatives may be affected by the following complications:

a. 2-Oxazoline monomers bearing free thiol groups are not applicable in cationic ring opening polymerization (CROP), since the thiol is a nucleophile that acts as termination agent for the cationic active centers [30];
b. Further, unprotected thiol groups are susceptible to oxidation to disulfides (e.g., with oxygen from air), which renders them inactive in thiol-ene click reactions and consequently may lead in poly(2-oxazoline)s to uncontrolled crosslinking, making storage and handling under ambient conditions difficult;
c. Free thiol-groups in poly(2-oxazoline)s could also interfere in biological applications with sulfur-containing biomolecules (in particular in living organisms) by nucleophilic or disulfide exchange reactions [10].

Furthermore, thiol moieties may adversely transform other reactive groups within the same polymer backbone, e.g., reduction of azide moieties [31]. Consequently, protection of these free thiol moieties along the polymer backbone is necessary. For many side chain functionalities in poly(2-oxazoline)s, e.g., aldehyde [32], amino [33], and carboxylic acid groups [34], a large number of protecting groups have been reported in the literature. So far, for mercapto-modified poly(2-oxazoline)s, only the 4-methoxybenzyl substituent has been discussed as protecting group [35]. Its cleavage requires quite harsh conditions with trifluoroacetic acid and anisole under elevated temperatures over extended periods of time [35], which may cause damage to sensitive moieties in the polymer.

An alternative approach employs photoremovable protecting groups (PPGs), which have been reported for various functionalities [36–44]. One of the early PPGs, which found broad application, is based on the 2-nitrobenzyl motif, and till the 1980s about six main categories of different PPG classes were described [41]. Until 2013, the spectrum of PPG systems was significantly enhanced, as elaborated by the exhaustive review of Klán et al. [36]. Some current research directions that are worthwhile to point out are as follows: concurrent implementation of complementary PPGs at solid interfaces, which allow selective deprotection in a lithographic manner [42]; long-wavelength-sensitive PPGs for biological and biomedical in vivo applications [43]; and two-photon-sensitive PPGs, which combine the advantages of longer wavelengths for deprotection with high spatial resolution [44]. Generally, PPGs provide the advantage of using light as sole means for cleavage under mild conditions, allowing for good spatio-temporal control and obviating the need for chemical reagents in the deprotection reaction [36,40].

In the present publication, we focus on the well-known photolabile 2-nitrobenzyl unit as PPG for novel thiol-modified poly(2-oxazoline)s. The efficient synthesis of an oxazoline monomer carrying a 2-nitrobenzyl-shielded thiol group and its copolymerization with 2-ethyl-2-oxazoline (EtOxa) is reported. As a proof of principle, the tandem reaction cascade depicted in Figure 1 was investigated with the synthesized polymer system by preliminary gelation experiments. This cascade comprises photodeprotection and simultaneous thiol-ene click coupling to result in network formation.

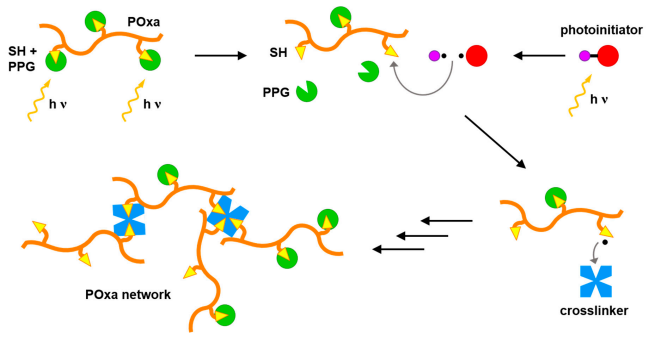


**Figure 1.** Schematic strategy of the tandem network formation by concurrent photodeprotection and thiol-ene click crosslinking ('POxa': poly(2-oxazoline), 'PPG': photoremovable protecting group, 'SH': thiol group).

## 2. Materials and Methods

Experimental details about the synthetic procedures and characterization methods are provided in the Supporting Information.

## 3. Results and Discussion

### *3.1. Monomer Synthesis*

The novel monomer 2-{2-[(2-nitrobenzyl) thio]ethyl}-4,5-dihydrooxazole (**4**), abbreviated NbMEtOxa, was prepared in four steps partially based on concepts from the literature (see Scheme 1) [45]. For the synthesis of 3-[(2-nitrobenzyl)thio] propanoic acid (**1**), the thiol group of mercaptopropionic acid was protected with *o*-nitrobenzyl bromide, according to reaction procedures published by Hensarling et al. and Pauloehrl et al. [46,47]. In the subsequent step, the carboxyl group was converted to the *N*-hydroxysuccinimide ester **2** and directly coupled with 2-chloroethylamine to yield amide **3**. Ring closure to the 2-oxazoline **4** was accomplished with potassium carbonate at elevated temperatures in acetonitrile. The overall yield of the 4-step synthesis route amounted to 47%, and corresponding $^{1}$H and $^{13}$C NMR spectra (see ESI, Figures S1 to S6) confirmed the presence of the title compound **4**.

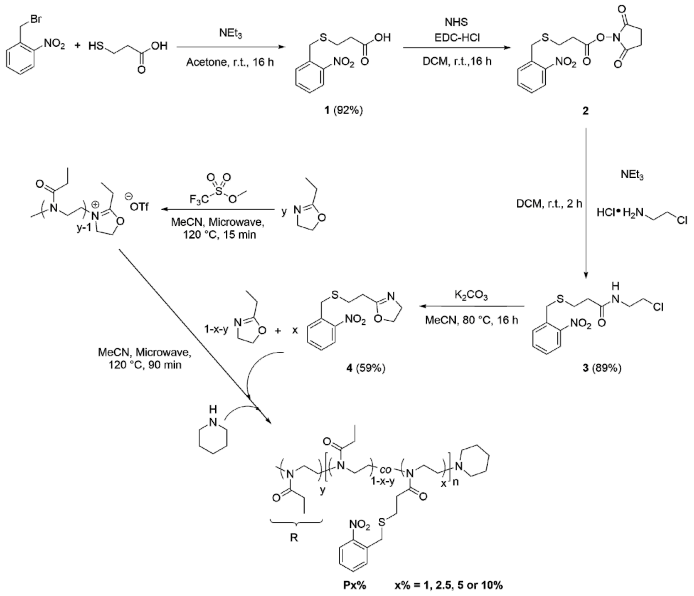


**Scheme 1.** Synthesis route for 2-{2-[(2-nitrobenzyl)thio]ethyl}-4,5-dihydrooxazole (NbMEtOxa) and the corresponding copolymerization using 2-ethyl-2oxazoline (EtOxa) as comonomer. The label R in the polymer structure denotes the EtOxa-homoblock of the initiator species with degree of polymerization y.

### 3.2. Polymer Synthesis

Copolymerization of NbMEtOxa with other 2-oxazolines allows one to incorporate properties of the respective comonomers into a single polymer architecture. The copolymer composition can be conveniently controlled by this approach via the comonomer mixing ratio in the reaction feed. In particular, for copolymers based on 2-alkyl-2-oxazolines, the thermoresponsivness in aqueous solution can be controlled by the types of alkyl groups and their combinations [8]. In our study, we employed commercially available EtOxa as a comonomer, which has been extensively used by many groups. After deprotection of the NbMEtOxa repeat unit, the free thiol groups were exploited for crosslinking of the copolymer, with the crosslinking density being tailored by the comonomer ratio of NbMEtOxa and EtOxa. Several polymerization attempts of the novel NbMEtOxa indicated problems with the common initiator methyl trifluoromethanesulfonate (MeOTf), as no reasonable amounts of polymer could be obtained. A potential impediment may be S-methylation by MeOTf, analogous to issues reported by Cesana and coworkers for the copolymerization of amino-functionalized oxazolines [33]. Various literature reports suggest a strategy with a preinitiator species for functionalized 2-oxazolines to circumvent such side reactions. There, a preceding reaction of an appropriate 2-alkyl-2-oxazoline and methylation agent (e.g., MeOTf or methyl tosylate) generates an initiator species for the subsequent polymerization of the problematic oxazoline monomers [32,33,35,48]. Based on these reports, we found that oligo(2-ethyl-2-oxazoline)-2-ethyl-2-oxazolinium trifluoromethanesulfonate (EtOxaOTf, formed from EtOxa and MeOTf) allowed successful copolymerization of EtOxa and NbMEtOxa. The copolymers with different NbMEtOxa contents (**P1%**, **P2.5%**, **P5%**, and **P10%**) were characterized by $^1$H NMR spectroscopy, gel permeation chromatography (GPC), and UV/Vis spectroscopy. Integration of both types of monomers into the same polymer backbone is corroborated by their respective proton signals in the $^1$H NMR spectrum, as exemplarily shown for **P10%** in Figure 2A. The relative ratio of 8.5 mol% for the NbMEtOxa repeat units in the polymer could be determined by comparing the integral of signal **a** ($\delta$ = 3.02 ppm) with that of signals **f** ($\delta$ = 7.41–7.93 ppm), which is in good agreement with the monomer feed of 10 mol%. The molar mass at peak maximum ($M_p$) of the copolymers, as determined by GPC (see ESI, Figure S14), matches the low NbMEtOxa content with the target molar mass of 15 kg mol$^{-1}$, but decreases with higher comonomer content ($M_p$ for P1%: 16.1 kg mol$^{-1}$; P2.5%: 13.7 kg mol$^{-1}$; P5%: 8.0 kg mol$^{-1}$; P10%: 5.6 kg mol$^{-1}$). For an ideal Gaussian curve, $\overline{M}_n$ corresponds to $M_p$, but due to the broader molar mass distributions and the presence of several polymer species $\overline{M}_n$ is not well defined and thus we provide $M_p$ for the maximum of the GPC trace. Molar mass distributions ($Đ$ = 1.3–3.2) were broader than expected for CROP of 2-oxazolines ($Đ$ typically around 1.2). These GPC traces show several local maxima that indicate the presence of multiple species. In addition, the UV detector signal deviates significantly from the RI detector signal. The aromatic protecting group of NbMEtOxa is the only functionality that can contribute to a UV absorption at the specific detector wavelength ($\lambda$ = 280 nm), while the EtOxa repeat unit possesses no such UV absorption. A deviation between the shapes of the UV and RI detector signal traces reflects a compositional drift for different molar masses. In order to quantify the absolute number of incorporated comonomer units, the corresponding response factors of each repeat unit type and both detectors must be known [49]. The response factor is defined by the specific detector sensitivity for a given type of repeat unit. For the copolymers discussed in this paper, no response factors can be determined, either for the EtOxa repeat unit, as it does not show any UV absorption, or for the NbMEtOxa repeat unit, as it does not form defined homopolymers. Nevertheless, a qualitative analysis of the compositional drift is possible by the following procedure to generate a UV-RI difference plot: (a) first, the UV and RI traces are normalized by dividing all signal intensity values with the one at the respective trace maxima; (b) then, the normalized RI trace is subtracted from the normalized UV trace. Even though this normalization procedure does remove information on the absolute number of repeat units in the polymer backbone and thus prevents quantitative analysis, this internal calibration yet allows qualitative comparison of the compositional drift between different samples.

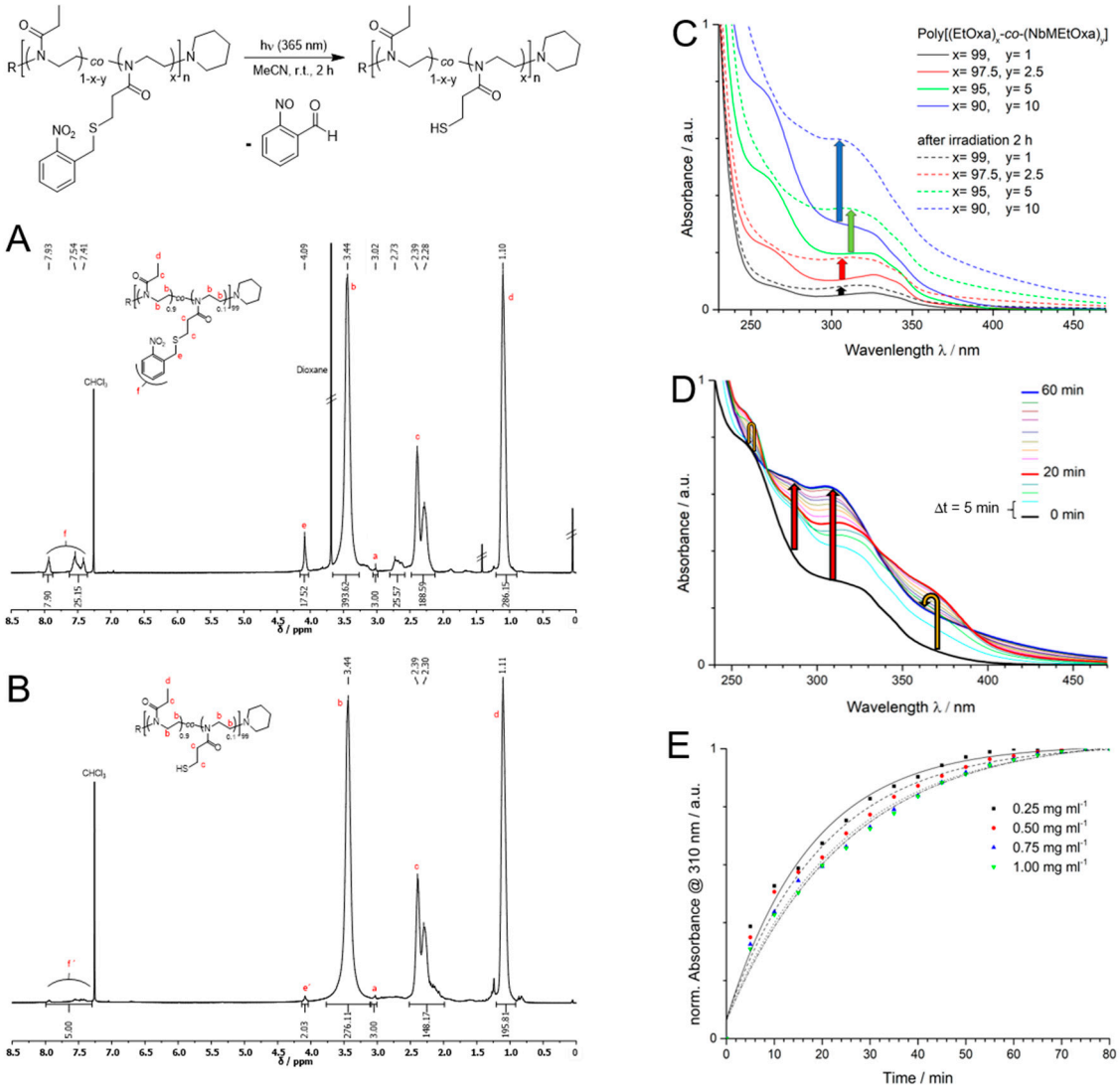


**Figure 2.** Deprotection reaction scheme for copolymer **P10%** and the corresponding $^1$H NMR spectra recorded before (**A**) and after irradiation with UV light ($\lambda$ = 365 nm) (**B**). R = EtOxa-homoblock of initiator species, signals **a** and **a′** correspond to the terminal methyl group of the initiator block R (the corresponding integrals are normalized to three protons), and signals **e′** and **f′** in (**B**) indicate residual PPGs after the deprotection step. These signals were used to calculate the degree of polymerization. In graph (**C**), UV/Vis spectra of polymers containing different amounts of protected thiol moieties in acetonitrile solution (c = 0.25 mg ml$^{-1}$) are depicted. Spectrum (**D**) shows the time-dependent absorbance change during deprotection of **P10%**. Deprotection kinetics (**E**) are shown for different polymer concentrations. The absorbance was measured at its maximum for *o*-nitrosobenzaldehyde at $\lambda_{max}$ = 310 nm. The dashed lines are drawn to guide the eye. The arrows indicate the change in absorbance with increasing time.

For the example of a perfectly random copolymer with fixed comonomer ratio, the proportionality between the UV and RI detector traces is independent of the degree of polymerization, as the overall composition is identical for every chain length. As consequence, the UV-RI difference plot would result in a straight line at zero value. In the case of a polymer composed of non-UV-active monomers, this procedure would yield the inverse of the normalized RI trace with -1 at minimum. In contrast, if the copolymer composition of UV-absorbing and non-UV-active comonomers varies for different chain lengths, non-zero values are expected in such a UV-RI difference plot. Positive values in the

UV-RI difference plot indicate polymer chains containing higher amounts of UV-absorbing units, while negative values represent the same but with higher content of non-UV-active comonomer in reference to the chain composition at the elution volume, where the normalized intensity of the UV trace equals that of the RI trace (intersection of both curves).

In our polymers, the significant deviations from the zero-line (abscissa) imply that the ratio between the UV-absorbing NbMEtOxa-related repeat units and the non-UV-active EtOxa repeat units is not uniform for all polymer chain lengths (see ESI, Figure S15). In essence, the UV-RI difference plots for all polymer samples (**P1%**, **P2.5%**, **P5%**, and **P10%**) show a positive peak at low molar masses (short chain lengths at high elution volumes) and a negative deflection in the intermediate region, while at high molar masses (long chains at low elution volumes) the amount of UV-absorber seems to increase again. The data suggest the coexistence of three different polymer architectures:

a. Low molar mass polymers (fraction 1) with high NbMEtOxa content that can be removed by deprotection (see discussion on photodeprodection further below);
b. Polymer chains (fraction 2) consisting of high EtOxa and low NbMEtOxa content;
c. High molar mass species (fraction 3) with UV-active groups.

The low molar mass polymers (fraction 1) with high content of UV-active species may be explained by a tendency for early chain termination of NbMEtOxa. This assumption is supported by the fact that the homopolymerization of NbMEtOxa solely led to oligomers even by employing the above presented two-step initiation strategy (see ESI, Table S1). In contrast, the EtOxa monomer supports extended chain growth leading to longer polymer chains with lower NbMEtOxa content (fraction 2). Furthermore, the *o*-nitrosobenzaldehyde PPGs from the NbMEtOxa repeat units in the polymer backbone may undergo side-reactions that lead to branched polymer species with high molar masses (fraction 3) and a high content of UV-active groups.

### *3.3. Photodeprotection*

Deprotection of the copolymers was performed in acetonitrile solution ($c$ = 0.25 mg ml$^{-1}$) by irradiation with UV light at a wavelength of $\lambda$ = 365 nm and radiant exposure of up to $H_e$ = 24 J cm$^{-2}$ (exposure time up to 2 h). Under these conditions, photoinduced cleavage of the *o*-nitrobenzyl PPG follows the mechanism of a Norrish type II reaction, forming 2-nitrosobenzaldehyde as side product (chemical reaction depicted in Figure 2) [36,39,40]. Successful fragmentation is clearly indicated by the decrease of the *o*-nitrobenzylic $^1$H NMR signal intensities at $\delta$ = 4.09 ppm (signal **e**) and $\delta$ = 7.41–7.93 ppm (signal **f**) in Figure 2A,B. The deprotection efficiency was determined by comparison of the signal integrals at $\delta$ = 4.09 ppm (signals **e** and **e'**) before and after irradiation, amounting to 90% after 2 h irradiation. Similar values are reported in the literature for carboxylates, which were protected with the same PPG [40]. Delaittre and coworkers reported quantitative deprotection of *o*-nitrobenzyl-masked thiol groups in polyacrylamide RAFT copolymers after 2 h irradiation time and workup [50]. In our case, extended irradiation times beyond 2 h showed no further increase in deprotection yield, potentially due to side reactions during CROP of the incorporated NbMEtOxa units, as discussed above for the high molar mass species (fraction 3). After deprotection, the UV-RI difference curves show a substantial loss of UV-active components for the low molar mass region (see ESI, Figure S15). The GPC traces indicate a high molar mass fraction with residual UV absorbance that result from persistent UV-active moieties that cannot be removed by light (see ESI, Figure S14). These moieties may be a consequence from NbMEtOxa side-reactions that yield branched polymers, which become insensitive to UV deprotection. Furthermore, additional high molar mass species are observed in the GPC traces of the deprotected samples, which may result from oxidative coupling of the liberated thiol groups.

Comparison of the UV/Vis spectra (Figure 2C), recorded before (solid lines) and after 2 h irradiation (dashed lines), showed an absorbance increase in the range of $\lambda$ = 300–350 nm, proportional to the concentration of the liberated *o*-nitrosobenzaldehyde with two local absorption maxima at 285 nm and 310 nm [50,51]. In Figure 2D, the time-dependent change of absorbance during deprotection is exemplarily shown for **P10%** at a concentration of $c$ = 0.25 mg ml$^{-1}$. With progressing time, the *o*-nitrosobenzaldehyde absorbance in the range of $\lambda$ = 270–350 nm steadily increases, as indicated by the red arrows. Interestingly, two additional temporary absorbance maxima around $\lambda$ = 265 and 350 nm appear during the first 20 min of irradiation and decrease again (indicated by the bent yellow arrows), which may be attributed to reactive intermediates [40,51–53]. The kinetic measurements in Figure 2E were performed using four different concentrations of **P10%**, as indicated in the figure legend, by following the absorbance of the *o*-nitrosobenzaldehyde maximum at $\lambda$ = 310 nm. Independent of the polymer concentration, the UV/Vis measurements show no further change in absorbance beyond 80 min of irradiation, indicating maximal deprotection of the thiol moieties. The small variations (flattening) in the kinetic curves for the different polymer concentrations can be attributed to an internal filter effect caused by the released *o*-nitrosobenzaldehyde that absorbs the incident light [36,40] and therefore decreases the amount of photons triggering the photoelimination.

### *3.4. Tandem Network Formation*

The free thiol groups along the polymer backbone provided by photodeprotection are a prerequisite for network formation by reaction with a separate crosslinker unit. Our proposed tandem reaction cascade employs photoactivated thiol-ene click coupling between such liberated thiol groups and vinyl moieties in the crosslinker. Specifically, pentaerythritol tetraacrylate (PETA) was used as tetrafunctional crosslinker and 2-hydroxy-2-methylpropiophenone (HMPP) as photoinitiator for radical activation. The reaction conditions reported by Ooi and coworkers were adapted to the increased molar ratio of thiol groups along the polymer backbone [54]. Crosslinking tests (Figure 3) were performed with 15 wt% polymer solutions of **P1%**, **P2.5%**, **P5%**, and **P10%**, in DMF, using UV light at a wavelength of $\lambda$ = 365 nm and radiant exposure of up to $H_e$ = 24 J cm$^{-2}$ (exposure time up to 2 h, each experiment with five replicates). Successful network formation is demonstrated in Figure 3 with a firm gel that retains its oblique shape when inverting the vial containing the mixture that was irradiated in a tilted position. Even though the initial photoexcited state during deprotection of the *o*-nitrobenzyl PPG may involve radical species [39], it was found that addition of the photoinitiator HMPP was crucial for gel formation via the thiol-ene click process. As no gel formation was observed in the absence of the photoinitiator, spontaneous thiol-Michael addition was excluded under these conditions. Neither did irradiation of a DMF solution of photoinitiator HMPP and the tetrafunctional acrylate crosslinker PETA (ESI, Figure S22, vial 2) nor irradiation of a mixture of HMPP and **P10%** (ESI, Figure S22, vial 1) alone lead to gel formation. In the presence of photoinitiator and crosslinker, successful network formation was achieved for **P10%** with a higher NbMEtOxa content after an irradiation time of 1 h by the formation of a non-flowing gel. In contrast, for copolymers containing lower amounts of NbMEtOxa (**P1%**, **P2.5%**, **P5%**) no gel formation was observed, even after doubling either the irradiation time, the photoinitiator concentration, or the polymer mass concentration. In order to preserve the positive intrinsic properties of poly(EtOxa), the NbMEtOxa content was limited to 10%, as this amount was already sufficient for crosslinking.

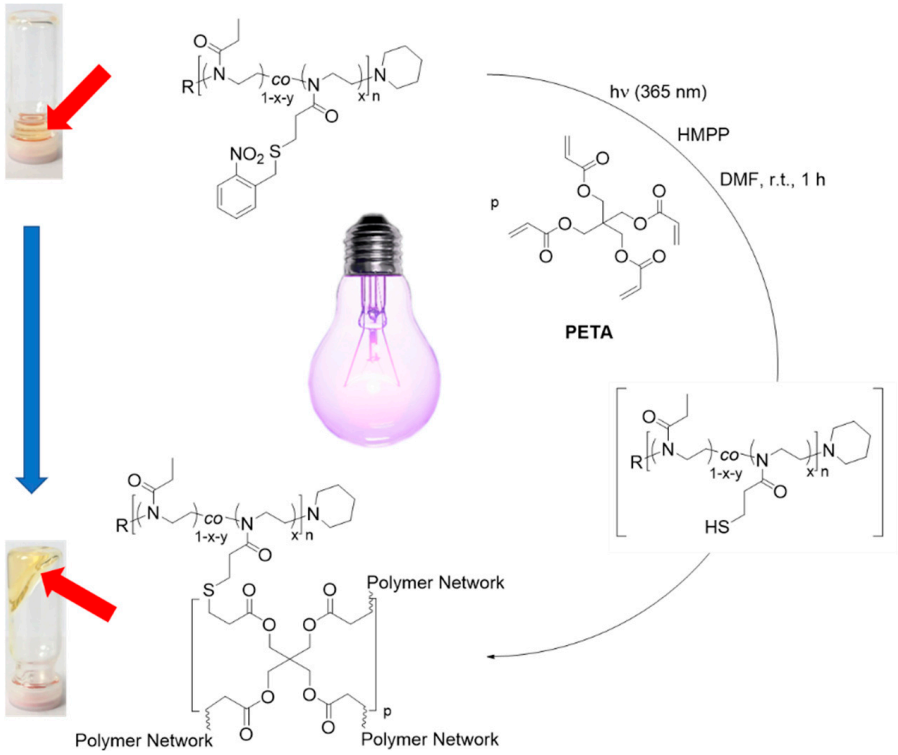


**Figure 3.** Tandem network formation by in situ photodeprotection and concurrent crosslinking of **P10%** with pentaerythritol tetraacrylate (PETA). The label R in the polymer structure denotes the initiator EtOxa-homoblock with degree of polymerization y. The photos (left) show the liquid-to-gel transition induced by UV irradiation of the tilted vial resulting in a rigid gel. Red arrows indicate liquid and gel, respectively.

## 4. Conclusions

In summary, we could demonstrate a novel tandem process for the photoinduced formation of a poly(oxazoline) network involving concurrent photodeprotection of polymer-associated thiol units and their thiol-ene click coupling to a vinyl crosslinker agent. For this purpose, a synthesis route for the novel monomer NbMEtOxa with overall yield of 47% was developed. Copolymerization with EtOxa led to polymers with masked thiol functions, for which nearly quantitative photodeprotection was achieved within 2 h at $\lambda$ = 365 nm ($H_e$ = 24 J cm$^{-2}$). Successful network formation via the tandem deprotection-crosslinking route requires a minimum ratio of NbMEtOxa repeat units (in the investigated system around 10%) in the macromolecular structure.

The unique feature of this strategy lies in the concurrent activation of functional groups and induction of a crosslinking reaction both triggered by light with high spatio-temporal control. This approach circumvents potential side reactions of free thiol groups that affect polymer stability and allow storage and convenient handling of a thiol-containing polymer.

Further studies will be directed to the improvement of the gelation efficiency at lower thiol group content (other types of crosslinkers, initiators, and solvents); extension of the tandem network formation concept to responsive polymer systems; and the exploration of potential applications in materials, biomedical, and surface sciences.

**Supplementary Materials:** The following are available online at http://www.mdpi.com/2073-4360/12/8/1767/s1.

**Author Contributions:** Conceptualization, N.J.; Investigation, N.J. and F.D.; Project administration and funding acquisition, U.J.; Writing—original draft, N.J., F.D. and U.J.; Writing—review & editing, N.J., F.D. and U.J. All authors have read and agreed to the published version of the manuscript.

**Funding:** Financial support from Deutsche Forschungsgesellschaft (DFG) Application D-A-CH Lead Agency Program "Self-Assembly of DNA Dendrimers in the Bulk and at Interfaces" (JO 370/5-1) is gratefully acknowledged.

**Acknowledgments:** N.J. thanks the Deutsche Forschungsgesellschaft (DFG) for funding (JO 370/5-1). Max Meier, Petra Frank, and Thorben Jaik are acknowledged for helpful discussions. We thank Thomas Paululat for help with the NMR measurements.

**Conflicts of Interest:** The authors declare no conflict of interest.

## References

1. Luxenhofer, R.; Han, Y.; Schulz, A.; Tong, J.; He, Z.; Kabanov, A.V.; Jordan, R. Poly(2-oxazoline)s as Polymer Therapeutics. *Macromol. Rapid Commun.* **2012**, *33*, 1613–1631. [CrossRef] [PubMed]
2. Knop, K.; Hoogenboom, R.; Fischer, D.; Schubert, U.S. Poly(ethylene glycol) in Drug Delivery: Pros and Cons as Well as Potential Alternatives. *Angew. Chem. Intern.* **2010**, *49*, 6288–6308. [CrossRef] [PubMed]
3. Adams, N.; Schubert, U.S. Poly(2-oxazolines) in biological and biomedical application contexts. *Adv. Drug Deliv. Rev.* **2007**, *59*, 1504–1520. [CrossRef] [PubMed]
4. Viegas, T.X.; Bentley, M.D.; Harris, J.M.; Fang, Z.; Yoon, K.; Dizman, B.; Weimer, R.; Mero, A.; Pasut, G.; Veronese, F.M. Polyoxazoline: Chemistry, Properties, and Applications in Drug Delivery. *Bioconj. Chem.* **2011**, *22*, 976–986. [CrossRef]
5. Tauhardt, L.; Kempe, K.; Gottschaldt, M.; Schubert, U.S. Poly(2-oxazoline) functionalized surfaces: From modification to application. *Chem. Soc. Rev.* **2013**, *42*, 7998–8011. [CrossRef]
6. Lorson, T.; Lübtow, M.M.; Wegener, E.; Haider, M.S.; Borova, S.; Nahm, D.; Jordan, R.; Sokolski-Papkov, M.; Kabanov, A.V.; Luxenhofer, R. Poly(2-oxazoline)s based biomaterials: A comprehensive and critical update. *Biomaterials* **2018**, *178*, 204–280. [CrossRef]
7. Hoogenboom, R. Poly(2-oxazoline)s: Alive and Kicking. *Macromol. Chem. Phys.* **2007**, *208*, 18–25. [CrossRef]
8. Hoogenboom, R. Poly(2-oxazoline)s: A Polymer Class with Numerous Potential Applications. *Angew. Chem.* **2009**, *48*, 7978–7994. [CrossRef]
9. Pizzi, D.; Humphries, J.; Morrow, J.P.; Fletcher, N.L.; Bell, C.A.; Thurecht, K.J.; Kempe, K. Poly(2-oxazoline) macromonomers as building blocks for functional and biocompatible polymer architectures. *Eur. Polym. J.* **2019**, *121*, 109258. [CrossRef]
10. Ahmad, N.; Colak, B.; Gibbs, M.J.; Zhang, D.-W.; Gautrot, J.E.; Watkinson, M.; Becer, C.R.; Krause, S. Peptide Cross-Linked Poly(2-oxazoline) as a Sensor Material for the Detection of Proteases with a Quartz Crystal Microbalance. *Biomacromolecules* **2019**, *20*, 2506–2514. [CrossRef]
11. Chujo, Y.; Yoshifuji, Y.; Sada, K.; Saegusa, T. A Novel Nonionic Hydrogel from 2-Methyl-2-oxazoline. *Macromolecules* **1989**, *22*, 1074–1077. [CrossRef]
12. Chujo, Y.; Sada, K.; Saegusa, T. Polyoxazoline Having a Coumarin Moiety as a Pendant Group. Synthesis and Photogelation. *Macromolecules* **1990**, *23*, 2693–2697. [CrossRef]
13. Chujo, Y.; Sada, K.; Saegusa, T. Reversible Gelation of Polyoxazoline by Means of Diels-Alder Reaction. *Macromolecules* **1990**, *23*, 2636–2641. [CrossRef]
14. Chujo, Y.; Sada, K.; Naka, A.; Nomura, R.; Saegusa, T. Synthesis and Redox Gelation of Disulfide-Modified Polyoxazoline. *Macromolecules* **1993**, *26*, 883–887. [CrossRef]
15. Kelly, A.M.; Hecke, A.; Wirnsberger, B.; Wiesbrock, F. Synthesis of Poly(2-oxazoline)-Based Hydrogels with Tailor-Made Swelling Degrees Capable of Stimuli-Triggered Compound Release. *Macromol. Rapid Commun.* **2011**, *32*, 1815–1819. [CrossRef]
16. Hartlieb, M.; Pretzel, D.; Kempe, K.; Fritzsche, C.; Paulus, R.M.; Gottschaldt, M.; Schubert, U.S. Cationic poly(2-oxazoline) hydrogels for reversible DNA binding. *Soft Matter* **2013**, *9*, 4693–4704. [CrossRef]
17. Gress, A.; Völkel, A.; Schlaad, H. Thio-Click Modification of Poly[2-(3-butenyl)-2-oxazoline]. *Macromolecules* **2007**, *40*, 7928–7933. [CrossRef]
18. Kempe, K.; Lobert, M.; Hoogenboom, R.; Schubert, U.S. Synthesis and characterization of a series of diverse poly(2-oxazoline)s. *J. Polym. Sci. A Polym. Chem.* **2009**, *47*, 3829–3838. [CrossRef]
19. Kempe, K.; Vollrath, A.; Schaefer, H.W.; Poehlmann, T.G.; Biskup, C.; Hoogenboom, R.; Hornig, S.; Schubert, U.S. Multifunctional Poly(2-oxazoline) Nanoparticles for Biological Applications. *Macromol. Rapid Commun.* **2010**, *31*, 1869–1873. [CrossRef]

20. Kempe, K.; Hoogenboom, R.; Jaeger, M.; Schubert, U.S. Three-Fold Metal-Free Efficient ("Click") Reactions onto a Multifunctional Poly(2-oxazoline) Designer Scaffold. *Macromolecules* **2011**, *44*, 6424–6432. [CrossRef]
21. Kempe, K.; Weber, C.; Babiuch, K.; Gottschaldt, M.; Hoogenboom, R.; Schubert, U.S. Responsive Glyco-poly(2-oxazoline)s: Synthesis, Cloud Point Tuning, and Lectin Binding. *Biomacromolecules* **2011**, *12*, 2591–2600. [CrossRef] [PubMed]
22. Dargaville, T.R.; Forster, R.; Farrugia, B.L.; Kempe, K.; Voorhaar, L.; Schubert, U.S.; Hoogenboom, R. Poly(2-oxazoline) Hydrogel Monoliths via Thiol-ene Coupling. *Macromol. Rapid Commun.* **2012**, *33*, 1695–1700. [CrossRef] [PubMed]
23. Blöhbaum, J.; Paulus, I.; Pöppler, A.-C.; Tessmar, J.; Groll, J. Influence of charged groups on the cross-linking efficiency and release of guest molecules from thiol–ene cross-linked poly(2-oxazoline) hydrogels. *J. Mater. Chem. B* **2019**, *7*, 1782–1794. [CrossRef] [PubMed]
24. Liebscher, J.; Teßmar, J.; Groll, J. In Situ Polymer Analogue Generation of Azlactone Functions at Poly(oxazoline)s for Peptide Conjugation. *Macromol. Chem. Phys.* **2020**, *221*, 1900500. [CrossRef]
25. Wang, Y.; Zheng, M.; Meng, F.; Zhang, J.; Peng, R.; Zhong, Z. Branched Polyethylenimine Derivatives with Reductively Cleavable Periphery for Safe and Efficient In Vitro Gene Transfer. *Biomacromolecules* **2011**, *12*, 1032–1040. [CrossRef]
26. Love, J.C.; Estroff, L.A.; Kriebel, J.K.; Nuzzo, R.G.; Whitesides, G.M. Self-Assembled Monolayers of Thiolates on Metals as a Form of Nanotechnology. *Chem. Rev.* **2005**, *105*, 1103–1170. [CrossRef]
27. Roth, P.J.; Boyer, C.; Lowe, A.B.; Davis, T.P. RAFT Polymerization and Thiol Chemistry: A Complementary Pairing for Implementing Modern Macromolecular Design. *Macromol. Rapid Commun.* **2011**, *32*, 1123–1143. [CrossRef]
28. Yoon, J.A.; Kamada, J.; Koynov, K.; Mohin, J.; Nicolaÿ, R.; Zhang, Y.; Balazs, A.C.; Kowalewski, T.; Matyjaszewski, K. Self-Healing Polymer Films Based on Thiol–Disulfide Exchange Reactions and Self-Healing Kinetics Measured Using Atomic Force Microscopy. *Macromolecules* **2012**, *45*, 142–149. [CrossRef]
29. Pepels, M.; Filot, I.; Klumperman, B.; Goossens, H. Self-healing systems based on disulfide–thiol exchange reactions. *Polym. Chem.* **2013**, *4*, 4955–4965. [CrossRef]
30. Glassner, M.; Vergaelen, M.; Hoogenboom, R. Poly(2-oxazoline)s: A comprehensive overview of polymer structures and their physical properties. *Polym. Int.* **2018**, *67*, 32–45. [CrossRef]
31. Cartwright, I.L.; Hutchinson, D.W.; Armstrong, V.W. The reaction between thiols and 8-azidoadenosine derivatives. *Nucleic Acids Res.* **1976**, *3*, 2331–2340. [CrossRef] [PubMed]
32. Taubmann, C.; Luxenhofer, R.; Cesana, S.; Jordan, R. First Aldehyde-Functionalized Poly(2-oxazoline)s for Chemoselective Ligation. *Macromol. Biosci.* **2005**, *5*, 603–612. [CrossRef] [PubMed]
33. Cesana, S.; Auernheimer, J.; Jordan, R.; Kessler, H.; Nuyken, O. First Poly(2-oxazoline)s with Pendant Amino Groups. *Macromol. Chem. Phys.* **2006**, *207*, 183–192. [CrossRef]
34. Zarka, M.T.; Nuyken, O.; Weberskirch, R. Amphiphilic Polymer Supports for the Asymmetric Hydrogenation of Amino Acid Precursors in Water. *Chem. A Eur. J.* **2003**, *9*, 3228–3234. [CrossRef]
35. Cesana, S.; Kurek, A.; Baur, M.A.; Auernheimer, J.; Nuyken, O. Polymer-Bound Thiol Groups on Poly(2-oxazoline)s. *Macromol. Rapid Commun.* **2007**, *28*, 608–615. [CrossRef]
36. Klán, P.; Šolomek, T.; Bochet, C.G.; Blanc, A.; Givens, R.; Rubina, M.; Popik, V.; Kostikov, A.; Wirz, J. Photoremovable Protecting Groups in Chemistry and Biology: Reaction Mechanisms and Efficacy. *Chem. Rev.* **2013**, *113*, 119–191. [CrossRef]
37. Bochet, C.G. Wavelength-selective cleavage of photolabile protecting groups. *Tetrahedron Lett.* **2000**, *41*, 6341–6346. [CrossRef]
38. Bochet, C.G. Orthogonal Photolysis of Protecting Groups. *Angew. Chem. Int.* **2001**, *40*, 2071–2073. [CrossRef]
39. Bochet, C.G. Photolabile protecting groups and linkers. *J. Chem. Soc. Perkin Trans.* **2002**, *1*, 125–142.
40. Wang, P. Photolabile Protecting Groups: Structure and Reactivity. *As. J. Org. Chem.* **2013**, *2*, 452–464. [CrossRef]
41. Pillai, V.N.R. Photoremoveable Protecting Groups in Organic Synthesis. *Synthesis* **1980**, *1980*, 1–26. [CrossRef]
42. Del Campo, A.; Boos, D.; Spiess, H.W.; Jonas, U. Surface Modification with Orthogonal Photosensitive Silanes for Sequential Chemical Lithography and Site-Selective Particle Deposition. *Angew. Chem. Int.* **2005**, *44*, 4707–4712. [CrossRef] [PubMed]
43. Vorobev, A.Y.; Moskalensky, A.E. Long-wavelength photoremovable protecting groups: On the way to in vivo application. *Comput. Struct. Biotechnol. J.* **2020**, *18*, 27–34. [CrossRef] [PubMed]

44. Hennig, A.-L.K.; Deodato, D.; Asad, N.; Herbivo, C.; Dore, T.M. Two-Photon Excitable Photoremovable Protecting Groups Based on the Quinoline Scaffold for Use in Biology. *J. Org. Chem.* **2020**, *85*, 726–744. [CrossRef] [PubMed]
45. Levy, A.; Litt, M. Polymerization of cyclic iminoethers. V. 1,3-oxazolines with hydroxy-, acetoxy-, and carboxymethyl-alkyl groups in the 2 position and their polymers. *J. Polym. Sci. A Polym. Chem.* **1968**, *6*, 1883–1894. [CrossRef]
46. Hensarling, R.M.; Hoff, E.A.; LeBlanc, A.P.; Guo, W.; Rahane, S.B.; Patton, D.L. Photocaged pendent thiol polymer brush surfaces for postpolymerization modifications via thiol-click chemistry. *J. Polym. Sci. Part. A Polym. Chem.* **2013**, *51*, 1079–1090. [CrossRef]
47. Pauloehrl, T.; Delaittre, G.; Bastmeyer, M.; Barner-Kowollik, C. Ambient temperature polymer modification by in situ phototriggered deprotection and thiol–ene chemistry. *Polym. Chem.* **2012**, *3*, 1740–1749. [CrossRef]
48. Kobayashi, S.; Iijima, S.; Igarashi, T.; Saegusa, T. Synthesis of a Nonionic Polymer Surfactant from Cyclic Imino Ethers by the Initiator Method. *Macromolecules* **1987**, *20*, 1729–1734. [CrossRef]
49. Kilz, P. Copolymer Analysis by LC Methods, including 2D Chromatography. In *Encyclopedia of Chromatography*; Cazes, J., Ed.; Marcel Dekker: New York, NY, USA, 2001; pp. 195–200.
50. Delaittre, G.; Pauloehrl, T.; Bastmeyer, M.; Barner-Kowollik, C. Acrylamide-Based Copolymers Bearing Photoreleasable Thiols for Subsequent Thiol–Ene Functionalization. *Macromolecules* **2012**, *45*, 1792–1802. [CrossRef]
51. Il'ichev, Y.V.; Schwörer, M.A.; Wirz, J. Photochemical Reaction Mechanisms of 2-Nitrobenzyl Compounds: Methyl Ethers and Caged ATP. *J. Am. Chem. Soc.* **2004**, *126*, 4581–4595. [CrossRef]
52. Patchornik, A.; Amit, B.; Woodward, R.B. Photosensitive Protecting Groups. *J. Am. Chem. Soc.* **1970**, *92*, 6333–6335. [CrossRef]
53. Barltrop, J.A.; Plant, P.J.; Schofield, P. Photosensitive protective groups. *Chem. Commun.* **1966**, *822*, 822–823. [CrossRef]
54. Ooi, H.W.; Jack, K.S.; Whittaker, A.K.; Peng, H. Photo-initiated Thiol–Ene "Click" Hydrogels from RAFT-Synthesized Poly(N-isopropylacrylamide). *J. Poly. Sci. Part A Poly. Chem.* **2013**, *51*, 4626–4636. [CrossRef]


© 2020 by the authors. Licensee MDPI, Basel, Switzerland. This article is an open access article distributed under the terms and conditions of the Creative Commons Attribution (CC BY) license (http://creativecommons.org/licenses/by/4.0/).

# 7 Thermoresponsive and Photocrosslinkable Poly(2-alkyl-2-oxazoline) Toolbox – Customizable Ultralow-Fouling Hydrogel Coatings for Blood Plasma Environments

**Published as:**

**Fiona Wiesner (née Diehl)**, Christian Petri, Simone Hageneder, Cleiton Kunzler, Sven Klees, Petra Frank, Matthias Pertiller, Jakub Dostalek, Wolfgang Knoll, and Ulrich Jonas, *Macromol. Rapid Commun.* **2023**, 2300549, doi: 10.1002/marc.202300549.

**Author Contributions:**

***Fiona Wiesner (née Diehl):*** Conception, Coordination, Data processing, Writing, Reviewing, Editing

*Christian Petri:* Polymer syntheses and analyses, Data generation and processing, SPR/OWS analysis, Writing, Reviewing, Editing

*Simone Hageneder:* SPR/OWS analyses

*Cleiton Kunzler:* AFM measurements

*Sven Klees:* TGA measurements

*Petra Frank:* Monomer Syntheses, GPC analysis

*Matthias Pertiller:* SPR/OWS analyses

*Jakub Dostalek:* Conception, Coordination, Writing, Reviewing, Funding, Editing

*Wolfgang Knoll:* Conception, Reviewing, Funding

*Ulrich Jonas:* Conception, Coordination, Writing, Reviewing, Editing, Funding, Corresponding author

**Supporting Information** can be found in the Appendix, page A16.

Macromolecular Rapid Communications
www.mrc-journal.de

# Thermoresponsive and Photocrosslinkable Poly(2-alkyl-2-oxazoline) Toolbox – Customizable Ultralow-Fouling Hydrogel Coatings for Blood Plasma Environments

*Fiona Wiesner (née Diehl), Christian Petri, Simone Hageneder, Cleiton Kunzler, Sven Klees, Petra Frank, Matthias Pertiller, Jakub Dostalek, Wolfgang Knoll, and Ulrich Jonas**

**This study focuses on developing surface coatings with excellent antifouling properties, crucial for applications in the medical, biological, and technical fields, for materials and devices in direct contact with living tissues and bodily fluids such as blood. This approach combines thermoresponsive poly(2-alkyl-2-oxazoline)s, known for their inherent protein-repellent characteristics, with established antifouling motifs based on betaines. The polymer framework is constructed from various monomer types, including a novel benzophenone-modified 2-oxazoline for photocrosslinking and an azide-functionalized 2-oxazoline, allowing subsequent modification with alkyne-substituted antifouling motifs through copper(I)-catalyzed azide-alkyne cycloaddition. From these polymers surface-attached networks are created on benzophenone-modified gold substrates via photocrosslinking, resulting in hydrogel coatings with several micrometers thickness when swollen with aqueous media. Given that poly(2-alkyl-2-oxazoline)s can exhibit a lower critical solution temperature in water, their temperature-dependent solubility is compared to the swelling behavior of the surface-attached hydrogels upon thermal stimulation. The antifouling performance of these hydrogel coatings in contact with human blood plasma is further evaluated by surface plasmon resonance and optical waveguide spectroscopy. All surfaces demonstrate extremely low retention of blood plasma components, even with undiluted plasma. Notably, hydrogel layers with sulfobetaine moieties allow efficient penetration by plasma components, which can then be easily removed by rinsing with buffer.**

## 1. Introduction

Antifouling substrate and surface materials, which protect an object from nonspecific adsorption of biomolecular entities and subsequent growth of biofilms, have gained critical importance in such versatile fields of science, like biomedicine (e.g. as coatings for medical devices and implants, such as urinal and breathing catheters, feeding tubes, injection equipment, temporary implants, blood filtration, to mention a few),[1] marine engineering (e.g. as coatings for ship bodies to improve their hydrodynamics and minimize their drag),[2] and sensor technologies (e.g. as protection layer for sensor transducers in contact with body fluids).[3,4] A particular challenge and demand presents the availability of surface coatings, which exhibit essentially no protein adsorption upon contact with human blood plasma (HBP) or whole blood. In the literature, a plethora of antifouling compounds has been developed and investigated,[5] with the most prominent examples comprising poly(ethylene glycol)/oligo(ethylene glycol) (PEG/OEG),[6] zwitterionic polymers,[7] and polysaccharide-based materials.[8] The

F. Wiesner (née Diehl), C. Petri, C. Kunzler, S. Klees, P. Frank, U. Jonas
Macromolecular Chemistry
Department Chemistry-Biology
University of Siegen
Adolf-Reichwein-Strasse 2, 57076 Siegen, Germany
E-mail: jonas@chemie.uni-siegen.de

The ORCID identification number(s) for the author(s) of this article can be found under https://doi.org/10.1002/marc.202300549

© 2023 The Authors. Macromolecular Rapid Communications published by Wiley-VCH GmbH. This is an open access article under the terms of the Creative Commons Attribution License, which permits use, distribution and reproduction in any medium, provided the original work is properly cited.

**DOI: 10.1002/marc.202300549**

S. Hageneder, M. Pertiller, J. Dostalek, W. Knoll
Biosensor Technologies
AIT-Austrian Institute of Technology GmbH
Konrad-Lorenz-Straße 24, Tulln an der Donau 3430, Austria

J. Dostalek
FZU-Institute of Physics
Czech Academy of Sciences
Na Slovance 2, Prague 182 21, Czech Republic

J. Dostalek, W. Knoll
Laboratory for Life Sciences and Technology (LiST)
Danube Private University
Konrad-Lorenz-Straße 24, Tulln an der Donau 3430, Austria

commonly accepted working principle of antifouling coatings implies the formation of a tightly bound water layer on the surface that hinders proteins and other biological entities to adsorb.[5] Consequently, a strong hydrophilicity for association of water molecules to the surface presents the main requirement identified for effective antifouling motifs. For ionic and zwitterionic compounds, the effectiveness to bind the hydrate layer is enhanced by electrostatic interactions, providing further resistance to protein adsorption.[9,10] Many procedures to increase the surface hydrophilicity, like anodization for metals and plasma treatments of conductive and non-conductive surfaces,[11] result in rather transient surface modification, while deposition of self-assembled monolayers (SAMs), polymer brushes, and hydrogel coatings often yield permanent effects. For the latter cases of surface-attached molecular entities, physicochemical characteristics, such as polymer chain flexibility, packing density, molecular mass, and surface charge, are crucial for potent antifouling qualities.[12,13]

A particular interesting class of powerful antifouling materials are polymer network-based hydrogels, which can retain substantial amounts of water due to the hydrophilic nature of the underlying polymer backbone. Such water-swollen polymer networks are held together either by physical or chemical crosslinks between the polymer chains, rendering the material insoluble and maintaining its structural integrity over extended periods of time, especially in the case of covalent crosslinks. The counteracting effects of the osmotic pressure of water hydrating the polymer segments, which leads to an expansive force, and the entropically driven tendency of the flexible chain segments to coil into a random conformation, inducing a contracting force, result in the equilibrium swelling state of the network.

Methods for chemical crosslinking entail 1) in situ crosslinking during polymerization and 2) post-polymerization crosslinking by external stimuli, such as UV light (photocrosslinking),[14–17] or temperature increase (thermal crosslinking).[18,19] In particular, the post-polymerization photocrosslinking technique enables the simultaneous preparation of ultra-thin polymer network coatings and covalent attachment to an organic surface material. Inorganic surfaces, like gold metal, may be pre-treated with an adhesion promoting layer bearing for example, benzophenone moieties in order to endow the substrate with photocrosslinking entities.

The potential of poly(2-alkyl-2-oxazoline)s, investigated in the present work, lies in their renown anti-fouling capacities, to serve as base material in photocrosslinked hydrogel architectures that can be further enhanced by other antifouling motifs via a modular click chemistry approach. Poly(2-alkyl-2-oxazoline)s possess a pseudo-peptidic backbone structure and, in addition to their antifouling properties, are characterized by a pronounced biocompatibility.[20,21] Depending on the specific alkyl substituent, they can also show a lower critical solution temperature (LCST) behavior in water, being hydrophilic and dissolved below the cloud point temperature, while undergoing rearrangement of the hydrogen-bonding arrangement with lower affinity of the polymer to water when heated above this point. This process ultimately results in phase separation into a polymer poor and a polymer rich fraction that eventually leads to polymer precipitation.[22] Such volume transitions resulting from the LCST behavior have been exploited for reversible actuation in advanced biosensor applications and are particularly suitable for responsive binding matrices.[23–29]

Poly(2-alkyl-2-oxazoline)s are prepared by cationic ring-opening polymerization (CROP), which allows control over the target molar mass while retaining a narrow mass dispersity, and enables the design of advanced polymer architectures via variation of the comonomer types and sequence. However, this preparation technique is sensitive toward nucleophilic substances or side groups and the cationic chain end can be easily terminated by those. Due to these inherent limitations, many functional monomer types including common crosslinker structures (e.g. based on thiol or amino groups) and antifouling motifs cannot be directly implemented in the CROP procedure. Yet, including a crosslinker functionality in the polymer backbone would provide convenient access to poly(2-oxazoline) network architectures, which are interesting for a variety of applications, such as surface coatings and sensor matrices.

In the field of surface coatings, the possibility to perform crosslinking via irradiation with UV light after deposition of the polymer on a respective substrate extends the radius of operation substantially. Preparation of photocrosslinked poly(2-alkyl-2-oxazoline) networks was successfully demonstrated employing thiol-ene coupling chemistry by incorporation of either unsaturated double bonds into the polyoxazoline scaffold,[30,31] or photocleavable-protected thiol side chains for simultaneous deprotection and crosslinking.[32] Furthermore, such networks could be also obtained from coumarin-modified poly(oxazoline)s via photodimerization upon UV irradiation.[33,34] These strategies suffer from the disadvantage of requiring two mutually reactive units in close proximity to successfully attain crosslinking, which becomes less probable owing to the restricted polymer dynamics compared to small molecules in solution. An additional problem may be the susceptibility to oxidation of the free thiol group involved in the thiol-ene coupling reaction. A photocrosslinker unit that avoids the above-mentioned issues is the well-known benzophenone moiety, as it is stable in the absence of UV light and only needs adjacent C—H bonds as requirement for the crosslinking process. The benzophenone motif was already utilized for the surface attachment of several different types of polymers.[15,35–37] For poly(2-alkyl-2-oxazoline)s, two generic methods for the preparation of substrate coatings via photoactivation of benzophenone groups are reported in the literature. The first strategy is based on substrate modification with respective benzophenone-containing silanes and subsequent polymer deposition followed by irradiation, which results in thin polymer layers of a few nanometers.[35] The second approach relies on the modification of the amine groups in a partially hydrolyzed poly(2-alkyl-2-oxazoline) with photoreactive benzophenone substituents.[38–40] Yet, in order to target a well-defined polymer architecture, incorporation of the benzophenone motif into an oxazoline monomer would provide full control over the composition of the comonomer feed during CROP and thereby the exact ratio of crosslinking sites along the polymer backbone. An early report of molecular frameworks that contain both a 2-oxazoline and a benzophenone structure was provided by Kappel et al.[41] in the context of pharmaceutical applications, but without reference to 2-alkyl-2-oxazoline polymers. When attempting the synthesis of 2-[(4-phenylphenoxy)methyl]-2-oxazoline following this procedure, in our hands we could isolate only the tautomer


© 2023 The Authors. Macromolecular Rapid Communications published by Wiley-VCH GmbH


15213927, 0, Downloaded from https://onlinelibrary.wiley.com/doi/10.1002/marc.202300549 by Cochrane Germany, Wiley Online Library on [28/11/2023]. See the Terms and Conditions (https://onlinelibrary.wiley.com/terms-and-conditions) on Wiley Online Library for rules of use; OA articles are governed by the applicable Creative Commons License

2-(4-benzoylphenoxymethylidene)-1,3-oxazolidine, which was not subjected to CROP. To circumvent the potential risk of tautomerization at the oxazoline ring, we report in the present manuscript the synthesis of a 2-oxazoline derivative with longer alkyl spacer connecting the benzophenone unit, and which is susceptible to copolymerization with other 2-alkyl-2-oxazolines via CROP.

Besides the direct copolymerization of oxazoline photocrosslinker monomers, the inclusion of specific functional groups into the poly(oxazoline) backbone, such as protic antifouling motifs, is difficult due to the sensitivity of CROP toward nucleophilic moieties. A versatile route to endow the polymer scaffold with functional substituents in a post-polymerization modification reaction is provided by azide click chemistry, which provides a toolbox for convenient and effective coupling of alkyne-containing motifs to the azide group. This strategy was exploited here by utilizing an azide-containing oxazoline as comonomer in CROP to yield azide-functionalized poly(2-alkyl-2-oxazoline)s.[42] The polymer backbones with azide modification were conjugated with suitable antifouling motifs in a modular crafting approach to further enhance the antifouling quality and to target respective applications via appropriate click combinations. At this stage, the soluble polymers could be fully analyzed by the standard polymer characterization methods to assess the efficiency of the click modification, which is rather difficult for an insoluble polymer network. Once such polymers were converted into hydrogel coatings by photocrosslinking, their characteristic properties, such as a) layer thickness, b) thermoresponsivity, and c) antifouling properties, were investigated by surface plasmon resonance (SPR) spectroscopy combined with optical waveguide spectroscopy (OWS). Specifically, the antifouling efficacy was analyzed by variation of the refractive index and thickness in the SPR/OWS sensor environment before and after a contact with biological fluids.[43]

## 2. Results and Discussion

In the following discussion, we describe the synthetic strategies for a family of photocrosslinkable poly(2-alkyl-2-oxazoline)s with antifouling backbone and pendent antifouling motifs, employing three components that can be freely combined in a modular approach via CROP. These three components consist of i) the benzophenone-based photocrosslinker monomer 2-[3-(4-benzoylphenoxy)propyl]-4,5-dihydro-1,3-oxazole (BPOxa), ii) the main monomers 2-ethyl-2-oxazoline (EtOxa) and 2-*iso*-propyl-2-oxazoline (iPrOxa) as building blocks for a non-fouling and potentially thermoresponsive polymer backbone, and iii) the azide-based oxazoline monomer 2-(3-azidopropyl)-4,5-dihydro-1,3-oxazole (AzOxa) for click coupling of the antifouling motifs that carry alkyne functions. The alkyne click agents themselves are comprised of different structural elements of the carboxy alkyne 4-pentynoic acid (COOH) for subsequent bioligand coupling, or of literature-known antifouling motifs based on the carboxybetaine 3-[dimethyl(prop-2-yn-1-yl)ammonio]propanoate (CB) and the sulfobetaine 3-[dimethyl(prop-2-yn-1-yl)ammonio]propane-1-sulfonate (SB), as well as the OEG units 2-{2-[2-(prop-2-yn-1-yloxy)ethoxy]ethoxy}ethan-1-ol (OEG) and 3-{dimethyl{2-[2-(prop-2-yn-1-yloxy)ethoxy]ethyl}ammonio}propane-1-sulfonate (OEG-SB). These alkyne motifs are all freely interchangeable to further expand the modular range of the click-modified polymer toolbox. We further analyze the thermal properties of the multicomponent copolymers in aqueous solution by turbidimetry for cloud point determination. After conversion of these copolymers into crosslinked, surface-attached copolymer networks and swelling with water or phosphate-buffered saline (PBS) to form hydrogel coatings, the response of their swelling ratios to temperature changes is characterized by SPR spectroscopy. Furthermore, SPR analysis of the hydrogel coatings in direct contact with HBP was performed to quantify their antifouling efficacy to adumbrate the performance in an anticipated application of biomedical context.

### 2.1. Monomer Synthesis, Polymerization, and Polymer Modification with Antifouling Motifs

#### *2.1.1. Photocrosslinker Monomer*

A 2-oxazoline with a benzophenone unit connected via a methoxy linkage has been reported in the literature.[48] In our hands, this synthesis procedure did not yield the expected oxazoline derivative 2-[4-benzoylphenoxy)methyl]-4,5-dihydro-1,3-oxazole (**u1** in Scheme S14, Supporting Information), but the tautomeric product 2-(4-benzoylphenoxymethylidene)-1,3-oxazolidine (**u2**), as discussed in detail in Chapter S17 (Supporting Information). To avoid potential problems with such tautomerism, we developed a synthesis route for BPOxa (**4**) with propylene spacer between the 2-oxazoline core and the benzophenone substituent (**Figure 1**A).

In a first step, 4-hydroxybenzophenone was coupled to ethyl-4-bromobutyrate in the presence of $K_2CO_3$, followed by alkaline hydrolysis with NaOH of the respective ester to yield 4-(benzoylphenoxy)butanoic acid (**1**). The resulting carboxylic acid functionality was then transformed into the *N*-hydroxysuccinimide (NHS) active ester **2** by reaction with trifluoroacetic anhydride (TFAA) and NHS, followed by amidation with 2-chloroethylamine. The obtained 4-(4-benzoylphenoxy)-*N*-(2-chloroethyl)butanamide (**3**) was then heated in the presence of anhydrous $K_2CO_3$, which induces a ring closure forming the final product BPOxa (**4**) with an overall yield of ≈65%.

#### *2.1.2. Main Monomers*

While the main monomer EtOxa (**6**) was commercially available, iPrOxa (**7**), and nPrOxa (**8**) were synthesized according to Witte and Seeliger.[49] In short, the corresponding alkyl nitriles (butyronitrile and isobutryonitrile) were reacted with 2-aminoethanol and $Cd(OAc)_2$ as catalyst to form the 2-alkyl-oxazoline ring in yields above 65%.

#### *2.1.3. Azide Monomer*

The azide monomer 2-(3-azidopropyl)-4,5-dihydro-1,3-oxazole (AzOxa, **13**, see **Figure 2**A) was prepared in analogy to the literature, in which the synthesis of the phenyl derivative was described.[50,51]

 © 2023 The Authors. Macromolecular Rapid Communications published by Wiley-VCH GmbH



15213927, 0, Downloaded from https://onlinelibrary.wiley.com/doi/10.1002/marc.202300549 by Cochrane Germany, Wiley Online Library on [28/11/2023]. See the Terms and Conditions (https://onlinelibrary.wiley.com/terms-and-conditions) on Wiley Online Library for rules of use; OA articles are governed by the applicable Creative Commons License

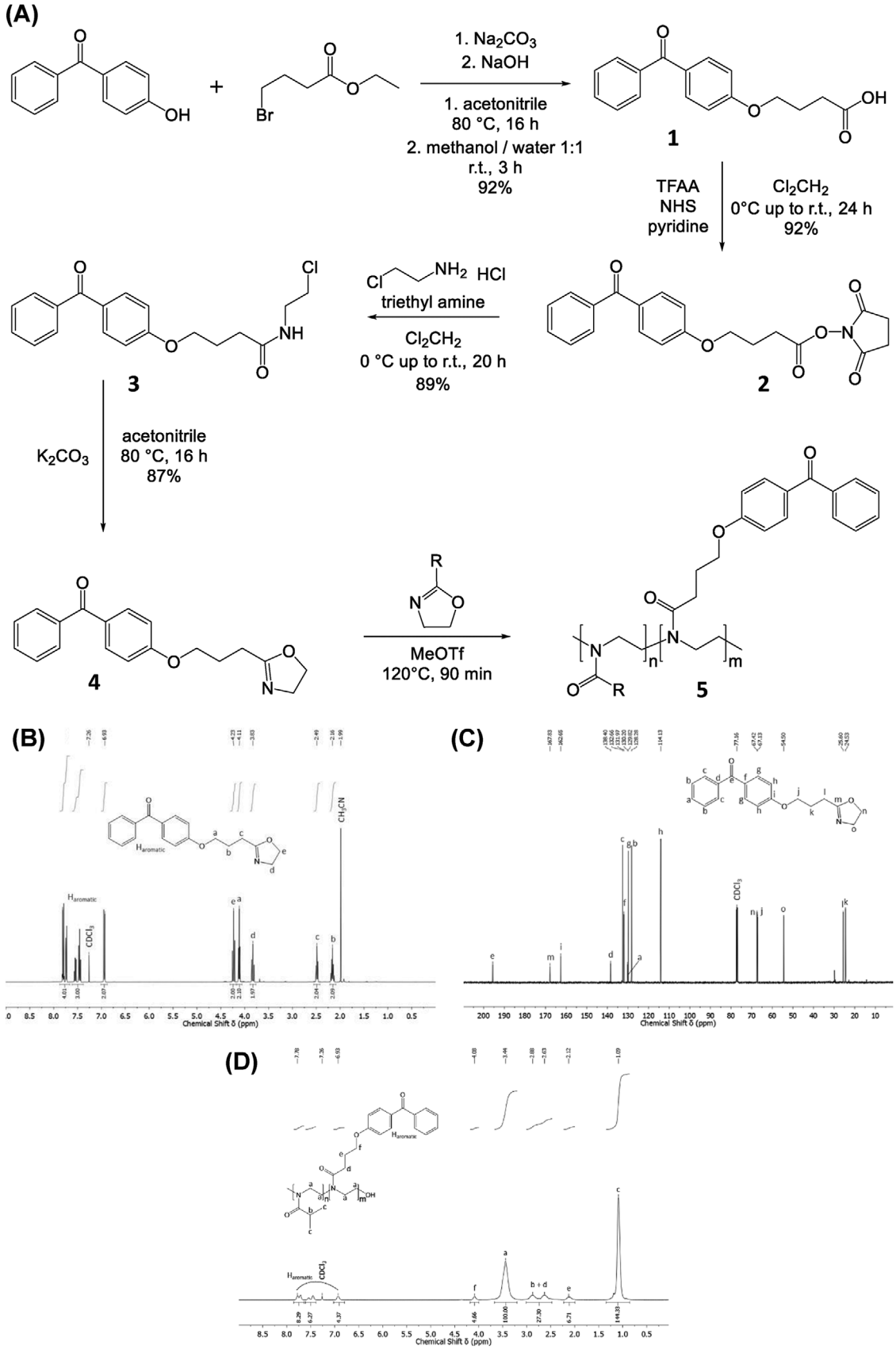



© 2023 The Authors. Macromolecular Rapid Communications published by Wiley-VCH GmbH


15213927, 0, Downloaded from https://onlinelibrary.wiley.com/doi/10.1002/marc.202300549 by Cochrane Germany, Wiley Online Library on [28/11/2023]. See the Terms and Conditions (https://onlinelibrary.wiley.com/terms-and-conditions) on Wiley Online Library for rules of use; OA articles are governed by the applicable Creative Commons License

**Figure 1.** A) Synthesis route for 2-[3-(4-benzoylphenoxy)propyl]-4,5-dihydro-1,3-oxazole (BPOxa, **4**) and its copolymerization (NHS = *N*-hydroxysuccinimide, TFAA = trifluoroacetic anhydride, MeOTf = methyl trifluoromethanesulfonate). B) $^{1}$H NMR spectrum of BPOxa (**4**) measured at r.t. in $CDCl_3$ (with a Larmor frequency of 400 MHz). C) $^{13}$C NMR spectrum of BPOxa (**4**), measured at r.t. with 100 MHz in $CDCl_3$. D) Representative $^{1}$H NMR spectrum of poly(iPrOxa$_{94}$-*co*-BPOxa$_6$), measured at r.t. with 400 MHz in $CDCl_3$.

In the first step, the bromine of ethyl-4-bromobuytrate was substituted by $NaN_3$ to yield ethyl-4-azidobutyrate (**9**), followed by alkaline hydrolysis of the ester leading to 4-azidobutanoic acid (**10**). The carboxylic acid was activated by conversion to the NHS ester **11** with 2,5-dioxopyrrolidin-1-yl 2,2,2-trifluoroacetate (*N*-trifluoroacetoxy succinimide, TFA-NHS) that was prepared according to reference.[52] Subsequently, 4-azido-*N*-(2-chloroethyl)butanamide (**12**) was obtained by amidation of **11** with 2-chloroethylamine hydrochloride. Cyclization of compound **12** in the presence of anhydrous $K_2CO_3$ led to the final product AzOxa (**13**) with an overall yield of 44% after the five synthesis steps.

### 2.1.4. Antifouling Motifs

The alkyne derivatives of the corresponding carboxy- and sulfobetaine were prepared by a ring opening reaction of propiolactone for CB (**14**), and propan-1,3-sulton for SB (**15**), respectively with dimethylamino-2-propyne, according to the literature.[53]

For synthesis of OEG (**16**, see **Scheme 1**), a threefold excess of triethylene glycol was deprotonated with sodium hydride and coupled to propargyl bromide. The monosubstituted product was separated from the reaction mixture by column chromatography on silica gel with an ethyl acetate/*n*-hexane mixture ($V/V$ = 3/1) as eluent. For the synthesis of the oligoethylene glycol-sulfobetaine conjugate, the terminal hydroxy functionality of OEG was transformed into the tosylate **17** as effective leaving group by reaction with 4-toluenesulfonyl chloride. Subsequent substitution with dimethylamine lead to derivative **18** with a dimethyl amino group, which was subjected to the ring opening reaction with propan-1,3-sulton, resulting in the final product OEG-SB (**19**). The overall yield of 41% for this four-step synthesis route is attributed to the mediocre yield of 55% in first reaction step. Attempts to synthesize the analogous OEG-

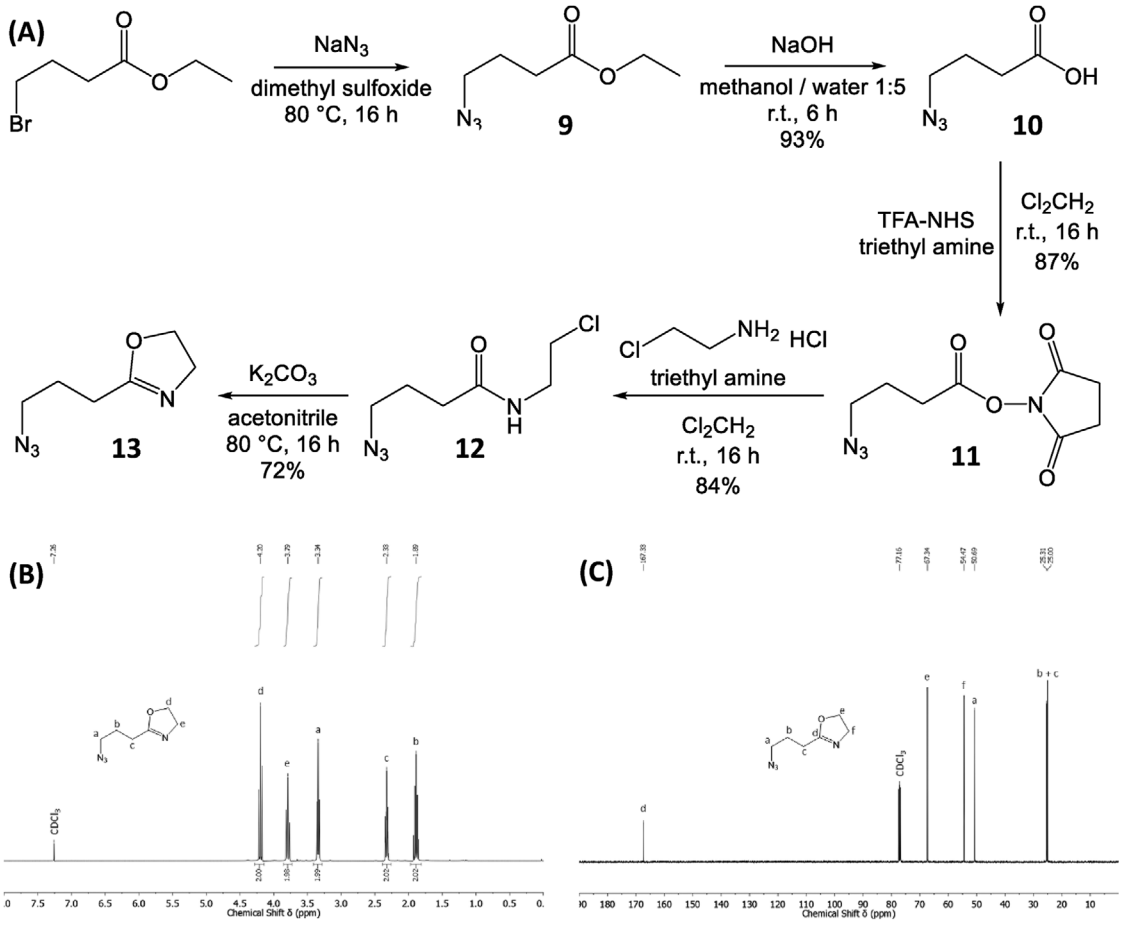


**Figure 2.** A) Synthesis of AzOxa (**13**) (TFA-NHS = 2,5-dioxopyrrolidin-1-yl 2,2,2-trifluoroacetate). B) $^{1}$H-NMR spectrum of AzOxa (**13**) and C) $^{13}$C-NMR spectrum of AzOxa (**13**), both measured at r.t. with 400 Hz in $CDCl_3$.

 © 2023 The Authors. Macromolecular Rapid Communications published by Wiley-VCH GmbH



15213927, 0, Downloaded from https://onlinelibrary.wiley.com/doi/10.1002/marc.202300549 by Cochrane Germany, Wiley Online Library on [28/11/2023]. See the Terms and Conditions (https://onlinelibrary.wiley.com/terms-and-conditions) on Wiley Online Library for rules of use; OA articles are governed by the applicable Creative Commons License

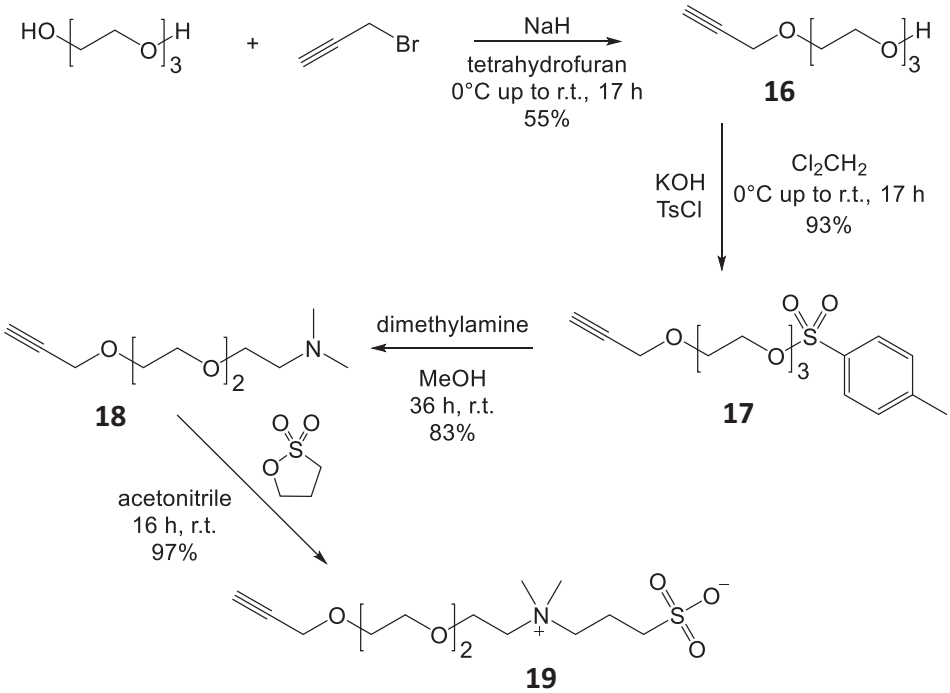


**Scheme 1.** Synthesis of OEG (**16**) and OEG-SB (**19**).

CB with carboxy betaine end group at the OEG chain were not successful in our hands, for details see Chapter S17 (Supporting Information).

### 2.1.5. Two-Component Copolymers

Copolymers containing one or more types of main monomers as first component and the photocrosslinker monomer **4** as second component are defined here as two-component copolymers. The copolymerization behavior of photocrosslinker **4** was investigated in various ratios with the 2-alkyl-2-oxazoline main monomers EtOxa (**6**), iPrOxa (**7**), nPrOxa (**8**), and combinations thereof. Details for the resulting poly(2-oxazoline) copolymers, such as composition, molar mass, dispersity *Đ*, and yield, are summarized in Table S1 (Supporting Information). The experimental data demonstrate good agreement between monomer feed and build-in ratio, and thus document the precise control over the polymer structures. The narrow molar mass distribution observed for almost all polymer systems indicate the quasi-living character of the performed polymerization reactions. Noteworthy, a general trend was observed for the series poly(EtOxa-*co*-BPOxa), with an increasing dispersity *Đ* from 1.17 for poly(EtOxa) up to 1.55 for poly($EtOxa_{90}$-*co*-$BPOxa_{10}$), which may be explained by the photocrosslinker monomer **4** apparently affecting the CROP mechanism by transfer or termination as potential side reactions. As expected, the glass points of the copolymers, as measured with modulated differential scanning calorimetry (M-DSC), vary systematically with the concentration of the BPOxa crosslinker units from 61.5 °C for pure poly(EtOxa) up to 66.5 °C for 100% poly(BPOxa), see Chapter S15 (Supporting Information).

### 2.1.6. Three-Component Copolymers

The three-component copolymers are defined by their composition, with the first component being the main monomer iPrOxa (**7**), the second component being the photocrosslinker monomer **4**, and the third component being the azide-modified 2-oxazoline monomer **13** (AzOxa). The selection of the main monomer iPrOxa was based on previous measurements of the cloud points for binary copolymer solutions in water (see Figure S11, Supporting Information). In such experiments, the cloud point temperatures between 35–45 °C observed for the iPrOxa-AzOxa combination are quite suitable for applications involving proteins and living tissue. In contrast, a rather high temperature range of 60–75 °C was found for the combination of the monomers EtOxa and AzOxa, which is inconvenient in a biological context. Furthermore, previously performed temperature-dependent swelling experiments of photocrosslinked hydrogel films in water showed a well-defined, sharp volume transition at 32 °C for poly(iPrOxa-*co*-BPOxa). Such thermoresponsive behavior under physiological conditions can be exploited for actuation in active plasmonics and advanced biosensor devices.[23–26]

Two photocrosslinkable iPrOxa-based poly(2-oxazoline)s with 6 and 10 mol% AzOxa (**13**), respectively, and 3 mol% benzophenone monomer **4** were synthesized using microwave-assisted CROP. Detailed information about the analysis of the three-component polymers is provided in the (Chapters S8,S9, Supporting Information) together with the data for the click-modified polymers discussed further below. Comparison of the iPrOxa homopolymer with the two-component polymers and the three-component polymers shows that both comonomers, the photocrosslinker **4** and the azide monomer **13**, lead to broadening of the molar mass distribution.

 © 2023 The Authors. Macromolecular Rapid Communications published by Wiley-VCH GmbH



15213927, 0, Downloaded from https://onlinelibrary.wiley.com/doi/10.1002/marc.202300549 by Cochrane Germany, Wiley Online Library on [28/11/2023]. See the Terms and Conditions (https://onlinelibrary.wiley.com/terms-and-conditions) on Wiley Online Library for rules of use; OA articles are governed by the applicable Creative Commons License

15213927, 0, Downloaded from https://onlinelibrary.wiley.com/doi/10.1002/marc.202300549 by Cochrane Germany, Wiley Online Library on [28/11/2023]. See the Terms and Conditions (https://onlinelibrary.wiley.com/terms-and-conditions) on Wiley Online Library for rules of use; OA articles are governed by the applicable Creative Commons License

#### 2.1.7. Click-Modifications

The azide-containing three-component copolymers were modified with the alkyne-functionalized antifouling motifs **14**, **15**, **16**, and **19** via copper(I)-catalyzed azide-alkyne cycloaddition (CuAAC), see **Figure 3**A. Furthermore, the commercially available 4-pentynoic acid (COOH, **20**) was also conjugated to the azide-based polymer by this coupling reaction to introduce free carboxylic acid functions into the polyoxazoline backbone, which also allows further functionalization, for example, with bioligands like antibodies. The progress of the CuAAC reaction was monitored by IR spectroscopy, following the azide absorption band located at ≈2100 $cm^{-1}$, which indicated complete conversion of the azide functionality. The CuAAC-modified polymers were dialyzed against water to remove copper sulfate, sodium ascorbate, and any excess of the respective alkynes.

The data from the SEC measurements indicated striking differences between the azide-containing parent polymer and the click-modified systems with pending antifouing motifs, even though the degree of polymerization does not change during the CuAAC click modification (apparent molar mass and dispersity data are presented in Figure 3D,E, the original GPC data are provided in Chapter S18, Supporting Information). For the parent system poly(iPrOxa$_{91}$-*co*-BPOxa$_3$-*co*-AzOxa$_6$) with 6 mol% azide functions, an average molar mass of 27.7 × $10^3$ g $mol^{-1}$ was determined, which corresponds very well to the expected values of 30–35 × $10^3$ g $mol^{-1}$ for the monomer-initiator ratio of ≈300/1 used in the CROP synthesis of this polymer. Notably, the polymers with the antifouling motifs in the side chains showed a trend to higher apparent molar masses and a considerable increase of their dispersities. Based on the masses of the alkyne fragments, the order of the polymer mass increase is expected to follow the side chain modification with $N_3$ < COOH < CB < OEG < SB < **OEG-SB**, resulting in an approximate maximum mass increase of 10% for **OEG-SB**. In contrast, the apparent molar mass as measured by SEC follows the unexpected order of the polymer functionality $N_3$ < COOH < OEG < **OEG-SB** < SB < CB with almost 30% apparent mass increase for CB. This might be explained as follows. In SEC analysis, the relative molar mass is deduced from the hydrodynamic radius of the polymer coil in relation to a calibration standard. Thus, the apparent increase of the molar mass in the CuAAC-modified polymers is based on the increase of their hydrodynamic radius. Such coil expansion is caused by the addition of the antifouling side chains with zwitterionic character, which results in polar and solvation effects that influence coil swelling and consequently result in ill-defined molar mass values.

Surprisingly, for the 10 mol% azide-functionalized base polymer poly(iPrOxa$_{87}$-*co*-BPOxa$_3$-*co*-AzOxa$_{10}$), the trend of the apparent molar mass variation is in stark contrast to the 6 mol% polymers above, showing the opposite behavior. Here, a significant decrease of the apparent molar mass was observed, diminishing from 28.3 × $10^3$ g $mol^{-1}$ for the parent polymer poly(iPrOxa$_{87}$-BPOxa$_3$-AzOxa$_{10}$), following the order $N_3$ > OEG > OEG-SB > SB > CB, to 9.5 × $10^3$ g $mol^{-1}$ for poly(iPrOxa$_{87}$-*co*-BPOxa$_3$-*co*-CB$_{10}$). This reversed trend may be caused by the increased number of charges on the backbone, which potentially leads to an aggregation of single polymer chains (coil to globule transition) and therefore a decrease in hydrodynamic radius and apparent average molar mass in SEC. This hypothesis is further corroborated by the opposing thermal response of poly(2-alkyl-2-oxazoline)s and polybetaines, reported in the literature.[54–56] Poly(2-alkyl-2-oxazoline)s can show a LCST behavior in aqueous media, for which an increase in the overall polarity leads to an improved water solubility and consequently an increase in the cloud point temperature. Yet, several polybetaine systems are known to possess an upper critical solution temperature (UCST) in water, which is based on the attractive interaction between the zwitterionic groups and exactly opposite to the LCST behavior of the poly(2-alkyl-2-oxazoline)s. In the case of the present polymer samples based on poly(iPrOxa$_{91}$-*co*-BPOxa$_3$-*co*-AzOxa$_6$) with a lower degree of modification of 6 mol%, the coupling of the antifouling motifs indeed increases the solubilization with water, leading to coil expansion, as observed by the apparent molar mass values from SEC, and an increased cloud point (see **Figure 4**). For the higher degree of modification with 10 mol% antifouling motifs, such competing UCST character by attractive zwitterion interaction in the side chains may become dominant over the polarity of the polyoxazoline backbone, which leads to a compaction of the polymer chains with the reduced hydrodynamic radius and consequently a lower apparent mass value in dimethylacetamide used as solvent in SEC. Yet, the overall hydrophilicity of the polymer seems to be further increased as reflected in a still higher cloud point compared to the 6 mol% samples (see Figure 4).

#### 2.1.8. Anchor Molecule

For attaching the polymers to a gold substrate by photoactivation, the gold anchor molecule with benzophenone groups BPdiS (**22**) was synthesized as previously reported.[25] Briefly, 3,3′-dithiodipropionic acid was converted into an active ester with NHS and TFAA in the first step. In the second step, a nucleophilic substitution of the active ester with (4-(aminomethyl)phenyl)(phenyl)methanone yielded the target molecule BPdiS (**22**) in an overall yield of ≈41%.

### 2.2. Thermal Properties of Aqueous Poly(2-oxazoline) Solutions

As the synthesized polymers are targeted for advanced biosensor applications, their behavior in aqueous environments needs to be understood. In this respect, we have studied the temperature-dependent solution behavior of two- and three-component copolymers in water by turbidimetry with a UV/VIS spectrometer and compared it to that of the respective poly(2-alkyl-2-oxazoline) homopolymers. All measurements were performed using 0.3 wt.% aqueous polymer solutions with a heating and cooling rate of 1 K $min^{-1}$, while recording the transmittance at a wavelength of 550 nm. The cloud point was defined as the temperature, at which a transmittance of 50% was reached.

**Figure 5**C shows the dramatic decrease of the cloud points from about 70 °C to 20 °C with increasing BPOxa content of up to 6 mol% for poly(EtOxa-*co*-BPOxa), and for poly(iPrOxa-*co*-BPOxa) a cloud point reduction from ≈40 °C to ≈20 °C. The drop of the cloud points with increasing BPOxa content can be attributed to the less hydrated benzophenone groups compared

 © 2023 The Authors. Macromolecular Rapid Communications published by Wiley-VCH GmbH

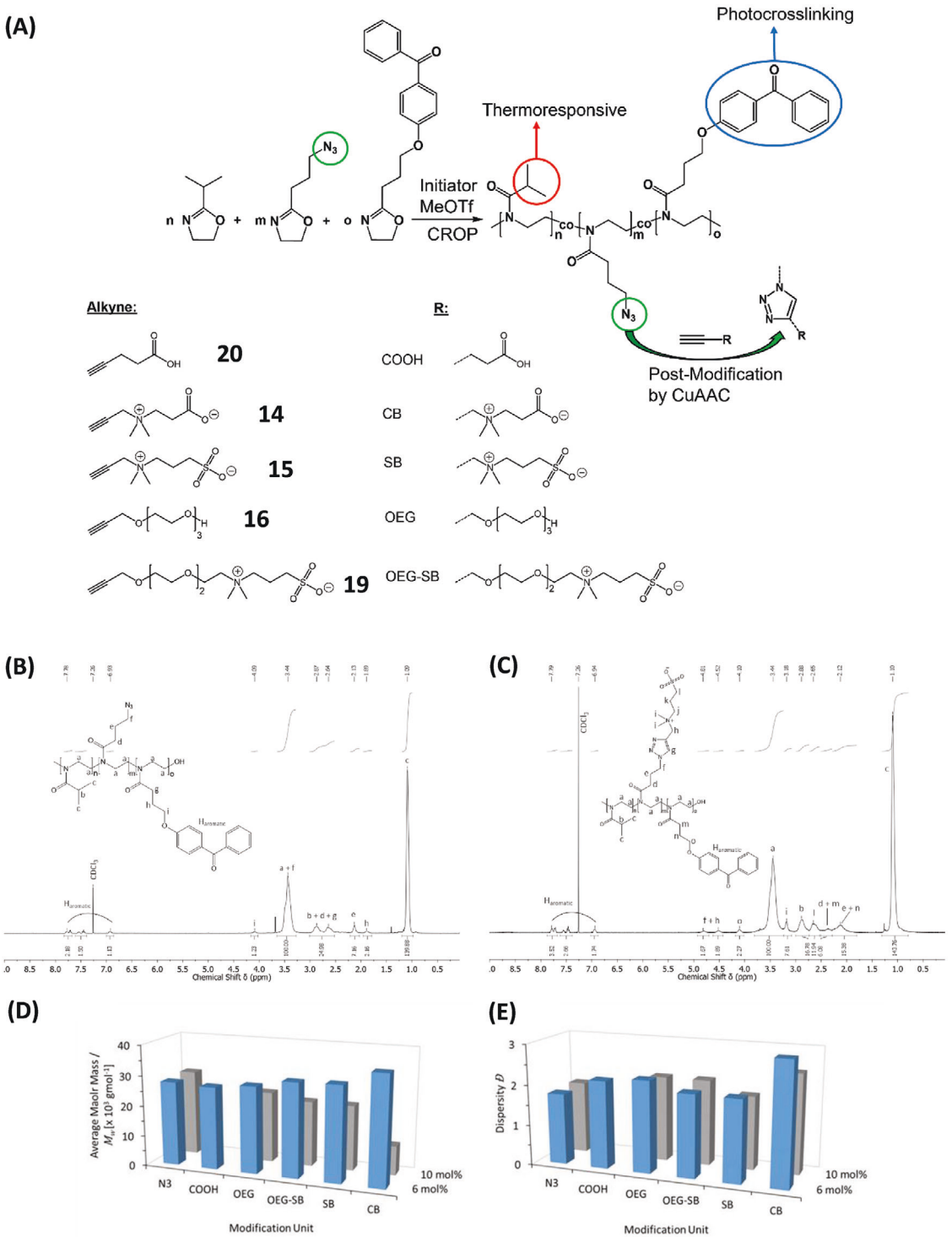


**Figure 3.** A) Synthesis and CuAAC click modification of the three-component copolymers containing iPrOxa (**7**) as main monomer, AzOxa (**13**) as modification side, and BPOxa (**4**) for photocrosslinking. B) $^1$H-NMR spectrum of poly(iPrOxa$_{87}$-BPOxa$_3$-AzOxa$_{10}$) in $CDCl_3$ before CuAAC click coupling. C) $^1$H-NMR spectrum of poly(iPrOxa$_{87}$-BPOxa$_3$-SB$_{10}$) in $CDCl_3$ after modification of AzOxa with SB. D) Apparent molar mass average and E) dispersity in dependence of the modification unit after CuAAC click coupling for the different antifouling motifs.

 © 2023 The Authors. Macromolecular Rapid Communications published by Wiley-VCH GmbH



15213927, 0, Downloaded from https://onlinelibrary.wiley.com/doi/10.1002/marc.202300549 by Cochrane Germany, Wiley Online Library on [28/11/2023]. See the Terms and Conditions (https://onlinelibrary.wiley.com/terms-and-conditions) on Wiley Online Library for rules of use; OA articles are governed by the applicable Creative Commons License

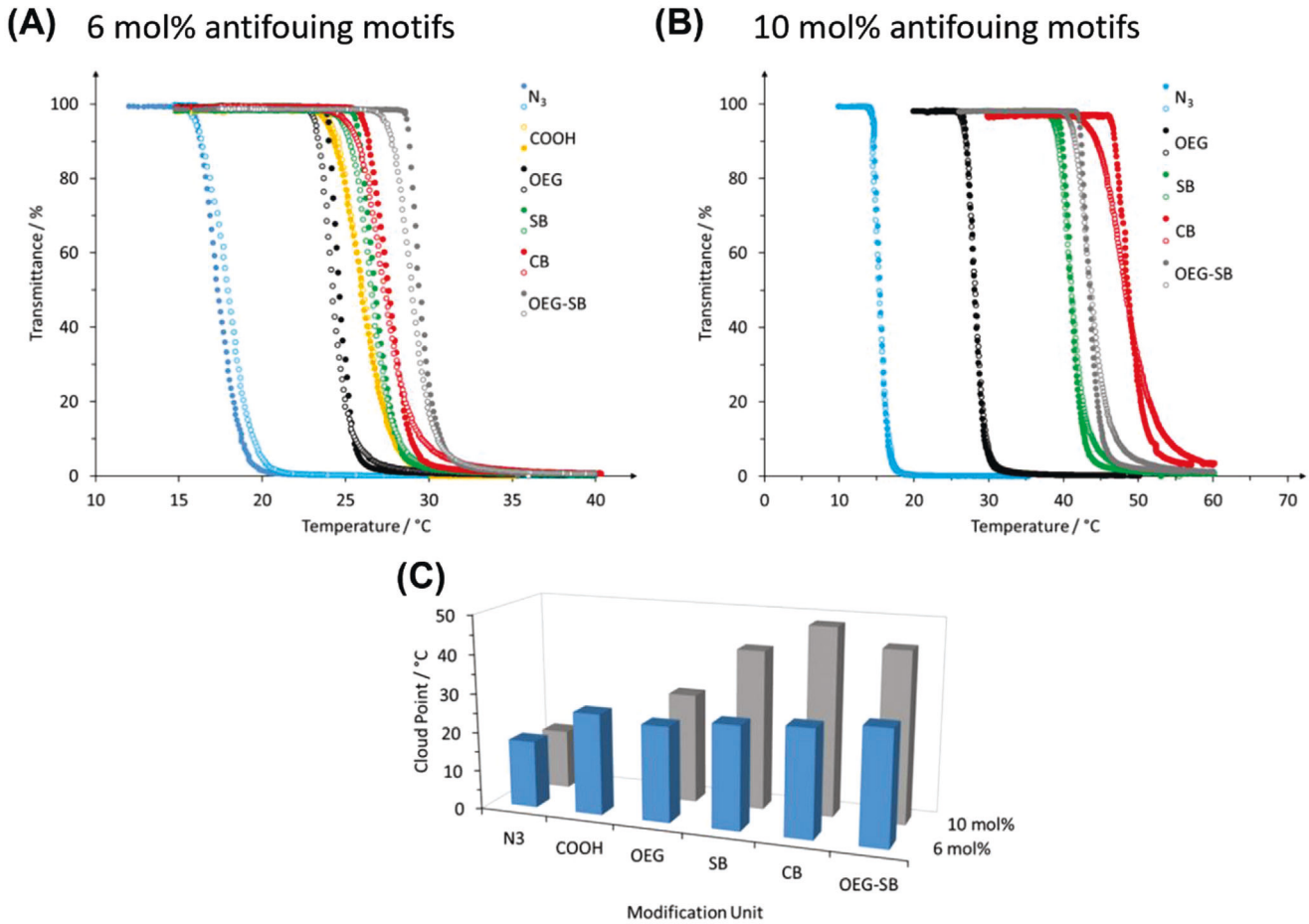


**Figure 4.** Cloud point dependence on type of functional group for 0.3 wt.% aqueous solutions of the poly(iPrOxa-*co*-BPOxa-*co*-AzOxa) systems, as determined by UV/VIS turbidity measurements at a wavelength of 650 nm and a heating rate of 1 K $min^{-1}$. A) Transmittance curves of non-modified and modified poly(iPrOxa$_{91}$-*co*-BPOxa$_3$-*co*-AzOxa$_6$) and B) poly(iPrOxa$_{87}$-*co*-BPOxa$_3$-*co*-AzOxa$_{10}$). C) Cloud point comparison between non-modified and modified poly(iPrOxa$_{91}$-*co*-BPOxa$_3$-*co*-AzOxa$_6$) and poly(iPrOxa$_{87}$-*co*-BPOxa$_3$-*co*-AzOxa$_{10}$).

to the more polar 2-ethyl and 2-isopropyl amide side chains. The transmittance curves in Figure 5A,B are characterized by sharp transitions for both, the heating and cooling cycles, demonstrating reversible LCST-type switching from a hydrophilic state below the cloud point temperature to a more hydrophobic state beyond this point. A hysteresis as narrow as 0.5 K was observed for the majority of the investigated polymers. Due to the insolubility of the copolymer poly(nPrOxa$_{94}$-*co*-BPOxa$_6$) in water, a comparison of the cloud point with the corresponding homopolymer poly(nPrOxa) could not be performed. Since the temperature range of the cloud points for poly(iPrOxa-*co*-BPOxa) between ≈20 °C and ≈40 °C is most appropriate for the anticipated biosensor applications, the cloud point measurements for the three-component polymers discussed below were only performed with the iPrOxa system.

After modification of the parent polymers poly(iPrOxa-*co*-BPOxa-*co*-AzOxa) containing 6% or 10% azide groups (abbreviated as N3 in Figure 4) by CuAAC click coupling with the alkyne motifs COOH (**20**), CB (**14**), OEG (**15**), SB (**16**), and OEG-SB (**19**), their cloud points in aqueous solutions were determined by turbidity measurements, as above. The experiments were performed with 0.3 wt.% aqueous polymer solutions and a heating rate of 1 K $min^{-1}$, recording the transmittance at a wavelength of 650 nm. Again, heating and cooling cycles were performed for each polymer solution and the cloud point was defined as the temperature, at which the transmittance dropped to 50%. A significant increase of the cloud point temperature was observed for all polymers after modification with the antifouling motif, as depicted in Figure 4. For the polymers with 6 mol% coupling sites, all types of modification showed a clear increase of the cloud point by ≈5–10 K starting from 18 °C for the 6 mol% azide-containing polymer. For the polymers with 10 mol% coupling sites, the cloud point increase was even more pronounced, specifically for the zwitterionic systems SB, CB, and OEG-SB, reaching almost 50 °C compared to 15 °C for the 10 mol% azide-containing polymer. All polymers could be reversibly switched from a hydrophilic to a hydrophobic state with a minor hysteresis between the heating and cooling cycle of ≈0.5 to 1 K. The plausible explanation for the observed cloud point increase in all alkyne-modified samples is a much stronger

 © 2023 The Authors. Macromolecular Rapid Communications published by Wiley-VCH GmbH



15213927, 0, Downloaded from https://onlinelibrary.wiley.com/doi/10.1002/marc.202300549 by Cochrane Germany, Wiley Online Library on [28/11/2023]. See the Terms and Conditions (https://onlinelibrary.wiley.com/terms-and-conditions) on Wiley Online Library for rules of use; OA articles are governed by the applicable Creative Commons License

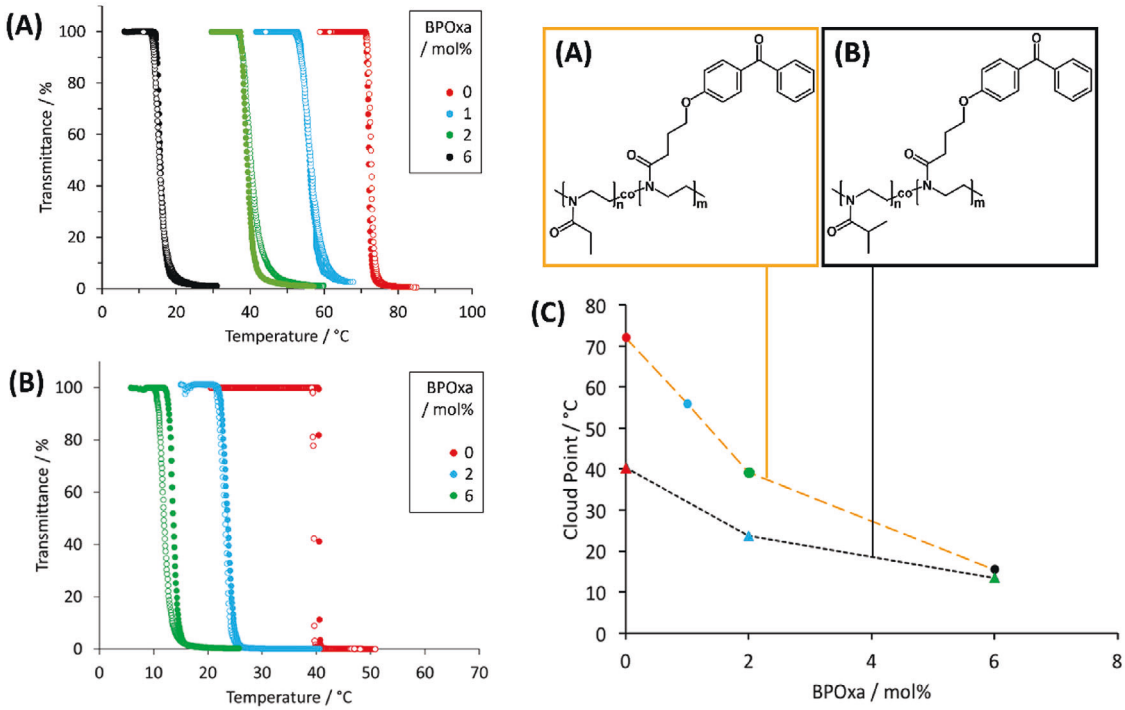


**Figure 5.** Transmittance curves at 550 nm for aqueous solutions of A) poly(EtOxa-*co*-BPOxa) and B) poly(iPrOxa-*co*-BPOxa) with polymer concentrations of 3 mg ml$^{-1}$, recorded with a heating and cooling rate of 1 K min$^{-1}$ (filled circles indicate heating and open circles cooling). C) Cloud point dependence on benzophenone content for poly(EtOxa-*co*-BPOxa) and poly(iPrOxa-*co*-BPOxa). Color codes in (C) correspond to BPOxa content in polymer samples of (A) and (B), respectively. Cloud point error: ±1 K.

hydration of the highly polar side chains, which results in a higher enthalpy of mixing $\Delta H_M$ compared to the non-modified parent polymer poly(iPrOxa-*co*-BPOxa-*co*-AzOxa).

### 2.3. Photocrosslinking and Thermal Properties of Poly(2-oxazoline) Networks

To investigate the temperature-dependent swelling of surface attached hydrogel films by SPR/OWS, the benzophenone-containing poly(2-alkyl-2-oxazoline) systems, comprising two- and three-component polymers, were photocrosslinked by irradiation with UV light. For the covalent attachment of such hydrogel layers during photocrosslinking, the SPR/OWS substrates were modified as follows. First, Au substrates were immersed into 1 mM solutions of BPdiS (**22**) in dimethyl sulfoxide and then rinsed with dimethyl sulfoxide and ethanol, followed by drying under a stream of nitrogen. Onto these BPdiS-coated substrate, the benzophenone-containing polymers were spin coated at 2000 rpm from a 6–10 wt.% ethanolic solution, resulting in layer thicknesses of 350–850 nm after drying. The dry polymer layers were irradiated with UV light of 365 nm an irradiation dose of 8 J cm$^{-2}$ (for two-component copolymers) and 12 J cm$^{-2}$ (for three-component copolymers) under exclusion of oxygen, to induce simultaneous crosslinking and covalent attachment to the substrate. The crosslinked samples were inserted into an electrically heatable SPR sample holder, in which the polymer network layers were swollen and rinsed with water for 60 min to ensure removal of residual soluble components in the hydrogel film. Initial reflectivity curve was recorded at room temperature and then, after each increasing temperature step, the layers were equilibrated for 15 min. The swelling properties were analyzed at each temperature step by SPR/OWS upon resonant excitation with attenuated total reflection in Kretschmann configuration. Under SPR/OWS conditions, surface plasmons and dielectric waveguide-guided waves are phase-matched with the excitation light beam to probe the polymer network films. This optical coupling is manifested as a series of narrow dips at distinct angles in the angular reflectivity spectra $R(\theta)$, see Figure S13 (Supporting Information). The refractive indices $n$ and thicknesses $d$ of the polymer films were determined from the angular reflectivity spectra $R(\theta)$ either in the dry ($n_{dry}$, $d_{dry}$) or swollen ($n_{swollen}$, $d_{swollen}$) state. As these measurements were performed in situ, the changes in thickness and refractive index could be tracked in real time upon variations of temperature or solvent. The swelling ratio $SR$ and surface mass density $\Gamma$ were calculated from the refractive indices and layer thicknesses according to Equations (2) and (3), see experimental part for more details.

**Figure 6** depicts the temperature-dependent swelling ratios, which are the inverse of the polymeric volume fractions $\Phi$, for the water-swollen hydrogels composed of different poly(2-alkyl-2-oxazoline) networks. The swelling ratios of these hydrogel layers at 20 °C follow the order of their cloud points in aqueous solution ($T_{CP}$), indicated above the chemical structures of each copolymer. Yet, the estimated center temperatures of the volume transitions for the polymer networks, at which the gel is half collapsed, lie significantly higher than the $T_{CP}$ of the respective polymer solutions. Here, the center temperature is defined in analogy to

 © 2023 The Authors. Macromolecular Rapid Communications published by Wiley-VCH GmbH



15213927, 0, Downloaded from https://onlinelibrary.wiley.com/doi/10.1002/marc.202300549 by Cochrane Germany, Wiley Online Library on [28/11/2023]. See the Terms and Conditions (https://onlinelibrary.wiley.com/terms-and-conditions) on Wiley Online Library for rules of use; OA articles are governed by the applicable Creative Commons License

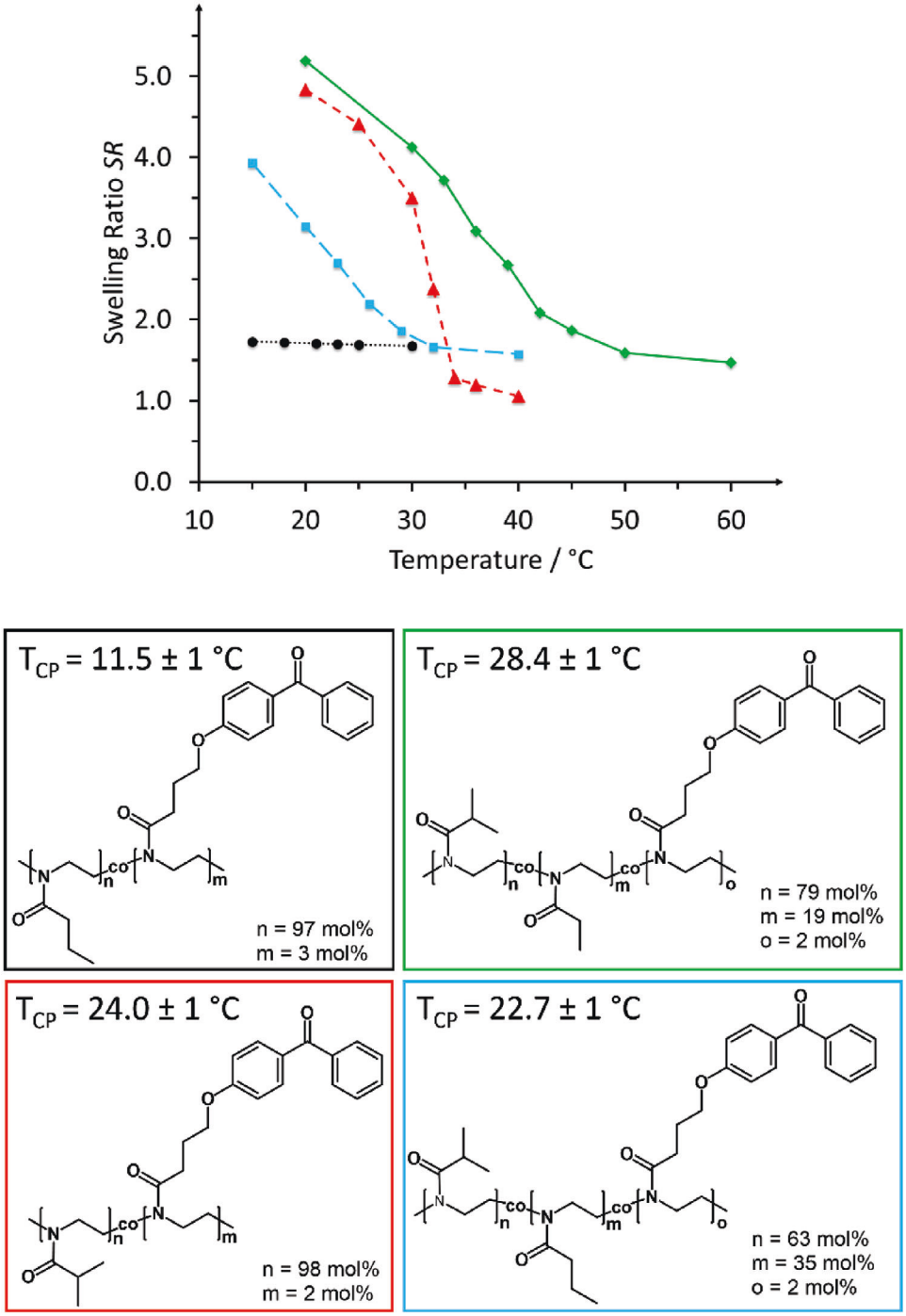


**Figure 6.** SPR/OWS measurements of the temperature-dependent swelling ratio in water for surface-attached hydrogel layers based on four different benzophenone-containing poly(2-alkyl-2-oxazoline)s.

the cloud point temperature, at which a transmittance of 50% is reached, and is estimated on the basis of the experimentally accessible temperature range. The shift of the transition temperature can be explained with the change in the polymer volume fraction from $\Phi \approx 0.03$ for the polymer solutions to $\Phi > 0.6$ in the hydrogels.

This trend follows the theoretical prediction of the phase transition curves, for which the branch on the right side of the LCST minimum increases with increasing polymer volume fractions and skews toward smaller volume fractions with increasing chain lengths.[57] This behavior is further illustrated for a range of varying volume fractions in the polymer solutions


© 2023 The Authors. Macromolecular Rapid Communications published by Wiley-VCH GmbH


15213927, 0, Downloaded from https://onlinelibrary.wiley.com/doi/10.1002/marc.202300549 by Cochrane Germany, Wiley Online Library on [28/11/2023]. See the Terms and Conditions (https://onlinelibrary.wiley.com/terms-and-conditions) on Wiley Online Library for rules of use; OA articles are governed by the applicable Creative Commons License

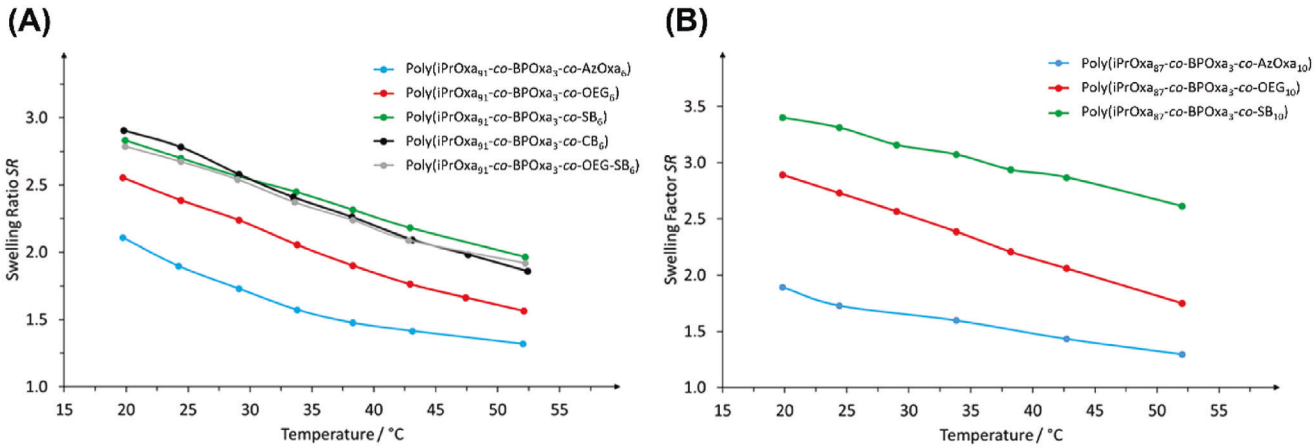


**Figure 7.** Temperature-dependent swelling of hydrogel films made from CuAAC-modified poly(2-alkyl-2-oxazoline)s with A) 6 mol% and B) 10 mol% antifouling motifs in comparison to the non-modified AzOxa systems (blue), as determined by OWS.

in Figure S10 (Supporting Information). For all investigated polymer systems, a substantial sigmoidal drop in the swelling ratio was observed with increasing temperature, except for poly(nPrOxa$_{97}$-*co*-BPOxa$_3$), in which the volume transition lies below the limiting minimum temperature of 15 °C accessible by the SPR equipment. These experiments confirm that the surface-attached poly(2-alkyl-2-oxazoline) hydrogel layers can be reversibly switched between a swollen and collapsed state by temperature variation around the volume phase transition (see Figure S14, Supporting Information). Simultaneously, the Young's modulus switches between a soft swollen network at low temperatures and a more rigid collapsed film above the volume phase transition, as observed by atomic force microscopy indentation measurements (see Figure S22, Supporting Information, red circles). An additional variation of the Young's modulus can be achieved via a different crosslinking density effected by modulation of the irradiation dose (see Figure S22, Supporting Information, green circles). A sharp volume transition was observed in the interval of ≈5 K for the two-component system poly(iPrOxa$_{98}$-*co*-BPOxa$_2$), which contains a single main monomer (iPrOxa) that is responsible for the LCST behavior. In contrast, the phase transition region is significantly widened to several x10 K for the two-component systems poly(iPrOxa$_{63}$-*co*-nPrOxa$_{35}$-*co*-BPOxa$_2$) and poly(iPrOxa$_{79}$-*co*-EtOxa$_{19}$-*co*-BPOxa$_2$) with a mixture of two LCST-inducing main comonomers (iPrOxa and nPrOxa, iPrOxa and EtOxa). Noteworthy, further broadening of the phase transition region was found for the surface-attached hydrogel layers with the three-component systems including the azide or antifouling motifs, as shown in **Figure 7**A.

Due to the high polarity of the zwitterionic side chains, the three-component polymer systems were irradiated with UV light dose of 12 J cm$^{-2}$ (compared to 8 J cm$^{-2}$ for the two-component samples), to ensure stable layer formation and prevent hydrogel layer delamination. The results depicted in Figure 7 show a significant increase of the swelling ratio upon introduction of the antifouling motifs by CuAAC modification, with the highest swelling ratios observed for the zwitterionic systems. Following the order of their cloud points in aqueous solution (Figure 4), which can be seen as an indicator for the polarity of the polymers, the swelling ratios of the OEG-modified polymers lie between the least polar parent azide polymers and the modified systems bearing highly polar zwitterionic groups. The increase of the swelling ratio is more pronounced for the polymers with a higher content of the respective modification motif (10 mol% vs 6 mol%), again following the trend of the cloud points in water shown above. All systems are characterized by a gradual decrease of the swelling ratio with increasing temperature over the range of 20–52 °C. The residual water content of the collapsed systems at the maximum temperature was found to be highest for the zwitterionic polymer systems. As above for the two-component copolymer systems, repeated heating and cooling cycles of the three-component samples demonstrated full reversibility of the swelling behavior.

### 2.4. Antifouling Properties of Modified Poly(2-oxazoline) Networks

HBP represents an important biological fluid, which is used in numerous bioanalytical techniques (e.g. detection of specific biomarkers of diseases) or therapy (for example, apheresis and dialysis). PBS is a frequently used medium in blood-related research, as it exhibits pH of 7.4 and contains key ions at concentration close to physiological conditions. To investigate the suitability of the three-component hydrogels as antifouling coatings in contact with HBP, polymer network layers were prepared on BPdis-modified gold surfaces by photocrosslinking, analogous to the SPR/OWS swelling experiments above. The three-component hydrogels were based on poly(iPrOxa$_{87}$-*co*-BPOxa$_3$-*co*-AzOxa$_{10}$), which was modified with 10 mol% of the antifouling motifs CB (14), SB (15), OEG (16), and OEG-SB (19), respectively. The swelling properties of these hydrogel films were first examined in PBS and afterward their changes occurring in contact with pooled HBP were assessed at room temperature (25 °C).

The reference hydrogel film from poly(iPrOxa$_{87}$-*co*-BPOxa$_3$-*co*-AzOxa$_{10}$) with unreacted azide groups ($N_3$), crosslinked with 5 J cm$^{-2}$, exhibited the lowest swelling ratio of $SR_{PBS} \approx 1.6$ in PBS (shown in **Figure 8**) compared to $SR_{H2O} \approx 1.7$ in water. The reduced swelling in PBS buffer compared to pure water for the uncharged polymer hints to a reduction of the solvent quality owing to the presence of ions. Introduction of OEG


© 2023 The Authors. Macromolecular Rapid Communications published by Wiley-VCH GmbH


15213927, 0, Downloaded from https://onlinelibrary.wiley.com/doi/10.1002/marc.202300549 by Cochrane Germany, Wiley Online Library on [28/11/2023]. See the Terms and Conditions (https://onlinelibrary.wiley.com/terms-and-conditions) on Wiley Online Library for rules of use; OA articles are governed by the applicable Creative Commons License

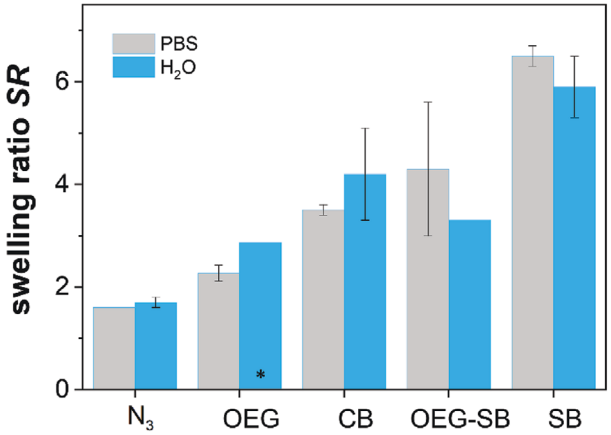


**Figure 8.** Swelling ratios (*SR*s) of poly(2-alkyl-2-oxazoline) hydrogel films with 10 mol% antifouling motifs, crosslinked with 5 J cm$^{-2}$ (* 12 J cm$^{-2}$) at the wavelength of 365 nm, and swollen in PBS (10 mM, pH 7.4) in grey and in water, blue. Error bars were derived from standard deviation of triplicates.

groups into the three-component copolymer led to a minor increase of the swelling ratio to $SR_{PBS} \approx 2.3$ in PBS, which is attributed to an enhanced hydrophilicity of the polymer system through the OEG side chains. Yet, in water the swelling ratio for this system is higher despite the increased degree of crosslinking ($SR_{H2O} \approx 2.8$ at 25 °C, 12 J cm$^{-2}$), again indicating a decrease in solvent quality for PBS. Even higher swelling ratios were observed for the hydrogel films comprising the zwitterionic CB groups with $SR_{PBS} \approx 3.5$ ($SR_{H2O} \approx 4.2$) and OEG-SB moieties with $SR_{PBS} \approx 4.3$ ($SR_{H2O} \approx 3.3$), respectively, while the most prominent effect was present in the SB system with the highest swelling ratio of $SR_{PBS} \approx 6.5$ ($SR_{H2O} \approx 5.9$). The substantial increase in swelling of the SB system can be explained by the inreased degree of ionization resulting from the lower p$K_a$ value of the corresponding sulfonic acid group (p$K_a$ typically below 1) compared to the carboxylic acid (p$K_a$ typically ≈5) related to the CB moiety.[58,59] This more pronounced ionization in the SB system promotes stronger solvation and consequently enhanced swelling.[60,61] Interestingly, the combination of the hydrophilic OEG chain with the highly polar SB motif for OEG-SB does not substantially increase the swelling ratio compared to the single CB functionalization, but rather leads to an intermediate swelling ratio in PBS. As OEG side chains are known to introduce a LCST behavior, a competing influence between OEG and SB (inherent UCST characteristics) might be responsible here. A further notable effect is the inversion of the swelling trend in pure water, for which the values of N3, OEG, and CB lie above the values in PBS, while for OEG-SB and SB the PBS values are higher. Apparently, the strong charge screening of the SB moieties in PBS prevents their electrostatic aggregation, which is accompanied by a stronger swelling. As investigated above for pure water (Figure 7), the hydrogel layers can be reversibly collapsed also in PBS buffer, shown in Figure S24 (Supporting Information).

After this initial assessment of the hydrogels in contact with PBS buffer, the effect of HBP on the swelling ratio *SR* and surface mass density Γ was investigated to evaluate their applicability as antifouling coatings. For this purpose, the films were

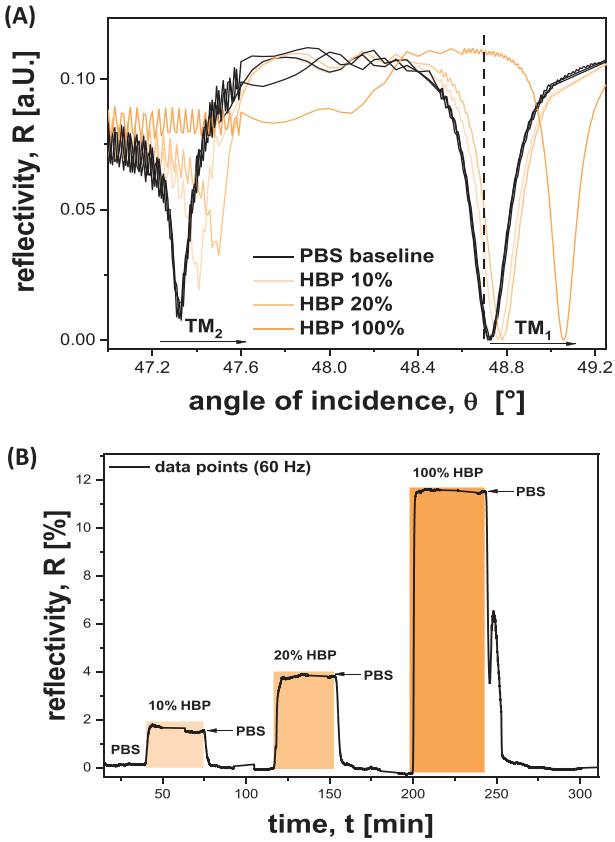


**Figure 9.** Examples of OWS measurements indicating the changes in reflectivity for poly(2-alky-2-oxazoline)-based hydrogel with SB moieties. A) Normalized reflectivity spectra R($\theta$) measured upon incubation with HBP diluted to 10 and 20% and with undiluted HBP. B) Respective kinetics of reflectivity changes measured over time at fixed angle $\theta = 48.7°$ (after baseline correction due to a drift in the signal). Colored sections indicate the contact time intervals with different dilutions of HBP.

first swollen in PBS to reach an equilibrium and to establish a baseline for the reflectivity value $R(\theta)$ at a fixed angle of 48.7°. This angle was positioned at the sharp slope of the resonance dip associated with the excitation of the $TM_1$ mode (see example in **Figure 9**A) to assess the effect of HBP in the kinetics mode of the SPR/OWS set-up. In this kinetics mode, the variation in reflectivity $R(\theta = 48.7°)$ was monitored upon changing the medium from PBS to whole HBP and HBP diluted to 10 and 20% with PBS with an incubation time of 15 min. The kinetics for the poly(2-alky-2-oxazoline)-SB polymer network in Figure 9B reveal an increase in the reflectivity upon incubation with HBP medium, and a drop reversing back to the original baseline upon subsequent rinsing with PBS. These observations indicate a complete release of all HPB components from the poly(2-alky-2-oxazoline)-based polymer networks after washing with PBS, with no irreversible attachment of HBP compounds being visible. All investigated poly(2-alky-2-oxazoline)-based hydrogel films showed the same qualitative behavior, suggesting that all systems perform as efficient protein-repellent antifouling coatings.

In order to determine changes occurring directly in contact with HBP, respective reflectivity scans $R(\theta)$ were measured and

 © 2023 The Authors. Macromolecular Rapid Communications published by Wiley-VCH GmbH



15213927, 0, Downloaded from https://onlinelibrary.wiley.com/doi/10.1002/marc.202300549 by Cochrane Germany, Wiley Online Library on [28/11/2023]. See the Terms and Conditions (https://onlinelibrary.wiley.com/terms-and-conditions) on Wiley Online Library for rules of use; OA articles are governed by the applicable Creative Commons License

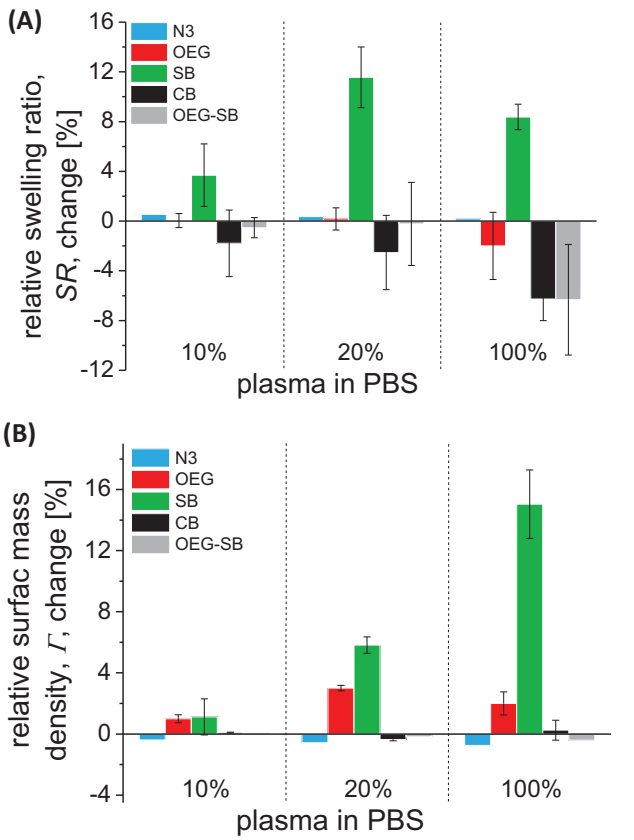


**Figure 10.** A) Relative swelling ratio change at different concentrations of HBP for hydrogel films with different side-chain motifs. Error bars indicate standard deviation from triplicates. Data fitted with asymptotic fit. Relative values calculated in respect to data for pure PBS (0% HBP). B) Relative surface mass density change at different concentrations of HBP for the same polymers as in (A).

by simultaneous probing with $TM_1$ and $TE_0$ modes the associated optical properties were determined. Angular reflectivity scans presented in Figure 9A show a shift of the $TM_1$ and $TM_2$ resonances to higher angles when contacted to HBP, reverting to the original positions after rinsing with PBS, in accordance with the kinetics data above. Bulk refractive index HBP sample was first determined as of $n_{solvent}$ = 1.3340, 1.3342, 1.3350, 1.3445 for 0, 10, 20, 100% HBP, respectively, from the critical angle position.

Then, variations in thickness $d_{swollen}$ and refractive index $n_{swollen}$ of the hydrogel layer were evaluated to follow changes in swelling ratio *SR* and surface mass density Γ, as summarized in **Figure 10**. The polymer networks carrying N3 and OEG motifs show no change in the *SR* and surface mass density Γ when contacted with HBP. Contrary to these samples, hydrogel films carrying OEG-SB and CB moieties behave differently as their *SR* decreased by ≈6% in pure HBP. Interestingly, an opposite effect was measured for the polymer networks with SB, for which *SR* increased by more than 7% in presence of whole HBP. All hydrogel films show no measurable change in surface mass density Γ when contacted with HBP, except the film made from the polymer bearing SB groups. The data suggest that only a minute amount of biomolecules was able to diffuse into the polymer network with N3, OEG, CB, and OEG-SB motifs. Apparently, the measured increase in surface mass density of $\Delta\Gamma = 28 \pm 15$ ng mm$^{-2}$ indicates that the hydrogel film with SB groups possesses a sufficiently open structure, through which HBP constituents can reversibly diffuse. These observations are particularly interesting, as the ability to reversibly uptake and release components from HBP is of high importance for applications in biosensing with such hydrogel films as binding matrices.

## 3. Conclusion

The present study demonstrates a remarkable performance of hydrogel coatings against fouling by undiluted human blood plasma, exploiting surface-attached, water-swollen polymer networks from photocrosslinkable poly(2-alkyl-2-oxazoline)s with pendent betaine moieties. The developed synthesis route, which allows full control over the polymer composition, employs a monomer toolbox comprising the novel benzophenone oxazoline BPOxa for photocrosslinking and the azide-functionalized oxazoline AzOxa for click-coupling of alkyne-modified antifouling motifs from the class of carboxy- and sulfobetaines. This approach provides access to a modular architecture with 2-alkyl-2-oxazolines as backbone-forming main monomers, which, depending on the substitution pattern, can entail an LCST-type thermoresponsiveness to reversibly vary the hydrogel film thickness with temperature. The analysis of the thermal response revealed a striking increase of several Kelvin for the volume transitions of water-swollen crosslinked networks in comparison to the cloud points of the polymers in solution, resulting from the higher polymer volume fraction in the networks with $\Phi > 0.6$ compared to the solutions with $\Phi \approx 0.03$. The SPR/OWS investigation of the hydrogel coatings in contact with human blood plasma shows specifically for the sulfobetaine-functionalized system an efficient penetration of the swollen polymer network by the plasma components, yet a complete release of all components upon rinsing with aqueous buffer, rendering this material as a versatile protein-repellant coating and promising matrix for advanced biosensor architectures.

## 4. Experimental Section

*Synthesis Procedures*: The syntheses routes for all monomers, polymers, antifouling motifs, and click-modified polymers as well as a list of the used materials and instrumentation can be found in the Supporting Information.

*Turbidimetry Measurements*: The temperature-dependent solution behavior of the polymers in water was determined by turbidimetry with UV/VIS spectroscopy. All measurements were performed using 0.3 wt.% aqueous polymer solutions with a heating and cooling rate of 1 K min$^{-1}$, while recording the transmittance at a wavelength of 550 or 650 nm. The cloud point was defined as the temperature, at which a transmittance of 50% was reached.

*Preparation of Surface Attached Hydrogel Films*: BK7 glass slides were coated with chromium (2 nm) and gold (50–55 nm) by vacuum thermal evaporation (HHV Auto 306 from HHV LTD). These substrates were directly immersed for 16 h into a 1 mM solution of 3,3′-disulfanediylbis[*N*-(4-benzoylbenzyl)propanamide] (BPdiS, **22**) dissolved in dimethyl sulfoxide in order to form a SAM. The samples were rinsed with ethanol and dried by a steam of nitrogen. Ethanolic solutions of the oxazoline-based polymers (6–10 wt.%) were deposited by spin coating (2000 rpm for 120 s) onto the BPdiS-modified gold substrates. The obtained polymer layers were dried for 4 h at 50 or 80 °C in a vacuum oven. The dry polymer layers

 © 2023 The Authors. Macromolecular Rapid Communications published by Wiley-VCH GmbH



15213927, 0, Downloaded from https://onlinelibrary.wiley.com/doi/10.1002/marc.202300549 by Cochrane Germany, Wiley Online Library on [28/11/2023]. See the Terms and Conditions (https://onlinelibrary.wiley.com/terms-and-conditions) on Wiley Online Library for rules of use; OA articles are governed by the applicable Creative Commons License

were crosslinked under argon atmosphere with UV light at wavelength of $\lambda = 365$ nm with irradiation doses between 4 and 20 J cm$^{-2}$.

*SPR/OWS Analysis of Swollen Thin Hydrogel Films*: The crosslinked polymer layers attached to the BPdiS-modified gold substrates were characterized in the dry and swollen state by surface plasmon resonance combined with optical waveguide spectroscopy (SPR/OWS). The optical system utilized attenuated total reflection in Kretschmann configuration as previously reported.[44] Briefly, a polarized He-Ne laser ($\lambda$= 632.8 nm) was sent through a high refractive index prism composed of LASFN9 glass, to which a glass substrate with a thin metal layer and anchored hydrogel film was optically matched by a high refractive index oil. A flow-cell with a volume of 25 µL was clamped against the glass substrate. This assembly was mounted on a rotation stage in order to measure changes in the reflected laser beam intensity as a function of the angle of incidence $R(\theta)$ by a photodiode connected to a lock-in amplifier (EG&G, Model 5210). The flow-cell was temperature-controlled by a Peltier element via a dedicated driver (LFI3751, Wavelength Electronics, USA). Tygon LMT-55 tubings (Ismatec, Germany) with an inner diameter of 0.25 or 0.62 nm were used with a peristaltic pump (Ismatec, Germany) to transport liquid samples over the sensor surface. The measured angular reflectivity scans $R(\theta)$ were fitted by a Fresnel reflectivity model with the software WinSpall (Max Planck Institute for Polymer Research, Mainz, Germany). By fitting multiple resonant features associated with the excitation of $TE_0$, $TM_1$ and $TM_2$ modes allowed the determination of the thickness $d_{dry}$ and the refractive index $n_{dry}$ of the polymer networks in the dry state (in contact with air) and the thickness $d_{swollen}$ and the refractive index $n_{swollen}$ of the swollen polymer networks (in contact with a liquid). Birefringence was omitted and thus all refractive indices were assumed to be identical for TM and TE polarizations. The optical parameters of all other materials below the polymer layers (Cr, Au, linkers) were determined by reference samples without polymer layers. The polymer volume fraction of the film in the swollen state was calculated by the effective medium theory from the measured refractive indices in the dry and swollen states, according to Equation (1).[45]

$$\Phi = \frac{n^2_{swollen} - n^2_{solvent}}{n^2_{swollen} + 2n^2_{solvent}} / \frac{n^2_{dry} - n^2_{solvent}}{n^2_{dry} + 2n^2_{solvent}} \quad (1)$$

Here, $n_{solvent}$ is the refractive index of solvent (water, PBS, or HBP).

The swelling ratio of the film was determined from the measured thicknesses in the dry state $d_{dry}$ and in contact with aqueous media $d_{swollen}$ following Equation (2).

$$SR = d_{swollen}/d_{dry} \quad (2)$$

Pooled HBP was obtained from Innovative Research (USA). Diffusion of biomolecules from HBP into the polymer network results in changes of the hydrogel swelling state and was expressed as variation in the surface mass density $\Gamma$, see Equation (3).

$$\Gamma = d_{swollen} \ (n_{swollen} - n_{solvent}) \ (\partial c/\partial n) \quad (3)$$

The ratio $\partial c/\partial n$ relates to changes of the refractive index with polymer concentration in water and is based on values of proteins reported in the literature.[46,47]

## Supporting Information

Supporting Information is available from the Wiley Online Library or from the author.

## Acknowledgements

This project had received funding from the European Union's Horizon 2020 Research and Innovation Program under grant agreement No 633937, project ULTRAPLACAD. Further, the authors thank for the financial support through the BMBF funded Project Medistorplast (13GW0349C) for FD, from Austrian Science Fund (FWF) via the project DIPLAB I 5119-B for SH, MP, and JD, and from Czech Science Fund (GACR) project APLOMA (22-30456J) for JD.

Open access funding enabled and organized by Projekt DEAL.

## Conflict of Interest

The authors declare no conflict of interest.

## Data Availability Statement

The data that support the findings of this study are available from the corresponding author upon reasonable request.

## Keywords

antifouling thermoresponsive hydrogel coatings, betaines, blood plasma, photocrosslinkable poly(2-oxazoline)s, SPR/OWS

Received: September 12, 2023
Revised: November 3, 2023
Published online:

[1] I. Banerjee, R. C. Pangule, R. S. Kane, *Adv. Mater.* **2011**, *23*, 690,
[2] J. B. Kristensen, R. L. Meyer, B. S. Laursen, S. Shipovskov, F. Besenbacher, C. H. Poulsen, *Biotechnol. Adv.* **2008**, *26*, 471.
[3] B. Liu, X. Liu, S. Shi, R. Huang, R. Su, W. Qi, Z. He, *Acta Biomater.* **2016**, *40*, 100.
[4] Y.-N. Chou, F. Sun, H.-C. Hung, P. Jain, A. Sinclair, P. Zhang, T. Bai, Y. Chang, T.-C. Wen, Q. Yu, S. Jiang, *Acta Biomater.* **2016**, *40*, 31,
[5] S. Chen, L. Li, C. Zhao, J. Zheng, *Polymer (Guildf)* **2010**, *51*, 5283.
[6] J. M. Harris, in *Poly(Ethylene Glycol) Chemistry* (Ed.: J. M. Harris), Springer Science+Business Media, New York **1992**, pp. 1–14.
[7] Q. Shao, S. Jiang, *Adv. Mater.* **2015**, *27*, 15.
[8] X. Liu, R. Huang, R. Su, W. Qi, L. Wang, Z. He, *ACS Appl. Mater. Interfaces* **2014**, *6*, 13034,.
[9] T. Goda, M. Tabata, M. Sanjoh, M. Uchimura, Y. Iwasaki, Y. Miyahara, *Chem. Commun.* **2013**, *49*, 8683.
[10] F. Wang, H. Zhang, B. Yu, S. Wang, Y. Shen, H. Cong, *Prog. Org. Coat.* **2020**, *147*, 105860.
[11] R. A. Wolf, in Proc. J. Vinyl and Additive Technology, Vol. *13*, **2007**, pp. 87–90.
[12] G. Gunkel, M. Weinhart, T. Becherer, R. Haag, W. T. S. Huck, *Biomacromolecules* **2011**, *12*, 4169.
[13] B. Liu, X. Liu, S.e Shi, R. Huang, R. Su, W. Qi, Z. He, *Acta Biomater.* **2016**, *40*, 100.
[14] D. Kuckling, M. E. Harmon, C. W. Frank, *Macromolecules* **2002**, *35*, 6377.
[15] P. W. Beines, I. Klosterkamp, B. Menges, U. Jonas, W. Knoll, *Langmuir* **2007**, *23*, 2231,
[16] C. Haslinger, A. Zahoranová, S. Baudis, *Monatsh. Chem.* **2023**, *154*, 459.
[17] L. Korchia, C. Bouilhac, V. Lapinte, C. Travelet, R. Borsali, J.-J. Robin, *Polym. Chem.* **2015**, *6*, 6029.
[18] R. Navarro, M. Pérez Perrino, O. Prucker, J. Rühe, *Langmuir* **2013**, *29*, 10932.
[19] K. Schuh, O. Prucker, J. Rühe, *Macromolecules* **2008**, *41*, 9284.
[20] R. Hoogenboom, H. Schlaad, *Polymers* **2011**, *3*, 467.

 © 2023 The Authors. Macromolecular Rapid Communications published by Wiley-VCH GmbH



15213927, 0, Downloaded from https://onlinelibrary.wiley.com/doi/10.1002/marc.202300549 by Cochrane Germany, Wiley Online Library on [28/11/2023]. See the Terms and Conditions (https://onlinelibrary.wiley.com/terms-and-conditions) on Wiley Online Library for rules of use; OA articles are governed by the applicable Creative Commons License

[21] R. Hoogenboom, *Angew. Chem., Int. Ed.* **2009**, *48*, 7978.
[22] R. Hoogenboom, H. M. L. Thijs, M. J. H. C. Jochems, B. M. Van Lankvelt, M. W. M. Fijten, U. S. Schubert, *Chem. Commun.* **2008**, 5758.
[23] F. Diehl, S. Hageneder, S. Fossati, S. K. Auer, J. Dostalek, U. Jonas, *Chem. Soc. Rev.* **2022**, *51*, 3926.
[24] D. Kotlarek, S. Fossati, P. Venugopalan, N. Gisbert Quilis, J. Slabý, J. Homola, M. Lequeux, F. Amiard, M. Lamy De La Chapelle, U. Jonas, J. Dostálek, *Nanoscale* **2020**, *12*, 9756,
[25] K. Sergelen, C. Petri, U. Jonas, J. Dostalek, *Biointerphases* **2017**, *12*, 051002.
[26] M. Toma, U. Jonas, A. Mateescu, W. Knoll, J. Dostalek, *J. Phys. Chem. C* **2013**, *117*, 11705.
[27] N. Gisbert Quilis, M. Van Dongen, P. Venugopalan, D. Kotlarek, C. Petri, A. Moreno Cencerrado, S. Stanescu, J. L. Toca Herrera, U. Jonas, M. Möller, A. Mourran, J. Dostalek, *Adv. Opt. Mater.* **2019**, *7*, 1900342.
[28] S. K. Auer, S. Fossati, Y. Morozov, U. Jonas, J. Dostálek, *J. Phys. Chem. B* **2022**, *126*, 3170.
[29] S. Hageneder, V. Jungbluth, R. Soldo, C. Petri, M. Pertiller, M. Kreivi, A. Weinhäusel, U. Jonas, J. Dostalek, *ACS Appl. Mater. Interfaces* **2021**, *13*, 27645.
[30] T. R. Dargaville, R. Forster, B. L. Farrugia, K. Kempe, L. Voorhaar, U. S. Schubert, R. Hoogenboom, *Macromol. Rapid Commun.* **2012**, *33*, 1695.
[31] A. Gress, A. Völkel, H. Schlaad, *Macromolecules* **2007**, *40*, 7928.
[32] N. Jung, F. Diehl, U. Jonas, *Polymers* **2020**, *12*, 1767.
[33] L. Korchia, C. Bouilhac, V. Lapinte, C. Travelet, R. Borsali, J.-J. Robin, *Polym. Chem.* **2015**, *6*, 6029.
[34] C. Haslinger, A. Zahoranová, S. Baudis, *Monatsh. Chem.* **2023**, *154*, 459.
[35] O. Prucker, C. A. Naumann, J. Rühe, W. Knoll, C. W. Frank, *J. Am. Chem. Soc.* **1999**, *121*, 8766.
[36] A. Mateescu, Y. Wang, J. Dostalek, U. Jonas, *Membranes* **2012**, *2*, 40.
[37] M. Gianneli, R. F. Roskamp, U. Jonas, B. Loppinet, G. Fytas, W. Knoll, *Soft Matter* **2008**, *4*, 1443.
[38] J. D. J. S. Samuel, T. Brenner, O. Prucker, M. Grumann, J. Ducree, R. Zengerle, J. Rühe, *Macromol. Chem. Phys.* **2010**, *211*, 195.
[39] B. L. Rivas, K. E. Geckeler, in *Advances in Polymer Science*, Springer-Verlag, Berlin **1992**, Vol. *102*, pp. 171–188.
[40] V. P. Dhende, S. Samanta, D. M. Jones, I. R. Hardin, J. Locklin, *ACS Appl. Mater. Interfaces* **2011**, *3*, 2830.
[41] J. C. Kappel, Y.i C. Fan, K. S. Lam, *J. Comb. Chem.* **2008**, *10*, 333.
[42] C. Petri, *Synthesis and Characterization of Novel Photocrosslinkable Poly(2-Oxazoline)-Based Hydrogel Systems for the Application as Biosensor Matrix. Dissertation*, University of Siegen, Siegen **2018**.
[43] M. M. Ouberai, K. Xu, M. E. Welland, *Biomaterials* **2014**, *35*, 6157.
[44] A. Aulasevich, R. F. Roskamp, U. Jonas, B. Menges, J. Dostálek, W. Knoll, *Macromol. Rapid Commun.* **2009**, *30*, 872.
[45] D. E. Aspnes, *Thin Solid Films* **1982**, *89*, 249.
[46] G. E. Perlmann, L. G. Longsworth, *J. Am. Chem. Soc.* **1948**, *70*, 2719.
[47] E. Stenberg, B. Persson, H. Roos, C. Urbaniczky, *J. Colloid Interface Sci.* **1991**, *143*, 513.
[48] B. Sudha, R. Kamble, S. Shashikanth, *J. Serb. Chem. Soc.* **2008**, *73*, 261.
[49] H. Witte, W. Seeliger, *Justus Liebigs Ann. Chem.* **1974**, *1974*, 996.
[50] T.-X. Lav, P. Lemechko, E. Renard, C. Amiel, V. Langlois, G. Volet, *React. Funct. Polym.* **2013**, *73*, 1001.
[51] G. Le Fer, C. Amiel, G. Volet, *Eur. Polym. J.* **2015**, *71*, 523.
[52] N. M. Leonard, J. Brunckova, *J. Org. Chem.* **2011**, *76*, 9169.
[53] L. Tauhardt, D. Pretzel, K. Kempe, M. Gottschaldt, D. Pohlers, U. S. Schubert, *Polym. Chem.* **2014**, *5*, 5751.
[54] J. Seuring, S. Agarwal, *ACS Macro Lett.* **2013**, *2*, 597.
[55] R. Hoogenboom, H. M. L. Thijs, M. J. H. C. Jochems, B. M. Van Lankvelt, M. W. M. Fijten, U. S. Schubert, *Chem. Commun.* **2008**, 5758.
[56] A. Laschewsky, *Polymers* **2014**, *6*, 1544.
[57] R. J. Young, P. A. Lovell, *Introduction to Polymers*, 3rd ed., CRC Press, Boca Raton, FL **2011**.
[58] M. Namazian, S. Halvani, M. R. Noorbala, *J. Mol. Struct.* **2004**, *711*, 13.
[59] L. Wu, J. Jasinski, S. Krishnan, *J. Appl. Polym. Sci.* **2012**, *124*, 2154.
[60] R. R. Netz, D. Andelman, *Phys. Rep.* **2003**, *380*, 1.
[61] N. Giovambattista, P. G. Debenedetti, P. J. Rossky, *J. Phys. Chem. B* **2007**, *111*, 9581.
[62] R. J. Scott, L.-Y. Lian, S. H. Muharram, A. Cockayne, S. J. Wood, B. W. Bycroft, P. Williams, W. C. Chan, *Bioorg. Med. Chem. Lett.* **2003**, *13*, 2449.
[63] S. Sakakibara, N. Inukai, *Bull. Chem. Soc. Jpn.* **1965**, *38*, 1979.
[64] M. T. Zarka, O. Nuyken, R. Weberskirch, *Chem. - Eur. J.* **2003**, *9*, 3228.
[65] S. M. Andreev, L. A. Pavlova, Y. A. Davidovich, S. V. Rogozhin, *Russ. Chem. Bull.* **1980**, *29*, 785.
[66] S. Asano, J. Gavrilyuk, D. R. Burton, C. F. Barbas, *ACS Med. Chem. Lett.* **2014**, *5*, 133.
[67] O. Norberg, L. Deng, M. Yan, O. Ramström, *Bioconjugate Chem.* **2009**, *20*, 2364.
[68] E. W. Della, P. A. Smith, *J. Org. Chem.* **1999**, *64*, 1798.

 © 2023 The Authors. Macromolecular Rapid Communications published by Wiley-VCH GmbH



15213927, 0, Downloaded from https://onlinelibrary.wiley.com/doi/10.1002/marc.202300549 by Cochrane Germany, Wiley Online Library on [28/11/2023]. See the Terms and Conditions (https://onlinelibrary.wiley.com/terms-and-conditions) on Wiley Online Library for rules of use; OA articles are governed by the applicable Creative Commons License

# 8 Hydrogel-Based Diffusion Barriers for Drug-Loaded Wound Dressings

## 8.1 Introduction

Diabetes mellitus represents one of the most rapidly growing health challenges of our time, with patient numbers increasing significantly worldwide.[1] One of the most severe complications associated with diabetes is the development of diabetic foot ulcers (DFU), which affect approximately one-quarter of all diabetic patients during their lifetime. According to the Centers for Disease Control and Prevention, 30.3 million people in the United States suffer from diabetes. The global prevalence of DFU in 2016 was 6.3%; while in Europe the prevalence averaged approximately 5.5%.[2] A study from 2005 showed that every 30 seconds worldwide, a lower limb amputation occurs due to diabetes.[3] Such chronic diabetic wounds not only severely impact patients' quality of life but also pose a substantial burden on healthcare systems.[4]

While conventional treatments for DFU encompass the intake of insulin, recent research has demonstrated remarkable therapeutic effects through topical insulin application.[5,6] This approach has shown promising results in promoting wound healing by improving local energy metabolism and enhancing protein synthesis. However, current treatment protocols require daily insulin applications, which presents a significant challenge. Diabetic patients typically have fragile skin,[7] and frequent wound dressing changes often result in additional tissue damage and pain, potentially compromising the healing process and patient comfort.

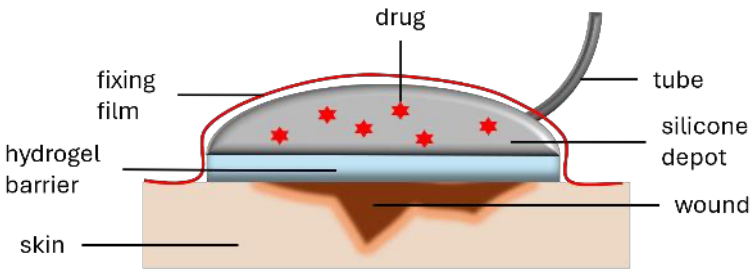


Figure 1. Schematic illustration of the envisioned wound dressing.

To address these challenges, the present work in this thesis focuses on the development of an innovative wound dressing system with an integrated insulin reservoir and a hydrogel-based diffusion barrier. This design aims to provide controlled, sustained insulin release over extended periods of time while reducing the frequency of dressing changes. Additionally, the

set-up is devised to be refilled *via* a tube system, further aiming to decrease the number of wound dressing changes. The concept leverages the inherent properties of hydrogels, which are well-known for their permeability to small molecules and excellent biocompatibility. These characteristics make them ideal candidates for controlled drug delivery applications in wound care.

The specific focus of this section of the thesis lies in the synthesis and characterization of photocrosslinkable acrylamide copolymers intended to serve as hydrogel diffusion-barrier materials. These materials will form the crucial interface between the insulin reservoir and the wound surface, controlling the rate of insulin delivery while maintaining an optimal wound healing environment. The main requirement for the hydrogel barrier will be maintaining a seamless connection between the silicone depot and the polymer network to prevent liquid bypass, while allowing the drug molecule solution to diffuse through the gel for a drug release over extended time frames.

This research was part of an industrial cooperation with the company OSCOMED (Sonneberg, Germany) founded through the Bundesministerium für Bildung und Forschung (BMBF), Germany.

## 8.2 Experimental Details

### 8.2.1 Equipment and Chemicals

All $^{1}$H and $^{13}$C NMR spectra were recorded with a spectrometer from Jeol Type ECZ 500. The $^{1}$H NMR measurements were recorded at a frequency of 500 MHz and the $^{13}$C NMR measurements at 126 MHz at room temperature (≈ 20 °C). The chemical shifts of the signals δ were specified in ppm. The peaks of the nondeuterated solvents were used as internal standard. All recorded spectra were analyzed with the software MestReNova. The sililcone substrates were pre-treated with a Sicatech corona generator Uni-System LF 1. For photocrosslinking, the UV crosslinker Bio-Link from LTF Labortechnik was used with a wavelength of 365 nm and a total energy of 13.0 J cm$^{-2}$ h$^{-1}$.

2,2'-Azobis[2-(2-imidazolin-2-yl)propane] dihydrochloride (AIPC, 97% - Waco Chemicals, Neuss, Germany) was used as received. Azobisisobutyronitrile (AIBN, 98% - Fluka, Charlotte, North Carolina, USA) and acrylamide (Am, Carl Roth, Karlsruhe, Germany) were both recrystallized from methanol twice. The solvents methanol (MeOH, 99.8%), ethyl acetate

(EtOAc, 99.8%% - btoh Fisher Scientific, Schwerte, Germany), ethanol (EtOH, technical grade), and acetone (99% - both VWR, Darmstadt, Germany) were used without further purification. Deuterated solvents for NMR analysis (Deutero, Kastellaun, Germany) were used as received. MilliQ-water was taken from a Merck Millipore system (σ = 18.2 MΩ cm, Millipore, Schwalbach, Germany). 1,4-Dioxane was dried with sodium and distilled afterwards. The two-component liquid silicone rubber Silopren™ LSR 2040 was provided by the collaborating enterprise OSCOMED (Sonneberg, Germany).

### 8.2.2 Synthesis Procedures

*Crosslinker Monomers*

BPAm was synthesized according to literature procedures.[8–10]

BPQAAm was synthesized according to a literature procedure.[11]

*Poly(Am-co-BPAm)*

Table 1. Synthetic details for the copolymerization of acrylamide (Am) with *N*-(4-benzophenyl) acrylamide (BPAm), using 2,2'-azobis [2-(2-imidazolin-2-yl) propane] dihydrochloride (AIPC) as initiator.

| ratio Am : **BPAm** | Am / mg (mmol) | BPAm / mg (µmol) | AIPC / mg (µmol) | yield / mg (%) |
|---|---|---|---|---|
| 99 : **1** | 500 (7.03) | 17.8 (71.0) | 9.63 (35.5) [d] | 210 (41) |
| 98.5 : **1.5** | 250 (3.52) [a] | 13.5 (53.6) [b] | 4.86 (17.9) [e] | 235 (89) |
| 98 : **2** | 250 (3.52) | 18.0 (71.5) [c] | 4.87 (18.0) [f] | 260 (97) |
| 97.5 : **2.5** | 250 (3.52) [a] | 22.4 (89.3) [b] | 4.88 (18.0) [e] | 265 (97) |
| 97 : **3** | 250 (3.52) [a] | 26.9 (107) [b] | 5.02 (18.5) [e] | 269 (97) |

[a] Taken from a stock solution in water (mass concentration $\beta$ = 100 g/l). [b] Taken from a stock solution in 1,4-dioxane ($\beta$ = 40 g/l ). [c] Taken from a stock solution in 1,4-dioxane ($\beta$ = 91.7 g/l). [d] Taken from a stock solution in 1,4-dioxane and water (*V*/*V* = 2 : 3, $\beta$ = 63.7 g/l). [e] Taken from a stock solution in water ($\beta$ = 40 g/l). [f] Taken from a stock solution in 1,4-dioxane and water (*V*/*V* = 2 : 3, $\beta$ = 21.8 g/l).

Am, BPAm, and AIPC were dissolved in a mixture of 1,4-dioxane and water (*V*/*V* = 2 : 3, total volume = 7 ml) and the reaction mixture was degassed by purging with argon for 40 min. For detailed weigh-ins, see Table 1. Afterwards, the reaction flasks were placed in a preheated

aluminum block (55 °C) for 16 h. The reaction mixtures were precipitated in ice-cooled MeOH (150 ml) and stirred for 48 h. The precipitate was dissolved in water (25 ml), or mixtures of water and 1,4-dioxane (~ *V*/*V* = 2:1, 40 ml) and dried via lyophlilization.

*Poly(Am-co-BPQAAm)*

Am, BPQAAm, and AIPC were dissolved in water (total volume = 7 ml) and the reaction mixture was degassed by purging with argon for 40 min. For detailed weigh-ins, see Table 2. Afterwards, the reaction flasks were placed in a preheated aluminum block (55 °C) for 16 h. The reaction mixtures were precipitated in ice-cooled acetone (150 ml) twice. The precipitate was then dried in vacuum overnight.

Table 2. Synthetic details for the copolymerization of acrylamide (Am) with [(4-benzoylphenyl)methyl]dimethyl[3-(prop-2-enamido)propyl] azanium bromide (BPQAAm), using 2,2'-azobis [2-(2-imidazolin-2-yl) propane] dihydrochloride (AIPC) as initiator.

| ratio Am : **BPQAAm** | Am [a] / mg (mmol) | BPQAAm [b] / mg (µmol) | AIPC [c] / mg (µmol) | yield / mg (%) |
|---|---|---|---|---|
| 99 : **1** | 250 (3.52) | 14 (32.5) | 4.41 (16.3) | 180 (68) |
| 98.5 : **1.5** | 250 (3.52) | 21.0 (48.8) | 4.41 (16.3) | 189 (67) |
| 98 : **2** | 250 (3.52) | 28.0 (65.0) | 4.41 (16.3) | 173 (63) |
| 97.5 : **2.5** | 250 (3.52) | 35.0 (81.3) | 4.41 (16.3) | 149 (52) |
| 97 : **3** | 250 (3.52) | 42.1 (97.5) | 4.41 (16.3) | 182 (61) |

[a] Taken from a stock solution in water (mass concentration $\beta$ = 100 g/l). [b] Taken from a stock solution in water ($\beta$ = 11.4 g/l). [c] Taken from a stock solution in water ($\beta$ = 40 g/l).

### 8.2.3 Silicone Sheet Fabrication

Silopren™ LSR 2040 component A (5 g) and component B (5 g) were dissolved in ethyl acetate (10 ml) by intense shaking for 16 h. The homogenized mixture was dried in vacuum at room temperature overnight. Subsequently, the dried mixture was filled into a syringe and deposited on a poly(ethylene terephthalate) (PET) sheet and covered with a second PET sheet. The PET-silicone-PET sandwich was then pressed between two glass slides fixed with two metal clamps. The molded silicone mixture was placed in a preheated oven at 180 °C for 3 h. After curation, the specimen was stripped from the PET sheets.

### 8.2.4 Crosslinking

*Crosslinking pre-tests*

The corresponding polymer (25 mg) was dissolved in water (1.5 ml) or a mixture of water and ethanol (1.5 ml, *V*/*V* = 1:1) and the polymer solution was poured into a polystyrene Petri dish. The sample was dried on a heating plate (24 h, 40 °C), forming a thin polymer layer on the bottom of the Petri dish. The polymer layers were irradiated with UV light for 30 min ($\lambda = 365$ nm, energy = 13.0 J/cm$^2$h). After that, demineralized water (1 ml) was added to each sample in order to evaluate the swelling behavior.

*Crosslinking on silicone*

The silicone specimen was moved beneath a corona discharge tip with an even speed. For deposition of an adhesion promotion layer, the surfactant-containing polymer poly(Am$_{94}$-*co*-BPAm$_1$-*co*-B35A$_5$) was dissolved in a mixture of water and ethanol (V/V = 1:1, $\beta$ = 2.5 g/l) and sprayed on the silicone surface, dried on a heating plate (2 h, 40 °C) and irradiated with UV light for 30 min ($\lambda$ = 365 nm, energy = 13.0 J/cm$^2$h). One droplet of a hydrogel pre-polymer dissolved in water or a mixture of water and ethanol (V/V = 1:1, $\beta$ = 17 g/l) was placed on the substrate, dried on a heating plate (2 h, 40 °C), and irradiated with UV light for 30 min ($\lambda$ = 365 nm, energy = 13.0 J cm$^{-}$2 h$^{-1}$). The silicone sample was placed in water for 1 min to swell the crosslinked polymers and the surface attachment of the hydrogel was evaluated.

## 8.3 Results and Discussion

### 8.3.1 Monomer synthesis

For the generation of polymer networks, two photocrosslinker monomers were synthesized: BPAm and BPQAAm. BPAm, a well-established crosslinker readily activated by UV irradiation, was synthesized according to literature procedures with high efficiency.[8–10] The synthesis involved exposing 4-aminobenzophenone to excess of acryloyl chloride, yielding 88% of the target monomer. Yet, this monomer suffers from a rather hydrophobic character with very poor solubility in water. In contrast, BPQAAm was designed to exhibit enhanced hydrophilicity due to the incorporation of a quaternary ammonium moiety in its structure. This monomer was prepared via a two-step reaction sequence following published protocols.[11] The first step involved selective bromination of 4-methylbenzophenone using *N*-bromosuccinimide with azobisisobutyronitrile (AIBN) as radical initiator, affording 4-bromomethyl

benzophenone in 84% yield. Subsequently, nucleophilic substitution between 4-bromomethyl benzophenone and *N*-[3-(dimethylamino)propyl]acrylamide in methyl-*tert.*-butyl ether resulted in precipitation of BPQAAm as the quaternary ammonium bromide salt with 90% yield. These high-yielding syntheses provided access to photocrosslinkers with complementary properties, enabling fine-tuning of the resultant polymer networks for specific applications.

### 8.3.2 Polymer synthesis

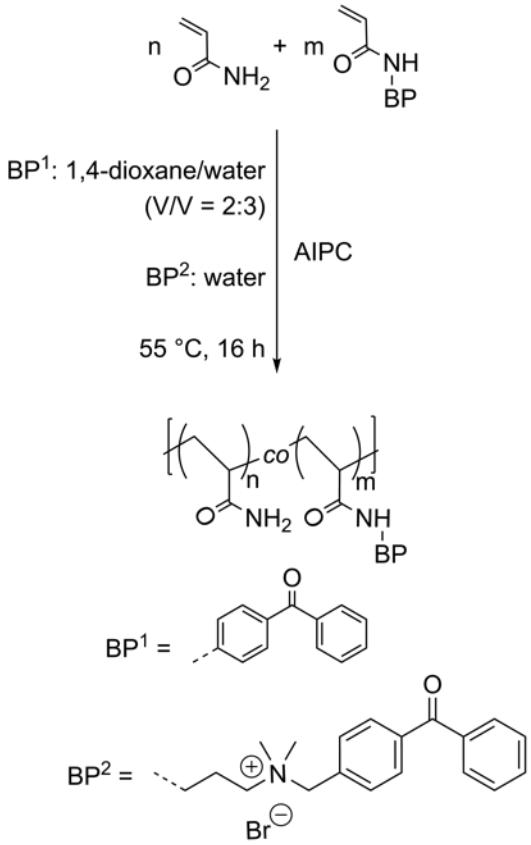


Scheme 1. Synthesis scheme for the hydrophilic acrylamide-based copolymers with $BP^1$ = BPAm, and $BP^2$ = BPQAAm.

Acrylamide, a well-established monomer for the preparation of hydrophilic polymers,[12] was selected as the primary component for the diffusion barrier in the drug delivery wound dressing, as described above. The polymer networks were prepared by copolymerizing acrylamide with either BPAm or BPQAAm *via* free radical polymerization (FRP) using AIPC as the water-soluble initiator (see Scheme 1). For the BPAm-containing systems, the crosslinker feed ratios were systematically varied from 1.0 to 3.0 mol% in 0.5 mol% increments. Notably, when BPAm content exceeded this range, the resulting polymers seemed to exhibit upper critical solution temperature (UCST) behavior, as their solubility in water rapidly increased

after heating the polymer-water mixture with a hot water bath. This rendered them unsuitable for the intended application and thereby established the optimal crosslinker concentration window. Due to the hydrophobic nature of BPAm, polymerizations were conducted in a water/1,4-dioxane mixture (*V*/*V* = 2 : 3), which ensured complete solubilization of both monomers and polymers while maintaining environmental compatibility. In contrast, BPQAAm copolymerizations were performed exclusively in aqueous media owing to the enhanced hydrophilicity of this crosslinker. The BPAm-containing copolymers achieved excellent yields ranging from 89% to 95%, with structural confirmation provided by $^{1}$H NMR spectroscopy (spectra provided in the Appendix, page A28). Interestingly, the BPQAAm-containing copolymers were obtained in lower yields between 52% and 68% and they could not be redissolved after isolation, neither in water, dimethyl sulfoxide (DMSO), MeOH, chloroform, acetonitrile, acetone, nor toluene. This could likely caused by the formation of high molecular weight polymers with significant chain entanglements functioning as physical crosslinks — a phenomenon frequently observed in aqueous polymerizations, which typically yield higher degrees of polymerization compared to reactions in organic media.[13] Consequently, subsequent crosslinking experiments were exclusively performed using the BPAm-functionalized copolymers.

### 8.3.3 Crosslinking tests

A comprehensive analysis of the crosslinking behavior was conducted through various experimental approaches. Initially, the intrinsic crosslinking capability of the polymer was evaluated by depositing a thin polymer layer within a polystyrene Petri dish and subjecting it to a prolonged UV irradiation of 30 min to ensure complete crosslinking for comparative assessment. The swelling behavior of the irradiated samples was subsequently evaluated by the addition of water. Successfully crosslinked samples exhibited immediate water uptake, forming rigid, manipulable gels within the Petri dish, whereas poorly crosslinked or non-crosslinked samples dissolved upon water addition, resulting in liquid solutions. While all samples demonstrated effective network formation, the degree of crosslinking correlated linearly with the concentration of the crosslinking agent, with lower crosslinker concentrations yielding comparatively weaker network structures.

For the intended wound dressing application, crosslinking the polymers onto a silicone depot surface was essential. Silicone samples were prepared using two-component Silopren LSR

2040, which required modification of the standard processing protocol due to its high viscosity (originally the silicone was designed for injection molding applications). To achieve appropriate handling conditions in the laboratory environment, both components were diluted with ethyl acetate to maintain mixability and processability without specialized injection molding equipment. Following component mixing, the solvent was removed through a combination of moderate heating (40°C) and vacuum application. The processed mixture was then applied between two PET film-covered glass slides secured with clamps to maintain uniform pressure distribution. The assembled construct was subsequently transferred to an oven for silicone curing (see Figure 2A), following a protocol developed in collaboration with Aliia Ibragimova during the research activities for her master thesis.

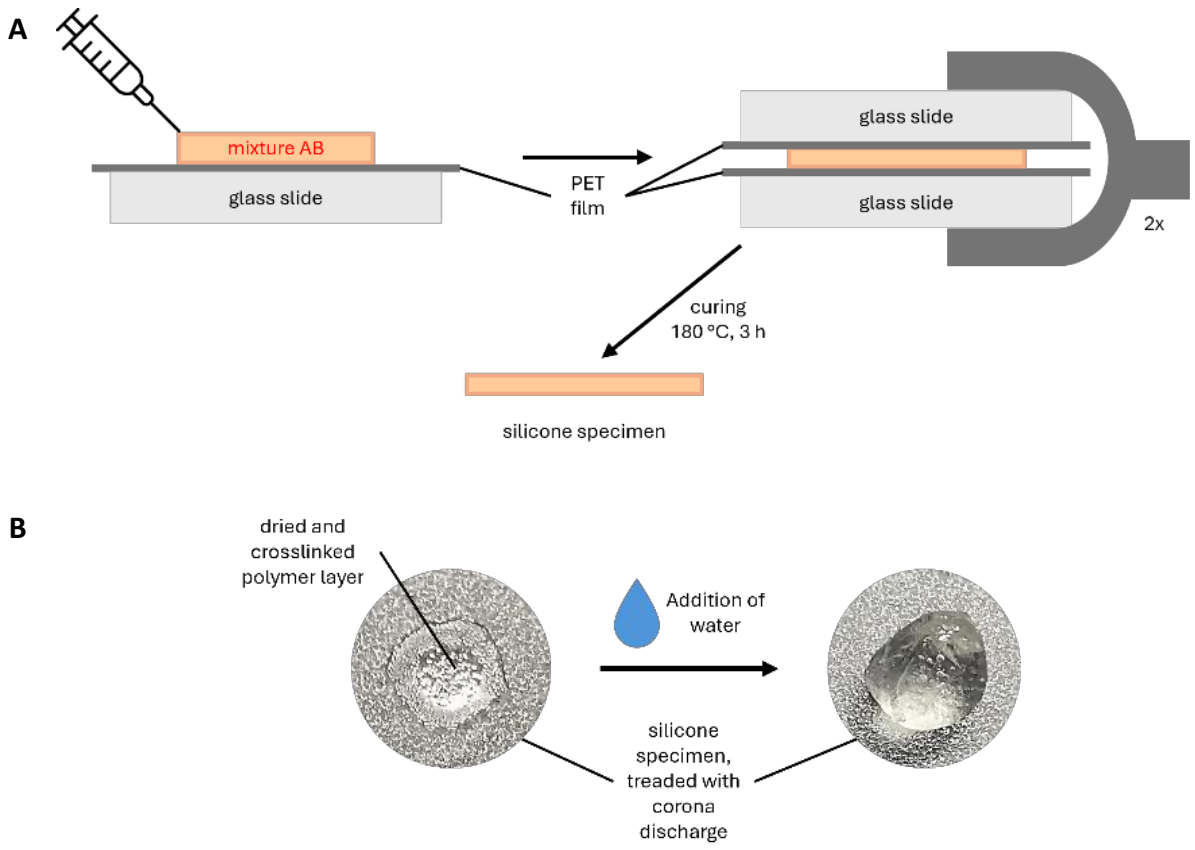


Figure 2. (A) Procedure for fabrication of the silicone specimens. (B) Crosslinking of poly(Am-*co*-BPAm) on a corona-treated silicone surface, showing that by swelling the formed network with water no adhesion to the underlying surface can be observed.

For surface-adhesion crosslinking experiments, the cured silicone samples underwent corona discharge treatment to increase surface hydrophilicity and promote polymer chain attachment during the crosslinking process. Similar testing protocols were applied to alternative silicone sheets provided by OSCOMED. Despite successful crosslinking within the

polymer chains of the hydrogel precursor across all experimental conditions, attachment to the silicone surfaces was not achieved (see Figure 2B). This failure in surface adhesion likely stems from fundamental physicochemical incompatibilities between the highly hydrophilic crosslinked acrylamide polymer networks and the inherently hydrophobic, chemically inert silicone substrate, even after surface activation via corona discharge.

## 8.4 Conclusion and Outlook

Despite challenges encountered in achieving direct attachment of polymer networks to the silicone surface, the use of hydrogels as permeable diffusion barriers in wound dressings remains a promising approach for diabetic foot ulcer (DFU) patient care. The critical requirement for the wound dressing design — maintaining a seamless connection between the silicone depot and the polymer network to prevent liquid bypass — highlighted the limitations of direct hydrogel-silicone interfaces.

The presented findings necessitated a strategic reconfiguration of the wound dressing setup to produce a functional prototype viable for industrial application. The alternative approach developed involves attaching the hydrogel polymer to an intermediate carrier material, which can then be effectively connected to the silicone depot. This modification addresses the interfacial challenges while preserving the beneficial diffusion properties of the hydrogel system. Building upon these discoveries, subsequent refinements to the wound dressing design were undertaken by Aliia Ibragimova in her PhD research. This collaborative effort culminated in a jointly developed innovation, documented in the invention disclosure included in the Appendix (page A29). This progression demonstrates how initial technical obstacles were transformed into opportunities for design improvement through systematic investigation and creative problem-solving.

The evolution of this wound dressing system illustrates the iterative nature of biomaterials development, where material interface challenges often drive innovative solutions that ultimately enhance therapeutic efficacy. The modified approach maintains the core advantages of hydrogel-based drug delivery while addressing practical implementation requirements critical for clinical translation in DFU management.

## References


1. Magliano, D.J.; Boyko, E.J. *IDF DIABETES ATLAS*; 10th ed.; International Diabetes Federation: Brussels, **2021**; ISBN 9782930229980.

2. Zhang, P.; Lu, J.; Jing, Y.; Tang, S.; Zhu, D.; Bi, Y. Global Epidemiology of Diabetic Foot Ulceration: A Systematic Review and Meta-Analysis. *Ann Med* **2017**, *49*, 106, doi:10.1080/07853890.2016.1231932.

3. Boulton, A.J.; Vileikyte, L.; Ragnarson-Tennvall, G.; Apelqvist, J. The Global Burden of Diabetic Foot Disease. *The Lancet* **2005**, *366*, 1719, doi:10.1016/S0140-6736(05)67698-2.

4. Rice, J.B.; Desai, U.; Cummings, A.K.G.; Birnbaum, H.G.; Skornicki, M.; Parsons, N.B. Burden of Diabetic Foot Ulcers for Medicare and Private Insurers. *Diabetes Care* **2014**, *37*, 651, doi:10.2337/dc13-2176.

5. Chauhan, S.; Jhawat, V.; Singh, R.P.; Yadav, A. Topical Delivery of Insulin Using Novel Organogel Formulations: An Approach for the Management of Diabetic Wounds. *Burns* **2024**, *50*, 1068, doi:10.1016/j.burns.2024.01.008.

6. Bhittani, M.K.; Rehman, M.; Altaf, H.N.; Altaf, O.S. Effectiveness of Topical Insulin Dressings in Management of Diabetic Foot Ulcers. *World J Surg* **2020**, *44*, 2028, doi:10.1007/s00268-019-05321-3.

7. David, P.; Singh, S.; Ankar, R. A Comprehensive Overview of Skin Complications in Diabetes and Their Prevention. *Cureus* **2023**, doi:10.7759/cureus.38961.

8. Beines, P.W.; Klosterkamp, I.; Menges, B.; Jonas, U.; Knoll, W. Responsive Thin Hydrogel Layers from Photo-Cross-Linkable Poly(N-Isopropylacrylamide) Terpolymers. *Langmuir* **2007**, *23*, 2231, doi:10.1021/la063264t.

9. Fadida, T.; Lellouche, J.P. Poly-N-(4-Benzoylphenyl)Methacrylamide Nanoparticles: Preparation, Characterization, and Photoreactivity Features. *Journal of Polymer Research* **2012**, *19*, doi:10.1007/s10965-012-0023-2.

10. Kommeren, S.; Dongmo, J.; Bastiaansen, C.W.M. Switchable Surface Structured Hydrogel Coatings. *Soft Matter* **2017**, *13*, 2239, doi:10.1039/c7sm00195a.

11. Morozov, Y.M.; Wiesner, F.; Grün, J.J.; Pertiller, M.; Fossati, S.; Schmidt, K.; Quilis, N.G.; Gusenbauer, C.; Zbiral, B.; Toca-Herrera, J.L.; et al. Microstructuring of Thermoresponsive Biofunctional Hydrogels by Multiphoton Photocrosslinking. *Adv Funct Mater* **2024**, *34*, doi:10.1002/adfm.202315578.

12. Yang, T.-H. Recent Applications of Polyacrylamide as Biomaterials. *Recent Patents on Materials Sciencee* **2008**, *1*, 29, doi:10.2174/1874464810801010029.

13. Valdebenito, A.; Encinas, M.V. Effect of Solvent on the Free Radical Polymerization of *N*,*N* -dimethylacrylamide. *Polym Int* **2010**, *59*, 1246, doi:10.1002/pi.2856.

# 9 Antiadhesive and Antibacterial Coatings for Short-Term Titanium Implants

**Published as:**

**F. Wiesner**, K. G. M. Schönewald, K. Vogel, N. Jung, B. Schwierz, M. Kipping, A. Ibragimova, J. Schumacher, C. Pritzel, C. R. V. Thiagarajan, U. Ritz, U. Jonas, Antiadhesive and Antibacterial Coatings for Short-Term Titanium Implants, Macromol. Rapid Commun. **2025**, 2400989, doi: 10.1002/marc.202400989.

**Author Contributions:**

***Fiona Wiesner (née Diehl):*** Conception, Coordination, Monomer syntheses and analyses, polymer syntheses and analyses, Coating procedures, Writing, Reviewing, Editing

*Karl G. M. Schönewald:* Cell and bacteria tests, Data evaluation

*Kira Vogel:* Cell and bacteria tests, Data evaluation

*Niklas Jung:* Monomer syntheses and analyses, polymer syntheses and analyses, Coating procedures

*Barbara Schwierz:* Cell and bacteria tests, Data evaluation

*Maren Kipping:* Monomer syntheses and analyses, Polymer syntheses and analyses

*Aliia Ibragimova:* Polymer syntheses and analyses

*Joshua Schumacher:* AFM measurements, Data evaluation, Writing

*Christian Pritzel:* ESEM measurements, Data evaluation

*Clinton R. V. Thiagarajan:* Monomer syntheses and analyses

*Ulrike Ritz:* Conception, Coordination, Writing, Reviewing, Editing, Funding, Corresponding author

*Ulrich Jonas:* Conception, Coordination, Writing, Reviewing, Editing, Funding, Corresponding author

**Supporting Information** can be found in the Appendix, page A34

Macromolecular Rapid Communications
www.mrc-journal.de

# Antiadhesive and Antibacterial Coatings for Short-Term Titanium Implants

*Fiona Wiesner, Karl G. M. Schönewald, Kira Vogel, Niklas Jung, Barbara Schwierz, Maren Kipping, Aliia Ibragimova, Joshua Schumacher, Christian Pritzel, Clinton R. V. Thiagarajan, Ulrike Ritz,* and Ulrich Jonas**

**This study presents a novel approach for the development of antifouling and antibacterial hydrogel coatings for short-term titanium implants to treat bone defects. Such implants provide temporary stabilization during bone healing and are intended to be explanted within a period of 12 months. The novel surface modification prevents complications during implant removal, like injury to tissue, nerves, or tendons due to adhesion to the untreated titanium surface. The coatings combine acrylamide-based hydrogels with photocrosslinkers possessing intrinsic antibacterial properties and anchor groups designed for titanium substrates. Comprehensive in vitro evaluations are conducted to assess the biocompatibility and efficacy of these coatings. The results demonstrate that the water-swellable polymer networks effectively prevent cell and tissue adhesion by their antifouling characteristics without inducing cytotoxicity. Importantly, these coatings also exhibit an intrinsic and non-leaching antibacterial effect covalently incorporated into the molecular framework, which addresses the limitations of current implant coating technologies that often rely on the incorporation of antibiotics or bactericidal agents. As the experimental data conclusively verify the effectiveness of the coatings in inhibiting cell adhesion and bacterial colonization, this technology shows great potential to significantly advance the field of short-term titanium implants.**

## 1. Introduction

Fractures are a worldwide occurring problem with a variety of different treatment possibilities depending on severity, localization, and risk factors. The analysis of the Global Burden of Diseases, Injuries, and Ris Factors Study (GBD) reported with 178 million new fractures, the large burden of fractures worldwide in the year 2019. Since 1990 the absolute number increased by 33.4% demonstrating the elevation of fractures in the elder society.[1] In Germany, the observed increase was by 14% (from 2009 to 2019).[2]

Depending on the type of fracture screws and/ or plates are surgically inserted to join and fix the bone fragments in an anatomically correct position, known as osteosynthesis. The duration of the metal implants depends on the type and localization of the fracture. In the case of hip or knee implants, it is desirable that the implant lasts as long as possible and integrates completely into the tissue.[3] Other implants have to be removed after some time; in this case, it is desirable, that the implant does not connect with the surrounding tissue to facilitate its removal without any tissue damage.[4] Implant removal currently accounts for approx. 30% of all elective operations in trauma surgery/orthopedics. If the fracture heals without complications, removal at the distal radius is recommended after 3–6 months, particularly after 9–12 months and diaphyseally after 12–24 months.[5,6]

F. Wiesner, N. Jung, M. Kipping, A. Ibragimova, C. R. V. Thiagarajan, U. Jonas
University of Siegen, Department of Biology and Chemistry
Macromolecular Chemistry
Adolf-Reichwein-Straße 2, 57076 Siegen, Germany
E-mail: jonas@chemie.uni-siegen.de

K. G. M. Schönewald, K. Vogel, B. Schwierz, U. Ritz
University Medical Center Mainz
Department of Orthopedics and Trauma Surgery
Langenbeckstraße 1, 55131 Mainz, Germany
E-mail: ritz@uni-mainz.de

J. Schumacher
University of Siegen, Department of Biology and Chemistry
Physical Chemistry I
Adolf-Reichwein-Straße 2, 57076 Siegen, Germany

C. Pritzel
University of Siegen, Department of Biology and Chemistry
Chemistry of Building Materials
Paul-Bonatz-Straße 9-11, 57076 Siegen, Germany

The ORCID identification number(s) for the author(s) of this article can be found under https://doi.org/10.1002/marc.202400989

© 2025 The Author(s). Macromolecular Rapid Communications published by Wiley-VCH GmbH. This is an open access article under the terms of the Creative Commons Attribution License, which permits use, distribution and reproduction in any medium, provided the original work is properly cited.

**DOI: 10.1002/marc.202400989**

Adhesion is a frequent complication when removing osteosynthesis material. Adhesions describe an abnormal hyperplasia of tissue that can take on different dimensions. It can mean the formation of a thin fibrous layer, but also thick scar tissue. This is often associated with chronic pain, dysfunction, and reduced quality of life for the patient.[7] After insertion of the implants, fibrous scar tissue forms as part of the defect healing process, and connective tissue adhesions to the implant occur. Tendons can also be affected, which can lead to permanent reduced mobility of the joint and periarthritis. This often leads to adhesion of the tendon to the material, resulting in an increased risk of tenosynovitis and tendon rupture. The most common and most serious complication is tenogenic stiffening of the joint. If material is subsequently removed, tenolysis is often indicated, in which the tendon is detached from the surrounding tissue, although the prognosis is poor and there is a risk of irreversible loss of function. The only safe strategy would be to prevent tendon adhesion.[4,8] Another serious complication is infection of the osteosynthesis material. The bacterium Staphylococcus aureus is particularly clinically relevant.[9]

Titanium is a very common implant material as it has a lower rate of failure and fewer complications, compared to other metal materials like steel. However, titanium implants exhibit a higher propensity for tissue adhesion compared to their stainless steel counterparts.[10] The tissue-adhesive properties of titanium implants, which are beneficial for long-term implants, may pose risks for the application of short-term implants, potentially leading to reduced range of motion, joint stiffness, and, in severe cases, neurovascular complications due to removal. These adhesion-related complications can result in protracted recovery periods, increased patient morbidity, and substantial psychological distress. Only a few articles deal with the question of how to use the biomechanical advantages of titanium for short-term implants and modify them to avoid tissue adhesion and thereby escaping the negative side effects during or after implant removal.[11] Furthermore, existing coatings for implants often lack robust covalent attachment to the titanium substrate, but instead rely on superficial application akin to wax deposition. In light of these challenges, the development of durable antiadhesive coatings for short-term titanium implants represents a promising strategy to mitigate post-implantation complications and reduce the risks associated with implant removal.

An additional medical complication presents the inherent risk of surgical site infection associated with implantation procedures often necessitates prolonged antibiotic therapy or revision surgery, imposing additional burdens on healthcare systems and patients alike. In fact, literature found with anti-adhesive coatings of titanium alloys mostly regards anti-adhesion of bacteria to avoid bacterial adhesion and infection at the implant site.[12,13] Many current approaches incorporate antibiotics, silver nanoparticles, or drug-release systems to mitigate infection risks.[14] This modification method potentially results in unstable coatings susceptible to removal or dissolution, compromising their efficacy in preventing cellular attachment. Moreover, leaching of the active agent, especially of antibiotics, may inadvertently promote bacterial resistance, induce adverse systemic effects, or fail to maintain constant antibacterial efficacy.[15]

To address the issues previously discussed, an ideal coating for short-term titanium implants would consist of an antifouling hydrogel covalently bound to the substrate, incorporating a non-leaching antibiotic motif. In this context, hydrogels derived from water-swollen polymer networks have emerged as a particularly effective class of materials for preventing protein and cell adhesion.[16] As such, they present an attractive solution to the challenges associated with short-term implants, potentially acting as a protective barrier against the surrounding cellular environment. The initial step in achieving this goal involves the development of a hydrophilic polymer network capable of binding to titanium.

The literature reports a diverse array of compounds suitable for hydrogel polymer networks. While some are derived from natural sources such as polysaccharides.[17] or polypeptides,[18] synthetic polymers, including polyacrylamides,[16] polyacrylates, and poly(2-oxazoline)s,[19] offer greater versatility. The advantage of synthetic polymers lies in the ability to tailor their properties through judicious selection of monomeric composition and subsequent modification reactions. This allows for precise control over characteristics such as chain length, molar mass, functional groups, and overall polymer architecture. To generate covalent polymer networks, two general strategies are applicable: the use of multifunctional crosslinker comonomers for in situ network formation during polymerization, or the activation of trigger-sensitive moieties in pre-formed single-chain polymers to enable post-polymerization crosslinking.[20] The latter approach offers the advantage of processing the soluble single-chain polymers into coatings before inducing network formation. Photocrosslinking presents a particularly convenient type of post-polymerization crosslinking, enabling network generation from pre-synthesized polymers through light irradiation, with azide.[21] and benzophenone derivatives.[22] being prominent examples of photocrosslinking groups. An additional prerequisite for the hydrogel coating is a strong covalent bonding to the titanium implant. Phosphonic acid groups have emerged as potent anchor units for robust attachment to oxidized titanium surfaces.[23] Antibacterial features can be incorporated into the polymer network via physical embedding or chemical attachment of active agents. To prevent loss of the antibacterial function over time, covalent bonding of the active species to the gel structure or imparting intrinsic antibacterial motifs directly to the polymer backbone are effective strategies.

In this study, we present a novel approach that combines antiadhesive acrylamide-based hydrogels with benzophenone photocrosslinkers possessing intrinsic antibacterial properties and phosphonic acid anchor groups specifically targeting titanium substrates. This particular design aims to address the multifaceted requirements of coatings for short-term titanium implants, potentially offering a significant advancement in implant technology.

## 2. Experimental Section

### 2.1. Equipment, Methods and Chemicals

#### *2.1.1. Equipment and Methods*

The reactions were performed under an inert gas atmosphere with dried glassware.

 © 2025 The Author(s). Macromolecular Rapid Communications published by Wiley-VCH GmbH



15213927, 0, Downloaded from https://onlinelibrary.wiley.com/doi/10.1002/marc.202400989, Wiley Online Library on [12/03/2025]. See the Terms and Conditions (https://onlinelibrary.wiley.com/terms-and-conditions) on Wiley Online Library for rules of use; OA articles are governed by the applicable Creative Commons License

All $^{1}$H and $^{13}$C NMR spectra were recorded with a spectrometer from Jeol Type ECZ 500. The $^{1}$H NMR measurements were recorded at a frequency of 500 MHz and the $^{13}$C NMR measurements at 126 MHz at room temperature (≈20 °C). $^{31}$P NMR (17.5 MHz) spectra were recorded at 28.5 °C on a Spinsolve 43 Phosphorus Benchtop NMR (Magritek, Aachen, Germany) with an internal NMR device reference. The chemical shifts of the signals $\delta$ were specified in ppm. The peaks of the undeuterated solvents were used as an internal standard. All recorded spectra were analyzed with the software MestReNova. The following abbreviations were utilized to describe NMR peak patterns: s = singlet, d = doublet, t = triplet, and dd = doublet of doublets.

Molar mass distributions and dispersities of polymers were measured by the Polymer Standard Service (PSS) SECcurity GPC system Agilent Technologies 1260 infinity. For measuring of RAFT-copolymers, the system was equipped with a PSS GRAM 100 Å column, and for measurement of FR-copolymers, a Gram Linear M column was used. In both cases, a 10 µm particle size pre-column was applied. A solution of DMAc with lithium bromide ($c$ = 1 g l$^{-1}$) was used as an eluent. For detection, an IR detector and a UV/Vis detector, adjusted to a wavelength of 280 nm, were applied. A sample volume of 20 µl was injected. A temperature of T ≈ 60 °C and a flow rate of 1 ml min$^{-1}$ were adjusted. The calibration curves were generated with poly(methyl methacrylate)-standards (PSS, Mainz), and the molar mass of the polymers was determined by the system software. Elemental analysis measurements were performed with the EA 3000 CHNS.

All cell culture plates (ultra-low attachment plates) or flasks used were from Cornig Inc. (New York, USA).

Titanium discs were manufactured from commercially pure grade 4 titanium (ISO 5832-2, Medartis, Basel, Switzerland). Discs measuring 14.5 mm in diameter/1.6 mm in thickness and 33.5 mm in diameter/1.6 mm in thickness were used in this study. The diameters were chosen to ensure that the discs would match the diameter of 6- and 24-well plates.

The titanium substrates were pre-treated with a Sicatech corona generator Uni-System LF1.

For photocrosslinking, the UV Crosslinker Bio-Link from LTF Labortechnik was used with a total energy of 8.6 J cm$^{-2}$.

Modified titanium discs were analyzed by environmental scanning electron microscopy (Quanta 250 FEG, FEI Deutschland GmbH, Dreieich, Germany) in low vac mode at 130 Pa and 20 keV, equipped with a combination of LF, GSE, and ET BSE detectors. Additional EDX was carried out with an EDS1, Apollo XL-SDD. The generated data was processed with the TEAMTM Enhanced V. 4.5 software.

For atomic force microscopy (AFM) experiments, tipless silicon FCL-5 cantilever with a nominal spring constant of 0.12 N m$^{-1}$ and a resonance frequency of 14 kHz (Applied NanoStructures, Inc., Mountain View, California, USA), Dry Borosilicate Glass Microspheres with a nominal diameter of 20 µm (Duke Standards, Fremont, California, USA), Norland Optical Adhesive 73 (Norland Products, Inc., Cranbury, New Jersey, USA), BLX-254 UV chamber (LTF Labortechnik, Wasserburg, Germany) equipped with T-8L UV light tubes for emission of UV light with a wavelength of 365 nm (Vilber Lourmat, Eberhardzell, Germany) and a TGT1 diffraction grating to visualize the bead-modified AFM tip (NT-MDT LLC, Moscow, Russia) were used. Scanning electron microscopy was performed using a CamScan CS24 electron microscope (Cambridge, UK). AFM measurements were performed using an MFP-3D-Bio atomic force microscope (Asylum Research, Santa Barbara, California, USA) and analyzed using Igor Pro 6.38B01 software (WaveMetrics, Lake Oswego, Oregon, USA). MilliQ-water was received from a Merck Millipore Direct Q 8 system (Millipore, Schwalbach, Germany) with a resistivity of 18.2 MΩ cm, hereinafter referred to as water. Force measurements were performed in polystyrene petri dishes (Sarstedt AG & Co. KG, Nümbrecht, Germany).

EVOS Fluoreszenz–Microscope (Thermo Fisher Scientific Inc. Waltham, USA), Digital microscope, Keyence BZ-X800 Series (Keyence Corporation of America Itasca, USA), Biological safety cabinets, NuAIRE, NU-440-600E, class II (NuAire Plymouth, USA), FACS (Cytoflex, Beckman Coulter, Brea, USA).

### 2.1.2. Chemicals

*N*-(2-hydroxyethyl) acrylamide (HEAm, 97%-Merck, Darmstadt, Germany), vinyl phosphonic acid (VPA, >= 90%-Sigma Aldrich, Steinheim, Germany), trifluoroacetic acid (TFA, 99%-Carl Roth, Karlsruhe, Germany), lithium bromide (LiBr, 98%-Alfa Aesar, Haverhill, Massachusetts, USA), 2,2′-azobis[2-(2-imidazolin-2-yl)propane] dihydrochloride (AIPC, 97%-Waco Chemicals, Neuss, Germany), and Lewatit MP62 (Lanxess, Köln, Germany) were used as received. Azobisisobutyronitrile (AIBN - Fluka, Charlotte, North Carolina, USA) and acrylamide (Am, Carl Roth, Karlsruhe, Germany) were both recrystallized from methanol twice. The solvents methanol (MeOH, 99.8%-Fisher Scientific, Schwerte, Germany), ethyl acetate (EtOAc, 99.8%), ethanol (EtOH, 99+%), ethanol absolute (abs. EtOH, 99,9+%), and *N,N*-dimethylacetamide (DMAc, 99.5% -all VWR, Darmstadt, Germany) were used without further purification. Deuterated solvents for NMR analysis (Deutero, Kastellaun, Germany) were used as received. MilliQ-water was taken from a Merck Millipore system ($\sigma$ = 18.2 MΩ cm, Millipore, Schwalbach, Germany).

### 2.1.3. Cell Culture

Media for both cell cultures DMEM/F-12 (1:1) (1X) + GlutaMAX-I Dulbecco´s Modified Eagle Medium F-12 Nutrient Mixture (Thermo Fisher, Waltham, USA) supplemented with 10% FCS (Biochrom GmbH, Berlin, Germany) and 1% Penicillin/Streptomycin (Sigma Aldrich, Steinheim, Germany). Tenocytes were isolated from waste material during surgery (see below), NHDF (normal human dermal fibroblasts) were purchased from Promocell (Heidelberg, Germany), L929 murine fibroblasts from ATCC (Manassas, USA), Accutase for cell detachment (Sigma Aldrich, Steinheim, Germany), for proliferation tests alamarBlue Cell Viability Reagent (Thermo Fisher, Waltham, USA), for cytotoxicity tests MTT (thiazolylblau-tetrazoliumbromid; Sigma Aldrich, Steinheim, Germany).

Human tenocytes were isolated from surgical tendon material obtained during the reconstruction of the anterior cruciate ligament (ACL plastic). The use of residual materials was approved by the ethics committee of the Landesärztekammer Rheinland-Pfalz in agreement with the university medical center and in


© 2025 The Author(s). Macromolecular Rapid Communications published by Wiley-VCH GmbH


15213927, 0, Downloaded from https://onlinelibrary.wiley.com/doi/10.1002/marc.202400989, Wiley Online Library on [12/03/2025]. See the Terms and Conditions (https://onlinelibrary.wiley.com/terms-and-conditions) on Wiley Online Library for rules of use; OA articles are governed by the applicable Creative Commons License

accordance with the principles expressed in the Declaration of Helsinki and the ICH Guidelines for GCP. All patients provided written consent. First, connective tissue, fatty tissue, and other types of tissue that were not required were carefully separated from the tendon material using a scalpel and forceps so that only the tendon structure remained intact. The cleaned tendon material was then cut into sterile 2 mm pieces using a scalpel. Depending on the size of the tendon, ≈10–20 pieces were prepared and transferred to a Petri dish and placed in cell culture medium containing ascorbic acid at a concentration of 50 µg $ml^{-1}$. Tenocytes grew out of the pieces and were approved to be tenocytes by fluorescent staining of typical markers.

#### 2.1.4. Microbiology Testing

Müller–Hinton–Agar (Thermo Fisher, Waltham, USA), BD Trypticase Soja–Agar (Becton Dickinson GmbH, New Jersey, USA), Mc Farland BSS 0.5 standard (Carl Roth GmbH + Co. KG, Karlsruhe, Germany), Staphylococcus aureus Culti–Loops subsp. ATCC 29213 (Fisher Scientific GmbH, Dreieich, Germany)

### 2.2. Synthesis Procedures

#### 2.2.1. Main Monomers

The main monomer *N*-(2-hydroxypropyl) acrylamide (HPAm) was prepared as reported elsewhere.[24] The acidic acid-based monomer *N*-(2-acetic acid) acrylamide (AaAm) was synthesized according to a published procedure.[25] The Boc-protected *N*-(2-aminoethyl) acrylamide (AEAm-Boc) was synthesized in a two-step reaction, according to the literature.[26] The Boc-protected *N*-(3-aminopropyl) acrylamide (APAm-Boc) was synthesized in a two-step reaction. In the first step, the single Boc-protected 1,3-diaminopropane (*N*-tert-butoxycarbonyl-1,3-diaminopropane) was synthesized according to a literature procedure.[27] In the second step, *N*-tert-butoxycarbonyl-1,3-diaminopropane was modified with acryloyl chloride to yield the corresponding vinylic monomer. The reaction was performed in analogy to the literature.[26]

#### 2.2.2. Crosslinker Monomers

The syntheses of the acrylamide-based crosslinker monomers-*N*-(4-benzophenyl)acrylamide (BPAm),[28–30] and [(4-benzoylphenyl)methyl]dimethyl[3-(prop-2-enamido)propyl]azanium bromide (BPQAAm).[31] were performed according to literature.

#### 2.2.3. Adhesion Monomers

Brij35 acrylate (B35A), was synthesized according to literature.[32]

#### 2.2.4. Chain Transfer Agents

The CTA 2-(dodecylthiocarbonothioylthio)-2-methylpropionic acid (DMP) was prepared in analogy to procedures published elsewhere.[33]

#### 2.2.5. Adhesion Polymer

The synthesis of the adhesion polymer poly($Am_{93}$-*co*-$BPAm_2$-*co*-$B35A_5$) was performed according to literature.[32]

#### 2.2.6. Anchor Polymers

Anchor polymers were synthesized via free radical polymerization according to the following general procedure. Vinyl phosphonic acid (VPA), *N*-(2-hydroxyethyl) acrylamide (HEAm), and 2,2′-azobis(isobutyronitrile) (AIBN) were dissolved in methanol (total volume $V_{total}$ = 5 ml) and the solutions purged with argon for 30 min while stirring. The solutions were placed in a pre-heated aluminum block (65 °C) and the reaction took place for 21 h. The reaction time was reached, and the polymerizations were quenched by cooling with liquid nitrogen and exposure to air. The polymers were precipitated in ice-cold ethyl acetate (120 ml), filtered off, and dried in a vacuum overnight. For specific amounts of educts, yields, and GPC analysis results, see Table S1 (Supporting Information).

#### 2.2.7. Co- and Terpolymers for Double Layer Coatings

For the preparation of double-layer coatings, 17 different polymers were synthesized via FR or RAFT polymerization. For each polymer, the monomers, initiator, and, in the case of RAFT polymerization, the CTA DMP were dissolved in methanol ($V_{total}$ = 2-5 ml). The reaction mixtures were purged with argon for 30 min and placed in a preheated oil bath or aluminum block (65 °C) for 16 to 24 h. After completion, the polymerizations were quenched by cooling with liquid nitrogen and exposure to air. All polymers were precipitated in ice-cooled ethyl acetate (200 ml) at least twice. The polymers were separated by centrifugation or filtration and dried under reduced pressure overnight. The specific amounts of educts, yields, and GPC analysis results are summarized in Tables S2 and S4 (Supporting Information).

#### 2.2.8. Deprotection of Polymers Containing Boc-Protected Amino Groups

In a dry 10 ml Schlenk tube typically 50–100 mg of the of polymers containing Boc-protected amino groups were dissolved in water (1.5 ml). To the mixture, TFA (0.5 ml) was added and the mixture was stirred at room temperature overnight. The polymers were precipitated in ice-cold THF. The precipitate was then redissolved in water and stirred with cationic ion exchange resin (Lewatit MP62) for 24 h. The resin was finally filtered off and the filtrate lyophilized. For specific amounts of educts, yields, and GPC analysis results, see Table S3 (Supporting Information).

### 2.3. Coating Procedures

#### 2.3.1. Coating of Poly(styrene) Well Plates

Aliquots of an adhesion polymer solution (70 µl for full coatings or one or two droplets for partial coatings, water/ethanol mixture


© 2025 The Author(s). Macromolecular Rapid Communications published by Wiley-VCH GmbH


15213927, 0, Downloaded from https://onlinelibrary.wiley.com/doi/10.1002/marc.202400989, Wiley Online Library on [12/03/2025]. See the Terms and Conditions (https://onlinelibrary.wiley.com/terms-and-conditions) on Wiley Online Library for rules of use; OA articles are governed by the applicable Creative Commons License

$V/V$ = 7:3, 2.5 mg ml$^{-1}$) were added in each well of a 24-well plate and the plate dried under reduced pressure overnight at $T$ = 40 °C. The dried polymer films were irradiated with UV-light ($\lambda$ = 254 nm) for 1 h. Afterward, the hydrogel precursor polymer stock solutions (200 µl for full coatings 10 µl for partial coatings, water/ethanol mixture $V/V$ = 7:3, 25 mg ml$^{-1}$) were deposited on top of the adhesion polymer film and dried in vacuo overnight at $T$ = 40 °C. The dried films were irradiated with UV-light ($\lambda$ = 254 nm) for 1 h. The polymer networks were washed by swelling in water for at least 1 h, rinsed with ethanol, and dried in vacuum at $T$ = 40 °C.

#### 2.3.2. Coating of Titanium Substrates

The circular titanium substrates were pre-cleaned by scrubbing with detergent (akuta by Dalli Werke, Stolberg, Germany) and rinsing with water. Subsequently, the substrates were exposed to a Hellmanex (VWR, Darmstadt, Germany) cleaning solution (3%) overnight at room temperature. The cleaned disks were rinsed with water and ethanol, dried in a nitrogen stream, and treated with a corona discharger for ≈10 s. Directly after the treatment, the titanium disks were immersed into water. For full coatings, the pre-treated titanium disks were immersed in an aqueous anchor polymer solution (1 mg ml$^{-1}$) overnight. For partial coatings, the pre-treated titanium disks were immersed halfway in an aqueous anchor polymer solution (1 mg ml$^{-1}$) overnight, by placing them upright into a suitable container. The titanium disks were then rinsed with water and ethanol, placed into 24 well plates, and dried under reduced pressure at $T$ = 40 °C for 2 h. Afterward, the hydrogel precursor polymer stock solutions (200 µl for full coatings or 100 µl for partial coatings, water/ethanol mixture, $V/V$ = 7:3, 25 mg ml$^{-1}$) were deposited on top of the anchor polymer film and dried in vacuo overnight at $T$ = 40 °C. The dried films were irradiated with UV-light ($\lambda$ = 254 nm) for 1 h. After completing crosslinking, the polymer networks were washed by swelling in water for at least 1 h, rinsed with ethanol, and dried in a vacuum at $T$ = 40 °C.

### 2.4. Analyses

#### 2.4.1. AFM Measurements

Force measurements were carried out on the hydrogel by measuring single force curves in air and force maps of 90 µm size with 100 force curves per force map in water. Individual force curves were analyzed by applying the software-implemented algorithm for offset correction to determine the point of contact and then applying the Hertz model to fit the approach curve from 0 to 40% of indentation depth. The radius of the indenter was assumed to be a spherical indenter with a radius of 10 µm having a Young´s modulus of 68 GPa and a Poisson ratio of 0.19 as defined in the software. For the sample, a Poisson ratio of 0.33 was assumed, according to the literature.[34]

### 2.5. In Vitro Tests

#### 2.5.1. Cytotoxicity Assay

In vitro cytotoxicity was analyzed analogously to ISO 10993-5 using the MTT ([3-(4,5-dimethylthiazol-2-yl)- 2,5-diphenyltetrazoliumbromid)]) assay. Mouse L929 cells (10000 cells well$^{-1}$) were seeded in a 96-well tissue culture plate for 24 h. Polymers either on 24 cell culture plates or titanium discs in 24 well plates were incubated in 1 mL cell media for 24 h. ≈100 µL of this extract was given to L929 cells in the 96-well plate. After an incubation time of 24 h, the MTT assay was performed, and the colorimetric readout was performed at a wavelength of 570 nm (reference wavelength 650 nm). Zinc diethyl dithiocarbamate (ZDEC) and zinc dibutyl dithiocarbamate (ZDBC) (Food and Drug Safety Center, Hatano Research Institute, Hadano, Japan) were used as positive controls as they induce a reproducible cytotoxic reaction.

#### 2.5.2. Lentiviral Transduction

Gene transfer of eGFP into NDHF and tenocytes was achieved by lentiviral transduction. The eGFP encoding lentiviral vector pHR0-SEW was used to prepare vector supernatants by transfection of 293T cells as previously described.[11,35] For gene transfer, 15.000 cells were seeded into 24-well tissue culture plates. Two rounds of transduction on days 1 and 3 were performed at a cumulative multiplicity of infection (MOI) of *100 to achieve 90–95% gene marking. Transduction efficiency was confirmed by flow cytometry.

#### 2.5.3. Adhesion Assays

For the investigation of cell adhesion and cell growth, 20 000 fibroblasts or tenocytes were seeded per well/titanium disc. The volume calculated for 20000 cells was pipetted onto the titanium discs or the coated well and as a control on uncoated cell culture wells. The fluorescence microscopic examination of cell growth and cell adhesion was carried out on day 1, day 3, and day 7 after sowing. The images were taken according to a standardized scheme to facilitate comparison of the images.

On the monitoring days, overview images were taken at magnifications of 2x and 4x as well as detailed images at a magnification of 10x. The image sections of the overview images were based on the following areas: I. Upper outer edge area, II. right outer edge area, III. lower outer edge area, IV. Left outer rim area and V. Centre. At least 3 experiments were carried out for each coated cell culture well or titanium disc.

In order to test whether the non-adherent cells were still viable, they were transferred to a culture well to test if they were still able to adhere and proliferate after contact with the polymer.

#### 2.5.4. Microbial Testing

The polymers used were analyzed for an intrinsic antimicrobial effect. The bacterium Staphylococcus aureus was used to


© 2025 The Author(s). Macromolecular Rapid Communications published by Wiley-VCH GmbH


15213927, 0, Downloaded from https://onlinelibrary.wiley.com/doi/10.1002/marc.202400989, Wiley Online Library on [12/03/2025]. See the Terms and Conditions (https://onlinelibrary.wiley.com/terms-and-conditions) on Wiley Online Library for rules of use; OA articles are governed by the applicable Creative Commons License

demonstrate this effect. Staphylococcus aureus was cultured and afterward diluted to a turbidity corresponding to McFarland Standard 4. Subsequently, 2 µl of this bacterial suspension and 1000 µl of culture medium were pipetted onto the coated titanium discs incubated at 37 °C for 24 h. After incubation, on the one hand, $OD_{600}$ was measured and on the other hand, the contaminated medium was plated on Mueller–Hinton culture media, and after 24 h colonies were documented photographically after spreading in order to record bacterial growth.

## 3. Results and Discussion

This chapter details the multi-step development process for effective hydrogel coatings on short-term titanium implants. First, the synthesis and evaluation of the monomer and polymer components are discussed, as these directly impact the hydrogel's key characteristics. The coating procedure is then described, outlining the methods for achieving uniform surface coverage on the titanium substrates. Finally, the biological performance of the coatings is evaluated through in vitro assessment of cellular response and bacterial colonization.

### 3.1. Monomer and Polymer Synthesis

An overview of the building blocks, which are divided into crosslinker monomers, interface-active monomers, main monomers, and the chain transfer agent, is given in **Scheme 1**, part I.

#### *3.1.1. Monomer Syntheses*

The coatings for the short-term titanium implants were developed using a variety of monomers with different functionalities. The first category comprises the crosslinker monomers, which have a double bond for polymerization and a photoreactive benzophenone unit to enable crosslinking between polymer chains upon irradiation. Two different crosslinker monomers were synthesized and evaluated. The first, BPAm, is a well-established photocrosslinker monomer.[36] The synthesis of BPAm was performed following literature procedures,[28–30] Briefly, 4-aminobenzophenone was exposed to an excess of acryloyl chloride, forming the BPAm monomer with a yield of 88%. However, BPAm has poor solubility in aqueous media, which would not be ideal for the biological environment surrounding the implants. Good solubility in water-based bodily fluids would be more beneficial for this application. The second photocrosslinker, BPQAAm, has a similar structure to BPAm but includes a quaternary ammonium unit in the spacer between the photoreactive and polymerizable moieties. The permanently positive charge of the ammonium group provides higher affinity toward water and is a common motif in antibacterial agents.[37] BPQAAm was synthesized in a two-step reaction sequence as previously published.[31] In the first step, bromination of 4- methylbenzophenone with *N*-bromosuccinimide and azobisisobutyronitrile (AIBN) was performed, yielding 84% of 4-bromomethyl benzophenone. In the second step, *N*-[3- (dimethylamino)propyl]acrylamide was quaternized with 4-bromomethyl benzophenone to yield 90% of the final product BPQAAm.

Another monomer type is the interface-active monomers, which promote adhesion to specific surfaces. The amphiphilic surfactant monomer B35A, with a hydrophobic alkyl chain, was used for less polar polymeric surfaces like polystyrene well plates, where the alkyl chains can adsorb through hydrophobic interactions. B35A was synthesized from the surfactant Brij 35 in 91% yield by substituting the terminal OH group with acryloyl chloride under basic conditions, according to the literature.[25] For the oxidized titanium surface, the commercially available vinyl phosphonic acid (VPA) was employed as anchor group.

The main monomers serve as the foundation for the hydrophilic polymer networks. Their highly hydrophilic characteristics complement the specific functions of the other monomer types, embedding them in an environment well-suited for strong interactions with aqueous solutions. The well-established hydrophilic monomers acrylamide (Am) and hydroxyethyl acrylamide (HEAm) were obtained from commercial suppliers, while the additional main monomers 2-hydroxypropyl acrylamide (HPAm).[24] and the acrylamide of glycine (AaAm).[25] were synthesized following published procedures. The synthesis of HPAm involved an exothermic reaction of 1-amino-2-propanol with acryloyl chloride, yielding 30% of the target monomer. For AaAm, a reaction between glycine and acryloyl chloride under basic conditions resulted in an 11% yield. Additionally, the Boc-protected monomers *N*-(2-aminoethyl)acrylamide-Boc (AEAm-Boc).[26] and *N*-(3-aminopropyl)acrylamide-Boc (APAm-Boc).[26,27] were synthesized in a two-step reaction sequence. The first step involved the reaction of the corresponding diamine with di-*tert*-butyl dicarbonate yielding 80% and 41% of the mono-Boc-functionalized diamine precursors, respectively. This step was followed by the conversion of the mono-Boc-functionalized diamines to the acrylamides using acryloyl chloride under mild basic conditions, resulting in 73% of AEAm-Boc and 94% of APAm-Boc. In addition to their role as a hydrophilic matrix base, the monomers AaAm, AEAm-Boc, and APAm-Boc offer the potential for post-polymerization modification with specific functional groups.

#### *3.1.2. Polymer Syntheses*

Two different polymerization methods were explored for the polymer structures shown in Scheme 1, part II: free radical polymerization (FRP) and reversible addition-fragmentation chain transfer polymerization (RAFT polymerization). FRP is easily implemented yet allows less control, leading to high molar masses with a broad distribution.[38] In contrast, RAFT polymerization provides a higher degree of control by employing chain transfer agents (CTAs) to mediate the interchange of active radical sites at the chain ends. This allows to target the molar mass of the polymer with dispersities $Đ$ as low as 1.2.[38] The CTA fragment remains as an end group in the RAFT polymers, which is in contrast to the FRP polymers that feature chain ends resulting from the initiator and termination reaction. All structures of the synthesized polymers can be found in the overview graphic (see Figure S1, Supporting Information). The effect of the structural difference in both polymer types on their performance as antiadhesive and antibacterial coatings was evaluated in in vitro


© 2025 The Author(s). Macromolecular Rapid Communications published by Wiley-VCH GmbH


15213927, 0, Downloaded from https://onlinelibrary.wiley.com/doi/10.1002/marc.202400989, Wiley Online Library on [12/03/2025]. See the Terms and Conditions (https://onlinelibrary.wiley.com/terms-and-conditions) on Wiley Online Library for rules of use; OA articles are governed by the applicable Creative Commons License

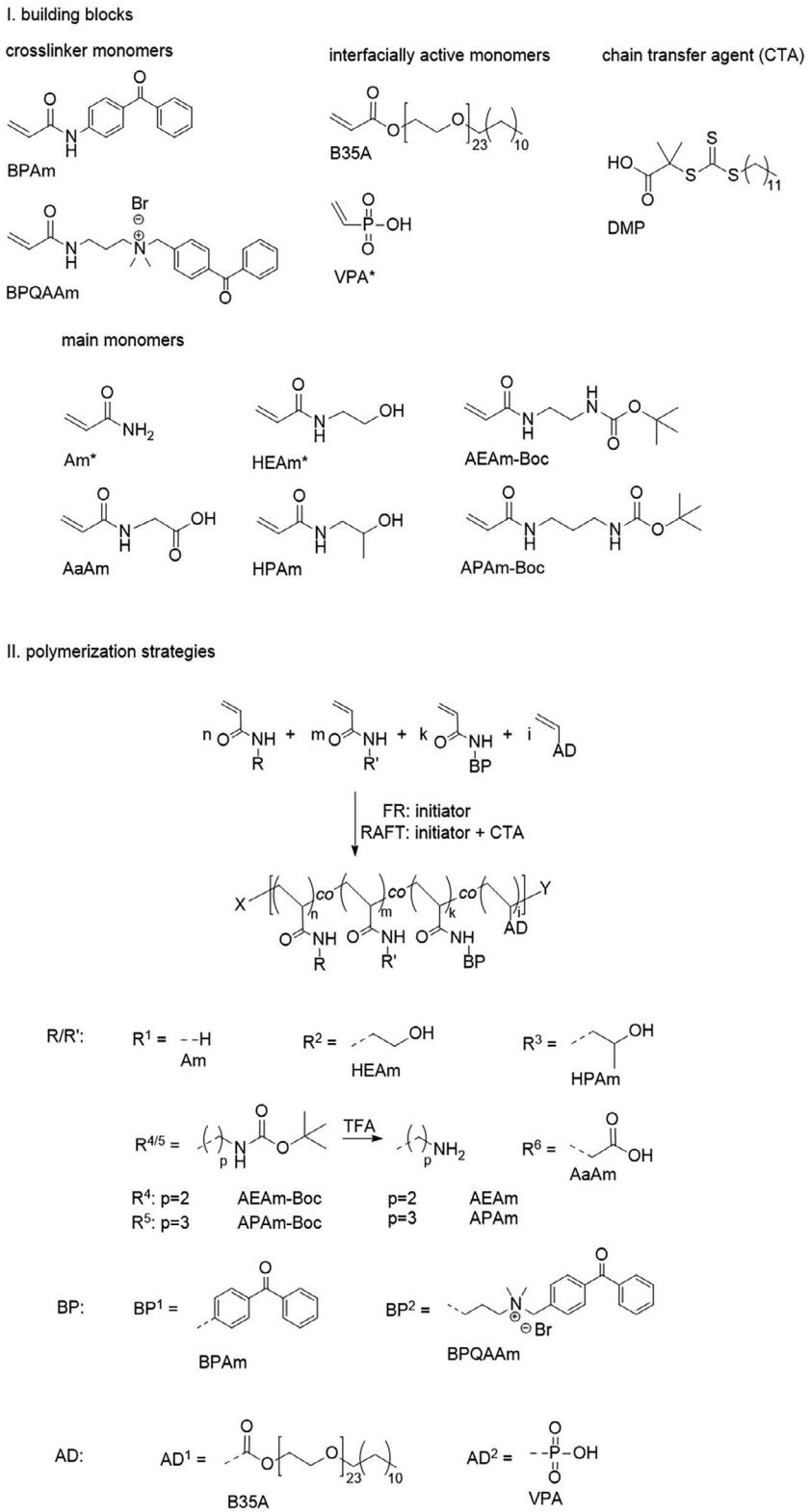


**Scheme 1.** Structures of the building blocks and synthesis strategies for the antifouling polymers, with AD = adhesion promoting group, BP = benzophenone crosslinker, and R/R' = main comonomer units (* commercially available compounds).

 © 2025 The Author(s). Macromolecular Rapid Communications published by Wiley-VCH GmbH



15213927, 0, Downloaded from https://onlinelibrary.wiley.com/doi/10.1002/marc.202400989, Wiley Online Library on [12/03/2025]. See the Terms and Conditions (https://onlinelibrary.wiley.com/terms-and-conditions) on Wiley Online Library for rules of use; OA articles are governed by the applicable Creative Commons License

with cells and bacteria, as described in the biological experiments further below.

DMP as CTA for the RAFT polymerizations was obtained with a yield of 39% in a one-pot reaction according to the literature.[33] by first adding carbon disulfide to a solution of *n*-dodecanethiol and triethylamine, followed by reaction with $\alpha$-bromoisobutyric acid.

The adhesion promoter polymer poly(Am-*co*-B35A-*co*-BPAm) (**AP0**, Figure S1, Supporting Information) provides covalent attachment of the hydrogel precursor polymers to polystyrene well plates and was prepared according to the literature.[32] via FRP of acrylamide, the surfactant monomer B35A, and the crosslinker monomer BPAm with a yield of 83%.

For attachment to titanium surfaces, a variety of phosphonic acid-containing anchor polymers (**AP1-AP4**, Figure S1, Supporting Information) were synthesized. Vinyl phosphonic acid (VPA) and hydroxyethyl acrylamide (HEAm) were copolymerized in varying ratios (2, 5, 10, and 20 mol% VPA) using AIBN as initiator. The GPC results indicate a rapid increase in dispersity $Đ$ with higher VPA content, from 1.6 for 2 mol% VPA to 3.0 for 20 mol% VPA, in line with literature reports.[39] However, the molar masses in the presence of VPA (30–34 kg mol$^{-1}$) matched the HEAm homopolymer equivalent prepared by FRP (32 kg mol$^{-1}$). It was challenging to determine the actual VPA content incorporated into the copolymers, as the $^{1}$H NMR signals of the HEAm and VPA-based repeat units overlap, precluding quantitative analysis. However, the $^{31}$P NMR spectra qualitatively show an increase in phosphorus content with higher VPA monomer feed, suggesting successful copolymerization.

A broad range of hydrogel precursor polymers (**A** – **P**, Figure S1, Supporting Information) were synthesized via both FRP and RAFT polymerization (see Tables S2–S4, Supporting Information). The reactions typically yielded 65–98% of the target polymers. The RAFT-derived polymers showed molar masses from 11 to 39 kg mol$^{-1}$, fluctuating around the target mass of 25 kg mol$^{-1}$, with low dispersities from 1.2 to 1.4. In contrast, the FRP products had higher molar masses (≈40–70 kg mol$^{-1}$) and broader dispersities between 2.2 and 3.8, as expected for uncontrolled polymerizations.[38] For the APAm-Boc and AEAm-Boc-containing polymers **A** and **B**, the Boc protecting groups were cleaved by reaction with TFA, and treated with a basic ion exchanger to yield the free amino side groups. This deprotection step resulted in a reduction of the apparent molar masses in GPC, likely due to the loss of the Boc group affecting the polymer hydrophilicity and consequently the hydrodynamic radii.

### 3.2. Coatings on Polystyrene and Titanium Substrates

The efficacy of the prepared polymers as hydrogel coatings in terms of antiadhesion was evaluated by modifying sterile tissue-grade polystyrene well plates with the polymers. Two different setups were employed: fully coated wells and partially coated wells. The partially coated wells were used to determine if the cells would remain viable and adhere near the coated area on the well plate bottom. The fully coated wells were specifically used for the toxicity and cell viability tests.

#### *3.2.1. Coatings on Polystyrene Well Plates*

The coating procedure involved first applying an adhesion polymer layer by dissolving the respective polymer in a water and ethanol mixture and adding it to the well. This layer was then dried and crosslinked using UV light. Subsequently, a layer of the hydrogel precursor polymer was added by applying a solution of the polymer on top of the adhesion polymer layer. This layer was then dried, crosslinked, and washed by adding water and allowing it to sit for 1 h. Finally, the wells were cleaned with ethanol and dried before performing the cell and bacteria tests.

#### *3.2.2. Coatings on Titanium Disks*

For the coating of titanium substrates, the above-described anchor polymers **AP1** – **AP4** (see Figure S1, Supporting Information) were developed. The circular titanium disks used as the substrate were prepared for the coating procedure by scrubbing with detergent, followed by rinsing with water and incubation in an alkaline cleaning solution. To activate the surface, the disks were exposed to a corona discharge for several seconds and placed directly into water to generate OH groups on the titanium surface. The cleaned and activated titanium disks were incubated in an anchor polymer solution overnight, rinsed with water and ethanol, and dried. The hydrogel precursor polymer was then dissolved and added to the disk, which was placed inside a well plate. The precursor polymer layer was dried, crosslinked with UV light, and washed by exposure to water. Finally, the disks were rinsed with ethanol, dried, and used for the in vitro tests, discussed further below. A workflow of the titanium sample preparation is shown in **Figure 1**.

#### *3.2.3. Contact Angle Measurements*

The effect of the modification steps on the titanium surface was analyzed by measuring the static and dynamic water contact angles (CAs) for titanium disks as received, after cleaning, and with the anchor polymer coatings. The results (see Figures S8 and S9, Supporting Information) show that the as-received titanium disks had relatively high water contact angles, ranging from 68° for static CA to ≈90° for dynamic CA. These comparably high CAs are rather unexpected for the polar titanium oxide material found on titanium under ambient conditions and suggest adsorbates that contaminate the surface. After applying the aforementioned cleaning procedure, the contact angles decreased significantly to 36° static CA and ≈45° dynamic CA. After application of the anchor polymer layer containing 10% VPA, even lower contact angle values of 29° static CA and 25° dynamic CA were observed. These findings indicate successful modification of the titanium surface with the anchor polymers and demonstrate the increased hydrophilicity of the coated substrates, facilitating the spreading of the aqueous hydrogel precursor solutions. As the titanium substrates with the hydrogel coating comprising the anchor polymer and the crosslinked hydrogel precursor were swollen and completely wetted by water, contact angles were too low to be measured.

 © 2025 The Author(s). Macromolecular Rapid Communications published by Wiley-VCH GmbH



15213927, 0, Downloaded from https://onlinelibrary.wiley.com/doi/10.1002/marc.202400989, Wiley Online Library on [12/03/2025]. See the Terms and Conditions (https://onlinelibrary.wiley.com/terms-and-conditions) on Wiley Online Library for rules of use; OA articles are governed by the applicable Creative Commons License

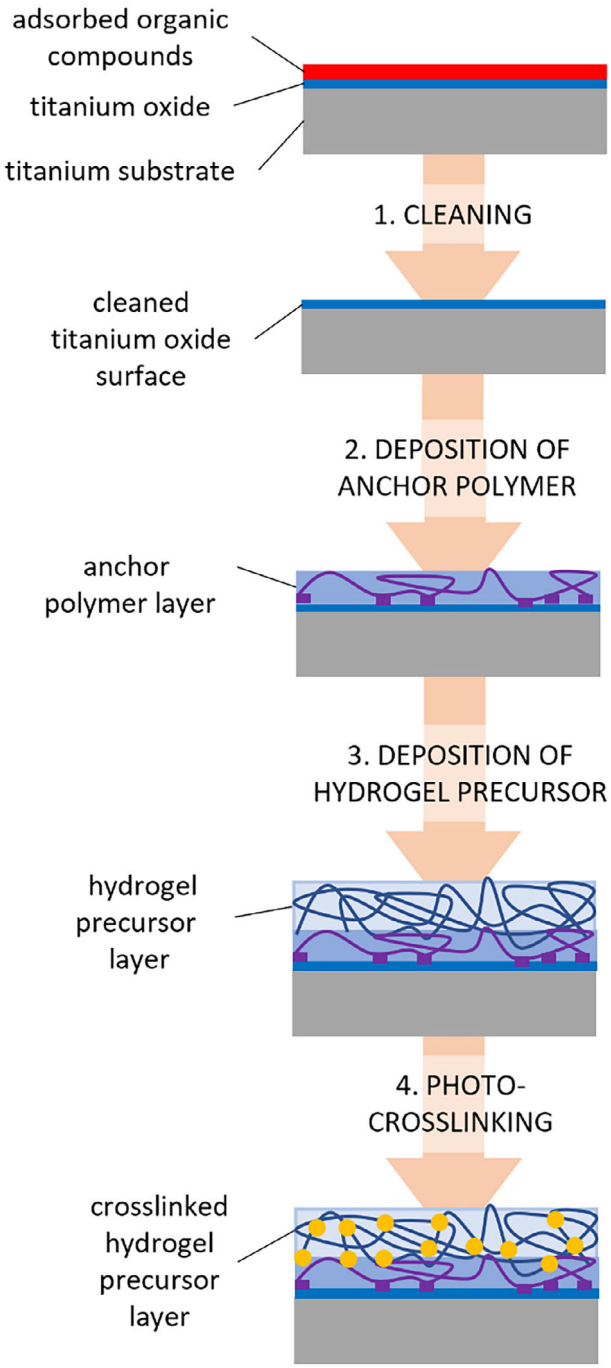


**Figure 1.** Schematic illustration of the process to generate a multi-layer coating on titanium substrates. The process involves the deposition of an anchor polymer layer, followed by the deposition of a hydrogel precursor layer and photocrosslinking inducing network formation. When implanted, this network absorbs water from the surrounding tissue to swell into the antiadhesive hydrogel coating.

#### *3.2.4. ESEM-EDX Measurements*

To corroborate the two-layer architecture of the polymer network coating, environmental scanning electron microscopy (ESEM) coupled with energy-dispersive X-ray (EDX) spectroscopy was utilized. **Figure 2** shows the results of this measurement for a polymer-coated titanium sheet, which was cooled with liquid nitrogen and cut in half to expose the cross-section. The ESEM-EDX analysis of the cross-section revealed the expected sandwich structure of the coating, with the carbon signal (black trace) following the position of the overall organic layers. A distinct peak in the phosphorus signal (violet trace) at the interface between the titanium substrate and the hydrogel precursor layer indicates the successful binding of the phosphonic acid-containing anchor polymer to the titanium surface.

#### *3.2.5. AFM Measurements*

The mechanical properties of the swollen hydrogel coatings on the titanium substrates were investigated using atomic force microscopy (AFM). For this purpose, the hydrogel layer was indented by a spherical tip with a diameter of ≈25 µm mounted on a cantilever with a spring constant of 250 ± 30 pN $nm^{-1}$ (for further details see Figures S12–S17, Supporting Information). From these measurements, Young's modulus of the hydrogel coatings was determined by a Hertzian model with a maximum value of 10.3 kPa and a full width at half maximum of 11.2 kPa, as derived from a Gaussian fit. These values are in good agreement with the typical range of 0.2 kPa to 50 kPa reported for Young's moduli of swollen hydrogels, depending on the degree of crosslinking.[40,41]

From optical inspection and morphological analysis with the above methods (ESEM and AFM) a homogeneous surface coating with the polymers was confirmed (see Figures S18–S21, Supporting Information).

### 3.3. In Vitro Experiments

#### *3.3.1. Cytotoxicity Tests*

Before proceeding with cell and bacterial tests, the cytotoxicity of the polymers was evaluated following the DIN ISO 10993-5 standard (Biological Evaluation of Medical Devices-Tests for In Vitro Cytotoxicity). The results revealed cell viability ranging from 50 to 220%, indicating varying effects of the polymers on the cells (see **Figure 3**). Materials with cell viability below 70% were deemed non-biocompatible and excluded from further investigation in cell culture and bacterial experiments.

The polymers **A** to **I** contain the end groups from RAFT polymerization and are more cytotoxic than the polymers **J** to **P** prepared by free radical polymerization. To reduce the number of tests to be performed on titanium substrates, the three best-performing polymers from different classes were selected: **A** was

 © 2025 The Author(s). Macromolecular Rapid Communications published by Wiley-VCH GmbH



15213927, 0, Downloaded from https://onlinelibrary.wiley.com/doi/10.1002/marc.202400989, Wiley Online Library on [12/03/2025]. See the Terms and Conditions (https://onlinelibrary.wiley.com/terms-and-conditions) on Wiley Online Library for rules of use; OA articles are governed by the applicable Creative Commons License

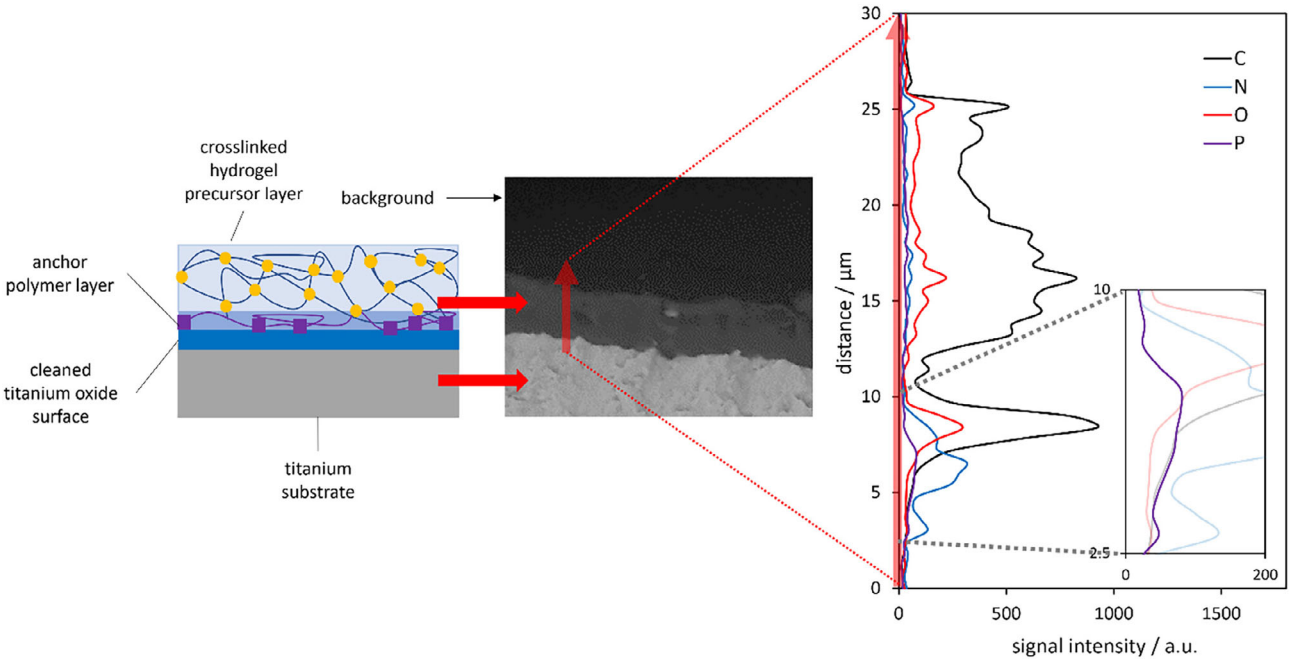


**Figure 2.** Environmental scanning electron microscopy (ESEM) image of the cross-section of a coated titanium substrate cut in half. The red arrow indicates the direction of the line scan for the EDX analysis shown on the right-hand side. The insert highlights the trace of the phosphorous signal (violet) from the anchor polymer layer.

chosen from the RAFT polymers with the lowest cytotoxicity from this group, **M** from the class of free radical polymerization, and **N** from free radical polymerization additionally including an antibacterial motif. As those polymers do not contain an anchor group for the titanium substrate, the titanium surface was first treated with a polymer containing a phosphonium anchor motif. As a first biological evaluation, the biocompatibility of the combined coating was confirmed (**Figure 4**).

### *3.3.2. Adhesion Tests*

Primary fibroblasts and tenocytes were seeded onto cell culture plates partially coated with the polymer. As illustrated in **Figure 5**, using tenocytes and the most promising polymer **N** as an example, the cells exclusively adhered to the uncoated areas of the plate. No cell adhesion occurred on the polymer-coated regions. Similarly, no adhesion was observed on fully coated plates.

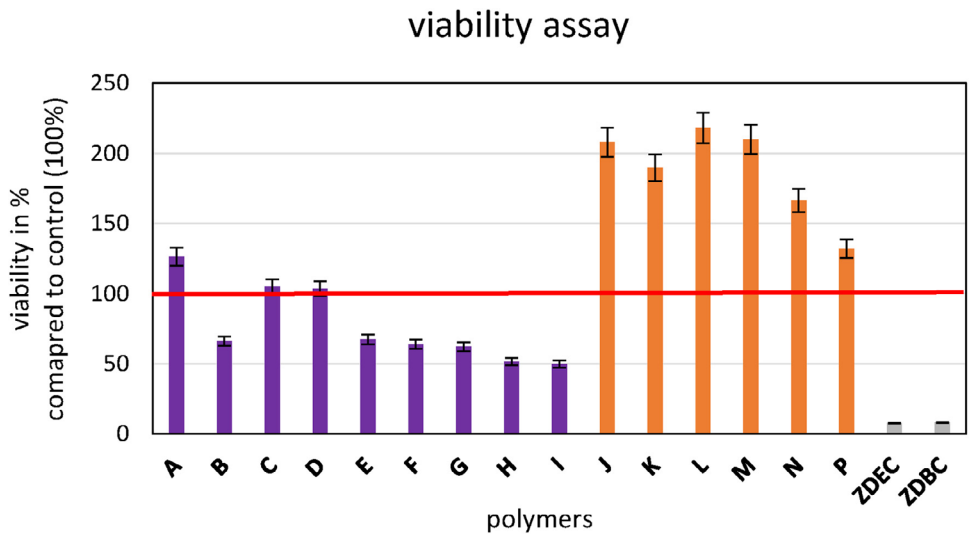


**Figure 3.** MTT tests performed analogous to ISO 10993-5 show the different effects of the tested polymers. The red line represents the viability with normal cultivation medium (100%); ZDEC and ZDBC: cytotoxic controls. Polymers synthesized by RAFT polymerization are shown in purple, while FRP-derived polymers are highlighted in orange.

 © 2025 The Author(s). Macromolecular Rapid Communications published by Wiley-VCH GmbH



15213927, 0, Downloaded from https://onlinelibrary.wiley.com/doi/10.1002/marc.202400989, Wiley Online Library on [12/03/2025]. See the Terms and Conditions (https://onlinelibrary.wiley.com/terms-and-conditions) on Wiley Online Library for rules of use; OA articles are governed by the applicable Creative Commons License

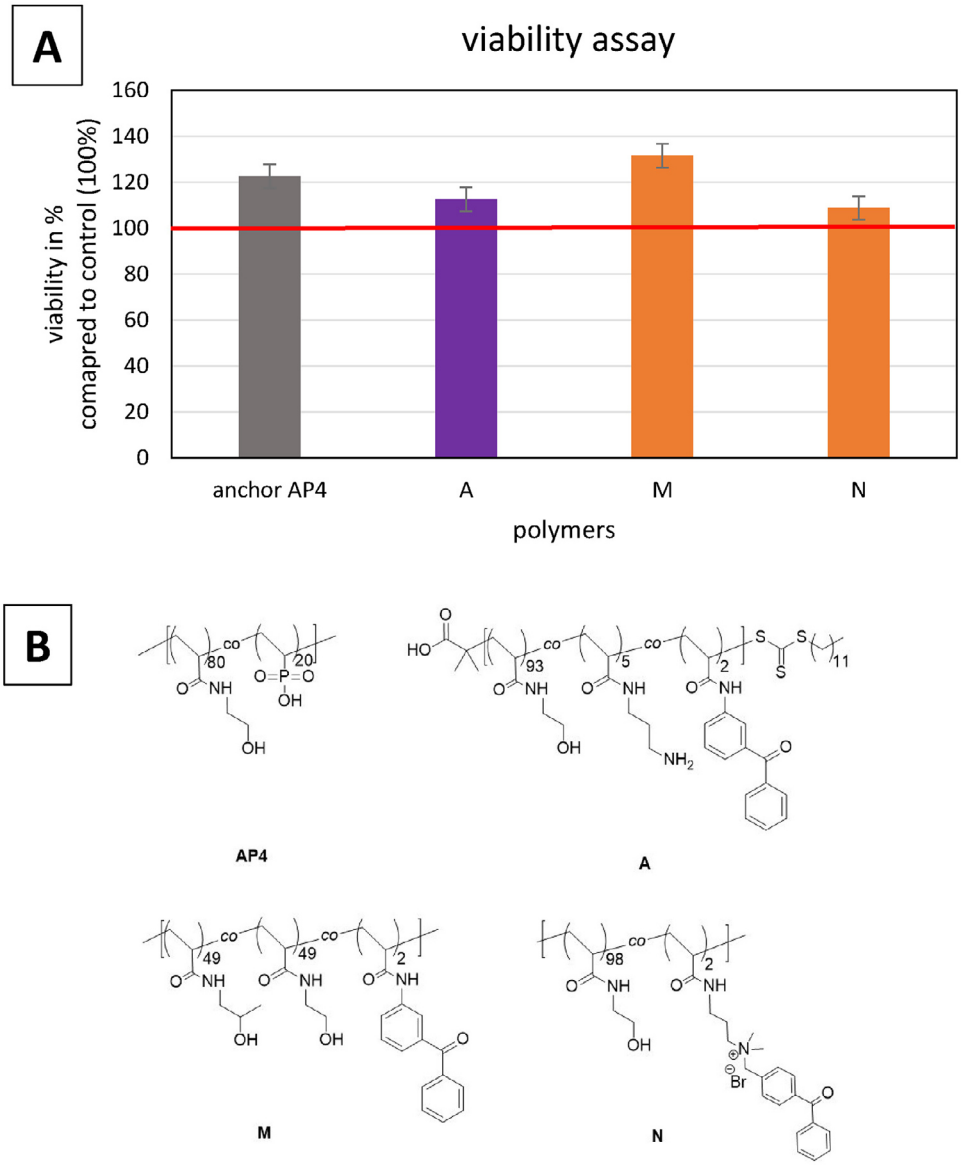


**Figure 4.** (A) MTT tests performed analogous to ISO 10993-5 show the different effects of the tested polymers. The red line represents the viability with a normal cultivation medium (100%). RAFT polymers are shown in purple, while FRP-derived polymers are colored in orange. (B) Structures of the polymers with the best performances.

However, the non-adherent cells remained viable, as demonstrated by their ability to adhere and proliferate after being transferred to a standard cell culture plate.

Polymers **A**, **M**, and **N** were subsequently applied to fully coated titanium discs. **Figure 6** illustrates the discs coated with polymers **A** and **M**. On these surfaces, cells not only adhered to the coated areas but also, in the case of polymer **A**, the coating dissolved from the titanium surface. Due to these findings, both polymers **A** and **M** were excluded from further analysis.

**Figure 7** demonstrates that cells adhere extensively, fully covering the surface of uncoated titanium discs (A and B). In contrast, no cell adhesion was observed on titanium surfaces coated with polymer **N**. Consistent with results from coated cell culture surfaces, the non-adherent cells remained viable, as evidenced by their ability to adhere and proliferate when transferred to uncoated titanium discs (data not shown).

Cells seeded on unmodified cell culture plates or titanium surfaces exhibit their typical phenotype with the formation of a dense cell layer and cell-cell contacts. Surface coating with polymer **N** abolished cell adhesion completely without being cytotoxic to the cells. This finding makes the investigated polymer coating particularly interesting for clinical applications in short-term implants, as it offers a potential method to minimize the risks associated with explantation. To our knowledge, no clinically proven surface modifications exist that reduce tissue or tendon adhesion to titanium implants in trauma surgery. Some experimentally tested

 © 2025 The Author(s). Macromolecular Rapid Communications published by Wiley-VCH GmbH



15213927, 0, Downloaded from https://onlinelibrary.wiley.com/doi/10.1002/marc.202400989, Wiley Online Library on [12/03/2025]. See the Terms and Conditions (https://onlinelibrary.wiley.com/terms-and-conditions) on Wiley Online Library for rules of use; OA articles are governed by the applicable Creative Commons License

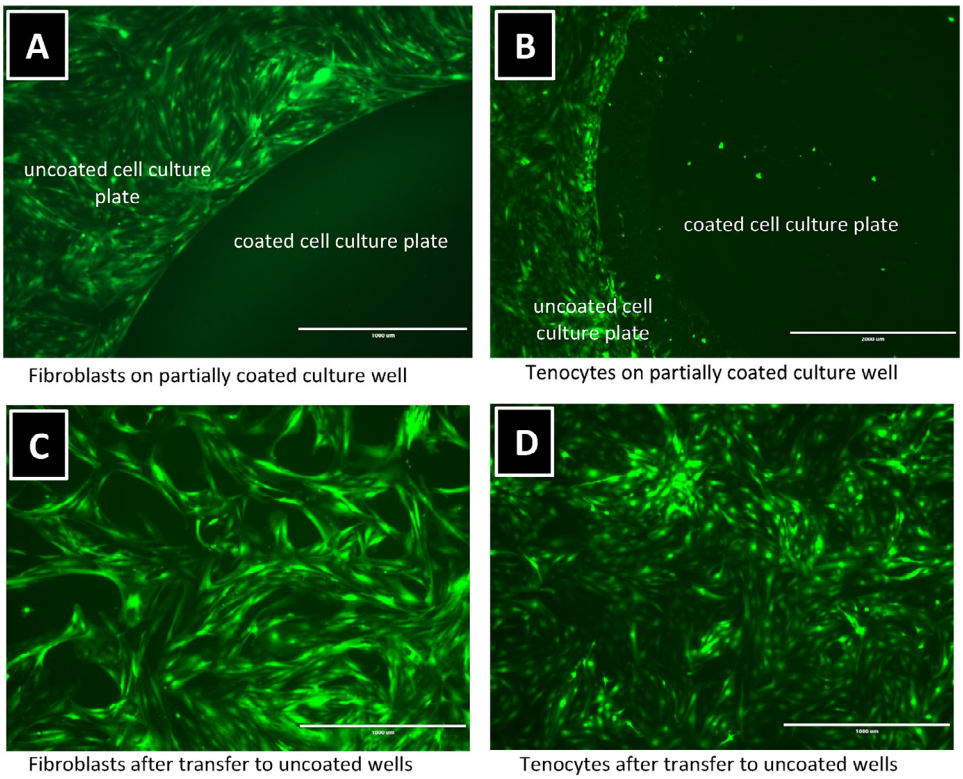


**Figure 5.** (A) Fibroblasts and (B) tenocytes seeded on partially coated cell culture plates with polymer N and after transfer to uncoated plates with (C) fibroblasts and (D) tenocytes. Similar observations were obtained with the polymers A and M (data not shown).

modifications based on polished titanium or in a titanium molybdenum alloy.[42,43] have been described in vitro and in vivo to inhibit tissue adhesion.[44] Kuhn et al. described reduced fibroblast adhesion and proliferation after plasma polymerization with hexamethyldisiloxane (HMDSO).[11] However, none of these modifications have made it into clinical practice.

### 3.3.3. Bacteria Tests

The bacterium mainly responsible for infections in the field of bone osteosynthesis is Staphylococcus aureus.[45] Therefore, this bacterial strain was applied to the polymer layers diluted in a medium and after 24 h the OD was measured. Moreover, the medium was seeded on agar plates and the colony forming units (CFU) was detected.

**Figure** 8A shows the measurement of the OD600, calculated compared to the control (100%). Polymer **N** inhibited bacterial growth almost completely. This was confirmed by plating of the incubated medium on agar plates and analysis of the CFU. Figure 8 further exemplary shows the colonies on the control plate (Figure 8B) in comparison to polymer **N** (Figure 8C), indicating a clear anti-microbial effect of polymer **N**.

Countless studies exist analyzing antibacterial implant modifications and some antibiotic-releasing osteosynthesis

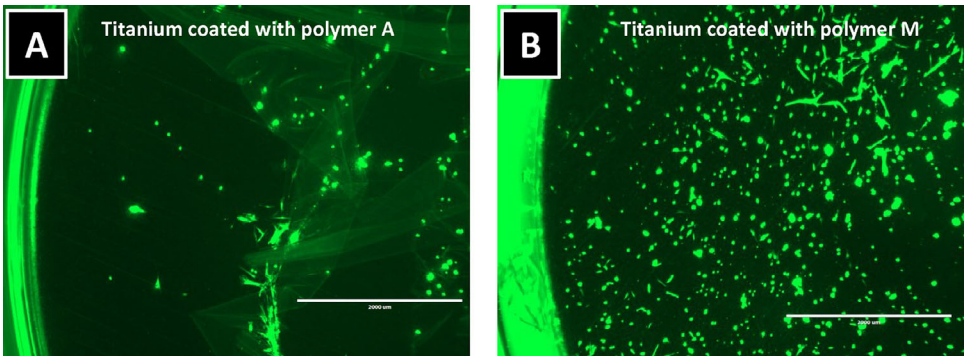


**Figure 6.** Fibroblasts seeded on fully coated titanium discs coated with (A) polymer A and (B) polymer M.

 © 2025 The Author(s). Macromolecular Rapid Communications published by Wiley-VCH GmbH



15213927, 0, Downloaded from https://onlinelibrary.wiley.com/doi/10.1002/marc.202400989, Wiley Online Library on [12/03/2025]. See the Terms and Conditions (https://onlinelibrary.wiley.com/terms-and-conditions) on Wiley Online Library for rules of use; OA articles are governed by the applicable Creative Commons License

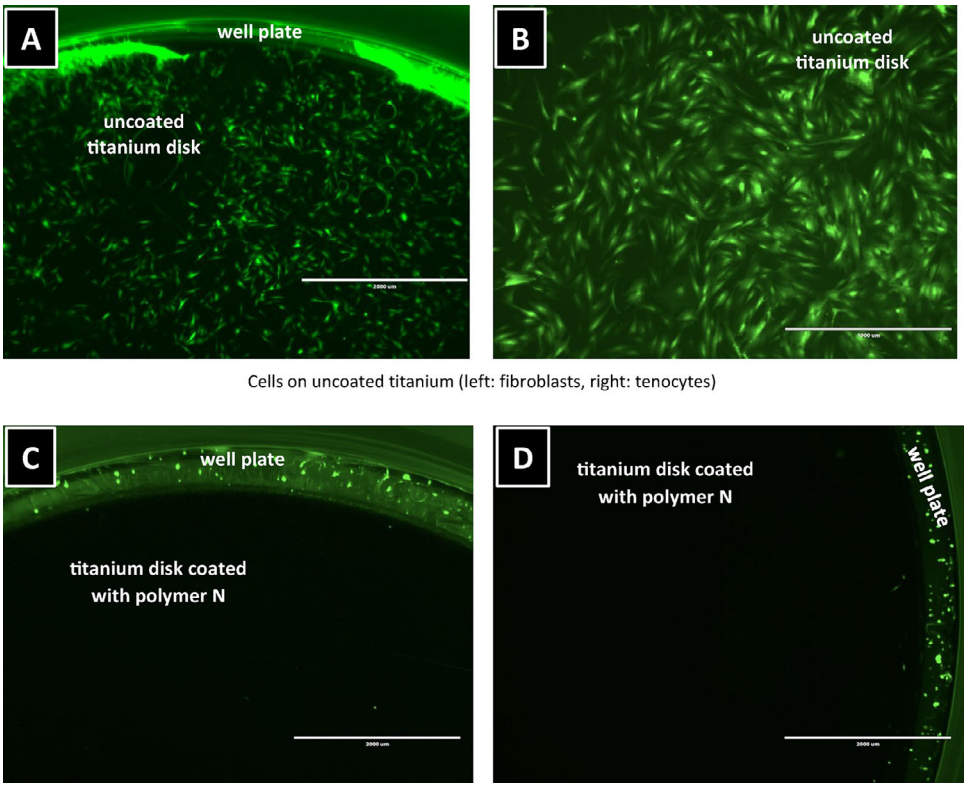


**Figure 7.** (A) Fibroblasts and (B) tenocytes seeded on uncoated titanium discs. (C) Fibroblasts and (D) tenocytes on titanium discs coated with polymer N.

materials are already used in clinical practice, e.g. gentamycin-releasing bone cement. As already described in the introduction, this is associated with various possible negative side effects like promoting bacterial resistance, inducing adverse systemic effects, or failing to maintain constant antibacterial efficacy.[13]

Polymer **N** exhibits effective intrinsic antibacterial properties that inhibit the growth of Staphylococcus aureus without causing the typical side effects associated with antibiotic treatments. While polymers with intrinsic antimicrobial activity have been previously described,[46] including their potential for immobilization on various surfaces, these materials primarily focus on preventing bacterial colonization. However, a secondary objective of many studies has been to promote tissue biocompatibility and cell adhesion. This is often achieved by combining antibacterial substrates with tissue-adhesion-promoting peptides, such as RGD.[47,48] Chitosan or streptavidin are other examples of molecules that combine intrinsic antibacterial properties with tissue-integrating effects.[49,50] In contrast, our study follows a different approach. The primary aim was to develop a surface modification specifically designed for short-term implants. This modification avoids tissue integration and adhesion while remaining non-cytotoxic. At the same time, it effectively inhibits bacterial colonization through intrinsic antibacterial properties, thereby avoiding the adverse side effects typically associated with antibiotic treatments. This innovation is exemplified by polymer **N**.

## 4. Conclusion

This study presents a novel approach combining antiadhesive acrylamide-based hydrogels with photocrosslinkers possessing intrinsic antibacterial properties and anchor groups specifically designed for titanium substrates.

The water-swellable polymer networks coated on short-term titanium implants effectively prevent cell and tissue adhesion without inducing cytotoxicity. Based on the non-adhesiveness, such polymer layers are expected to circumvent injuries during implant removal caused by tight implant tissue integration. Intrinsic antibacterial effects have been integrated into the molecular framework of these coatings via the specific structure of the cationic crosslinker BPQAAm and have been demonstrated to successfully inhibit bacterial colonization. This avoids the use of additional antibiotics or bactericidal agents that tend to leach from the coating in a rather uncontrolled manner. Based on these findings this innovative coating design demonstrates significant potential to advance short-term titanium implant technology, addressing key challenges related to tissue adhesion and infection risks.

Future investigations should focus on further validating the performance of the coatings in appropriate in vivo models. Successful translation of this coating technology into clinical applications could lead to reduced complications associated with the removal of short-term trauma implants, eventually improving therapeutic results and patient well-being.

 © 2025 The Author(s). Macromolecular Rapid Communications published by Wiley-VCH GmbH



15213927, 0, Downloaded from https://onlinelibrary.wiley.com/doi/10.1002/marc.202400989, Wiley Online Library on [12/03/2025]. See the Terms and Conditions (https://onlinelibrary.wiley.com/terms-and-conditions) on Wiley Online Library for rules of use; OA articles are governed by the applicable Creative Commons License

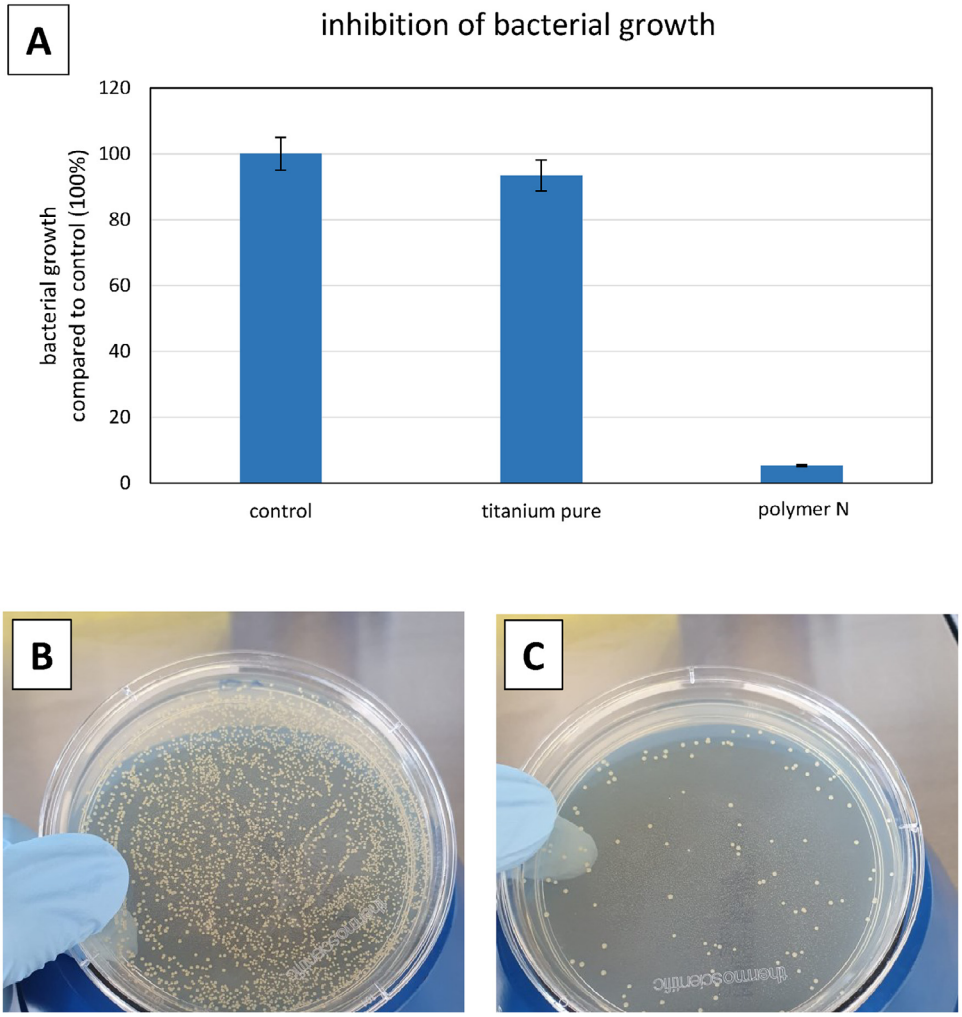


**Figure 8.** (A) Measurement of bacterial growth ($OD_{600}$) on the coated titanium discs compared to pure LB-medium (control 100%). CFUs 24 h after plating of the incubated medium. (B) Medium, (C) polymer N.

## Supporting Information

Supporting Information is available from the Wiley Online Library or from the author.

## Acknowledgements

U.R. and U.J. contributed equally to this work. This project has received funding from the BMBF Project "Medistorplast-Wundauflagen mit Wirkstoffdepot für effizientere Therapie chronischer Wunden" (13GW0349C) for FW and AI. The authors further thank the Deutsche Forschungsgemeinschaft (DFG) (JO 370/5-1) for supporting NJ. CVRT was funded through the project „PermAFog-Entwicklung von neuartigen, umweltschonenden permanenten Antifog-Additiv-Masterbatches für Polyolefinfolien in Gewächsanwendungen' of the Landwirtschaftliche Rentenbank (Förderkennzeichen: 854 798). Furthermore, the authors are thankful for receiving experimental support through Mateusz Andruschko and Sabine Fuchs for $^{31}$P NMR spectroscopy, Thomas Paululat for $^{1}$H and $^{13}$C NMR spectroscopy, and Renée Sophie Hoffmann for help with the CA measurements. The authors thank Petra Frank for synthetic support. The helpful discussions with Holger Schönherr and Manuela Kilian are highly appreciated. The authors are very thankful to Stefan Stein, and Georg Speyer Haus, for providing the eGFP lentiviral system. This research article is part of the doctoral theses of Karl Schönewald, Kira Vogel, and Barbara Schwartz.

Open access funding enabled and organized by Projekt DEAL.

## Conflict of Interest

Patent: WO2024094645A1-"Nonstick polymer coatings for short-term implants", Inventors: Niklas Jung, Ulrich Jonas, Fiona Wiesner (née Diehl), Clinton Richard Viktor Thiagarajan, Ulrike Ritz, Karl Michael Georg Schönewald, Kira Vogel

## Data Availability Statement

The data that support the findings of this study are available in the supplementary material of this article.

## Keywords

antiadhesive and antibacterial hydrogel coatings, antifouling, fibroblasts, photocrosslinkable poly(acrylamides), short-term titanium implants, tenocytes

 © 2025 The Author(s). Macromolecular Rapid Communications published by Wiley-VCH GmbH



15213927, 0, Downloaded from https://onlinelibrary.wiley.com/doi/10.1002/marc.202400989, Wiley Online Library on [12/03/2025]. See the Terms and Conditions (https://onlinelibrary.wiley.com/terms-and-conditions) on Wiley Online Library for rules of use; OA articles are governed by the applicable Creative Commons License

Received: December 11, 2024
Revised: February 24, 2025
Published online:

[1] J. A. Cauley, *Lancet Healthy Longevity* **2021**, *2*, e535.
[2] M. Rupp, N. Walter, C. Pfeifer, S. Lang, M. Kerschbaum, W. Krutsch, F. Baumann, V. Alt, *Dtsch Arztebl Int.* **2021**, *118*, 665.
[3] J. T. Evans, J. P. Evans, R. W. Walker, A. W. Blom, M. R. Whitehouse, A. Sayers, *Lancet* **2019**, *393*, 647.
[4] W. Wu, R. Cheng, J. das Neves, J. Tang, J. Xiao, Q. Ni, X. Liu, G. Pan, D. Li, W. Cui, B. Sarmento, *J. Controlled Release* **2017**, *261*, 318.
[5] D. I. Vos, M. H. Verhofstad, *Eur. J. Trauma Emerg. Surg.* **2013**, *39*, 327.
[6] K. Izadpanah, M. Jaeger, D. Maier, N. Südkamp, *OP-J.* **2016**, *32*, 120.
[7] J. Liao, X. Li, Y. Fan, *Bioact. Mater.* **2023**, *26*, 387.
[8] R. Liechti, R. Babst, U. Hug, B.-C. Link, B. J. M. van de Wall, M. Knobe, F. J. P. Beeres, *Eur. J. Trauma Emerg. Surg.* **2022**, *48*, 2369.
[9] J. S. H. Wong, A. L. H. Lee, C. Fang, H. C. H. Leung, A. H. Y. Liu, R. C. K. So, C. S. Y. Yung, T.-M. Wong, F. Leung, *J. Orthop. Surg.* **2022**, *30*, 10225536221118519.
[10] T. Stich, F. Alagboso, T. Křenek, T. Kovářík, V. Alt, D. Docheva, *Bioeng. Transl. Med.* **2022**, *7*, e10239.
[11] S. Kuhn, J. Kroth, U. Ritz, A. Hofmann, C. Brendel, L. P. Müller, R. Förch, P. M. Rommens, *J. Mater. Sci. Mater. Med.* **2014**, *25*, 2549.
[12] F. Wang, W. Peng, D. Huo, J. Zhang, S. Deng, L. Huang, S. Tan, *J. Mater. Chem. B* **2024**, *12*, 5917.
[13] V. Allizond, S. Comini, A. M. Cuffini, G. Banche, *Antibiotics* **2022**, *11*, 529.
[14] A. Barik, N. Chakravorty, *Trends in Biomedical Research*, Springer, Berlin, Germany **2019**.
[15] Z. Hao, M. Wang, L. Cheng, M. Si, Z. Feng, Z. Feng, *Front. Bioeng. Biotechnol.* **2024**, *11*, 1337543.
[16] D. Chan, J. Chien, E. Axpe, L. Blankemeier, S. W. Baker, S. Swaminathan, V. A. Piunova, D. Y. Zubarev, C. L. Maikawa, A. K. Grosskopf, J. L. Mann, H. T. Soh, E. A. Appel, *Adv. Mater.* **2022**, *34*, 2109764.
[17] O. Pop-Georgievski, D. Kubies, J. Zemek, N. Neykova, R. Demianchuk, E. M. Chánová, M. Šlouf, M. Houska, F. Rypáček, *Beilstein J. Nanotechnol.* **2015**, *6*, 617.
[18] M. Dettin, A. Zamuner, G. Iucci, G. M. L. Messina, C. Battocchio, G. Picariello, G. Gallina, G. Marletta, I. Castagliuolo, P. Brun, *J. Pept. Sci.* **2014**, *20*, 585.
[19] F. Wiesner, C. Petri, S. Hageneder, C. Kunzler, S. Klees, P. Frank, M. Pertiller, J. Dostalek, W. Knoll, *Macromol. Rapid Commun.* **2024**, *45*, 2300549.
[20] A. Mateescu, Y. Wang, J. Dostalek, U. Jonas, *Membranes* **2012**, *2*, 40.
[21] K. Schuh, O. Prucker, J. Rühe, *Macromolecules* **2008**, *41*, 9284.
[22] O. Prucker, T. Brandstetter, J. Rühe, *Biointerphases* **2018**, *13*, 010801.
[23] L. Zeininger, L. Portilla, M. Halik, A. Hirsch, *Chem.-Eur. J.* **2016**, *22*, 13506.
[24] B. D. Fairbanks, H. Thissen, G. Maurdev, P. Pasic, J. F. White, L. Meagher, *Biomacromolecules* **2014**, *15*, 3259.
[25] R. Ayala, C. Zhang, D. Yang, Y. Hwang, A. Aung, S. S. Shroff, F. T. Arce, R. Lal, G. Arya, S. Varghese, *Biomaterials* **2011**, *32*, 3700.
[26] D. Roy, B. S. Sumerlin, *ACS Macro Lett.* **2012**, *1*, 529.
[27] K. Chiba, M. Asanuma, M. Ishikawa, Y. Hashimoto, K. Dodo, M. Sodeoka, T. Yamaguchi, *Chem. Commun.* **2017**, *53*, 8751.
[28] P. W. Beines, I. Klosterkamp, B. Menges, U. Jonas, W. Knoll, *Langmuir* **2007**, *23*, 2231.
[29] S. Kommeren, J. Dongmo, C. W. M. Bastiaansen, *Soft Matter* **2017**, *13*, 2239.
[30] T. Fadida, J. P. Lellouche, *J. Polym. Res.* **2012**, *19*, 23.
[31] Y. M. Morozov, F. Wiesner, J. J. Grün, M. Pertiller, S. Fossati, K. Schmidt, N. G. Quilis, C. Gusenbauer, B. Zbiral, J. L. Toca-Herrera, et al., *Adv. Funct. Mater.* **2024**, *34*, 2315578.
[32] S. Freese, S. Diraoui, A. Mateescu, P. Frank, C. Theodorakopoulos, U. Jonas, *Gels* **2020**, *6*, 1.
[33] A. Postma, T. P. Davis, R. A. Evans, G. Li, G. Moad, M. S. O'Shea, *Macromolecules* **2006**, *39*, 5293.
[34] D. Tranchida, E. Sperotto, T. Staedler, X. Jiang, H. Schönherr, *Adv. Eng. Mater.* **2011**, *13*, B369.
[35] C. Brendel, U. Müller-Kuller, S. Schultze-Strasser, S. Stein, L. Chen-Wichmann, A. Krattenmacher, H. Kunkel, A. Dillmann, M. N. Antoniou, M. Grez, *Gene Ther.* **2012**, *19*, 1018.
[36] A. Kibrom, R. F. Roskamp, U. Jonas, B. Menges, W. Knoll, H. Paulsen, R. L. C. Naumann, *Soft Matter* **2011**, *7*, 237.
[37] M. N. Nadagouda, P. Vijayasarathy, A. Sin, H. Nam, S. Khan, J. B. M. Parambath, A. A. Mohamed, C. Han, *Med. Chem. Res.* **2022**, *31*, 1663.
[38] R. J. Young, P. A. Lovell, *Introduction to Polymers*, CRC Press, Boca Raton, Florida, USA, **2011**.
[39] R. E. Dey, X. Zhong, P. J. Youle, Q. G. Wang, I. Wimpenny, S. Downes, J. A. Hoyland, D. C. Watts, J. E. Gough, P. M. Budd, *Macromolecules* **2016**, *49*, 2656.
[40] M. D. A. Norman, S. A. Ferreira, G. M. Jowett, L. Bozec, E. Gentleman, *Nat. Protoc.* **2021**, *16*, 2418.
[41] M. J. N. Junk, R. Berger, U. Jonas, *Langmuir* **2010**, *26*, 7262.
[42] J. S. Hayes, J. L. Welton, R. Wieling, R. G. Richards, *J. Biomed. Mater. Res. B Appl. Biomater.* **2012**, *100B*, 611.
[43] D. O. Meredith, L. Eschbach, M. O. Riehle, A. S. G. Curtis, R. G. Richards, *J. Orthop. Res.* **2007**, *25*, 1523.
[44] A. I. Pearce, S. G. Pearce, K. Schwieger, S. Milz, E. Schneider, C. W. Archer, R. G. Richards, *J. Orthop. Res.* **2008**, *26*, 1377.
[45] X. Zou, X. Li, K. He, Q. Song, R. Yin, *Eur. J. Clin. Microbiol. Infect. Dis.* **2024**, *44*, 213.
[46] M. Haktaniyan, M. Bradley, *Chem. Soc. Rev.* **2022**, *51*, 8584.
[47] Y. He, X. Wan, K. Xiao, W. Lin, J. Li, Z. Li, F. Luo, H. Tan, J. Li, Q. Fu, *Biomater. Sci.* **2019**, *7*, 5369.
[48] M. Hoyos-Nogués, F. Velasco, M.-P. Ginebra, J. M. Manero, F. J. Gil, C. Mas-Moruno, *ACS Appl. Mater. Interfaces* **2017**, *9*, 21618.
[49] M. Lehnert, M. Gorbahn, M. Klein, B. Al-Nawas, I. Köper, W. Knoll, M. Veith, *J. Biomed. Mater. Res., Part A* **2012**, *100A*, 388.
[50] J. D. C. Tardelli, M. A. Schiavon, A. C. Reis, *Carbohydr. Polym.* **2024**, *344*, 122496.

 © 2025 The Author(s). Macromolecular Rapid Communications published by Wiley-VCH GmbH



15213927, 0, Downloaded from https://onlinelibrary.wiley.com/doi/10.1002/marc.202400989, Wiley Online Library on [12/03/2025]. See the Terms and Conditions (https://onlinelibrary.wiley.com/terms-and-conditions) on Wiley Online Library for rules of use; OA articles are governed by the applicable Creative Commons License

# 10 Patent: Nonstick Polymer Coatings for Short-Term Implants

**Published as:**

Niklas Jung, Ulrich Jonas, **Fiona Diehl**, Clinton R. V. Thiagarajan, Ulrike Ritz Karl G. M. Schönewald and Kira Vogel (2022) Nonstick Polymer Coatings for Short-term Implants (DE102022128813A1), Deutsches Patent- und Markenamt.

**Author Contributions:**

*Niklas Jung:* Monomer syntheses and analyses, polymer syntheses and analyses, Coating procedures

*Ulrich Jonas:* Conception, Coordination, Writing, Reviewing, Editing

***Fiona Wiesner (née Diehl):*** Conception, Coordination, Monomer syntheses and analyses, polymer syntheses and analyses, Coating procedures, Graphics, Reviewing, Editing

*Clinton R. V. Thiagarajan:* Monomer syntheses and analyses

*Ulrike Ritz:* Conception, Coordination, Writing, Reviewing, Editing

*Karl G. M. Schönewald:* Cell and bacteria tests, Data evaluation

*Kira Vogel*: Cell and bacteria tests, Data evaluation

**Details** can be found in the Appendix, page A38.

(12) NACH DEM VERTRAG ÜBER DIE INTERNATIONALE ZUSAMMENARBEIT AUF DEM GEBIET DES PATENTWESENS (PCT) VERÖFFENTLICHTE INTERNATIONALE ANMELDUNG

(19) **Weltorganisation für geistiges Eigentum**
Internationales Büro

(43) **Internationales Veröffentlichungsdatum**
**10. Mai 2024 (10.05.2024)**

WIPO | PCT

(10) **Internationale Veröffentlichungsnummer**
**WO 2024/094645 A1**

(51) **Internationale Patentklassifikation:**
*C08F 220/58* (2006.01) *C09D 133/24* (2006.01)
*C08F 8/12* (2006.01)

(21) **Internationales Aktenzeichen:** PCT/EP2023/080274

(22) **Internationales Anmeldedatum:**
30. Oktober 2023 (30.10.2023)

(25) **Einreichungssprache:** Deutsch

(26) **Veröffentlichungssprache:** Deutsch

(30) **Angaben zur Priorität:**
10 2022 128 813.7
31. Oktober 2022 (31.10.2022) DE

(71) **Anmelder: UNIVERSITÄT SIEGEN** [DE/DE]; Adolf-Reichwein-Straße 2a, 57076 Siegen (DE). **UNIVERSITÄTSMEDIZIN DER JOHANNES GUTENBERG-UNIVERSITÄT MAINZ** [DE/DE]; Langenbeckstraße 1, 55131 Mainz (DE).

(72) **Erfinder: JUNG, Niklas**; Universität Siegen, Adolf-Reichwein-Straße 2, 57076 Siegen (DE). **JONAS, Ulrich**; Universität Siegen, 57076 Siegen (DE). **DIEHL, Fiona**; Universität Siegen, Adolf-Reichwein-Straße 2, 57076 Siegen (DE). **THIAGARAJAN, Clinton Richard Viktor**; Universität Siegen, Adolf-Reichwein-Straße 2, 57076 Siegen (DE). **RITZ, Ulrike**; Universitätsmedizin der Johannes Gutenberg-Universität Mainz, Langenbeckstraße 1, 55131 Mainz (DE). **SCHÖNEWALD, Karl Michael Georg**; Universitätsmedizin der Johannes Gutenberg-Universität Mainz, Langenbeckstraße 1, 55131 Mainz (DE). **VOGEL, Kira**; Universitätsmedizin der Johannes Gutenberg-Universität Mainz, Langenbeckstraße 1, 55131 Mainz (DE).

(74) **Anwalt: LAHRTZ, Fritz**; Simmons & Simmons LLP, Lehel Carré, Thierschplatz 6, 80538 München (DE).

(81) **Bestimmungsstaaten** *(soweit nicht anders angegeben, für jede verfügbare nationale Schutzrechtsart)*: AE, AG, AL, AM, AO, AT, AU, AZ, BA, BB, BG, BH, BN, BR, BW, BY, BZ, CA, CH, CL, CN, CO, CR, CU, CV, CZ, DE, DJ, DK, DM, DO, DZ, EC, EE, EG, ES, FI, GB, GD, GE, GH, GM, GT, HN, HR, HU, ID, IL, IN, IQ, IR, IS, IT, JM, JO, JP, KE, KG, KH, KN, KP, KR, KW, KZ, LA, LC, LK, LR, LS, LU, LY, MA, MD, MG, MK, MN, MU, MW, MX, MY, MZ, NA, NG, NI, NO, NZ, OM, PA, PE, PG, PH, PL, PT, QA, RO, RS, RU, RW, SA, SC, SD, SE, SG, SK, SL, ST, SV, SY, TH, TJ, TM, TN, TR, TT, TZ, UA, UG, US, UZ, VC, VN, WS, ZA, ZM, ZW.

(84) **Bestimmungsstaaten** *(soweit nicht anders angegeben, für jede verfügbare regionale Schutzrechtsart)*: ARIPO (BW, CV, GH, GM, KE, LR, LS, MW, MZ, NA, RW, SC, SD, SL, ST, SZ, TZ, UG, ZM, ZW), eurasisches (AM, AZ, BY, KG, KZ, RU, TJ, TM), europäisches (AL, AT, BE, BG, CH, CY, CZ, DE, DK, EE, ES, FI, FR, GB, GR, HR, HU, IE, IS, IT, LT, LU, LV, MC, ME, MK, MT, NL, NO, PL, PT, RO, RS, SE, SI, SK, SM, TR), OAPI (BF, BJ, CF, CG, CI, CM, GA, GN, GQ, GW, KM, ML, MR, NE, SN, TD, TG).

**Veröffentlicht:**
— *mit internationalem Recherchenbericht (Artikel 21 Absatz 3)*

**(54) Title:** NONSTICK POLYMER COATINGS FOR SHORT-TERM IMPLANTS

**(54) Bezeichnung:** ANTIADHÄSIVE POLYMER-BESCHICHTUNGEN FÜR KURZZEITIMPLANTATE

**(57) Abstract:** The present invention relates to hydrophilic (co)polymers having chemically reactively (covalently) bound anchor groups and/or crosslinker molecules that permit attachment to the parent substrate or linkage of these polymers to networks. The invention further relates to hydrogels and coatings, especially implant coatings, comprising the polymers of the invention, and to medical devices, such as implants, that have been coated with a coating of the invention.

**(57) Zusammenfassung:** Die vorliegende Erfindung betrifft hydrophile (Co-)Polymere mit chemisch reaktiv (kovalent) gebundenen Ankergruppen und/oder Vernetzermolekülen, welche eine Anknüpfung an das zugrundeliegende Substrat bzw. eine Verknüpfung dieser Polymere zu Netzwerken erlauben. Die Erfindung betrifft ferner Hydrogele und Beschichtungen, insbesondere Implantatbeschichtungen, die die erfindungsgemäßen Polymere umfassen, sowie medizinische Vorrichtungen, wie Implantate, die mit einer erfindungsgemäßen Beschichtung überzogen sind.

WO 2024/094645 A1

# Antiadhäsive Polymer-Beschichtungen für Kurzzeitimplantate

## Gebiet der Erfindung

Die vorliegende Erfindung betrifft hydrophile (Co-)Polymere mit chemisch reaktiv (kovalent) gebundenen Ankergruppen und/oder Vernetzermolekülen, welche eine Anknüpfung an das zugrundeliegende Substrat bzw. eine Verknüpfung dieser Polymere zu Netzwerken erlauben. Die Beschichtung von Kurzzeitimplantaten mit solchen wasserquellbaren Polymernetzwerken (Hydrogelen) verhindert eine Adhäsion von Zellen und Gewebe auf der Oberfläche (Antifouling), ohne dass eine Zytotoxizität von ihr ausgeht, und erzielt gleichzeitig eine intrinsische antibakterielle Wirkung, ohne dass eine Beigabe zusätzlicher Antibiotika oder Bakterizide notwendig ist. Da das umliegende Gewebe nicht an einem antiadhäsiv beschichteten Implantat haften kann, wird dieses nicht bei der Entfernung des Implantates geschädigt. Außerdem wird durch die intrinsische antibakterielle Wirkung von bestimmten Beschichtungen einer häufig im Zuge einer Implantation vorkommenden Infektion vorgebeugt.

Die beschriebenen Beschichtungen können als Modifikationen für handelsübliche, medizinisch zugelassene Implantate dem Zweck dienen, die Wiederentnahme des Kurzzeitimplantats nach abgeschlossener Tragedauer zu vereinfachen und Komplikationen während der Implantation und Tragezeit zu prävenieren.

## Hintergrund der Erfindung

Moderne Implantate in Unfallchirurgie und Orthopädie, welche dem Patienten mit einer Tragedauer von maximal 12 Monaten implantiert werden (Kurzzeitimplantate), finden weitläufig Anwendung, um eine temporäre Stützfunktion des Knochenapparates zu erzielen, beispielsweise nach einem akuten Unfall. Sie bestehen häufig aus Titan und müssen bei Komplikationen, spätestens aber nach beendeter Tragedauer entfernt werden.

Die Anforderungen an derartige Kurzzeitimplantate sind konträr zu denen für Langzeitimplantate, welche mehrere Jahre bis Jahrzehnte im Körper des Patienten verbleiben (beispielsweise Hüft- oder Knieimplantate). Bei Langzeitimplantaten ist eine vollständige Integration des Implantates in das körpereigene Gewebe erwünscht, um eine permanente und stabile Stützfunktion zu erreichen. Im Gegensatz dazu ist es für Kurzzeitimplantate erstrebenswert, dass sich die Implantate nicht mit dem umliegenden Gewebe verbinden, um Rupturen bei der Entfernung vorzubeugen. Gründe für die Notwendigkeit einer Implantatentfernung können Adhärenzen von umliegendem Gewebe an der Oberfläche sein. Dabei bilden Titanimplantate häufiger als beispielsweise Stahlimplantate solche Adhärenzen aus. Die Adhärenz von Sehnen an eine Implantatplatte, insbesondere an einer Titanoberfläche, kann zu Bewegungseinschränkungen bis hin zur Versteifung von Gelenken, beispielsweise im Bereich der Hand und des Handgelenkes führen.

Sollten Nerven an der Oberfläche der Platte adhärieren, wie es zum Beispiel bei der Plattenosteosynthese des Humerusschaftes geschehen kann, wird hierdurch die operative Entfernung der Platte deutlich erschwert und das Risiko eines bleibenden Nervenschadens signifikant erhöht. Solche vermeidbaren Komplikationen sind für den Patienten häufig mit stärkeren Schmerzen, verlängerten Heilungsprozessen und einer erhöhten psychischen Belastung verbunden. Zusätzlich geht grundlegend mit einer jeden Implantation ein gesteigertes Infektionsrisiko einher. Im Falle einer Infektion sind meist eine Antibiotikagabe und/oder ein Implantatwechsel mit einem verlängerten

Krankenhausaufenthalt die Folge, wodurch die physische und psychische Belastung für den Patienten sowie die Kosten für das Gesundheitssystem steigen und gleichzeitig die Kapazitäten in medizinischen Institutionen beansprucht werden. Eine antiadhäsive Beschichtung könnte sowohl die Komplikationen nach der Implantation reduzieren als auch die Risiken bei der Implantatentfernung minimieren.

Für antiadhäsive Beschichtungen von Kurzzeitimplantaten sind zum jetzigen Zeitpunkt keine relevanten, patentierten Systeme bekannt. Im Gegensatz zu Oberflächenmodifikationen von Kurzzeitimplantaten sind bereits einige Beschichtungen für Langzeitimplantate zur Verbesserung derer Eigenschaften bekannt. Dokumentierte Beschichtungen bestehen z.B. aus (click-funktionalisierten) Polymeren [1-3] oder Hydroxylapatit und anderen Calciumverbindungen. [4,5] Diese wirken zumeist osteokonduktiv, um eine gute Integration des Implantates in das umliegende Gewebe zu ermöglichen. Das bedeutet, dass diese Beschichtungstypen nicht antiadhäsiv wirken, sondern, im Gegenteil, die Zelladhäsion an das Implantat fördern.

Weitere Methoden der Implantatbeschichtungen erfordern spezielle Prozesse, wie Plasmabehandlungen, Laserabscheidungsverfahren, oder Anodisierungen, welche wiederum ein aufwändigeres Equipment benötigen und damit auch erhöhte Kosten in Verbindung stehen. Außerdem sind solche Methoden nicht oder nur bedingt für komplexere Geometrien geeignet.

Darüber hinaus gibt es bereits Veröffentlichungen zu Implantatmodifikationen, welche eine antibakterielle Wirkung hervorrufen. Der Großteil dieser Beschichtungen basiert auf antibiotika-, bakterizid-, silber- oder kupferhaltigen Überzügen. [5,6] Dabei werden häufig Antibiotika über einen begrenzten Zeitraum vom Implantat an das umliegende Gewebe abgegeben, um einer Infektion vorzubeugen. Diese Antibiotikaabgabe wiederum kann durchaus zu Resistenzen oder allergischen Reaktionen führen. Metallionenbasierte Bakterizide hingegen können zu einer lokalen Toxizität führen.

Neben Metallimplantaten werden bioresorbierbare Implantate als vielversprechende Kurzzeitimplantate gehandelt, da diese keine Entfernung nach Beendigung der Tragedauer erfordern. Allerdings weisen zersetzbare Implantate unterschiedliche physikalischen Eigenschaften zu Metallen auf, wie eine geringere Duktilität und Zugfestigkeit. Insbesondere bieten diese Implantate nicht über ihre gesamte Implementierungsdauer hinweg eine gleichbleibend starke Stabilisierung des Knochenapparates, sondern büßen im Rahmen des Zersetzungsprozesses an Stabilität ein. [7,8] Für entsprechende klinische Fragestellungen, bei denen eine konstante Robustheit des Implantates erforderlich ist, sind aus diesem Grund bioresorbierbare Implantate nur bedingt geeignet. Auch die Abbauprodukte des bioresorbierbaren Implantats, die lokal in hohen Konzentrationen vorliegen können, dürfen nicht zytotoxisch sein, da sie ansonsten zu unerwünschten Reaktionen führen könnten. Der Körper muss in der Lage sein, diese Produkte zu verstoffwechseln bzw. abzubauen. [8]

Entsprechend besteht die Aufgabe der vorliegenden Erfindung darin, neuartige und vorteilhafte Polymerbeschichtung bereitzustellen, die unter anderem den Einsatz von Implantaten als Kurzeitimplantate erlauben.

## Zusammenfassung der Erfindung

Die zugrundeliegende Aufgabe wird durch die Bereitstellung eines erfindungsgemäßen (Co-)Polymers gelöst.

Die hier beschriebenen und dem Hydrogel zugrundeliegenden Polymerketten der vorliegenden Erfindung bestehen aus hydrophilen Hauptmonomeren, und Vernetzermonomeren, teilweise mit antibakteriell wirksamen Strukturmotiven, und/oder dedizierten Ankergruppen für das entsprechende

Implantatsubstrat. Durch die gezielte Wahl dieser modular kombinierbaren Monomere ist es möglich, gleichzeitig biokompatible, antiadhäsive und antibakterielle Polymernetzwerke herzustellen.

Für diese Erfindung ist die Verknüpfung der Polymerketten mit benzophenonderivatbasierten Vernetzermonomeren durch Bestrahlung mit UV-Licht ein besonderer Vorteil. Durch eine solche photochemisch aktivierte Netzwerkbildung können extrem dünne (im Sub-Mikrometerbereich), gleichmäßige und kovalent angebundene Beschichtungen der Implantatoberfläche erhalten werden. Auch bei komplexeren Implantatgeometrien kann eine solche lichtinduzierte Vernetzung der Polymerbeschichtung durchgeführt werden. Zusätzlich erlaubt der UV-Bestrahlungsschritt eine simultane Sterilisation des Implantats. Durch die Einführung eines antibakteriellen Strukturmotivs (bspw. eine quartäre Ammoniumgruppe, welche durch die ionische Struktur einen antibakteriellen Effekt aufweist) in die Polymerketten für die Beschichtungen kann das Infektionsrisiko während der Operation für den Patienten reduziert werden, um eine Beeinträchtigung der Wundheilung und Geweberegeneration zu verhindern. Dafür entfallen in der hier beschriebenen Erfindung bakterizide Wirkstoffe, die dem Implantat zusätzlich beigefügt werden müssen, da die antibakterielle Wirkung alleine durch die intrinsische Beschaffenheit des antiadhäsiven Hydrogels gewährleistet wird. Eine ungewünschte freie Migration solcher nichtgebundenen Wirkstoffe in das umliegende Milieu (Gewebe, Knochen, Organe etc.) wird somit vermieden.

Zusätzlich ist die Polymernetzwerkbeschichtung im trockenen Zustand äußerst hart und mechanisch stabil und quillt erst nach der Implantation im Körper zum weichen, antiadhäsiven und antibakteriellen Hydrogel. Außerdem bedarf die hier dargestellte Erfindung keiner technisch aufwändigen Prozesse und besteht lediglich aus dem Inkubieren des Implantatsubstrats (Einschichtsystem) und/oder der Applikation einer Polymerlösung auf das Implantat (Sandwichaufbau) sowie der nach Trocknung erfolgenden Bestrahlung mit einer UV-Lampe.

Dies sind weitreichende Neuerungen in der Beschichtungsentwicklung von Implantaten.

Basierend auf den vorgehend genannten überraschenden Erkenntnissen wurde die vorliegende Erfindung realisiert, welche wie folgt zusammengefasst werden kann:

1. **Polymer** aufweisend eine Struktur der allgemeinen Formel (I)

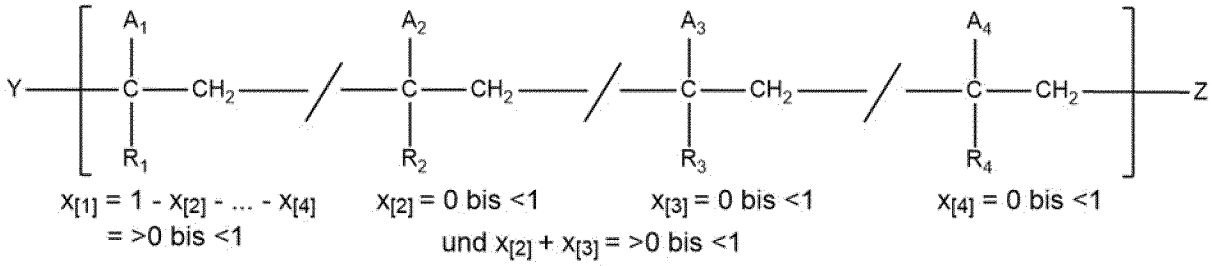


**(I)**

wobei

$A_1$ -H oder -$CH_3$ ist;

$A_2$ -H oder -$CH_3$ ist;

$A_3$ -H oder -$CH_3$ ist;

$A_4$ -H oder -$CH_3$ ist;

$R_1$, für jede Wiederholungseinheit, unabhängig ausgewählt ist aus der Gruppe bestehend aus

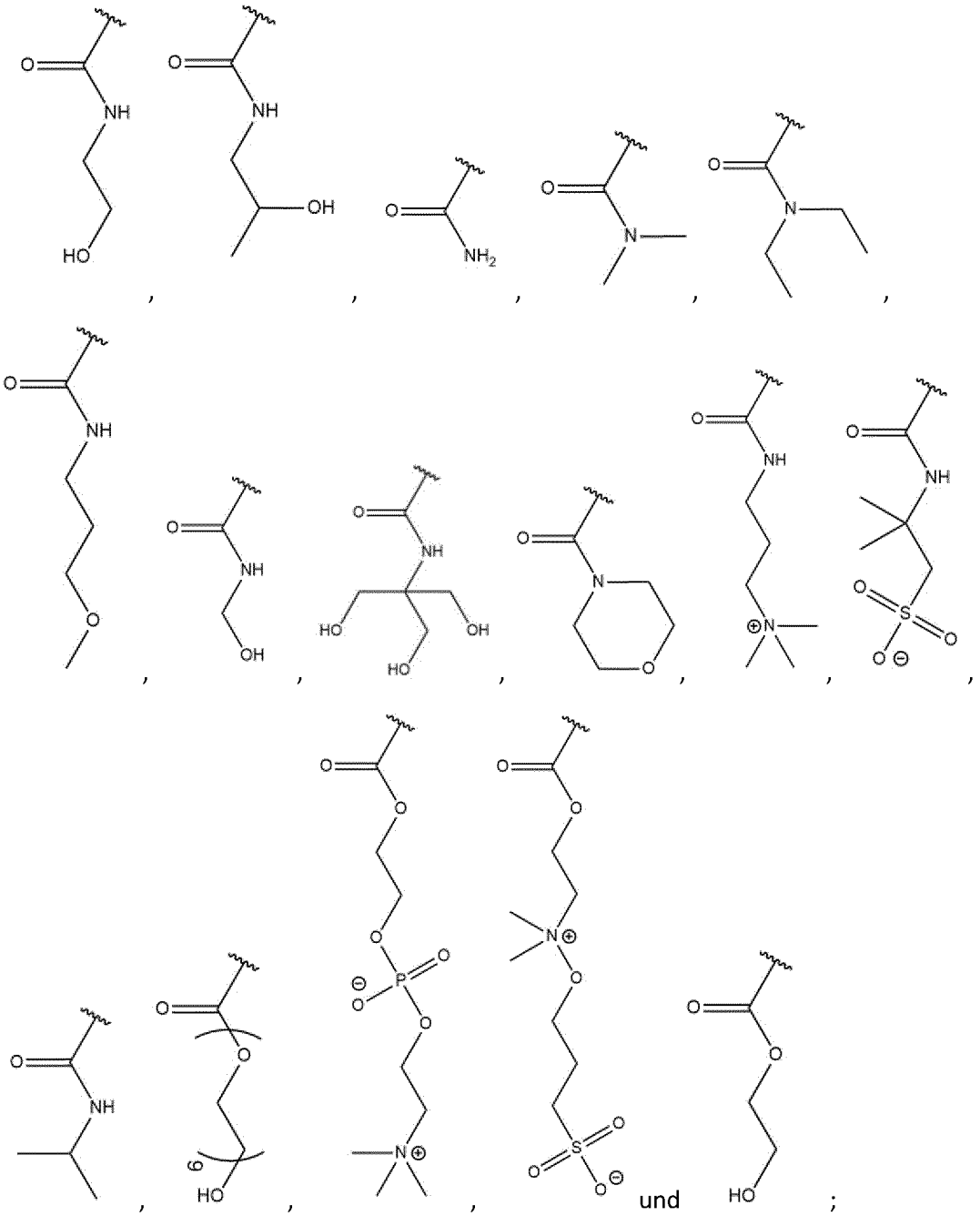

und ;

$R_2$, für jede Wiederholungseinheit, unabhängig ausgewählt ist aus der Gruppe bestehend aus

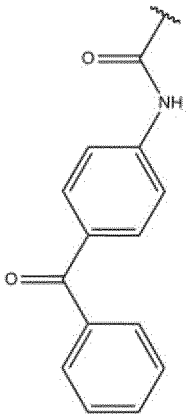

und

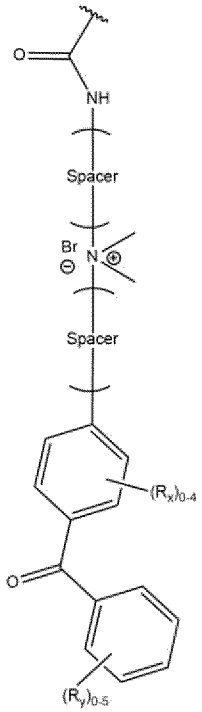

,

wobei jeder „Spacer“ jeweils unabhängig voneinander ausgewählt ist aus der Gruppe bestehend aus linearen oder verzweigten Alkylketten und linearen oder verzweigten Ethylen- oder Propylenoxidketten, vorzugweise unabhängig voneinander ausgewählt aus linearen oder verzweigen $C_{1-20}$-Alkylketten;

Rx, jeweils unabhängig voneinander, -OH, Halogen (Br, Cl, I, oder F), Halogen-$C_{1-4}$ Alkyl (z.B. -$CF_3$, -$CCL_3$, -$CBr_3$, -$Cl_3$), -$NH_2$, -$C_{1-4}$ Alkyl, -$C_{2-4}$ Alkenyl, -$C_{2-4}$ Alkinyl, -$OC_{1-4}$ Alkyl, -$OC_{2-4}$ Alkenyl, -$OC_{2-4}$ Alkinyl -$NO_2$, -SH, -$SO_2H$, -$SO_3H$, -NCS, -SCN, -COOH oder Cyano ist; und

Ry, jeweils unabhängig voneinander, -OH, Halogen (Br, Cl, I, oder F), Halogen-$C_{1-4}$ Alkyl (z.B. -$CF_3$, -$CCL_3$, -$CBr_3$, -$Cl_3$), -$NH_2$, -$C_{1-4}$ Alkyl, -$C_{2-4}$ Alkenyl, -$C_{2-4}$ Alkinyl, -$OC_{1-4}$ Alkyl, -$OC_{2-4}$ Alkenyl, -$OC_{2-4}$ Alkinyl -$NO_2$, -SH, -$SO_2H$, -$SO_3H$, -NCS, -SCN, -COOH oder Cyano ist;

$R_3$, für jede Wiederholungseinheit, unabhängig ausgewählt ist aus der Gruppe bestehend aus

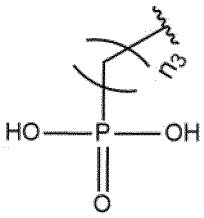

,

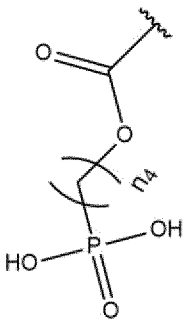

,

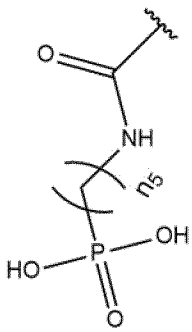

,

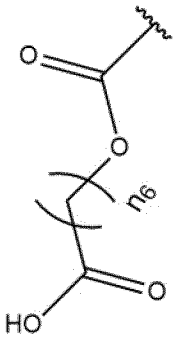

,

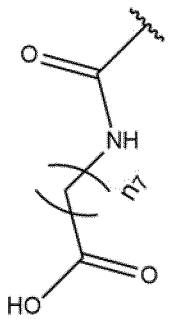

,

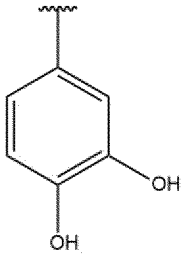

, 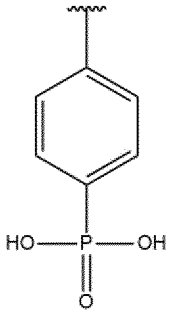

und 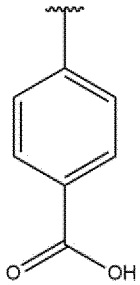

,

wobei $n_3$, $n_4$, $n_5$, $n_6$ und $n_7$ jeweils unabhängig voneinander 0, 1, 2, 3, 4, 5, 6, 7, 8, 9, 10, 11, 12, 13, 14, 15, 16, 17 oder 18 ist;

$R_4$, für jede Wiederholungseinheit, unabhängig ausgewählt ist aus der Gruppe bestehend aus

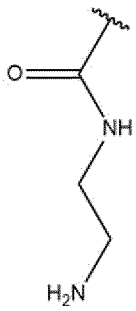

, 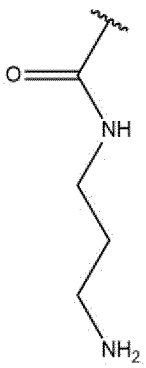

und 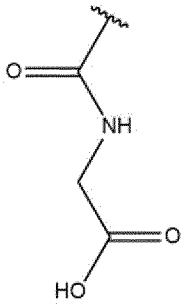

;

Y ein Fragment A eines Kettenübertragungsreagenzes oder eine Endgruppe ist; und

Z ein Fragment B des Kettenübertragungsreagenzes oder eine Endgruppe ist.

2. Polymer gemäß Ausführungsform 1, wobei $R_1$, für jede Wiederholungseinheit, unabhängig ausgewählt ist aus der Gruppe bestehend aus

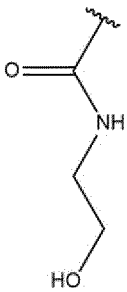

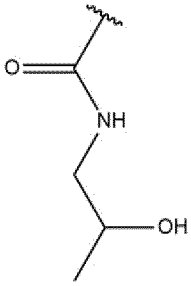

und .

3. Polymer gemäß Ausführungsform 1, wobei $R_1$, für jede Wiederholungseinheit,

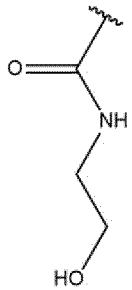

ist.

4. Polymer gemäß Ausführungsform 1, wobei $R_1$, für jede Wiederholungseinheit,

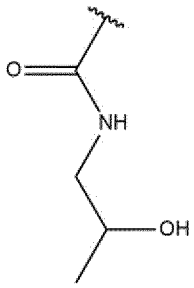

ist.

5. Polymer gemäß einer der Ausführungsformen 1 bis 4, wobei $A_1$ -H ist.

6. Polymer gemäß einer der Ausführungsformen 1 bis 4, wobei $A_1$ $-CH_3$ ist.

7. Polymer gemäß einer der Ausführungsformen 1 bis 6, wobei $R_2$, für jede Wiederholungseinheit, unabhängig ausgewählt ist aus der Gruppe bestehend aus

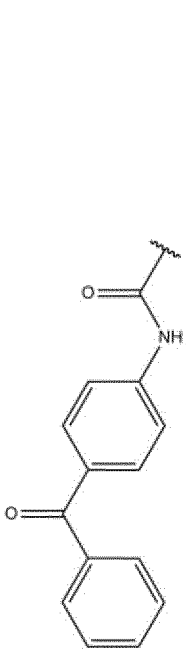

und

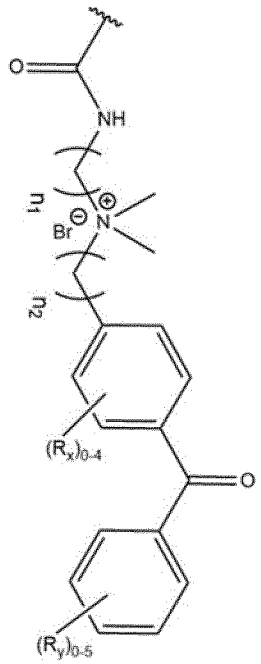

,

wobei $n_1$ und $n_2$ jeweils unabhängig voneinander 1, 2, 3, 4, 5, 6, 7, 8, 9, 10, 11, 12, 13, 14, 15, 16, 17, 18, 19 oder 20 ist;

$R_x$, jeweils unabhängig voneinander, -OH, Halogen (Br, Cl, I, oder F), Halogen-$C_{1-4}$ Alkyl (z.B. $-CF_3$, $-CCL_3$, $-CBr_3$, $-Cl_3$), $-NH_2$, $-C_{1-4}$ Alkyl, $-C_{2-4}$ Alkenyl, $-C_{2-4}$ Alkinyl, $-OC_{1-4}$ Alkyl, $-OC_{2-4}$ Alkenyl, $-OC_{2-4}$ Alkinyl $-NO_2$, -SH, $-SO_2H$, $-SO_3H$, -NCS, -SCN, -COOH oder Cyano ist; und

$R_y$, jeweils unabhängig voneinander, -OH, Halogen (Br, Cl, I, oder F), Halogen-$C_{1-4}$ Alkyl (z.B. $-CF_3$, $-CCL_3$, $-CBr_3$, $-Cl_3$), $-NH_2$, $-C_{1-4}$ Alkyl, $-C_{2-4}$ Alkenyl, $-C_{2-4}$ Alkinyl, $-OC_{1-4}$ Alkyl, $-OC_{2-4}$ Alkenyl, $-OC_{2-4}$ Alkinyl $-NO_2$, -SH, $-SO_2H$, $-SO_3H$, -NCS, -SCN, -COOH oder Cyano ist.

8. Polymer gemäß einer der Ausführungsformen 1 bis 6, wobei $R_2$, für jede Wiederholungseinheit, unabhängig ausgewählt ist aus der Gruppe bestehend aus

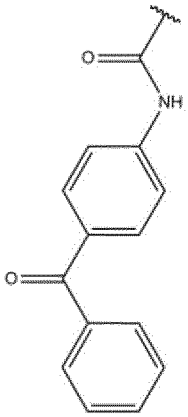


und

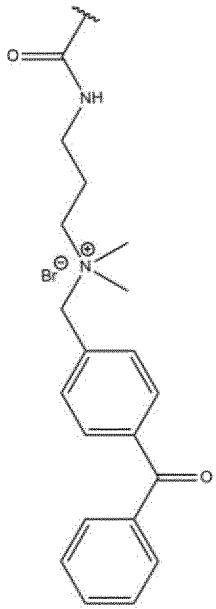


.

9. Polymer gemäß einer der Ausführungsformen 1 bis 6, wobei $R_2$, für jede Wiederholungseinheit,

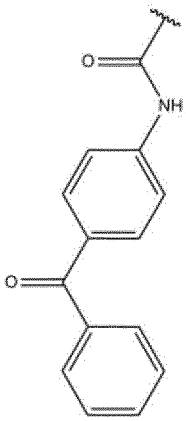


ist.

10. Polymer gemäß einer der Ausführungsformen 1 bis 6, wobei $R_2$, für jede Wiederholungseinheit,

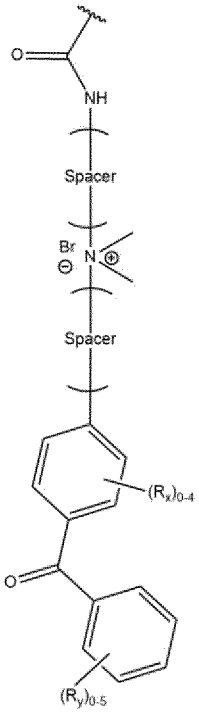

ist,

wobei jeder „Spacer“ jeweils unabhängig voneinander ausgewählt ist aus der Gruppe bestehend aus linearen oder verzweigten Alkylketten und linearen oder verzweigten Ethylen- oder Propylenoxidketten, vorzugweise unabhängig voneinander ausgewählt aus linearen oder verzweigen $C_{1-20}$-Alkylketten;

$R_x$, jeweils unabhängig voneinander, -OH, Halogen (Br, Cl, I, oder F), Halogen-$C_{1-4}$ Alkyl (z.B. $-CF_3$, $-CCL_3$, $-CBr_3$, $-Cl_3$), $-NH_2$, $-C_{1-4}$ Alkyl, $-C_{2-4}$ Alkenyl, $-C_{2-4}$ Alkinyl, $-OC_{1-4}$ Alkyl, $-OC_{2-4}$ Alkenyl, $-OC_{2-4}$ Alkinyl $-NO_2$, -SH, $-SO_2H$, $-SO_3H$, -NCS, -SCN, -COOH oder Cyano ist; und

$R_y$, jeweils unabhängig voneinander, -OH, Halogen (Br, Cl, I, oder F), Halogen-$C_{1-4}$ Alkyl (z.B. $-CF_3$, $-CCL_3$, $-CBr_3$, $-Cl_3$), $-NH_2$, $-C_{1-4}$ Alkyl, $-C_{2-4}$ Alkenyl, $-C_{2-4}$ Alkinyl, $-OC_{1-4}$ Alkyl, $-OC_{2-4}$ Alkenyl, $-OC_{2-4}$ Alkinyl $-NO_2$, -SH, $-SO_2H$, $-SO_3H$, -NCS, -SCN, -COOH oder Cyano ist.

11. Polymer gemäß einer der Ausführungsformen 1 bis 6, wobei $R_2$, für jede Wiederholungseinheit,

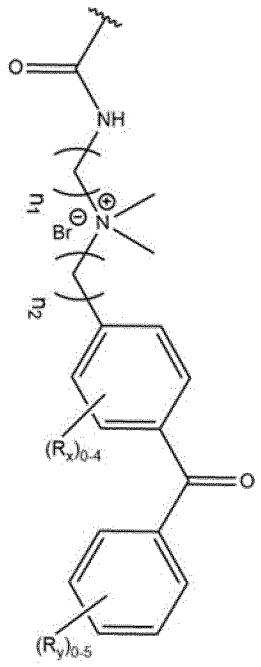


ist,

wobei $n_1$ und $n_2$ jeweils unabhängig voneinander 1, 2, 3, 4, 5, 6, 7, 8, 9, 10, 11, 12, 13, 14, 15, 16, 17, 18, 19 oder 20 ist;

$R_x$, jeweils unabhängig voneinander, -OH, Halogen (Br, Cl, I, oder F), Halogen-$C_{1-4}$ Alkyl (z.B. $-CF_3$, $-CCL_3$, $-CBr_3$, $-Cl_3$), $-NH_2$, $-C_{1-4}$ Alkyl, $-C_{2-4}$ Alkenyl, $-C_{2-4}$ Alkinyl, $-OC_{1-4}$ Alkyl, $-OC_{2-4}$ Alkenyl, $-OC_{2-4}$ Alkinyl $-NO_2$, -SH, $-SO_2H$, $-SO_3H$, -NCS, -SCN, -COOH oder Cyano ist; und

$R_y$, jeweils unabhängig voneinander, -OH, Halogen (Br, Cl, I, oder F), Halogen-$C_{1-4}$ Alkyl (z.B. $-CF_3$, $-CCL_3$, $-CBr_3$, $-Cl_3$), $-NH_2$, $-C_{1-4}$ Alkyl, $-C_{2-4}$ Alkenyl, $-C_{2-4}$ Alkinyl, $-OC_{1-4}$ Alkyl, $-OC_{2-4}$ Alkenyl, $-OC_{2-4}$ Alkinyl $-NO_2$, -SH, $-SO_2H$, $-SO_3H$, -NCS, -SCN, -COOH oder Cyano ist.

12. Polymer gemäß einer der Ausführungsformen 1 bis 6, wobei $R_2$, für jede Wiederholungseinheit,

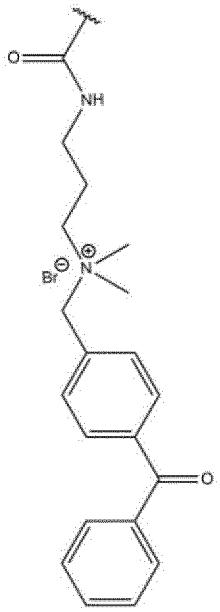


ist.

13. Polymer gemäß einer der Ausführungsformen 1 bis 12, wobei $A_2$ -H ist.

14. Polymer gemäß einer der Ausführungsformen 1 bis 12, wobei $A_2$ $-CH_3$ ist.

15. Polymer gemäß einer der Ausführungsformen 1 bis 14, wobei $R_3$, für jede Wiederholungseinheit, unabhängig ausgewählt ist aus der Gruppe bestehend aus

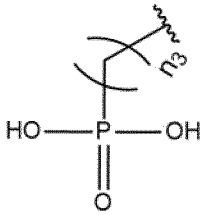
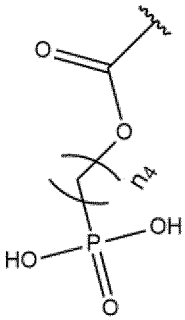
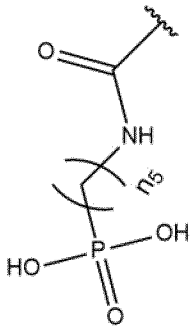
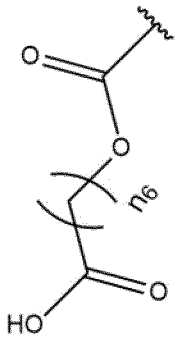
und
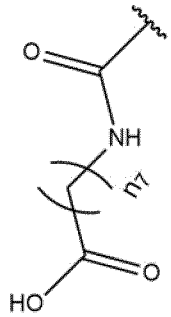
,

wobei $n_3$, $n_4$, $n_5$, $n_6$ und $n_7$ jeweils unabhängig voneinander 0, 1, 2, 3, 4, 5, 6, 7, 8, 9, 10, 11, 12, 13, 14, 15, 16, 17 oder 18 ist.

16. Polymer gemäß einer der Ausführungsformen 1 bis 14, wobei $R_3$, für jede

Wiederholungseinheit, 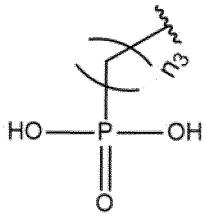 ist, wobei $n_3$ 0, 1, 2, 3, 4, 5, 6, 7, 8, 9, 10, 11, 12, 13, 14, 15, 16, 17 oder 18 ist.

17. Polymer gemäß einer der Ausführungsformen 1 bis 14, wobei $R_3$, für jede

Wiederholungseinheit, 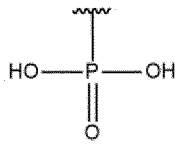 ist.

18. Polymer gemäß einer der Ausführungsformen 1 bis 14, wobei $R_3$, für jede Wiederholungseinheit, unabhängig ausgewählt ist aus der Gruppe bestehend aus

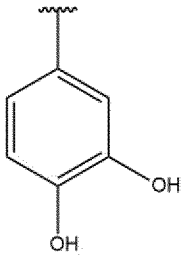
,
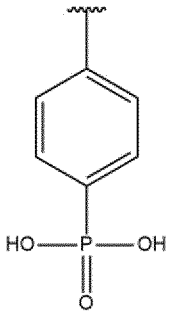
und
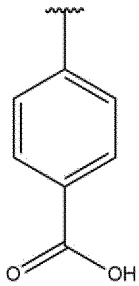
.

19. Polymer gemäß einer der Ausführungsformen 1 bis 18, wobei $A_3$ $-H$ ist.

20. Polymer gemäß einer der Ausführungsformen 1 bis 18, wobei $A_3$ $-CH_3$ ist.

21. Polymer gemäß einer der Ausführungsformen 1 bis 20, wobei $R_4$, für jede Wiederholungseinheit,

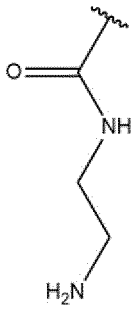

ist.

22. Polymer gemäß einer der Ausführungsformen 1 bis 20, wobei $R_4$, für jede Wiederholungseinheit,

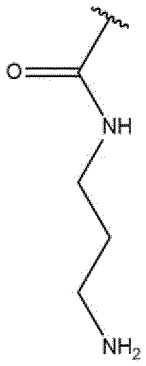

ist.

23. Polymer gemäß einer der Ausführungsformen 1 bis 20, wobei $R_4$, für jede Wiederholungseinheit,

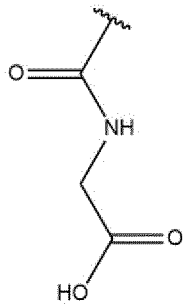

ist.

24. Polymer gemäß einer der Ausführungsformen 1 bis 23, wobei $A_4$ -H ist.

25. Polymer gemäß einer der Ausführungsformen 1 bis 23, wobei $A_4$ $-CH_3$ ist.

26. Polymer gemäß Ausführungsform 1, wobei

$R_1$, für jede Wiederholungseinheit, unabhängig ausgewählt ist aus der Gruppe bestehend aus

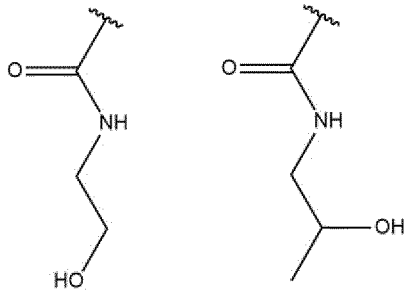

und ;

$R_2$, für jede Wiederholungseinheit, unabhängig ausgewählt ist aus der Gruppe bestehend aus

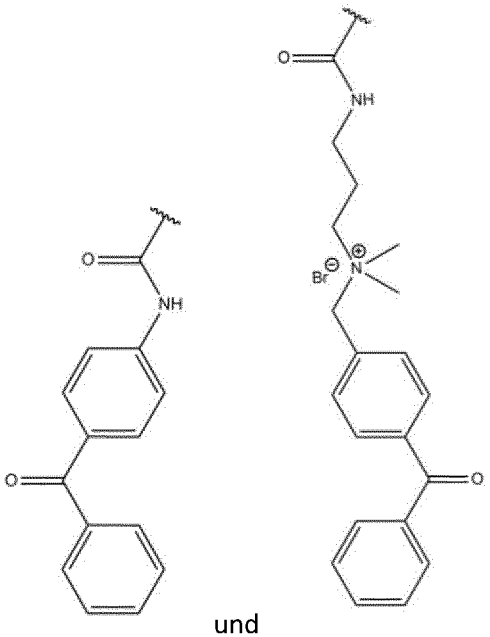

und ;

$R_3$, für jede Wiederholungseinheit, 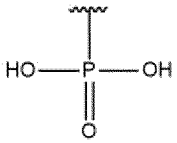 ist; und

$R_4$, für jede Wiederholungseinheit, unabhängig ausgewählt ist aus der Gruppe bestehend aus

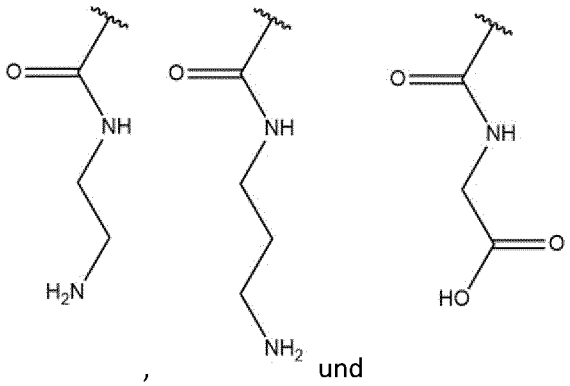

, und .

27. Polymer gemäß Ausführungsform 26, wobei $A_1$ -H ist, $A_2$ -H ist, $A_3$ -H ist, und $A_4$ -H ist.

28. Polymer gemäß einer der Ausführungsformen 1 bis 27, wobei Z ein Fragment A eines Kettenübertragungsreagenzes und Y ein Fragment B des Kettenübertragungsreagenzes ist.

29. Polymer gemäß einer der Ausführungsformen 1 bis 28, wobei das Kettenübertragungsreagenz ausgewählt ist aus der Gruppe bestehend aus Dithioester, Trithiocarbonate, Xanthate und Carbamate.

30. Polymer gemäß einer der Ausführungsformen 1 bis 27, wobei Y 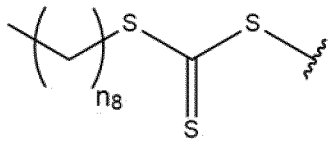

ist, und Z 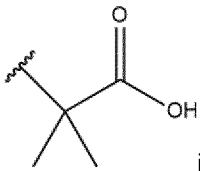

ist;

wobei $n_8$ eine Ganzzahl von 1 bis 24 ist, vorzugsweise eine Ganzzahl von 1 bis 14, weiter bevorzugt eine Ganzzahl von 1 bis 11; am bevorzugtesten 1 oder 11 ist.

31. Polymer gemäß einer der Ausführungsformen 1 bis 27, wobei Y und Z jeweils eine Endgruppe ist.

32. Polymer gemäß einer der Ausführungsformen 1 bis 31, wobei $x_{[2]}$ >0 bis <1 ist.

33. Polymer gemäß einer der Ausführungsformen 1 bis 32, wobei $x_{[3]}$ >0 bis <1 ist.

34. Polymer gemäß einer der Ausführungsformen 1 bis 33, wobei $x_{[4]}$ >0 bis <1 ist.

35. Polymer gemäß einer der Ausführungsformen 1 bis 31, wobei $x_{[2]}$ 0 ist und $x_{[3]}$ >0 bis <1 ist; und optional $x_{[4]}$ >0 bis <1 ist.

36. Polymer gemäß einer der Ausführungsformen 1 bis 31, wobei $x_{[2]}$ >0 bis <1 ist und $x_{[3]}$ 0 ist; und optional $x_{[4]}$ >0 bis <1 ist.

37. Polymer gemäß einer der Ausführungsformen 1 bis 31, wobei $x_{[2]}$ >0 bis <1 ist und $x_{[3]}$ >0 bis <1 ist; und optional $x_{[4]}$ >0 bis <1 ist.

38. Polymer gemäß Ausführungsform 1, ausgewählt aus der Gruppe bestehend aus

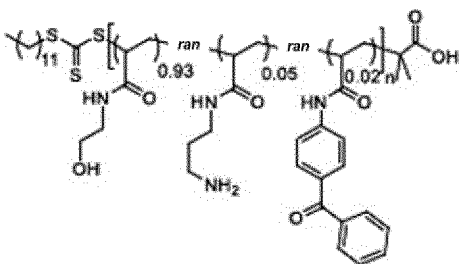
,
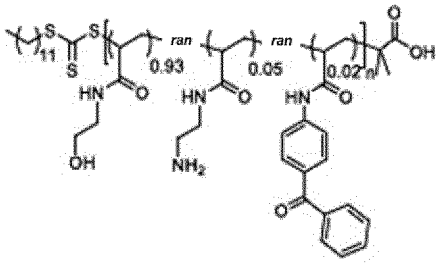
,
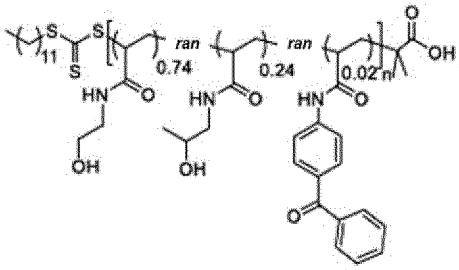
,
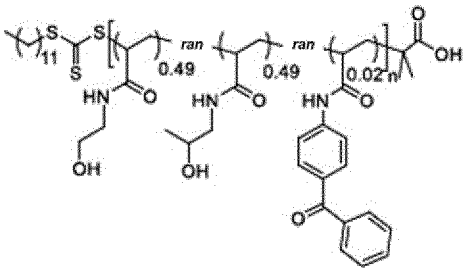
,
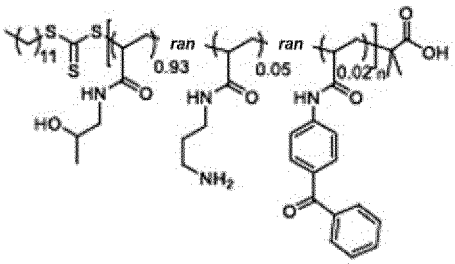
,
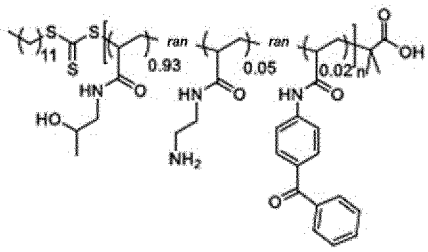
,
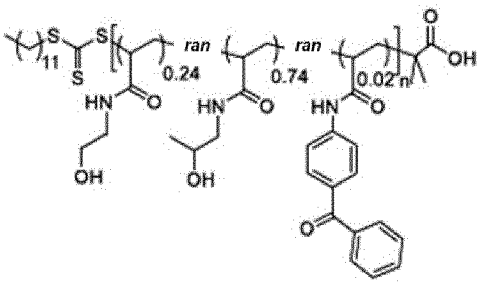
,
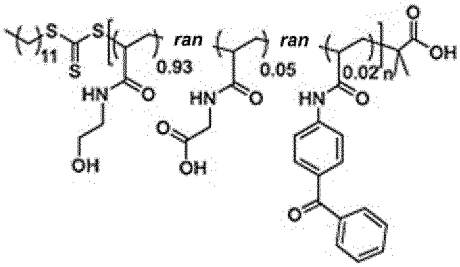
,
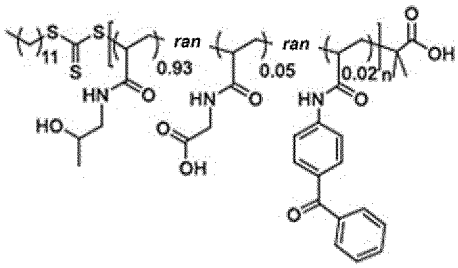
,
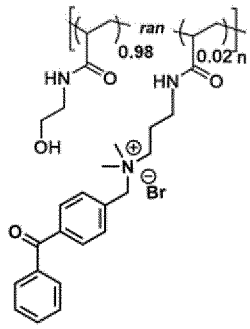
,
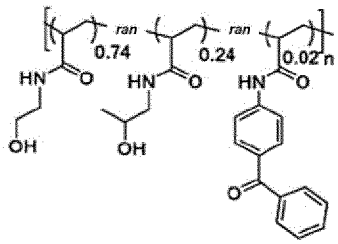
,

5

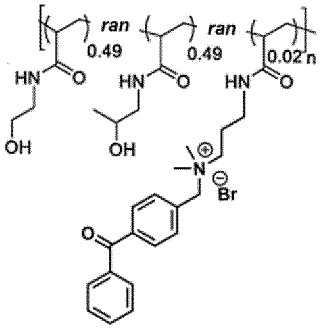

,
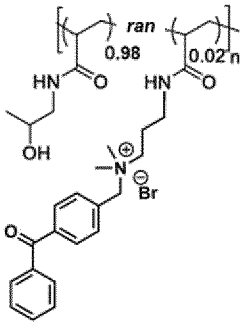

,
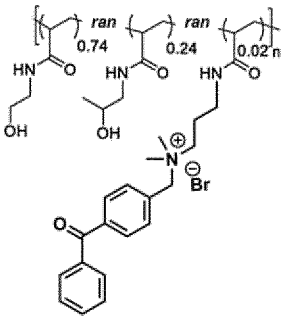

,

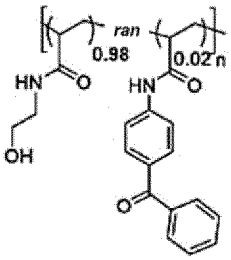

,
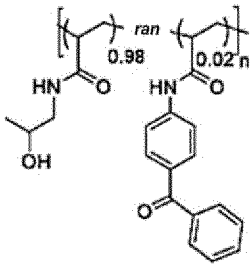

,
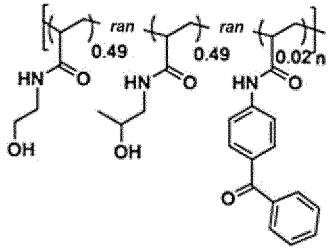

,

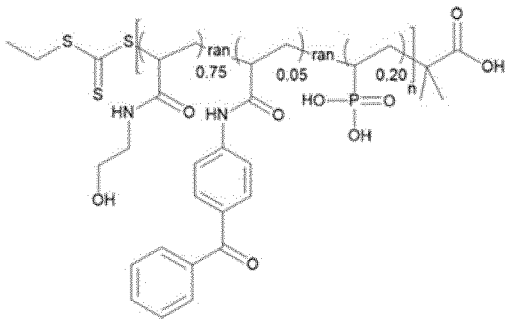

, und
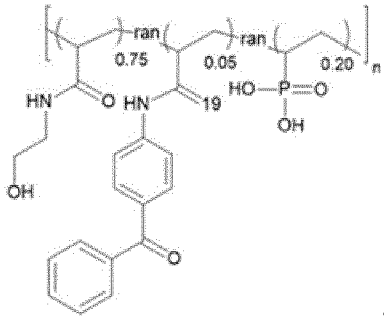

;

wobei n eine Ganzzahl von 2 bis 100.000 ist, wie beispielsweise eine Ganzzahl von 50 bis 10.000, z.B. eine Ganzzahl von 100 bis 2.000.

39. Polymer gemäß Ausführungsform 1, ausgewählt aus der Gruppe bestehend aus

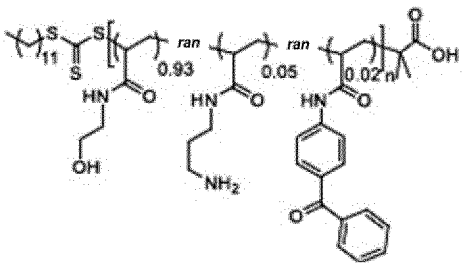

,
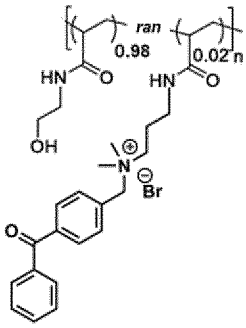

und
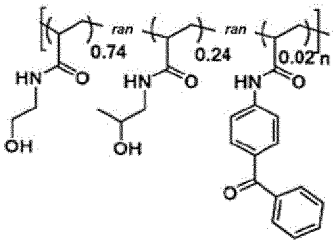

wobei n eine Ganzzahl von 2 bis 100.000 ist, wie beispielsweise eine Ganzzahl von 50 bis 10.000, z.B. eine Ganzzahl von 100 bis 2.000.

40. Polymer gemäß Ausführungsform 1, ausgewählt aus der Gruppe bestehend aus

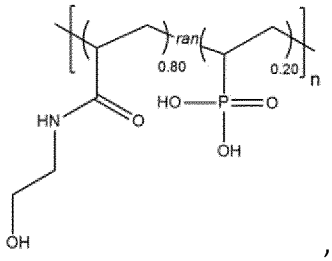

,
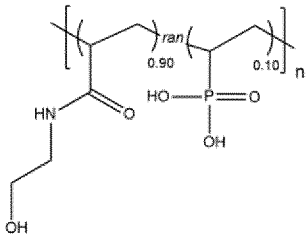

,
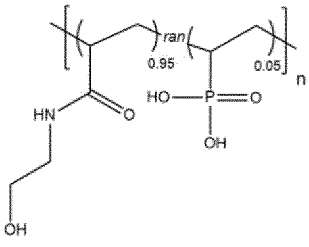

,
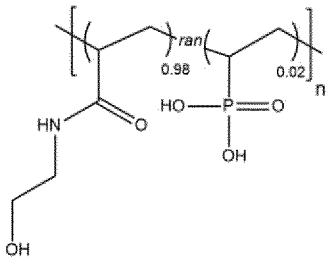

, und ;
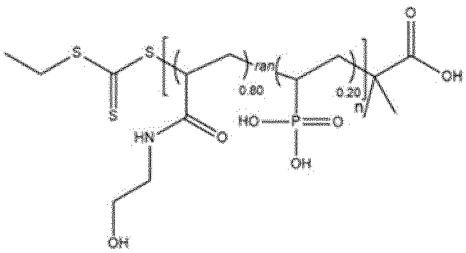


wobei n eine Ganzzahl von 2 bis 100.000 ist, wie beispielsweise eine Ganzzahl von 50 bis 10.000, z.B. eine Ganzzahl von 100 bis 2.000.

41. Polymer gemäß Ausführungsform 1, ausgewählt aus der Gruppe bestehend aus

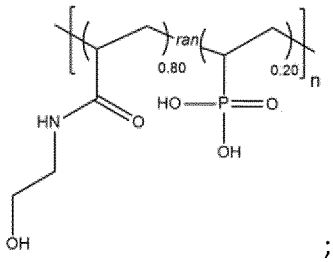

;

wobei n eine Ganzzahl von 2 bis 100.000 ist, wie beispielsweise eine Ganzzahl von 50 bis 10.000, z.B. eine Ganzzahl von 100 bis 2.000.

42. **Hydrogel**, umfassend ein vernetztes Polymer gemäß einer der Ausführungsformen 1 bis 41.

43. **Beschichtung**, umfassend mindestens eine Schicht, die ein Polymer gemäß einer der Ausführungsformen 1 bis 41 umfasst.

44. Beschichtung gemäß Ausführungsform 43, umfassend eine erste Schicht, die ein Polymer gemäß Ausführungsform 35 umfasst, und eine zweite Schicht, die ein Polymer gemäß Ausführungsform 36 umfasst.

45. Beschichtung gemäß Ausführungsform 44, wobei die erste und zweite Schichtmiteinander kreuzvernetzt sind.

46. Beschichtung gemäß Ausführungsform 43, die eine Schicht umfasst, die ein Polymer gemäß Ausführungsform 37 umfasst.

47. **Metallhaltiges Substrat**, dadurch gekennzeichnet, dass mindestens ein Teil seiner Oberfläche mit einer Beschichtung überzogen ist, welche mindestens eine Schicht umfasst, die ein Polymer gemäß einer der Ausführungsformen 1 bis 41 umfasst.

48. Substrat gemäß Ausführungsform 47, wobei die Beschichtung eine Beschichtung gemäß einer der Ausführungsformen 43 bis 46 ist.

49. Substrat gemäß Ausführungsform 47 oder 48, wobei das Substrat aus einem Metall besteht.

50. Substrat gemäß einer der Ausführungsformen 47 bis 49, wobei das Metall ausgewählt ist aus der Gruppe bestehend aus Titan, Titanlegierungen, Aluminium, Aluminiumlegierungen, Zink, Zinklegierungen, Zinn, Zinnlegierungen, Zirkonium, Zirkoniumlegierungen, Tantal, Tantallegierungen, Kobalt, Kobaltlegierungen, Nickel, Nickellegierungen, Kupfer, Kupferlegierungen, Magnesium, Magnesiumlegierungen, Molybdän, Molybdänlegierungen, Niob, Nioblegierungen, Chrom, Chromlegierungen, Eisen, Eisenlegierungen, rostfreier Stahl, und Metalloxiden davon.

51. Substrat gemäß einer der Ausführungsformen 47 bis 51, wobei das Metall ein Metalloxid umfasst.

52. Substrat gemäß Ausführungsform 51, wobei das Metalloxid ausgewählt ist aus der Gruppe bestehend aus $TiO_2$, $AlO_2$, ZnO, $ZrO_2$, ITO, IZO, $NiO_x$, $NiCoO_x$, $MoO_x$ $Fe_2O_3$, und $Nb_2O_5$.

53. Substrat gemäß einer der Ausführungsformen 51 bis 54, wobei das Substrat Titan, Titanoxid, oder eine Titanlegierung umfasst oder daraus besteht.

54. Substrat gemäß Ausführungsform 53, wobei die Titanlegierung Ti6Al4V oder Ti6AL4V ELI ist.

55. Substrat gemäß Ausführungsform 53, wobei das Titanoxid $TiO_2$ ist.

56. **Vorrichtung**, umfassend ein Substrat gemäß einer der Ausführungsformen 47 bis 55.

57. Vorrichtung gemäß Ausführungsform 56, wobei das Substrat mindestens einen Teil der Oberfläche der Vorrichtung bildet.

58. Vorrichtung gemäß Ausführungsform 56 oder 57, wobei die Vorrichtung eine medizinische Vorrichtung ist.

59. Vorrichtung gemäß einer der Ausführungsformen 56 bis 58, wobei die Vorrichtung ein Implantat ist.

60. **Verwendung** einer Vorrichtung gemäß Ausführungsform 59 als Kurzzeitimplantat.

61. **Verfahren** zur Beschichtung eines Substrats, umfassend die Schritte

    (a) Bereitstellen eines metallhaltigen Substrates, und

    (b) In-Kontakt-Bringen des Substrates mit einer Lösung des Polymers gemäß einer der Ausführungsformen 1 bis 41;

    (c) gegebenenfalls Trocknen des Substrates; und

    (d) gegebenenfalls UV-Bestrahlung.

62. **Verfahren** zur Beschichtung einer Vorrichtung, umfassend die Schritte

    (a) Bereitstellen einer Vorrichtung, umfassend ein metallhaltiges Substrat, und

(b) In-Kontakt-Bringen der Vorrichtung bzw. des Substrates mit einer Lösung des Polymers gemäß einer der Ausführungsformen 1 bis 41;

(c) gegebenenfalls Trocknen des Substrates; und

(d) gegebenenfalls UV-Bestrahlung.

63. Verfahren gemäß Ausführungsform 61 oder 62, wobei Schritt (b) ein erstes In-Kontakt-Bringen der Vorrichtung bzw. des Substrates mit einer Lösung des Polymers gemäß Ausführungsform 39, gefolgt von einem zweiten In-Kontakt-Bringen der Vorrichtung bzw. des Substrates mit einer Lösung des Polymers gemäß Ausführungsform 40 umfasst (Zwei-Schicht-System).

64. Verfahren gemäß Ausführungsform 61 oder 62, wobei Schritt (b) das In-Kontakt-Bringen der Vorrichtung bzw. des Substrates mit einer Lösung des Polymers gemäß Ausführungsform 41 umfasst (Einschichtsystem).

65. Verfahren gemäß einer der Ausführungsformen 61 bis 64, wobei das In-Kontakt-Bringen das Besprühen oder Begießen mit oder Eintauchen in der/die Lösung umfasst.

66. **Verwendung** des Polymers gemäß einer der Ausführungsform 1 bis 41 als antiadhäsive Beschichtung, vorzugsweise als antiadhäsive Beschichtung auf einer medizinischen Vorrichtung, ferner bevorzugt als antiadhäsive Beschichtung auf einem Implantat.

67. **Polymer** gemäß einer der Ausführungsformen 1 bis 41 **zur Verwendung** in einem Verfahren zu Behandlung einer Knochenfraktur in einem Patienten, das Verfahren umfassend

a) Bereitstellen eines Implantats, umfassend ein Substrat, das dadurch gekennzeichnet ist, dass mindestens ein Teil seiner Oberfläche mit einer Beschichtung überzogen ist, welche mindestens eine Schicht umfasst, die ein Polymer gemäß einer der Ausführungsformen 1 bis 45 umfasst; und

b) Einsetzen des Implantats an einer Knochenreparaturstelle oder im Bereich der Knochenfraktur im Patienten.

68. Polymer zur Verwendung gemäß Ausführungsform 67, wobei das Implantat das Implantat der Ausführungsform 59 ist.

69. **Monomer** aufweisend eine Struktur der allgemeinen Formel (II)

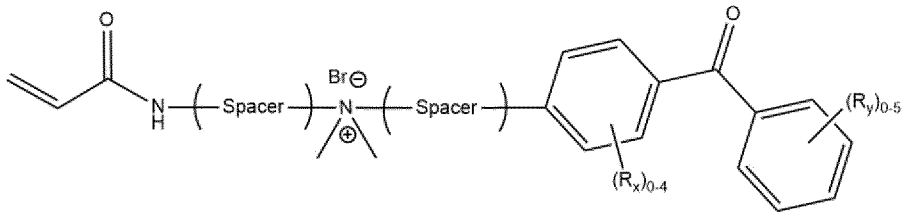


(II)

wobei jeder „Spacer“ jeweils unabhängig voneinander ausgewählt ist aus der Gruppe bestehend aus linearen oder verzweigten Alkylketten und linearen oder verzweigten Ethylen- oder Propylenoxidketten, vorzugweise unabhängig voneinander ausgewählt aus linearen oder verzweigen $C_{1-20}$-Alkylketten;

$R_x$, jeweils unabhängig voneinander, -OH, Halogen (Br, Cl, I, oder F), Halogen-$C_{1-4}$ Alkyl (z.B. -$CF_3$, -$CCL_3$, -$CBr_3$, -$CI_3$), -$NH_2$, -$C_{1-4}$ Alkyl, -$C_{2-4}$ Alkenyl, -$C_{2-4}$ Alkinyl, -$OC_{1-4}$ Alkyl, -$OC_{2-4}$ Alkenyl, -$OC_{2-4}$ Alkinyl -$NO_2$, -SH, -$SO_2H$, -$SO_3H$, -NCS, -SCN, -COOH oder Cyano ist; und

$R_y$, jeweils unabhängig voneinander, -OH, Halogen (Br, Cl, I, oder F), Halogen-$C_{1-4}$ Alkyl (z.B. -$CF_3$, -$CCL_3$, -$CBr_3$, -$CI_3$), -$NH_2$, -$C_{1-4}$ Alkyl, -$C_{2-4}$ Alkenyl, -$C_{2-4}$ Alkinyl, -$OC_{1-4}$ Alkyl, -$OC_{2-4}$ Alkenyl, -$OC_{2-4}$ Alkinyl -$NO_2$, -SH, -$SO_2H$, -$SO_3H$, -NCS, -SCN, -COOH oder Cyano ist.

70. **Monomer** aufweisend eine Struktur der allgemeinen Formel (IIa)

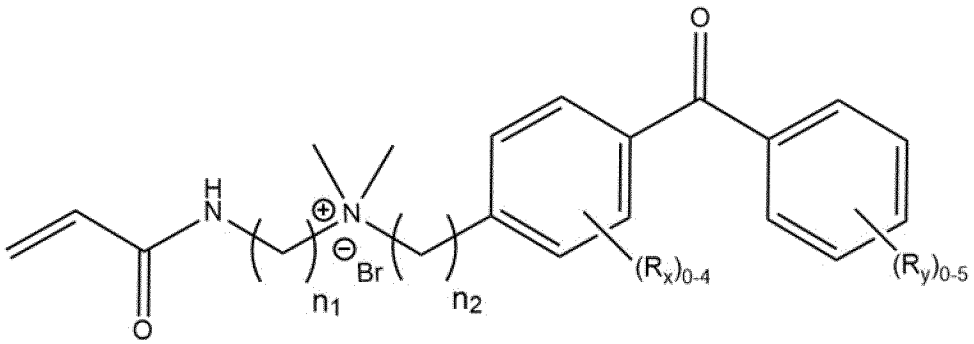


(IIa)

wobei $n_1$ und $n_2$ jeweils unabhängig voneinander 1, 2, 3, 4, 5, 6, 7, 8, 9, 10, 11, 12, 13, 14, 15, 16, 17, 18, 19 oder 20 ist;

$R_x$, jeweils unabhängig voneinander, -H, -OH, Halogen (Br, Cl, I, oder F), Halogen-$C_{1-4}$ Alkyl (z.B. -$CF_3$, -$CCL_3$, -$CBr_3$, -$CI_3$), -$NH_2$, -$C_{1-4}$ Alkyl, -$C_{2-4}$ Alkenyl, -$C_{2-4}$ Alkinyl, -$OC_{1-4}$ Alkyl, -$OC_{2-4}$ Alkenyl, -$OC_{2-4}$ Alkinyl -$NO_2$, -SH, -$SO_2H$, -$SO_3H$, -NCS, -SCN, -COOH oder Cyano ist; und

$R_y$, jeweils unabhängig voneinander, -H, -OH, Halogen (Br, Cl, I, oder F), Halogen-$C_{1-4}$ Alkyl (z.B. -$CF_3$, -$CCL_3$, -$CBr_3$, -$CI_3$), -$NH_2$, -$C_{1-4}$ Alkyl, -$C_{2-4}$ Alkenyl, -$C_{2-4}$ Alkinyl, -$OC_{1-4}$ Alkyl, -$OC_{2-4}$ Alkenyl, -$OC_{2-4}$ Alkinyl -$NO_2$, -SH, -$SO_2H$, -$SO_3H$, -NCS, -SCN, -COOH oder Cyano ist.

71. Monomer gemäß Ausführungsform 70, wobei $n_1$ 1 bis 10 ist.

72. Monomer gemäß Ausführungsform 70, wobei $n_1$ 1 bis 5 ist.

73. Monomer gemäß Ausführungsform 70, wobei $n_1$ 1 bis 3 ist.

74. Monomer gemäß Ausführungsform 70, wobei $n_1$ 3 ist.

75. Monomer gemäß einer der Ausführungsformen 70 bis 74, wobei $n_2$ 1 bis 10 ist.

76. Monomer gemäß einer der Ausführungsformen 70 bis 74, wobei $n_2$ 1 bis 5 ist.

77. Monomer gemäß einer der Ausführungsformen 70 bis 74, wobei $n_2$ 1 bis 3 ist.

78. Monomer gemäß einer der Ausführungsformen 70 bis 74, wobei $n_2$ 1 ist.

79. Monomer gemäß einer der Ausführungsformen 69 bis 78, wobei $(R_x)_{0-4}$ $(R_x)_0$ ist.

80. Monomer gemäß einer der Ausführungsformen 69 bis 79, wobei $(R_y)_{0-4}$ $(R_y)_0$ ist.

81. Monomer gemäß Ausführungsform 70, welches folgende Struktur aufweist.

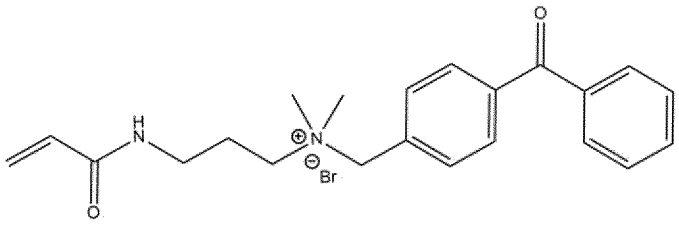


82. Verwendung eines Monomers gemäß einer der Ausführungsformen 69 bis 81 als Photovernetzer.

# 11 General Conclusion and Outlook

The results presented in this thesis demonstrate the performance and versatility of tailored hydrogels across diverse applications in the biomedical field. Throughout the investigations, it transpired that it is crucial to clarify the distinct properties for specific applications during the initial stages of polymer design. This approach of integrating application-specific requirements into the foundational design framework has proven essential for achieving desired functionality in hydrogel systems.

The review article of responsive hydrogels combined with plasmonic systems revealed significant potential in sensing and actuation applications. The integration of these technologies presents promising opportunities for advanced bioanalytical systems operating in contact with human tissue, as well as a future basis for microscopic devices capable of navigating through complex vascular networks to perform precise, targeted interventions either autonomously or *via* remote control.

Further advancing the field, a novel approach was presented utilizing multiphoton absorption-based crosslinking for the precise preparation of thermoresponsive, biofunctional NIPAAm hydrogel microstructures. This methodology opens new avenues for developing stimuli-actuated microstructures suitable for micromachines and actively tunable interfaces that enhance bioanalytical technologies.

The development of a tandem photoinduced process for poly(2-alkyl-2-oxazoline) network formation represents another significant contribution. This process, involving concurrent photodeprotection of polymer-associated thiol units and their thiol-ene click coupling to vinyl crosslinker agents, offers diverse potential applications across materials science, biomedical engineering, and surface modification technologies.

The performed research also yielded a comprehensive toolbox for thermoresponsive and photocrosslinkable poly(2-alkyl-2-oxazoline)s with ultralow-fouling characteristics. The remarkable performance of these hydrogel coatings against fouling by undiluted human blood plasma, achieved through surface-attached, water-swollen polymer networks based on poly(2-alkyl-2-oxazoline)s with pendent betaine moieties, establishes them as promising matrices for advanced biosensor architectures.

Although the investigation into drug-loaded wound dressings with permeable hydrogel membranes for continuous drug delivery to chronic DFU necessitated modifications to the initial experimental design, the foundational concept remains promising. Further refinement of this approach could significantly improve wound treatment protocols and reduce the burden of complications for diabetes patients globally.

Notable progress was also made in developing implant coatings that combine antiadhesive acrylamide-based hydrogels with photocrosslinkers possessing intrinsic antibacterial properties and anchor groups specifically designed for titanium substrates. While additional validation through appropriate *in vivo* models is required, successful clinical translation of this coating technology could substantially reduce complications associated with short-term trauma implant removal, thereby improving therapeutic outcomes and patient quality of life.

Looking forward, the integration of these various hydrogel technologies presents opportunities for even more sophisticated, application-specific systems. The convergence of responsive behavior, biofunctionality, and advanced fabrication techniques is expected to yield increasingly well-tailored solutions for complex biomedical challenges. Given the versatility and adaptability demonstrated throughout this research, hydrogel systems are poised to make substantial contributions to future healthcare approaches, potentially revolutionizing treatment modalities across multiple medical disciplines.

## Acknowledgements

First and foremost, I thank Ulrich Jonas for providing me the opportunity to deepen my understanding of chemistry through my PhD studies in his research group. His guidance, mentorship throughout these years, and creation of a positively reinforcing environment have enabled me to thrive. I am grateful to Petra Frank for her structured and meticulous lab management. Her exceptional practical skills were instrumental in the smooth progression of my research. The group of macromolecular chemistry has been my academic home since I joined as a bachelor's research student in 2016. I am grateful to all group members I've encountered during my time in the labs. The welcoming atmosphere, enjoyable group activities, thought-provoking conversations, and collaborative spirit fostered lasting relationships. I especially thank Thorben Jaik and Niklas Jung, my first lab supervisors, who guided my initial steps in research and witnessed my scientific development over the years. Special thanks go to Silvia Freese, Aliia Ibragimova, and Ali Balasini, who stood beside me through the challenging times of PhD candidacy. Your scientific support, friendship, and ability to bring laughter made this journey memorable. I am thankful for the opportunity to supervise many talented students whose curiosity, eagerness to learn, and unique abilities made mentoring a rewarding experience. The collaborations with external research partners have been invaluable learning experiences. I particularly thank Ulrike Ritz and Jakub Dostalek for sharing their expertise through our interdisciplinary projects. Our scientific discussions were always enlightening.

Beyond the academic sphere, my family and friends provided unwavering support through research challenges – even when the intricacies of my synthesis problems were beyond their comprehension. Further on, I am truly thankful for always having my four-pawed colleague Kalle at my side, purring away the distress after long working days. Finally, I am deeply grateful to my partner and now husband, Chrisitan Wiesner, who has supported me since the beginning. His genuine interest in my work (Including profound questions about dynamic light scattering during Sunday breakfast- Haha!) and patience with my exhausted, hungry, and stressed states on difficult days have been invaluable.

This journey would not have been possible without each of you.
I am truly fortunate to have you all in my life.
Thank you.

# Appendix

## Index

Supporting Information:
Microstructuring of Thermoresponsive Biofunctional Hydrogels by Multiphoton Photocrosslinking ……. A1

Supporting Information:
Plasmon-Enhanced Multiphoton Polymer Crosslinking for Selective Modification of Plasmonic Hotspots …… A8

Supporting Information:
Thiol-Substituted Poly(2-Oxazoline)s with Photolabile Protecting Groups - Tandem Network Formation by Light ……. A10

Supporting Information:
Thermoresponsive and Photocrosslinkable Poly(2-alkyl-2-oxazoline) Toolbox – Customizable Ultralow-Fouling Hydrogel Coatings for Blood Plasma Environments … A16

Experimental Details:
Hydrogel-Based Diffusion Barriers for Drug-Loaded Wound Dressings ……. A28

Invention Disclosure:
Hydrogel-Based Diffusion Barriers for Drug-Loaded Wound Dressings ……. A29

Supporting Information:
Antiadhesive and Antibacterial Coatings for Short-Term Titanium Implants ……. A34

Patent Description:
Nonstick Polymer Coatings for Short-Term Implants…… A38

ADVANCED FUNCTIONAL MATERIALS

Supporting Information

for *Adv. Funct. Mater.*, DOI 10.1002/adfm.202315578

Microstructuring of Thermoresponsive Biofunctional Hydrogels by Multiphoton Photocrosslinking

*Yevhenii M. Morozov*, Fiona Wiesner (née Diehl), Jonas J. Grün, Matthias Pertiller, Stefan Fossati, Katharina Schmidt, Nestor Gisbert Quilis, Claudia Gusenbauer, Barbara Zbiral, Jose Luis Toca-Herrera, Sven Klees, Clinton Richard Victor Thiagarajan, Ulrich Jonas* and Jakub Dostalek**



**Microstructuring of Thermoresponsive Biofunctional Hydrogels by Multiphoton Photocrosslinking**

*Yevhenii M. Morozov*, Fiona Wiesner (née Diehl), Jonas J. Grün, Matthias Pertiller, Stefan Fossati, Katharina Schmidt, Nestor Gisbert Quilis, Claudia Gusenbauer, Barbara Zbiral, Jose Luis Toca-Herrera, Sven Klees, Clinton Richard Victor Thiagarajan, Ulrich Jonas*, and Jakub Dostalek**



**$^1$H and $^{13}$C NMR Spectra of Monomers**

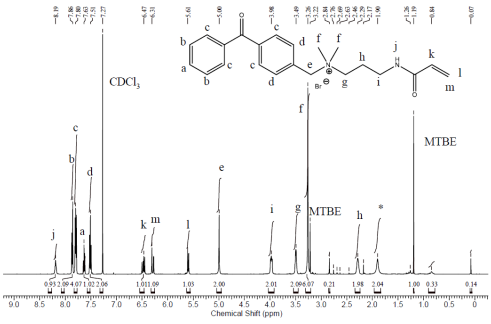


**Figure S1.** $^1$H NMR spectrum (500 MHz) of BPQAAm in $CDCl_3$ with assigned signals. Shows one impurity at 1.90 ppm, marked with an asterisk.

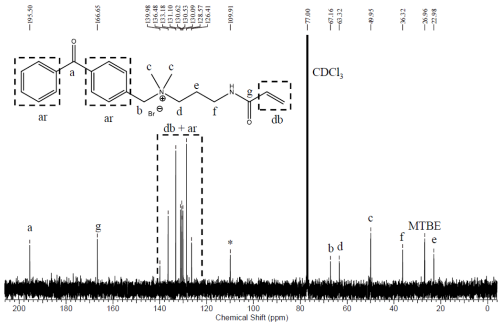


**Figure S2.** $^{13}$C NMR (125 MHz) spectrum of BPQAAm in $CDCl_3$ with assigned signals, with one impurity at 109.9 ppm.





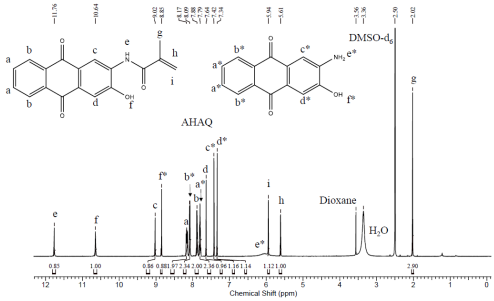


**Figure S3.** $^1$H NMR (500 MHz) spectrum of MAAHAQ in DMSO-*d6* with assigned signals. The product was obtained as a mixture of the educt AHAQ (signals are marked with an asterisk) and the product.

**Co- and Terpolymer Synthesis Details**

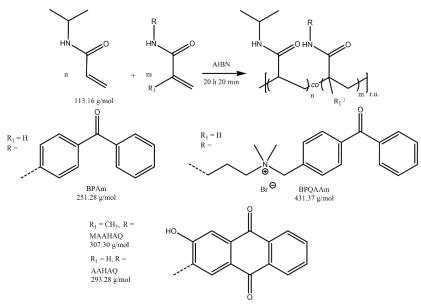


**Scheme S1.** Synthesis of NIPAAm copolymers containing the crosslinker monomers BPAm, BPQAAm, AAHAQ, and MAAHAQ.

**Table S1.** Summary for all copolymerization reactions with the used amounts of NIPAAm [M1] and a comonomer (BPAm, AAHAQ, BPQAAm, MAAHAQ) [M2]. Further given are the initiator amounts [I] and the yields of the reactions. GRJ- indicates the specific sample number.

| GRJ- | [M1]:[M2]:[I] | M2 / mg (µmol) | AIBN / mg (µmol) | Yield / mg (%) | *Đ* | *Mp* / kg mol$^{-1}$ |
|---|---|---|---|---|---|---|
| Poly(NIPAm$_n$-*co*-BPAm$_m$) | | | | | | |
| 031 [a,b] | 99/1/0.5 | 11.2 (44.6) | 3.66 (22.3) | 173.0 (34) | - | - |
| 031-1 | 99/1/0.5 | 11.2 (44.6) | 3.66 (22.3) | 410.8 (80) | 2.97 | 110.6 |
| 033-1 [c,d] | 99/1/0.5 | 19.3 (44.6) | 3.66 (22.3) | 335.0 (65) | 2.57 | 101.0 |
| 035 | 95/5/0.5 | 58.4 (233) | 3.82 (23.2) | 450.2 (81) | 2.55 | 153.1 |
| Poly(NIPAm$_n$-*co*-BPQAAm$_m$) | | | | | | |
| 033 [b] | 99/1/0.5 | 19.3 (44.6) | 3.66 (22.3) | 289.0 (56) | - | - |
| 037 [e] | 95/5/0.5 | 50.2 (116) | 1.91 (11.6) | 210.1 (70) | 2.39 | 74.9 |
| Poly(NIPAm$_n$-*co*-AAHAQ$_m$) | | | | | | |
| 032 [b,f] | 99/1/0.5 | 13.1 (44.6) | 3.66 (22.3) | - | - | - |
| 032-1 [b,g] | 99/1/0.5 | 13.1 (44.6) | 3.66 (22.3) | 112.1 (22) | 1.30 | 56.1 |
| 032-2 [d] | 99/1/0.5 | 13.1 (44.6) | 3.66 (22.3) | 205.3 (40) | 1.39 | 30.2 |
| 036 | 95/5/0.5 | 68.2 (233) | 3.82 (23.2) | 170.0 (30) | 1.56 | 36.9 |
| 041 | 99/1/1 | 13.1 (44.6) | 7.33 (44.6) | 178.2 (35) | 1.37 | 32.0 |
| 042 | 95/5/1 | 68.2 (233) | 7.63 (46.5) | 290.6 (51) | 1.74 | 28.1 |
| 043 [h] | 99/1/0.5 | 13.1 (44.6) | 3.66 (22.3) | 202.3 (39) | 1.38 | 25.2 |
| 045 [i,h] | 99/1/0.5 | 13.1 (44.6) | 3.66 (22.3) | 243.1 (47) | 1.45 | 24.2 |
| 046 [h] | 99/1/1 | 13.1 (44.6) | 7.33 (44.6) | 212.7 (41) | 1.47 | 23.4 |
| Poly(NIPAm$_n$-*co*-MAAHAQ$_m$) | | | | | | |
| 044 [d] | 99/1/0.5 | 13.1 (44.6) [j] | 3.66 (22.3) | 265 (52) | 1.33 | 27.8 |
| 047 [e] | 95/5/0.5 | 35.7 (116) [k] | 1.91 (11.6) | 195 (68) | 1.62 | 35.4 |





[a] Methanol was used as solvent.
[b] The reaction temperature was 60 °C.
[c] The polymer was redissolved in 1,4-Dioxane for the precipitation.
[d] The reaction was carried out with an oil bath.
[e] 3.5 ml of solvent were used and half of the NIPAm (250 mg, 2.20 mmol).
[f] DMF was used without further purification.
[g] The polymer was redissolved in MeOH for the precipitation.
[h] The reaction temperature was set to 80 °C.
[i] The reaction time was increased to 44 h 30 min.
[j] The actual used amount was calculated using the $^1$H-spectrum and a total of 20.1 mg the product was used.
[k] The actual used amount was calculated using the $^1$H-spectrum and a total of 56.2 mg of the product were used.

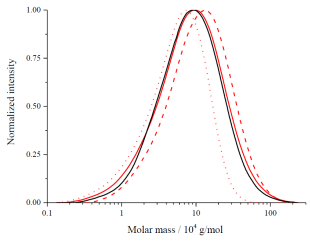


**Figure S4.** Recorded molar mass distribution (RI detector) of poly(NIPAm$_m$-co-BPAm$_n$) (red) and poly(NIPAm$_m$co-BPQAAm$_n$) polymers (black). For the BPAm copolymers, the corresponding curves were modified (GRJ-31-1, GRJ-035, GRJ-033-1).





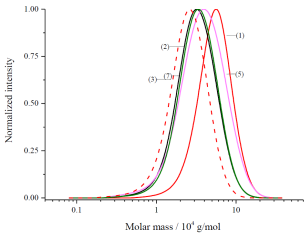


**Figure S5.** Molar mass distributions recorded by GPC (RI detector) of poly(NIPAm$_m$-co-AAHAQ$_n$). Curves are colored according to the induced change starting from the reference poly(NIPAm$_{98}$-co-AAHAQ$_2$) (2) in black, prepared at 65°C with 0.5 mol% feed-in of AIBN. The induced changes in the reaction temperature are shown in red. The dashed red line shows an increase to 80 °C (3) and the solid red line a decrease to 60 °C (1). The pink line corresponds to a 5% feed-in of AAHAQ (5) and the green line to a feed-in of 1% AIBN (7).

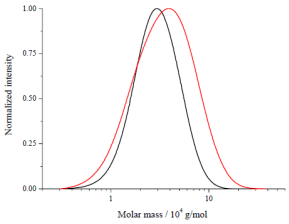


**Figure S6.** Recorded molar mass distribution (RI detector) of poly(NIPAm$_m$-co-MAAHAQ$_n$). The copolymers with 1% feed-in are shown in black and the 5% feed-in of MAAHAQ is shown in red.





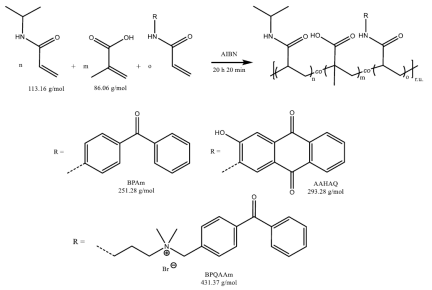


**Scheme S2.** Synthesis of NIPAAm and MAA-based terpolymers containing the crosslinker monomers BPAm, BPQAAm, AAHAQ, and MAAHAQ.

**Table S2.** Summary for all terpolymerization reactions with the used amounts of NIPAAm [M1], MAA [M2] and a crosslinker monomer (BPAm, AAHAQ, BPQAAm, MAAHAQ) [M3]. Further given are the initiator amounts [I] and the yields of the reactions. GRJ- indicates the specific sample number.

| GRJ- | [M1]:[M2]:[M3]:[I] | [M1] / mg (mmol) | [M2] / mg (mmol) | [M3] / mg (µmol) | [I] / mg (µmol) | Yield / mg (mmol) | *Mp* / kg mol$^{-1}$ (*Đ*) |
|---|---|---|---|---|---|---|---|
| Poly(NIPAm$_{90}$-*co*-MAA$_5$-*co*-AAHAQ$_5$) | | | | | | | |
| 048 | 90/5/5/0.5 | 225 (1.99) | 9.5 (0.11) | 34.0 (110) | 1.81 (11.0) | 180 (67) | 34.0 (1.68) |
| Poly(NIPAm$_{94}$-*co*-MAA$_5$-*co*-BPAm$_1$) | | | | | | | |
| 049 | 94/5/1/0.5 | 250 (2.21) | 10.1 (0.12) | 5.91 (23.5) | 1.93 (11.8) | 215 (81) | 138.1 (3.03) |
| Poly(NIPAm$_{94}$-*co*-MAA$_5$-*co*-BPQAAm$_1$) | | | | | | | |
| 050 | 94/5/1/0.5 | 250 (2.21) | 10.1 (0.12) | 10.1 (23.5) | 1.93 (11.8) | 198 (73) | 97.0 (1.89) |

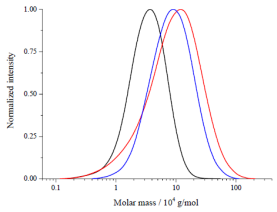


**Figure S7.** Recorded molar mass distribution (RI detector) of the three terpolymers poly(NIPAm$_{90}$-co-MAA$_5$-co-AAHAQ$_5$) (black), poly(NIPAm$_{94}$-co-MAA$_5$-co-BPAm$_1$) (red) and poly(NIPAm$_{94}$-co-MAA$_5$-co-BPQAAm$_1$) (blue).

**$^1$H and $^{13}$C NMR Spectra of Polymers**

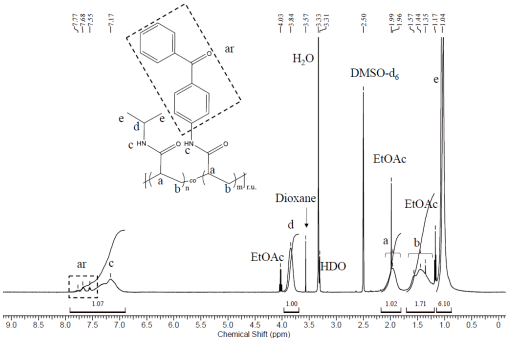


**Figure S8.** $^1$H NMR (500 MHz) spectrum of poly(NIPAm$_{99}$-*co*-BPAm$_1$) in DMSO-*d6* with assigned signals.





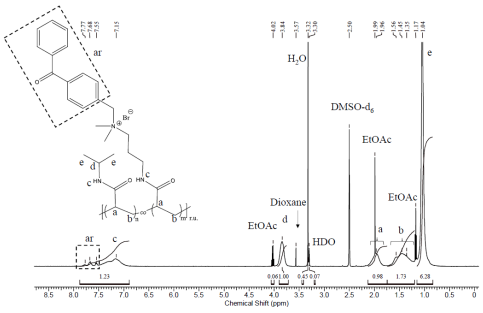


**Figure S9.** $^1$H NMR (500 MHz) spectrum of poly(NIPAm$_{99}$-*co*-BPQAAm$_1$) in DMSO-*d6* with assigned signals.

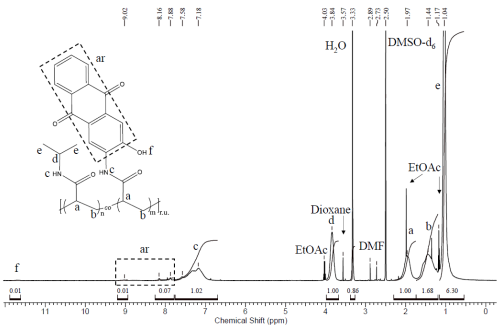


**Figure S10.** $^1$H NMR (500 MHz) spectrum of poly(NIPAm$_{99}$-*co*-AAHAQ$_1$) in DMSO-*d6* with assigned signals.





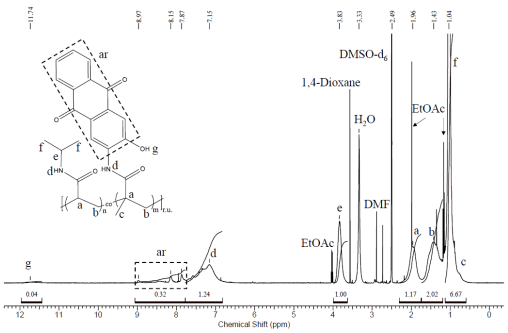


**Figure S11.** $^1$H NMR (500 MHz) spectrum of poly(NIPAm$_{95}$-co-MAAHAQ$_5$) in DMSO-*d6* with assigned signals.

**UV/VIS Absorption Spectra of Polymers**

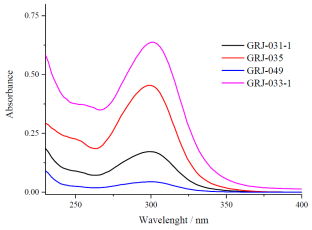


**Figure S12**. UV/VIS measurements of all poly(NIPAm$_m$-co-BPAm$_n$) (0.3 g/l) in DMSO. GRJ-033-1 had a concentration of 0.8 g/l.





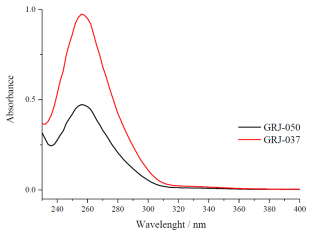


**Figure S13.** UV/VIS measurements of all poly(NIPAm$_m$-co-BPQAAm$_n$) (0.3 g/l) in DMSO. The corresponding concentrations are 0.2 g/l (GRJ-037) and 0.15 g/l (GRJ-050).

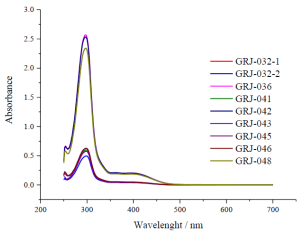


**Figure S14.** UV/VIS measurements of all poly(NIPAm$_m$-co-AAHAQ$_n$) (0.3 g/l) in DMSO.

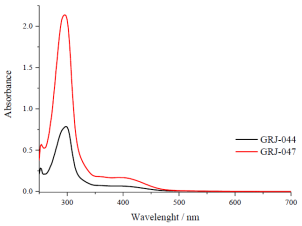


**Figure S15.** UV/VIS measurements of all poly(NIPAm$_m$-co-MAAHAQ$_n$) (0.3 g/l) in DMSO.

**Crosslinker Built-In Ratios**

**Table S3.** Comparison of the crosslinker feed-in and build-in ratios, determinded by calculation from $^1$H NMR spectra and UV/VIS spectroscopy. Depending on the method used for characterization, different error sources lead to variations in the determined built-in ratios.

| GRJ- | Crosslinker feed-in / mol% | Crosslinker built-in determined by UV/VIS spectroscopy / mol% | Crosslinker built-in determined by NMR spectroscopy / mol% |
|---|---|---|---|
| Poly(NIPAm$_m$-*co*-BPAm$_n$), SD: 8% | | | |
| 31 | 1 | - | 1.8 |
| 31-1 | 1 | 0.8 | 1.8 |
| 033-1 | 1 | 1.1 | 2.5 |
| 35 | 5 | 2.2 | 7.0 |
| Poly(NIPAm$_m$-*co*-BPQAAm$_n$), SD: 2% | | | |
| 037 | 5 | 5.3 | 4.5 |
| Poly(NIPAm$_m$-*co*-AAHAQ$_n$), SD: 5% | | | |
| 032-1 | 1 | 0.7 | 0.6 |
| 032-2 | 1 | 1.3 | 1.4 |
| 043 | 1 | 1.7 | 1.8 |
| 045 | 1 | 1.6 | 2.0 |
| 036 | 5 | 7.5 | 7.0 |
| 042 | 5 | 7.4 | 8.2 |
| 041 | 1 | 1.6 | 1.8 |
| 046 | 1 | 1.7 | 1.8 |
| Poly(NIPAm$_m$-*co*-MAAHAQ$_n$), SD: 3% | | | |
| 44 | 1 | 1.2 | 2.6 |
| 47 | 5 | 3.5 | 6.4 |





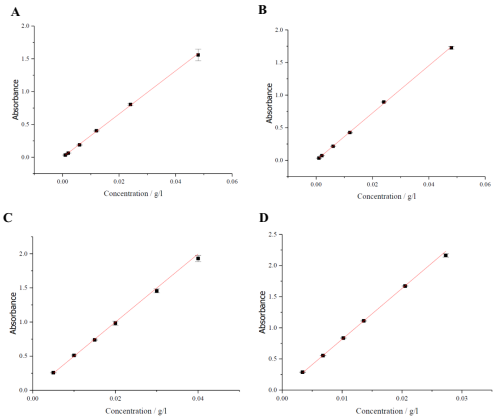


**Figure S16.** Calibration curves from UV-VIS characterization of the four different crosslinker monomers (**A**) BPAm, (**B**) BPQAAm), (**C**) AAHAQ, and (**D**) MAAHAQ. Here, the UV-VIS absorbance is plotted against the monomer concentration.





**SPR Measurement**

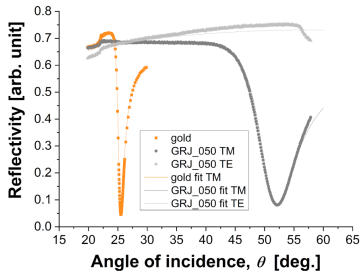


**Figure S17.** Angular SPR measurement of the poly(NIPAAm$_{94}$-*co*-MAA$_5$-BPQAAm$_1$) layer obtained by spin-coating of a 150 µL volume of the polymer solution (2% w/w in EtOH) at 2,000 rpm for 60 s on a 50 nm gold slide (25 µm to 25 µm size) and dried overnight at 50 °C in a vacuum oven. Fitting parameters give 97.4 nm to the resulting polymer layer in dry. "GRJ_050" is a code name for the poly(NIPAAm$_{94}$-*co*-MAA$_5$-BPQAAm$_1$) polymer.

**Lithography Setup**

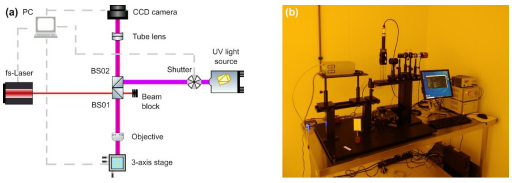


**Figure S18.** General-purpose home-built multiphoton absorption lithography setup[1]: (a) schematic of the optical setup and (b) photography of the setup.

[1]Y. M. Morozov, N. G. Quilis, F. Diehl, S. Klees, J. Grün, U. Jonas, J. Dostalek, *SPIE Proc.* **2022**, *12145*, 1214502.





**Microscopy Images**

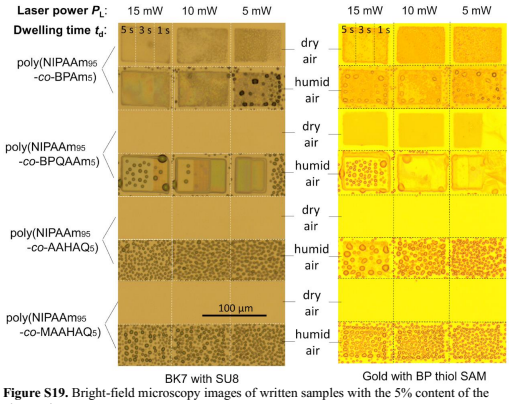


**Figure S19.** Bright-field microscopy images of written samples with the 5% content of the photoactive monomers.

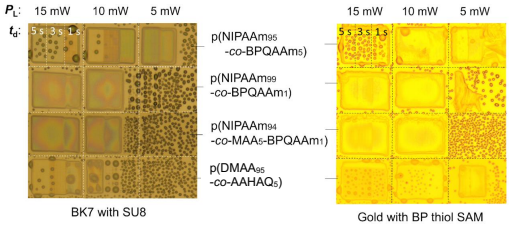


**Figure S20.** Bright-field microscopy images of written NIPAAm- and BPQAAm-based polymers showing the effect of the different amounts of the crosslinker and the presence of the MMA compound on the crosslinking ability. The Figure also illustrates the effect of the attachment of the AAHAQ photoactive compound to a different polymer backbone (to the DMAA main chain instead of the NIPAAm one) on the crosslinking process (the bottom row).

**AFM Images and Hight Profiles**

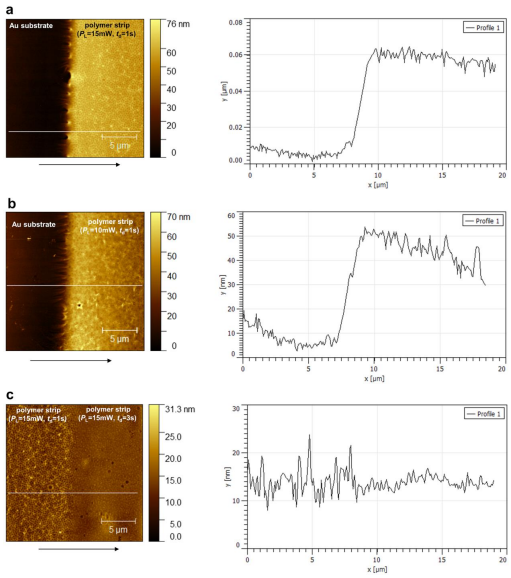


**Figure S21.** AFM topography images and height profiles (along white lines) of the written poly(NIPAAm$_{95}$-*co*-BPQAAm$_5$) sample: (a) transition between the gold substrate and the polymer structure made with $P_L$ of 15 mW and $t_d$ of 1 s; (b) transition between the gold substrate and the polymer structure made with $P_L$ of 10 mW and $t_d$ of 1 s; (c) and transition between the polymer structure made with $P_L$ of 15 mW and $t_d$ of 1 s and the polymer structure made with $P_L$ of 15 mW and $t_d$ of 3 s. Black arrows indicate the laser polarization during the crosslinking process.





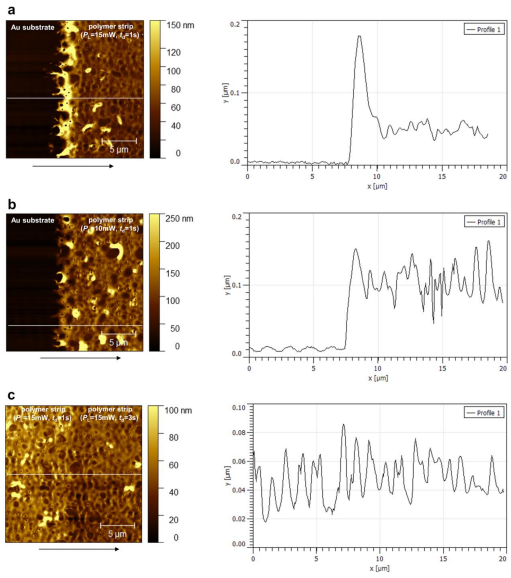


**Figure S22.** AFM topography images and height profiles (along white lines) of the written poly(NIPAAm$_{95}$-co-BPAm$_5$) sample: (a) transition between the gold substrate and the polymer structure made with $P_L$ of 15 mW and $t_d$ of 1 s; (b) transition between the gold substrate and the polymer structure made with $P_L$ of 10 mW and $t_d$ of 1 s; and (c) transition between the polymer structure made with $P_L$ of 15 mW and $t_d$ of 1 s and the polymer structure made with $P_L$ of 15 mW and $t_d$ of 3 s. Black arrows indicate the laser polarization during the crosslinking process.





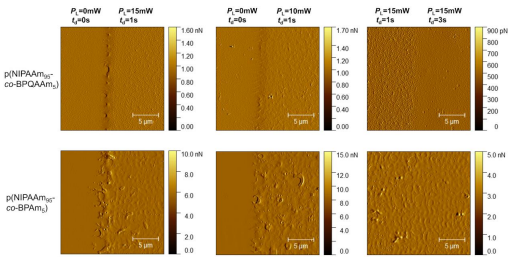


**Figure S23.** AFM peak force amplitude maps of the written poly(NIPAAm$_{95}$-*co*-BPQAAm$_5$) and poly(NIPAAm$_{95}$-*co*-BPAm$_5$) samples.

**Copolymer poly(DMAA$_{95}$-co-AAHAQ$_5$) Synthesis Details**

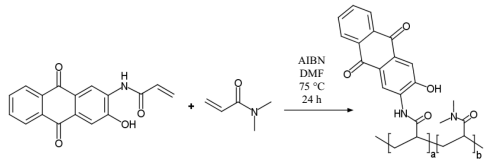


**Scheme S3.** Synthesis of poly(DMAA$_{95}$-*co*-AAHAQ$_5$).





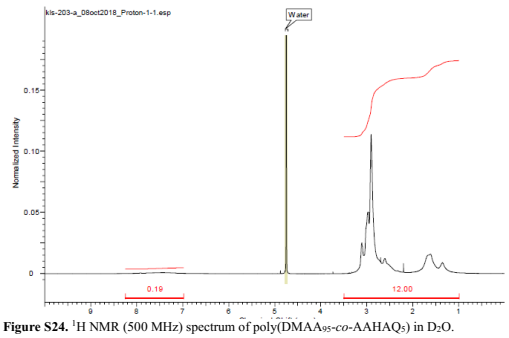


**Figure S24.** $^1$H NMR (500 MHz) spectrum of poly(DMAA$_{95}$-*co*-AAHAQ$_5$) in $D_2O$.

**Crosslinking Experiments**

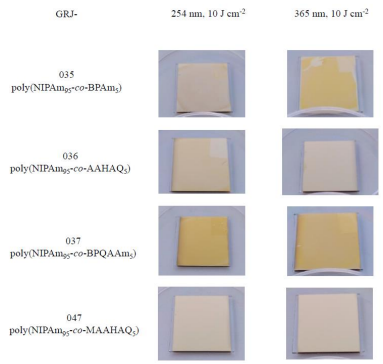


**Figure S25.** One-photon crosslinking experiments of the four copolymers with a feed-in of 5% of the crosslinker (BPAm, AAHAQ, BPQAAm, and MAAHAQ). The upper right part of

the gold substrates was blocked during the exposure of the light (254 and 365) nm with an energy of 10 J $cm^{-2}$ and can be seen as a reference if a network could be formed. For GRJ-047 a network formation could later on be confirmed for an irradiation at 254 nm, which cannot be seen on the photo.

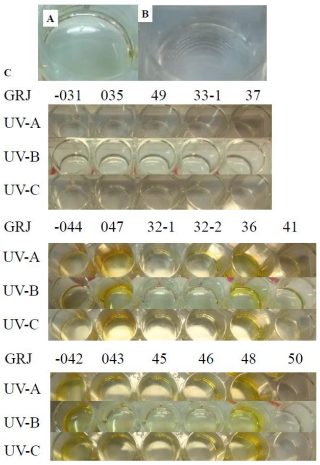


**Figure S26.** (A) An example of a copolymer that did not crosslink. (B) An example of a successfully crosslinked copolymer. (C) Results of the crosslinking experiments at different UV wavelengths (UV-A/B/C).





**Table S4.** Overview of the ability to crosslink of different copolymers with 5% feed-in of BPAm, BPQAAm, AAHAQ and MAAHAQ and 0.5% of AIBN.

| | | Crosslinkability | |
|---|---|---|---|
| GRJ- | Crosslinker | UV-A | UV-C |
| 35 | BPAm | ✓ | ✓ |
| 37 | BPQAAm | ✓ | ✓ |
| 36 | AAHAQ | X | ✓ |
| 47 | MAAHAQ | X | ✓ |





**Table S5.** Determined crosslinkability of the corresponding co- and terpolymers with the feed-in of the monomers NIPAm [M1] and the corresponding crosslinker [M2] as well as theinitiator AIBN [I] after UV-A, B, and C irradiation. For the terpolymers [M1] denotes the feed-in for NIPAm, [M2] for MAA, [M3] for the crosslinker and [I] the initiator.

| GRJ- | $[M_1]:[M_2]:[I]$ | Crosslink ability |
|---|---|---|
| Poly(NIPAm$_m$-*co*-BPAm$_n$) | | UV-A/B/C |
| 031 | 99/1/0.5 | (✓) |
| 031-1 | 99/1/0.5 | ✓ |
| 033-1 | 99/1/0.5 | ✓ |
| 035 | 95/5/0.5 | ✓ |
| Poly(NIPAm$_m$-*co*-BPQAAm$_n$) | | |
| 033 | 99/1/0.5 | (✓) |
| 37 | 95/5/0.5 | ✓ |
| Poly(NIPAm$_m$-*co*-AAHAQ$_n$) | | |
| 32 | 99/1/0.5 | (✓) |
| 032-1 | 99/1/0.5 | X |
| 032-2 | 99/1/0.5 | X |
| 036 | 95/5/0.5 | ✓ |
| 041 | 99/1/1 | X |
| 042 | 95/5/1 | ✓ |
| 043 | 99/1/0.5 | X |
| 045 | 99/1/0.5 | X |
| 046 | 99/1/1 | X |
| Poly(NIPAm$_m$-*co*-MAAHAQ$_n$) | | |
| 044 | 99/1/0.5 | X |
| 047 | 99/5/0.5 | ✓ |
| Poly(NIPAm$_{90}$-*co*-MAA$_5$-*co*-AAHAQ$_5$) | | |
| 048 | 90/5/5/0.5 | ✓ |
| Poly(NIPAm$_{94}$-*co*-MAA$_5$-*co*-BPAm$_1$) | | |
| 049 | 94/5/1/0.5 | ✓ |
| Poly(NIPAm$_{94}$-*co*-MAA$_5$-*co*-BPQAAm$_1$) | | |
| 050 | 94/5/1/0.5 | ✓ |





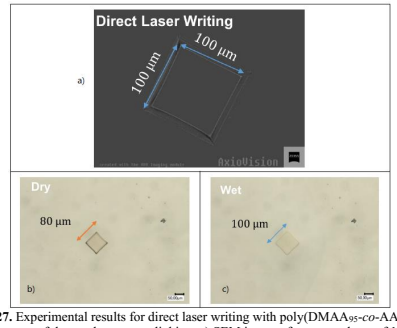


**Figure S27.** Experimental results for direct laser writing with poly(DMAA$_{95}$-*co*-AAHAQ$_5$) indicating successful two-photon crosslinking. a) SEM image of a square shape of 100 × 100 $\mu m^2$ size. b+c) Optical microscope images of the square in dry (b) and swollen state (c).

**SPRi Setup**

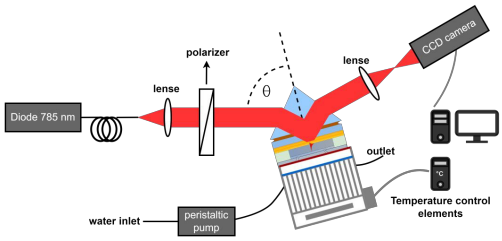


**Figure S28.** A schematic of the home-built surface plasmon resonance imaging (SPRi) setup.

**List of Abbreviations**

**List S1.** List of abbreviations used in the paper (in alphabetic order).

| Abbreviation | Definition |
|---|---|
| 3D | three-dimensional |
| AAHAQ | 2-acrylamido-3-hydroxyanthraquinone |
| AFM | atomic force microscopy |
| AIBN | azobisisobutyronitrile |
| ANCO | chromophore of AAHAQ and MAAHAQ |
| BCH | chromophore of BPQAAm |
| BK7 | pure optical borosilicate-crown glass |
| BNCO | chromophore of BPAm |
| BPAm | *N*-(4-benzoylphenyl)acrylamide |
| BP disulfide, BPdiS | 3,3'-disulfanediylbis(N-(4-benzoylbenzyl)propanamide |
| BPQAAm | [(4-benzoylphenyl)methyl]dimethyl[3-(prop-2-enamido)propyl]azanium bromide |
| CCD | charge-coupled device |
| DMAA | *N*,*N*-dimethyl acrylamide |
| DMAc | *N*,*N*-dimethylacetamide |
| DMF | dimethylformamide |
| DMSO | dimethyl sulfoxide |
| EtOH | ethanol |
| IgG | immunoglobulin G |
| LCST | lower critical solution temperature |
| MAA | methacrylic acid |
| MAAHAQ | 2-methacrylamido-3-hydroxyanthrquinone |
| miliQ water | highly-purified water |
| NIPAAm | *N*-isopropyl acrylamide |
| NIR | near-infrared |
| NMR | nuclear magnetic resonance |
| pH | “potential of hydrogen” = acidity |
| pNIPAAm | poly(*N*-isopropyl acrylamide) |





| | |
|---|---|
| RAFT | radical addition-fragmentation chain transfer |
| RI | refractive index |
| SAM | self-assembled monolayer |
| SEC | size-exclusion chromatography |
| SI | supporting information |
| SPR | surface plasmon resonance |
| SPRi | surface plasmon resonance imaging |
| SU-8 | SU-8 negative photoresist |
| TLC | thin-layer chromatography |
| UV | ultra-violet |
| VI | LabVIEW virtual instrument |
| VIS | visible light |

Supporting information to:

# Plasmon-Enhanced Multiphoton Polymer Crosslinking for Selective Modification of Plasmonic Hotspots

Yevhenii M. Morozov,[†*] Nestor Gisbert Quilis,[∥] Stefan Fossati,[⊥] Laura de Laporte,[Δ] Claudia Gusenbauer,[§] Andreas Weber,[▲] Jose Luis Toca-Herrera,[▲] Fiona Wiesner (née Diehl),[‡] Ulrich Jonas,[‡] and Jakub Dostalek[⊥#*]

[†] Center for Health & Bioresources, AIT-Austrian Institute of Technology, Giefinggasse 4, Vienna, 1210, Austria

[∥] Biosensor Technologies, AIT-Austrian Institute of Technology, Konrad-Lorenz-Strasse 24, Tulln an der Donau, 3430, Austria

[⊥] FZU-Institute of Physics, Czech Academy of Sciences, Na Slovance 2, Prague, 182 21, Czech Republic

[Δ] DWI-Leibniz Institute for Interactive Materials, Forckenbeckstrasse 50, Aachen, 52056, Germany

[§] Institute of Wood Technology and Renewable Materials, University of Natural Resources and Life Sciences, Vienna, Konrad-Lorenz-Strasse 24, Tulln an der Donau, 3430, Austria

[▲] Institute of Biophysics, University of Natural Resources and Life Sciences, Vienna, Muthgasse 11/II, Vienna, 1190, Austria

[‡] Macromolecular Chemistry, Department of Chemistry and Biology, University of Siegen, Adolf Reichwein-Straße 2, Siegen, 57074, Germany

[#] LiST-Life Sciences Technology, Danube Private University, Viktor-Kaplan-Strasse 2, Wiener Neustadt, 2700, Austria

* Correspondence should be directed to: Yevhenii.Morozov@ait.ac.at; dostalek@fzu.cz

Characterization of the threshold for burning

The observation was carried out for pDMAA-based polymer network fabricated with the Nanoscribe system as can be seen in Figure S1.

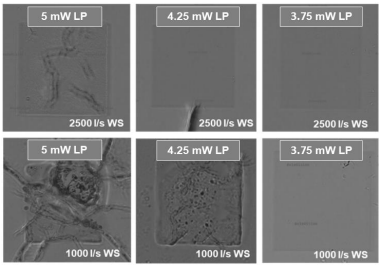


**Figure S1.** Optical microscope images of the inscribed square-shaped structures with varying laser power (LP) and writing speed (WS) of the poly(DMAA$_{96}$-*co*-AAHAQ$_4$) polymer.



Near-field optical simulations

Figure S2 illustrates a trend in the near-field enhancement of electric field intensity in vicinity to arrays of AuNPs with increasing diameter *D*.

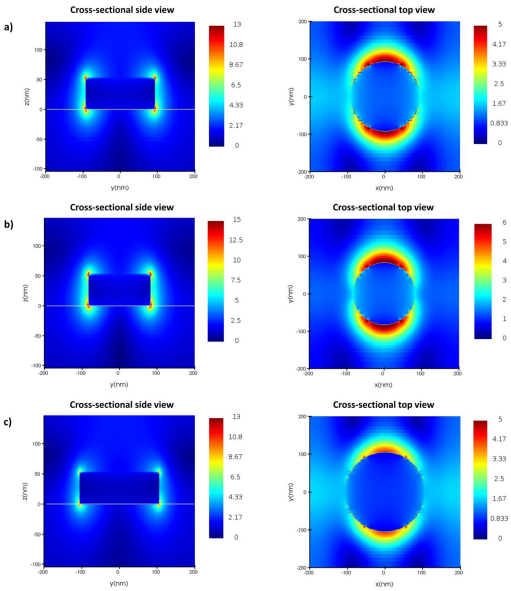


**Figure S2.** Lumerical FDTD simulation results for AuNP array having (a) $D$ = 185 nm at $\lambda$ = 780 nm; (b) $D$ = 165 nm at $\lambda$ = 785 nm; and (c) $D$ = 210 nm at $\lambda$ = 780 nm. The background refractive index was set to 1.45. All cross-sections were made through the NP centers. Electric field magnitude values are normalized to those of the incident (excitation) plane wave.



Determination of the 1D swelling ratio of the poly(DMAA$_{96}$-*co*-AAHAQ$_4$) copolymer

Figure S3 demonstrates the angular reflectivity spectra measured for poly(DMAA$_{96}$-*co*-AAHAQ$_4$) copolymer film with a home-built angular surface plasmon resonance setup.[1] The polymer films were prepared on the top of a flat 50 nm thick gold film that was modified with a self-assembled monolayer formed from benzophenone-disulfide. These spectra were fitted with a Fresnel reflectivity-based model. For a dry layer in contact with air (Figure S3a), a thickness of 154 nm was determined for the assumed refractive index of 1.45. Subsequently, the reflectivity spectrum was recorded for the same polymer film that was swollen in water (Figure S3b) and a thickness of 357 nm and a refractive index of 1.35 was determined under the assumption that the polymer surface mass density does not change. These results translate to a swelling ratio of 2.3 was determined between the dry and swollen layers in the perpendicular direction to the surface (1D swelling). The photographs of a suspended poly(DMAA$_{96}$-*co*-AAHAQ$_4$) copolymer film in air and water are shown in Figure S3c.

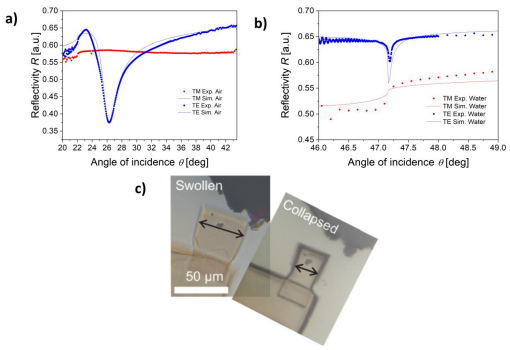


**Figure S3.** Angular reflectivity spectra measured for poly(DMAA$_{96}$-*co*-AAHAQ$_4$) copolymer film in (a) dry and (b) swollen in water. (c) Photographs of the suspended poly(DMAA$_{96}$-*co*-AAHAQ$_4$) copolymer film in air and water.

Control MPC experiment without matching $\lambda_{LSP}$ with $\lambda_L$

MPC-prepared structures on the substrate, where the LSPR wavelength was not aligned with that of the NIR fs laser was characterized with AFM as presented in Figure S4.

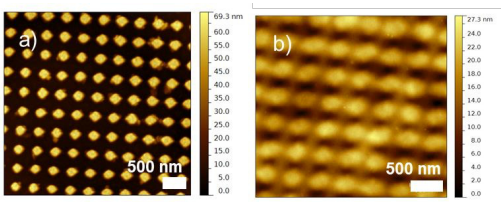


**Figure S4.** (a) AFM image of the bare AuNP array with AuNPs diameter of 210 nm; (b) AFM image of the poly(DMAA$_{96}$-*co*-AAHAQ$_4$) covered AuNP array irradiated with a laser power of 3.75 mW and a writing speed of 2,500 lines per second and rinsed with ethanol.

Experimental observation of LSPR shift due to the deposition of polymer layer

Topography of bare arrays of AuNPs were characterized by AFM (Figure S5a) and then the transmission LSPR spectra were measured before and after the pNIPAAm-based polymer layer deposition (Figure S5b)

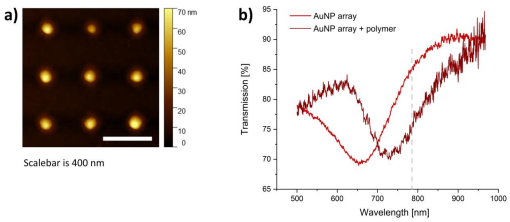


**Figure S5.** (a) AFM image of the bare AuNP array with AuNPs diameter of 165 ± 10 nm; (b) Corresponding white-light transmission spectra of bare AuNP array and AuNP array covered with a 100 nm layer of poly(NIPAAm$_{94}$-*co*-MAA$_5$-BPQAAm$_1$) terpolymer; dashed grey line indicates the fs laser wavelength $\lambda_L$.



Characterization of the PE-MPC with pNIPAAm-based polymer network.

Figure S6 illustrates the measurements with preparation of PE-MPC samples with pNIPAAm-based hydrogel where a signaling strip was written by using conditions above the threshold (so the polymer was crosslinked over the whole area in between AuNPs). Figure S7 provides details on AFM observation of height topography of the collapsed and dried pNIPAAm-based network locally attached to AuNPs depending on the drying temperature.

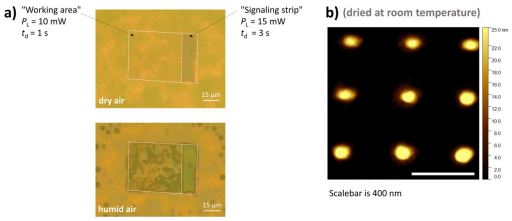


**Figure S6**. Plasmonically enhanced MPC experiment with the thermoresponsive poly(NIPAAm$_{94}$-*co*-MAA$_5$-BPQAAm$_1$) terpolymer. (a) Bright-field microscopy image of the written "patch" in the polymer layer in dry and humid air; (b) AFM image of the "working area" of the sample after the recording dried at room temperature.



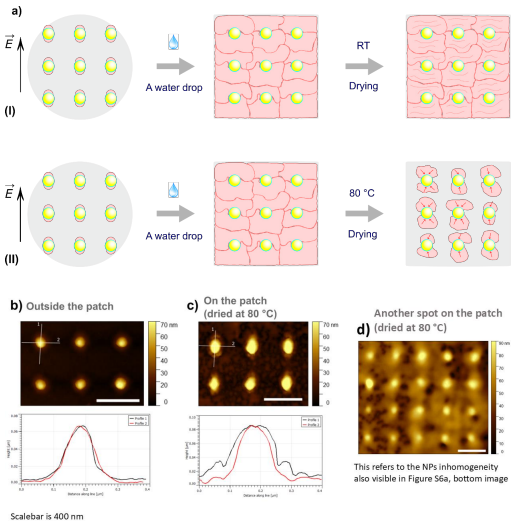


**Figure S7.** (a) A schematic showing the mechanism of the hydrogel shrinkage during drying at different temperatures: (I) at room temperature – the hydrogel shrinks slightly only in the vertical (perpendicular to the sample surface) direction; (II) at the elevated temperature of 80 °C – the hydrogel shrinks significantly also in the horizontal (in the sample plane) direction to its original shape; the black arrow indicates the polarization of the laser beam during plasmonically enhanced MPC. (b) AFM image of the sample outside the patch. (c)-(d) AFM images of the "working area" at different spots of the sample dried at the elevated 80 °C temperature.



References

(1) Morozov, Y. M.; Diehl, F.; Grün, J. J.; Pertiller, M.; Fossati, S.; Schmidt, K.; Quilis, N. G.; Gusenbauer, C.; Zbiral, B.; Toca-Herrera, J. L.; Klees, S.; Thiagarajan, C. R. V.; Jonas, U.; Dostalek, J. Microstructuring of thermoresponsive biofunctional hydrogels by multiphoton photocrosslinking. *Adv. Func. Mat.* **2024**, *34* (26), 2315578.

Supporting Information

**Thiol-Substituted Poly(2-Oxazoline)s with Photolabile Protecting Groups - Tandem Network Formation by Light**

*Niklas Jung, Fiona Diehl, Ulrich Jonas**

Macromolecular Chemistry, University of Siegen, Adolf-Reichwein Strasse 2, 57076 Siegen, Germany

*corresponding author Email address: jonas@chemie.uni-siegen.de

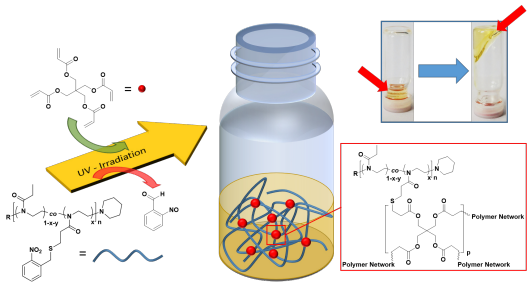


Schematic representation of tandem network formation by concurrent photodeprotection and thiol-ene click coupling (red arrows indicate liquid and gel, respectively).

## Table of Content

Experimental Part ..... 1

Synthesis of 2-{2-[(2-Nitrobenzyl)thio]ethyl}-4,5-dihydrooxazole (NbMEtOx) ..... 2

Synthesis of $CH_3$-Poly[(2-ethyl-2-Oxazoline)$_{1-x}$-co-(NbMEtOx)$_x$]-piperidine (Px%) ..... 5

Gelformation using Pentaerythritol tetraacrylate (PETA) ..... 6

Attempts to synthesize a NbMEtOxa Homopolymer ..... 6

NMR Spectra of NbMEtOxa and Precursors ..... 8

NMR Spectra of Polymers before and after Deprotection ..... 11

GPC Data of Polymers ..... 15

UV/Vis Spectra of Polymers ..... 16

Gel Formation ..... 21

## Experimental Part

***Materials***

Acetone (VWR Chemicals, 99.8%) was distilled before use. Further, 2-ethyl-2-oxazoline (EtOxa, Alfa Aesar 99%), methyl trifluoromethanesulfonate (MeOTf, Alfa Aesar, 97%), triethylamine ($NEt_3$, ChemSolute, 99%), and 2-methyl-2oxazoline (MeOxa, Sigma Aldrich, 98%) were dried over $CaH_2$ and distilled under inert gas or vacuum prior to use. For polymerizations anhydrous acetonitrile (MeCN, VWR, max. 0.001% $H_2O$) and for further experiments acetonitrile (MeCN, VWR Chemicals, 99+%) was used. Deuterated solvents were purchased from Deutero GmbH. 2-Chloroethylamine hydrochloride (Alfa Aesar, 98+%), dichloromethane (DCM, Fisher Scientific, 99.8%), diethyl ether (Acros Organics, 99.5%), *N,N*-dimethylformamide (DMF, Carl Roth, 99.8%), 1,4-dioxane (Carl Roth, 99.5%), ethyl acetate (EtOAc, VWR Chemicals, 99.8%), 1-ethyl-3-(3-dimethylaminopropyl)carbodiimide hydrochloride (EDC-HCl, Carl Roth, 99+%), hexanes (Fisher Scientific), hydrochloric acid (VWR Chemicals, 37%), 2-hydroxy-2-methylpropiophenone (HMPP, CIBA, 97%), *N*-hydroxysuccinimide (NHS, Alfa Aesar, 98+%), 3-mercaptopropionic acid (Alfa Aesar, 99%), magnesium sulfate hexahydrate (Carl Roth, 99+%), methanol (MeOH, Fisher Scientific, 99.8%), 2-nitrobenzyl bromide (Alfa Aesar, 98+%), pentaerythritol tetraacrylate (PETA, Sigma Aldrich), piperidine (Alfa Aesar, 99%), potassium carbonate (Bernd Kraft) and sodium hydrogencarbonate (J.T. Baker) were used as received.

***Methods***

The molar masses and the molar mass distribution ($Đ$) of the synthesized poly(2-oxazoline)s were measured using a PSS system (Agilent 1260) equipped with an autosampler, RI detector and an UV-detector type Agilent VWD Series 1260. The absorption was measured at $\lambda = 280$ nm. A so-called Gram Linear M column, equipped with a 10 µm particle size precolumn was utilized at $T \approx 60$ °C. As eluent dimethylacetamide (DMAc) mixed with 1 g $l^{-1}$ LiBr was used and 20 µl of the polymer-samples were injected. The flow rate of the system was 1 ml $min^{-1}$. The calibration curve was measured using PMMA standards (PSS, Mainz). Other gel permeation chromatography (SEC) experiments were carried out on an Agilent 1200-System consisting of a degasser, an isocratic pump, an autosampler, a RI-detector, a UV-detector (Lambda 1010, Bischoff), and a SDV Linear M column. THF was used as eluent with a flow rate of 1 ml $min^{-1}$. Calibration was performed with polystyrene standards (PSS, Mainz). The UV/Vis measurements were performed using an Evolution 220 UV-Visible spectrophotometer and a PCCU 1 Peltier control and cooling unit from Thermo Scientific. NMR spectroscopy was performed using a Bruker AV 400 spectrometer or a Joel ECZ 500 spectrometer. All measurements were performed at room temperature. The $^1$H NMR spectra were recorded at 400 or 500 MHz and $^{13}$C NMR spectra at 101 or 126 MHz. Chemical shifts ($\delta$) are given in ppm and are referenced to the undeuterated signal of the used solvent. Polymerizations were performed using a Discover SP Microwave System equipped with an Explorer 12 Hybrid Autosampler from CEM. Crosslinking and photodeprotection experiments were carried out in a UV-crosslinker UVP-CL1000, operating at $\lambda = 365$ nm ($H_e = 12.0$ J $cm^{-2}$ per 1 h).

***Synthesis of 2-{2-[(2-Nitrobenzyl)thio]ethyl}-4,5-dihydrooxazole (NbMEtOx)***

***A: Synthesis of 3-[(2-Nitrobenzyl)thio]propanoic acid (1)***

3-Mercaptopropionic acid (1.98 g, 18.7 mmol, 1.62 ml) and anhydrous $NEt_3$ (1.44 g, 14.2 mmol, 1.98 ml) were stirred in anhydrous acetone (60 ml) for 30 min at 0 °C. Then 2-nitrobenzyl bromide (2.02 g, 9.4 mmol) was added in portions under nitrogen. The reaction was stirred overnight at room temperature. The formed triethylamine hydrobromide was filtered-off and the crude product was isolated via rotary evaporation. The crude product was redissolved in dichloromethane (60 ml), washed with 0.5 M HCl (4 x 20 ml) and brine (20 ml). The organic

phase was dried over $MgSO_4$, filtrated and the product was concentrated via rotary evaporation. The obtained yellowish, highly viscous residue was stirred with hexanes (60 ml) for 30 min to obtain a yellowish-white powder as product. The title compound was filtered-off, washed with small portions of cold hexanes and dried in vacuo. TLC: $R_f$: 0 – 0.32 (EtOAc : hexanes 2:1) - Yield: 2.08 g (8.62 mmol, 92%) - $^1$H NMR (400 MHz, $CDCl_3$) $\delta$ 10.90 (s, 1H), 7.98 (dd, 1H, $J$ = 8.1, 1.3 Hz,), 7.57 (td, 1H, $J$ = 7.5, 1.3 Hz), 7.51 – 7.39 (m, 2H), 4.10 (s, 2H), 2.75 – 2.69 (m, 2H), 2.65 – 2.59 (m, 2H) ppm; $^{13}$C NMR (101 MHz, $CDCl_3$) $\delta$ 177.7, 148.9, 134.0, 133.3, 132.0, 128.5, 125.6, 34.4, 33.8, 26.7 ppm.



***B: Synthesis of 2,5-Dioxopyrrolidin-1-yl 3-[(2-nitrobenzyl)thio]propanoate (2)***

3-((2-Nitrobenzyl)thio)propanoic acid (2.08 g, 8.62 mmol), $NEt_3$ (1.43 g, 14.1 mmol, 2.0 ml) and NHS (1.62 g, 14.1 mmol) were dissolved in DCM (60 ml). To the yellowish mixture, EDC-HCl (2.70 g, 14.1 mmol) was added and the mixture was stirred at room temperature overnight. The mixture was washed with 1 M HCl (3 x 40 ml), water (3 x 40 ml) and brine (2 x 40 ml). The aqueous phases were combined and extracted with DCM (30 ml). The solvent was evaporated and the crude product was directly used for preparation of compound **3**.

***C: Synthesis of N-(2-chloroethyl)-3-[(2-nitrobenzyl)thio]propenamide (3)***

Compound **2** (2.98 g, 8.8 mmol) was dissolved in DCM (30 ml) and cooled to 0 °C. To this solution 2-chloroethylamine hydrochloride (2.05 g, 17.6 mmol) and $NEt_3$ (1.78 g, 17.6 mmol, 2.5 ml) were added and the mixture was stirred for 45 min at 0 °C. Afterwards, the cooling bath was removed and the solution was stirred until TLC (EtOAc : hexanes 4:1, $R_f$: 0.65 [product **3**]) showed complete conversion (around 2 h). The mixture was diluted with DCM (30 ml) and 1 M HCl (20 ml) was added. The organic phase was further washed with 1 M HCl (2 x 20 ml), brine (20 ml) and saturated aq. $NaHCO_3$ (3 x 20ml) The organic phase was dried with $MgSO_4$, filtrated and the solvent was evaporated under reduced pressure. The product was isolated as yellow-white solid. Yield: 2.34 g (7.7 mmol, 89%) - $^1$H NMR (400 MHz, $CDCl_3$) $\delta$ 7.96 (dd, 1H, $J$ = 8.1, 1.3 Hz), 7.56 (td, 1H, $J$ = 7.5, 1.3 Hz), 7.49 (dd, 1H, $J$ = 7.7, 1.4 Hz), 7.45 – 7.39 (m, 1H), 6.09 (br.s, 1H), 4.09 (s, 2H), 3.64 – 3.56 (m, 4H), 2.76 (t, 2H, $J$ = 7.1 Hz), 2.44 (t, 2H, $J$ = 7.1 Hz) ppm. $^{13}$C NMR (101 MHz, $CDCl_3$) $\delta$ 171.3, 148.8, 134.0, 133.3, 132.2, 128.5, 125.5, 44.0, 41.4, 36.5, 33.8, 27.8 ppm.

***D: Ring formation to 2-{2-[(2-Nitrobenzyl)thio]ethyl}-4,5-dihydrooxazole (NbMEtOxa) (4)***

Amide **3** (2.31 g, 7.7 mmol) was dissolved in MeCN (50 ml). Anhydrous $K_2CO_3$ (2.74 g, 19.9 mmol) was added to the solution and stirred at 80 °C until TLC (EtOAc, $R_f$: 0.20 [product **4**])



showed full conversion (around 16 h). After cooling the reaction suspension, the solids were decanted and then passed through a syringe filter (PTFE, 0.45 µm). Then, the solvent was evaporated and the product was dried in vacuum overnight. The obtained yellow oil was dissolved in DCM, passed through a syringe filter (PTFE, 0.45 µm), and the solvent was removed in vacuo. Afterwards the crude product was passed through a short silica column (eluent: EtOAc) and then the solvent was evaporated. The product appeared as light brownish solid after drying in vacuum overnight. Yield: 1.22 g (4.57 mmol, 59%) - $^1$H NMR (400 MHz, $CDCl_3$) δ 7.96 (dd, 1H, $J$ = 8.1, 1.3 Hz), 7.55 (td, 1H, $J$ = 7.5, 1.3 Hz), 7.48 (dd, 1H, $J$ = 7.7, 1.5 Hz), 7.44 – 7.37 (m, 1H), 4.21 (t, 2H, $J$ = 9.5 Hz), 4.09 (s, 2H), 3.81 (t, 2H, $J$ = 9.5 Hz), 2.76 – 2.70 (m, 2H), 2.55 – 2.48 (m, 2H) ppm. $^{13}$C NMR (101 MHz, $CDCl_3$) $\delta$ 166.6, 148.8, 134.1, 133.2, 132.0, 128.3, 125.5, 67.5, 54.5, 33.7, 28.5, 28.2 ppm.

***Synthesis of $CH_3$-Poly[(2-ethyl-2-Oxazoline)$_{1-x}$-co-(NbMEtOx)$_x$]-piperidine (Px%)***

All polymerizations were performed according to the following procedure. As example, the polymerization using 10 mol% NbMEtOxa is described.

Briefly, MeOTf (5.61 mg, 34 µmol) and EtOxa (10.17 mg, 100 µmol) were dissolved in anhydrous MeCN (1091 mg) in a glovebox. Then the mixture was stirred under microwave irradiation for 15 min at 120 °C. Afterwards, the solution was transferred into a glovebox, in which EtOxa (384 mg, 3.88 mmol) and NbMEtOxa (103.3 mg, 0.38 mmol) were added to the vial. The final concentration was adjusted to $c$ = 2 mol l$^{-1}$ by adding anhydrous MeCN. Then, the mixture was stirred under microwave irradiation for 90 min at 120 °C. The polymerization was stopped by adding 1 M methanolic piperidine solution (0.2 ml) and the resulting mixture was stirred at room temperature overnight. The polymer was precipitated in ice-cold diethyl ether, redissolved in 1,4-dioxane, filtrated and freeze dried. Yield: 370 mg (74%) - $^1$H NMR (500 MHz, $CDCl_3$) $\delta$ 8.02 – 7.87 (8H), 7.62 – 7.35 (25H), 4.15 – 4.03 (17H), 3.66 – 3.27 (401H), 3.06 – 2.98 (3H), 2.80 – 2.58 (26H), 2.48 – 2.12 (192H), 1.21 – 0.89 (292H) ppm.



***Deprotection Procedure***

The corresponding copolymer (100 mg, 6.7 µmol) was filled into a microwave vial and dissolved in MeCN (30 ml). The vial was sealed with a silicone cap and the mixture was purged with Ar for 15 min. Afterwards, the vial was placed in a UV crosslinking chamber with a wavelength of $\lambda$ = 365 nm for 2 h ($H_e$ = 24 J cm$^{-2}$). Then the polymer was recovered by precipitation into ice-cold diethyl ether. The precipitate was collected and thoroughly washed with diethyl ether. Finally, the product was dried in vacuum overnight.

***Kinetics of Photodeprotection***

Solutions of different polymer concentrations were prepared in MeCN. Each solution was added to a 1 cm square quartz cell. The cells were irradiated at λ = 365 nm in a UV crosslinking chamber ($H_e$ = 12 J cm$^{-2}$ per 1 h). After 5 min, the irradiation was stopped and the cells immediately transferred to a UV spectrometer, where the absorbance was recorded at $\lambda$ = 310 nm.

***Gelformation using Pentaerythritol tetraacrylate (PETA)***

The polymer **P10%** containing protected thiol groups (50 mg, 3.3 µmol, 36.3 µmol thiol groups) and PETA (0.7 equiv. with respect to thiol groups) were dissolved in degassed DMF to obtain a concentration of 15 wt%. Then HMPP (2.7x10$^{-3}$ mg, 1.64x10$^{-2}$ µmol, 2.5 µl) was added. The vial was sealed and remaining oxygen was removed by a freeze-pump-thaw cycle. Afterwards, the vial was placed in a UV crosslinker ($\lambda$ = 365 nm, $H_e$ = 12 J cm$^{-2}$) for 1 h.

***Attempts to synthesize a NbMEtOxa Homopolymer***

MeOTf and MeOxa were dissolved in anhydrous MeCN and stirred for 15 minutes in the microwave oven at 120 °C with an initial power of 140 W. Then, NbMEtOxa was added in a glovebox to the reaction mixture. The reaction vial was transferred back to the microwave oven

and further stirred for 90 min (120°C, initial power 140 W). Subsequently, the polymerization was quenched by adding water (0.2 ml) and stirred for 4 hours at room temperature. The polymer was precipitated into ice-cold diethyl ether, dissolved in 1,4-dioxane and dried via lyophilization. The individual reaction parameters are listed in the following table.

Table S1: Tabular representation of the initial weights of MeOTf, MeCN, MeOxa, NbMEtOxa, yields, and GPC analysis data for NbMEtOxa homopolymers.

| No. | MeOTf /mg (µmol) | MeCN /g | MeOxa /mg (µmol) | NbMEtOxa /g (mmol) | Yield /mg (%) | $\bar{M}_n$ /kDa | $Đ$ |
|---|---|---|---|---|---|---|---|
| 1 | 3.1 (19) | 1.2 | 3.8 (45) | 0.20 (0.77) | - [a] | - [a] | - [a] |
| 2 | 4.4 (27) | 1.8 | 5.1 (60) | 0.27 (1.0) | - [a] | - [a] | - [a] |
| 3 | 2.9 (17) | 2.3 | 6.2 (73) | 0.19 (0.72) | 20 (10) | 1.3 | 2.9 |

[a] Homopolymer could not be isolated.



## NMR Spectra of NbMEtOxa and Precursors

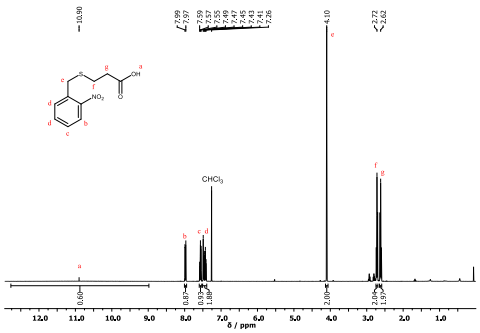


Figure S1: $^{1}$H NMR (400 MHz) spectrum of 3-[(2-nitrobenzyl)thio]propanoic acid (**1**) recorded in $CDCl_3$.

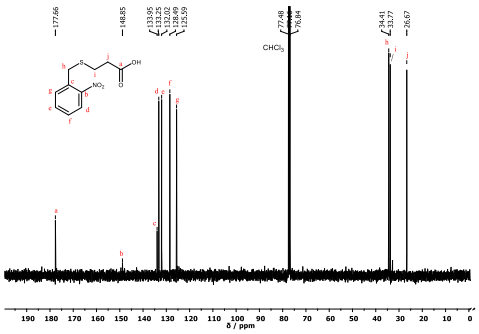


Figure S2: $^{13}$C NMR (101 MHz) spectrum of 3-[(2-nitrobenzyl)thio]propanoic acid (**1**) recorded in $CDCl_3$.



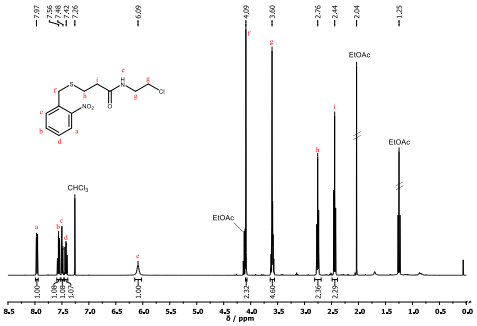


Figure S3: $^{1}$H NMR (400 MHz) spectrum of *N*-(2-chloroethyl)-3-[(2-nitrobenzyl)thio]propenamide (**3**) recorded in $CDCl_3$.

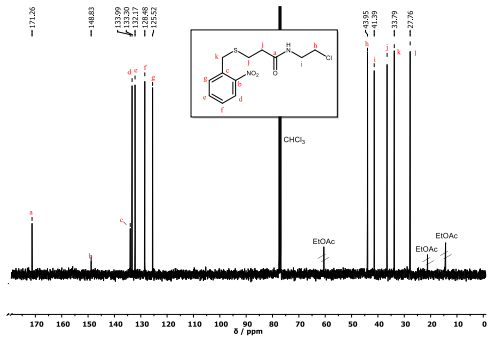


Figure S4: $^{13}$C NMR (101 MHz) spectrum of *N*-(2-chloroethyl)-3-[(2-nitrobenzyl)thio]propenamide (**3**) recorded in $CDCl_3$.



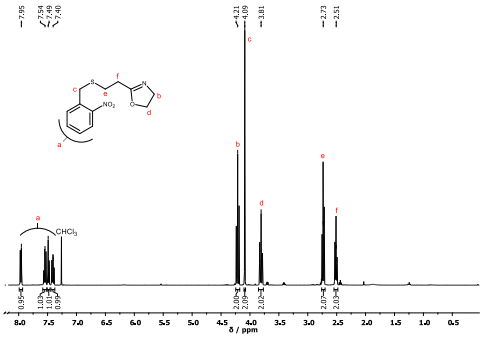


Figure S5: $^{1}$H NMR (400 MHz) spectrum of 2-{2-[(2-nitrobenzyl)thio]ethyl}-4,5-dihydrooxazole (NbMEtOx) (**4**) recorded in $CDCl_3$.

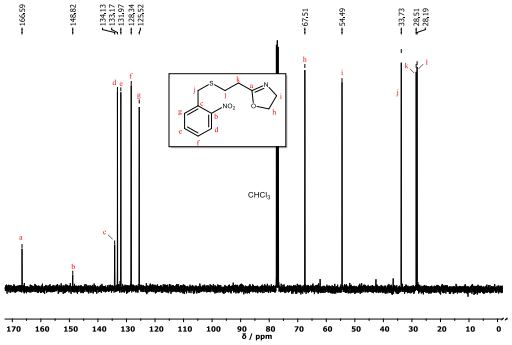


Figure S6: $^{13}$C NMR (101 MHz) spectrum of 2-{2-[(2-nitrobenzyl)thio]ethyl}-4,5-dihydrooxazole (NbMEtOx) (**4**) recorded in $CDCl_3$.

## NMR Spectra of Polymers before and after Deprotection

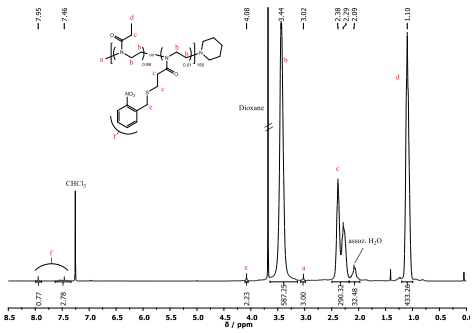


Figure S7: $^1$H NMR (500 MHz) spectrum of **P1%** recorded in $CDCl_3$.

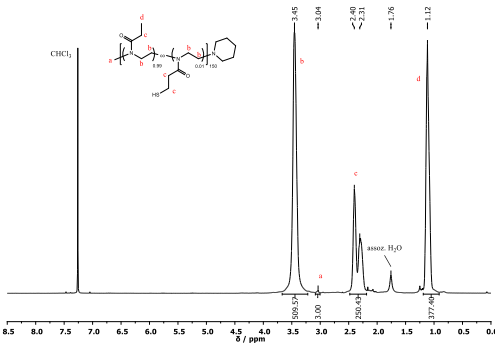


Figure S8: $^1$H NMR (500 MHz) spectrum of **P1%** after deprotection recorded in $CDCl_3$.



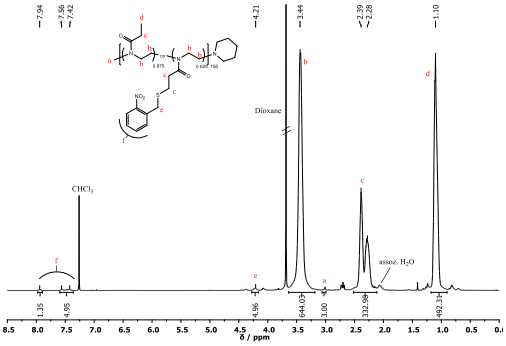


Figure S9: $^1$H NMR (500 MHz) spectrum of **P2.5%** recorded in $CDCl_3$.

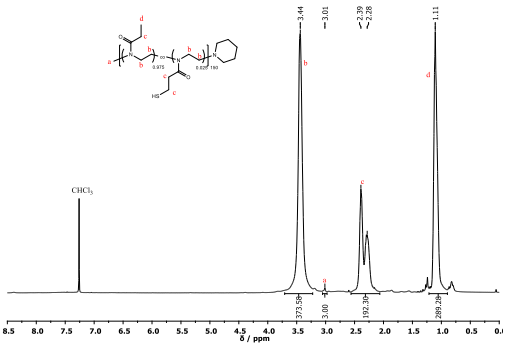


Figure S10: $^1$H NMR (500 MHz) spectrum of **P2.5%** after deprotection, recorded in $CDCl_3$.



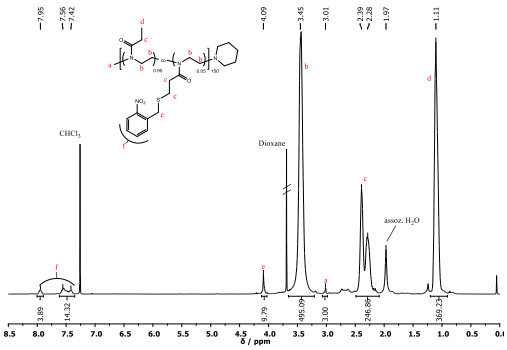


Figure S11: $^1$H NMR (500 MHz) spectrum of **P5%** recorded in $CDCl_3$.

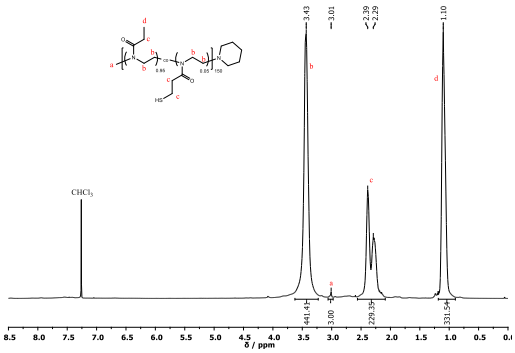


Figure S12: $^1$H NMR (500 MHz) spectrum of **P5%** after deprotection, recorded in $CDCl_3$.



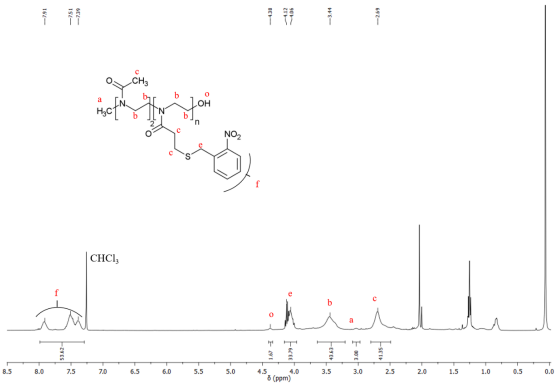


Figure S13: $^1$H NMR (400 MHz) spectrum of the NbMEtOxa homopolymer, recorded in $CDCl_3$.

## GPC Data of Polymers

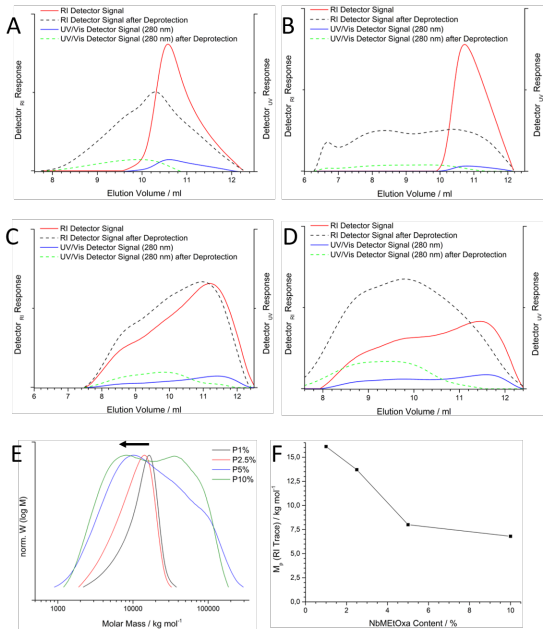


Figure S14: GPC elugrams of the different copolymers containing NbMEtOxa. The content of NbMEtOxa increased in the order from **P1%** (A), **P2.5%** (B), **P5%** (C) to **P10%** (D). DMAc containing LiBr (1 g $l^{-1}$) was used as eluent for each measurement. In graph (E), the RI GPC traces for all copolymers (**P1%**, **P2.5%**, **P5%**, **P10%**) are plotted to illustrate the change in molar mass at peak maximum ($M_p$), as indicated in panel (F).



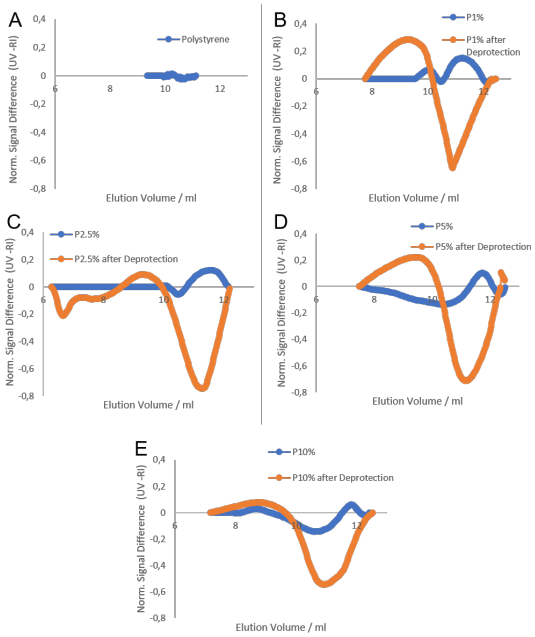


Figure S15: Qualitative analysis of the compositional drift by UV-RI difference plots for a polystyrene (PS) standard 5630 g $mol^{-1}$ (A), **P1%** (B), **P2.5%** (C), **P5%** (D) to **P10%** (E) based on the following procedure: (1) first the UV and RI traces were normalized by dividing all signal intensity values with the one at the respective trace maxima and (2) then the normalized RI trace was subtracted from the normalized UV trace. The reference trace (A) shows a close to zero-value line as expected for the PS homopolymer. The blue lines show the copolymer systems before and the orange lines after irradiation with UV light ($\lambda$ = 365 nm, $H_e$ = 12 J $cm^{-2}$, 1 h).



## UV/Vis Spectra of Polymers

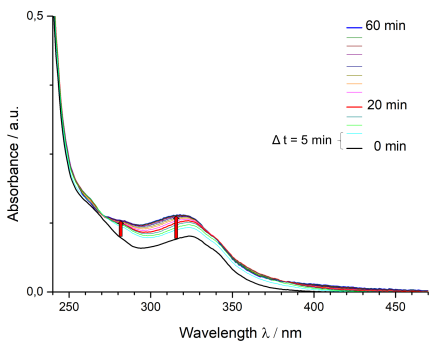


Figure S16: Time-dependent UV/Vis absorbance vs. wavelength scans of **P1%**. Red arrows indicate the change in absorption with increasing time.

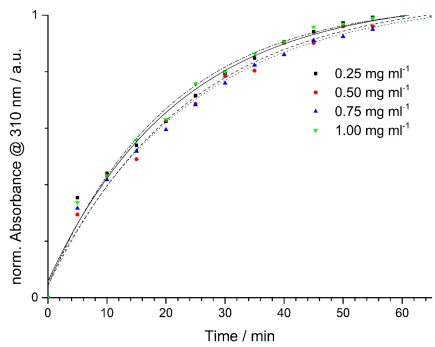




Figure S17: Deprotection kinetics of **P1%** at different concentrations. The absorbance was measured at $\lambda$ = 310 nm.

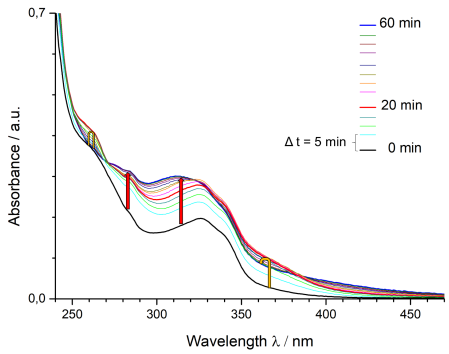


Figure S18: Time-dependent UV/Vis absorbance vs. wavelength scans of **P2.5%**. Red and yellow arrows indicate the change in absorption with increasing time.

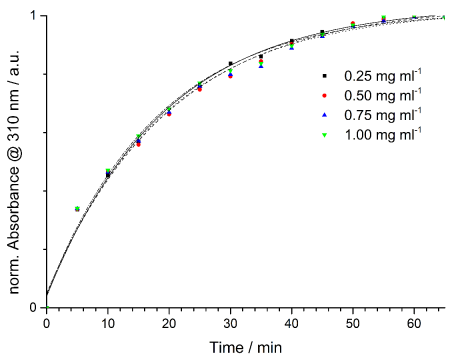

Figure S19: Deprotection kinetics of **P2.5%** at different concentrations. The absorbance was measured at $\lambda$ = 310 nm.

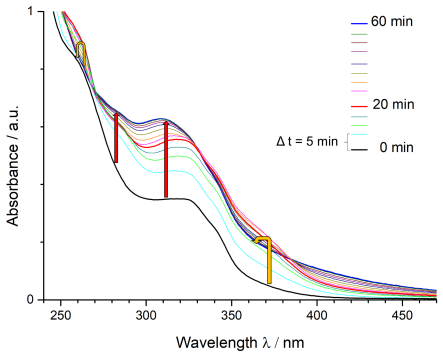


Figure S20: Time-dependent UV/Vis absorbance vs. wavelength scans of **P5%**. Red and yellow arrows indicate the change in absorption with increasing time.



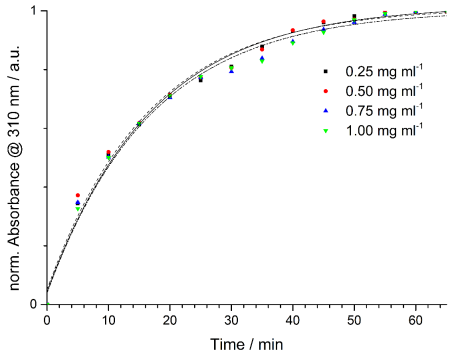


Figure S21: Deprotection kinetics of **P5%** at different concentrations. The absorbance was measured at $\lambda$ = 310 nm.



## Gel Formation

Table S2: Quantities of polymer, crosslinker PETA and DMF used for crosslinking tests. Photoinitiator HMPP (2.7 µg, 1.64x10$^{-2}$ µmol, 2.5 µl) was added to reaction vials 2 to 6.

| Vial | Polymer | Mass Polymer / mg (content of Thiols / µmol) | Mass PETA[a] / mg (µmol, µl) | Total Volume DMF / µl |
|---|---|---|---|---|
| **1** | P10% | 50 (36.3) | - | 331 |
| **2** | - | - | 2.3 (25.4, 21.5) | 350 |
| **3** | P1% | 50 (3.4) | 0.21 (2.4, 2.0) | 348 |
| **4** | P2.5% | 50 (10.4) | 0.65 (7.3, 6.1) | 344 |
| **5** | P5% | 50 (18.1) | 1.15 (12.7, 10.7) | 340 |
| **6** | P10% | 50 (36.3) | 2.3 (25.4, 21.5) | 331 |

[a] Mass of PETA was taken from a freshly prepared stock solution in DMF ($\beta$ = 107 mg ml$^{-1}$).



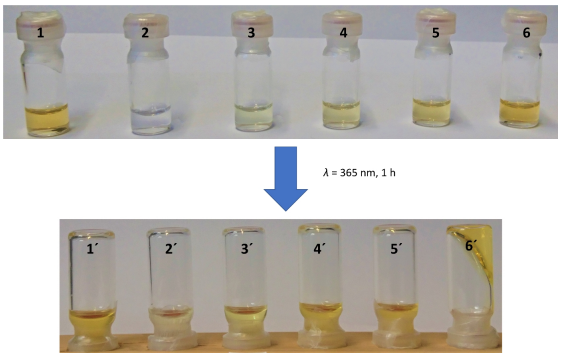


Figure S22: Images of reaction vials before (upper picture) and after irradiation (lower picture, vial numbers are marked with a prime). The vial numbers correspond to numbering in Table S2. The concentration of polymer was 15 wt% in DMF. Vials **1** and **2** were used as control. Successful network formation in vial **6'** is corroborated by the triangular shape of the rigid gel after irradiation of the tilted vial.

Macromolecular Rapid Communications

Supporting Information

for *Macromol. Rapid Commun.*, DOI 10.1002/marc.202300549

Thermoresponsive and Photocrosslinkable Poly(2-alkyl-2-oxazoline) Toolbox – Customizable Ultralow-Fouling Hydrogel Coatings for Blood Plasma Environments

*Fiona Wiesner (née Diehl), Christian Petri, Simone Hageneder, Cleiton Kunzler, Sven Klees, Petra Frank, Matthias Pertiller, Jakub Dostalek, Wolfgang Knoll and Ulrich Jonas**

**Supporting Information**

# Thermoresponsive and Photocrosslinkable Poly(2-alkyl-2-oxazoline) Toolbox - Customizable Ultralow-Fouling Hydrogel Coatings for Blood Plasma Environments

Fiona Wiesner (née Diehl), Christian Petri, Simone Hageneder, Cleiton Kunzler, Sven Klees, Jakub Dostalek, Wolfgang Knoll, Ulrich Jonas*

F. Wiesner (née Diehl), C. Petri, C. Kunzler, S. Klees, P. Frank, U. Jonas
Macromolecular Chemistry, Department Chemistry-Biology, University of Siegen, Adolf-Reichwein-Strasse 2, 57076 Siegen, Germany

M. Pertiller, J. Dostalek, W. Knoll, S. Hageneder
Biosensor Technologies, AIT-Austrian Institute of Technology GmbH, Konrad-Lorenz-Straße 24, 3430 Tulln an der Donau, Austria

J. Dostalek
FZU-Institute of Physics, Czech Academy of Sciences, Na Slovance 2, 182 21 Prague, Czech Republic

J. Dostalek, W. Knoll
Laboratory for Life Sciences and Technology (LiST), Danube Private University, Konrad-Lorenz-Straße 24, 3430 Tulln an der Donau, Austria

## S1 Materials

Chemicals were purchased from Alfa Aesar (trifluoroacetic anhydride, *N*-hydroxysuccinimide, 2-aminoethanol, iso-butyronitrile, 4-hydroxybenzophenone, 2-chloroethylamine hydrochloride, ethyl 4-bromobutyrate, 4-methylbenzophenone, sodium azide, sodium carbonate and calcium hydride), Fluorochem (methyl trifluoromethanesulfonate), Fisher Scientific (dimethylsulfoxide) and Prolabo (anhydrous acetonitrile) and were used as received, unless otherwise noted. EtOxa, iPrOxa, and nPrOxa were refluxed over $CaH_2$ and stored under



dry nitrogen atmosphere. 2-Aminoethanol was distilled under reduced pressure prior to use. Anhydrous sodium carbonate $K_2CO_3$ was dried in vacuum at 130 °C prior to use. All syntheses steps were carried out under dry argon gas atmosphere, unless noted otherwise. All polymerization reactions were carried out under dry nitrogen atmosphere.

## S2 Instrumentation

$^1$H NMR (400 MHz) and $^{13}$C NMR (100 MHz) spectra were recorded on a Bruker AV 400 spectrometer. FT-IR spectroscopy was carried out on a Bruker Tensor 27. Size exclusion chromatography (SEC) was carried out on a PSS-System consisting of a degasser, an isocratic pump, an autosampler (Agilent 1200), a UV-detector Lambda 1010 (Bishoff), a RI-detector RI-71 (Shodex) and a SDV Linear M column or PSS GRAM 100 Å column, respectively. A 0.1 wt% solution of LiBr dissolved in dimethylacetamide (DMAc) was used as eluent with a flow rate of 1 ml min$^{-1}$. All polymers were synthesized by microwave assisted cationic ring opening polymerization, using a microwave reactor type Discover LabMate. Thermal Analysis was performed on a Differential Scanning Calorimeter (DSC) TA Instruments Q 1000. Cloud point analysis was performed on a UV/VIS spectrophotometer type Thermo Scientfic Evolution 201/220, using 0.3 wt% aqueous polymer solution with a heating and cooling rate of 1 K min$^{-1}$.

## S3 Synthesis of the Photocrosslinker Monomer BPOxa

**4-(4-Benzoylphenoxy)butanoic acid (1)** was synthesized according to literature. [62] Anhydrous sodium carbonate was added to a solution of 4-hydroxybenzophenone (10.6 mmol, 2.09 g) in acetonitrile (60 ml). After stirring for 30 min, ethyl 4-brombutyrate (10.6 mmol, 1.91 ml) was added and the mixture was heated up to 80 °C until thin layer chromatography (TLC, *n*-hexane/ethyl acetate, 4:1, $R_f$ = 0.41) indicated complete conversion of the educt, which was obtained after 16 h. The solvent was evaporated, and the residue dissolved in ethyl acetate (100 ml), followed by washing with water (3x 50 ml). The solvent was again evaporated, and the crude ester was used without further purification in the next reaction step. The crude product (10.6 mmol) was dissolved in a mixture of methanol (80 ml) and aqueous NaOH (80 mmol, 3.20 g, 80 ml $H_2O$), and stirred at room temperature (r.t.) until



a TLC (n-hexane/ethyl acetate/acidic acid, 1:1:0.1; $R_f$ = 0.62) indicated complete conversion of the educt, which was obtained after 3 h. The solution was acidified with 4 M HCl to pH = 1 and the formed precipitate filtered off and washed several times with small portions of cold water. The remaining product was dried in vacuum at 60 °C with$P_2O_5$.

Yield: 92% (2.75g, 9,69 mmol) of a white solid; TLC (n-hexane/ethyl acetate/acidic acid, 1:1:0.1; $R_f$ = 0.62); m.p. 84 – 86 °C; IR ($\nu$/cm$^{-1}$): 3119 (COOH), 1596 (C=O), 1282, 1227, 1142; $^1$H NMR (400 MHz, $CDCl_3$, $\delta$/ppm): 2.17 (m, 2H), 2.62 (t, J = 7.15 Hz, 2H), 4.12 (t, J = 6.07 Hz, 2H), 6.94 – 7.83 ppm (various m, Ar H); $^{13}$C NMR (100 MHz, $CDCl_3$, $\delta$/ppm): 25.8, 31.5, 68.4, 115.3, 129.4, 130.7, 131.0, 133.2, 133.7, 139.5, 164.4, 177.1, 197.6 ppm.

**2,5-Dioxopyrrolidin-1-yl 4-(4benzoylphenoxy)butanoate (2)** was synthesized utilizing procedures from the literature.[52] Pyridine (58.8 mmol, 5 ml), trifluoroacetic anhydride (14.2 mmol, 2 ml) and *N*-hydroxysuccinimide (14.5 mmol, 1.67 g) were added to a solution of compound **1** (3.40 mmol, 0.96 g) in dichloromethane (30 ml) and stirred for 30 min at 0 °C, followed by stirring at r.t. for additional 24 h. The reaction mixture was then diluted with dichloromethane (90 ml) and 0.5 M HCl was added. The layers were separated, and the organic layer was washed with 0.5 M HCl (2x 60 ml) and saturated aqueous $NaHCO_3$. The organic layer was dried with anhydrous $MgSO_4$ and the solvent evaporated.

Yield: 92% (3.12 mmol, 1.19 g); TLC (*n*-hexane/ethyl acetate, 1:1; $R_f$ = 0.42); IR ($\nu$/cm$^{-1}$): 3063 (C-$H_{aromatic}$), 2945 (C-H), 1813, 1782, 1728 (C=O); $^1$H NMR (400 MHz, $CDCl_3$, $\delta$/ppm): 2.27 (m, 2H), 2.84 – 2.89 (t, 6H), 4.15 (t, $J$ = 5.98 Hz, 2H), 6.96 – 7.83 (various m, Ar H); $^{13}$C NMR (100 MHz, $CDCl_3$, $\delta$/ppm): 24.4, 25.7, 27.8, 66.3, 114.2, 128.3, 129.9, 130.5, 132.7, 138.4, 162.3, 168.4, 169.2, 194.7.

**4-(4-Benzoylphenoxy)-N-(2-chloroethyl)butanamide (3).**[63] Compound **2** (3.1 mmol, 1.19 g) was dissolved in dichloromethane (25 ml) and cooled to 0 °C. 2-Chloroethylamine hydrochloride (6.19 mmol, 0.72 g) and triethyl amine (6.2 mmol, 0.86 ml) were added. After 45 min the ice water bath was removed and the reaction mixture stirred at r.t. until a TLC (*n*-hexane/ethyl acetate, 1:1; $R_f$ = 0.24) indicated complete conversion of the educts, which was obtained after 20 h. The reaction mixture was diluted with dichloromethane (10 ml) and aqueous HCl (0.5 M) was added. The layers were separated, and the organic layer was washed

with aqueous HCl (0.5 M, 2x 25 ml) followed by washing with saturated aqueous $NaHCO_3$ (2x 25 ml). The organic layer was dried with $MgSO_4$ and the solvent evaporated.

Yield: 89% (2.76 mmol, 0.95 g); TLC (*n*-hexane/ethyl acetate, 1:1; $R_f$ = 0.24); IR ($\nu$/cm$^{-1}$): 3302 (NH), 3068 (C-$H_{aromatic}$), 2963 (C-H), 1728 (C=O); $^1$H NMR (400 MHz, $CDCl_3$, $\delta$/ppm): 2.17 (m, 2H), 2.44 (t, *J* = 7.22 Hz, 2H), 3.61 (m, 4H), 4.09 (t, *J* = 5.98 Hz, 2H), 6.93 – 7.81 ppm (various m, Ar H); $^{13}$C NMR (100 MHz, $CDCl_3$, $\delta$/ppm): 25.0, 32.7, 41.3, 44.2, 67.2, 77.2, 114.1, 128.3, 129.3, 130.3, 132.1, 132.7, 138.4, 162.6, 172.5, 195.7.

**2-[3-(4-Benzoylphenoxy)propyl]-4,5-dihydro-1,3-oxazole (4)** was synthesized employing literature procedures.[64] Compound **3** (2.3 mmol, 0.80 g) was dissolved in acetonitrile (25 ml) and $K_2CO_3$ (4.6 mmol, 0.64 g) was added under argon atmosphere. The reaction mixture was stirred at 80 °C until TLC (*n*-hexane/ethyl acetate, 1:1; $R_f$ = 0.35) indicated complete conversion of the educt after about 16 h. The insoluble $K_2CO_3$ was removed by filtration and the solvent was evaporated to obtain the product as a slightly brownish viscous oil.

Yield: 87% (2.0 mmol, 0.62 g); TLC (*n*-hexane/ethyl acetate, 1:1): $R_f$ = 0.35; IR ($\nu$/cm$^{-1}$): 3057 (C-$H_{aromatic}$), 2939 (C-H), 1651 (C=O), 1597 (C=N); $^1$H NMR (400 MHz, $CDCl_3$, $\delta$/ppm): 2.17 (m, 2H), 2.50 (t, *J* = 7.33 Hz, 2H), 3.84 (t, *J* = 9.44 Hz, 2H), 4.12 (t, *J* = 6.14 Hz, 2H), 4.25 (t, *J* = 9.55 Hz, 2H), 6.96 – 7.80 (various m, Ar H); $^{13}$C NMR (100 MHz, $CDCl_3$, $\delta$/ppm): 24.5, 25.6, 54.5, 67.1, 67.4, 114.1, 128.3, 129.8, 132.0, 132.7, 138.4, 162.7, 167.8, 195.7.



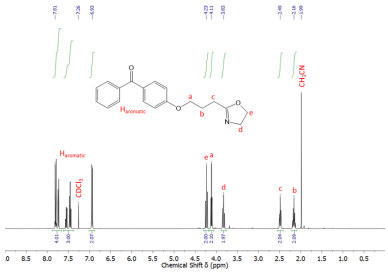

**Figure S1.** $^1$H NMR spectrum of BPOxa (**4**) measured at r.t. in $CDCl_3$ (with a Larmor frequency of 400 MHz).

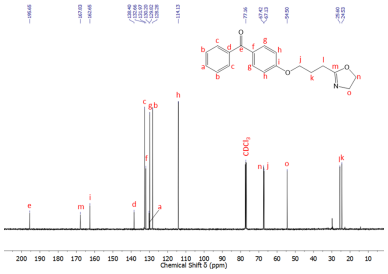

**Figure S2.** $^{13}$C NMR spectrum of BPOxa (**4**), measured at r.t. with 100 MHz in $CDCl_3$.



## S4 Synthesis of 2-Alkyl-2-Oxazoline Main Monomers iPrOxa and nPrOxa

**2-Isopropyl-2-oxazoline (iPrOxa, 7) and 2-*n*-propyl-2-oxazoline (nPrOxa, 8)** were synthesized according to literature.[49]

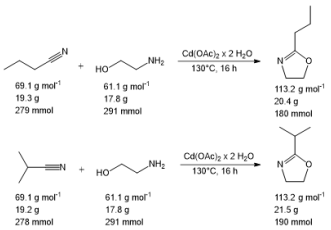


**Scheme S1.** Synthesis of nProxa (**8**) and iPrOxa (**7**).

To 2-aminoethanol (291 mmol, 17.8 g) either butyronitrile (279 mmol, 19.3 g) or isobutryonitrile (278 mmol, 19.2 g), and $Cd(OAc)_2$ x 2 $H_2O$ (15.0 mmol, 4.01 g) were added, respectively. The obtained solution was heated up to 130°C for 16 h and the respective products isolated by fractional distillation under reduced pressure.

Yield (iPrOxa, **7**): 65% (20.4 g, 180 mmol). $^1$H NMR (400 MHz, $CDCl_3$, $\delta$/ppm): 4.30 – 4.17 (m, 2H), 3.88 – 3.76 (m, 2H), 2.56 (ddtd, *J* = 13.9, 8.1, 7.0, 5.8 Hz, 1H), 1.19 (d, *J* = 7.1 Hz, 6H). $^{13}$C NMR (101 MHz, $CDCl_3$, $\delta$/ppm): 172.2, 66.9, 54.0, 27.8, 19.3.

Yield (nPrOxa, **8**): 68% (21.5 g, 190 mmol). $^1$H NMR (400 MHz, $CDCl_3$, $\delta$/ppm): 4.22 (td, *J* = 9.4, 0.5 Hz, 2H), 3.89 – 3.76 (m, 2H), 2.25 (tt, *J* = 7.8, 1.3 Hz, 2H), 1.74 – 1.59 (m, 2H), 0.97 (t, *J* = 7.4 Hz, 3H). $^{13}$C NMR (101 MHz, $CDCl_3$, $\delta$/ppm): 168.2, 66.9, 54.2, 29.7, 19.2, 13.6.

## S5 Synthesis of the Azide-Containing Monomer AzOxa

**2,5-Dioxopyrrolidin-1-yl 2,2,2-trifluoroacetate (TFA-NHS)** was synthesized according to literature.[65]



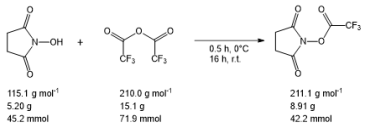


**Scheme S2.** Synthesis of 2,5-dioxopyrrolidin-1-yl 2,2,2-trifluoroacetate (TFA-NHS).

A 50 ml Schlenk flask was charged with trifluoroacetic anhydride (TFAA, 71.9 mmol, 15.1 g) and cooled to 0°C. Then, *N*-hydroxysuccinimide (NHS, 45.2 mmol, 5.20 g) was added and the reaction stirred for 30 min at this temperature, followed by stirring at r.t. for additional 16 h. The excess of TFAA was removed and the residue redissolved twice in toluene (20 ml) and the solvent evaporated.

Yield: 93% (42.2 mmol, 8.90 g).

**Ethyl-4-azidobutanoate (9)** was synthesized referring to literature.[50]

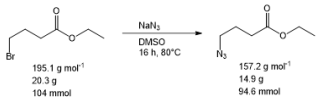


**Scheme S3.** Synthesis of ethyl-4-azidobutanoate (**9**).

Ethyl-4-bromobutanoate (104 mmol, 20.3 g, 15 ml) and $NaN_3$ (365 mmol, 23.7 g) were added to dimethyl sulfoxide (100 ml) and the mixture was heated up to 80°C for 16 h. After cooling to r.t., DCM (200 ml) was added and the organic layer was washed with water (5x 100 ml), dried over $MgSO_4$ and the solvent evaporated.

Yield: 91% (94.6 mmol, 14.9 g). IR (cm$^{-1}$) = 2939 (C-H), 2094 ($N_3$), 1729 (C=O). $^1$H NMR (400 MHz, $CDCl_3$, $\delta$/ppm): 4.10 (q, *J* = 7.1 Hz, 2H), 3.31 (t, *J* = 6.7 Hz, 2H), 2.36 (t, *J* = 7.2 Hz, 2H), 1.87 (p, *J* = 7.0 Hz, 2H), 1.22 (td, *J* = 7.1, 0.5 Hz, 3H). $^{13}$C NMR (101 MHz, $CDCl_3$, $\delta$/ppm): 172.7, 60. 6, 50.7, 31.2, 24.3, 14.2.

**4-Azidobutanoic acid (10)** was synthesized referring to literature.[62]

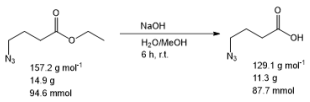


**Scheme S4.** Synthesis of 4-azidobutanoic acid (**10**).

To compound **9** aq. NaOH (200 mmol, 8.0 g, 200 ml) and methanol (40 ml) were added. The solution was stirred at r.t. for 6 h, acidified with HCl (4 M) to pH = 1 and extracted with diethyl ether (4x 100 ml). The organic layer was dried with $MgSO_4$ and the solvent evaporated.

Yield: 93% (87.7 mmol, 11.3 g). IR (cm$^{-1}$) = 3095 (OH), 2939 (C-H), 2093 ($N_3$), 1705 (C=O). $^1$H NMR (400 MHz, $CDCl_3$, $\delta$/ppm); 11.48 (s, 1H), 3.35 (t, $J$ = 6.7 Hz, 2H), 2.45 (t, $J$ = 7.2 Hz, 2H), 1.98 – 1.81 (m, 2H). $^{13}$C NMR (101 MHz, $CDCl_3$, $\delta$/ppm): 179.4, 50.5, 31.0, 23.9.

**2,5-Dioxopyrrolidin-1-yl 4-azidobutanoate (11)** was synthesized referring to literature:[65]

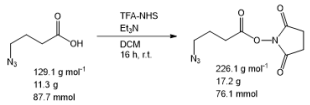


**Scheme S5.** Synthesis of 2,5-dioxopyrrolidin-1-yl 4-azidobutanoate (**11**).

Compound **10** (87.7 mmol, 11.3 g) was dissolved in dichloromethane (200 ml) and TFA-NHS (128 mmol, 27.0 g) and triethyl amine (500 mmol, 51.0 g) were added. The solution was stirred at r.t. for 16 h, followed by the addition of dichloromethane (100 ml). The organic layer was washed with aqueous 0.1 M HCl (3x 100 ml), saturated $NaHCO_3$ (2x 100 ml) solution and dried with $MgSO_4$. After evaporation of the solvent, a highly viscous yellowish liquid remained, which became solid after 3 days.

Yield: 87% (76.1 mmol, 17.2 g). IR (cm$^{-1}$) = 2947 (C-H), 2097 ($N_3$), 1813, 1783, 1729 (C=O). $^1$H NMR (400 MHz, $CDCl_3$, $\delta$/ppm): 3.41 (t, $J$ = 6.6 Hz, 2H), 2.80 (s, 4H), 2.69 (t, $J$ = 7.2 Hz, 2H), 1.98 (p, $J$ = 6.9 Hz, 2H). $^{13}$C NMR (101 MHz, $CDCl_3$, $\delta$/ppm): 169.2, 168.0, 50.0, 28.1, 25.6, 24.1.

**4-Azido-*N*-(2-chloroethyl)butanamide (12)** was synthesized according to literature.[50]



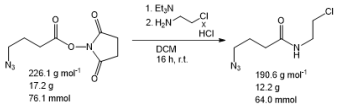


**Scheme S 6.** Synthesis of 4-azido-*N*-(2-chloroethyl)butanamide (**12**).

Compound **11** (76.1 mmol, 17.2 g) was dissolved in DCM (150 ml) and 2-chloroethylamine hydrochloride (150 mmol, 17.4 g) and triethyl amine (360 mmol, 36.5 g, 50 ml) were added. The solution was stirred at r.t. for 16 h, followed by the addition of dichloromethane (100 ml). The organic layer was washed with aq. 1 M HCl (3x 100 ml) and $NaHCO_3$ (2x 100 ml), dried with $MgSO_4$ and the solvent evaporated, giving the product as highly viscous yellowish liquid.

Yield: 84% (64.0 mmol, 12.2 g). IR (cm$^{-1}$) = 3296 (NH), 2935 (C-H), 2093 ($N_3$), 1646 (C=O). $^1$H NMR (400 MHz, $CDCl_3$, $\delta$/ppm): 6.57 (d, $J$ = 5.8 Hz, 1H), 3.59 – 3.45 (m, 4H), 3.29 (t, $J$ = 6.6 Hz, 2H), 2.25 (t, $J$ = 7.3 Hz, 2H), 1.92 – 1.79 (m, 2H). $^{13}$C NMR (101 MHz, $CDCl_3$, $\delta$/ppm): 172.25, 50.65, 43.63, 41.21, 32.93, 24.69.

**2-(3-Azidopropyl)-2-oxazoline (13)** was synthesized referring to literature.[64]

**Scheme S7.** Synthesis of 2-(3-azidopropyl)-2-oxazoline (AzOxa, **13**).

To compound **12** (49.8 mmol, 9.50 g) anhydrous acetonitrile (120 ml) and $K_2CO_3$ (65.8 mmol, 9.10 g) were added, and the reaction mixture was heated up to 80 °C for 16 h. The reaction mixture was allowed to cool to r.t. and filtered (0.4 µm syringe filter) and the solvent evaporated. The resulting product was then connected to fine vacuum line overnight. $CaH_2$ was added and the mixture stirred at r.t. for 16 h, followed by distillation under reduced pressure (0.5 mbar), giving the product as a colorless liquid.



Yield: 72% (35.9 mmol, 5.50 g). IR (cm$^{-1}$) = 2940 (C-H), 2093 ($N_3$), 1667 (N=C-O). $^1$H NMR (400 MHz, $CDCl_3$, $\delta$/ppm): 4.28 – 4.14 (m, 2H), 3.85 – 3.73 (m, 2H), 3.34 (t, $J$ = 6.7 Hz, 2H), 2.33 (tt, $J$ = 7.3, 1.4 Hz, 2H), 1.97 – 1.81 (m, 2H). $^{13}$C NMR (101 MHz, $CDCl_3$, $\delta$/ppm): 167.3, 77.2, 67.3, 54.5, 25.3, 25.0.

## S6 Synthesis of Alkyne-Containing Antifouling Motifs (SB, CB, OEG, and OEG-SB) for Click Modification

**3-[Dimethyl(prop-2-yn-1-yl)ammonio]propanoate, CB 14)** was synthesized according to literature.[53]

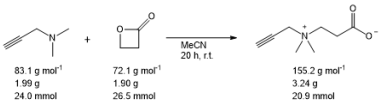


**Scheme S8.** Synthesis of CB (**14**).

Propiolactone (26.5 mmol, 1.90 g) was added to a solution of dimethylamino-2-propin (24.0 mmol, 1.99 g) in acetonitrile (57 ml) and stirred for 18 h at r.t. The formed precipitate was filtered off, washed with small portions of cold acetonitrile, and dried under reduced pressure.

Yield: 88% (20.6 mmol, 3.3 g) of a white solid. IR (cm$^{-1}$) = 3190 (H-C≡C), 2963 (C-H) 2123 (C≡C). $^1$H NMR (400 MHz, $D_2O$, $\delta$/ppm): 4.25 (d, $J$ = 2.0 Hz, 2H), 3.74 – 3.63 (m, 2H), 3.17 (s, 6H), 2.74 – 2.64 (m, 2H). $^{13}$C NMR (101 MHz, $D_2O$ + DMSO-$d_6$, $\delta$/ppm): 177.5, 83.3, 62.9, 55.9, 51.9, 32.4.

**3-[Dimethyl(prop-2-yn-1-yl)ammonio]propane-1-sulfonate, SB (15)** was synthesized according to literature.[53]

**Scheme S9.** Synthesis of SB (**15**).

Propan-1,3-sulton (29.5 mmol, 3.6 g) was added to a solution of dimethylamino-2-propin (26.8 mmol, 2.23 g) in acetonitrile (57 ml) and stirred for 24 h at r.t. The formed precipitate was filtered off, washed with small portions of cold acetonitrile, and dried under reduced pressure.

Yield: 58% (15.6 mmol, 3.2 g) of a white solid. IR (cm$^{-1}$) = 3190 (H-C≡C), 2963 (C-H) 2123 (C≡C). $^1$H NMR (400 MHz, $D_2O$, $\delta$/ppm): 4.30 (s, 2H), 3.68 – 3.57 (m, 2H), 3.22 (s, 6H), 3.01 (t, $J$ = 7.2 Hz, 2H), 2.33 – 2.20 (m, 2H). $^{13}$C NMR (101 MHz, $D_2O$ + DMSO-$d_6$, $\delta$/ppm): 83.2, 71.9, 63.9, 55.9, 48.8, 19.9.

**2-{2-[2-(Prop-2-yn-1-yloxy)ethoxy]ethoxy}ethan-1-ol, OEG (16)** was synthesized according to literature.[66]

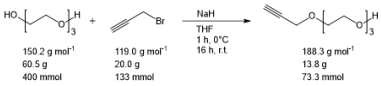


**Scheme S10.** Synthesis of OEG (**16**).

Triethylene glycol (400 mmol, 60.5 g, 54.0 ml) was dissolved in tetrahydrofuran (200 ml) and NaH was added portion wise at 0°C. The reaction was stirred at 0 °C for 1 h and propargyl bromide (133 mmol, 20.0 g, 12.7 ml) was added, followed by stirring at r.t. for additional 16 h. During the reaction, the solution turned brownish, and a white solid was formed. The reaction was quenched with ice cold water (100 ml) and the mixture extracted with dichloromethane (3x 50 ml). The organic layer was washed with brine (2x 50 ml), dried over anhydrous $Na_2SO_4$ and the solvent evaporated. The product was isolated by column chromatography (silica gel, ethyl acetate/*n*-hexane = 3:1), giving the title compound as a slightly yellowish oil.

Yield: 55% (73.3 mmol, 13.8 g). $^1$H NMR (400 MHz, $CDCl_3$, $\delta$/ppm): 4.20 (d, $J$ = 2.4 Hz, 2H), 3.75 – 3.64 (m, 10H), 3.63 – 3.59 (m, 2H), 2.60 – 2.45 (m, 1H), 2.43 (t, $J$ = 2.4 Hz, 1H). $^{13}$C NMR (101 MHz, $CDCl_3$, $\delta$/ppm): 58.5, 61.9, 69.2, 70.5, 70.5, 70.8, 72.6, 74.7, 79.7.

**2-{2-[2-(prop-2-yn-1-yloxy)ethoxy]ethoxy}ethyl 4-methylbenzenesulfonate (17)** was synthesized according to literature.[67]

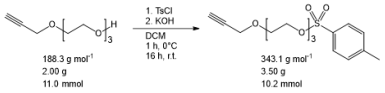


**Scheme S11.** Synthesis scheme for 2-{2-[2-(prop-2-yn-1-yloxy)ethoxy]ethoxy}ethyl-4-methylbenzenesulfonate (**17**).

Compound **16** (11.0 mmol, 2.00 g) and 4-toluenesulfonyl chloride (12.0 mmol, 2.22 g) were dissolved in dichloromethane (10 ml) and KOH (43.3 mmol, 2.38 g) was added at 0°C. The reaction mixture was stirred at r.t. for 16 h, and quenched with ice cold water (25 ml). The product was extracted with dichloromethane (3x 100 ml). The organic phases were combined and dried with $MgSO_4$ and solvent was removed under reduced pressure. The product appeared as colorless liquid.

Yield: 93% (10.2 mmol, 3.50 g). $^1$H NMR (400 MHz, $CDCl_3$, $\delta$/ppm): 7.84 – 7.74 (m, 2H), 7.37 – 7.30 (m, 2H), 4.18 (d, $J$ = 2.4 Hz, 2H), 4.17 – 4.14 (m, 2H), 3.71 – 3.66 (m, 4H), 3.66 – 3.61 (m, 2H), 3.58 (s, 4H), 2.44 (d, $J$ = 0.6 Hz, 3H), 2.42 (t, $J$ = 2.4 Hz, 1H). $^{13}$C NMR (101 MHz, $CDCl_3$, $\delta$/ppm): 58.5, 68.8, 69.2, 69.4, 70.6, 70.7, 70.9, 74.7, 79.8, 128.1, 130.0, 133.2, 144.9.

***N,N*-Dimethyl-2-{2-[2-(prop-2-yn-1-yloxy)ethoxy]ethoxy}ethan-1-amine (18)** was synthesized according to literature.[68]

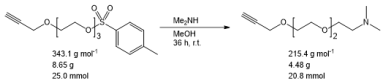


**Scheme S12.** Synthesis of N,N-dimethyl-2-{2-[2-(prop-2-yn-1-yloxy)ethoxy]ethoxy}ethan-1-amine (**18**).



Compound **17** (25.0 mmol, 8.65 g) was dissolved in methanolic dimethylamine (100 mmol, 50.0 ml). The reaction was conducted at r.t. for 35 h and the solvent removed under reduced pressure. The remaining brownish residue was dissolved in water (50 ml ml) and extracted with dichloromethane (5x 30 ml). The combined organic phase was washed with slightly basic water (2x 50 ml water + 5 ml $NH_4OH$ (25 wt%)) and brine (2x 50 ml), dried with $MgSO_4$ and the solvent evaporated.

Yield: 83% (20.8 mmol, 4.48 g) of a yellowish oil. $^1$H NMR (400 MHz, $CDCl_3$, $\delta$/ppm): 4.19 (d, $J$ = 2.4 Hz, 2H), 3.71 – 3.59 (m, 8H), 3.56 (t, $J$ = 5.9 Hz, 2H), 2.49 (t, $J$ = 5.9 Hz, 2H), 2.44 – 2.39 (m, 1H), 2.24 (s, 6H), 2.22 (d, $J$ = 3.1 Hz, 6H). $^{13}$C NMR (101 MHz, $CDCl_3$, $\delta$/ppm): 79.8, 74.6, 70.7, 70.5, 70.5, 69.5, 69.2, 59.0, 58.5, 46.0.

**3-{Dimethyl{2-[2-(prop-2-yn-1-yloxy)ethoxy]ethyl}ammonio}propane-1-sulfonate, OEG-SB (19)** was synthesized according to literature.[53]

**Scheme S13.** Synthesis of OEG-SB (**19**).

Compound **18** (9.29 mmol, 2.00 g) and 1,3-propanesultone (8.45 mmol, 1.03 g) were dissolved in acetonitrile (7 ml) and the resulting mixture stirred at r.t. for 16 h. A white precipitate was formed, which was filtered off and washed with diethyl ether (3x 30 ml). The product was then dried under reduced pressure.

Yield: 97% (8.19 mmol, 2.98 g). $^1$H NMR (400 MHz, $D_2O$, $\delta$/ppm): 4.25 (s, 2H), 3.98 (dq, $J$ = 5.0, 2.5 Hz, 2H), 3.80 – 3.69 (m, 8H), 3.66 – 3.60 (m, 2H), 3.60 – 3.52 (m, 2H), 3.19 (s, 6H), 2.98 (t, $J$ = 7.3 Hz, 2H), 2.30 – 2.20 (m, 2H), 2.07 (s, 1H). $^{13}$C NMR (101 MHz, $D_2O$ + DMSO-$d_6$, $\delta$/ppm): 80.6, 77.7, 71.2, 71.0, 71.0, 70.2, 65.6, 65.0, 64.6, 64.6, 64.6, 59.4, 53.1, 53.1, 53.0, 48.9, 19.9.



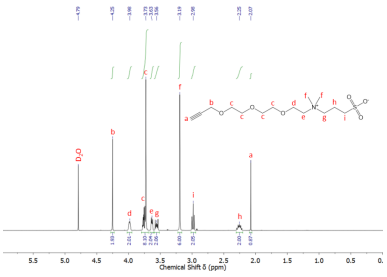


**Figure S3.** $^1$H-NMR spectrum of OEG-SB (**19**), measured at r.t. with 400 MHz in DMSO-d6.

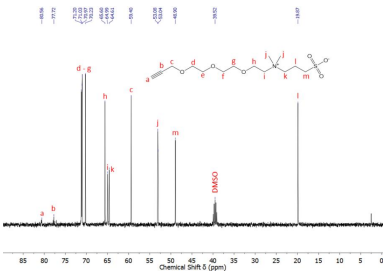


**Figure S4.** $^{13}$C-NMR spectrum of OEG-SB (**19**), measured at r.t. with 100 MHz in DMSO-d6.

## S7 Two-Component Copolymerization of BPOxa with 2-Alkyl-2-Oxazolines

All polymers (**5**) were synthesized as follows: The respective monomers were added via an Eppendorf pipette to a solution of methyl trifluoromethanesulfonate (MeOTf) in acetonitrile



($c_1$ = 3.5 mg ml$^{-1}$ or $c_2$ = 1.75 mg ml$^{-1}$) under inert gas atmosphere in a glove box and polymerized in a microwave reactor at 120 °C for 90 min. After quenching the reaction with water, the polymers were precipitated in ice-cold diethyl ether, filtered off and washed several times with small portions of diethyl ether. Polymers were then isolated by drying under reduced pressure and characterized by $^1$H NMR spectroscopy and SEC with the individual data provided in **Table S1**.

**Table S1.** Summarized experimental data of benzophenone containing two-component copolymers.

| Monomer Feed | Polymer Composition[a)] | $M_{w,SEC}$[b)] /$10^{-3}$ g $mol^{1}$ | Đ [c)] | Cloud Point / °C[d)] | Yield / % |
|---|---|---|---|---|---|
| $EtOxa_{100}$ | Poly($EtOxa_{100}$) | 36.9 | 1.17 | 72.0 ± 1 | 90 |
| $EtOxa_{99}$-$BPOxa_1$ | Poly($EtOxa_{99}$-*co*-$BPOxa_1$) | 23.0 | 1.29 | 56.0 ± 1 | 94 |
| $EtOxa_{97}$-$BPOxa_3$ | Poly($EtOxa_{98}$-*co*-$BPOxa_2$) | 30.3 | 1.47 | 39.1 ± 1 | 87 |
| $EtOxa_{95}$-$BPOxa_5$ | Poly($EtOxa_{94}$-*co*-$BPOxa_6$) | 27.6 | 1.54 | 15.5 ± 1 | 93 |
| $EtOxa_{89}$-$BPOxa_{11}$ | Poly($EtOxa_{90}$- *co*-$BPOxa_{10}$) | 25.0 | 1.55 | N/A[e)] | 91 |
| $BPOxa_{100}$ | Poly($BPOxa_{100}$) | 45.1 | 1.51 | N/A[e)] | 66 |
| $iPrOxa_{100}$ | Poly($iPrOxa_{100}$) | 23.9 | 1.13 | 40.2 ± 1 | 81 |
| $iPrOxa_{95}$-$BPOxa_5$ | Poly($iPrOxa_{94}$-*co*-$BPOxa_6$) | 17.0 | 1.36 | 13.5 ± 1 | 81 |
| $nPrOxa_{100}$ | Poly($nPrOxa_{100}$) | 33.0 | 1.18 | 25 ± 1 | 61 |
| $nPrOxa_{95}$-$BPOxa_5$ | Poly($nPrOxa_{94}$-*co*-$BPOxa_6$) | 31.6 | 1.49 | N/A[e)] | 72 |
| $EtOxa_{97}$-$BPOxa_3$ | Poly($EtOxa_{97}$-*co*-$BPOxa_3$) | 31.3 | 1.67 | 40.0 ± 1 | 76 |
| $iPrOxa_{98}$-$BPOxa_2$ | Poly($iPrOxa_{98}$-*co*-$BPOxa_2$) | 29.4 | 1.54 | 24.0 ± 1 | 79 |
| $iPrOxa_{65}$-$nPrOxa_{33}$-$BPOxa_2$ | Poly($iPrOxa_{63}$-*co*-$nPrOxa_{35}$-*co*-$BPOxa_2$) | 30.1 | 1.89 | 22.7 ± 1 | 65 |
| $iPrOxa_{79}$-$EtOxa_{19}$-$BPOxa_2$ | Poly($iPrOxa_{79}$-*co*-$EtOxa_{19}$-*co*-$BPOxa_2$) | 32.2 | 2.1 | 28.4 ± 1 | 86 |
| $nPrOxa_{97}$-$BPOxa_3$ | Poly($nPrOxa_{97}$-*co*-$BPOxa_3$) | 41.6 | 1.24 | 12.0 ± 1 | 75 |

Monomer/Initiator (M/I) Ratio: 300/1. [a)] As calculated by $^1$H NMR spectra. [b)] As determined by SEC analysis. [c)] Đ $M_w/M_n$ calculated by GPC analysis. [d)] As determined by turbidity measurements of a 0.3 wt% aqueous solution. [e)] Polymer does not dissolve in water.



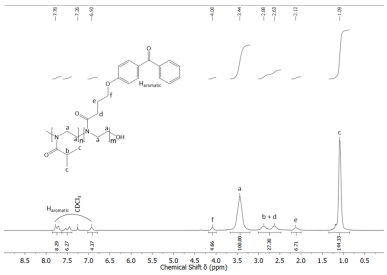


**Figure S5.** Representative $^1$H NMR spectrum of poly($iPrOxa_{94}$-*co*-$BPOxa_6$), measured at r.t. with 400 MHz in $CDCl_3$.

**Figure S5** shows a typical $^1$H NMR spectrum of poly(2-alkyl-2-oxazoline) copolymerized with the BPOxa photocrosslinker monomer. The methyl groups of the iso-propyl side chain show a chemical shift of 1.09 ppm and the polymer backbone of 3.44 ppm. Signals at 2.12, 2.63 and 4.08 belong to the propylene spacer between the benzophenone moiety and the polymer backbone. Signals observed at 6.93–7.78 ppm are attributed to the aromatic protons of the benzophenone system.

## S8 Synthesis of Three-Component Poly(2-Alkyl-2-Oxazoline) Copolymers with Azide- and Photocrosslinker Units

Temperature program for microwave-assisted synthesis:

Power: 140 W, Ramp: 2 min, Hold Time: 90 min, Temperature: 120°C

All polymerization reactions were quenched with water (12.5 mmol, 0.20 g, 0.2 ml) and isolated by drying under reduced pressure at 50°C. Compositions: PEC112a1-a5 - poly($iPrOxa_{91}$-*co*-$BPOxa_3$-*co*-$AzOxa_6$); PEC115a1-a5 - poly($iPrOxa_{87}$-*co*-$BPOxa_3$-*co*-$AzOxa_{10}$)



**Table S2.** Summarized experimental data of AzOxa and benzophenone-containing three-component copolymers PEC112a1-a5 = poly($iPrOxa_{91}$-*co*-$BPOxa_3$-*co*-$AzOxa_6$) and PEC115a1-a5 = poly($iPrOxa_{87}$-*co*-$BPOxa_3$-*co*-$AzOxa_{10}$).

| Exp.-Nr. | Monomer Feed [mg/mmol] iPrOxa | BPOxa | AzOxa | M/I Ratio[a)] |
|---|---|---|---|---|
| PEC1112a1 | 782 / 6.92 | 62 / 0.20 | 60 /0.39 | 313 |
| PEC1112a2 | 778 / 6.88 | 59 / 0.19 | 59 / 0.38 | 311 |
| PEC1112a3 | 780 / 6.90 | 69 / 0.22 | 62 / 0.40 | 314 |
| PEC1112a4 | 783 / 6.93 | 62 / 0.20 | 60 / 0.39 | 313 |
| PEC1112a5 | 788 / 6.97 | 60 / 0.19 | 61 / 0.40 | 315 |
| PEC115a1 | 794 / 7.01 | 59 / 0.19 | 126 / 0.82 | 334 |
| PEC115a2 | 791 / 6.99 | 57 / 0.18 | 118 / 0.77 | 331 |
| PEC115a3 | 793 / 7.00 | 58 / 0.19 | 123 / 0.80 | 333 |
| PEC115a4 | 791 / 6.99 | 58 / 0.19 | 121 / 0.78 | 332 |

[a)] Initiator stock solution (acetonitrile/MeOTf): 1.5 ml/4 mg (0.024 mmol, 3.50 mg ≙ 2.70 mg $ml^{-1}$ of MeOTf). Monomer/Initiator (M/I) Ratio: 300/1.

Yields = 81% (3.65 g) for the combined reaction yields of PEC112a1-a5 and yields = 73% (2.85 g) for the combined reaction yields of PEC115a1-a5.



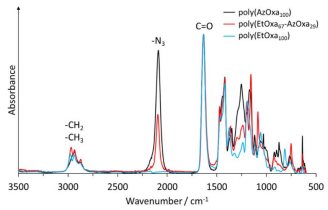


**Figure S6.** Comparison of IR spectra for poly($AzOxa_{100}$) (**black**), poly($EtOxa_{67}$-$AzOxa_{29}$) (**red**) and poly($EtOxa_{100}$) (**blue**).

## S9 Click Reaction of Azide-Containing Three-Component Copolymers with COOH and Antifouling Motifs (SB, CB, OEG, and OEG-SB)

For the modification 500 mg (PEC112) and 400 mg (PEC115) of the respective azide-containing polymers were dissolved at r.t. in a mixture of water/*tert*.-BuOH (20 ml; 1/1 ratio). Then the respective alkyne was added, followed by the addition of $CuSO_4$ x 5 $H_2O$ (0.28 mmol; 70 mg) and sodium ascorbate (0.50 mmol; 100 mg). The reaction solution was stirred for 16 h and then dialyzed against water (membrane MWCO = 3500 Da) for 3 days. The modified polymer was then isolated by freeze-drying from water.

**Table S3.** Click reaction of poly($iPrOxa_{91}$-*co*-$BPOxa_3$-*co*-$AzOxa_6$) containing 6 mol% azide functionalities with the alkyne fragments COOH, SB, CB, OEG, and OEG-SB.

| | Modification Unit -COOH | -SB | -CB | -OEG | -OEG-SB |
|---|---|---|---|---|---|
| Alkyne Feed (mg / mmol) | 80 / 0.82 | 85 / 0.42 | 85 / 0.45 | 100 / 0.53 | 125 / 0.37 |
| Polymer Yield (mg / %) | 391 / 78 | 407 / 81 | 444 / 89 | 370 / 74 | 472 / 94 |

**Table S4.** Click reaction of poly(iPrOxa$_{87}$-*co*-BPOxa$_3$-*co*-AzOxa$_{10}$) containing 10 mol% azide functionalities with the alkyne fragments COOH, SB, CB, OEG, and OEG-SB.

| | Modification Unit | | | | |
|---|---|---|---|---|---|
| | -COOH | -SB | -CB | -OEG | -OEG-SB |
| Alkyne Feed (mg/mmol) | 80 / 0.82 | 85 / 0.42 | 85 / 0.45 | 100 / 0.53 | 125 / 0.37 |
| Polymer Yield (mg/%) | -/- | 400 / 100 | 340 / 85 | 310 / 78 | 300 / 75 |

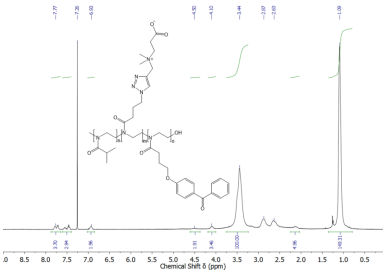

**Figure S7.** $^1$H-NMR spectrum of poly(iPrOxa$_{87}$-BPOxa$_3$-CB$_{10}$), measured at r.t. with 400 MHz in $CDCl_3$.



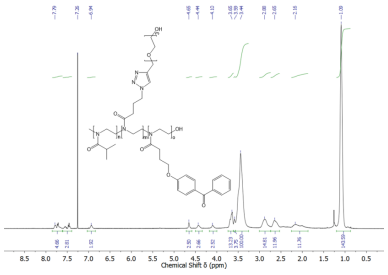

**Figure S8.** $^1$H-NMR spectrum of poly(iPrOxa$_{87}$-BPOxa$_3$-OEG$_{10}$), measured at r.t. with 400 MHz in $CDCl_3$.

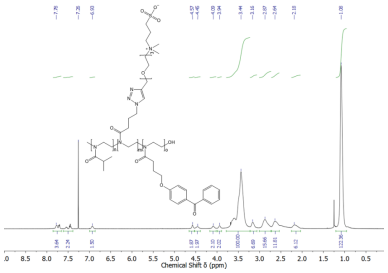

**Figure S9.** $^1$H-NMR spectrum of poly(iPrOxa$_{87}$-BPOxa$_3$-OEG-SB$_{10}$), measured at r.t. with 400 MHz in $CDCl_3$.



**Table S5.** Analytical data of non-modified and modified poly(iPrOxa-*co*-BPOxa-*co*-AzOxa).

| Exp.-Nr. | Polymer Composition[a)] | $M_w$[b)] [ $10^3$ g mol$^{-1}$] | Dispersity Đ[c)] | Yield / % |
|---|---|---|---|---|
| PEC112a | poly(iPrOxa$_{91}$-*co*-BPOxa$_3$-*co*-AzOxa$_6$)[d)] | 27.7 | 1.76 | 81 |
| PEC112-COOH | poly(iPrOxa$_{91}$- *co*-BPOxa$_3$-*co*-COOH$_6$) | 27.1 | 2.17 | 57 |
| PEC112-SB | poly(iPrOxa$_{91}$-*co*-BPOxa$_3$-*co*-SB$_6$) | 31.2 | 2.02 | 43 |
| PEC112-CB | poly(iPrOxa$_{91}$-*co*-BPOxa$_3$-*co*-CB$_6$) | 35.8 | 3.14 | 41 |
| PEC112-OEG | poly(iPrOxa$_{91}$-*co*-BPOxa$_3$-*co*-OEG$_6$) | 28.5 | 2.27 | 48 |
| PEC112-OEG-SB | poly(iPrOxa$_{91}$-*co*-BPOxa$_3$-*co*-OEG-SB$_6$) | 30.9 | 2.03 | 56 |
| PEC115a | poly(iPrOxa$_{87}$-*co*-BPOxa$_3$-*co*-AzOxa$_{10}$)[d)] | 28.3 | 1.80 | 73 |
| PEC115-SB | poly(iPrOxa$_{87}$-*co*-BPOxa$_3$-*co*-SB$_{10}$) | 21.4 | 1.82 | 44 |
| PEC115-CB | poly(iPrOxa$_{87}$-*co*-BPOxa$_3$-*co*-CB$_{10}$) | 9.5 | 2.46 | 39 |
| PEC115-OEG | poly(iPrOxa$_{87}$-*co*-BPOxa$_3$-*co*-OEG$_{10}$) | 23.4 | 2.12 | 52 |
| PEC115-OEG-SB | poly(iPrOxa$_{87}$-*co*-BPOxa$_3$-*co*-OEG-SB$_{10}$) | 21.5 | 2.09 | 51 |

[a)] As calculated from $^1$H NMR analysis. [b)] As determined by SEC analysis. [c)] Calculated from SEC analysis. [d)] Monomer/initiator (M/I) ratio: 300/1.

## S10 Synthesis of the Disulfide Anchor BPdiS for Au-Substrates

**Bis(2,5-dioxopyrrolidin-1-yl) 3,3'-disulfanediyldipropanoate (21).**[52] To a mixture of 3,3'-disulfanediyldipropionic acid (4.99 mmol, 1.05 g) and dichloromethane (35 ml) pyridine (61.95 mmol, 4.9 g, 5 ml) was added and the resulting solution cooled with an ice-water bath to 0 °C. NHS (16.77 mmol, 1.93 g) and TFA (16.33 mmol, 3.43 g, 2.3 ml) were added and the solution was stirred at 0 °C for 30 min, followed by warming up to r.t. and stirring for additional 16 h. Dichloromethane (60 ml) was added to the solution and the organic layer washed with aq. HCl (0.5 M, 3x 60 ml) and saturated $NaHCO_3$ (2x 60 ml). The separated organic layer was



dried over anhydrous $MgSO_4$ and the solvent evaporated, giving the title compound as a slightly brownish solid.

Yield 82% (4.09 mmol, 1.66 g); $^1$H NMR (400 MHz, $CDCl_3$, $\delta$/ppm): 4.54 (s, 2H), 3.02–3.08 (various m, 8H); $^{13}$C NMR (100 MHz, $CDCl_3$, $\delta$/ppm): 25.7, 31.2, 32.4, 167.3, 169.1.

**3,3'-disulfanediylbis[N-(4-benzoylbenzyl)propanamide], BPdiS (22)** was synthesized as previously reported.[25] Compound **21** (0.74 mmol, 0.30 g) was dissolved in dimethyl sulfoxide (14 ml) and cooled with an ice-water bath to 0 °C. [4-(aminomethyl)phenyl](phenyl)methanone hydrochloride (3.30 mmol, 0.70 g) dissolved in simethyl sulfoxide (6 ml) and triethylamine (3.20 mmol, 0.45 ml) were added and the solution stirred for 16 h at r.t. Dichloromethane (20 ml) was added. The organic layer was washed with water (2x 20 ml) and the formed precipitate in the organic layer was filtered off and washed with small portions of dichloromethane several times. The remaining product was dried in vacuum overnight.

Yield: 51% (0.38 mmol, 226 mg); IR (cm$^{-1}$): $\nu$ = 3295 (N-H), 3052 (C-H$_{aromatic}$), 2907 (C-H), 1641 (C=O); $^1$H NMR (400 MHz, DMSO, $\delta$/ppm): 2.61 (t, $J$ = 7.07 Hz, 2H), 2.93 (t, $J$ = 7.12 Hz, 2H), 4.39 (d, J = 5.90, 2H), 7.42 – 7.71 (various m, Ar H); $^{13}$C NMR (100 MHz, $CDCl_3$, $\delta$/ppm): 33.9, 34.9, 41.9, 127.2, 128.5, 129.5, 129.8, 132.6, 135.5, 137.2, 144.5, 170.3, 195.4.

## S11 Cloud Points of Aqueous Poly(2-alkyl-2-oxazoline) Solutions Depending on AzOxa Content and Polymer Volume Fractions

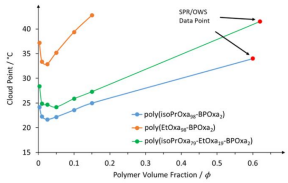


**Figure S10.** Phase diagram illustrating the dependence of the cloud point on polymer volume fraction for poly(EtOxa$_{98}$-*co*-BPOxa$_2$), poly(iPrOxa$_{79}$-*co*-EtOxa$_{19}$-*co*-BPOxa$_2$) and poly(iPrOxa$_{98}$-*co*-BPOxa$_2$) for a degree of polymerization of around 250, as determined by turbidity measurements in aqueous solution (heating only) with a heating rate of 1 K min$^{-1}$. Phase transition temperatures (indicated as "SPR/OWS data point") were determined by temperature dependent OWS.

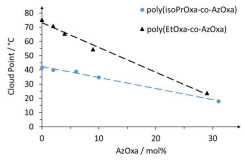


**Figure S11.** Dependence of the cloud point on AzOxa content for poly(iPrOxa-*co*-AzOxa) and poly(EtOxa-*co*-AzOxa), as determined by UV/VIS turbidity measurements of a 0.3 wt% aqueous polymer solution at a wavelength of 550 nm and a heating rate of 1 K min$^{-1}$.



## S12 Dependence of the Swelling Ratio for Poly(EtOxa$_{97}$-*co*-BPOxa$_3$) Networks on the UV Irradiation Dose and Temperature

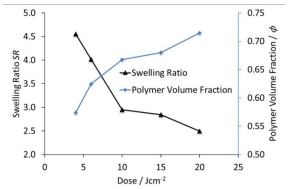


**Figure S12.** Dependence of the swelling ratio on the UV irradiation dose for Poly(EtOxa$_{97}$-*co*-BPOxa$_3$) as determined from SPR/OWS measurements. M/I = 300/1.

The diagram depicted in **Figure S12** shows the correlation between irradiation dose and swelling ratio for poly(EtOxa$_{97}$-*co*-BPOxa$_3$). Highly swollen hydrogel networks were obtained for low irradiation doses, whereby increasing dose result in higher crosslinking densities and therewith a decrease of the swelling ratio. For the investigated polymer system poly(EtOxa$_{97}$-*co*-BPOxa$_3$) swelling ratios between 2.5 and 4.6 were observed for irradiation dose of 20 J cm$^{-2}$ and for 4 J cm$^{-2}$, respectively, indicating that surface attached photocrosslinkable poly(2-alkyl-2-oxazoline) based hydrogels of varying swelling ratios were successfully fabricated by irradiation with UV light of different dose at wavelength of 365 nm. The polymer volume fraction, calculated from equation (1) in the main text, shows the opposite behavior. Here, the polymer volume content increases for higher irradiation dose. Both observations result from the increasing elastic retraction force of the swollen network.



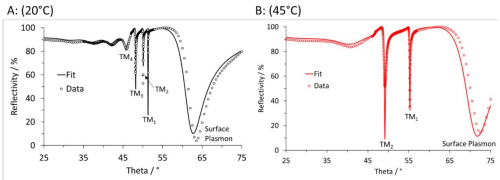


**Figure S13.** Fit and data points of the SPR/OWS angular reflectivity spectra of a swollen (**A**, 20°C) and collapsed (**B**, 45°C) poly(2-isoPrOxa$_{98}$-BPOxa$_2$) hydrogel layer sustaining at least two waveguide modes, measured with transverse magnetic (TM) polarization of the incident laser beam.

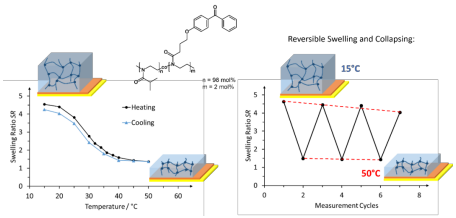


**Figure S14.** Reversibility of the swelling and collapsing for poly(iPrOxa$_{98}$-*co*-BPOxa$_2$) networks in aqueous media as determined from SPR/OWS measurements.

The reversibility of the temperature-dependent swelling and collapsing was analyzed by heating and cooling cycles for crosslinked poly(iPrOxa$_{98}$-*co*-BPOxa$_2$) networks swollen in aqueous media. A small hysteresis was observed for the first measurement cycle (**Figure S14** left), resulting from the slow response time of the polymer system. Additional heating and cooling cycles (**Figure S14** right) showed similar results, corroborating fully reversible switching between the swollen and collapsed state by changing the environmental temperature.



## S13 Swelling Behavior of Polymer Networks in PBS Buffer Solutions

Since such polymer systems are targeted for application as biosensor matrix, the influence of buffer, which inevitably will be used in the context of biological analytes and medical samples, on their thermal swelling response needs to be known. For this purpose, the influence of crosslinking density and salt concentration (PBS buffer solution) was investigated for the polymer system poly(isoPrOxa$_{87}$-BPOxa$_3$-SB$_{10}$). Thereby, the temperature-dependent swelling was measured for hydrogel layers photocrosslinked with varying irradiation dose of 5, 8, and 12 J cm$^{-2}$ (**Figure S15A**), and the initial swelling ratio was recorded for PBS buffer concentrations of 0, 1, 5 and 10 M (**Figure S15B**), respectively.

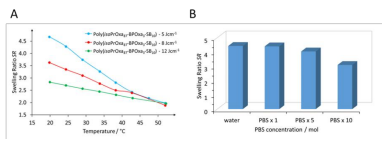


**Figure S15.** Dependence of the swelling ratio on the UV irradiation dose (in water) (**A**) and varying PBS buffer concentration (for an irradiation dose of 5 J cm$^{-2}$) (**B**) for poly(iPrOxa$_{87}$-*co*-BPOxa$_3$-*co*-SB$_{10}$) hydrogel films, as determined by OWS.

It was found that the swelling ratio was significantly influenced by the irradiation dose, which increased from *SR* = 2.8 for 12 J cm$^{-2}$ up to *SR* = 4.7 for 5 J cm$^{-2}$, which follows the expected trend for increasing crosslinking density. Similar results were already described for the polymer system poly(EtOxa$_{97}$-*co*-BPOxa$_3$) above (see **Chapter S12**). For all three irradiation doses, a linear decrease of the swelling ratio with increasing temperature was observed, as already described for the 12 J cm$^{-2}$ sample in **Figure S15B** above. At the highest temperature of 52 °C all three systems reach almost equal swelling ratios of 1.9-2.0, which can be assigned to the fully collapsed state of these hydrogel systems. These measurements indicate the strong influence of the elastic retraction force of the hydrogel network, which is much more pronounced for highly crosslinked networks. The swelling ratio measurements performed for

different PBS buffer concentrations showed a decreasing swelling ratio for an increasing salt concentration. Here, charge screening of the betaine groups by the ions from the PBS buffer reduces repulsive forces between identical charges and leads to a compaction of the hydrogel layer.

## S14 Mechanical Properties of Surface-Attached Poly(iPrOxa$_{98}$-*co*-BPOxa$_2$)

Mechanical properties of surface attached poly(2-alkly-2-oxazoline) based hydrogels were exemplarily investigated for poly(iPrOxa$_{98}$-*co*-BPOxa$_2$) by AFM nano indentation. Therefore, the respective polymer was spin coated at 2000 rpm from a 6 wt% ethanolic solution onto 4-(3-triethoxysilyl)propoxybenzophenone (BPTES) modified silicone substrates. Samples were then dried at 50°C under reduced pressure, followed by crosslinking at wavelength of 365 nm of varying dose (4 and 8 J cm$^{-2}$) under exclusion of oxygen. Layer thicknesses were then analyzed by AFM scratch test, resulting in dry state layer thickness of approximately 400 nm. The surface attached layers were then exposed to water for 2 h and the Young's modulus of the swollen films assessed by force maps at 25 °C. Same measurements were performed for collapsed state hydrogel layers at 38 °C. For each single measurement point, cantilever bending was fixed at 20 nm. This procedure was adopted for both samples, whereby the elastic modulus of the hydrogels corresponds to a Gaussian fit of the force map distribution, resulting in a representative value for each sample. Fitting of the force curves was performed using Hertz cone model, due to the shape of the tip and indentation depth, whereby all measurements were in the repulsive region to exclude a contribution of the underlying substrate.



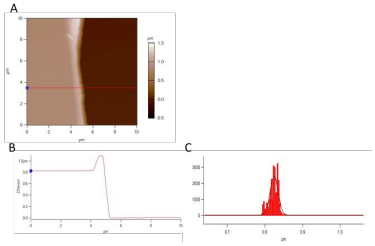


**Figure S16. (A)** AFM height image, **(B)** cross section and **(C)** histogram analysis of dry state poly(iPrOxa$_{98}$-*co*-BPOxa$_2$) crosslinked at 365 nm with 4 J cm$^{-2}$. The mean value for the film thickness was 825 nm (STD: 10.5 nm).

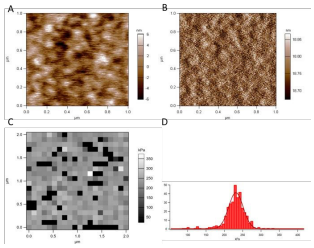


**Figure S17.** AFM tapping mode image in water at 25 °C for poly(iPrOxa$_{98}$-*co*-BPOxa$_2$) crosslinked at 365 nm with 4 J cm$^{-2}$. **(A)** Height image and **(B)** amplitude image. **(C)** Force map and **(D)** histogram fitted with Gaussian function for young's modulus analysis.



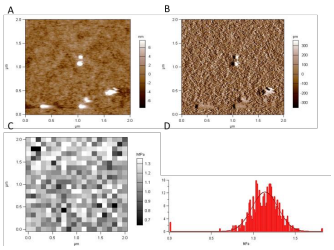


**Figure S18.** AFM tapping mode image in water at 38 °C for poly(iPrOxa$_{98}$-*co*-BPOxa$_2$) crosslinked at 365 nm with 4 J cm$^{-2}$. **(A)** Height image and **(B)** amplitude image. **(C)** Force map and **(D)** histogram fitted with Gaussian function for young's modulus analysis.

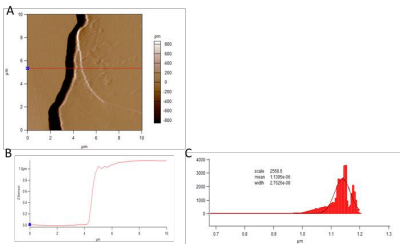


**Figure S19. (A)** AFM height image, **(B)** cross section and **(C)** histogram analysis of dry state poly(iPrOxa$_{98}$-*co*-BPOxa$_2$) crosslinked at 365 nm with 8 J cm$^{-2}$.



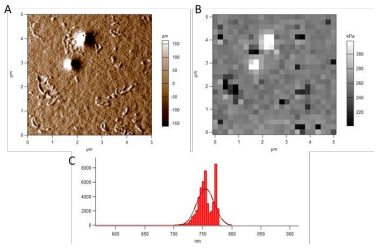


**Figure S20. (A)** AFM amplitude image, **(B)** force map and **(C)** histogram analysis of swollen state poly(iPrOxa$_{98}$-*co*-BPOxa$_2$) crosslinked at 365 nm with 8 J cm$^{-2}$ at 25 °C in water.

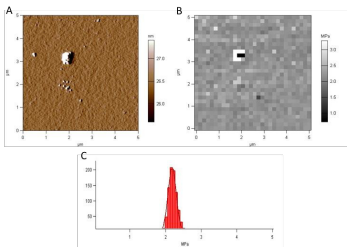


**Figure S21. (A)** AFM amplitude image, **(B)** force map and **(C)** histogram analysis of poly(iPrOxa$_{98}$-*co*-BPOxa$_2$) crosslinked at 365 nm with 8 J cm$^{-2}$ at 38 °C in water.

**Table S6.** Young's modulus dependency on irradiation dose and temperature for poly(iPrOxa$_{98}$-*co*-BPOxa$_2$) networks measured in water.

| Dose / J cm$^{-2}$ | Temperature / °C | Young Modulus / kPa |
|---|---|---|
| 4 | 25 | 193 ± 15.9 |
| 4 | 38 | 1140 ± 155.3 |
| 8 | 25 | 417 ± 39.0 |
| 8 | 38 | 2190 ± 111.1 |

Results summarized in **Table S6**, depict the dependency of the Young's modulus on crosslinking density and temperature. For swollen state layers measured at 25 °C, it was found that an increasing irradiation dose from 4 to 8 J cm$^{-2}$ increases the Young's modulus by a factor of two, approximately. The same result was obtained for collapsed state layers investigated at 38 °C, which is above the phase transition temperature of poly(iPrOxa$_{98}$-*co*-BPOxa$_2$). In both cases, the rise of the Young's modulus results from the higher crosslinking density and thus a higher polymer volume content of the respective hydrogel layers. Comparison of swollen state and collapsed hydrogel layers of the same irradiation dose show an increase of the Young's modulus by a factor of six. Here, the increasing Young's modulus results from the higher polymer volume content of the hydrogel layers induced by the environmental temperature.



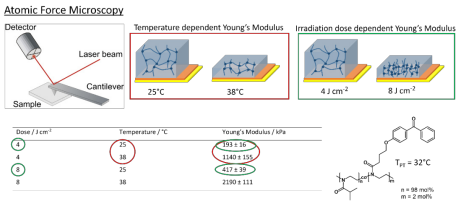


**Figure S22.** AFM measurements for poly(iPrOxa$_{98}$-*co*-BPOxa$_2$) networks in aqueous medium at different temperatures.

## S15 Glass Transition Temperatures

Glass transition temperatures $T_g$ were determined as a function of benzophenone groups using modulated differential scanning calorimetry modulated dynamic scanning calorimetry (M-DSC). Here, an oscillating heating profile (**Figure S23A**) is overlaid to a linear temperature ramp, which allows the separation of the total heat flow into a reversing and a non-reversing component, whereas the non-reversing component is obtained by subtracting the reversing from the total heat flow. By using this method, simultaneously occurring events like glass transition $T_g$ and thermal relaxation processes can be separately detected from each other. Samples were analyzed in sealed aluminum pans, whereby an empty pan of identical type was used as reference. Measurements were conducted for the system poly(EtOxa-*co*-BPOxa) of varying benzophenone concentrations at a temperature range from 0 °C to 140 °C. The heating/cooling rate applied for all measurements was 5 K/min with a modulation period of 60 s and an amplitude of ±0.796 K (**Figure S23A**). For all measurements at least two heating and cooling cycles were performed, whereby $T_g$ was determined using the second heating cycle of each experiment.



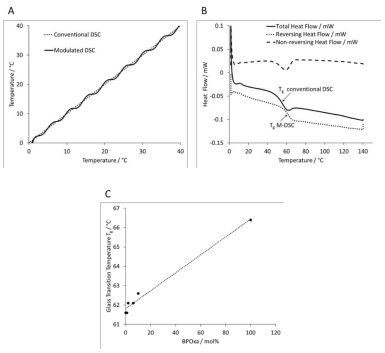


**Figure S23. (A)** Modulated DSC heating ramp and **(B)** deconvoluted signals (total heat flow, reversing heat flow, non-reversing heat flow) for M-DSC heating experiment for poly(EtOxa). Heating rate M-DSC: 5 K min$^{-1}$ ± 0.796 K min$^{-1}$. **(C)** Glass transition temperature $T_g$ for different poly(EtOxa-*co*-BPOxa). M/I = 150/1 .

The diagram shown in **Figure S23B** depicts the second heating cycle of poly(EtOxa), whereby the total heat flow is additionally deconvoluted into a reversing and a non-reversing component. The conventional DSC signal, represented by the total heat flow, shows a typical combination of the $T_g$ and an enthalpy relaxation process occurring at the nearly equal temperatures. These two overlapping events are clearly separated from each other in the reversing and the non-reversing heat flow, resulting in much higher accuracy for the determination of $T_g$. The process of enthalpy relaxation, observed in the non-reversing heat flow, is presumed to be related to molecular conformation changes, resulting from a decrease of free volume and chain mobility in the glassy state. Results of the BPOxa depending $T_g$ summarized in **Figure S23C**, demonstrate a relatively low impact of the large benzophenone group on $T_g$, whereby the lowest value was observed for poly(EtOxa$_{100}$) and the highest value



for poly(BPOxa$_{100}$). Copolymers composed of both monomers show values of $T_g$ between both homopolymers with a linear relation.

## S16 Temperature-Dependent Swelling

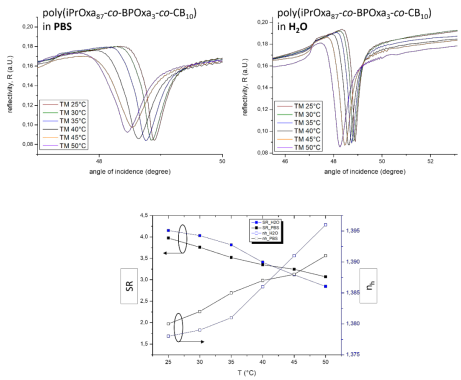


**Figure S24.** SPR/OWS curves for the temperature-dependent swelling, determined for a hydrogel film made from poly(iPrOxa$_{87}$-*co*-BPOxa$_3$-*co*-CB$_{10}$).

## S17 Unsuccessful Synthesis Approaches

*Alternative Benzophenone Crosslinker Monomer*

Unsuccessful attempt of synthesizing a benzophenone 2-oxazoline derived photocrosslinker according to literature. Here, the benzophenone moiety was linked by a methylene bridge to

the 2-oxazoline ring. As a result, a tautomeric form **u1** (**Scheme S14**) of the intended product was observed and confirmed by $^{1}$H NMR, $^{13}$C NMR, and IR spectroscopy, which results from the C-H acidic proton (**u1**) of the methylene bridge.

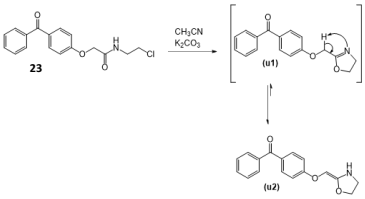


**Scheme S14.**Tautomeric structure of 2-[4-benzoylphenoxy)methyl]-4,5-dihydro-1,3-oxazole (**u1**) to 2-(4-benzoylphenoxymethylidene)-1,3-oxazolidine (**u2**).

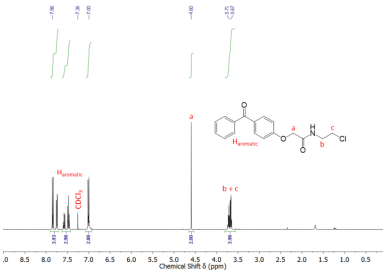


**Figure S25.** $^{1}$H NMR spectrum of 2-(4-benzoylphenoxy)-*N*-(2-chloroethyl)acetamide (**23**), measured at r.t. with 400 MHz in $CDCl_3$.



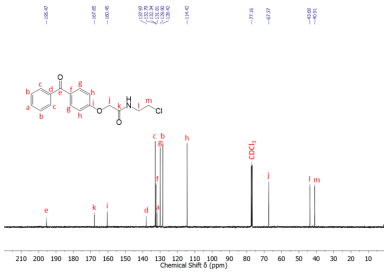


**Figure S26.** $^{13}$C NMR spectrum of 2-(4-benzoylphenoxy)-*N*-(2-chloroethyl)acetamide (**23**), measured at r.t. with 100 MHz in $CDCl_3$.

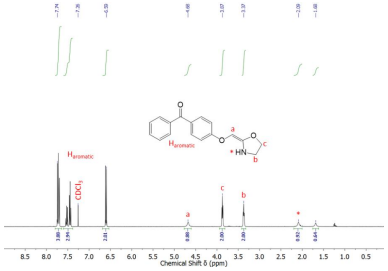


**Figure S27.** $^{1}$H NMR spectrum of 2-(4-benzoylphenoxymethylidene)-1,3-oxazolidine (**u2**), measured at r.t. with 400 MHz in $CDCl_3$.



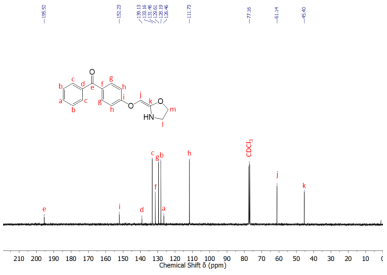


**Figure S28.**$^{13}$C NMR spectrum of 2-(4-benzoylphenoxymethylidene)-1,3-oxazolidine (**u2**), measured at r.t. with 100 MHz in $CDCl_3$.

*Oligoethylene glycol-Carboxybetaine Conjugate with Alkyne Functionality (OEG-CB)*

**3-{Dimethyl{2-[2-(prop-2-yn-1-yloxy)ethoxy]ethyl}ammonio}propanoate**

This chapter describes different approaches for the synthesis of $EO_2$-carboxybetaine combinations, similar to the compound synthesized in **Chapter S6**.

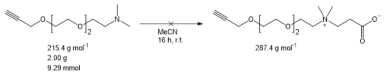


**Scheme S15.** Unsuccessful synthesis attempt #1 for OEG-CB.

1. *N*,*N*-dimethyl-2-{2-[2-(prop-2-yn-1-yloxy)ethoxy]ethoxy}ethan-1-amine (0.93 mmol, 200 mg) and β-propiolactone (1.02 mmol, 73.6 mg) were dissolved in acetonitrile (2 ml) and stirred for 16 h at r.t. As TLC indicated no conversion of the educt, the reaction temperature was raised to 50°C for 24 h. TLC indicated still no conversion of the educt.

2. In a second approach, the reaction was performed, using β-propiolactone as solvent. The reaction mixture was stirred for 16 h at r.t. A white precipitate was formed, which was



filtered off and dried under reduced pressure. $^{1}$H NMR indicated that the title compound was not obtained.

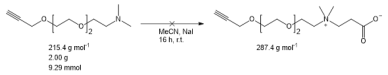


**Scheme S16.** Unsuccessful synthesis attempt #3 for OEG-CB.

3. A third approach included the addition of sodium iodide, which was added to get a better leaving group. Therefore, *N*,*N*-dimethyl-2-{2-[2-(prop-2-yn-1-yloxy)ethoxy]ethoxy}ethan-1-amine (0.45 mmol, 100 mg) and β-propiolactone (051 mmol, 36.8 mg) were dissolved in acetonitrile. NaI (0.046 mmol, 6.90 mg) was added, and the resulting solution was stirred at r.t. for 16 h. A white solid was formed during the reaction, which was removed and analyzed. The recorded $^{1}$H NMR spectrum indicated that the desired product was not formed.

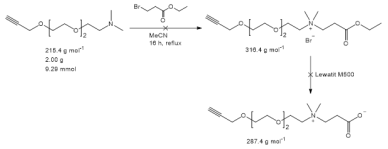


**Scheme S17.** Unsuccessful synthesis attempts #4 and #5 for OEG-CB.

4. For the synthesis of the title compound another approach was tested, using *N*,*N*-dimethyl-2-{2-[2-(prop-2-yn-1-yloxy)ethoxy]ethoxy}ethan-1-amine (0.90 mmol, 200 mg) and ethyl 3-bromopropionate (0.95 mmol, 172 mg) dissolved in acetonitrile (1.5 ml). The resulting reaction mixture was stirred at 60°C for 3 days.

5. The same reaction was performed by dissolving *N*,*N*-dimethyl-2-{2-[2-(prop-2-yn-1-yloxy)ethoxy]ethoxy}ethan-1-amine (0.90 mmol, 200 mg) in ethyl 3-bromopropionate (3.80 mmol, 680 mg). The resulting reaction mixture was also stirred at 60°C for days. In both cases, the desired product was not formed.

**3-{Dimethyl{2-[2-(prop-2-yn-1-yloxy)ethoxy]ethyl}ammonio}butanoate**

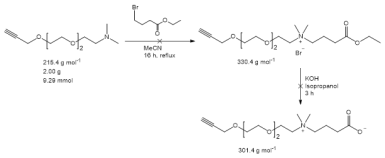


**Scheme S18.** Unsuccessful synthesis attempt #6 for OEG-CB.

6. The last approach of synthesizing a combination of a carboxybetaine and oligoethylene glycol, was done by dissolving *N*,*N*-dimethyl-2-{2-[2-(prop-2-yn-1-yloxy)ethoxy]ethoxy}ethan-1-amine (0.70 mmol, 150 mg) and ethyl 4-bromobutyrate (0.77 mmol, 150 mg) in acetonitrile (2 ml). The resulting reaction mixture was heated to reflux for 16 h and then allowed to cool to r.t. Acetonitrile was evaporated under reduced pressure, but the desired product was not formed.



**S18 GPC Analysis Data**

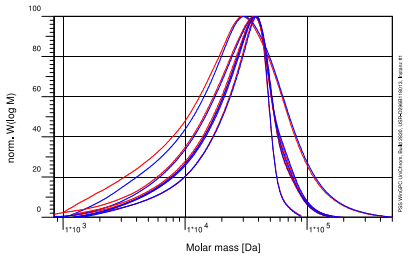


**Kurve 1 :** Vial 61: PEC112a1-N3 - 1
**Kurve 2 :** Vial 61: PEC112a1-N3 - 1
**Kurve 3 :** Vial 63: PEC112a1-SB - 1
**Kurve 4 :** Vial 63: PEC112a1-SB - 1
**Kurve 5 :** Vial 64: PEC112a1-CB - 1
**Kurve 6 :** Vial 64: PEC112a1-CB - 1
**Kurve 7 :** Vial 65: PEC112a1-OEG3 - 1
**Kurve 8 :** Vial 65: PEC112a1-OEG3 - 1
**Kurve 9 :** Vial 66: PEC112a1-OEG2-SB - 1
**Kurve 10 :** Vial 66: PEC112a1-OEG2-SB - 1

| | I1: RID 1, RI Signal | I1: VWD 1, Signal | I1: RID 1, RI Signal | I1: VWD 1, Signal | I1: RID 1, RI Signal | I1: VWD 1, Signal | I1: RID 1, F |
|---|---|---|---|---|---|---|---|
| **Mn :** | 1,5768e4 | 1,5566e4 | 1,5475e4 | 1,6466e4 | 1,1409e4 | 1,3663e4 | 1,2602e4 |
| **Mw :** | 2,7677e4 | 2,7620e4 | 3,1197e4 | 3,1855e4 | 3,5835e4 | 3,7773e4 | 2,8548e4 |
| **Mz :** | 3,5769e4 | 3,5862e4 | 4,5761e4 | 4,6359e4 | 8,5316e4 | 8,4014e4 | 4,3850e4 |
| **Mv :** | 0,000000 | 0,000000 | 0,000000 | 0,000000 | 0,000000 | 0,000000 | 0,000000 |
| **D :** | 1,7552e0 | 1,7744e0 | 2,0160e0 | 1,9346e0 | 3,1409e0 | 2,7646e0 | 2,2653e0 |
| **[n]:** | 0,000000 | 0,000000 | 0,000000 | 0,000000 | 0,000000 | 0,000000 | 0,000000 |
| **Vp :** | 8,4785e0 | 8,4652e0 | 8,4948e0 | 8,4815e0 | 8,7622e0 | 8,6988e0 | 8,5015e0 |
| **Mp :** | 3,8609e4 | 3,9129e4 | 3,7983e4 | 3,8493e4 | 2,9167e4 | 3,1040e4 | 3,7731e4 |
| **FI :** | 3,3744e3 | 1,8059e2 | 3,6492e3 | 1,6544e2 | 1,7268e3 | 8,2587e1 | 5,2800e3 |
| **< 842** | 0,00 | 0,00 | 0,00 | 0,00 | 0,00 | 0,00 | 0,00 |
| **w% :** | 100,00 | 100,00 | 100,00 | 100,00 | 100,00 | 100,00 | 100,00 |
| **> 500744** | 0,00 | 0,00 | 0,00 | 0,00 | 0,00 | 0,00 | 0,00 |

**Projekt :** C:\GPC-Daten\2016\Oktober.LDX
**Datum :** Freitag 14.10.16 08:08:30
**Kostenstelle :**
**Zeichen :**



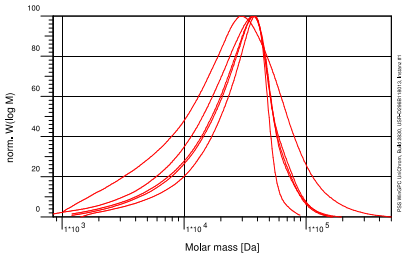


**Kurve 1 :** Vial 61: PEC112a1-N3 - 1
**Kurve 2 :** Vial 63: PEC112a1-SB - 1
**Kurve 3 :** Vial 64: PEC112a1-CB - 1
**Kurve 4 :** Vial 65: PEC112a1-OEG3 - 1
**Kurve 5 :** Vial 66: PEC112a1-OEG2-SB - 1

| | I1: RID 1, RI Signal | I1: RID 1, RI Signal | I1: RID 1, RI Signal | I1: RID 1, RI Signal | I1: RID 1, RI Signal | |
|---|---|---|---|---|---|---|
| **Mn :** | 1,5768e4 | 1,5475e4 | 1,1409e4 | 1,2602e4 | 1,4818e4 | g/mol |
| **Mw :** | 2,7677e4 | 3,1197e4 | 3,5835e4 | 2,8548e4 | 3,0152e4 | g/mol |
| **Mz :** | 3,5769e4 | 4,5761e4 | 8,5316e4 | 4,3850e4 | 4,4017e4 | g/mol |
| **Mv :** | 0,000000 | 0,000000 | 0,000000 | 0,000000 | 0,000000 | g/mol |
| **D :** | 1,7552e0 | 2,0160e0 | 3,1409e0 | 2,2653e0 | 2,0349e0 | |
| **[n]:** | 0,000000 | 0,000000 | 0,000000 | 0,000000 | 0,000000 | ml/g |
| **Vp :** | 8,4785e0 | 8,4948e0 | 8,7622e0 | 8,5015e0 | 8,5020e0 | ml |
| **Mp :** | 3,8609e4 | 3,7983e4 | 2,9167e4 | 3,7731e4 | 3,7712e4 | g/mol |
| **FI :** | 3,3744e3 | 3,6492e3 | 1,7268e3 | 5,2800e3 | 3,3994e3 | ml*V |
| **< 842** | 0,00 | 0,00 | 0,00 | 0,00 | 0,00 | |
| **w% :** | 100,00 | 100,00 | 100,00 | 100,00 | 100,00 | |
| **> 500744** | 0,00 | 0,00 | 0,00 | 0,00 | 0,00 | |

**Projekt :** C:\GPC-Daten\2016\Oktober.LDX
**Datum :** Freitag 14.10.16 08:09:50
**Kostenstelle :**
**Zeichen :**



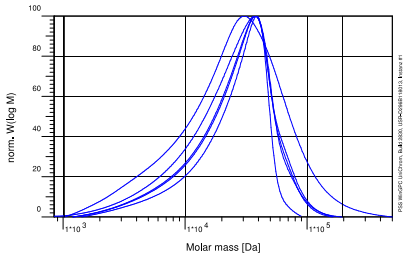


**Kurve 1 :** Vial 61: PEC112a1-N3 - 1
**Kurve 2 :** Vial 63: PEC112a1-SB - 1
**Kurve 3 :** Vial 64: PEC112a1-CB - 1
**Kurve 4 :** Vial 65: PEC112a1-OEG3 - 1
**Kurve 5 :** Vial 66: PEC112a1-OEG2-SB - 1

| | I1: VWD 1, Signal | I1: VWD 1, Signal | I1: VWD 1, Signal | I1: VWD 1, Signal | I1: VWD 1, Signal | |
|---|---|---|---|---|---|---|
| **Mn :** | 1,5566e4 | 1,6466e4 | 1,3663e4 | 1,4294e4 | 1,6087e4 | g/mol |
| **Mw :** | 2,7620e4 | 3,1855e4 | 3,7773e4 | 2,9349e4 | 3,0881e4 | g/mol |
| **Mz :** | 3,5862e4 | 4,6359e4 | 8,4014e4 | 4,4263e4 | 4,4531e4 | g/mol |
| **Mv :** | 0,000000 | 0,000000 | 0,000000 | 0,000000 | 0,000000 | g/mol |
| **D :** | 1,7744e0 | 1,9346e0 | 2,7646e0 | 2,0533e0 | 1,9197e0 | |
| **[n]:** | 0,000000 | 0,000000 | 0,000000 | 0,000000 | 0,000000 | ml/g |
| **Vp :** | 8,4652e0 | 8,4815e0 | 8,6988e0 | 8,4882e0 | 8,4887e0 | ml |
| **Mp :** | 3,9129e4 | 3,8493e4 | 3,1040e4 | 3,8237e4 | 3,8218e4 | g/mol |
| **FI :** | 1,8059e2 | 1,6544e2 | 8,2587e1 | 2,4233e2 | 1,5042e2 | ml*V |
| **< 1022** | 0,00 | 0,00 | 0,00 | 0,10 | 0,00 | |
| **w% :** | 100,00 | 100,00 | 98,74 | 99,90 | 100,00 | |
| **> 195260** | 0,00 | 0,00 | 1,26 | 0,00 | 0,00 | |

**Projekt :** C:\GPC-Daten\2016\Oktober.LDX
**Datum :** Freitag 14.10.16 08:11:42
**Kostenstelle :**
**Zeichen :**

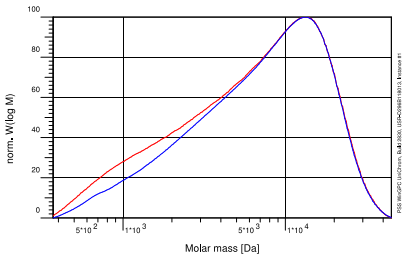


**Sample :** Vial 62: PEC115-CB - 1
**Integration from:** Monday 16.01.17 22:48:54
**Integration to :** Monday 16.01.17 22:53:12
**Calibration File :** GRAM 100A DMAc_LiBr_20160917.CAL
**MHK + A (CaL):** 0,000E+0
**Int.stand.+cal.:** 14,030 ml
**Pump :** PSS SECcurity
**Concentration :** 0,000 g/l
**Column 1 :** PSS GRAM 100A
**Detector 1 :** I1: IsoPump 1, Pressure
**Detector 2 :** I1: RID 1, RI Signal
**Detector 3 :** I1: VWD 1, Signal A
**Operator :** usr

**Eluent :** DMAc + LiBr 0,1
**MHK + K (CaL):** 1,000E+0 ml/g
**Int.stand.+sam.:** 13,950 ml
**Flowrate :** 1,000 ml/min
**Inject volume :** 20,000 ul
**Temperature :** 60,000 °C
**Delay volume :** 0,000 ml
**Delay volume :** 0,170 ml
**Delay volume :** 0,000 ml
**Acquisition interval :** 1,000 sec

8,329 ml
12,642 ml

**I1: RID 1, RI Signal** **I1: VWD 1, Signal A**

| | | | |
|---|---|---|---|
| **Mn :** | 3,2220e3 | 3,8517e3 | g/mol |
| **Mw :** | 9,0016e3 | 9,4702e3 | g/mol |
| **Mz :** | 1,5383e4 | 1,5270e4 | g/mol |
| **Mv :** | 0,000000 | 0,000000 | g/mol |
| **D :** | 2,7938e0 | 2,4587e0 | |
| **[n]:** | 0,000000 | 0,000000 | ml/g |
| **Vp :** | 9,6101e0 | 9,5967e0 | ml |
| **Mp :** | 1,2380e4 | 1,2557e4 | g/mol |
| **A :** | 9,8041e2 | 3,8480e1 | ml*V |
| **< 370** | 0,00 | 0,00 | |
| **w% :** | 100,00 | 100,00 | |
| **> 44952** | 0,00 | 0,00 | |

**Project :** C:\GPC-Daten\2016\December.LDX
**Date :** Friday 20.01.17 09:54:51

**Account :**
**Sign :**

S44

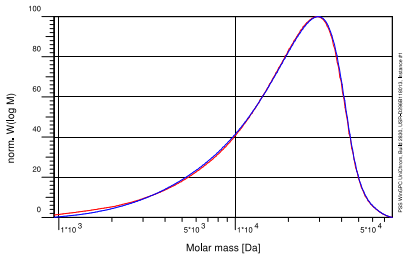


**Sample :** Vial 61: PEC115-SB - 1
**Integration from:** Monday 16.01.17 22:32:02
**Integration to :** Monday 16.01.17 22:36:03
**Calibration File :** GRAM 100A DMAc_LiBr_20160917.CAL
**MHK + A (CaL):** 0,000E+0
**Int.stand.+cal.:** 14,030 ml
**Pump :** PSS SECcurity
**Concentration :** 0,000 g/l
**Column 1 :** PSS GRAM 100A
**Detector 1 :** I1: IsoPump 1, Pressure
**Detector 2 :** I1: RID 1, RI Signal
**Detector 3 :** I1: VWD 1, Signal A
**Operator :** usr

**Eluent :** DMAc + LiBr 0,1
**MHK + K (CaL):** 1,000E+0 ml/g
**Int.stand.+sam.:** 13,950 ml
**Flowrate :** 1,000 ml/min
**Inject volume :** 20,000 ul
**Temperature :** 60,000 °C
**Delay volume :** 0,000 ml
**Delay volume :** 0,170 ml
**Delay volume :** 0,000 ml
**Acquisition interval :** 1,000 sec

7,850 ml
11,878 ml

**I1: RID 1, RI Signal** **I1: VWD 1, Signal A**

| | | | |
|---|---|---|---|
| **Mn :** | 1,1137e4 | 1,1771e4 | g/mol |
| **Mw :** | 2,1265e4 | 2,1444e4 | g/mol |
| **Mz :** | 2,8884e4 | 2,8988e4 | g/mol |
| **Mv :** | 0,000000 | 0,000000 | g/mol |
| **D :** | 1,9094e0 | 1,8218e0 | |
| **[n]:** | 0,000000 | 0,000000 | ml/g |
| **Vp :** | 8,7663e0 | 8,7529e0 | ml |
| **Mp :** | 2,9046e4 | 2,9433e4 | g/mol |
| **A :** | 2,1592e3 | 7,6197e1 | ml*V |
| **< 940** | 0,00 | 0,00 | |
| **w% :** | 100,00 | 100,00 | |
| **> 77640** | 0,00 | 0,00 | |

**Project :** C:\GPC-Daten\2016\December.LDX
**Date :** Friday 20.01.17 09:53:08

**Account :**
**Sign :**

S45

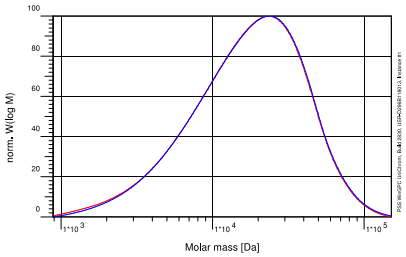


**Sample :** Vial 63: PEC115-OEG3 - 1
**Integration from:** Monday 16.01.17 23:04:26
**Integration to :** Monday 16.01.17 23:08:55
**Calibration File :** GRAM 100A DMAc_LiBr_20160917.CAL
**MHK + A (CaL):** 0,000E+0
**Int.stand.+cal.:** 14,030 ml
**Pump :** PSS SECcurity
**Concentration :** 0,000 g/l
**Column 1 :** PSS GRAM 100A
**Detector 1 :** I1: IsoPump 1, Pressure
**Detector 2 :** I1: RID 1, RI Signal
**Detector 3 :** I1: VWD 1, Signal A
**Operator :** usr

**Eluent :** DMAc + LiBr 0,1
**MHK + K (CaL):** 1,000E+0 ml/g
**Int.stand.+sam.:** 13,950 ml
**Flowrate :** 1,000 ml/min
**Inject volume :** 20,000 ul
**Temperature :** 60,000 °C
**Delay volume :** 0,000 ml
**Delay volume :** 0,170 ml
**Delay volume :** 0,000 ml
**Acquisition interval :** 1,000 sec

7,428 ml
11,931 ml

**I1: RID 1, RI Signal** **I1: VWD 1, Signal A**

| | | | |
|---|---|---|---|
| **Mn :** | 1,0520e4 | 1,1047e4 | g/mol |
| **Mw :** | 2,3132e4 | 2,3399e4 | g/mol |
| **Mz :** | 3,8973e4 | 3,9061e4 | g/mol |
| **Mv :** | 0,000000 | 0,000000 | g/mol |
| **D :** | 2,1990e0 | 2,1180e0 | |
| **[n]:** | 0,000000 | 0,000000 | ml/g |
| **Vp :** | 9,0345e0 | 9,0211e0 | ml |
| **Mp :** | 2,2298e4 | 2,2597e4 | g/mol |
| **A :** | 9,7423e3 | 3,8077e2 | ml*V |
| **< 885** | 0,00 | 0,00 | |
| **w% :** | 100,00 | 100,00 | |
| **> 151466** | 0,00 | 0,00 | |

**Project :** C:\GPC-Daten\2016\December.LDX
**Date :** Friday 20.01.17 09:55:43

**Account :**
**Sign :**

S46

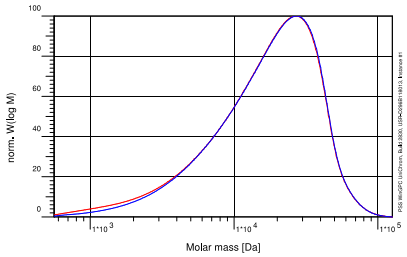


**Sample :** Vial 64: PEC115-OEG2-SB - 1
**Integration from:** Monday 16.01.17 23:20:59
**Integration to :** Monday 16.01.17 23:25:45
**Calibration File :** GRAM 100A DMAc_LiBr_20160917.CAL
**MHK + A (CaL):** 0,000E+0
**Int.stand.+cal.:** 14,030 ml
**Pump :** PSS SECcurity
**Concentration :** 0,000 g/l
**Column 1 :** PSS GRAM 100A
**Detector 1 :** I1: IsoPump 1, Pressure
**Detector 2 :** I1: RID 1, RI Signal
**Detector 3 :** I1: VWD 1, Signal A
**Operator :** usr

**Eluent :** DMAc + LiBr 0,1
**MHK + K (CaL):** 1,000E+0 ml/g
**Int.stand.+sam.:** 13,950 ml
**Flowrate :** 1,000 ml/min
**Inject volume :** 20,000 ul
**Temperature :** 60,000 °C
**Delay volume :** 0,000 ml
**Delay volume :** 0,170 ml
**Delay volume :** 0,000 ml
**Acquisition interval :** 1,000 sec

7,527 ml
12,326 ml

**I1: RID 1, RI Signal** **I1: VWD 1, Signal A**

| | | | |
|---|---|---|---|
| **Mn :** | 9,3301e3 | 1,0280e4 | g/mol |
| **Mw :** | 2,1167e4 | 2,1526e4 | g/mol |
| **Mz :** | 3,1766e4 | 3,1856e4 | g/mol |
| **Mv :** | 0,000000 | 0,000000 | g/mol |
| **D :** | 2,2686e0 | 2,0939e0 | |
| **[n]:** | 0,000000 | 0,000000 | ml/g |
| **Vp :** | 8,8568e0 | 8,8434e0 | ml |
| **Mp :** | 2,6576e4 | 2,6928e4 | g/mol |
| **A :** | 1,8358e4 | 6,1959e2 | ml*V |
| **< 560** | 0,00 | 0,00 | |
| **w% :** | 100,00 | 100,00 | |
| **> 126282** | 0,00 | 0,00 | |

**Project :** C:\GPC-Daten\2016\December.LDX
**Date :** Friday 20.01.17 09:56:12

**Account :**
**Sign :**

S47

# Diffusion Barrier Hydrogel Wound Dressings

## NMR Spectra

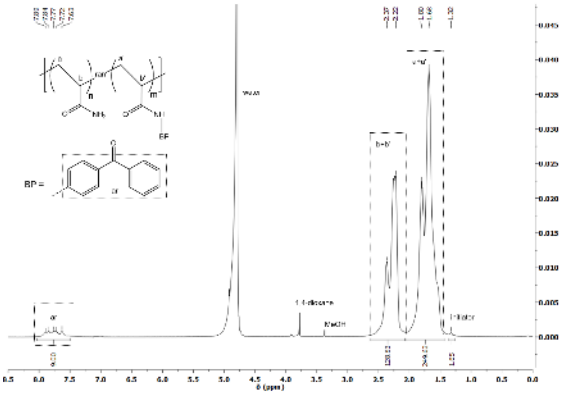

Figure S. $^{1}$H NMR spectrum of poly(Am$_{99}$-*co*-BPAm$_{1}$), recorded in $D_2$0.

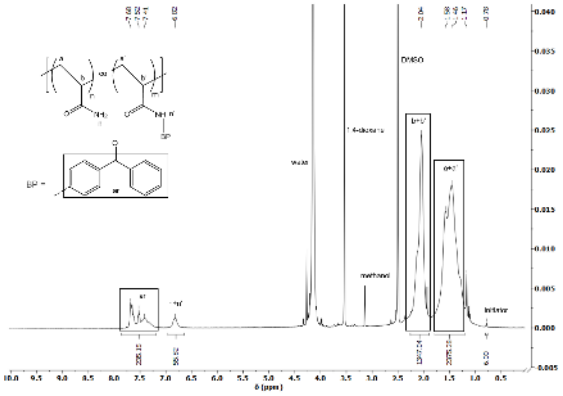

Figure S1. $^{1}$H NMR spectrum of poly(Am$_{98.5}$-*co*-BPAm$_{1.5}$), recorded in DMSO-d6.

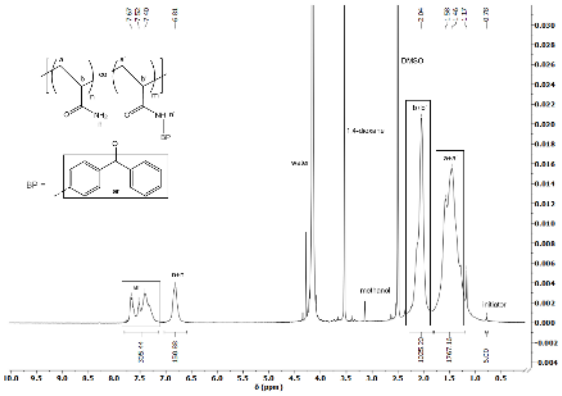

Figure S2. $^{1}$H NMR spectrum of poly(Am$_{98}$-*co*-BPAm$_{2}$), recorded in DMSO-d6.

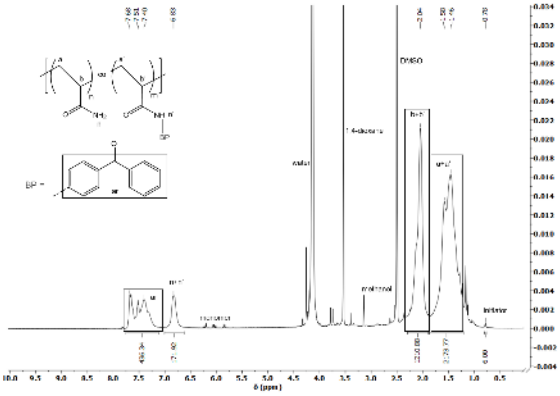

Figure S3. $^{1}$H NMR spectrum of poly(Am$_{97.5}$-*co*-BPAm$_{2.5}$), recorded in DMSO-d6.

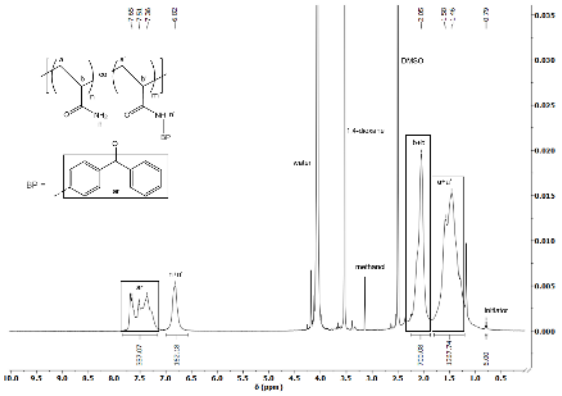

Figure S4. $^{1}$H NMR spectrum of poly(Am$_{97}$-*co*-BPAm$_{3}$), recorded in DMSO-d6.

## Anhang

### Explanation of the Invention Fabric-Supported Hydrogel Membranes for Wound Dressings with A Polymer Foil Drug Reservoir

**Field of the invention**

The present invention relates to a wound dressing consisting of a drug reservoir, a fabric-supported hydrogel membrane with or without addition of silica and/or silicone particles as reinforcement materials, a perforated medical polymer foil as the foundation, and optionally a layer of medical fabric in contact with the skin. The refillable drug depot from polymer foil stores an active substance in form of an aqueous medical solution, which is supplied to a chronic wound through the pores of the hydrogel membrane with a hydrogel-controlled release rate. The fabric-reinforced hydrogel membrane ensures moderate delivery of a drug acting as a barrier between the depot and the wound.

**Fabrication strategies**

There are several possibilities for fabrication of the hydrogel-based composite wound dressing. **Figures 1-3** schematically illustrate step by step possible fabrication strategies. According to the first approach (**Fig.1**), circular samples are precision-cut from a polymer foil (step 1-I.), establishing a foundational substrate. Following this, holes are punctured in the central region of the polymer substrate disks (step 1-II.). Then, the punctured polymer substrates undergo corona discharge treatment (step 1-III.) to enhance surface energy of the polymer, ensuring improved adhesion of subsequent layers of the wound dressing. The process continues with the application of a polymer mesh (e.g., poly(ethylene terephthalate) - PET) for mechanical reinforcement of the hydrogel film and the deposition of a hydrogel precursor polymer solution (step 1-IV.). Then the polymer solution is dried at 40 °C and exposed to UV-light to induce photocrosslinking (step 1-V.), ensuring attachment of the hydrogel polymer both to the polymer mesh and the polymer foil while simultaneously creating a polymeric network. Additional layers of hydrogel polymer are prepared via addition of more polymer solution on top of the crosslinked layer, with sequential drying and photocrosslinking processes conducted twice (step 1-VI.). The next step involves bonding of a second polymer foil at the outer rim to the base foil through gluing or welding processes (step 1-VII.), forming the back wall and resulting in an enclosure around the crosslinked membrane structure. This step introduces the drug reservoir character to the composite





structure. The final step during application of the construct in a medical context is the injection of an aqueous solution containing active drugs, like insulin (step 1-VIII.), which swells the crosslinked polymer network to a permeable hydrogel layer that allows diffusion of aqueous media and pharmaceutically active components through this layer. This procedure concludes the development of a polymer-based drug delivery system that offers controlled and targeted release of therapeutic agents.

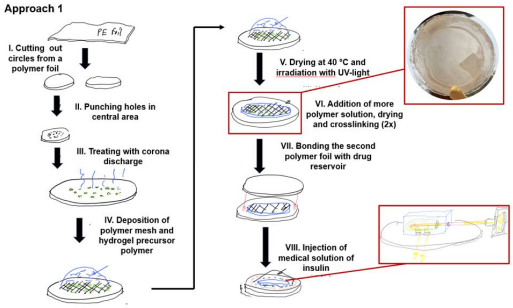


**Fig. 1.** Fabrication process of the hydrogel-based composite wound dressing (approach 1).

The second strategy (**Fig.2**) involves the following steps: firstly, holes punched into a large piece of polymer foil (step 2-I.), exemplified by polyethylene (PE). Subsequently, the polymer foil undergoes corona discharge treatment (step 2-II.) to enhance surface properties and adhesion. Following this, a circular polymer mesh (e.g., PET) saturated with a polymer solution is carefully added to the treated substrate (step 2-III.). The composite structure undergoes a drying process at 40 °C (step 2-IV.). The subsequent step involves irradiation with UV-light to induce photocrosslinking of the hydrogel precursor polymer (step 2-V.). The process is further advanced by the addition of more polymer solution, followed by the repetition of drying at 40 °C and UV-light irradiation (step 2-VI. by repetition of steps 2-IV. and 2-V.) to obtain three layers of hydrogel polymer. Finally, the hydrogel-based membrane is cut out (step 2-VII.). This approach allows simultaneous fabrication of several membranes on the polymer foil substrate, to which a back wall to form the drug





reservoir can be attached through gluing or welding processes, as illustrated above in **Fig. 1**, step 1-VII.

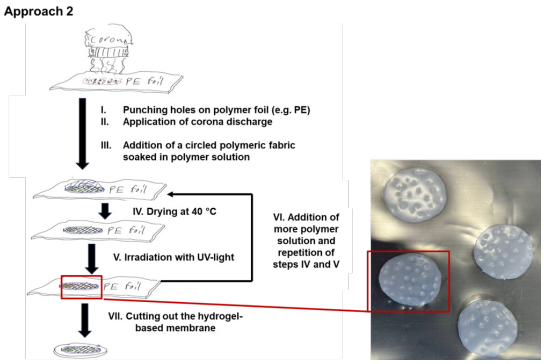


**Fig. 2.** Fabrication process of the hydrogel-based composite wound dressing (approach 2).

Another strategy (**Fig.3**) as modification of approach 2 involves the following steps: holes are precisely punched into a polymer foil (step 3-I.). Then the polymer foil undergoes corona discharge treatment (step 3-II.). Following these preparatory steps, the hydrogel-based composite membrane, prepared according to a specified procedure described in the chapter **„Preparation of fabric-supported hydrogel membrane"**, is carefully placed onto the polymer foil (step 3-III.). A polymer solution is then added onto the sandwich assembly and dried to eventually attach the membrane to the polymer foil via photocrosslinking. For this bonding step the composite structure is subjected to a drying process at 40 °C and irradiation with UV-light. The final step involves precise cutting of the hydrogel-based membrane out of the flat substrate foil. This approach also allows simultaneous fabrication of several membranes on the same polymer foil substrate, to which the backing foils for drug reservoir formation can be attached through gluing or welding processes.





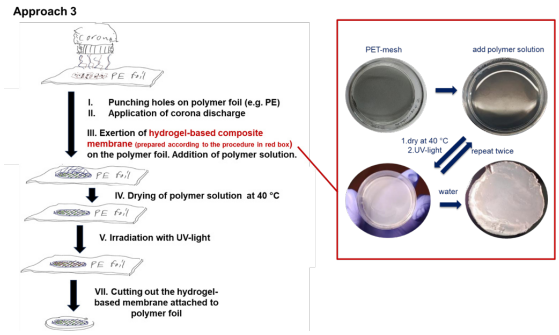


**Fig. 3**. Fabrication process of the hydrogel-based composite wound dressing (approach 3).

**Motivation**

Healing of chronic wounds or ulcers is significantly slower and complex compared to acute wounds since they do not follow a regular wound recovery course.[1]

Chronic wounds caused by diabetes are a specialized field of research due to the specific considerations that must be taken in account for this unique case.[1,2] One main complication in diabetes is the so-called "diabetic foot ulcer (DFU)" which can be defined as a chronic, non-healing wound at the patient's feet that may lead to high hospital costs, limitations in mobility, and in extreme cases to amputation of limbs or even to death of the patients.[1]

Conventional methods of DFUs therapy include debridement, fighting infection, off-loading the area of high pressure at the feet and application of wound dressings.[3] The choice of the dressing depends e.g. on the wound type,[4] on the costs, wound exudates control, and other factors.[5] Often dressings contain certain active substances to improve the healing process.[6] For instance, autologous human keratinocytes,[7] iodine complex - hyiodine,[8] silver particles,[9] phenytoin,[10] ciprofloxacin,[11] *aloe vera extract*,[12] and other substances[6] are typically suggested for this purpose.

According to some studies,[11,13–16] there is a promising potential of insulin being used as an active substance for the topic treatment of diabetic wounds, because the hormone plays a significant role in the wound healing process,[11,13–16] and it is cheaper and easier available than other growth factors.[13] Topical application of insulin stimulates processes that promote wound healing such as keratinocyte migration, fibroblastic reaction, collagen deposition, formation of new blood vessels in healing tissues.[11,13–16] It also regulates re-epithelialization and inflammatory responses and, in contrast to the systemic insulin treatment, topical application of insulin does not influence blood glucose levels in the body. However, topical insulin treatment is not a standardized procedure in DFU treatments, and it is only rarely used as local injections, cream, spray, dressings.[11,13–16]

Hydrogels are very promising materials for wound dressing applications, since they provide moist environment, can be loaded with bioactive components, and maintain substantial drug release, some are oxygen and nutrients permeable, non-toxic, biocompatible, and biodegradable, and do not cause immune response of the organism.[2,6]

Up to now, there already exist medicated dressings that contain drugs and other active components, such as bioactive substances that stimulate natural tissue growth,[17,18] antimicrobial agents,[6,9] pain relievers, or natural extracts.[12,19] Nevertheless, none of these examples is yet widely and universally used due to the high cost and difficulties in the control of drug release. Therefore, the necessity of an effective and affordable hydrogel wound dressing that would allow constant supply of an active component to the wound is at present still an open issue.

**Summary of the invention**

The embodiment of the wound dressing comprises a refillable medical polymer-based drug reservoir, a fabric-supported hydrogel membrane with or without incorporated silica or silicone particles, a perforated medical polymer foil (e.g., PE, PP, PET) as substrate, and a layer of a medical fabric (e.g., PET) in contact with the skin. The drug depot allows storage and thus constant availability of an active substance and its supply to a chronic wound. The polymer foil (e.g., PE, PP, PET) used for the drug reservoir is airtight and waterproof which prevents leakage and contamination of the active substance solution contained inside. The repeated addition of the active substance through an appropriated port structure in the





reservoir ensures reduced frequency of dressing changes, thus decreasing the threat for infection as well as reduction of the discomfort and pain endured by a patient.

The fabric-supported hydrogel membrane has all the advantages of hydrogel materials combined with improved mechanical stability due to covalent attachment to a polymer mesh (e.g., PET). The membrane consists of a biocompatible hydrogel with adapted porosity for moderate release of an active substance from the drug depot through the hydrogel pores to the wound. Additional reinforcement of the hydrogel-based membrane with a polymer mesh allows easier handling of the membrane in terms of workability, transporting and attachment to other parts of the wound dressing. Since pores of any fabric are clearly larger than hydrogel pores, its presence within the membrane does not impede drug diffusion through the hydrogel. It is also possible to additionally increase mechanical stability and handling of the hydrogels via incorporation of benzophenone-silane (BPTES)-modified silica or silicone particles. Moreover, the fabric-reinforced hydrogel membrane is affixed to a medical-grade perforated polymer foil (e.g., PE, PP, PET) substrate (Fig. 1-3), serving as the structural basis for the wound dressing. This configuration enhances the mechanical stability and shear stress resistance of the overall composite wound dressing design.

A vide range of polymeric materials can be used to form hydrogel layers on the surface of a polymer mesh (e.g., PET) ensuring coverage of the fabric-pores. For example, polymers based on acrylamide and its derivatives such as *N*-(2-hydroxyethyl)acrylamide (HEAm) are well-known as highly hydrophilic, biocompatible, anti-fouling materials which are commercially available and can be easily copolymerized with benzophenone derivatives via free radical polymerisation. HEAm-based polymers are also used as carrier materials for the transport of bioactive substances or the use in self-healing materials. Other classes of polymers, such as poly(2-alkyl-2-oxazoline)s synthesised via cationic ring opening polymerization, are also suitable for applications in wound dressings due to their high hydrophilicity, anti-fouling properties and high biocompatibility. Poly(2-alkyl-2-oxazoline)s can also be easily modified, which allows high tunability of their properties according to specific applications. As well as for polyacrylamides, poly(2-alkyl-2-oxazoline) copolymers can be synthesized with benzophenone-containing side groups, which allow formation of polymeric networks upon photocrosslinking. Photocrosslinking enables control over crosslink density by varying intensity, duration, and wavelength of the applied irradiation. Copolymers that contain benzophenone groups in their structure can be covalently attached to polymer-meshes (e.g., PET) thus forming a coherent membrane that possesses the





combined properties of hydrogels (e.g., high water uptake and storage, high porosity, softness, and flexibility, non-inflammatory, and bio-compatibility) and the mechanical stability and integrity of a fabric. The possibility of inclusion of BPTES-modified silica or silicone particles can further improve mechanical stability of hydrogels without affecting the primary functions of the hydrogels. The benzophenone groups attached to the surface of the particles ensure covalent binding of the particles to the polymer.

The utilization of perforated medical-grade polymer foil (e.g., PE, PP, PET) as the substrate material guarantees controlled drug release into the wound without leakage of the liquid from the drug reservoir, concurrently conferring mechanical stability and resistance to shear stress upon the composite wound dressing.

The medical fabric which is in contact with the skin allows the release of the active substance into the wound since its mesh-size is substantially larger than the pores of the hydrogels. It may be furnished with antibacterial properties, and it is anti-adhesive and thus can be in direct contact with the wound surface without sticking to the wound. This allows a painless dressing change avoiding scarring. The medical fabric can consist of PET or polyamide, for example, which are already commercially available and approved for medical purposes (wound care).

The wound dressing can be sterilized and is stored in the dry state separately from an active component solution, which positively affects the shelf-life of both – the wound dressing and the drug. The solution of an active component should be added to the drug depot right before application to the wound, upon which the aqueous medium swells the photocrosslinked polymer network to form the permeable hydrogel just upon dressing application. This handling procedure makes the whole setup easy to transport, store and distribute without restriction to a certain medication or drug types. Since the hydrogels which are suitable for the membrane application typically do not interact with medical substances, e.g., insulin as the present example, the use of the wound dressing can be extended to aqueous solutions of many different active components.

**Novelty of the invention**

Hydrogel-based wound dressings have advantages over traditional wound dressings due to diversity of their properties. Besides providing moist environment, protecting the wound from





external contaminations and injury, hydrogel wound dressings can also supply active components to the wound that can promote the natural healing process and reduce the possibility of infection and inflammation.[2,6] Currently, there is a variety of medicated dressings available that contain drugs and other bioactive substances such as growth factors to stimulate natural tissue growth,[17,18] silver particles[9] or ionic silver as antimicrobial agents,[6] pain relievers, antibiotics, patient's own stem cells,[6] or natural extracts.[9,12] Thus, drug-loaded hydrogel wound dressings can address several problems simultaneously, such as generating an environment stimulating the healing process and deliver further medication. However, due to the restricted volume of the hydrogel body in the wound dressing the total amount of active components that can be embedded and released are limited and require a change of dressing if the drug reservoir is depleted.

The current invention presents a wound dressing with a liquid reservoir, which can be refilled multiple times during application, and that offers a prolongated release of an active substance without requiring a voluminous layer of hydrogel material. Since the drug depot stores an active substance solution, the main function of the hydrogel is to act as a barrier between the drug reservoir and the wound. Because the hydrogel membrane is mechanically reinforced with a medical polymer fabric, the amount of hydrogel polymer can be reduced to the minimal quantity required to sufficiently cover and close the pores of the polymer-mesh. This overall strategy significantly reduces the amount of hydrogel material needed and improves the mechanical properties of the hydrogel, making the membrane easy to handle, transport and attach to other parts of the wound dressing. Additional improvement of the mechanical stability of the hydrogels can be achieved by incorporation of surface-modified silica or silicone particles. The presence of covalently bound particles within the hydrogel offers substantial increase of robustness and facilitates handling of the hydrogel-based membrane without affecting its primary functions. The hydrogel-based membrane is attached to a medical-grade polymer foil, which additionally enhances the mechanical stability of the wound dressing. The non-fouling properties of chosen hydrogel precursor polymers make the membrane suitable for a diverse range of bioactive substances since the hydrogel precursor polymers do not interfere with polypeptide-compounds such as insulin. Therefore, the wound dressing can potentially be used for delivery of many active substances that exist in the form of an aqueous solution.

A brief comparison with some patents in given in **Table 3**.

**Examples**

**Polymer synthesis**

For polymer synthesis *N*-(2-hydroxyethyl)acrylamide (HEAm, 97%, stabilized with hydroquinone monomethyl ether, Aldrich Chemistry) was used without further purification. 2-methyl-2-oxazoline (MeOx, 98%, Sigma-Aldrich), 2-ethyl-2-oxazoline (EtOx, 99%, Alfa Aesar), methyltrifluormethansulfonat (MeOTf, 97%, Alfa Aesar), acetonitrile (MeCN, ≥ 99.9%, Chemsolute) were distilled prior use. 2-[3-(4-benzoylphenoxy)propyl]-2-oxazoline (BPOx) and *N*-(4-benzoylphenyl) acrylamide (BPAm) were synthesized according to the literature.[20]

2,2`-Azobis(2-methylpropionitrile) (AIBN, 98%, Fluka Analytical, Germany), methanol (technical grade, ≥ 98.5%, VWR) and ethanol (≥ 99.8%, Carl Roth) were used without purification.

**Copolymer CP1: poly(HEAm$_{99}$-*co*-BPAm$_{1}$)**

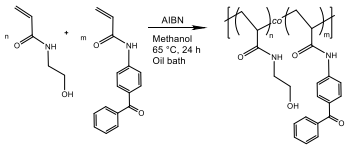


**Scheme 1.** Free radical copolymerization of HEAm with BPAm in MeOH.

HEAm (500 mg, 4.34 mmol), BPAm (11.02 mg,40 µmol) and AIBN (3.57 mg, 21.7 µmol) were dissolved in 8 ml of methanol, and the reaction mixture was purged with argon for 30 min (**Scheme 1**). The reaction was carried out at 65 °C (oil bath) for 24 h and quenched by cooling with liquid nitrogen and exposure to air. The polymer was precipitated twice in 600 ml of ice-cold ethyl acetate, dissolved in water and isolated by lyophilization.

$^{1}$H-NMR (MeOH-d4, 500 MHz, $\delta$ / ppm): 7.77-7.52 (Ar-H), 5.33 (-OH), 3.62 ($CH_2$-OH), 3.10 ($CH_2$-N), 2.02 ($CH_2$-CO-backbone), 1.57 ($CH_2$-backbone).

GPC (DMAc+1 g/L LiBr): $\bar{M}n$ = 38 kDa, $\bar{M}p$ = 150 kDa, $Đ$ = 4.21





**Copolymer CP2 and CP3: poly(EtOx$_{98.5}$-*co*-BPOx$_{1.5}$) and poly(MeOx$_{98.5}$-*co*-BPOx$_{1.5}$)**

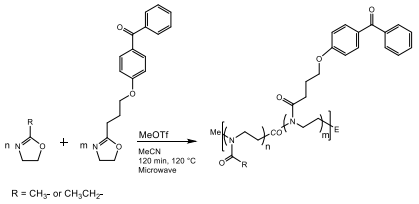


**Scheme 2.** Cationic ring opening polymerization (CROP) of 2-alkyl-2-oxazolines in MeCN.

For the microwave-assisted cationic ring-opening polymerization (CROP) of the respective 2-alkyl-2-oxazolines (**Scheme 2**), the respective monomer (MeOx or EtOx), MeOTf and BPOx were placed under inert gas conditions (glovebox) in a microwave reaction vessel and dissolved in MeCN. Polymerization was performed in a microwave reactor (reactions conditions are shown in **Table 1**). Polymerization was quenched with MeOH (0.2 ml) and the reaction mixture was stirred for 16 h at room temperature. The polymers were purified by 2-fold precipitation in ice-cold diethyl ether (600 ml) and isolated by lyophilization from water.

**Table 1.** Reaction conditions of copolymerization of 2-alkyl-2-oxazolines.

| Polymer | Monomer mg/mmol | BPOx mg/µmol | MeOTf mg/µmol | MeCN ml | Microwave conditions |
|---|---|---|---|---|---|
| poly(EtOx$_{98.5}$-*co*-BPOx$_{1.5}$) | 500/5.04 | 23.4/76 | 2.71/16.5 | 1.75 | 120 °C ramp 2:00 120 min |
| poly(MeOx$_{98.5}$-*co*-BPOx$_{1.5}$) | 500 /5.87 | 27.3/88 | 2.16/19.2 | | |

**Poly(MeOx$_n$-*co*-BPOx$_m$):**

1H-NMR ($CDCl_3$, 500 MHz, δ / ppm): 7.73-6.94 (Ar-H), 4.06 ($CH_2$-O), 3.44 ($CH_2$-backbone), 2.13-2.10 ($CH_2$-CO/$CH_3$-CO)

GPC (DMAc+1 g/L LiBr): $\bar{M}n$ = 41 kDa, $\bar{M}p$ = 55 kDa, $Đ$ = 1.36





**Poly(EtOx$_n$-*co*-BPOx$_m$):**

1H-NMR ($CDCl_3$, 500 MHz, δ / ppm): 7.70-6.93 (Ar-H), 4.12 ($CH_2$-O), 3.44 ($CH_2$-backbone), 2.40-2.30 ($CH_2$-CO), 1.12 (-$CH_3$)

GPC (DMAc+1 g/L LiBr): $\bar{M}n$ = 31 kDa, $\bar{M}p$ = 42 kDa, $Đ$ = 1.35

**Synthesis of silicone particles:**

**Procedure[22]:**

Siloxane-based PDMS-particles were prepared by the hydrolysis and condensation of the silicon precursors tetraethyl orthosilicate (TEOS) and dimethydiethoxylsilane (DMDES) using a modified Stöber process. A co-solvent containing ethanol (23 ml) and distilled water (1.5 ml) was added to a round-bottom flask. Then, 1 ml of monomers of various molar ratios of DMDES to TEOS was added to the solution. A 25% $NH_4OH$ solution was slowly added dropwise to the aqueous dispersion and stirred for 16 h at room temperature or at 60 °C Exact combinations of reagents and workup procedures are presented in **Table 2**.

The particles were collected by centrifugation at 8,000 rpm for 10 min or by dialysis against ethanol. The precipitates were redispersed in distilled water and ethanol for washing and then centrifuged to collect the particles. The washing procedures were repeated three times.

**Table 2.** Composition of reaction mixtures for synthesis of siloxane-based PDMS-particles.

| Sample | DMDES:TEOS mol% ratio | DMDES mg (mmol) | TEOS mg (mmol) | 25% $NH_4OH$ ml | Comment |
|---|---|---|---|---|---|
| 1 | 80:20 | 670 (4.5) | 240 (1.1) | 3.4 | r.t. (centrifuged) |
| 2 | | | | | 60 °C (dialyzed) |
| 3 | 60:40 | 500 (3.4) | 470 (2.3) | 3.4 | r.t. (centrifuged) |

**Synthesis of silica particles:**

**Procedure[23]:**

Silica-particles were prepared by the hydrolysis and condensation of the silicon precursor tetraethyl orthosilicate (TEOS) using a modified Stöber process. A round-bottom flask was charged with a combination of aqueous ammonia (32%, 10 ml) and absolute ethanol





(125 ml), heated up to 40°C, followed by the addition of 5 ml TEOS solution in 20 ml of absolute ethanol (pre-heated at 40 °C). The mixture was stirred at 700 rpm overnight at 40 °C and became slightly turbid. The particles were collected by centrifugation at 8,000 rpm for 10 min. The precipitates were redispersed in distilled water and ethanol for washing and then centrifuged to collect the particles. The washing procedures were repeated three times.

Both silica and silicone particles were analysed by scanning electron microscopy and dynamic light scattering techniques. The size of the particles varies from 100 nm up to 400 nm depending on specific reaction conditions.

**Modification of the surface of silica-particles with BPTES:**

For surface modification of silica-particles with appropriate photocrosslinking groups, a corresponding amount of BPTES solution in ethanol (0.1 mol/L) was added to a dispersion of $SiO_2$-particles in absolute ethanol (to ensure dilution factor of 100 for BPTES-solution). Then the particles were dispersed via ultrasonification (5 min). The dispersion was stirred overnight in the darkness with the rotation speed of 700 rpm. After incubation in the BPTES-solution, the particles were purified by 5x centrifugation with solvent exchange (from absolute ethanol to water). Then the purified BPTES-modified $SiO_2$-particles were redispersed in a corresponding amount of water (ultrasonification for 5 mins). In the next step, an aqueous solution of a corresponding polymer (20 mg/ml) was prepared. Then polymer solution was combined with dispersion of BPTES-modified $SiO_2$-particles in water and the mixture was stirred overnight (moderate stirring). The membranes were prepared by the standard procedure (see below).

## Preparation of fabric-supported hydrogel membrane:

1. Cutting out a circular sample from a polymer-mesh (further PET-mesh) with diameter ~ 3 cm.
2. Weighing the plain sample (circled PET-mesh).
3. Cleaning of the sample with ethanol to remove organic contaminants.
4. Insertion of the sample into a Petri dish (prior washed with ethanol) with excess amount of ethanol or water to pre-wet the PET-mesh in the respective solvent.
5. Dissolving 60 or 90 mg of polymer in 3 or 4.5 ml of ethanol or water.

6. Removal of the solvent and the PET-mesh from the Petri dish.
7. Addition of 1.5 ml of polymer solution to the Petri dish.
8. Insertion of the PET-mesh into the polymer solution.
9. Placement of the Petri dish on a heating plate and drying the polymer solution at 40 °C.
10. Crosslinking the polymer on the PET mesh at 365 nm under nitrogen stream for 60 min.
11. After crosslinking the first polymer layer, repeat steps 7-10 once or two more times for 2 or 3 polymer layers, respectively. Flipping of the mesh is necessary before drying the second layer of the polymer.
12. After crosslinking the last polymer layer, addition of excess amount of water to the Petri dish to swell the hydrogel.
13. Removal of excess amount of water and letting the sample to dry at room temperature (**Fig. 4**).
14. Weighing the ready sample.

In case of membranes with BPTES-modified $SiO_2$-particles inclusion (**Fig. 5**), the modified particles were dispersed in the polymer solution and the preparation of a fabric-supported hydrogel membrane was performed according to the above-mentioned procedure.

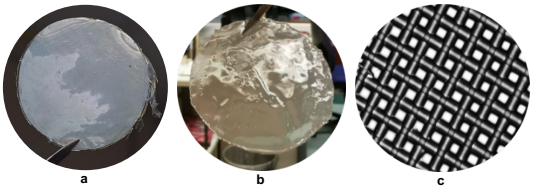


**Fig. 4.** Example of a fabric-supported hydrogel (poly(MeOx$_{98.5}$-*co*-BPOx$_{1.5}$) membrane in **a:** collapsed (dried at r.t.) and **b:** swollen states of the hydrogel, **c:** optical microscope image of the membrane, 5x magnification.





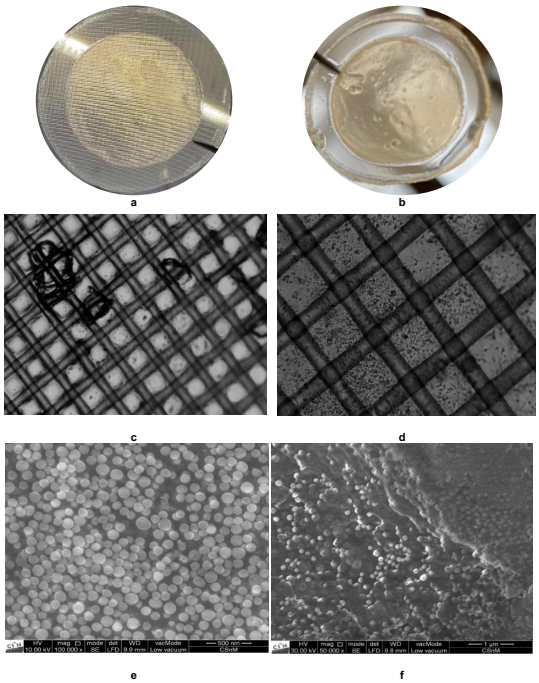


**Fig. 5.** Example of a fabric-supported hydrogel (poly(EtOx$_{98.5}$-*co*-BPOx$_{1.5}$)) membrane with inclusion of BPTES-modified silica particles (18 wt%), **a:** collapsed (dried at r.t.) and **b:** swollen states of hydrogel, optical microscope images of the membrane **c:** 5x and **d:** 10x magnification, SEM images of the membrane **e** and **f.**





### Water permeability test:

To test the ability of the fabric-reinforced hydrogel membrane to significantly hinder water flow, thereby ensuring controlled slow delivery of a drug to the wound, a water permeability test was designed (**Fig. 6**). For this, the membrane was placed on a tube-shaped glass adapter with spherically ground joint (part 1, **Fig. 6**), fixed with a rubber ring, then the second glass piece with a larger diameter was applied on the other side (bottom part 2 in **Fig. 6**). The whole setup was fixed with a metal clamp. Then water was added dropwise to the membrane. A satisfactory result means that the membrane can restrain the water flow providing very slow permeability of the water through the pores of the hydrogel.

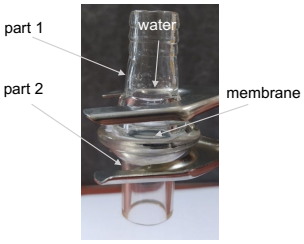


**Fig. 6.** Design of the water permeability test.

### Insulin diffusion test:

To test the ability of insulin to defuse through the pores of the hydrogel membrane, an insulin diffusion test was developed. For that, the membrane was placed in between two glass parts with plastic tubes at their ends (**Fig. 7, a**). A rubber ring was used as a fixator between the glass parts and the membrane. The two glass parts were fixed together with a metal bracket. To ensure equal pressure from both sides of the setup, it was placed horizontally. On one side of the setup (side A) 10 ml of insulin solution in the appropriate buffer, prepared according to the literature,[21] was added. The other side (side B) contained buffer of the same composition except insulin. After 24 h a UV-VIS measurements were performed to





observe if insulin was able to defuse through the membrane from side A to side B (**Fig. 7, b**).

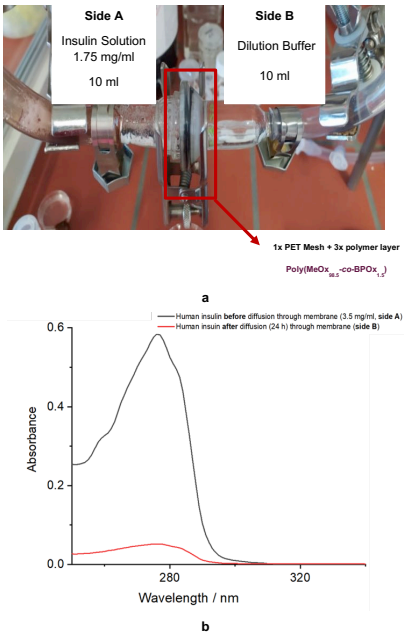


**Fig. 7. a:** Setup of the insulin diffusion test; **b:** UV-VIS spectra of insulin before and after diffusion through the hydrogel-based membrane.

**Table 3.** Patent search

| Patent | Main idea | Link | Comment |
|---|---|---|---|
| Dressing device US10667956B2 | "The invention relates to a transparent, absorbent device for the dressing of wounds and insertion sites of percutaneous and drug delivery devices. In particular, the device provides 360 degree or complete circumferential protection of a wound or insertion site of a percutaneous or drug delivery device and comprises a hydrogel center and an absorbent material surrounding the hydrogel center." | https://patents.google.com/patent/US10667956B2/en?q=drug+delivery+wound+dressing&oq=drug+delivery+wound+dressings+ | Visually the device has similarities to the current invention but **does not have a drug reservoir** – it has a possibility to insert a percutaneous or a drug delivery device through the insertion site of a percutaneous medical device. Thus, the **device does not store a drug** that is further released through the hydrogel centre. Used polymers do not match polymers used in the current invention |
| Apertured hydrogel compositions and wound dressings EP3145556B1 | "The present invention provides a method of forming a composition comprising: providing a layer of water-swellable hydrogel, wherein the hydrogel has embedded therein a reinforcement sheet of liquid water-permeable material, the layer of hydrogel having a wound-facing side and a non-wound-facing side;" | https://patents.google.com/patent/EP3145556B1/en | The **only similarity** to the present invention is the **reinforcement of the hydrogel layer with a reinforcement sheet of liquid-water-permeable material embedded in the hydrogel** Used polymers do not match polymers used in the current invention |
| Flexible hydrogel wound dressings WO2015059501A1 | «There is provided a wound dressing comprising a backing layer having disposed thereon a discontinuous layer of hydrogel, wherein the discontinuous layer of hydrogel is in the form of discrete islands of hydrogel on the backing layer. The backing layer is preferably a non-hydrogel-containing layer. The backing layer acts to support the discrete islands of hydrogel, so that they can remain in an array when, for example, placed on a wound. The backing layer is preferably a flexible material, such that it can conform around the contours of a human body.» | https://patents.google.com/patent/WO2015059501A1/en | The wound dressing is supported by fabric material, but the setup and arrangement does not match the current invention. Most of used polymers do not match polymers used in the current invention, only match – HEAm-based polymers. |
| Hydrogel composites and wound dressings US20110135726A1 | " The present invention provides an absorbent hydrogel composite for use in the manufacture of an article for application to a fluid-emitting surface, e.g. a wound, the composite having a laminar structure comprising first and second layers, the first layer being a surface contacting layer comprising a porous net structure having a surface contacting face and an outwardly directed face, the second layer | https://patents.google.com/patent/US20110135726A1/en?q=hydrogels+wound+dressings&oq=hydrogels+for+wound+dressings+ | The similarity with the current invention is mainly in the fact that the hydrogel layer in their dressing **may optionally be associated with a reinforcing fabric sheet, which may suitably be embedded in (integral with) the hydrogel.** |





| | | | |
|---|---|---|---|
| | comprising a low-crosslinked absorbent hydrogel disposed over the outwardly directed face of the first layer and arranged so that in use it is in fluid flow communication with the surface through apertures of the net structure. **The absorbent hydrogel may optionally be associated with a reinforcing sheet, for example a reinforcing fabric, which may suitably be embedded in (integral with) the hydrogel."** | | Used polymers do not match polymers used in the current invention. |
| Dressing set WO1996034633A1 | A dressing set comprising a **non-occlusive backing**, which optionally has at least one adhesive side, **a reservoir** in area is smaller than or at most equal to the backing and comprises one or more layers and **at least one pharmaceutically active compound**, and optionally one or more peel strips, release papers or similar arrangement protecting the reservoir and/or the optional adhesive side of said backing characterized in, that a) a foil having an area being larger than or at least equal to the area of the reservoir, is located between the reservoir and the backing b) the foil consists of at least one hydrophilic or hydrophilized polymer, c) the foil in a dry, moisture free state is substantially occlusive, and d) the foil after moisture absorption is substantially non-occlusive. | https://patents.google.com/patent/WO1996034633A1/en?q=wound+dressings+drug+reservoir&oq=wound+dressings+with+drug+reservoirs+ | The device consists essentially of a drug reservoir, hydrogel layer and a backing layer where hydrogel is in between the reservoir and the backing. **However, the reservoir is made of a compress, swab, or matrix, not a depot. Th hydrogel layer is not reinforced with a fabric.** Most of used polymers do not match polymers used in the current invention, only match – AAm-based polymers. |
| | | | |

**References:**


(1) Shah, S. A.; Sohail, M.; Khan, S.; Minhas, M. U.; de Matas, M.; Sikstone, V.; Hussain, Z.; Abbasi, M.; Kousar, M. Biopolymer-Based Biomaterials for Accelerated Diabetic Wound Healing: A Critical Review. *Int. J. Biol. Macromol.* **2019**, *139*, 975–993. https://doi.org/10.1016/j.ijbiomac.2019.08.007.

(2) Gianino, E.; Miller, C.; Gilmore, J. Smart Wound Dressings for Diabetic Chronic Wounds. *Bioengineering* **2018**, *5* (3), 51. https://doi.org/10.3390/bioengineering5030051.

(3) Sabolinski, M. L.; Capotorto, J. V. Comparative Effectiveness of a Human Fibroblast-Derived Dermal Substitute and a Viable Cryopreserved Placental Membrane for the Treatment of Diabetic Foot Ulcers. *J. Comp. Eff. Res.* **2019**, *8* (14), 1229–1238. https://doi.org/10.2217/cer-2019-0001.







(4) Wagner, F. W. The Dysvascular Foot: A System for Diagnosis and Treatment. *Foot Ankle* **1981**, *2* (2), 64–122. https://doi.org/10.1177/107110078100200202.

(5) Lavery, L. A.; Davis, K. E.; Berriman, S. J.; Braun, L.; Nichols, A.; Kim, P. J.; Margolis, D.; Peters, E. J.; Attinger, C. WHS Guidelines Update: Diabetic Foot Ulcer Treatment Guidelines: DFU Guidelines. *Wound Repair Regen.* **2016**, *24* (1), 112–126. https://doi.org/10.1111/wrr.12391.

(6) Moura, L. I. F.; Dias, A. M. A.; Carvalho, E.; de Sousa, H. C. Recent Advances on the Development of Wound Dressings for Diabetic Foot Ulcer Treatment—A Review. *Acta Biomater.* **2013**, *9* (7), 7093–7114. https://doi.org/10.1016/j.actbio.2013.03.033.

(7) Lobmann, R.; Pittasch, D.; Mühlen, I.; Lehnert, H. Autologous Human Keratinocytes Cultured on Membranes Composed of Benzyl Ester of Hyaluronic Acid for Grafting in Nonhealing Diabetic Foot Lesions. *J. Diabetes Complications* **2003**, *17* (4), 199–204. https://doi.org/10.1016/S1056-8727(02)00218-0.

(8) Sobotka, L.; Smahelova, A.; Pastorova, J.; Kusalova, M. A Case Report of the Treatment of Diabetic Foot Ulcers Using a Sodium Hyaluronate and Iodine Complex. *Int. J. Low. Extrem. Wounds* **2007**, *6* (3), 143–147. https://doi.org/10.1177/1534734607304684.

(9) Jung, R.; Kim, Y.; Kim, H.-S.; Jin, H.-J. Antimicrobial Properties of Hydrated Cellulose Membranes With Silver Particles. *J. Biomater. Sci. Polym. Ed.* **2009**, *20* (3), 311–324. https://doi.org/10.1163/156856209X412182.

(10) Shaw, J.; Hughes, C. M.; Lagan, K. M.; Stevenson, M. R.; Irwin, C. R.; Bell, P. M. The Effect of Topical Phenytoin on Healing in Diabetic Foot Ulcers: A Randomized Controlled Trial1: Topical Phenytoin on Healing in Diabetic Foot Ulcers. *Diabet. Med.* **2011**, *28* (10), 1154–1157. https://doi.org/10.1111/j.1464-5491.2011.03309.x.

(11) Hanam, S. R.; Singleton, C. E.; Rudek, W. The Effect of Topical Insulin on Infected Cutaneous Ulcerations in Diabetic and Nondiabetic Mice. *J. Foot Surg.* **1983**, *22* (4), 298–301.

(12) Inpanya, P.; Faikrua, A.; Ounaroon, A.; Sittichokechaiwut, A.; Viyoch, J. Effects of the Blended Fibroin/Aloe Gel Film on Wound Healing in Streptozotocin-Induced Diabetic Rats. *Biomed. Mater.* **2012**, *7* (3), 035008. https://doi.org/10.1088/1748-6041/7/3/035008.

(13) Vatankhah, N.; Jahangiri, Y.; Landry, G. J.; Moneta, G. L.; Azarbal, A. F. Effect of Systemic Insulin Treatment on Diabetic Wound Healing: Insulin Therapy and Diabetic Foot Ulcer. *Wound Repair Regen.* **2017**, *25* (2), 288–291. https://doi.org/10.1111/wrr.12514.

(14) Apikoglu-Rabus, S.; Izzettin, F. V.; Turan, P.; Ercan, F. Effect of Topical Insulin on Cutaneous Wound Healing in Rats with or without Acute Diabetes. *Clin. Exp. Dermatol.* **2010**, *35* (2), 180–185. https://doi.org/10.1111/j.1365-2230.2009.03419.x.

(15) Oryan, A.; Alemzadeh, E. Effects of Insulin on Wound Healing: A Review of Animal and Human Evidences. *Life Sci.* **2017**, *174*, 59–67. https://doi.org/10.1016/j.lfs.2017.02.015.

(16) Lima, M. H. M.; Caricilli, A. M.; de Abreu, L. L.; Araújo, E. P.; Pelegrinelli, F. F.; Thirone, A. C. P.; Tsukumo, D. M.; Pessoa, A. F. M.; dos Santos, M. F.; de Moraes, M. A.; Carvalheira, J. B. C.; Velloso, L. A.; Saad, M. J. A. Topical Insulin Accelerates Wound Healing in Diabetes by Enhancing the AKT and ERK Pathways: A Double-Blind Placebo-Controlled Clinical Trial. *PLoS ONE* **2012**, *7* (5), e36974. https://doi.org/10.1371/journal.pone.0036974.

(17) Wang, W.; Lin, S.; Xiao, Y.; Huang, Y.; Tan, Y.; Cai, L.; Li, X. Acceleration of Diabetic Wound Healing with Chitosan-Crosslinked Collagen Sponge Containing Recombinant







Human Acidic Fibroblast Growth Factor in Healing-Impaired STZ Diabetic Rats. *Life Sci.* **2008**, *82* (3–4), 190–204. https://doi.org/10.1016/j.lfs.2007.11.009.

(18) Matsumoto, Y.; Kuroyanagi, Y. Development of a Wound Dressing Composed of Hyaluronic Acid Sponge Containing Arginine and Epidermal Growth Factor. *J. Biomater. Sci. Polym. Ed.* **2010**, *21* (6–7), 715–726. https://doi.org/10.1163/156856209X435844.

(19) Fujita, N.; Sakaguchi, I.; Kobayashi, H.; Ikeda, N.; Kato, Y.; Minamino, M.; Ishii, M. An Extract of the Root of Lithospermun Erythrorhison Accelerates Wound Healing in Diabetic Mice. *Biol. Pharm. Bull.* **2003**, *26* (3), 329–335. https://doi.org/10.1248/bpb.26.329.

(20) Petri, Christian. Synthesis and Characterization of Novel Photocrosslinkable Poly(2-Oxazoline)-Based Hydrogel Systems for the Application as Biosensor Matrix, 2018.

(21) Ohno, Y.; Seki, T.; Kojima, Y.; Miki, R.; Egawa, Y.; Hosoya, O.; Kasono, K.; Seki, T. Investigation of Factors That Cause Insulin Precipitation and/or Amyloid Formation in Insulin Formulations. *J. Pharm. Health Care Sci.* **2019**, *5* (1), 22. https://doi.org/10.1186/s40780-019-0151-5.

(22) Baipaywad, Phornsawat; Kim, Yunkyung; Wi, Jung-Sub; Paik, Taejong; Park, Hansoo (2017). *Size-controlled synthesis, characterization, and cytotoxicity study of monodisperse poly(dimethylsiloxane) particles. Journal of Industrial and Engineering Chemistry, (), S1226086X17302113–*. doi:10.1016/j.jiec.2017.04.023

(23) Retsch, Markus. (2009). Complex Materials via Colloidal Crystallization.

Macromolecular Rapid Communications

# Supporting Information

for *Macromol. Rapid Commun.*, DOI 10.1002/marc.202400989

## Antiadhesive and Antibacterial Coatings for Short-Term Titanium Implants

*Fiona Wiesner, Karl G. M. Schönewald, Kira Vogel, Niklas Jung, Barbara Schwierz, Maren Kipping, Aliia Ibragimova, Joshua Schumacher, Christian Pritzel, Clinton R. V. Thiagarajan, Ulrike Ritz* and Ulrich Jonas**



# Supporting Information

## Antiadhesive and Antibacterial Coatings for Titanium Implants

Fiona Wiesner,[1] Karl G. M. Schönewald,[2] Kira Vogel,[2] Niklas Jung,[1] Barbara Schwierz,[2] Maren Kipping,[1] Aliia Ibragimova,[1] Joshua Schumacher,[3] Christian Pritzel,[4] Clinton R. V. Thiagarajan,[1] Ulrike Ritz,*[2] and Ulrich Jonas*[1]

[1]University of Siegen, Department of Biology and Chemistry, Macromolecular Chemistry, Adolf-Reichwein-Straße 2, 57076 Siegen, Germany – Email: jonas@chemie.uni-siegen.de

[2]University Medical Center Mainz, Technology Transfer, Langenbeckstraße 1, 55131 Mainz, Germany

[3]University of Siegen, Department of Biology and Chemistry, Physical Chemistry I, Adolf-Reichwein-Straße 2, 57076 Siegen, Germany

[4]University Medical Center Mainz, Department of Orthopedics and Trauma Surgery, Langenbeckstraße 1, 55131 Mainz, Germany – Email: ritz@uni-mainz.de

[5]University of Siegen, Department of Biology and Chemistry, Chemistry of Building Materials, Paul-Bonatz-Straße 9-11, 57076 Siegen, Germany

*contributed equally, corresponding authors



### S1. Polymer Synthesis

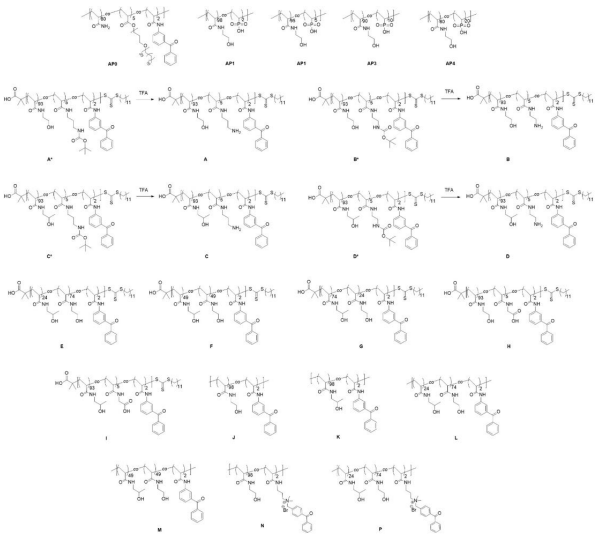


Figure S1. Overview about all synthesized polymers including their abbreviations.



Table S1. Educts, yields, and GPC results for the copolymerization of VPA and HEAm with different built-in ratios of VPA (c(VPA)). Synthetic details for the adhesion promoter polymer AD0 can be found in literature. [1]

| # | c(VPA) | VPA[a,b] | | HEAm[a,b] | | AIBN[a] | | Yield | | GPC | |
|---|---|---|---|---|---|---|---|---|---|---|---|
| | % | mg | µmol | mg | µmol | mg | µmol | mg | % | $\overline{M}_n$ / kg mol$^{-1}$ | *Đ* |
| **AP1** | 2 | 3.84 | 35.5 | 200 | 1.74 | 1.46 | 8.88 | 170 | 83 | 30 | 1.6 |
| **AP2** | 5 | 9.87 | 91.4 | 200 | 1.74 | 1.50 | 9.16 | 180 | 85 | 37 | 2.1 |
| **AP3** | 10 | 20.8 | 193 | 200 | 1.74 | 1.59 | 9.67 | 189 | 85 | 49 | 2.1 |
| **AP4** | 20 | 46.9 | 434 | 200 | 1.74 | 1.79 | 10.9 | 204 | 82 | 31 | 3.0 |

[a] taken from a stock solution in MeOH (*β* = 100 mg/ml) in case of #**1** to #**4**.

Table S2. Educts, yields, and GPC results for the RAFT copolymerization of the polymers **A** - **I** with different comonomers.

| # | Monomers Name / mg(mmol) | | BPAm / mg (µmol) | DMP / mg (µmol) | AIBN / mg (µmol) | Yield % | GPC $\overline{M}_n$ / kg mol$^{-1}$ | *Đ* |
|---|---|---|---|---|---|---|---|---|
| **A*** | HEAm 362 (3.14) | APAm-Boc 38.0 (0.17) | 16.61 (66.2) | 6.02 (17.0) | 2.80 (17.4) | 92 | 35 | 1.3 |
| **B*** | HEAm 364 (3.16) | AEAm-Boc 36.0 (0.17) | 16.72 (66.6) | 6.06 (17.0) | 2.80 (17.4) | 98 | 33 | 1.2 |
| **C*** | HPAm 366 (2.83) | APAm-Boc 34.0 (0.15) | 15.07 (60.0) | 5.44 (15.0) | 2.40 (15.0) | 76 | 15 | 1.1 |
| **D*** | HPAm 367 (2.84) | AEAm-Boc 32.0 (.015) | 15.07 (60.0) | 5.46 (15.0) | 2.40 (15.0) | 78 | 11 | 1.2 |
| **E** | HEAm 289 (2.51) | HPAm 110 (0.85) | 17.2 (67.4) | 6.12 (16.8) | 2.80 (17.4) | 83 | 35 | 1.2 |
| **F** | HEAm 198 (1.72) | HPAm 212 (1.73) | 16.73 (65.6) | 6.28 (17.3) | 2.80 (17.4) | 73 | 39 | 1.2 |
| **G** | HPAm 308 (2.38) | HEAm 97 (0.84) | 16.23 (63.6) | 5.86 (16.1) | 2.80 (17.4) | 66 | 36 | 1.4 |
| **H** | HEAm 377 (3.27) | AaAm 22.0 (0.17) | 17.33 (69.0) | 6.28 (17.3) | 2.80 (17.4) | 67 | 32 | 1.3 |
| **I** | HPAm 380 (2.94) | AaAm 20.0 (0.15) | 15.58 (61.8) | 5.63 (15.5) | 2.50 (15.5) | 66 | 34 | 1.4 |

Table S3. GPC data before and after deprotection of the RAFT copolymers **A** - **D**.

| # | Monomers | GPC (before deprotection) $\overline{M_n}$ / kDa | GPC (before deprotection) Đ | GPC (after deprotection) $\overline{M_n}$ / kDa | GPC (after deprotection) Đ | Yield / mg | Yield / % |
|---|---|---|---|---|---|---|---|
| **A** | HEAm - APAm | 34.7 | 1.3 | 34.6 | 1.3 | 92 | 92 |
| **B** | HEAm - AEAm | 38.0 | 1.2 | 33.3 | 1.2 | 98 | 98 |
| **C** | HPAm - APAm | 39.3 | 1.2 | 14.5 | 1.2 | 38 | 76 |
| **D** | HPAm - AEAm | 32.0 | 1.3 | 10.9 | 1.2 | 39 | 78 |

Table S4. Educts, yields, and GPC results for the FRP of the polymers **J** - **P** with different comonomers.

| # | HEAm / mg (mmol) | HPAm / mg (mmol) | Crosslinker Name / mg (µmol) | AIBN / mg (µmol) | Yield % | GPC $\overline{M_n}$ / kDa | GPC Đ |
|---|---|---|---|---|---|---|---|
| **J** | 500 (4.34) | - | BPAm 22.3 (88.6) | 3.64 (22.2) | 79 | 52 | 3.2 |
| **K** | - | 400 (3.10) | BPAm 15.58 (62.0) | 2.50 (15.5) | 79 | 60 | 2.3 |
| **L** | 500 (4.34) | 182 (1.41) | BPAm 29.5 (117) | 4.82 (29.3) | 82 | 69 | 3.8 |
| **M** | 212 (1.73) | 198 (1.72) | BPAm 16.73 (65.6) | 2.80 (17.4) | 75 | 63 | 2.5 |
| **N** | 500 (4.34) | - | BPQAAm 38.2 (88.6) | 3.64 (22.2) | 83 | 40 | 3.8 |
| **P** | 289 (2.51) | 110 (0.85) | BPQAAm 29.1 (67.4) | 2.82 (17.2) | 91 | 42 | 2.2 |

## S2. Polymer Analysis

### S2.1 NMR Spectroscopy



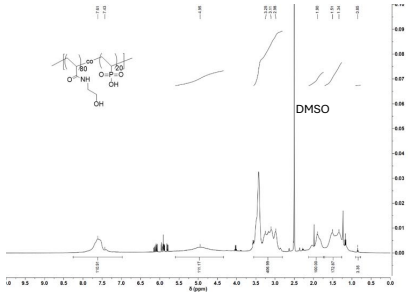


Figure S2. $^{1}$H NMR spectrum of **AP4** measured in DMSO-d6.

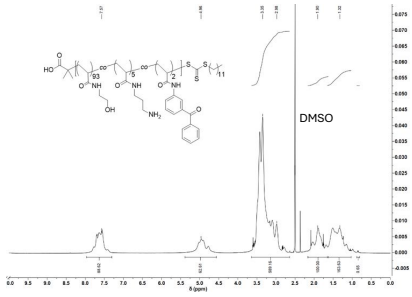


Figure S3. $^{1}$H NMR spectrum of polymer **A**, measured in DMSO-d6.



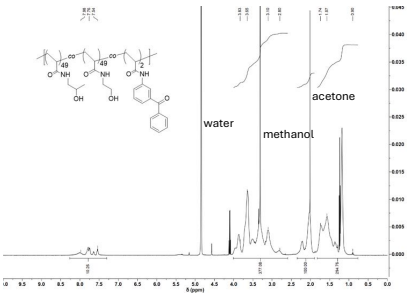


Figure S4. $^{1}$H NMR spectrum of polymer **M**, measured in methanol-d3.

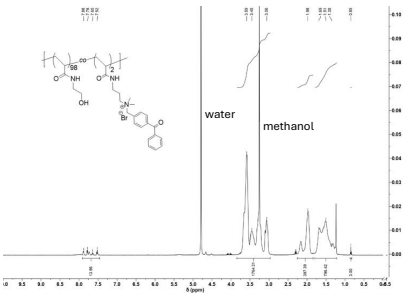


Figure S5. $^{1}$H NMR spectrum of polymer **N**, measured in methanol-d3.



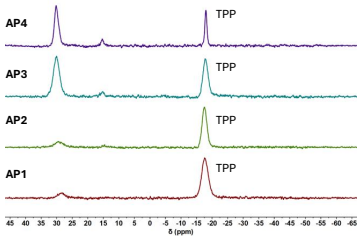


Figure S6. $^{31}$P NMR measurement of the anchor polymers **AP1** – **AP4** with triphenyl phosphate (TPP) as standard.

## S3. Polymer Network Analysis

### S3.1 Contact Angle Measurements

*Static contact angles measurements*

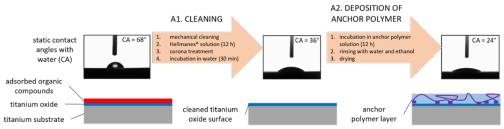


Figure S7. Procedure for performing the static contact angle measurements.

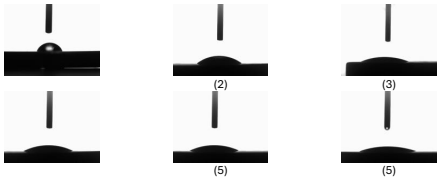


Figure S8. Static contact angles with water on (1) Ti as-received (CA = 68°), (2) cleaned titanium (CA = 36°), (3) Ti with **AP1** (CA = 22°), (4) Ti with **AP2** (CA = 25°), (5) Ti with **AP3** (CA = 24°), and (6) Ti with **AP4** (CA = 18°).

*Dynamic contact angle measurements*

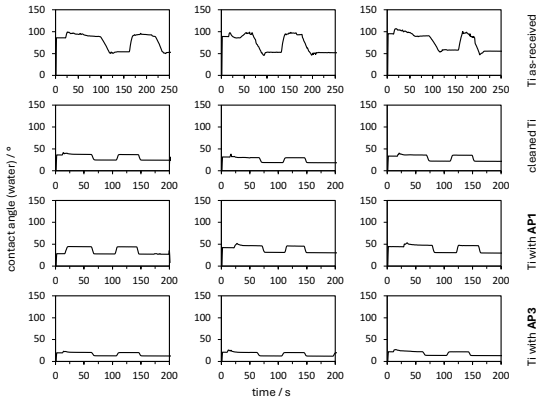


Figure S9. Graphs of the dynamic contact angle measurements with water.



## S2.2 Environmental Scanning Electron Microscopy

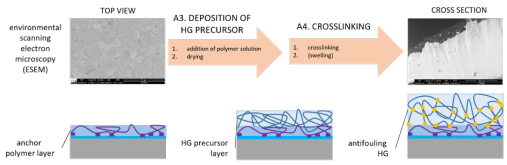


Figure S10. Workflow for the ESEM-EDX measurements.

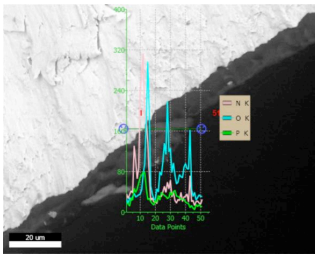


Figure S11. Results of the EDX line scan of the cross-section (raw data).

## S2.3 Atomic Force Microscopy

*Preparation of the cantilever*

The following procedure was adapted from Norman et al. [2] To place the adhesive onto the end of the cantilever, the tipless cantilever was mounted into the AFM holder. The adhesive was dropped onto a microscopy slide, which was placed in the sample holder of the AFM. The optical camera system was used to bring the cantilever into contact with the adhesive, allowing the distance between the two to be controlled visually. Contact-mode force curves were acquired in order to carefully dip the end of the cantilever into the adhesive, allowing an intimate contact with a dwelling time of 10 seconds and a trigger of 0.1 V. Afterwards, a microscopy slide coated with silica beads was placed in the sample holder of the AFM. The cantilever was carefully lowered above a bead visible in the optical camera system and then force curves with a deflection volt trigger of 1 V were recorded until the cantilever touched the bead and the adhesive was allowed to get into contact with the bead for a dwelling time of 10 seconds. In order to fix the attached



bead to the cantilever, the modified cantilever was exposed to UV irradiation for 15 minutes at a wavelength of 365 nm. After conducting the force measurements, the cantilever was sputtered with gold for SEM imaging.

*Quality assessment and calibration of the modified cantilever*

The successful modification of the cantilever was checked by scanning electron microscopy and by AFM. By measuring an AFM height image over a calibration grid made of sharp and upwards-facing cantilever-tips, the three-dimensional structure of the attached bead could be visualized and confirmed a highly homogeneous surface of the bead as can be seen in Figure S12.

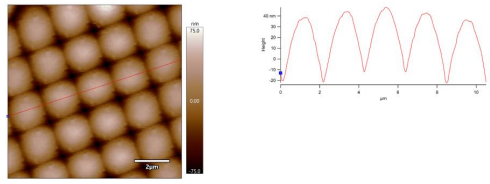

Figure S12. AFM height image of the calibration grid exposing upwards-facing AFM-tips (left) and cross-section analysis (right).

Additionally, the cantilever was imaged by electron microscopy as can be seen in Figure S13.

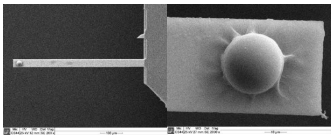

Figure S13. SEM secondary electron image of the top view of the modified cantilever (left) and a higher magnification of the bead with the sample holder tilted by 45° (right).

In the SEM images, the highly homogeneous glass bead can be seen without any impurities in the contact region. The bead-modified cantilever was then mounted to the AFM and force curves were recorded in order to determine the elastic modulus of the hydrogel-coated substrate. In order to determine said value, the spring constant was determined based on the thermal calibration method. For that, the virtual deflection was measured by measuring a force curve over the maximum distance possible in air without having a trigger. The change in the deflection of the cantilever during the z-movement was fitted and automatically subtracted from the subsequent measurements. Afterwards, the mounted cantilever was pressed 200 times on a glass slide which was previously cleaned using an acetone-saturated wipe. By plotting the measured deflection



against the z-distance and fitting the contact part of this fit, the inverse optical lever sensitivity was determined. For that, the determined slopes for all force curves were plotted in a histogram and the mean value was calculated based on a Gaussian fit. In order to determine the cantilevers spring constant, the temperature-induced oscillations of the cantilever were recorded and the resonance frequency was fitted according to the equipartition theorem.[1] Knowing the inverse optical lever sensitivity, the cantilevers spring constant could be determined and was found to be 250 ± 30 pN nm$^{-1}$. This process was repeated three times and the mean value was calculated. After determining the spring constant, the InvOLS value could be determined prior to new experiments based on the thermal spectrum of the cantilever as described before, ranging from 400 to 550 nm/V depending on the position of the laser on the cantilever.

Force probing on the hydrogel in the dry state revealed a relatively stiff surface which cannot be indented by the very soft cantilever as can be seen in Figure S14.

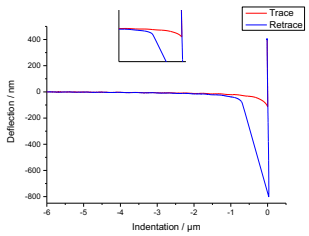


Figure S14. Deflection-indentation plot of the dry network from the hydrogel precursor polymer, measured in air.

Upon approaching the surface, long-range attractive forces lead to a bending of the cantilever towards the surface. As soon as the cantilever touches the surface, no indentation is observed, but only bending of the cantilever. Fitting of the force curve according to the Hertzian model yields apparent moduli exceeding 200 MPa. For this reason, the cantilever with a spring constant of 250 pN/nm is not suited for indentation measurements of the dry polymer network.

Force measurements in water on the swollen hydrogel coating yielded the force curves shown in Figure S15, where no adhesion is present and indentation of the hydrogel layer can be observed.

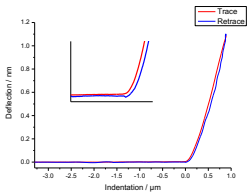


Figure S15. Force-indentation plot of the swollen hydrogel coating measured in water.

After measuring the force maps, by fitting the Hertzian model to the approach curves as can be seen in Figure S16 the Young´s modulus was determined. Inhomogeneous force curves were neglected.

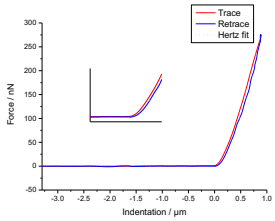


Figure S16. Force-indentation plot of the swollen hydrogel measured in water. The dotted black line corresponds to the Hertzian fit.

The measured Young´s moduli yield a distribution as can be seen in Figure S17. Eighteen force maps were excluded due to inhomogeneities during the measurement of those curves measured. A Gaussian fit has been fitted to the data to determine the mean value and the full width half maximum is taken to describe the distribution of the Young´s moduli.



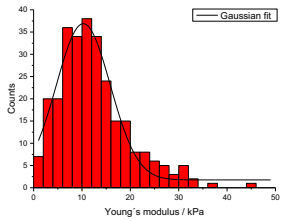


Figure S17. Histogram of the Young´s moduli determined from three separate force maps.

### S2.4 Coverage of the Titanium Specimens

Figure S18. Exemplary photograph of two polymer network-coated titanium disks with the specimen on the left showing a partially (drop-) coated sample and the specimen on the right an completely covered surface.

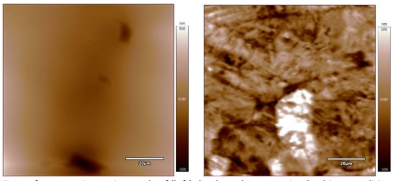

Figure S19. AFM surface scans in tapping mode of (left) the dry polymer coating (ambient conditions) and (right) the untreated titanium surface.



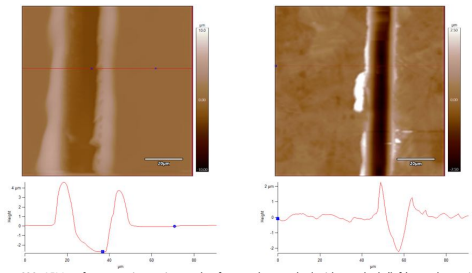

Figure S20. AFM surface scans in tapping mode of a sample scratched with a scalpel: (left) sample previously coated with polymer (ambient conditions) and (right) untreated titanium surface. The bottom pictures depict their corresponding height profiles (red line in the surface map visualizes the height profile line scan).

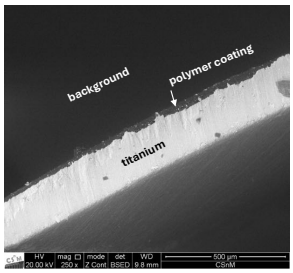


Figure S21. ESEM picture of the cross section of a coated titanium substrate, showing even surface coverage.

### Literature


1 Freese, S.; Diraoui, S.; Mateescu, A.; Frank, P.; Theodorakopoulos, C.; Jonas, U. Polyolefin-Supported Hydrogels for Selective Cleaning Treatments of Paintings. *Gels* **2020**, 6, doi:10.3390/gels6010001.

2 Cook, S. M.; Lang, K. M.; Chynoweth, K. M.; Wigton, M.; Simmonds, R. W.; Schäffer, T. E. Practical Implementation of Dynamic Methods for Measuring Atomic Force Microscope Cantilever Spring Constants. Nanotechnology **2006**, *17* (9), 2135–2145. https://doi.org/10.1088/0957-4484/17/9/010.

**Beschreibung der Abbildungen**

**Abbildung 1:** Tenozyten-Adhäsion auf Zellkulturplatte, beschichtet versus unbeschichtet.

**Abbildung 2:** Tenozyten-Adhäsion auf Titanscheiben. beschichtet (A) versus unbeschichtet (B)

**Abbildung 3:** *Staph. Aureus* CFUs nach Inkubation auf einer mit nicht antibakteriell wirkendem Polymer beschichteten Platte (A) versus einer mit antibakteriell wirkendem Polymer beschichteten Platte (B).

**Ausführliche Beschreibung der Erfindung**

Wie bereits oben erwähnt, stellt die vorliegende Erfindunghydrophile (Co-)Polymere mit chemisch reaktiv (kovalent) gebundenen Ankergruppen und/oder Vernetzermolekülen bereit, welche eine Anknüpfung an das zugrundeliegende Substrat bzw. eine Verknüpfung dieser Polymere zu Netzwerken erlauben. Die Beschichtung von Kurzeitimplantaten mit solchen wasserquellbaren Polymernetzwerken (Hydrogelen) verhindert eine Adhäsion von Zellen und Gewebe auf der Oberfläche (Antifouling), ohne dass eine Zytotoxizität von ihr ausgeht, und erzielt gleichzeitig gegebenenfalls eine intrinsische antibakterielle Wirkung, ohne dass eine Beigabe zusätzlicher Antibiotika oder Bakterizide notwendig ist. Da das umliegende Gewebe nicht an einem antiadhäsiv beschichteten Implantat haften kann, wird dieses nicht bei der Entfernung des Implantates geschädigt. Außerdem wird durch die gegebenenfalls intrinsische antibakterielle Wirkung der Beschichtung einer möglichen im Zuge einer Implantation vorkommenden Infektion vorgebeugt.

Die hier beschriebenen und dem Hydrogel zugrundeliegenden Polymerketten bestehen aus hydrophilen Hauptmonomeren, und Vernetzermonomeren, teilweise mit antibakteriell wirksamen Strukturmotiven, und/oder dedizierten Ankergruppen für das entsprechende Implantatsubstrat. Durch die gezielte Wahl dieser modular kombinierbaren Monomere ist es möglich, gleichzeitig biokompatible, antiadhäsive und antibakterielle Polymernetzwerke herzustellen.

Bei der Darstellung der erfindungsgemäßen (Co-)Polymeren ist von einer zufälligen Verteilung der Wiederholungseinheiten aus den verwendeten Monomeren auszugehen. Die bei einer normalen Polymerkette angegebene Anzahl von Wiederholungseinheiten „n“ ist in diesem Fall nur bedingt anwendbar, da die Wiederholungseinheiten innerhalb der Polymerkette nicht einer regelmäßigen Abfolge wiederholt folgen. Aus diesem Grund wurde auf die Angabe einer Wiederholungseinheit „n“ in den nachfolgenden Formeln, insbesondere der allgemeinen Formel (I), verzichtet. Im vorliegenden Fall wäre es deshalb auch möglich in den nachfolgenden Formeln Wiederholungseinheiten zu definieren, die im Bereich von n = 2 – 100.000, wie beispielsweise von 50-10.000, liegen können. Mit den eckigen Klammern ist dennoch eine wiederholende Abfolge der in Frage kommenden Wiederholungseinheiten entsprechend der üblichen Polymerkettendarstellung nach dem Stand der Technik angedeutet. Es könnte daher die Angabe „n“ an den eckigen Klammern in den nachfolgenden Formeln angegeben





werden, auf die jedoch aus den vorher genannten Gründen verzichtet wurde. Die Darstellung der Copolymerzusammensetzung aus unterschiedlichen Monomeren mit " / " ist entsprechend der Empfehlung nach IUPAC gewählt.

Erfindungsgemäß wird in einem ersten Aspekt ein (Co-)Polymer der allgemeinen Strukturformel (I) mit einer zufälligen Verteilung der Wiederholungseinheiten bereitgestellt:

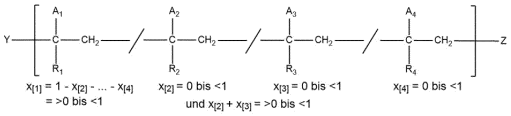


**(I)**

wobei $A_1$, $A_2$, $A_3$, $A_4$, $R_1$, $R_2$, $R_3$, $R_4$, Y und Z wie hierin beschrieben sind.

Die zufällige Verteilung der Wiederholungseinheiten ist mit den Zusammensetzungen (Stoffmengenanteilen) x angegeben, wobei x mit $x_{[1]}$, $x_{[2]}$, $x_{[3]}$ und $x_{[4]}$ eine molekulare Struktur einer Anzahl von Wiederholungseinheiten darstellt und die Summe der Stoffmengenanteile x der Wiederholungseinheiten mit $x_{[1]}$, $x_{[2]}$,$x_{[3]}$ und $x_{[4]}$ = 1 beträgt.

$A_1/R_1$, $A_2/R_2$, $A_3/R_3$ und $A_4/R_4$ entsprechen den Wiederholungseinheiten aus Hauptmonomer, Ankermonomer, Crosslinkermonomer bzw. Comonomer. Die jeweiligen durch $A_1/R_1$, $A_2/R_2$, $A_3/R_3$ und $A_4/R_4$ definierten Monomertypen können im erfindungsgemäßen Polymer identisch sein. Jedoch kann ein erfindungsgemäßes Polymer auch Kombinationen verschiedener Wiederholungseinheiten desselben Monomertyps umfassen. Entsprechend können sich die jeweiligen Wiederholungseinheiten desselben Monomertyps im Rest R unterscheiden. Beispielsweise kann ein erfindungsgemäßes Polymer unterschiedliche Wiederholungseinheiten des durch $A_1/R_1$ definierte Hauptmonomers umfassen, welche sich, z.B., im Rest $R_1$ unterscheiden.

Insbesondere wird ein Polymer bereitgestellt, welches eine Struktur der allgemeinen Formel (I) aufweist

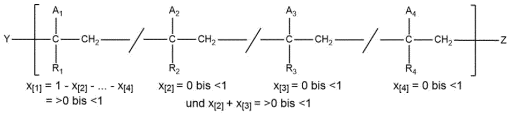


**(I)**

wobei

$A_1$ -H oder $-CH_3$ ist;

$A_2$ -H oder $-CH_3$ ist;





$A_3$ -H oder $-CH_3$ ist;

$A_4$ -H oder $-CH_3$ ist;

$R_1$, für jede Wiederholungseinheit, unabhängig ausgewählt ist aus der Gruppe bestehend aus

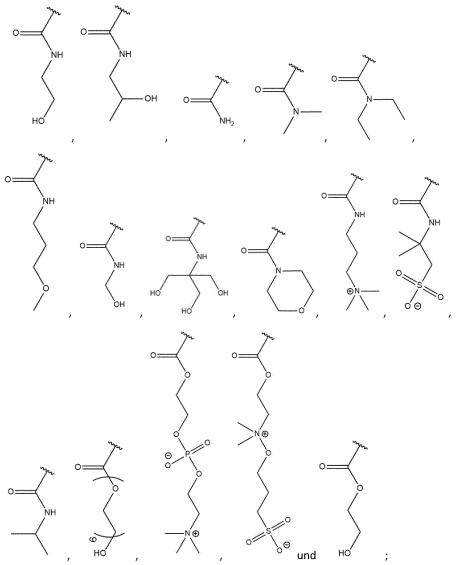


$R_2$, für jede Wiederholungseinheit, unabhängig ausgewählt ist aus der Gruppe bestehend aus





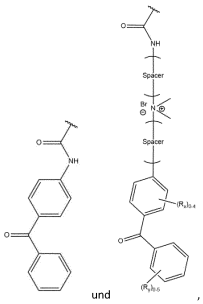


wobei jeder „Spacer“ jeweils unabhängig voneinander ausgewählt ist aus der Gruppe bestehend aus linearen oder verzweigten Alkylketten und linearen oder verzweigten Ethylen- oder Propylenoxidketten, vorzugweise unabhängig voneinander ausgewählt aus linearen oder verzweigen $C_{1-20}$-Alkylketten;

$R_x$, jeweils unabhängig voneinander, -OH, Halogen (Br, Cl, I, oder F), Halogen-$C_{1-4}$ Alkyl (z.B. $-CF_3$, $-CCL_3$, $-CBr_3$, $-Cl_3$), $-NH_2$, $-C_{1-4}$ Alkyl, $-C_{2-4}$ Alkenyl, $-C_{2-4}$ Alkinyl, $-OC_{1-4}$ Alkyl, $-OC_{2-4}$ Alkenyl, $-OC_{2-4}$ Alkinyl $-NO_2$, -SH, $-SO_2H$, $-SO_3H$, -NCS, -SCN, -COOH oder Cyano ist; und

$R_y$, jeweils unabhängig voneinander, -OH, Halogen (Br, Cl, I, oder F), Halogen-$C_{1-4}$ Alkyl (z.B. $-CF_3$, $-CCL_3$, $-CBr_3$, $-Cl_3$), $-NH_2$, $-C_{1-4}$ Alkyl, $-C_{2-4}$ Alkenyl, $-C_{2-4}$ Alkinyl, $-OC_{1-4}$ Alkyl, $-OC_{2-4}$ Alkenyl, $-OC_{2-4}$ Alkinyl $-NO_2$, -SH, $-SO_2H$, $-SO_3H$, -NCS, -SCN, -COOH oder Cyano ist;

$R_3$, für jede Wiederholungseinheit, unabhängig ausgewählt ist aus der Gruppe bestehend aus

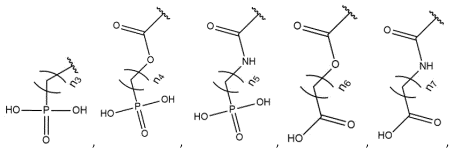

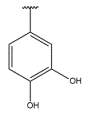
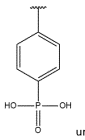
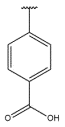

, und ,

wobei $n_3$, $n_4$, $n_5$, $n_6$ und $n_7$ jeweils unabhängig voneinander 0, 1, 2, 3, 4, 5, 6, 7, 8, 9, 10, 11, 12, 13, 14, 15, 16, 17 oder 18 ist;

$R_4$, für jede Wiederholungseinheit, unabhängig ausgewählt ist aus der Gruppe bestehend aus

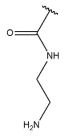
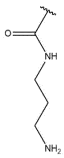
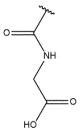

, und ;

Y ein Fragment A eines Kettenübertragungsreagenzes oder eine Endgruppe ist; und

Z ein Fragment B des Kettenübertragungsreagenzes oder eine Endgruppe ist.

Gemäß einiger bevorzugter Ausführungsformen ist $R_1$, für jede Wiederholungseinheit, unabhängig ausgewählt aus der Gruppe bestehend aus

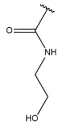
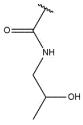

und .

Gemäß einiger besonders bevorzugter Ausführungsformen ist $R_1$, für jede Wiederholungseinheit,





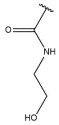

.

Gemäß einiger besonders bevorzugter Ausführungsformen ist $R_1$, für jede Wiederholungseinheit,

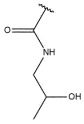

.

Gemäß einiger Ausführungsformen ist $A_1$ -H.

Gemäß einiger Ausführungsformen ist $A_1$ $-CH_3$.

Gemäß einiger besonders bevorzugter Ausführungsformen ist $R_1$, für jede Wiederholungseinheit,

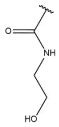

; und $A_1$ -H.

Gemäß einiger besonders bevorzugter Ausführungsformen ist $R_1$, für jede Wiederholungseinheit,

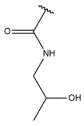

; und $A_1$ -H.

Gemäß einiger Ausführungsformen ist $R_2$, für jede Wiederholungseinheit, unabhängig ausgewählt aus der Gruppe bestehend aus





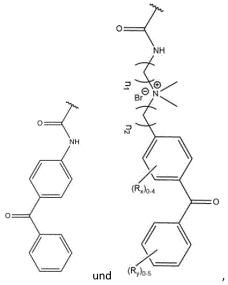

und ,

wobei $n_1$ und $n_2$ jeweils unabhängig voneinander 1, 2, 3, 4, 5, 6, 7, 8, 9, 10, 11, 12, 13, 14, 15, 16, 17, 18, 19 oder 20 ist;

$R_x$, jeweils unabhängig voneinander, -OH, Halogen (Br, Cl, I, oder F), Halogen-$C_{1-4}$ Alkyl (z.B. $-CF_3$, $-CCL_3$, $-CBr_3$, $-Cl_3$), $-NH_2$, $-C_{1-4}$ Alkyl, $-C_{2-4}$ Alkenyl, $-C_{2-4}$ Alkinyl, $-OC_{1-4}$ Alkyl, $-OC_{2-4}$ Alkenyl, $-OC_{2-4}$ Alkinyl $-NO_2$, -SH, $-SO_2H$, $-SO_3H$, -NCS, -SCN, -COOH oder Cyano ist; und

$R_y$, jeweils unabhängig voneinander, -OH, Halogen (Br, Cl, I, oder F), Halogen-$C_{1-4}$ Alkyl (z.B. $-CF_3$, $-CCL_3$, $-CBr_3$, $-Cl_3$), $-NH_2$, $-C_{1-4}$ Alkyl, $-C_{2-4}$ Alkenyl, $-C_{2-4}$ Alkinyl, $-OC_{1-4}$ Alkyl, $-OC_{2-4}$ Alkenyl, $-OC_{2-4}$ Alkinyl $-NO_2$, -SH, $-SO_2H$, $-SO_3H$, -NCS, -SCN, -COOH oder Cyano ist.

Gemäß einiger Ausführungsformen ist $R_2$, für jede Wiederholungseinheit, unabhängig ausgewählt aus der Gruppe bestehend aus





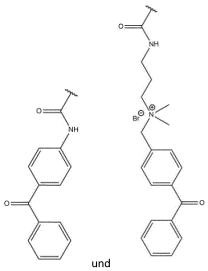

und .

Gemäß einiger Ausführungsformen ist $R_2$, für jede Wiederholungseinheit,

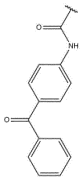

.

Gemäß einiger Ausführungsformen ist $R_2$, für jede Wiederholungseinheit,

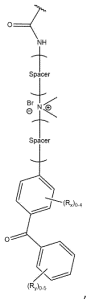


,

wobei jeder „Spacer" jeweils unabhängig voneinander ausgewählt ist aus der Gruppe bestehend aus linearen oder verzweigten Alkylketten und linearen oder verzweigten Ethylen- oder Propylenoxidketten, vorzugweise unabhängig voneinander ausgewählt aus linearen oder verzweigen $C_{1-20}$-Alkylketten;

$R_x$, jeweils unabhängig voneinander, -OH, Halogen (Br, Cl, I, oder F), Halogen-$C_{1-4}$ Alkyl (z.B. $-CF_3$, $-CCL_3$, $-CBr_3$, $-CI_3$), $-NH_2$, $-C_{1-4}$ Alkyl, $-C_{2-4}$ Alkenyl, $-C_{2-4}$ Alkinyl, $-OC_{1-4}$ Alkyl, $-OC_{2-4}$ Alkenyl, $-OC_{2-4}$ Alkinyl $-NO_2$, -SH, $-SO_2H$, $-SO_3H$, -NCS, -SCN, -COOH oder Cyano ist; und

$R_y$, jeweils unabhängig voneinander, -OH, Halogen (Br, Cl, I, oder F), Halogen-$C_{1-4}$ Alkyl (z.B. $-CF_3$, $-CCL_3$, $-CBr_3$, $-CI_3$), $-NH_2$, $-C_{1-4}$ Alkyl, $-C_{2-4}$ Alkenyl, $-C_{2-4}$ Alkinyl, $-OC_{1-4}$ Alkyl, $-OC_{2-4}$ Alkenyl, $-OC_{2-4}$ Alkinyl $-NO_2$, -SH, $-SO_2H$, $-SO_3H$, -NCS, -SCN, -COOH oder Cyano ist.

Gemäß einiger Ausführungsformen ist $R_2$, für jede Wiederholungseinheit,

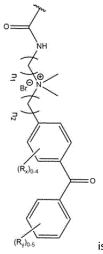

ist,





wobei $n_1$ und $n_2$ jeweils unabhängig voneinander 1, 2, 3, 4, 5, 6, 7, 8, 9, 10, 11, 12, 13, 14, 15, 16, 17, 18, 19 oder 20 ist;

$R_x$, jeweils unabhängig voneinander, -OH, Halogen (Br, Cl, I, oder F), Halogen-$C_{1-4}$ Alkyl (z.B. $-CF_3$, $-CCL_3$, $-CBr_3$, $-CI_3$), $-NH_2$, $-C_{1-4}$ Alkyl, $-C_{2-4}$ Alkenyl, $-C_{2-4}$ Alkinyl, $-OC_{1-4}$ Alkyl, $-OC_{2-4}$ Alkenyl, $-OC_{2-4}$ Alkinyl $-NO_2$, -SH, $-SO_2H$, $-SO_3H$, -NCS, -SCN, -COOH oder Cyano ist; und

$R_y$, jeweils unabhängig voneinander, -OH, Halogen (Br, Cl, I, oder F), Halogen-$C_{1-4}$ Alkyl (z.B. $-CF_3$, $-CCL_3$, $-CBr_3$, $-CI_3$), $-NH_2$, $-C_{1-4}$ Alkyl, $-C_{2-4}$ Alkenyl, $-C_{2-4}$ Alkinyl, $-OC_{1-4}$ Alkyl, $-OC_{2-4}$ Alkenyl, $-OC_{2-4}$ Alkinyl $-NO_2$, -SH, $-SO_2H$, $-SO_3H$, -NCS, -SCN, -COOH oder Cyano ist.

Gemäß einiger Ausführungsformen ist $R_1$, für jede Wiederholungseinheit,

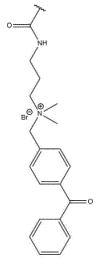

.

Gemäß einiger Ausführungsformen ist $A_2$ -H.

Gemäß einiger Ausführungsformen ist $A_2$ $-CH_3$.

Gemäß einiger Ausführungsformen ist $R_2$, für jede Wiederholungseinheit, unabhängig ausgewählt aus der Gruppe bestehend aus





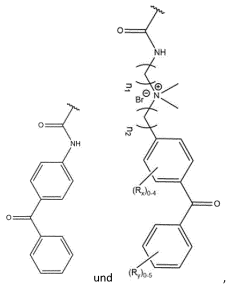

und ,

wobei $n_1$ und $n_2$ jeweils unabhängig voneinander 1, 2, 3, 4, 5, 6, 7, 8, 9, 10, 11, 12, 13, 14, 15, 16, 17, 18, 19 oder 20 ist;

$R_x$, jeweils unabhängig voneinander, -OH, Halogen (Br, Cl, I, oder F), Halogen-$C_{1-4}$ Alkyl (z.B. $-CF_3$, $-CCL_3$, $-CBr_3$, $-CI_3$), $-NH_2$, $-C_{1-4}$ Alkyl, $-C_{2-4}$ Alkenyl, $-C_{2-4}$ Alkinyl, $-OC_{1-4}$ Alkyl, $-OC_{2-4}$ Alkenyl, $-OC_{2-4}$ Alkinyl $-NO_2$, -SH, $-SO_2H$, $-SO_3H$, -NCS, -SCN, -COOH oder Cyano ist; und

$R_y$, jeweils unabhängig voneinander, -OH, Halogen (Br, Cl, I, oder F), Halogen-$C_{1-4}$ Alkyl (z.B. $-CF_3$, $-CCL_3$, $-CBr_3$, $-CI_3$), $-NH_2$, $-C_{1-4}$ Alkyl, $-C_{2-4}$ Alkenyl, $-C_{2-4}$ Alkinyl, $-OC_{1-4}$ Alkyl, $-OC_{2-4}$ Alkenyl, $-OC_{2-4}$ Alkinyl $-NO_2$, -SH, $-SO_2H$, $-SO_3H$, -NCS, -SCN, -COOH oder Cyano ist; und

$A_2$ ist -H.

Gemäß einiger Ausführungsformen ist $(R_x)_{0-4}$ $(R_x)_0$.

Gemäß einiger Ausführungsformen ist $(R_y)_{0-4}$ $(R_y)_0$.

Gemäß einiger bevorzugter Ausführungsformen ist $R_2$, für jede Wiederholungseinheit, unabhängig ausgewählt aus der Gruppe bestehend aus





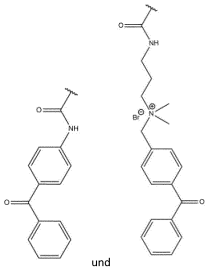

und ; und $A_2$ ist -H.

Gemäß einiger Ausführungsformen ist $R_3$, für jede Wiederholungseinheit, unabhängig ausgewählt aus der Gruppe bestehend aus

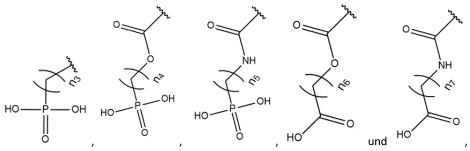

und ,

wobei $n_3$, $n_4$, $n_5$, $n_6$ und $n_7$ jeweils unabhängig voneinander 0, 1, 2, 3, 4, 5, 6, 7, 8, 9, 10, 11, 12, 13, 14, 15, 16, 17 oder 18 ist.

Gemäß einiger Ausführungsformen ist $R_3$, für jede Wiederholungseinheit, , wobei $n_3$ 0, 1, 2, 3, 4, 5, 6, 7, 8, 9, 10, 11, 12, 13, 14, 15, 16, 17 oder 18 ist.

Gemäß einiger Ausführungsformen ist $R_3$, für jede Wiederholungseinheit, 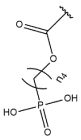 , wobei $n_4$ 0, 1, 2, 3, 4, 5, 6, 7, 8, 9, 10, 11, 12, 13, 14, 15, 16, 17 oder 18 ist.

Gemäß einiger Ausführungsformen ist $R_3$, für jede Wiederholungseinheit, 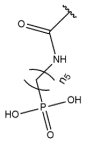 , wobei $n_5$ 0, 1, 2, 3, 4, 5, 6, 7, 8, 9, 10, 11, 12, 13, 14, 15, 16, 17 oder 18 ist.

Gemäß einiger Ausführungsformen ist $R_3$, für jede Wiederholungseinheit, 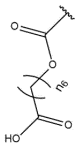 , wobei $n_6$ 0, 1, 2, 3, 4, 5, 6, 7, 8, 9, 10, 11, 12, 13, 14, 15, 16, 17 oder 18 ist.

Gemäß einiger Ausführungsformen ist $R_3$, für jede Wiederholungseinheit, 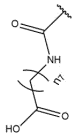 , wobei $n_7$ 1, 2, 3, 4, 5, 6, 7, 8, 9, 10, 11, 12, 13, 14, 15, 16, 17 oder 18 ist.





Gemäß einiger bevorzugter Ausführungsformen ist $R_3$, für jede Wiederholungseinheit,

.

Gemäß einiger Ausführungsformen ist $R_3$, für jede Wiederholungseinheit, unabhängig ausgewählt aus der Gruppe bestehend aus

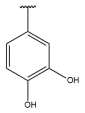 , 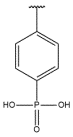 und 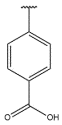 .

Gemäß einiger Ausführungsformen ist $A_3$ -H.

Gemäß einiger Ausführungsformen ist $A_3$ $-CH_3$.

Gemäß einiger bevorzugter Ausführungsformen ist $R_3$, für jede Wiederholungseinheit, ,

, wobei $n_3$ 0, 1, 2, 3, 4, 5, 6, 7, 8, 9, 10, 11, 12, 13, 14, 15, 16, 17 oder 18 ist; und $A_3$ ist -H.

Gemäß einiger bevorzugter Ausführungsformen ist $R_3$, für jede Wiederholungseinheit,

; und $A_3$ ist -H.

Gemäß einiger Ausführungsformen ist $R_3$, für jede Wiederholungseinheit, unabhängig ausgewählt aus der Gruppe bestehend aus

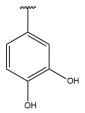 , 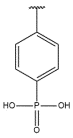 und 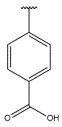 ; und $A_3$ ist -H.





Gemäß einiger Ausführungsformen ist $R_4$, für jede Wiederholungseinheit,

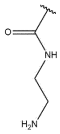 .

Gemäß einiger Ausführungsformen ist $R_4$, für jede Wiederholungseinheit,

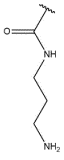 .

Gemäß einiger Ausführungsformen ist $R_4$, für jede Wiederholungseinheit,

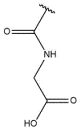 .

Gemäß einiger Ausführungsformen ist $A_4$ -H.

Gemäß einiger Ausführungsformen ist $A_4$ $-CH_3$.

Gemäß einiger bevorzugter Ausführungsformen ist $R_4$, für jede Wiederholungseinheit,





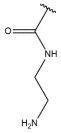 , und $A_4$ ist -H.

Gemäß einiger bevorzugter Ausführungsformen ist $R_4$, für jede Wiederholungseinheit,

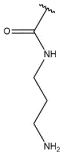 , und $A_4$ ist -H.

Gemäß einiger bevorzugter Ausführungsformen ist $R_4$, für jede Wiederholungseinheit,

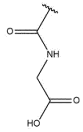 , und $A_4$ ist -H.

Gemäß einiger bevorzugter Ausführungsformen ist $R_1$, für jede Wiederholungseinheit, unabhängig ausgewählt aus der Gruppe bestehend aus

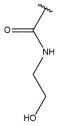 und 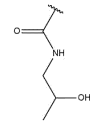 ;

ist $R_2$, für jede Wiederholungseinheit, unabhängig ausgewählt ist aus der Gruppe bestehend aus

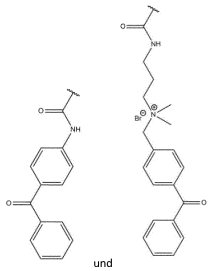

und ;

ist $R_3$, für jede Wiederholungseinheit, ; und

ist $R_4$, für jede Wiederholungseinheit, unabhängig ausgewählt aus der Gruppe bestehend aus

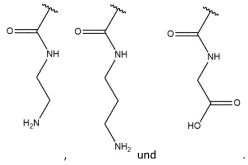

, und .

Gemäß einiger bevorzugter Ausführungsformen ist $R_1$, für jede Wiederholungseinheit, unabhängig ausgewählt aus der Gruppe bestehend aus





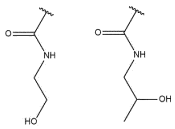

und ;

ist $R_2$, für jede Wiederholungseinheit, unabhängig ausgewählt ist aus der Gruppe bestehend aus

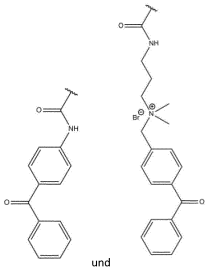

und ;

ist $R_3$, für jede Wiederholungseinheit, ;

ist $R_4$, für jede Wiederholungseinheit, unabhängig aus der Gruppe bestehend aus

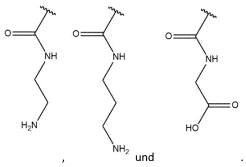

, und .





Gemäß einiger Ausführungsformen ist $A_1$ -H, $A_2$ -H, $A_3$ -H, und $A_4$ -H.

Z ein Fragment A eines Kettenübertragungsreagenzes und Y ein Fragment B des Kettenübertragungsreagenzes.

Geeignete Kettenübertragungsreagenzien für die Reversible Addition-Fragmentation Chain Transfer (RAFT) Polymerisation sind dem Fachmann gut bekannt, und sind in der Regel den Klassen der Dithioester, Trithiocarbonate, Xanthate und Carbamate zu entnehmen.

Im Falle einer Atom Transfer Radical Polymerization (ATRP) Reaktion entsprechen die endständigen Variablen Y und Z des Polymers den üblicherweise vorkommenden Endgruppen, vorzugsweise -Cl und -Br, bzw. organische Fragmente aus der ATRP-Initiatorkomponente, welche üblicherweise aus Organohalogeniden, wie beispielsweise Tetrachlorkohlenstoff, halogenierten Estern, halogenierten Alkylbenzolen und Sulfonylhalogeniden, bestehen.

Im Falle der Freien Radikalischen (FR) Polymerisation entsprechen die endständigen Variablen Y und Z des Polymers den üblicherweise vorkommenden gesättigten oder ungesättigten organischen Endgruppen oder abstrahierten Wasserstoffatomen, die durch Übertragungs-, Disproportionierungs- oder Kombinationsreaktionen entstehen, sowie Initiatorfragmenten, wie z.B. der Isobutyronitrilrest von Azobis(isobutyronitril) (AIBN).

Nicht-einschränkende Beispiele von Kettenübertragungsreagenzien, welche ebenfalls in den Ausführungsbeispielen eingesetzt wurden, sind

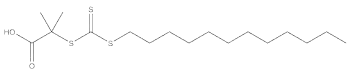

2-{[(Dodecylthio)carbothioyl]-thio}-2-methylpropansäure (DMP), und

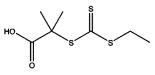

2-{[(Ethylthio)carbothioyl]-thio}-2-methylpropansäure (EMP).

Gemäß einiger bevorzugter Ausführungsformen ist Y 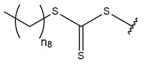 , und Z ist

;

wobei $n_8$ 1, 2, 3, 4, 5, 6, 7, 8, 9, 10, 11, 12, 13, 14, 15, 16, 17, 18, 19, 20, 21, 22, 23 oder 24 ist.

Gemäß einiger bevorzugter Ausführungsformen ist $n_8$ 1, 2, 3, 4, 5, 6, 7, 8, 9, 10, 11, 12, 13, 14, 15, 16, 17, 18, 19 oder 20.





Gemäß einiger bevorzugter Ausführungsformen ist $n_8$ 1, 2, 3, 4, 5, 6, 7, 8, 9, 10, 11, 12, 13, 14 oder 15.

Gemäß einiger bevorzugter Ausführungsformen ist $n_8$ 1, 2, 3, 4, 5, 6, 7, 8, 9, 10 oder 11.

Gemäß einiger besonders bevorzugter Ausführungsformen ist $n_8$ 1.

Gemäß einiger besonders bevorzugter Ausführungsformen ist $n_8$ 11.

Gemäß einiger Ausführungsformen ist Y und Z jeweils eine Endgruppe.

Gemäß einiger bevorzugter Ausführungsformen ist $x_{[2]}$ >0 bis <1.

Gemäß einiger bevorzugter Ausführungsformen ist $x_{[3]}$ >0 bis <1.

Gemäß einiger bevorzugter Ausführungsformen ist $x_{[4]}$ >0 bis <1.

Gemäß einiger besonders bevorzugter Ausführungsformen ist $x_{[2]}$ 0 und $x_{[3]}$ >0 bis <1; und optional ist $x_{[4]}$ >0 bis <1. In diesen Ausführungsformen kann das Polymer vorteilhafterweise als Ankerpolymer in einem Zwei-Schicht-Systeme Anwendung finden.

Gemäß einiger besonders bevorzugter Ausführungsformen ist $x_{[2]}$ >0 bis <1 und $x_{[3]}$ 0; und optional ist $x_{[4]}$ >0 bis <1. In diesen Ausführungsformen kann das Polymer vorteilhafterweise als antiadhäsives Polymer in einem Zwei-Schicht-Systeme Anwendung finden.

Gemäß einiger besonders bevorzugter Ausführungsformen ist $x_{[2]}$ >0 bis <1 und $x_{[3]}$ >0 bis <1; und optional ist $x_{[4]}$ >0 bis <1. In diesen Ausführungsformen kann das Polymer vorteilhafterweise sowohl als Ankerpolymer als auch als antiadhäsives Polymer in einem Einschichtsystem Anwendung finden.

Beispielhafte Polymere gemäß der Erfindung sind in der nachfolgenden Tabelle 1 aufgeführt.

**Tabelle 1**

| Abkürzung | Struktur | Name | Polymerisationstyp |
|---|---|---|---|
| P1 | 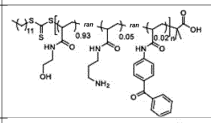 | RAFT-Poly(HEAm$_{93}$-*ran*-APAm$_{5}$-*ran*-BPAm$_{2}$)-DMP | Reversible Addition-Fragmentation Chain Transfer (RAFT) Polymersiation |
| P2 | 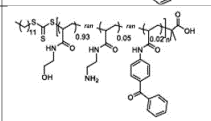 | RAFT-Poly(HEAm$_{93}$-*ran*-AEAm$_{5}$-*ran*-BPAm$_{2}$)-DMP | Reversible Addition-Fragmentation Chain Transfer (RAFT) Polymersiation |

| | | | |
|---|---|---|---|
| P3 | 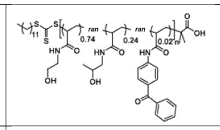 | RAFT-Poly(HEAm$_{74}$-*ran*-HPAm$_{24}$-*ran*-BPAm$_{2}$)-DMP | Reversible Addition-Fragmentation Chain Transfer (RAFT) Polymersiation |
| P4 | 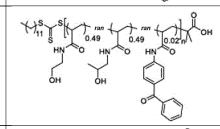 | RAFT-Poly(HEAm$_{49}$-*ran*-HPAm$_{49}$-*ran*-BPAm$_{2}$)-DMP | Reversible Addition-Fragmentation Chain Transfer (RAFT) Polymersiation |
| P5 | 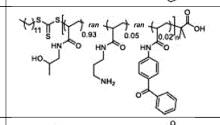 | RAFT-Poly(HPAm$_{93}$-*ran*-APAm$_{5}$-*ran*-BPAm$_{2}$)-DMP | Reversible Addition-Fragmentation Chain Transfer (RAFT) Polymersiation |
| P6 | 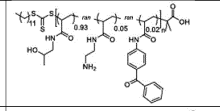 | RAFT-Poly(HPAm$_{93}$-*ran*-AEAm$_{5}$-*ran*-BPAm$_{2}$)-DMP | Reversible Addition-Fragmentation Chain Transfer (RAFT) Polymersiation |
| P7 | 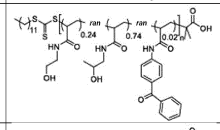 | RAFT-Poly(HEAm$_{24}$-*ran*-HPAm$_{74}$-*ran*-BPAm$_{2}$)-DMP | Reversible Addition-Fragmentation Chain Transfer (RAFT) Polymersiation |
| P8 | 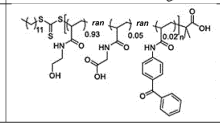 | RAFT-Poly(HEAm$_{93}$-*ran*-AaAm$_{5}$-*ran*-BPAm$_{2}$)-DMP | Reversible Addition-Fragmentation Chain Transfer (RAFT) Polymersiation |





| | | | |
|---|---|---|---|
| P9 | 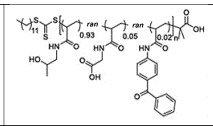 | RAFT-Poly(HPAm$_{93}$-*ran*-AaAm$_{5}$-*ran*-BPAm$_{2}$)-DMP | Reversible Addition-Fragmentation Chain Transfer (RAFT) Polymersiation |
| P10 | 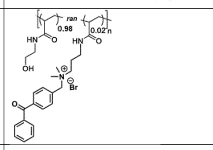 | Poly(HEAm$_{98}$-*ran*-BPQAAm$_{2}$) | Freie Radikalische (FR) Polymerisation |
| P11 | 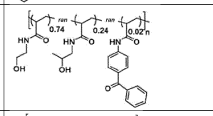 | Poly(HEAm$_{74}$-*ran*-HPAm$_{24}$-*ran*-BPAm$_{2}$) | Freie Radikalische (FR) Polymerisation |
| P12 | 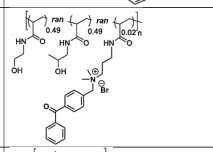 | Poly(HEAm$_{49}$-*ran*-HPAm$_{49}$-*ran*-BPQAAm$_{2}$) | Freie Radikalische (FR) Polymerisation |
| P13 | 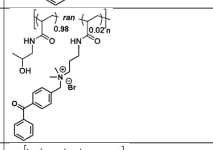 | Poly(HPAm$_{98}$-*ran*-BPQAAm$_{2}$) | Freie Radikalische (FR) Polymerisation |
| P14 | 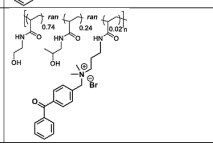 | Poly(HEAm$_{74}$-*ran*-HPAm$_{24}$-*ran*-BPQAAm$_{2}$) | Freie Radikalische (FR) Polymerisation |





| | | | |
|---|---|---|---|
| P15 | 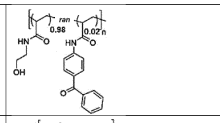 | Poly(HEAm$_{98}$-*ran*-BPAm$_{2}$) | Freie Radikalische (FR) Polymerisation |
| P16 | 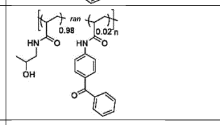 | Poly(HPAm$_{98}$-*ran*-BPAm$_{2}$) | Freie Radikalische (FR) Polymerisation |
| P17 | 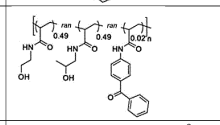 | Poly(HEAm$_{49}$-*ran*-HPAm$_{49}$-*ran*-BPAm$_{2}$) | Freie Radikalische (FR) Polymerisation |
| P18 | 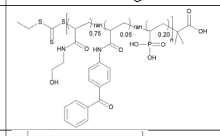 | RAFT-Poly(HEAm$_{75}$-*ran*-VPA$_{20}$-*ran*-BPAm$_{5}$)-EMP | Reversible Addition-Fragmentation Chain Transfer (RAFT) Polymersiation |
| P19 | 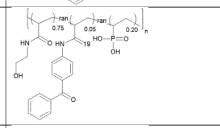 | Poly(HEAm$_{75}$-*ran*-VPA$_{20}$-*ran*-BPAm$_{5}$) | Freie Radikalische (FR) Polymerisation |
| AP1 | 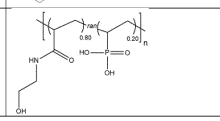 | Poly(HEAm$_{80}$-*ran*-VPA$_{20}$) | Freie Radikalische (FR) Polymerisation |





| | | | |
|---|---|---|---|
| AP2 | 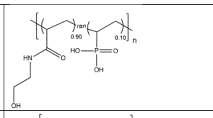 | Poly(HEAm$_{90}$-*ran*-VPA$_{10}$) | Freie Radikalische (FR) Polymerisation |
| AP3 | 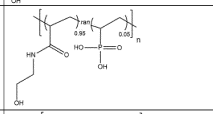 | Poly(HEAm$_{95}$-*ran*-VPA$_{5}$) | Freie Radikalische (FR) Polymerisation |
| AP4 | 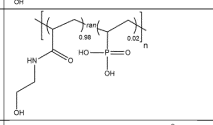 | Poly(HEAm$_{98}$-*ran*-VPA$_{2}$) | Freie Radikalische (FR) Polymerisation |
| AP5 | 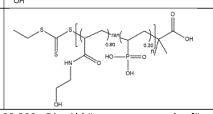 | RAFT-Poly(HEAm$_{80}$-*ran*-VPA$_{20}$)-EMP | Reversible Addition-Fragmentation Chain Transfer (RAFT) Polymersiation |

n = 2 bis 100.000. Die Abkürzung -*ran*- steht für die zufällige (englisch: random) Abfolge der Wiederholungseinheiten im Copolymer. Molmassen (FR): 50 - 500 kg/mol. Molmassen (RAFT): 2 – 40 kg/mol. Bei allen spezifischen Polymerstrukturen entspricht die im Index geschriebene Zahl dem molaren Verhältnis des Feed-ins. Beispiel: Poly(HEAm$_{98}$-*ran*-BPAm$_{2}$) bedeutet, dass 98 mol% HEAm und 2 mol% BPAm als Stoffmengenverhältnis zu Beginn der Polymerisation verwendet wurden.

Besonders bevorzugte Polymere gemäß der Erfindung sind:

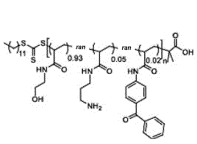
,
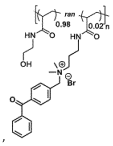
und
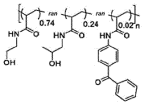
,

wobei n eine Ganzzahl von 2 bis 100.000 ist, wie beispielsweise eine Ganzzahl von 50 bis 10.000, z.B. eine Ganzzahl von 100 bis 2.000.

Ein besonders bevorzugtes Ankerpolymer gemäß der Erfindung ist:

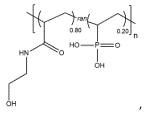

,

wobei n eine Ganzzahl von 2 bis 100.000 ist, wie beispielsweise eine Ganzzahl von 50 bis 10.000, z.B. eine Ganzzahl von 100 bis 2.000.

Basierend auf den vorhergehend beschriebenen Polymeren der Erfindung stellt die vorliegende Erfindung in einem weiteren Aspekt ein **Hydrogel** bereit, welches ein vernetztes Polymer gemäß der Erfindung umfasst.

In einem weiteren Aspekt stellt die vorliegende Erfindung eine **Beschichtung** bereit, welche mindestens eine Schicht umfasst, die ein Polymer gemäß der Erfindung umfasst.

Eine Beschichtung gemäß der Erfindung kann verschiedene Anwendungsformen annehmen, die von der Art der Herstellung und der Polymerzusammensetzung abhängen. Beispielhafte Anwendungsformen schließen Einschicht- und Zweischicht-(Sandwich)-Systeme ein.

Gemäß einiger Ausführungsformen umfasst die Beschichtung eine Schicht, die ein Polymer der allgemeinen Formel (I) mit $x_{[2]}$ >0 bis <1, $x_{[3]}$ >0 bis <1; und optional $x_{[4]}$ >0 bis <1 umfasst.

Gemäß einiger weitere Ausführungsformen umfasst die Beschichtung eine erste Schicht, die ein Polymer der allgemeinen Formel (I) mit $x_{[2]}$ 0, $x_{[3]}$ >0 bis <1; und optional x[4] >0 bis <1 umfasst, und eine zweite Schicht, die ein Polymer der allgemeinen Formel (I) mit $x_{[2]}$ >0 bis <1, $x_{[3]}$ = 0; und optional x[4] >0 bis <1 umfasst. In diesen Ausführungsformen können die erste und zweite Schichte in vorteilhafterweise miteinander kreuzvernetzt sein.

In einem weiteren Aspekt stellt die vorliegend Erfindung ein **metallhaltiges Substrat** bereit, dass dadurch gekennzeichnet ist, dass mindestens ein Teil seiner Oberfläche mit einer Beschichtung überzogen ist, welche mindestens eine Schicht umfasst, die ein Polymer gemäß der Erfindung umfasst.

Gemäß einiger Ausführungsformen ist mindestens ein Teil der Oberfläche des metallhaltigen Substrats mit einer Beschichtung gemäß der Erfindung überzogen.

Gemäß einiger Ausführungsformen ist die vollständige Oberfläche des metallhaltigen Substrats mit einer erfindungsgemäßen Beschichtung überzogen.

Gemäß einiger Ausführungsformen besteht das Substrat aus einem Metall.

Gemäß einiger Ausführungsformen besteht das Substrat aus einem Metall, das in Implantaten Verwendung findet.

Beispielhafte Metalle, die als Substrat gemäß der Erfindung dienen können, schließen Titan, Titanlegierungen, Aluminium, Aluminiumlegierungen, Zink, Zinklegierungen, Zinn, Zinnlegierungen,





Zirkonium, Zirkoniumlegierungen, Tantal, Tantallegierungen, Kobalt, Kobaltlegierungen, Nickel, Nickellegierungen, Kupfer, Kupferlegierungen, Magnesium, Magnesiumlegierungen, Molybdän, Molybdänlegierungen, Niob, Nioblegierungen, Chrom, Chromlegierungen, Eisen, Eisenlegierungen, rostfreier Stahl, und Metalloxide davon ein.

Beispielhafte, jedoch nicht einschränkende, Metalle, die üblicherweise Verwendung in Implantaten finden, sind Kobalt-Chrom-Molybdän-Legierungen, z.B. implavit® CoCrMo, unlegiertes Titan (Reintitan), Titan-Aluminium-Vanadium-Legierungen wie TiAl6V4 oder Ti6AL4V ELI, Titan-Aluminium-Niob-Legierungen wie TiAl6Nb7, und rostfreier Stahl.

Gemäß einiger Ausführungsformen umfasst das Metall ein Metalloxid, vorzugsweise auf seiner Oberfläche.

Nicht-einschränkende Beispiele für Metalloxide schließen $TiO_2$, $AlO_2$, ZnO, $ZrO_2$, ITO, IZO, $NiO_x$, $NiCoO_x$, $MoO_x$ $Fe_2O_3$, oder $Nb_2O_5$ ein.

Gemäß einiger Ausführungsformen umfasst das Metall Titanoxid, beispielswiese $TiO_2$.

Gemäß einiger Ausführungsformen umfasst oder besteht das Substrat aus Titan, Titanoxid oder einer Titanlegierung. Beispielhafte Titanlegierung sind oben beschrieben.

In einem weiteren Aspekt stellt die vorliegend Erfindung eine **Vorrichtung** bereit, die ein erfindungsgemäßes Substrat umfasst.

Gemäß einiger Ausführungsformen bildet das Substrat mindestens einen Teil der Oberfläche der Vorrichtung.

Gemäß einiger Ausführungsformen bildet das Substrat die vollständige Oberfläche der Vorrichtung.

Gemäß einiger Ausführungsformen ist die Vorrichtung eine medizinische Vorrichtung, wie beispielswiese ein Implantat.

Entsprechend stellt die vorliegende Erfindung in einem besonderen Aspekt ein Implantat bereit, welches dadurch gekennzeichnet ist, dass mindestens ein Teil seiner metallhaltigen Oberfläche mit einer erfindungsgemäßen Beschichtung überzogen ist. Weitere Ausführungsformen ergeben sich aus den zuvor beschriebenen.

Wie oben bereits erwähnt verhindert eine Beschichtung von, beispielsweise, Implantaten mit den erfindungsgemäßen Polymernetzwerken unter anderem eine Adhäsion von Zellen und Gewebe auf der Oberfläche des Implantats. Somit eignen sich Implantate, die eine erfindungsgemäße Beschichtung aufweisen, besonders als Kurzzeitimplantate. Entsprechend stellt die vorliegende Erfindung in einem weiteren Aspekt die Verwendung eines erfindungsgemäßen Implantats als Kurzzeitimplantat bereit.

In weiteren Aspekten stellt die vorliegende Erfindung Verfahren zur Beschichtung von Substraten und Vorrichtungen (wie beispielsweise von medizinischen Vorrichtungen, wie ein Implantat) bereit.

Insbesondere stellt die vorliegende Erfindung ein **Verfahren** zur Beschichtung eines Substrats bereit, umfassend die Schritte

(a) Bereitstellen eines metallhaltigen Substrates, und

(b) In-Kontakt-Bringen des Substrates mit einer Lösung eines Polymers gemäß der Erfindung;

(c) gegebenenfalls Trocknen des Substrates; und





(d) gegebenenfalls UV-Bestrahlung.

Ferner stellt die vorliegende Erfindung ein **Verfahren** zur Beschichtung einer Vorrichtung, wie beispielsweise einer medizinischen Vorrichtung, bereit, umfassend die Schritte

(a) Bereitstellen einer Vorrichtung, umfassend ein metallhaltiges Substrat, und

(b) In-Kontakt-Bringen der Vorrichtung bzw. des Substrates mit einer Lösung eines Polymers gemäß der Erfindung;

(c) gegebenenfalls Trocknen des Substrates; und

(d) gegebenenfalls UV-Bestrahlung.

Gemäß einiger Ausführungsformen umfasst Schritt (b) ein erstes In-Kontakt-Bringen der Vorrichtung bzw. des Substrates mit einer Lösung eines Polymer der allgemeinen Formel (I) mit $x_{[2]}$ 0, $x_{[3]}$ >0 bis <1; und optional x[4] >0 bis <1, gefolgt von einem zweiten In-Kontakt-Bringen der Vorrichtung bzw. des Substrates mit einer Lösung eines Polymer der allgemeinen Formel (I) mit $x_{[2]}$ >0 bis <1, $x_{[3]}$ = 0; und optional $x_{[4]}$ >0 bis <1 (Zwei-Schicht-System). Nach dem ersten In-Kontakt-Bringen und dem zweiten In-Kontakt-Bringen kann jeweils ein Trocknungsschritt erfolgen.

Gemäß einiger Ausführungsformen umfasst Schritt (b) das In-Kontakt-Bringen der Vorrichtung bzw. des Substrates mit einer Lösung eines Polymers der allgemeinen Formel (I) mit $x_{[2]}$ >0 bis <1, $x_{[3]}$ >0 bis <1; und optional $x_{[4]}$ >0 bis <1 (Einschichtsystem).

Das In-Kontakt-Bringen kann durch jedes dem Fachmann zum Aufbringen von Polymerlösungen auf Oberflächen bekannten Verfahren erfolgen, wie beispielsweise durch das Besprühen oder Begießen mit oder Eintauchen in der/die Lösung/en.

Am Ende der Prozedur kann ein "Waschschritt" erfolgen, um nicht anhaftende Polymerreste und/oder niedermolekulare Verbindungen zu entfernen.

In einem weiteren Aspekt stellt die vorliegend Erfindung die **Verwendung** eines erfindungsgemäßen Polymers als antiadhäsive Beschichtung, vorzugsweise als antiadhäsive Beschichtung auf einer medizinischen Vorrichtung, ferner bevorzugt als antiadhäsive Beschichtung auf einem Implantat, bereit.

In einem weiteren Aspekt stellt die vorliegend Erfindung ein erfindungsgemäßes **Polymer zur Verwendung** in einem Verfahren zu Behandlung einer Knochenfraktur in einem Patienten bereit, wobei das Verfahren die folgenden Schritte umfasst

a) Bereitstellen eines Implantats, umfassend ein Substrat, das dadurch gekennzeichnet ist, dass mindestens ein Teil seiner Oberfläche mit einerBeschichtung überzogen ist, welche mindestens eine Schicht umfasst, die ein erfindungsgemäßes Polymer umfasst; und

b) Einsetzen des Implantats an einer Knochenreparaturstelle oder im Bereich der Knochenfraktur im Patienten.

Gemäß einiger Ausführungsformen ist die Beschichtung eine erfindungsgemäße Beschichtung.

Gemäß einiger Ausführungsformen ist das Implantat ein erfindungsgemäßes Implantat.

In einem weiteren Aspekt stellt die vorliegende Erfindung ein Monomer bereit, welches eine Struktur der allgemeinen Formel (II) aufweist





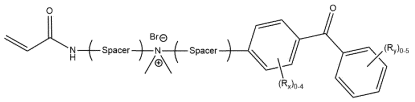

(II);

wobei jeder „Spacer" jeweils unabhängig voneinander ausgewählt ist aus der Gruppe bestehend aus linearen oder verzweigten Alkylketten und linearen oder verzweigten Ethylen- oder Propylenoxidketten, vorzugweise unabhängig voneinander ausgewählt aus linearen oder verzweigen $C_{1-20}$-Alkylketten;

$R_x$, jeweils unabhängig voneinander, -OH, Halogen (Br, Cl, I, oder F), Halogen-$C_{1-4}$ Alkyl (z.B. $-CF_3$, $-CCL_3$, $-CBr_3$, $-Cl_3$), $-NH_2$, $-C_{1-4}$ Alkyl, $-C_{2-4}$ Alkenyl, $-C_{2-4}$ Alkinyl, $-OC_{1-4}$ Alkyl, $-OC_{2-4}$ Alkenyl, $-OC_{2-4}$ Alkinyl $-NO_2$, -SH, $-SO_2H$, $-SO_3H$, -NCS, -SCN, -COOH oder Cyano ist; und

$R_y$, jeweils unabhängig voneinander, -OH, Halogen (Br, Cl, I, oder F), Halogen-$C_{1-4}$ Alkyl (z.B. $-CF_3$, $-CCL_3$, $-CBr_3$, $-Cl_3$), $-NH_2$, $-C_{1-4}$ Alkyl, $-C_{2-4}$ Alkenyl, $-C_{2-4}$ Alkinyl, $-OC_{1-4}$ Alkyl, $-OC_{2-4}$ Alkenyl, $-OC_{2-4}$ Alkinyl $-NO_2$, -SH, $-SO_2H$, $-SO_3H$, -NCS, -SCN, -COOH oder Cyano ist.

Gemäß einiger Ausführungsformen stellt die vorliegende Erfindung ein Monomer bereit, welches eine Struktur der allgemeinen Formel (IIa) aufweist

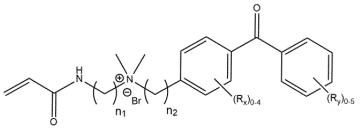

(IIa)

wobei $n_1$ und $n_2$ jeweils unabhängig voneinander 1, 2, 3, 4, 5, 6, 7, 8, 9, 10, 11, 12, 13, 14, 15, 16, 17, 18, 19 oder 20 ist;

$R_x$, jeweils unabhängig voneinander, -OH, Halogen (Br, Cl, I, oder F), Halogen-$C_{1-4}$ Alkyl (z.B. $-CF_3$, $-CCL_3$, $-CBr_3$, $-Cl_3$), $-NH_2$, $-C_{1-4}$ Alkyl, $-C_{2-4}$ Alkenyl, $-C_{2-4}$ Alkinyl, $-OC_{1-4}$ Alkyl, $-OC_{2-4}$ Alkenyl, $-OC_{2-4}$ Alkinyl $-NO_2$, -SH, $-SO_2H$, $-SO_3H$, -NCS, -SCN, -COOH oder Cyano ist; und

$R_y$, jeweils unabhängig voneinander, -OH, Halogen (Br, Cl, I, oder F), Halogen-$C_{1-4}$ Alkyl (z.B. $-CF_3$, $-CCL_3$, $-CBr_3$, $-Cl_3$), $-NH_2$, $-C_{1-4}$ Alkyl, $-C_{2-4}$ Alkenyl, $-C_{2-4}$ Alkinyl, $-OC_{1-4}$ Alkyl, $-OC_{2-4}$ Alkenyl, $-OC_{2-4}$ Alkinyl $-NO_2$, -SH, $-SO_2H$, $-SO_3H$, -NCS, -SCN, -COOH oder Cyano ist.

Gemäß einiger Ausführungsformen ist $n_1$ 1, 2, 3, 4, 5, 6, 7, 8, 9 oder 10.

Gemäß einiger Ausführungsformen ist $n_1$ 1, 2, 3, 4 oder 5.

Gemäß einiger Ausführungsformen ist $n_1$ 1, 2 oder 3.

Gemäß einiger Ausführungsformen ist $n_1$ 3.

Gemäß einiger Ausführungsformen ist $n_2$ 1, 2, 3, 4, 5, 6, 7, 8, 9 oder 10.

Gemäß einiger Ausführungsformen ist $n_2$ 1, 2, 3, 4 oder 5.

Gemäß einiger Ausführungsformen ist $n_2$ 1, 2 oder 3.

Gemäß einiger Ausführungsformen ist $n_2$ 1.

Gemäß einiger Ausführungsformen weißt das Monomer der Formel (IIa) folgende Struktur auf

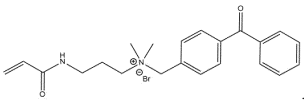

Monomere der Formel (II) oder (IIa) sind multifunktional, d.h. sie fungieren als Monomer, Photovernetzer und weisen ferner eine antibakterielle Wirkung auf.

In einem weiteren Aspekt stellt die vorliegende Erfindung die **Verwendung** eines Monomers der Formel (II) oder (IIa) als Photovernetzer bereit.

Nachdem diese Erfindung allgemein beschrieben wurde, kann ein weiteres Verständnis unter Bezugnahme auf die nachfolgenden spezifischen Ausführungsbeispiele erhalten werden, welche nur zur Veranschaulichung dient und nicht einschränkend gewertet werden soll, sofern nichts anderweitig angegeben wird.

**Ausführungsbeispiele**

**1. Synthese der Polymere**

Die dem Hydrogel zugrundeliegenden Polymerketten werden aus Kombinationen von zwei bis vier der entsprechenden Monomere *via* freier radikalischer Polymerisation oder „reversible addition-fragmentation chain transfer polymerization" (RAFT-Polymerisation) unter Zugabe von Radikalinitiatoren und etwaigen Kettenübertragungsreagenzien (im Falle der RAFT-Polymerisation) hergestellt. Die in den vorliegenden Ausführungsbeispielen synthetisierten Polymer sind in der obigen Tabelle 1 aufgeführt, und wurden mit den Bezeichnungen P1-P19 und AP1 bis AP5 abgekürzt.

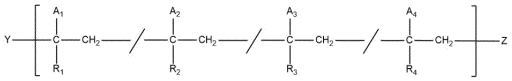

$x_{[1]} = 1 - x_{[2]} - \ldots - x_{[4]} = >0$ bis <1 $\quad x_{[2]} = 0$ bis <1 und $x_{[2]} + x_{[3]} = >0$ bis <1 $\quad x_{[3]} = 0$ bis <1 $\quad x_{[4]} = 0$ bis <1

**(I)**

mit $A_1$ = -H, $A_2$ = -H, $A_3$ = -H, und $A_4$ = -H.





Generische Polymerstruktur: a) hydrophiles Hauptmonomer ($R_1$), b) Benzophenonderivat als Vernetzermonomer ($R_2$), c) Ankermonomer für Titanoberflächen ($R_3$) und d) Comonomer ($R_4$), sowie e) Kettenübertragungsreagenz (Z und Y) bzw. Endgruppen (Z und Y).

**1.1 Wiederholungseinheiten und Reagenzien**

a) Hydrophiles Hauptmonomer:

$R_1$:

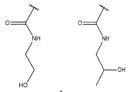

oder .

Die synthetisierten Polymere bestehen aus mindestens einem der o.g. Hauptmonomere oder aus deren Kombinationen in veränderlichen Verhältnissen mit Anteilen von 20-99.5 mol%.

b) Benzophenonderivat als Vernetzermonomer:

$R_2$:

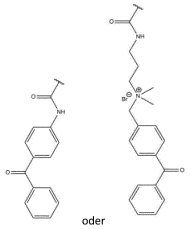

oder ;

Die synthetisierten Polymere beinhalten eines der o.g. benzophenonbasierten Vernetzermonomere in einem Anteil von 0.5-10 mol%. Durch das Vernetzermonomer mit quaternärer Ammoniumgruppe kann eine intrinsische antibakterielle Wirkung der Beschichtung hervorgerufen werden.

c) Ankermonomer für Titanoberflächen:

$R_3$:

Die Polymerbeschichtung enthält das Ankermonomer Vinylphosphonsäure (VPA) mit einem Anteil von 1-50 mol% in der Ankerpolymerschicht (Sandwichaufbau) oder im Beschichtungspolymer (Einschichtsystem).

d) Comonomer:

$R_4$:

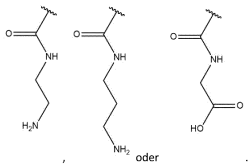

, oder .

Die synthetisierten Polymere beinhalten eines der o.g. Comonomere in einem Anteil von 0.5-10 mol%.

e) Kettenübertragungsreagenz (Z und Y)

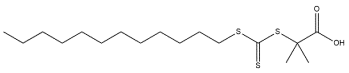

2-{[(Dodecylthio)carbothioyl]-thio}-2-methylpropansäure (DMP)

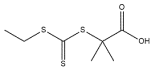

2-{[(Ethylthio)carbothioyl]-thio}-2-methylpropansäure (EMP)

Die in der hier beschriebenen Ausführungsbeispielen synthetisierten Polymere beinhalten das Kettenübertragungsreagenz 2-{[(Dodecylthio)carbothioyl]-thio}-2-methylpropansäure (DMP) oder 2 {[(Ethylthio)carbothioyl]-thio}-2-methylpropansäure (EMP) mit einem Anteil von 0-2 mol% (0 mol% = freie radikalische Polymerisation, >0 mol% = RAFT-Polymerisation).





f) Radikalinitiator:

Der Anteil des Intitiators Azobisisobutyronitril (AIBN) oder 2,2'-Azobis[2-(2-imidazolin-2-yl)propan]dihydrochlorid (AIPC) beträgt 0.1-5 mol%.

**1.2 *Synthesevorschrift für Coplyomere***

Für die Synthesen der Polymere P1 bis P19 sowie AP1 bis AP5 wurden in einem 10 ml Schlenkkolben jeweils die entsprechenden Monomere, der Initiator und gegebenenfalls das Kettenübertragungsreagenz (engl. „chain transfer agent", CTA) in Methanol (2-5 ml, gilt für P1-P17 und AP2-AP4) oder einem Wasser/1,4-Dioxan-Gemisch (V/V = 3:7, 2-5 ml, gilt für P18, P19, AP1 und AP5) gelöst. Die spezifischen Edukte und deren Mengen können der Tabelle 2 entnommen werden. Die Reaktionsmischung wurde durch Spülen mit Argon (30 min) entgast. Die Reaktionsgefäße wurden in ein vorgeheiztes Ölbad (65 °C) oder einen vorgeheizten Aluminiumblock (65 °C) für 16 bis 24 Stunden platziert. Die Reaktion wurde durch Kühlen mit flüssigem Stickstoff und Exposition des Gemisches mit Sauerstoff beendet. Die Polymere wurden mindestens zweimal in eisgekühltem Ethylacetat (200 ml) gefällt, daraufhin abfiltriert bzw. abzentrifugiert und über Nacht im Vakuum getrocknet.

Im Falle der Polymere P1, P2, P8 und P9 wurde das isolierte Polymer in Wasser (2.5 ml) aufgenommen und unter Zugabe von Trifluoressigsäure (0.5 ml) entschützt. Das Gemisch wurde bei Raumtemperatur über Nacht gerührt und danach in eisgekühltem Tetrahydrofuran (200 ml) ausgefällt. Der Niederschlag wurde abfiltriert und mit dem kationischen Anionenaustauscherharz Lewatit MP62 für 24 Stunden gerührt. Der Anionenaustauscher wurde danach abfiltriert und das Filtrat mittels Lyophilisation getrocknet.

**Tabelle 2**

| Nr. | Monomer(e) $A_1/R_1$ Name / mg / (mmol) | | Monomer $A_2/R_2$ Name / mg / (µmol) | Monomer $A_3/R_3$ Name / mg / (µmol) | Monomer $A_4/R_4$ Name / mg / (mmol) | CTA Name / mg / (µmol) | Initiator Name / mg / (µmol) |
|---|---|---|---|---|---|---|---|
| **P1** | HEAm 362 (3.14) | -- | BPAm 16.61 (66.2) | -- | APAm-Boc 38.0 (16.6) | DMP 6.02 (17.0) | AIBN 2.80 (17.4) |
| **P2** | HEAm 364 (3.16) | -- | BPAm 16.72 (66.6) | -- | AEAm-Boc 36.0 (17.0) | DMP 6.06 (17.0) | AIBN 2.80 (17.4) |
| **P3** | HEAm 289 (2.51) | HPAm 110 (0.85) | BPAm 17.2 (67.4) | -- | -- | DMP 6.12 (16.8) | AIBN 2.80 (17.4) |
| **P4** | HEAm 198 (1.72) | HPAm 212 (1.73) | BPAm 16.73 (65.6) | -- | -- | DMP 6.28 (17.3) | AIBN 2.80 (17.4) |
| **P5** | -- | HPAm 366 (2.83) | BPAm 15.07 (60.0) | -- | APAm-Boc 34.0 (14.8) | DMP 5.44 (15.0) | AIBN 2.40 (15.0) |

| | | | | | | | |
|---|---|---|---|---|---|---|---|
| **P6** | -- | HPAm/ 367 (2.84) | BPAm 15.07 (60.0) | -- | AEAm-Boc 32.0 (15.0) | DMP 5.46 (15.0) | AIBN 2.40 (15.0) |
| **P7** | HPAm 308 (2.38) | HEAm 97 (0.84) | BPAm 16.23 (63.6) | -- | -- | DMP 5.86 (16.1) | AIBN 2.80 (17.4) |
| **P8** | HEAm 377 (3.27) | -- | BPAm 17.33 (69.0) | -- | AaAm 22.0 (17.0) | DMP 6.28 (17.3) | AIBN 2.80 (17.4) |
| **P9** | -- | HPAm 380 (2.94) | BPAm 15.58 (61.8) | -- | AaAm 20.0 (15.0) | DMP 5.63 (15.5) | AIBN 2.50 (15.5) |
| **P10** | HEAm 500 (4.34) | -- | BPQAAm 38.2 (88.6) | -- | -- | -- | AIBN 3.64 (22.2) |
| **P11** | HEAm 500 (4.34) | HPAm 182 (1.41) | BPAm 29.5 (117) | -- | -- | -- | AIBN 4.82 (29.3) |
| **P12** | HEAm 212 (1.73) | HPAm 198 (1.72) | BPQAAm 28.3 (65.6) | -- | -- | -- | AIBN 2.91 (17.7) |
| **P13** | -- | HPAm 400 (3.10) | BPQAAm 26.7 (62.0) | -- | -- | -- | AIBN 2.59 (15.8) |
| **P14** | HEAm 289 (2.51) | HPAm 110 (0.85) | BPQAAm 29.1 (67.4) | -- | -- | -- | AIBN 2.82 (17.2) |
| **P15** | HEAm 500 (4.34) | -- | BPAm 22.3 (88.6) | -- | -- | -- | AIBN 3.64 (22.2) |
| **P16** | -- | HPAm 400 (3.10) | BPAm 15.58 (62.0) | -- | -- | -- | AIBN 2.50 (15.5) |
| **P17** | HEAm 212 (1.73) | HPAm 198 (1.72) | BPAm 16.73 (65.6) | -- | -- | -- | AIBN 2.80 (17.4) |
| **P18** | HEAm 200 (1.74) | -- | BPAm 29.1 (116) | VPA 50.0 (463) | -- | EMP 2.60 (11.6) | AIPC 3.75 (11.6) |
| **P19** | HEAm 200 (1.74) | -- | BPAm 29.1 (116) | VPA 50.0 (463) | -- | -- | AIPC 3.75 (11.6) |
| **AP1** | HEAm 200 (1.74) | -- | -- | VPA 46.9 (434) | -- | -- | AIPC 3.52 (10.9) |





| | | | | | | | |
|---|---|---|---|---|---|---|---|
| **AP2** | HEAm 200 (1.74) | -- | -- | VPA 20.8 (193) | -- | -- | AIBN 1.64 (8.88) |
| **AP3** | HEAm 200 (1.74) | -- | -- | VPA 9.87 (91.4) | -- | -- | AIBN 1.64 (8.88) |
| **AP4** | HEAm 200 (1.74) | -- | -- | VPA 3.84 (35.5) | -- | -- | AIBN 1.64 (8.88) |
| **AP5** | HEAm 200 (1.74) | -- | -- | VPA 46.9 (434) | -- | EMP 2.45 (10.9) | AIPC 3.52 (10.9) |

Mit CTA = chaint transfer agent (Kettenübertragungsreagenz), HEAm = *N*-(2-Hydroxyethyl)acrylamid, HPAm = *N*-(2-Hydroxypropyl)acrylamid, BPAm = *N*-(4-Benzoylphenyl)acrylamid, BPQAAm = [(4-Benzoylphenyl)methyl]dimethyl[3-(prop-2-enamido)-propyl]ammoniumbromid, VPA = Vinylphosphonsäure, APAm-Boc = *N-tert*-Butyloxycarbonyl-(*N'*-3-aminopropyl)acrylamid, AEAm-Boc= *N-tert*-Butyloxycarbonyl-(*N'*-3-aminoethyl)acrylamid, DMP = 2-{[[(Dodecylthio)carbothioyl]-thio}-2-methylpropansäure, EMP = 2-{[[(Ethylthio)carbothioyl]-thio}-2-methylpropansäure, AIBN = Azobis(isobutyronitril), AIPC = 2,2'-Azobis[2-(2-imidazolin-2-yl)propan]dihydrochlorid.

**Tabelle 3**

| Polymer-abkürzung | Ausbeute | Zahlenmittel der Molmasse $\overline{M_n}$ | Dispersität $Đ$ |
|---|---|---|---|
| **P1** | 92% | 34.6 kg/mol | 1.33 |
| **P2** | 98% | 33.3 kg/mol | 1.18 |
| **P3** | 83% | 34.9 kg/mol | 1.23 |
| **P4** | 73% | 39.4 kg/mol | 1.19 |
| **P5** | 76% | 14.5 kg/mol | 1.13 |
| **P6** | 78% | 10.9 kg/mol | 1.18 |
| **P7** | 66% | 36.3 kg/mol | 1.36 |
| **P8** | 67% | 31.9 kg/mol | 1.25 |
| **P9** | 66% | 34.0 kg/mol | 1.38 |
| **P10** | 83% | 40.4 kg/mol | 3.83 |
| **P11** | 82% | 69.3 kg/mol | 3.78 |
| **P12** | 76% | -- | -- |
| **P13** | 88% | -- | -- |
| **P14** | 91% | -- | -- |
| **P15** | 79% | 52.4 kg/mol | 3.21 |
| **P16** | 79% | -- | -- |
| **P17** | 75% | -- | -- |





| | | | |
|---|---|---|---|
| **P18** | 65% | -- | -- |
| **P19** | 85% | -- | -- |
| **AP1** | 60% | -- | -- |
| **AP2** | 85% | -- | -- |
| **AP3** | 85% | -- | -- |
| **AP4** | 83% | -- | -- |
| **AP5** | 73% | -- | -- |

**2. Beschichtungsverfahren**

Für das Beschichtungsverfahren werden zwei unterschiedliche Strategien angewendet, welche mit Polymeren unterschiedlicher Kombination der oben genannten Monomerspezies durchgeführt werden können.

1. Sandwichaufbau: Das Titansubstrat wird in einer Lösung des Ankerpolymers inkubiert, welches aus Hauptmonomer und Ankermonomer besteht. In einem zweiten Schritt wird eine Lösung des Beschichtungspolymers bestehend aus Hauptmonomer und Vernetzermonomer durch ein einfaches Verfahren (*Beispiel:* Sprühen oder Eintauchen) aufgetragen und eingetrocknet. Die Vernetzung der trockenen Polymerschichten wird durch Bestrahlung mit UV-Licht induziert und simultan das Implantat sterilisiert.

2. Einschichtsystem: Das Titansubstrat wird in einer Lösung des Polymers inkubiert, welches aus Hauptmonomer, Ankermonomer und Vernetzermonomer besteht, und anschließend getrocknet. Die Vernetzung der trockenen Polymerschicht wird durch Bestrahlung mit UV-Licht induziert und simultan das Implantat sterilisiert.

*Beschichtungsprozedur:* Die Titanscheiben für Zelladhäsionstests wurden über Nacht in einer wässrigen Hellmanexlösung (1-3%) gerührt. Anschließend wurden die Scheiben mit reichlich Wasser und Ethanol gespült und im Stickstoffstrom getrocknet. Die getrockneten Titansubstrate wurden mit einem Coronaentlader behandelt und unverzüglich in Wasser getaucht. Danach wurden sie über Nacht in wässrigen Lösungen des Einschichtpolymers (P18, P19) oder des Ankerpolymers (1-10 $mg \cdot ml^{-1}$) inkubiert. Die Scheiben wurden nach Abspülen mit Wasser und Ethanol im Vakuumofen (10 mbar, 40°C) getrocknet.

1. Für den Sandwichaufbau wurden Stammlösungen der Polymere P1 bis P17 in einer Wasser/Ethanol-Mischung (70:30 V/V) mit einer Konzentration von 25 $mg \cdot ml^{-1}$ hergestellt. Auf die Substrate wurden dann 200 µl der zu testenden Polymerlösung gegeben und diese im Vakuumofen (10 mbar, 40°C) eingedampft. Daraufhin wurden die Scheiben für eine Stunde mit UV-Licht einer Wellenlänge von 254 nm bestrahlt. Die beschichteten Substrate wurden durch Inkubation in Wasser für mehrere Stunden gewaschen und abschließend im Vakuumofen (10 mbar, 40°C) getrocknet.

2. Für das Einschischtsystem (Polymere P18 und P19) wurden die Scheiben für eine Stunde mit UV-Licht einer Wellenlänge von 254 nm bestrahlt, die beschichteten Substrate durch Inkubation in Wasser für mehrere Stunden gewaschen und abschließend im Vakuumofen (10 mbar, 40°C) getrocknet.

**3. Zelladhäsions- und Bakterientests**





Vor den Zell- und Bakterientests wurde die Zytotoxizität der Polymere analog zur DIN ISO 10993-5-Norm überprüft (Biologische Beurteilung von Medizinprodukten – Prüfung auf In-vitro-Zytotoxizität). Diese Tests zeigten, dass die genutzten Polymere keinerlei zytotoxische Wirkung entfalten.

In einem ersten Zellversuch wurden primäre Fibroblasten bzw. Tenozyten auf mit Polymer teilbeschichteten Zellkulturplatten ausgesät. Abbildung 1 zeigt am Beispiel der Tenozyten, dass die Zellen ausschließlich auf dem unbeschichteten Teil der Platte wachsen. Auf dem mit Polymer beschichteten Teil findet keine Adhäsion der Zellen statt. Auch auf voll beschichteten Platten konnte keine Zelladhäsion detektiert werden, jedoch konnte gezeigt werden, dass die nicht adhärenten Zellen vital sind, da sie nach Überführung auf eine Zellkulturplatte adhärierten und proliferierten.

Anschließend wurde das Polymer wie zuvor beschrieben auf Titanscheiben aufgebracht und die Adhäsion der Zellen untersucht. Abbildung 2A zeigt, dass auf der mit Polymer beschichteten Titanoberfläche keinerlei Zelladhäsion stattfindet. Abbildung 2B zeigt die Adhäsion der Zellen auf einer unbeschichteten Titanplatte. Wie schon bei der beschichteten Zellkulturoberfläche konnte gezeigt werden, dass auch die nicht adhärenten Zellen vital sind, da sie nach Überführung auf eine nicht beschichtete Titanplatte adhärierten und proliferierten.

Das Bakterium, das hauptsächlich für die Infektionen im Bereich der Knochenosteosynthese verantwortlich ist, ist der *Staphylococcus aureus*. Daher wurde dieser Bakterienstamm in Medium verdünnt auf den Polymerschichten aufgebracht und nach 24 h das Medium in unterschiedlichen Verdünnungen auf Agarplatten ausgesät und die CFU (colony forming units) detektiert. In der Kontrolle, die mit einem nicht antibakteriell wirkenden Polymer auf einer Platte inkubiert wurde, sieht man eine hohe Anzahl von CFUs (Abbildung 3A), wohingegen auf der Probe, die auf einer mit einem antibakteriell wirkenden Polymer beschichteten Platte inkubiert wurde, keine CFUs nachgewiesen werden konnten (Abbildung 3B), was für eine deutliche antimikrobielle Wirkung der entsprechenden Polymere spricht.

**Tabelle 3: Bewertung der Zelladhäsionstests**

| Polymer-abkürzung | Zelltyp | Kein Wachstum | Keine Zytotoxizität | Kein Bakterien-wachstum |
|---|---|---|---|---|
| P1 | Fibroblasten | +++++ | +++++ | |
| P1 | Tenozyten | ++++ | +++++ | |
| P2 | Fibroblasten | +++++ | + | |
| P3 | Fibroblasten | ++++ bis +++++ | ++ | |
| P4 | Fibroblasten | ++++ bis +++++ | + | |
| P4 | Tenozyten | ++ | + | |
| P5 | Fibroblasten | ++++ | +++++ | |
| P6 | Fibroblasten | + | +++++ | |
| P7 | Fibroblasten | +++++ | + | |
| P7 | Tenozyten | ++++ | o | |
| P8 | Fibroblasten | ++++ | o | |
| P9 | Fibroblasten | ++ ++ | o | |

| | | | | |
|---|---|---|---|---|
| P10 | Fibroblasten | +++++ | +++++ | Staph.aureus +++++ |
| P10 | Tenozyten | ++++ | +++++ | |
| P11 | Fibroblasten | +++++ | +++++ | |
| P11 | Tenozyten | o | +++++ | |
| P12 | Fibroblasten | +++++ | +++++ | |
| P12 | Tenozyten | +++ ++ | +++++ | |
| P14 | Fibroblasten | +++ | +++++ | |
| P14 | Tenozyten | ++++ | +++++ | |
| P15 | Fibroblasten | o | +++++ | Staph.aureus o |
| P15 | Tenozyten | ++++ | +++++ | |
| P16 | Fibroblasten | + | +++++ | |
| P16 | Tenozyten | ++++ | +++++ | |

Bewertung von o bis +++++ (o = höheres Zell-/Bakterienwachstum bzw. höhere Zytotoxizität und +++++ = geringeres Zell-/Bakterienwachstum bzw. geringere Zytotoxizität).

Zusammenfassend lässt sich sagen, dass die Beschichtungen eine Adhäsion von Fibroblasten (Hauptzelltyp des menschlichen Bindegewebes) und Tenozyten (charakteristische Zelle der menschlichen Sehne) erfolgreich verhindern konnten, ohne zytotoxisch auf diese zu wirken. Außerdem konnte eine antibakterielle Wirkung spezieller Polymerstrukturen nachgewiesen werden.





**Referenzen**


[1] C. A. Jeffrey, A medical implant and a method of coating a medical implant, WO2018107243 A1, Dec 15, 2017.

[2] A. P. Shete, A. A. Nisal, A. K. Lele, A process for coating a biomedical implant with a biocompatible polymer and a biomedical implant therefrom, WO2018173074 A1, Mar 23, 2018.

[3] Y. Lee, S. A. Kang, T. H. Choi, J. U. Park, S. A. Kim, et al., Method for coating implant using heat, WO2020231073 A1, May 07, 2020.

[4] H.-E. Kim, S.-M. Lee, J. Kim, S. M. Chung, Method for manufacturing hydroxyapatite-coated zirconia implant by means of dip coating using hydroxyapatite sol, WO2020204254 A1, May 15, 2019.

[5] H. D. Link, Verfahren zum Herstellen einer Implantatbeschichtung und entsprechendes Implantat, WO2012163950 May 30, 2012.

[6] H.-G. Neumann, C. Prinz, Antibacterial and osteoinductive implant coating, method of producing such coating, and implant coated with same, EP2617439 B1, Jan 15, 2013.

[7] E. Wintermantel, S.-W. Ha, Springer, Medizintechnik – Life Science Engeneering, 2008, DOI: 10.1007/978-3-540-74925-7.

[8] N. G. Grün, N. Donohue, P. Holweg, A.-M. Weinberg, J. Miner. Stoffwechs. Muskuloskelet. Erkrank., (25), 82–89, Resorbierbare Implantate in der Unfallchirurgie, 2018, DOI: 10.1007/s41970-018-0041-6.






**Patentansprüche**

1. **Polymer** aufweisend eine Struktur der allgemeinen Formel (I)

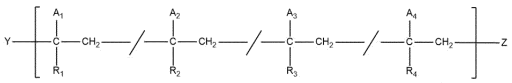

$x_{[1]} = 1 - x_{[2]} - ... - x_{[4]} = >0$ bis <1 $x_{[2]} = 0$ bis <1 und $x_{[2]} + x_{[3]} = >0$ bis <1 $x_{[3]} = 0$ bis <1 $x_{[4]} = 0$ bis <1

**(I)**

wobei

$A_1$ -H oder $-CH_3$ ist;

$A_2$ -H oder $-CH_3$ ist;

$A_3$ -H oder $-CH_3$ ist;

$A_4$ -H oder $-CH_3$ ist;

$R_1$, für jede Wiederholungseinheit, unabhängig ausgewählt ist aus der Gruppe bestehend aus

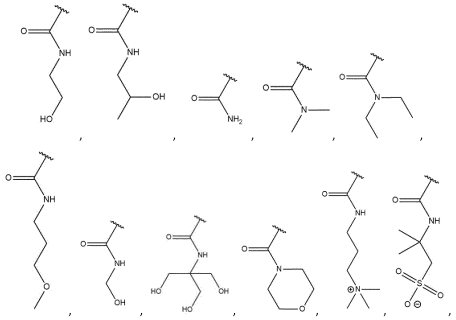





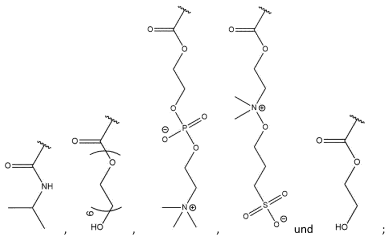

und ;

$R_2$, für jede Wiederholungseinheit, unabhängig ausgewählt ist aus der Gruppe bestehend aus

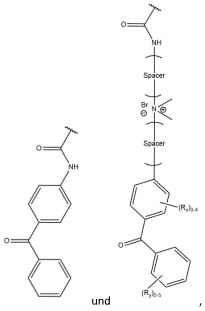

und ,

wobei jeder „Spacer" jeweils unabhängig voneinander ausgewählt ist aus der Gruppe bestehend aus linearen oder verzweigten Alkylketten und linearen oder verzweigten Ethylen- oder Propylenoxidketten, vorzugweise unabhängig voneinander ausgewählt aus linearen oder verzweigen $C_{1-20}$-Alkylketten;

$R_x$, jeweils unabhängig voneinander, -OH, Halogen (Br, Cl, I, oder F), Halogen-$C_{1-4}$ Alkyl (z.B. $-CF_3$, $-CCL_3$, $-CBr_3$, $-Cl_3$), $-NH_2$, $-C_{1-4}$ Alkyl, $-C_{2-4}$ Alkenyl, $-C_{2-4}$ Alkinyl, $-OC_{1-4}$ Alkyl, $-OC_{2-4}$ Alkenyl, $-OC_{2-4}$ Alkinyl $-NO_2$, -SH, $-SO_2H$, $-SO_3H$, -NCS, -SCN, -COOH oder Cyano ist; und

$R_y$, jeweils unabhängig voneinander, -OH, Halogen (Br, Cl, I, oder F), Halogen-$C_{1-4}$ Alkyl (z.B. $-CF_3$, $-CCL_3$, $-CBr_3$, $-Cl_3$), $-NH_2$, $-C_{1-4}$ Alkyl, $-C_{2-4}$ Alkenyl, $-C_{2-4}$ Alkinyl, $-OC_{1-4}$ Alkyl, $-OC_{2-4}$ Alkenyl, $-OC_{2-4}$ Alkinyl $-NO_2$, -SH, $-SO_2H$, $-SO_3H$, -NCS, -SCN, -COOH oder Cyano ist;

$R_3$, für jede Wiederholungseinheit, unabhängig ausgewählt ist aus der Gruppe bestehend aus

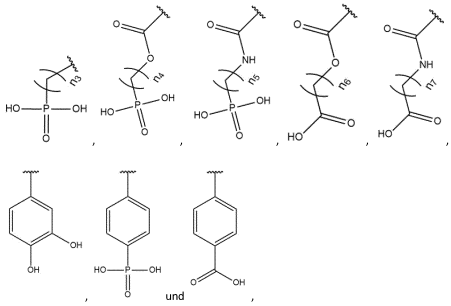

wobei $n_3$, $n_4$, $n_5$, $n_6$ und $n_7$ jeweils unabhängig voneinander 0, 1, 2, 3, 4, 5, 6, 7, 8, 9, 10, 11, 12, 13, 14, 15, 16, 17 oder 18 ist;

$R_4$, für jede Wiederholungseinheit, unabhängig ausgewählt ist aus der Gruppe bestehend aus

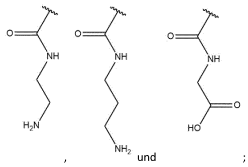

Y ein Fragment A eines Kettenübertragungsreagenzes oder eine Endgruppe ist; und

Z ein Fragment B des Kettenübertragungsreagenzes oder eine Endgruppe ist.

2. Polymer gemäß Anspruch 1, wobei $R_1$, für jede Wiederholungseinheit, unabhängig ausgewählt ist aus der Gruppe bestehend aus





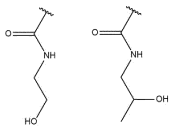

3. Polymer gemäß Anspruch 1 oder 2, wobei $R_2$, für jede Wiederholungseinheit, unabhängig ausgewählt ist aus der Gruppe bestehend aus

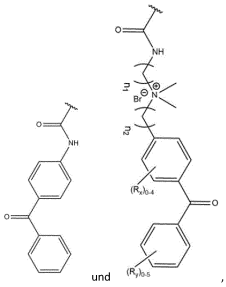

wobei $n_1$ und $n_2$ jeweils unabhängig voneinander 1, 2, 3, 4, 5, 6, 7, 8, 9, 10, 11, 12, 13, 14, 15, 16, 17, 18, 19 oder 20 ist;

$R_x$, jeweils unabhängig voneinander, -OH, Halogen (Br, Cl, I, oder F), Halogen-$C_{1-4}$ Alkyl (z.B. $-CF_3$, $-CCL_3$, $-CBr_3$, $-Cl_3$), $-NH_2$, $-C_{1-4}$ Alkyl, $-C_{2-4}$ Alkenyl, $-C_{2-4}$ Alkinyl, $-OC_{1-4}$ Alkyl, $-OC_{2-4}$ Alkenyl, $-OC_{2-4}$ Alkinyl $-NO_2$, -SH, $-SO_3H$, $-SO_3H$, -NCS, -SCN, -COOH oder Cyano ist; und

$R_y$, jeweils unabhängig voneinander, -OH, Halogen (Br, Cl, I, oder F), Halogen-$C_{1-4}$ Alkyl (z.B. $-CF_3$, $-CCL_3$, $-CBr_3$, $-Cl_3$), $-NH_2$, $-C_{1-4}$ Alkyl, $-C_{2-4}$ Alkenyl, $-C_{2-4}$ Alkinyl, $-OC_{1-4}$ Alkyl, $-OC_{2-4}$ Alkenyl, $-OC_{2-4}$ Alkinyl $-NO_2$, -SH, $-SO_3H$, $-SO_3H$, -NCS, -SCN, -COOH oder Cyano ist.

4. Polymer gemäß Anspruch 1 oder 2, wobei $R_2$, für jede Wiederholungseinheit, unabhängig ausgewählt ist aus der Gruppe bestehend aus





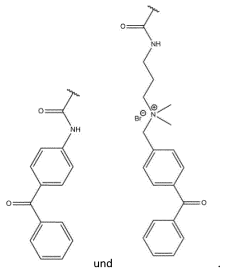

5. Polymer gemäß einem der Ansprüche 1 bis 4, wobei $R_3$, für jede Wiederholungseinheit, unabhängig ausgewählt ist aus der Gruppe bestehend aus

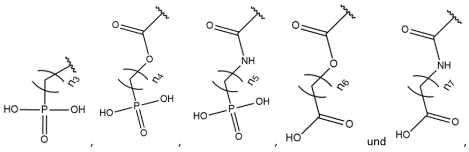

wobei $n_3$, $n_4$, $n_5$, $n_6$ und $n_7$ jeweils unabhängig voneinander 0, 1, 2, 3, 4, 5, 6, 7, 8, 9, 10, 11, 12, 13, 14, 15, 16, 17 oder 18 ist.

6. Polymer gemäß einem der Ansprüche 1 bis 4, wobei $R_3$, für jede Wiederholungseinheit,

ist.

7. Polymer gemäß einem der Ansprüche 1 bis 6, wobei $R_4$, für jede Wiederholungseinheit,





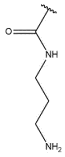

ist.

8. Polymer gemäß einem der Ansprüche 1 bis 7, wobei $A_1$, $A_2$ $A_3$ und $A_4$ jeweils -H sind.

9. Polymer gemäß Anspruch 1, wobei

$R_1$, für jede Wiederholungseinheit, unabhängig ausgewählt ist aus der Gruppe bestehend aus

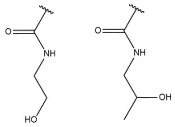

$R_2$, für jede Wiederholungseinheit, unabhängig ausgewählt ist aus der Gruppe bestehend aus

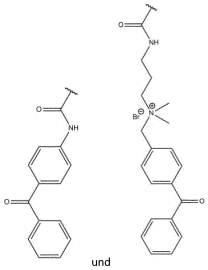

$R_3$, für jede Wiederholungseinheit, ist; und

$R_4$, für jede Wiederholungseinheit, unabhängig ausgewählt ist aus der Gruppe bestehend aus

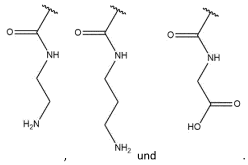

, und .

10. Polymer gemäß Anspruch 9, wobei $A_1$ -H ist, $A_2$ -H ist, $A_3$ -H ist, und $A_4$ -H ist.

11. Polymer gemäß einem der Ansprüche 1 bis 10, wobei Y 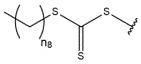 ist, und Z

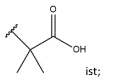

ist;

wobei $n_8$ eine Ganzzahl von 1 bis 24 ist, vorzugsweise eine Ganzzahl von 1 bis 14, weiter bevorzugt eine Ganzzahl von 1 bis 11; am bevorzugtesten 1 oder 11 ist.

12. Polymer gemäß einem der Ansprüche 1 bis 10, wobei Y und Z jeweils eine Endgruppe ist.

13. Polymer gemäß einem der Ansprüche 1 bis 12, wobei $x_{[2]}$ 0 ist und $x_{[3]}$ >0 bis <1 ist; und optional $x_{[4]}$ >0 bis <1 ist.

14. Polymer gemäß einem der Ansprüche 1 bis 12, wobei $x_{[2]}$ >0 bis <1 ist und $x_{[3]}$ 0 ist; und optional $x_{[4]}$ >0 bis <1 ist.

15. Polymer gemäß einem der Ansprüche 1 bis 12, wobei $x_{[2]}$ >0 bis <1 ist und $x_{[3]}$ >0 bis <1 ist; und optional $x_{[4]}$ >0 bis <1 ist.

16. Polymer gemäß Anspruch 1, ausgewählt aus der Gruppe bestehend aus





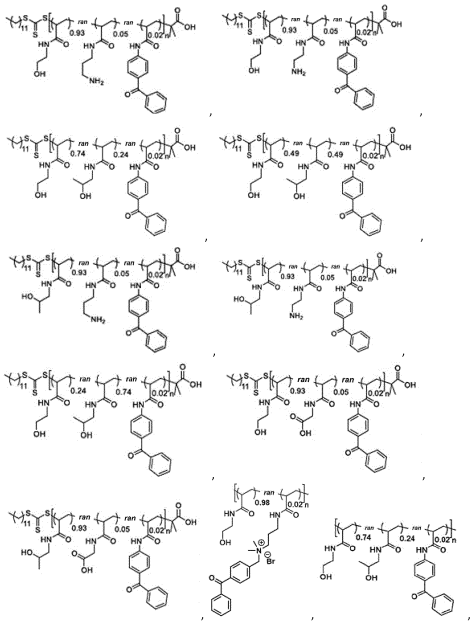





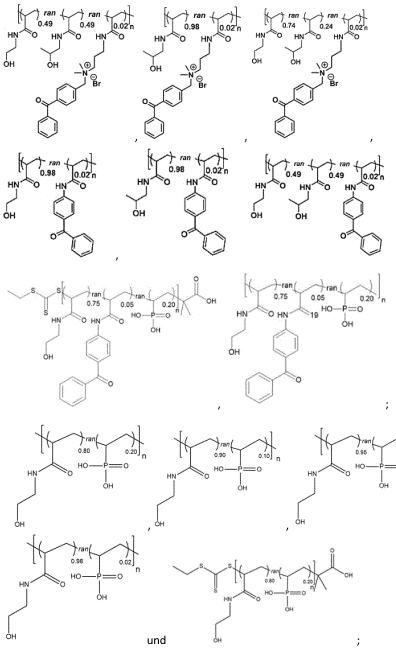

und ;

wobei n eine Ganzzahl von 2 bis 100.000 ist, wie beispielsweise eine Ganzzahl von 50 bis 10.000, z.B. eine Ganzzahl von 100 bis 2.000.

17. **Hydrogel**, umfassend ein vernetztes Polymer gemäß einem der Ansprüche 1 bis 16.

18. **Beschichtung**, umfassend mindestens eine Schicht, die ein Polymer gemäß einem der Ansprüche 1 bis 16 umfasst.





19. Beschichtung gemäß Anspruch 18, umfassend eine erste Schicht, die ein Polymer gemäß Anspruch 13 umfasst, und eine zweite Schicht umfasst, die ein Polymer gemäß Anspruch 14 umfasst.

20. Beschichtung gemäß Anspruch 18, die eine Schicht umfasst, die ein Polymer gemäß Anspruch 15 umfasst.

21. **Metallhaltiges Substrat**, dadurch gekennzeichnet, dass mindestens ein Teil seiner Oberfläche mit einer Beschichtung überzogen ist, welche mindestens eine Schicht umfasst, die ein Polymer gemäß einem der Ansprüche 1 bis 16 umfasst.

22. Substrat gemäß Anspruch 21, wobei das Substrat Titan oder eine Titanlegierung umfasst oder daraus besteht, vorzugsweise wobei das Titan oder die Titanlegierung ein Titanoxid umfasst.

23. **Vorrichtung**, umfassend ein Substrat gemäß Anspruch 21 oder 22.

24. Vorrichtung gemäß Anspruch 23, wobei die Vorrichtung eine medizinische Vorrichtung ist.

25. Vorrichtung gemäß Anspruch 24, wobei die medizinische Vorrichtung ein Implantat ist.

26. **Verwendung** einer Vorrichtung gemäß Anspruch 25 als Kurzzeitimplantat.

27. **Verwendung** des Polymers gemäß einem der Ansprüche 1 bis 16 als antiadhäsive Beschichtung, vorzugsweise als antiadhäsive Beschichtung auf einer medizinischen Vorrichtung, ferner bevorzugt als antiadhäsive Beschichtung auf einem Implantat.

28. **Monomer** aufweisend eine Struktur der allgemeinen Formel (II)

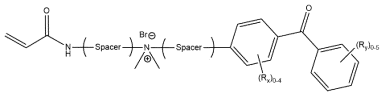

(II)

wobei jeder „Spacer" jeweils unabhängig voneinander ausgewählt ist aus der Gruppe bestehend aus linearen oder verzweigten Alkylketten und linearen oder verzweigten Ethylen- oder Propylenoxidketten, vorzugweise unabhängig voneinander ausgewählt aus linearen oder verzweigen $C_{1-20}$-Alkylketten;

$R_x$, jeweils unabhängig voneinander, -OH, Halogen (Br, Cl, I, oder F), Halogen-$C_{1-4}$ Alkyl (z.B. $-CF_3$, $-CCL_3$, $-CBr_3$, $-Cl_3$), $-NH_2$, $-C_{1-4}$ Alkyl, $-C_{2-4}$ Alkenyl, $-C_{2-4}$ Alkinyl, $-OC_{1-4}$ Alkyl, $-OC_{2-4}$ Alkenyl, $-OC_{2-4}$ Alkinyl $-NO_2$, -SH, $-SO_2H$, $-SO_3H$, -NCS, -SCN, -COOH oder Cyano ist; und

$R_y$, jeweils unabhängig voneinander, -OH, Halogen (Br, Cl, I, oder F), Halogen-$C_{1-4}$ Alkyl (z.B. $-CF_3$, $-CCL_3$, $-CBr_3$, $-Cl_3$), $-NH_2$, $-C_{1-4}$ Alkyl, $-C_{2-4}$ Alkenyl, $-C_{2-4}$ Alkinyl, $-OC_{1-4}$ Alkyl, $-OC_{2-4}$ Alkenyl, $-OC_{2-4}$ Alkinyl $-NO_2$, -SH, $-SO_2H$, $-SO_3H$, -NCS, -SCN, -COOH oder Cyano ist.

29. **Monomer** gemäß Anspruch 28, aufweisend eine Struktur der allgemeinen Formel (IIa)

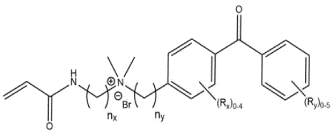

(IIa)

wobei $n_x$ und $n_y$ unabhängig voneinander eine Ganzzahl von 1 bis 20 sind;

$R_x$, jeweils unabhängig voneinander, -H, -OH, Halogen (Br, Cl, I, oder F), Halogen-$C_{1-4}$ Alkyl (z.B. -$CF_3$, -$CCL_3$, -$CBr_3$, -$Cl_3$), -$NH_2$, -$C_{1-4}$ Alkyl, -$C_{2-4}$ Alkenyl, -$C_{2-4}$ Alkinyl, -$OC_{1-4}$ Alkyl, -$OC_{2-4}$ Alkenyl, -$OC_{2-4}$ Alkinyl -$NO_2$, -SH, -$SO_3H$, -$SO_3H$, -NCS, -SCN, -COOH oder Cyano ist; und

$R_y$, jeweils unabhängig voneinander, -H, -OH, Halogen (Br, Cl, I, oder F), Halogen-$C_{1-4}$ Alkyl (z.B. -$CF_3$, -$CCL_3$, -$CBr_3$, -$Cl_3$), -$NH_2$, -$C_{1-4}$ Alkyl, -$C_{2-4}$ Alkenyl, -$C_{2-4}$ Alkinyl, -$OC_{1-4}$ Alkyl, -$OC_{2-4}$ Alkenyl, -$OC_{2-4}$ Alkinyl -$NO_2$, -SH, -$SO_3H$, -$SO_3H$, -NCS, -SCN, -COOH oder Cyano ist.

30. Monomer gemäß Anspruch 28 oder 29, welches folgende Struktur aufweist.

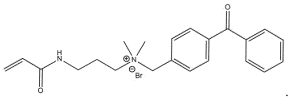

.

31. Verwendung eines Monomers gemäß einem der Ansprüche 28 bis 30 als Photovernetzer.





1/2

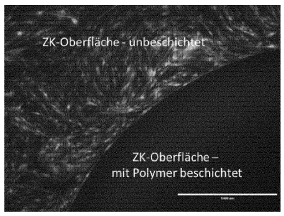


**Abbildung 1**

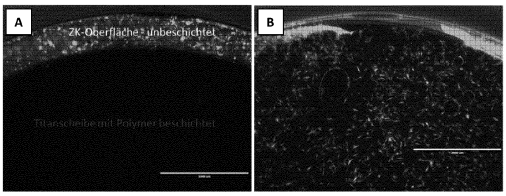


**Abbildung 2**



2/2

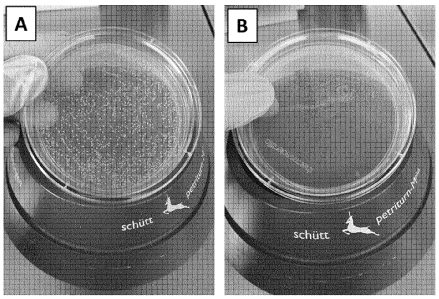


**Abbildung 3**

**INTERNATIONAL SEARCH REPORT**

International application No.
**PCT/EP2023/080274**

**A. CLASSIFICATION OF SUBJECT MATTER**
***C08F 220/58***(2006.01)i; ***C08F 8/12***(2006.01)i; ***C09D 133/24***(2006.01)i

According to International Patent Classification (IPC) or to both national classification and IPC

**B. FIELDS SEARCHED**

Minimum documentation searched (classification system followed by classification symbols)
C08F

Documentation searched other than minimum documentation to the extent that such documents are included in the fields searched

Electronic data base consulted during the international search (name of data base and, where practicable, search terms used)
EPO-Internal, WPI Data

**C. DOCUMENTS CONSIDERED TO BE RELEVANT**

| Category* | Citation of document, with indication, where appropriate, of the relevant passages | Relevant to claim No. |
|---|---|---|
| X | C. Yoshikawa et al. "Photo-crosslinked coatings based on 2-hydroxypropyl acrylamide for the prevention of biofouling - Journal of Materials Chemistry B (RSC Publishing)" *J. Mater. Chem. B*, Vol. 2, 14 June 2019 (2019-06-14), pages 3520-3527, Retrieved from the Internet: https://pubs.rsc.org/en/content/articlelanding/2019/tb/c9tb00044e [retrieved on 2024-01-31] DOI: 10.1039/C9TB00044E XP093126128 scheme 1, figure 4 | 1-4, 10, 14, 16, 19, 23 |
| X | US 2018346634 A1 (RODRIGUEZ-EMMENEGGER CESAR [CZ] ET AL.) 06 December 2018 (2018-12-06) example 2 | 28, 29 |
| X | US 10254567 B2 (NOVARTIS AG [CH]) 09 April 2019 (2019-04-09) page 1, lines 32-33; example 2 | 28, 29, 31 |
| A | WO 2012170706 A2 (SURMODICS INC [US]; SWAN DALE G [US] ET AL.) 13 December 2012 (2012-12-13) example 1; table 3 | 1-31 |

☐ Further documents are listed in the continuation of Box C. ☑ See patent family annex.

* Special categories of cited documents:
"A" document defining the general state of the art which is not considered to be of particular relevance
"E" earlier application or patent but published on or after the international filing date
"L" document which may throw doubts on priority claim(s) or which is cited to establish the publication date of another citation or other special reason (as specified)
"O" document referring to an oral disclosure, use, exhibition or other means
"P" document published prior to the international filing date but later than the priority date claimed
"T" later document published after the international filing date or priority date and not in conflict with the application but cited to understand the principle or theory underlying the invention
"X" document of particular relevance; the claimed invention cannot be considered novel or cannot be considered to involve an inventive step when the document is taken alone
"Y" document of particular relevance; the claimed invention cannot be considered to involve an inventive step when the document is combined with one or more other such documents, such combination being obvious to a person skilled in the art
"&" document member of the same patent family

| Date of the actual completion of the international search | Date of mailing of the international search report |
|---|---|
| **31 January 2024** | **12 February 2024** |
| Name and mailing address of the ISA/EP<br>**European Patent Office**<br>**p.b. 5818, Patentlaan 2, 2280 HV Rijswijk**<br>**Netherlands**<br>Telephone No. **(+31-70)340-2040**<br>Facsimile No. **(+31-70)340-3016** | Authorized officer<br>**Plehiers, Mark**<br>Telephone No. |

Form PCT/ISA/210 (second sheet) (January 2015)

## INTERNATIONAL SEARCH REPORT
**Information on patent family members**

International application No.
**PCT/EP2023/080274**

| Patent document cited in search report | | | Publication date (day/month/year) | Patent family member(s) | | | Publication date (day/month/year) |
|---|---|---|---|---|---|---|---|
| US | 2018346634 | A1 | 06 December 2018 | CA | 2984965 | A1 | 10 November 2016 |
| | | | | CZ | 306039 | B6 | 07 July 2016 |
| | | | | EP | 3292161 | A2 | 14 March 2018 |
| | | | | US | 2018346634 | A1 | 06 December 2018 |
| | | | | WO | 2016177354 | A2 | 10 November 2016 |
| US | 10254567 | B2 | 09 April 2019 | CA | 3010331 | A1 | 31 August 2017 |
| | | | | CA | 3116257 | A1 | 31 August 2017 |
| | | | | EP | 3419966 | A1 | 02 January 2019 |
| | | | | JP | 6546352 | B2 | 17 July 2019 |
| | | | | JP | 2019504169 | A | 14 February 2019 |
| | | | | TW | 201736332 | A | 16 October 2017 |
| | | | | US | 2017242275 | A1 | 24 August 2017 |
| | | | | US | 2019179170 | A1 | 13 June 2019 |
| | | | | WO | 2017145024 | A1 | 31 August 2017 |
| WO | 2012170706 | A2 | 13 December 2012 | US | 2013143056 | A1 | 06 June 2013 |
| | | | | WO | 2012170706 | A2 | 13 December 2012 |

Form PCT/ISA/210 (patent family annex) (January 2015)

## INTERNATIONALER RECHERCHENBERICHT

Internationales Aktenzeichen
**PCT/EP2023/080274**

**A. KLASSIFIZIERUNG DES ANMELDUNGSGEGENSTANDES**
INV. C08F220/58 C08F8/12 C09D133/24
ADD.

Nach der Internationalen Patentklassifikation (IPC) oder nach der nationalen Klassifikation und der IPC

**B. RECHERCHIERTE GEBIETE**

Recherchierter Mindestprüfstoff (Klassifikationssystem und Klassifikationssymbole )
C08F

Recherchierte, aber nicht zum Mindestprüfstoff gehörende Veröffentlichungen, soweit diese unter die recherchierten Gebiete fallen

Während der internationalen Recherche konsultierte elektronische Datenbank (Name der Datenbank und evtl. verwendete Suchbegriffe)

EPO-Internal, WPI Data

**C. ALS WESENTLICH ANGESEHENE UNTERLAGEN**

| Kategorie* | Bezeichnung der Veröffentlichung, soweit erforderlich unter Angabe der in Betracht kommenden Teile | Betr. Anspruch Nr. |
|---|---|---|
| X | C. Yoshikawa et al.: "Photo-crosslinked coatings based on 2-hydroxypropyl acrylamide for the prevention of biofouling - Journal of Materials Chemistry B (RSC Publishing)", J. Mater. Chem. B, Bd. 2 14. Juni 2019 (2019-06-14), Seiten 3520-3527, XP093126128, DOI: 10.1039/C9TB00044E Gefunden im Internet: URL:https://pubs.rsc.org/en/content/articlelanding/2019/tb/c9tb00044e [gefunden am 2024-01-31] Schema 1, Abb. 4 ----- -/-- | 1-4,10, 14,16, 19,23 |

☒ Weitere Veröffentlichungen sind der Fortsetzung von Feld C zu entnehmen ☒ Siehe Anhang Patentfamilie

* Besondere Kategorien von angegebenen Veröffentlichungen :
"A" Veröffentlichung, die den allgemeinen Stand der Technik definiert, aber nicht als besonders bedeutsam anzusehen ist
"E" frühere Anmeldung oder Patent, die bzw. das jedoch erst am oder nach dem internationalen Anmeldedatum veröffentlicht worden ist
"L" Veröffentlichung, die geeignet ist, einen Prioritätsanspruch zweifelhaft erscheinen zu lassen, oder durch die das Veröffentlichungsdatum einer anderen im Recherchenbericht genannten Veröffentlichung belegt werden soll oder die aus einem anderen besonderen Grund angegeben ist (wie ausgeführt)
"O" Veröffentlichung, die sich auf eine mündliche Offenbarung, eine Benutzung, eine Ausstellung oder andere Maßnahmen bezieht
"P" Veröffentlichung, die vor dem internationalen Anmeldedatum, aber nach dem beanspruchten Prioritätsdatum veröffentlicht worden ist

"T" Spätere Veröffentlichung, die nach dem internationalen Anmeldedatum oder dem Prioritätsdatum veröffentlicht worden ist und mit der Anmeldung nicht kollidiert, sondern nur zum Verständnis des der Erfindung zugrundeliegenden Prinzips oder der ihr zugrundeliegenden Theorie angegeben ist
"X" Veröffentlichung von besonderer Bedeutung;: die beanspruchte Erfindung kann allein aufgrund dieser Veröffentlichung nicht als neu oder auf erfinderischer Tätigkeit beruhend betrachtet werden
"Y" Veröffentlichung von besonderer Bedeutung;: die beanspruchte Erfindung kann nicht als auf erfinderischer Tätigkeit beruhend betrachtet werden, wenn die Veröffentlichung mit einer oder mehreren Veröffentlichungen dieser Kategorie in Verbindung gebracht wird und diese Verbindung für einen Fachmann naheliegend ist
"&" Veröffentlichung, die Mitglied desselben Patentfamilie ist

| Datum des Abschlusses der internationalen Recherche | Absendedatum des internationalen Rechercherichts |
|---|---|
| 31. Januar 2024 | 12/02/2024 |

| Name und Postanschrift der Internationalen Rechercherbehörde | Bevollmächtigter Bediensteter |
|---|---|
| Europäisches Patentamt, P.B. 5818 Patentlaan 2 NL - 2280 HV Rijswijk Tel. (+31-70) 340-2040, Fax: (+31-70) 340-3016 | Plehiers, Mark |

1

Formblatt PCT/ISA/210 (Blatt 2) (April 2005)



## INTERNATIONALER RECHERCHENBERICHT

Internationales Aktenzeichen
**PCT/EP2023/080274**

**C. (Fortsetzung) ALS WESENTLICH ANGESEHENE UNTERLAGEN**

| Kategorie* | Bezeichnung der Veröffentlichung, soweit erforderlich unter Angabe der in Betracht kommenden Teile | Betr. Anspruch Nr. |
|---|---|---|
| X | US 2018/346634 A1 (RODRIGUEZ-EMMENEGGER CESAR [CZ] ET AL) 6. Dezember 2018 (2018-12-06) Beispiel 2 ----- | 28,29 |
| X | US 10 254 567 B2 (NOVARTIS AG [CH]) 9. April 2019 (2019-04-09) Seite 1, Zeilen 32-33; Beispiel 2 ----- | 28,29,31 |
| A | WO 2012/170706 A2 (SURMODICS INC [US]; SWAN DALE G [US] ET AL.) 13. Dezember 2012 (2012-12-13) Beispiel 1; Tabelle 3 ----- | 1-31 |

1

Formblatt PCT/ISA/210 (Fortsetzung von Blatt 2) (April 2005)



## INTERNATIONALER RECHERCHENBERICHT

Angaben zu Veröffentlichungen, die zur selben Patentfamilie gehören

Internationales Aktenzeichen
**PCT/EP2023/080274**

| Im Recherchenbericht angeführtes Patentdokument | | Datum der Veröffentlichung | Mitglied(er) der Patentfamilie | | | Datum der Veröffentlichung |
|---|---|---|---|---|---|---|
| US 2018346634 | A1 | 06-12-2018 | CA | 2984965 | A1 | 10-11-2016 |
| | | | CZ | 306039 | B6 | 07-07-2016 |
| | | | EP | 3292161 | A2 | 14-03-2018 |
| | | | US | 2018346634 | A1 | 06-12-2018 |
| | | | WO | 2016177354 | A2 | 10-11-2016 |
| US 10254567 | B2 | 09-04-2019 | CA | 3010331 | A1 | 31-08-2017 |
| | | | CA | 3116257 | A1 | 31-08-2017 |
| | | | EP | 3419966 | A1 | 02-01-2019 |
| | | | JP | 6546352 | B2 | 17-07-2019 |
| | | | JP | 2019504169 | A | 14-02-2019 |
| | | | TW | 201736332 | A | 16-10-2017 |
| | | | US | 2017242275 | A1 | 24-08-2017 |
| | | | US | 2019179170 | A1 | 13-06-2019 |
| | | | WO | 2017145024 | A1 | 31-08-2017 |
| WO 2012170706 | A2 | 13-12-2012 | US | 2013143056 | A1 | 06-06-2013 |
| | | | WO | 2012170706 | A2 | 13-12-2012 |

Formblatt PCT/ISA/210 (Anhang Patentfamilie) (April 2005)